International Conference on Mechanical Engineering 2015
(ICME 2015) 18 – 20 December, 2015, Dhaka, Bangladesh

Paper ID : 005

Design, Fabrication and Experimental Study of a Single Plane Balancing Machine

Rifat Mahmud[1, a)], Abu Jafar Rasel[2, b)] and M. Ashiqur Rahman[1, c)]

[1]*Department of Mechanical Engineering, Bangladesh University of Engineering and Technology, Dhaka 1000, Bangladesh*
[2]*Department of Mechanical and Production Engineering, Ahsanullah University of Science and Technology, Dhaka 1208, Bangladesh*

a)Corresponding author: 08rifat@gmail.com
b)moner71@gmail.com
c)ashiq@me.buet.ac.bd

Abstract. A new technique to measure the unbalanced mass of a single plane rotor with a designed and fabricated balancing machine has been focused in this paper. Here, the unbalanced force of the rotor is transmitted to the vibrating deflector via a support and the amount of deflection is converted to corresponding change in electric voltage by using a proximity sensor. The shaft position is measured with the help of a light sensor. All the data these two transducers gather are presented to the computer simultaneously to plot two graphs showing the binary values of the corresponding sensors versus time. Comparing these graphs, the phase angle of the unbalanced force is determined. Further, the binary values of the proximity sensor is converted to corresponding displacement values. Using them for three known unbalanced masses, displacement versus unbalanced mass graph is plotted. The amount of unknown unbalanced mass for a measured displacement can be found from this graph.

INTRODUCTION

Rotating machineries are commonly used in almost all mechanical systems. Vibration caused by mass imbalance is a common problem in such machineries. Excessive vibration can cause unacceptable noise and substantially reduce the life of bearings. This unbalanced force is changed with change in speed of the rotor and changing the dynamic behavior of the whole system continuously [1].

There are two types of unbalance, single plane (static unbalance) and multi-plane (dynamic unbalance). If the unit being balanced is very short in length in relation to its diameter, single-plane balancing will normally be acceptable. Traditional single plane balancing involves placing the unit on low friction bearings allowing it to rotate and "settle" with the "heaviest" point falling to the bottom. Material is then removed from this point. This process is then repeated until no obvious "heavy" point seems to exist. Martinson [2] as early as 1870 developed a balancing machine where the ‘heavy spot' was marked by hand. At low speeds (sub-critical) the ‘heavy spot’ would coincide with the ‘high spot’ of the whirl according to Jeffcott’s analysis [3]. Rathbone [4] used astrobo-vibroscope to study the vibration of a large rotor. Ribary [4] presented a graphical construction that balanced using only the amplitude taken from an initial run and three trial weight runs. Somervaille [5] considerably simplified the graphical construction of Ribary. Somervaille’s construction is also known as the four circle method of balancing that is still in use today.

The literature review of balancing machine reveals that most of the earlier researchers focused on force transducers to find out the amount of unbalanced mass present in the test rotor. On the contrary, the distinct feature of the machine designed and constructed, in this paper, is that it uses only the displacement transducers to plot a reference curve from which the location and amount of unknown unbalanced mass are determined.

The rest of the paper is structured as follows. Section 2 presents the concept of the proposed machine with schemas and flowcharts. Section 3 shows the design and fabrication of the machine. Section 4 comprises of the experimental results obtained by using the fabricated machine. And lastly section 5 concludes the paper with a brief performance study.

CONCEPT OF THE PROPOSED SINGLE PLANE BALANCING MACHINE

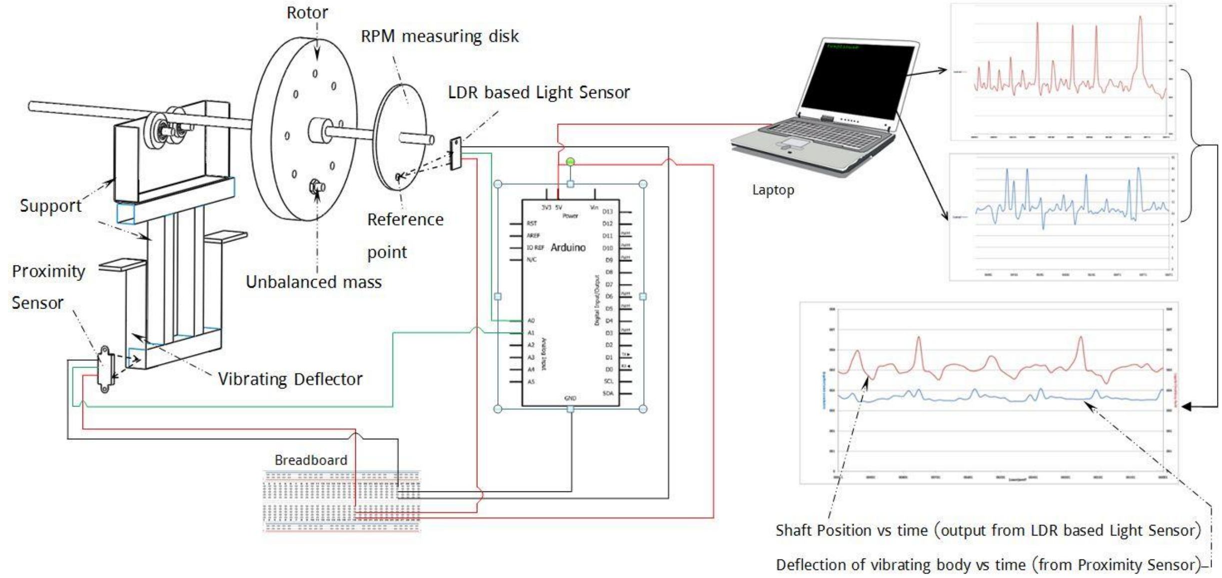

FIGURE 1. Schematic diagram showing the basic working principle with single plane unbalanced rotor.

Before starting the motor, the setup at a glance -

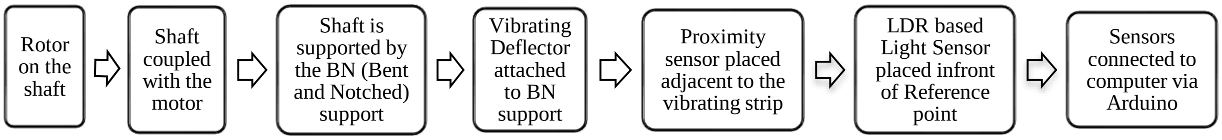

When rotor with unbalanced mass is attached to the machine and the motor is switched on –

Electrically generated data from these two sensors are plotted simultaneously from which the position of the unbalanced mass is found. The measurement of deflections of the deflector strip, for three known masses, gives a reference curve which is used to determine the amount of unbalanced mass. To bring the system in a balanced state, an exactly equal amount of counter mass is added just opposite to the unbalanced mass detected earlier.

After proper balancing -

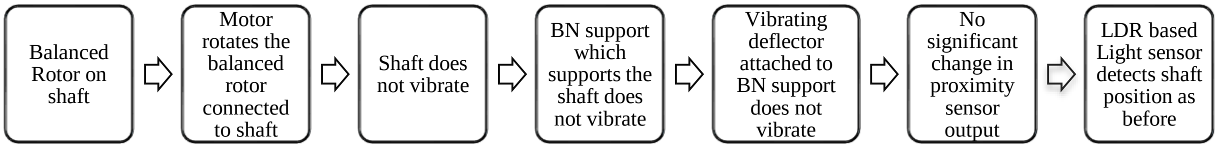

THE DESIGNED AND FABRICATED BALANCING MACHINE

The overall dimension of the setup is 125 cm × 60 cm × 55 cm.

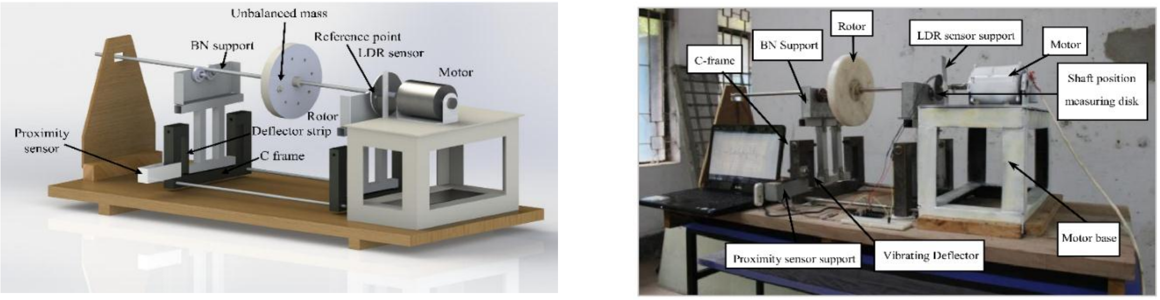

(a) (b)

FIGURE 2. (a) Full design of the setup; (b) Fabricated balancing machine.

Major Electrical Components

The primary transducers (proximity sensor and light sensor) sense and digitalize the analog readings obtained from the vibrating deflector and shaft position measuring disk respectively. The digital data is sent to the computer via an Arduino board where they are monitored and captured to show the final output in graphical form.

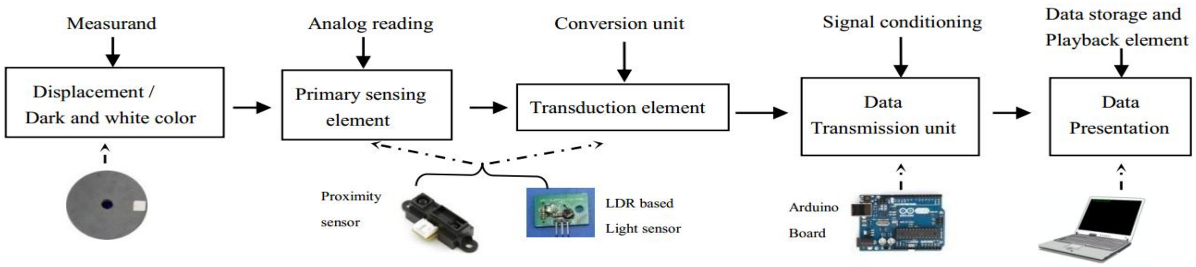

FIGURE 3. The electrical setup at a glance.

Primary Sensing and Transduction Element

Proximity Sensor and Light Sensor (LDR Based)

A proximity sensor emits beam of electromagnetic radiation and looks for changes in the return signal and correspondingly changes the voltage output.

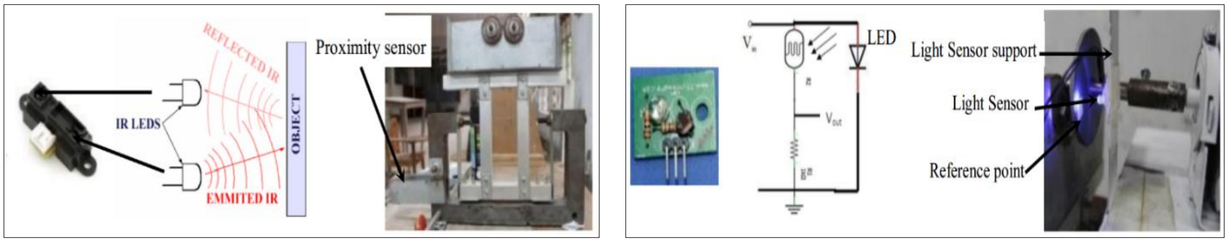

(a) (b)

FIGURE 4. Sensor, its operating principle and location in the machine (a) Proximity sensor; (b) Light sensor.

A LDR based light sensor is a light-controlled variable resistor whose resistance decreases with increasing incident light intensity. When LED light is reflected back by the dark colored shaft position measuring disk, voltage output is low and when by the reflexive material, voltage output is high. Details of the two sensors can be found in [6].

Data Transmission

Arduino and Serial Communication

Arduino is an open-source physical computing platform based on a simple microcontroller board and a development environment for writing program. The program used for Arduino in this setup can be found in [6]. The built-in analog-to-digital converter circuit of an Arduino reads the changing voltage input and converts it to an analogous number between 0 and 1023 (binary voltage value). Arduino sends these data bits to the computer one by one or serially in the form of Highs (1) and Lows (0).

Data Presentation

Monitoring the Sensor Output Voltage and Capturing the Monitored Data

Arduino software has a built-in monitor (serial monitor) which facilitates monitoring the sensor output voltage. It only shows the values but does not capture them. To capture the data, a special software named "Coolterm" has been used. "Coolterm" captures and saves data in a text file which can be exported to any plotter to plot the graphs.

PERFORMANCE EVALUATION

Determination of Vibration Amplitude, Amount of Unbalanced Mass and Phase Angle

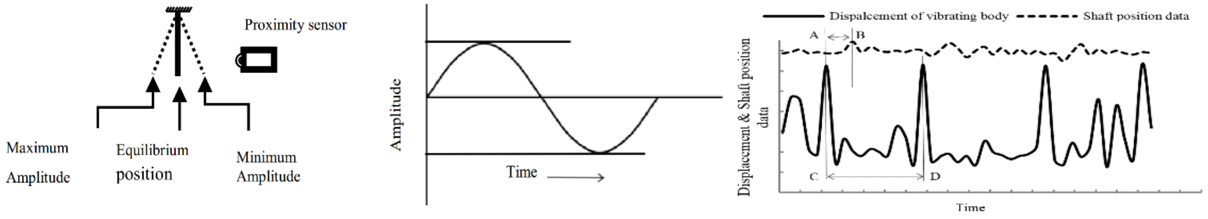

(a) (b)

FIGURE 5. (a) Deflection of the vibrating deflector. (b) Determination of the phase angle, φ

- Due to the addition of unbalanced mass, the deflector strip vibrates and generates a binary value (sensor output voltage value) that is converted to distance by the formula taken from catalog of the proximity sensor,

  $$\text{Distance (mm) from the sensor} = 12343.85 \times (\text{sensor output voltage value})^{-1.15} \qquad (1)$$

  The graph showing distance versus binary voltage value gives the maximum and minimum distance of the vibrating deflector from the proximity sensor's position. These data gives the amplitude of vibration,

  $$\text{Amplitude of vibration or Deflection from equilibrium position} = \frac{\text{Maximum distance - Minimum distance}}{2} \qquad (2)$$

- The deflector strip can be approximated as a linear spring i.e. the deflection versus unbalanced mass is a straight line. Adding 3 known masses in the standard rotor (having no residual unbalance) and measuring the deflection, the reference graph is plotted. For a measured deflection, this graph yields the amount of unbalance for a test rotor.

- The phase angle is determined from the consolidated graph plotted from the output of two sensors.

$$\text{Phase angle, } \phi = 2\pi \times \frac{AB}{CD} \tag{3}$$

Where, *AB* = Distance between the displacement peak value and the adjacent shaft peak value (Fig. 7. (b))
CD = Distance between two consecutive peaks of the displacement of vibrating deflector (Fig. 7. (b))

Experimental study

Different amount of known unbalanced masses were placed at 145^0 CCW (with respect to the white spot on the shaft position measuring disk). Next these positions were measured in terms of phase angles to check and verify the soundness of the entire experimental procedure.

Proximity Sensor Calibration and Rotating Disk without Unbalanced Mass

From the calibration graph of Fig. 6 (a), it is seen that voltage output from the proximity sensor fluctuates harshly if the object is less than 150 mm from the sensor. Hence the proximity sensor is placed 204 mm far from the vibrating deflector strip.

From Fig. 6 (b), it is observed that there is no significant peak in the displacement curve (the tiny peaks are for the unavoidable electric noise in the sensors) which indicates that the deflector is steady when the rotor runs without unbalanced mass. This ensures its use as a standard rotor for determining the reference graph of deflection versus unbalanced mass.

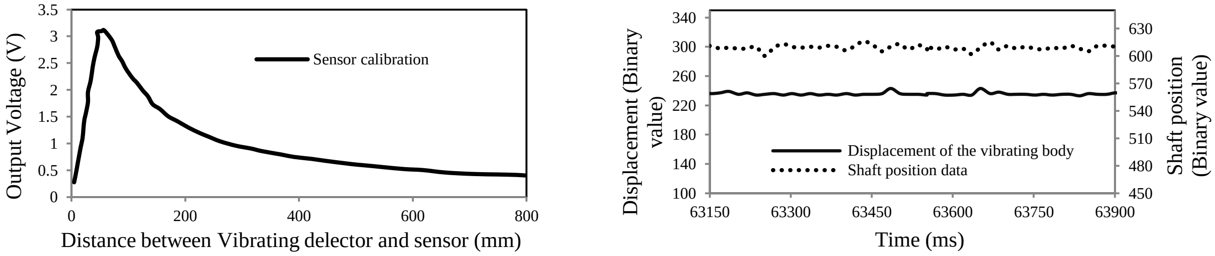

(a) (b)

FIGURE 6. (a) Proximity senor voltage output vs. displacement (b) The output of two sensors when the disk rotates without unbalanced mass.

Rotating Disk with Unbalanced Mass of 20 gm

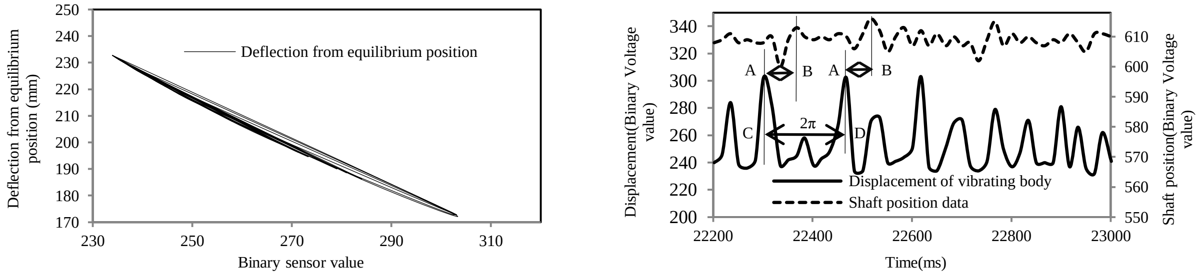

(a) (b)

FIGURE 7. With unbalanced mass 20 gm. (a) Binary value converted to displacement (mm); (b) Graph plotted from the output of two sensors.

From Fig. 7 (a), maximum distance = 235 mm and minimum distance = 173 mm. Using equation (2),

$$\text{Amplitude of vibration or Deflection from equilibrium position} = \frac{235\text{-}173}{2}\,\text{mm} = 31\,\text{mm}$$

From Fig. 7 (b), $\frac{AB}{CD}=\frac{2.65}{6.46}=0.41$; Using equation (3), Measured phase angle, φ = $360^0\times 0.41=147.6^0$ (CCW)

Rotating Disk with Unbalanced Mass of 60 gm

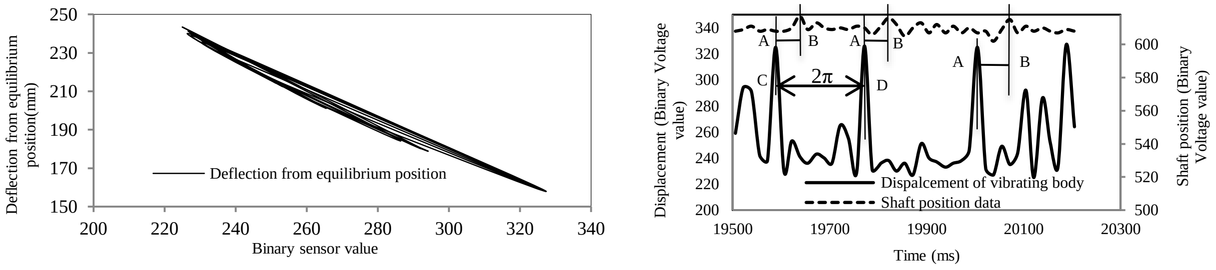

(a) (b)

FIGURE 8. With unbalanced mass 60 gm. (a) Binary value converted to displacement; (b) Graph plotted from the output of two sensors.

From Fig. 8 (a), maximum distance = 242 mm and minimum distance = 158 mm. Using equation (2),

$$\text{Amplitude of vibration or Deflection from equilibrium position} = \frac{242\text{-}158}{2}\,\text{mm} = 42\,\text{mm}$$

From Fig. 8 (b), $\frac{AB}{CD}=\frac{2.65}{6.90}=0.39$; Using equation (3), Measured phase angle, φ = $360^0\times 0.39=140.4^0$ (CCW)

Rotating Disk with Unbalanced Mass of 80 gm

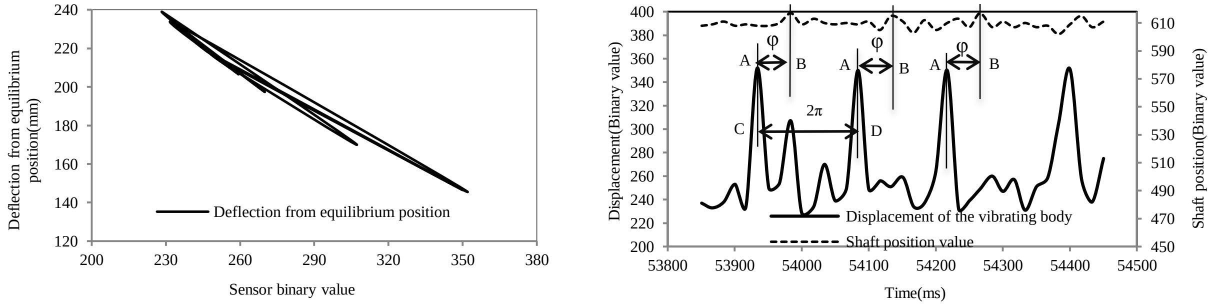

(a) (b)

FIGURE 9. With unbalanced mass 80 gm. (a) Binary value converted to displacement; (b) Graph plotted from the output of two sensors.

From Fig. 9 (a), maximum distance = 238 mm and minimum distance = 142 mm. Using equation (2),

$$\text{Amplitude of vibration or Deflection from equilibrium position} = \frac{238\text{-}142}{2}\,\text{mm} = 48\,\text{mm}$$

From Fig. 9 (b), $\frac{AB}{CD}=\frac{2.65}{6.60}=0.40$; Using equation (3), Measured phase angle, φ = $360^0\times 0.40 = 144.4^0$ (CCW)

The Reference Curve to Determine the Amount of Unbalanced Mass

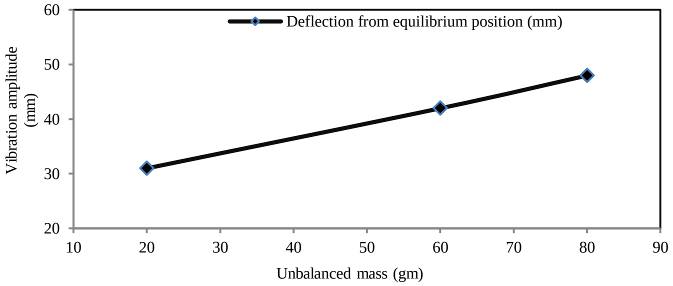

FIGURE 10. Relation between unbalanced mass and vibration amplitude.

Figure 10 shows the reference curve for determining the amount of unbalanced mass as explained earlier. The reference curve is plotted using the experimental data. As expected, it is a straight line.

Result and Discussion

Table 1. Summary of the results

Unbalanced mass (gm.)	Measured Phase angle in degree (CCW)	Actual Phase angle in degree (CCW)	% Error	Deflection (mm)
20	147.6	145	1.79	31
60	140.4	145	3.17	42
80	144.4	145	0.413	48

CONCLUSION

This paper presents a new approach for measuring unbalanced mass of a thin rotor with a designed and fabricated single plane balancing machine. If a rotor is unbalanced, there will be a peak in the vibration amplitude and this peak will dominate its frequency spectrum. This peak value, along with the reference peak value of shaft position is combined here to find the location and amount of unbalanced mass by using two sensors. The low value of percentage error shown in table 1 implies that the results are pretty accurate.

REFERENCES

1. H. K. Yadav, S. H. Upadhyay, and S.P. Harsha, Procedia Eng. **64**, 593–602 (2013).
2. C. Jackson, *The Practical Vibration Primer* (Gulf Publication, Houston, 1979). p. 153.
3. A. G. Parkinson, M. S. Darlow, A.J. Smalley, and R. H. Badgley, J. Sound Vibration **68**, 489–506 (1980).
4. S. Zhou and J. Shi, Shock Vib. Dig. **33**, 361-371 (2001).
5. Y. G. Kang, J. Sheen and S. N. Wang, J. Sound Vibration **199**, 349–368 (1997).
6. R. Mahmud, and A. J. Rasel, "Design, fabrication and performance evaluation of a dynamic balancing machine," B.Sc. thesis, Bangladesh University of Engineering and Technology, 2014.

International Conference on Mechanical Engineering 2015
(ICME 2015) 18 – 20 December, 2015, Dhaka, Bangladesh

Paper ID : 014

Study on Energy Recuperation Boom System in Electro-Hydraulic Excavator Using Secondary System

Debdatta Das[1, a)] and S.M.Rifat Iftekher[2, b)]

[1]*Graduate Student of Mechanical Engineering, University of Ulsan, Ulsan, 680-749, Republic of Korea*
[2]*Department of Mechanical Engineering, Chittagong University of Engineering and Technology, Chittagong 4349, Bangladesh*

[a)]Corresponding author: debdattacuet@gmail.com
[b)]rifatiftu2@gmail.com

Abstract. In recent research, researchers are predominantly focused on energy saving on hydraulic systems. The demand for energy saving and green emission of construction machinery, especially hydraulic excavators, has been enormously increased. As a result, electro-hydraulic system, which are flourished and successfully fruitful to automobile industry, is recently introduced to electro-hydraulic excavators. The efficiency of a hydraulic excavators is very low even though they have large power-to-size ratios. The electro-hydraulic configuration reduces hydraulic interferences among the actuators and losses which is prevalent in conventional hydraulic excavators. This paper predominantly investigates the energy saving for the electro-hydraulic excavator. By analyzing the excess energy of hydraulic cylinders in the conventional hydraulic excavator, a new boom potential energy recuperation system is proposed. In this system, a secondary unit is introduce. Meanwhile, the simulation models of the proposed energy recuperation system are constructed by AMESim software. In cementation, a controlling strategy, which is used to control the electro-hydraulic excavator to emulate mandates conferred by a driver and to optimize the energy saving procedure of the generator and battery, is also introduced in this paper. A series of simulation has been performed for clarifying the effectiveness of the energy saving electro-hydraulic excavator in boom cylinder and all the parameters of this circuit are taken from the real system. The measures to improve the energy recuperation efficiency of the proposed system are presented.

INTRODUCTION

Hydraulic systems in a wide diversity of forms are indispensable components of many modern work machines. Several technologies are accumulated to minimize energy consumption and emission with the raising demand of energy saving and environmental protection in the world range. Meanwhile, the cost of fuel has been grown swiftly and also, the pollution and global warming has become a significant problem day by day. Hence, the reductions of energy consumption and pollution become essential and indispensable demands [1, 2]. Hydraulic excavators are widely applied in construction. A typical hydraulic excavator is shown in Fig. 1. However, one remarkable drawback in this applications is the low energy efficiency, due to the complex working condition and frequent load changing, only 20% of the engine output power is utilized in a conventional type excavator as well as the energy conversions in power systems and hydraulic systems. In individual engine driven power systems, the fuel economy is usually decreased due to the variation of working points [3-6]. And electro-hydraulic power systems are the efficient solution, which has been successfully applied to vehicles, is also paid much attention in the field of construction machinery, especially electro-hydraulic excavators [1, 2, 7 and 11].

Energy recuperation is an effective approach to reduce the energy losses in hydraulic systems. In hydraulic cylinder led circuits, energy can be recuperated through cross connection hydraulic [8], accumulator [9], and electrical storage [10]. Electrical regeneration with accumulator approach is suitable for hybrid or electrical power driven hydraulic machines which provide batteries or super capacitors. Good control property is another weighty aspect that the development of hydraulic systems pursues. The normal control strategies with power managements cannot be simply applied to hydraulic excavators because their working conditions vary in a wide range and fluctuate tempestuously. As a result, electro-hydraulic systems with suitable control methods and energy managements have been paddled out for excavators in recent years.

FIGURE 1. A typical hydraulic excavator.

For overcoming the drawback of the conventional designs of excavators and to satisfy the current demands, this paper proposes one operative accomplishment for excavator design using electro-hydraulic actuators. In this system, it is recognized that the potential energy derived from a gravity-assisted or retraction of a hydraulic actuator may be stored and later returned to the system as necessity. The proposed system is simulated by AMESim software. The energy recovery efficiency of the proposed system is clearly verified through simulation results in comparison with the conventional energy recuperate system. Depending on the working circumstance and power management, a control strategy is designed for the excavator to get higher working efficiency and saving energy. A series of simulation has been analysis the effectiveness of the proposed system.

STRUCTURE OF ELECTRO-HYDRAULIC EXCAVATORS

The operation body of a hydraulic excavator casually has three cylinders: boom cylinder, arm cylinder, and bucket cylinder. The boom control system is deliberated in this study as one example to verify the suggested electro-hydraulic excavator. Fig. 2(a) schematic diagram the conventional control circuit with hydraulic components for the boom cylinder. It mainly consists of oil supply, actuators, control valves, regeneration unit and electric energy storage elements. The supplied flow line will connect with the large chamber or the small chamber of the boom cylinder, and the piston will be extended or retracted, respectively. The vital problem of this system is a huge power needed to operate the operation. Because in power extraction mode boom is up, so in this time piston and weight are working against to the gravitational force and it requires a huge energy to overcome. The extra cost will weaken the energy-saving advantage of the system.

To reduce all of the difficulties, increasing saving energy and lowering the initial consumption energy have to think in different way. The core idea of the proposed system is to regenerate the energy with high efficiency and reduce all of the difficulties. The proposed system schematic diagram is shown in Fig. 2(b).

It is the combination of electro-hydraulic actuators. The boom cylinder is controlled by the hydraulic circuit combined with an electric motor, a hydraulic pump, solenoid valve and on off valves to follow the given working command and energy storage components. There are two modes in the operation of the system, extraction mode and retraction mode which are the same as the operation of the boom arm or the bucket actuator of the excavator. In the extraction mode, the piston rod will be pushed to drive the boom to a desired position by supplying hydraulic fluid to the large chamber of the cylinder. The energy required to lift the testing load against the gravity force is provided by the pressurized fluid from the hydraulic pump. The higher lifting load position, the more potential energy is created. On the contrary, the gravity force acting on the cylinder rod will cause it to lower in the retraction mode, consequently release the potential energy accumulated in the extraction mode. In order to save the power obtained from the potential energy, an electrical generator with an electrical battery is included into the hydraulic control circuit. The generator is operated by using a hydraulic motor which is set in the hydraulic line connecting between the large chamber of the cylinder. To operate the proposed electro-hydraulic excavator with high efficiency and high energy saving capability, a control strategy is design as displayed in Fig. 3.

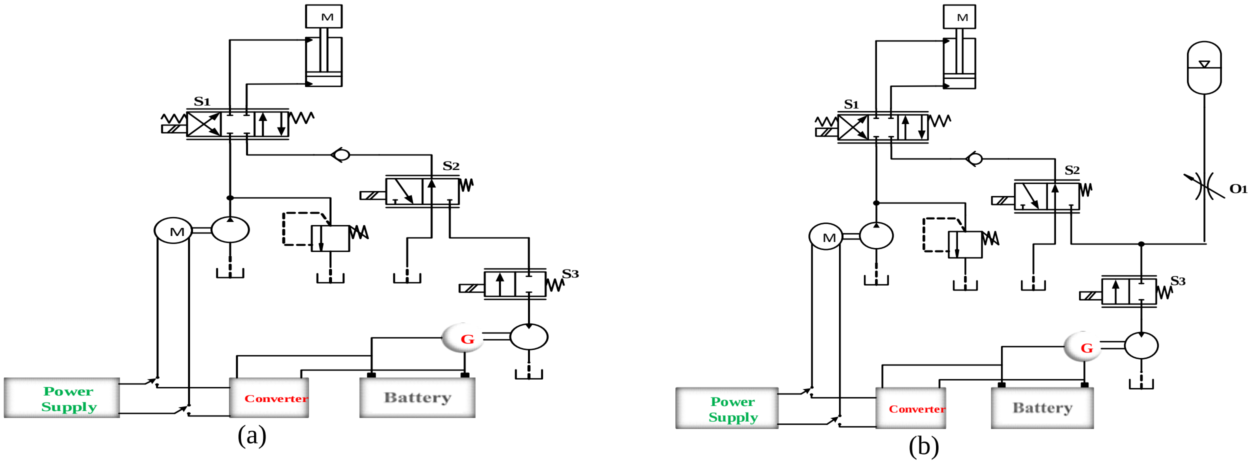

(a) (b)

FIGURE 2. (a) Schematic of conventional system; (b) Schematic of proposed system.

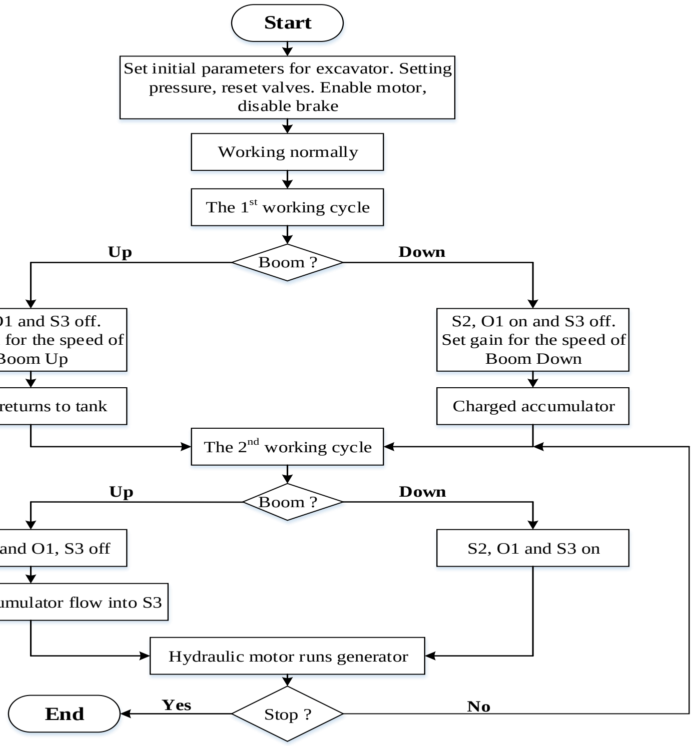

FIGURE 3. Working flow chart of the proposed system.

SIMULATION RESULTS AND ANALYSIS

To verify the performance of the conventional and proposed system, a series of simulation has been carried out by using AMESim software and the AMESim model of conventional and proposed system are shown in Fig. 4(a) and (b) respectively. Therefore, the internal dynamics of the different components can be neglected in the current study, as they are routinely built in AMESim. The aim of this research is to validate the impact of energy recuperation and improving efficiency. Based on the working circumstance of the excavator, the speed and torque of the generator with be run by controlling the electric motor and the accumulator to obtain the maximum efficiency and the highest saving energy. All the parameters of this system are taken from the real excavator which are depicted in Table 1.

Table 1. Setting parameters for the AMESim model.

Components	Value	Unit
Hydraulic Cylinder	63×42×660 (Piston dia. × Rod dia. × Length of Stroke)	mm
Electric Motor	700	rpm
Hydraulic Pump	34.3	cc/rev
	2500	rpm
Relief Valve Pressure	350	bar
Hydraulic Motor	34.3	cc/rev
	900	rpm
Weight	500	kg
Accumulator Gas Precharge Pressure	100	bar
Accumulator Working Pressure	100~300	bar
Accumulator Volume	08	litter

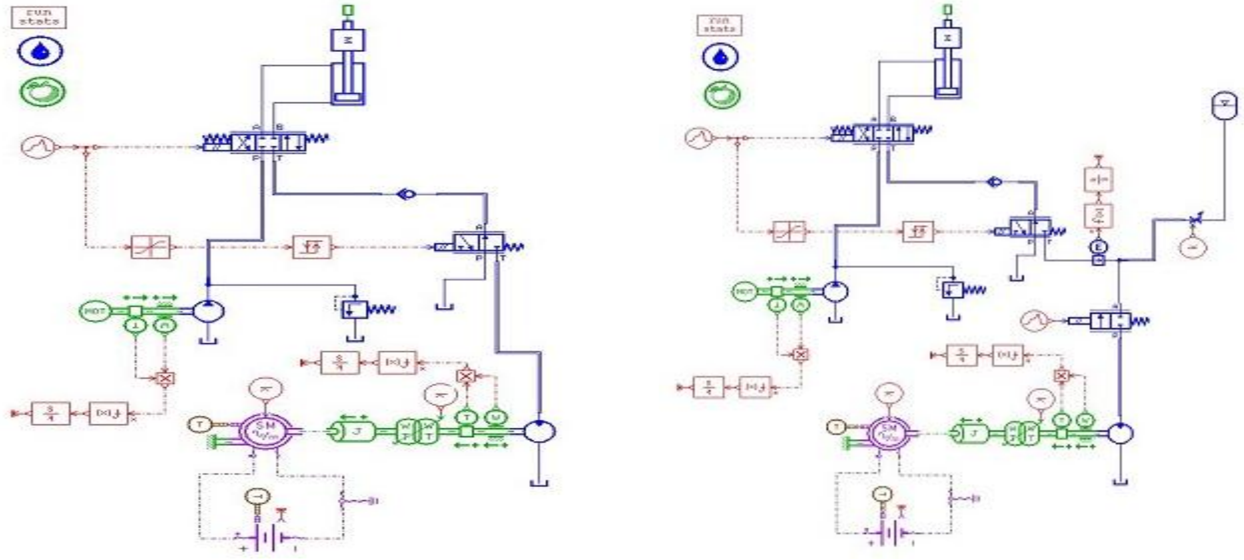

(a) (b)

FIGURE 4. (a) AMESim model of conventional system; (b) AMESim model for proposed system.

This paper deals with both conventional and proposed system. Here, the cylinder was tested with 660mm of full extraction and then full retraction in case of 500kg working load. Fig. 5(a) and (b) shows the signal input and rod displacement for the both system respectively. Fig. 5(b) depicts that the working performances of the two system are quite analogous. For boom up, rod displacement takes more time to reach its desired position because it has to work against gravitational force and load. Rod displacement of both system looks almost analogous and follows the signal input. Meanwhile, the simulation results are different in a consumption of energy and it shows in Fig. 6 (a) and (b) shows the input or consumption and generated energy for the conventional and proposed system. The input energy of the conventional system is much higher than the proposed system for conducting. Consequently, generated energy of the proposed system is lower than the conventional on because in the first cycle of the proposed system, accumulator is charged and then started to generate energy in the generator from the second cycle. By using the proposed circuit, the input or consumption power is 104.75 KJ while the generated power is 43.52 KJ and conventional circuit, the input or consumption power is 211.59 KJ while the generated power 59.62 KJ. However, when compared with the energy consumption in case of using the conventional circuit, the saved energy by using the proposed circuit is obtained by using Eq. (1). So analyzing this results, the proposed system has the ability to increase the efficiency almost 40.30% higher than conventional one although the generated energy is lower.

$$
\begin{aligned}
Saved\ Energy &= \frac{\left(\sum E_{consumption}\right)_{Proposed\ System}}{\left(\sum E_{consumption}\right)_{Conv.\ System}} \\
&= \frac{\sum \left(E_{consumption} - E_{generated}\right)_{Proposed\ System}}{\sum \left(E_{consumption} - E_{generated}\right)_{Conv.\ System}} \\
&= \frac{\left(104.75 - 43.5\right)_{Proposed\ System}}{\left(211.59 - 59.62\right)_{Conv.\ System}} \\
&= 40.30\% \qquad (1)
\end{aligned}
$$

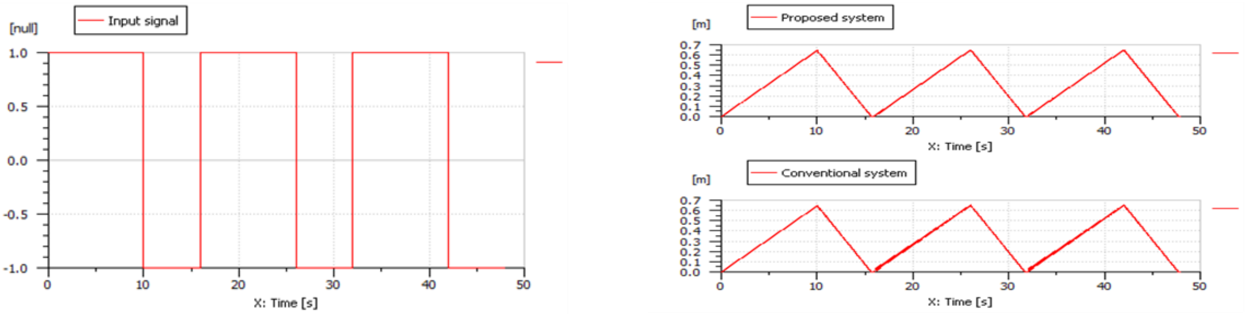

(a) (b)

FIGURE 5. (a) Input signal; (b) Rod displacement.

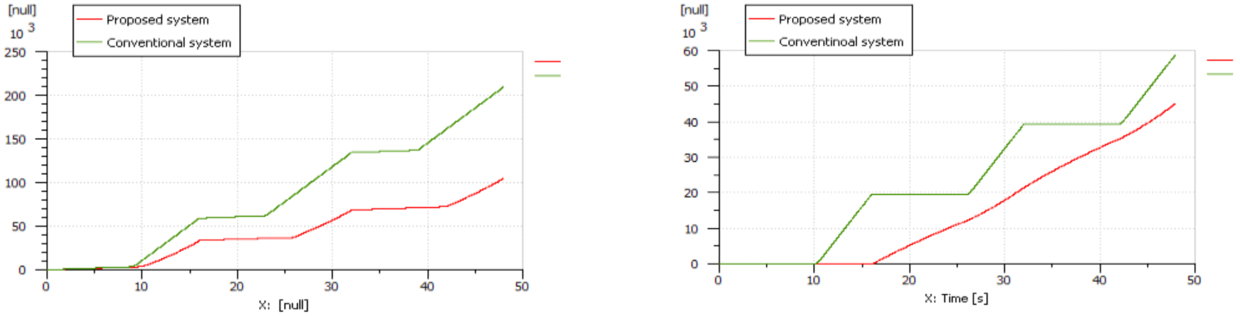

(a) (b)

FIGURE 6. (a) Input energy for conventional and proposed system; (b) Generated energy for conventional and proposed system.

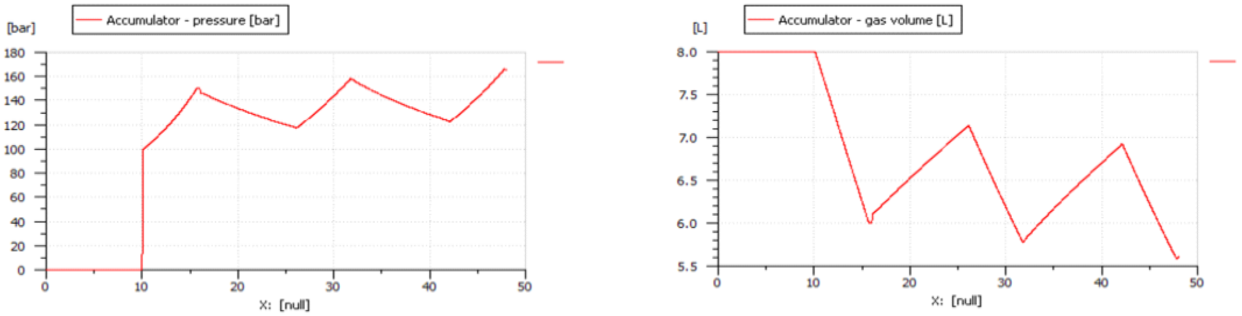

(a) (b)

FIGURE 7. (a) Gas pressure of accumulator; (b) Gas volume of accumulator.

Figure 7 depicts the pressure and gas volume of the accumulator for the proposed system. The initial gas pressure is 100 bar and gas volume 8 litter. When boom down, the gas pressure is increasing and boom up decreasing. But accumulator gas pressure increasing and decreasing rate are not identical because in boom up process, the chamber and accumulator pressure both assist to drive the hydraulic motor. For that reason accumulator pressure discharge is lower than charge.

According to the mechanical characteristics of the generator, high efficiency depends on high speed and continuous rotation. If generator swirls continually, SOC (State of Charge) can ascend smoothly. This proposed system has that ability and depicts in Fig. 8. But in the conventional system, SOC is not ascending smoothly. During a whole working period, the value of SOC in conventional system is 60.4% and in the proposed system is 60.8% with smooth ascending. From the results, it is obvious that the proposed electro-hydraulic excavator with the suggested control strategy can operate with higher efficiency and has an energy saving capability compere with conventional boom system. The proposed system working principle and control strategy are very simple.

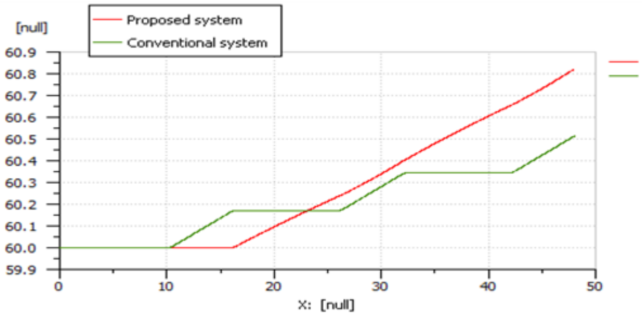

FIGURE 8. State of charge of battery.

CONCLUSIONS

The boom control performance of the electro-hydraulic with a potential energy saving system is studied in this paper. Energy recuperation is benignant to the working efficiency of an electro-hydraulic excavator. The characteristics of the control system are analyzed by simulation. The effectiveness of the electro-hydraulic excavator is verified by means of simulation. The results prove that the proposed electro-hydraulic excavator with its control strategy can increase the working efficiency for the excavators.

As a result, when applying the proposed one into the real excavator, such as 5 tons excavator, the working effectiveness and the energy saving capability will be significantly increased when compared with the proposed system. So this proposed system can become an optimal selection for the heavy industry in a near future with energy saving.

REFERENCES

1. H. Zhang, Y. Zhu, G. Tian, Q. Chen and Y. Chen, SAE Transactions: J. of Engines **113**(**3**), 408-417 (2004).
2. N. J. Schouten, M.A. Salman and N. A. Kheir, IEEE Transactions on Control Systems Technology **10**(**3**), 460-468 (2002).
3. Q. Xiao, Q.F. Wang and Y.T. Zhang, Automation in Construction **17**(**4**), 361–367 (2008).
4. Q.F. Wang, Y.T. Zhang, Q. Xiao, Chinese J. of Mechanical Engineering **41**(12**)** 135–140, (2005).
5. D.Y. Wang, C. Guan, S.X. Pan, M.J. Zhang, X. Lin, Automation in Construction **18**(**3**), 249–257 (2009).
6. J. Choi, H. Kim, S. Yu and K. Yi, J. of Mechanical Science and Technology **25**(**6**), 1557–1563 (2011).
7. J. I. Yoon, K. K. Ahn and D. Q. Truong, “A study on an energy saving electro-hydraulic excavator,” in Proceedings ICCAS-SICE International Joint Conference, 2009, pp. 3825-3830.
8. B. Yao, “Integrated mechatronic design of precision and energy saving electrohydraulic systems,” in proceedings 7th International Conference on Fluid Power Transmission and Control, 2009, pp. 360–372.
9. J. Nyman, J. Bärnström and K. Rydberg, “Use of accumulators to reduce the need of electric power in hydraulic lifting systems,” in proceedings 8th Scandinavian International Conference on Fluid Power-2003, pp. 311–326.
10. T. Minav, L. Laurila and J. Pyrhönen, Automation in Construction **30**, 144–150 (2013).
11. T. L. Lin, Q. F. Wang, B. Z. Hu and W. Gong, Automation in Construction **19**(8), 1016-1026 (2010).

Selection of Software for Mechanical Engineering Undergraduates

C.T.Cheah[1)], C.S.Yin[1)], T.Halim[1)], J.Naser[1)], and A.S Blicblau[1, a)]

[1]*Swinburne University of Technology, Faculty of Science Engineering and Technology, PO Box 218 Hawthorn, Victoria, Australia, 3122.*

[a)] Corresponding author: ablicblau@swin.edu.au

Abstract. A major problem with the undergraduate mechanical course is the limited exposure of students to software packages coupled with the long learning curve on the existing software packages. This work proposes the use of appropriate software packages for the entire mechanical engineering curriculum to ensure students get sufficient exposure real life design problems. A variety of software packages are highlighted as being suitable for undergraduate work in mechanical engineering, e.g. simultaneous non-linear equations; uncertainty analysis; 3-D modeling software with the FEA; analysis tools for the solution of problems in thermodynamics, fluid mechanics, mechanical system design, and solid mechanics.

INTRODUCTION

With the growing complexity of engineering problems and advancement of computer hardware, computational skills have become a necessary tool for engineers. Despite the importance of computational skills, not all the subjects in a mechanical engineering curriculum in SUT are integrated with computational skills. In some subjects where computational skills are being integrated, the software packages themselves have a long learning curve and not used consistently throughout the curriculum. The current software packages that are being used: IDEAS, ANSYS, Mathematica, AVL Swift, and AutoCAD are some of the best in their respective categories [1-5]. Even though these software packages are robust, they are not user-friendly, time-consuming and more suitable for research level rather than undergraduate studies. The problem to be addressed is the inconsistent usage of the software packages throughout the ME curriculum, and to highlight those that are suitable for engineering applications.

OVERVIEW OF THE SOFTWARE PACKAGES USED AND IMPLEMENTATION

The automotive, aviation and large manufacturing industries have long moved to three-dimensional (3-D) modeling. This movement has been followed by the medium sized manufacturing company, albeit at a slow speed due to the exorbitant cost of converting their legacy two-dimensional (2-D) to 3-D models [6, 7]. The transition to 3-D modeling gives the companies a competitive edge as it allows the customers to visualize the part/system and simulation analysis to be done by the engineers without having to build the actual prototype. Recent CAD software packages are designed to allow collaboration among engineering teams, which allows engineers at a different location to work on the same model [8-10]. These advantages allow for a reduction in production cost and time-to-market.

Computer Simulation Analysis

There are two types of computer simulation analysis that mechanical engineers are interested in, namely finite element analysis (FEA) for structural analysis and computational fluid dynamics (CFD) for fluid flow analysis. CFD was introduced in the 1960s, but only available to mainstream engineering users twenty years later, in the 1980s and FEA became available just slightly before CFD. Recent CFD software packages can handle more complex geometries and boundary conditions due to the change in the algorithm used, from finite difference method to finite element method [11]. The analysis approach for FEA and CFD work [12-14] very much in an identical way, the main difference is that the geometry of interest in CFD analysis is often the inverse of FEA analysis. For example, a water pipe, FEA analysis would focus on the pipe constructed from plate elements; CFD analysis would focus on the interior of the pipe constructed using solid elements.

The advantage of computer simulation analysis is the elimination of prototype building until the design is finalized; however, complex FEA and CFD analysis require a substantial computational power (supercomputers). For a computer simulation analysis to be efficiently executed, a single software package, which can perform structural, thermal, vibration, motion, and fluid flow is required as it eliminates the need to create multiple models and repeat numerous calculations.

Mathematical Packages

Engineering industry is moving towards computer simulation analysis to save time and cost of a product. Due to this the number of software packages was steadily increasing over the years, and it is necessary for the users or organization to choose the right software packages to be able to implement computer simulation analysis efficiently. This work looks at computer packages implemented in the undergraduate curriculum for appropriate for the different area in mechanical engineering.

The mathematical software package can be classified into two groups, namely: numerical packages (e.g. MATLAB, MathCAD, and TK Solver) and symbolic packages (e.g. Mathematica, Maple, and Derive). Numerical packages evaluate an expression, for example, the value of the derivative of x^2, by requiring a value of x to be entered and returning a numeric answer. Symbolic packages can return x as an answer to the problem. However, advanced mathematical software packages such as MATLAB [15] and Mathematica [16] both numerical and symbolic calculation, albeit performing better in their respective categories. Mathematica is written in custom, object-oriented version of C, this design allows it to be embedded in other software as a mathematics engine. Its capabilities can be categorized into four groups: numerical computation, symbolic computation, graphics, and programming.

Thermodynamics has been taught for many years [16-18] where students are still referring to property tables and solving problems with hand calculators despite the increase in computational ability. Due to this approach, the complexity of homework problems is limited and practically eliminates any design problems as they often introduce non-linearities, e.g. log-mean temperature differences or fourth order temperature dependence. EES [19] is a non-linear algebraic equation solver with an extensive library of built-in functions for thermodynamics and transport properties of fluids e.g. steam tables, refrigerant properties, psychometric, and combustion gas data. It uses the equation of state approach rather than internal tabular data to determine the properties of real fluids.

IMPLEMENTATION OF SOFTWARE

Nonlinear simultaneous equation solver

EES was developed to help students in doing design problems for thermodynamics and fluid mechanics subjects. Engineers are always concerned about minimizing or maximizing a set of parameters as part of their design, and this comes with uncertainty as nature cannot be controlled and off-the-shelf part comes with tolerances. The Min/Max and Uncertainty Analysis function would aid students in their design and give them a better understanding of the aspects of the design.

Case Study 1. Drag force and speed determination.

An airplane has a mass of 50000 kg, wing area of 300 m2, the thickness of airfoil, D = 30 mm, with a maximum lift coefficient of 3.2, cruising at an altitude of 12500 m. You are required to determine (a) the takeoff speed at sea level, assuming it is 20 % over the stall speed, (b) find the minimum total drag coefficient on the wing at minimum flight speed for the length of chord varies from 0.6m to 3m, and then calculate the total drag force.

Solution Case Study 1.

The calculations from EES are output into a straightforward format as shown in Figure 1a. Moreover, the total drag force as calculated is shown in graphical output a shown in Figure 1b.

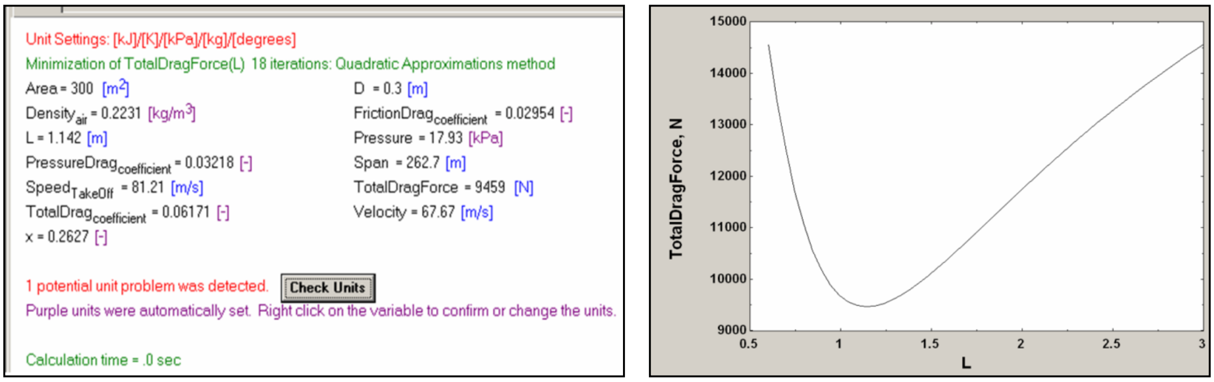

Unit Settings: [kJ]/[K]/[kPa]/[kg]/[degrees]
Minimization of TotalDragForce(L) 18 iterations: Quadratic Approximations method

Area = 300 [m^2]
Density$_{air}$ = 0.2231 [kg/m^3]
L = 1.142 [m]
PressureDrag$_{coefficient}$ = 0.03218 [-]
Speed$_{TakeOff}$ = 81.21 [m/s]
TotalDrag$_{coefficient}$ = 0.06171 [-]
x = 0.2627 [-]
D = 0.3 [m]
FrictionDrag$_{coefficient}$ = 0.02954 [-]
Pressure = 17.93 [kPa]
Span = 262.7 [m]
TotalDragForce = 9459 [N]
Velocity = 67.67 [m/s]

1 potential unit problem was detected.
Purple units were automatically set. Right click on the variable to confirm or change the units.

Calculation time = .0 sec

(a) (b)

FIGURE 1. (a) Sample EES calculations and (b) Sample EES graphical output

Structural analysis problems

Finite element analysis (FEA) is a common and useful when dealing with structural analysis and engineering problems, but its accuracy has always been a concern for engineers. Solidworks software is known as one of the relatively mature parametric feature-base ones, which integrates CAD/CAM/CAE. The SolidWorks/CosmosWorks (SWCW) structural analysis programs were used for FEA analysis that is integrated with SolidWorks [20, 21].

Case Study 2. Distributed pressure load on circular plate analysis

A circular steel plate (E=208GPa, v=0.3) with 228.6 mm diameter and 4.79 mm thickness is clamped at the edge. A pressure of 100 kPa is applied. You are required to determine the Von Mises stress and deflection of the plate using SWCW and compare it with theoretical results.

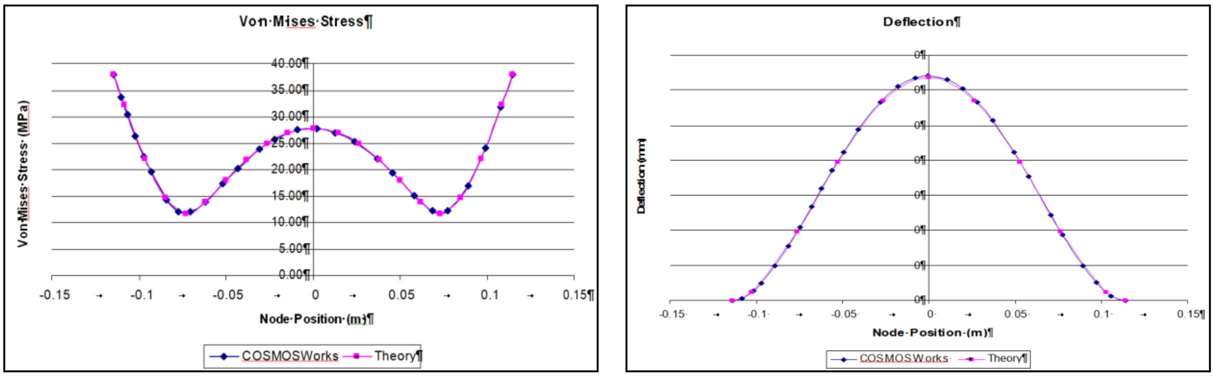

(a) (b)

FIGURE 2. (a) Comparison of von Mises Stress between SWCW FEA and theoretical approach and (b) comparison of deflection between SWCW FEA and theoretical approach.

Solution Case Study 2.

The Von Mises stress comparison between SWCW and theoretical formula are given in Figure 2a whereas the deflection results in the comparison between SWCW and theoretical formula are shown in Figure 2b.

Design for Fluid flow problems

CFD is a vital part of CAE, which enables engineers to simulate, visualize and analyze fluid flow and heat transfer of a system.

Case Study 3. The flow of water.

A case study of a ball valve design modified from SolidWorks/CosmosFloWorks (SWCFW)is shown to highlight the capabilities of the software package in enabling ME students to simulate, visualize and analyze fluid flow. This case study covers the flow of water across a ball valve assembly before and after some design changes. It is helpful for engineers who want to analyze design variations of their product.

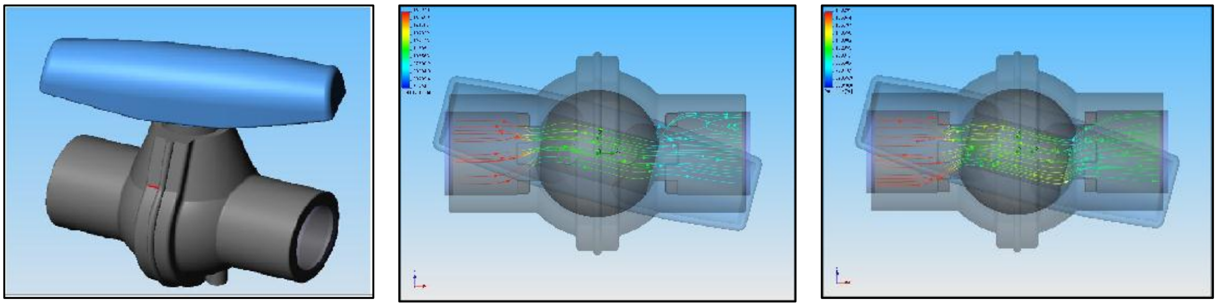

(a) (b) (c)

FIGURE 3. (a) ball valve assembly (b) trajectory flow (c) trajectory flow with modifications using SolidWorks/CosmosFloWorks

Solution Case Study 3.

Shown in Figure 3a is the ball valve assembly and in Figure 3b the trajectory flow of water on standard design with Figure 3c showing trajectory flow of water after 1.5 mm fillet is added onto the passage. If the same problem were to be presented in classroom tutorial, students would be able to calculate the pressure drop across the passage but they would not be able to visualize the turbulence of the first design

Motion in an engine

Case Study 4. Valve Cam design

Motion simulation is a very important tool in mechanical engineering designs as they often involved moving components or mechanism. With SolidWorks/CosmosWorks, students would be able to simulate the motion and animate the results without having to learn a new interface. SolidWorks/CosmosWorks was used to analyze an engine overhead cam to ensure that the rocker does not lose contact with the cam using minimal force to minimize wear and tear.

Solution Case Study 4.

The modeling of the valve cam design with the engine overhead cam assembly is given in Figure 4a, and the engine overhead cam with a spring is given in Figure 4(b). The results of the force magnitude analysis are shown in Figure 4(c). An iterative design could be carried out to determine the lowest spring stiffness while maintaining contact between the cam and rocker to prolong system life.

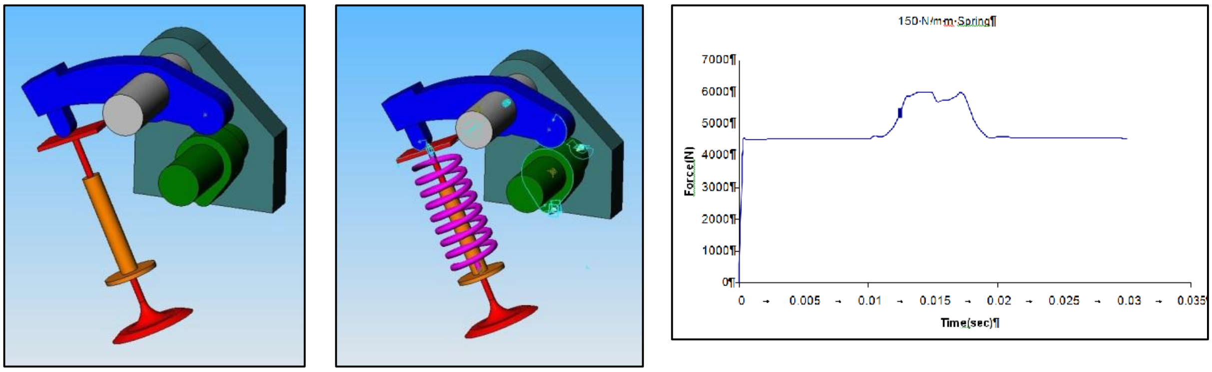

(a) (b) (c)

FIGURE 4. (a) valve cam design. (b) engine overhead cam with spring (c) force magnitude analysis

SOFTWARE IMPLEMENTATION AND LIMITATIONS

Comparing solutions from EES and analytical methods that EES is exceptionally accurate in solving non-linear simultaneous algebraic equations. Both MATLAB and Mathematica can perform similar functions such as symbolic and numerical integration, a command line syms (variable name) has to be inputted first in MATLAB to define the symbol used. Another strong point of MATLAB is that it is widely used in the field of engineering. Both MATLAB and Mathematica are the premier all-purpose mathematical package, but students have to proficient in their respective programming language to utilize fully the software package capabilities.

SolidWorks/CosmosWorks also offer frequency, buckling, thermal, optimization, nonlinear, drop test and fatigue analysis on top of the commonly used static analysis. This puts SolidWorks/CosmosWorks on par with ANSYS in terms of analysis capability, but SolidWorks/CosmosWorks offers three types of shell mesh compared to more than 300 on ANSYS and its analysis accuracy on other types of analysis is yet to be determined. Nevertheless, SolidWorks/CosmosWorks ease-of-use offers a great advantage to students who never had any experience with FEA analysis. SolidWorks/CosmosfloWorks can do analysis on internal flow, external flow, rotating flow, non-Newtonian fluids, etc.

Its robust analysis capability is almost equivalent to high-end CFD packages such as FLUENT and AVL/SWIFT/FIRE, except for intricate analysis such as engine combustion and nuclear power simulation. SolidWorks/CosmosMotion is fully embedded in SolidWorks and powered by ADAMS® (The Multibody Dynamics Simulation Solution), high-end virtual prototyping software from MSC [22]. CosmosMotion would enable engineers to size springs/dampers/motors/actuators, design cams/gears, determine power/force, and check for interference in their design. These capabilities and the capacity to export the results directly to SolidWorks/CosmosWorks under the same program to do FEA analysis would come in handy for students who are doing mechanical design.

CONCLUSION

By means of computer-aided engineering, students would be more exposed to real-life design problems, which also mean that lecturers in the respective subject have to modify the existing problems in the textbooks to accommodate for the use of software packages. With more exposure to real life problem and proficiency in using the software packages, students would be more comfortable in tackling their final year project. They could do a simplified analysis on either EES or SolidWorks (and its modules) to get a ‘preliminary’ result, and then ‘fine tune’ it with more robust analysis software packages such as ANSYS or AVL SWIFT/FIRE.

REFERENCES

[1] AST AST, Manual AF (AVL GmbH, Graz, Germany, 2009).

[2] Autodesk A. R11 Reference Manual (Autodesk, Guildford Surrey England, 2011).

[3] Guide AC-SM. Ansys Inc. ANSYS CFX Release, **14,** 150 (2011).

[4] Manual I-DU. Integrated Design Engineering Analysis Software (SDRC, Milford, OH. 1988).

[5] Wolfram. Mathematica available at http://www.wolfram.com/mathematica/ (2014)

[6] R Kumar, Ph.D thesis "Model-dependent inference of 3D information from a sequence of 2D images" (UMass, Amherst, 1992).

[7] V. Nanjundaswamy, A. Kulkarni, Z. Chen, P. Jaiswal, A. Verma, and R. Rai, “Intuitive 3D Computer-Aided Design (CAD) System With Multimodal Interfaces”. in ASME 2013 International Design Engineering Technical Conferences and Computers and Information in Engineering Conference, Volume 2A: 33rd Computers and Information in Engineering Conference (ASME, Portland, 2013)

[8] C. Emmer, A. Fröhlich, and J. Stjepandic, *Advanced engineering visualization with standardized 3D formats. Product Lifecycle Management for Society* (Springer, Berlin, 2013) p584.

[9] P.H. Huang, C.Y. Chen, C.J. Chang, D. Lo, and C.C. Huang, Manufacturing & Service Industries **22,** 556 (2012).

[10] V. Vyatkin, Industrial Informatics, IEEE Transactions **9,** 1234 (2013).

[11} D.A. Patterson and J.L. Hennessy, *Computer organization and design: the hardware/software interface* (Newnes, San Francisco, 2013).

[12] J.H. Tan, E.Y. Ng, C.P. Tan, and N. Liu, Progress in Computational Fluid Dynamics, an International Journal **13,** 238 **(**2013).

[13] P.J. Waterman, Desktop Engineering **16**, 34 (2010).

[14] P. Waurzyniak, Manufacturing Engineering **149**, 39 (2012).

[15] H. Moore, *MATLAB for Engineers* (Prentice Hall Press, Upper Saddle River, 2014).
[17] N. Mulop, K.M. Yusof, and Z. Tasir, Procedia-Social and Behavioral Sciences **56**, 703 (2012).
[18] K. Bain, A. Moon, M.R. Mack, and M.H. Towns, A review of research on the teaching and learning of thermodynamics at the university level, Chem. Educ. Res. Pract., **15**, 320 (2014).
[19] V.D. Kulkarni and P.S. Tambade, Eurasian Journal of Physics and Chemistry Education **5,** 2 **(**2012).
[20] S. Klein, Engineering Equation Solver (EES) for Microsoft Windows Operating System: Academic Professional Version (F-Chart Software, Madison, 2012).
[21] R. Shih, Solidworks and Engineering Graphics: An Integrated Approach (SDC Publications, Waltham, 2013).
[22] MSC SOFTWARE. ADAMS (MSC Software Corporation, California, 2012).

International Conference on Mechanical Engineering 2015
(ICME 2015) 18 – 20 December, 2015, Dhaka, Bangladesh

Paper ID : 032

The Influence of Brick Kilns on Seasonal Variation of Particulate Matter Concentration in Dhaka City

M. M. Islam[1, a)] and S. Afrin[1, b)]

[1]*Department of Civil Engineering, Bangladesh University of Engineering and Technology (BUET), Dhaka, Bangladesh*

[a)]Corresponding author: maksimulislam075@gmail.com
[b)]sadiaafrinbuet@gmail.com

Abstract. This paper represents the effects of brick kilns on the seasonal variation of particulate matter in the air of Dhaka. Trends in air quality over the past decade show large seasonal variations in both $PM_{2.5}$ and PM_{10} concentrations, exceeding the national standards during dry season, while remaining somewhat below the standards during rainy season. Wet deposition due to precipitation is considered as the reason for this seasonal variation. The aim of the study is to establish brick kilns as one of the sources of PM by analyzing air quality and meteorological data statistically with the help of Pearson Correlation Coefficient and statistical P-value and thus a major factor of seasonal variation as brick kilns are in operation only in dry period of the country. To assess the effect of brick kilns, wind speed and direction were considered among the meteorological parameters as emissions of brick kilns located at the northern periphery of the city are transported by wind. However, precipitation was also correlated with PM to identify the effect of wet deposition. The number of rainy days in a month during the wet period has been found to have strong negative correlation with average monthly PM concentrations. However, the daily amount of rainfall during the rainy period does not seem to have any effect on the daily PM concentration as $PM_{2.5\text{-}10}$ showed insignificant negative correlation, while $PM_{2.5}$ showed insignificant positive correlation. This indicates that although precipitation in general may promote wet deposition of particulates, the daily rainfall itself does not significantly dictate the magnitude of PM and therefore it may not be a significant factor for seasonal variation. High PM concentrations have been found to be associated with winds coming from northern and north-western directions during the dry season, suggesting that the brick kiln clusters situated in the northern periphery of the city are contributing to the degraded air quality by emitting particulate matter. The results of the study indicate that effect of wet deposition due to precipitation on the reduction of PM is very low and closure of brick kilns during rainy season is the main reason of the seasonal variation of particulate matter in Dhaka city.

INTRODUCTION

Bangladesh is the ninth-most polluted country in the world according to the statistics of the global Environmental Performance Index for 2014 [1]. Dhaka, the capital of Bangladesh, is one of the 20 megacities in the world [2] and facing severe urban air pollution problems. Based on publicly available air quality data from 1,100 cities including cities with populations of more than 100,000 people, WHO assessed that Dhaka is among the top 20 cities with the worst air pollution problem [3].This is primarily due to the high population density in this city (around 8,111 per square kilometer) which places its inhabitants at high risk of significant health impacts due to exposure to airborne contaminants. Vehicular emission, brick kilns and re-suspended dust from roads have been identified as major sources of air pollution in Dhaka city [4]. Among the air quality parameters in Dhaka city, the Particulate Matter (PM) has been the most widely studied due to its strong correlation with health outcomes and more recently due to its high concentrations in Dhaka city exceeding national ambient air quality standards during most parts of the year.

In Dhaka city, the major sources of PM_{10} have been found to be soil dust, road dust and motor vehicle emissions, while brick-kilns and motor vehicles have been found to be the main contributors to $PM_{2.5}$ [5], [6]. Among various sources, brick kiln is of particular importance as it is a seasonal pollution source and the brick kiln industry is one of the fastest-growing sectors, supporting the booming infrastructure and construction industry. With a current manufacturing capacity of about 12 billion bricks a year from 4,500 brick kilns surrounding all major cities, the industry is expected to grow 50% by 2020 [7], [8]. The brick manufacturing is primarily confined to the dry periods (October to March) as current technologies do not allow production during wet periods (April to September).The contribution of brick kiln emissions to the ambient air quality have previously estimated from the source apportionment studies conducted in 2001-2002, 2005-2006 and 2007-2009 [9, 10, 11]. These studies estimated an average of 30 – 40% contribution of brick kilns to total ambient $PM_{2.5}$ in Dhaka city during dry season.

Bangladesh has a subtropical monsoon climate characterized by wide seasonal variations in precipitation, moderately warm temperatures, and high humidity with minor regional climatic differences. Air quality of Dhaka is also characterized by high seasonal variation (Fig. 1).The daily PM_{10} and $PM_{2.5}$ concentrations exceed the national standards [12] (50 $\mu g/m^3$ and 150 $\mu g/m^3$ for PM_{10} and 15 $\mu g/m^3$and 65$\mu g/m^3$ for $PM_{2.5}$ for annual and 24-hour averaging period, respectively) by a factor of about two during the dry season, whereas during the wet season the ambient concentrations of PM have been found to be somewhat lower. The objective of the study is to establish brick kilns as the major source of this seasonal variation by statistically analyzing meteorological data.

MATERIALS AND METHODS

This study is based on the air quality data of Shangshad Bhaban Continuous Air Monitoring Station (CAMS) [13], which is located in an open, flat area approximately 150 meters away from the heavily trafficked Rokeya Sharani and 300 meters from Manik Mia Avenue. 24 hr average concentrations of $PM_{2.5}$ and PM_{10} are also measured at the CAMS using high volume PM_{10} and $PM_{2.5}$ samplers. Daily data of $PM_{2.5}$ and PM_{10} are available from April 2002 to May 2004; and monthly data are available from April 2002 to December 2010. The PM_{10} concentrations have been divided into two size fractions, $PM_{2.5}$ and $PM_{2.5-10}$ (=PM_{10} – $PM_{2.5}$) for this study.

Meteorological data for Dhaka city have been collected from two sources: Shangshad Bhaban CAMS and Bangladesh Meteorological Department (BMD). In Shangshad Bhaban CAMS, recorded data on rainfall are available from October 2002 to May 2004 as hourly averages. Daily wind speed and wind direction data have been collected from Bangladesh Meteorological Department (BMD); these data are not available at the Shangshad Bhaban CAMS. The BMD maintains a network of surface and upper air observatories, radar and satellite stations, agro-meteorological observatories, geomagnetic and seismological observatories and meteorological telecommunication systems. Data of almost all meteorological parameter are available at BMD since 1953.

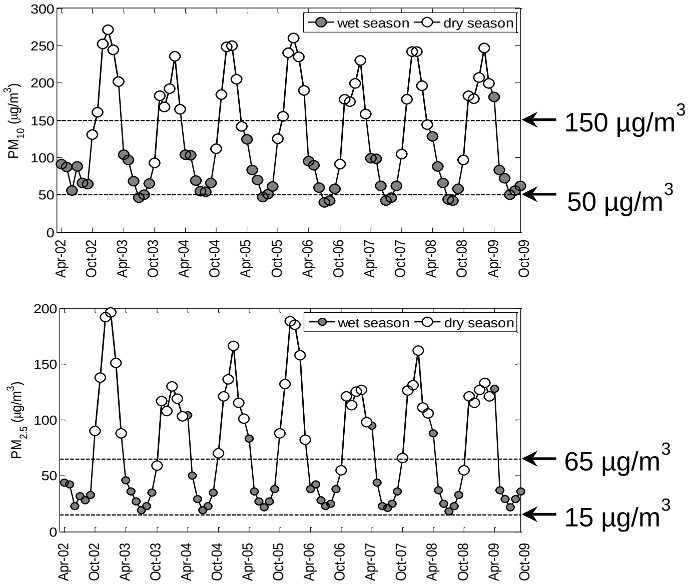

FIGURE 1. Monthly average PM_{10} and $PM_{2.5}$ trend in Dhaka city as measured at the Shangshad Bhaban CAMS.

It was mentioned earlier, the daily recorded PM data from the Shangshad Bhaban CAMS is only available for the period October 2002 to May 2004, while monthly PM data are available up to 2010. In order to assess the influences of brick kilns, the CAMS daily PM data from October 2002 to May 2004 have been used. The Shangshad Bhaban CAMS meteorological data was used for the period during which it was available, whereas for the remaining periods, meteorological data from BMD were used. For the analysis, the October 2002 to May 2004 period was further subdivided into three periods which are referred to as Dry period-1 (October 2002 to March 2003), Wet period (April 2003 to September 2003) and Dry period-2 (October 2003 to March 2004). Generally each period has its own unique meteorological conditions that can affect the concentrations of the particulate matter. Dry period is characterized by dry soil conditions, low relative humidity, low or no rainfall and prevailing winds of low speed from the northwest. Heavy rainfall occurs in wet period, which is characterized by high relative humidity, prevailing winds from southeast and a closure of brick-kiln operation. Pearson's correlation was used to determine the degree of association between different climatic variables and PM concentrations. A significance level of 5% ($p = 0.05$) has been chosen to be the threshold for determining the significance of the correlation coefficient.

RESULTS AND DISCUSSIONS

The number of rainy days in a month during the wet period has been found to have strong negative correlation with average monthly PM concentrations (Fig. 2) with correlation coefficients -0.85 and -0.94 for $PM_{2.5}$ and $PM_{2.5-10}$, respectively. This indicates that during the closure period of the brick kilns in the wet season, the prevalence of PM in air is strongly associated with rainfall period. However, the daily amount of rainfall during the wet period does not seem to have any effect on the daily PM concentration as $PM_{2.5-10}$ showed insignificant negative correlation ($r = -0.15$, $p = 0.379$), while $PM_{2.5}$ showed insignificant positive correlation ($r = 0.06$, $p = 0.734$) (see Fig. 3). This indicates that although precipitation in general may promote wet deposition of particulates, the daily rainfall itself does not significantly dictate the magnitude of PM concentrations and therefore it may not be a significant indicator

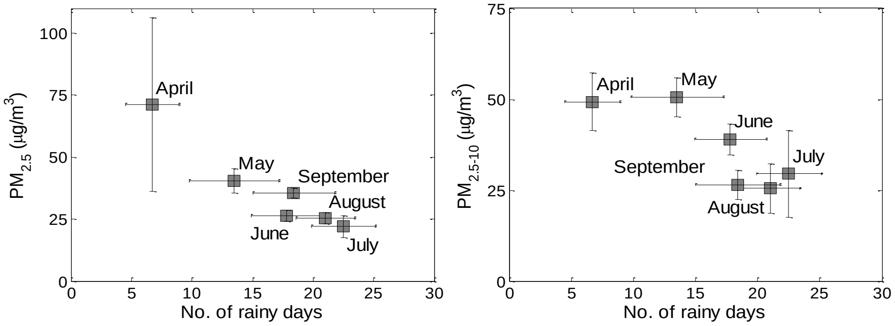

FIGURE 2. Average monthly PM concentrations against number of rainy days in a month during wet period showing a decrease in particulate matter concentration with increased number of rainy days.

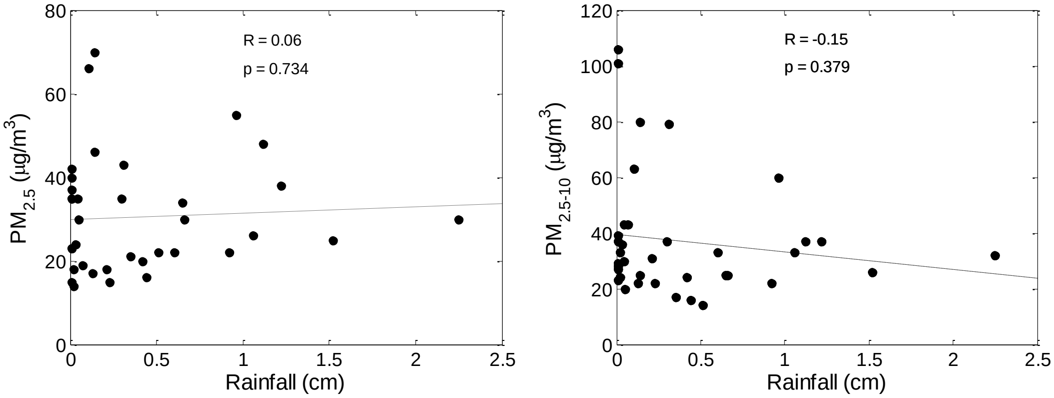

FIGURE 3. Scatter plot of different PM fractions and rainfall intensity during wet period showing a weak correlation between them. The dashed line represents the trend of the relationship as determined through linear regression.

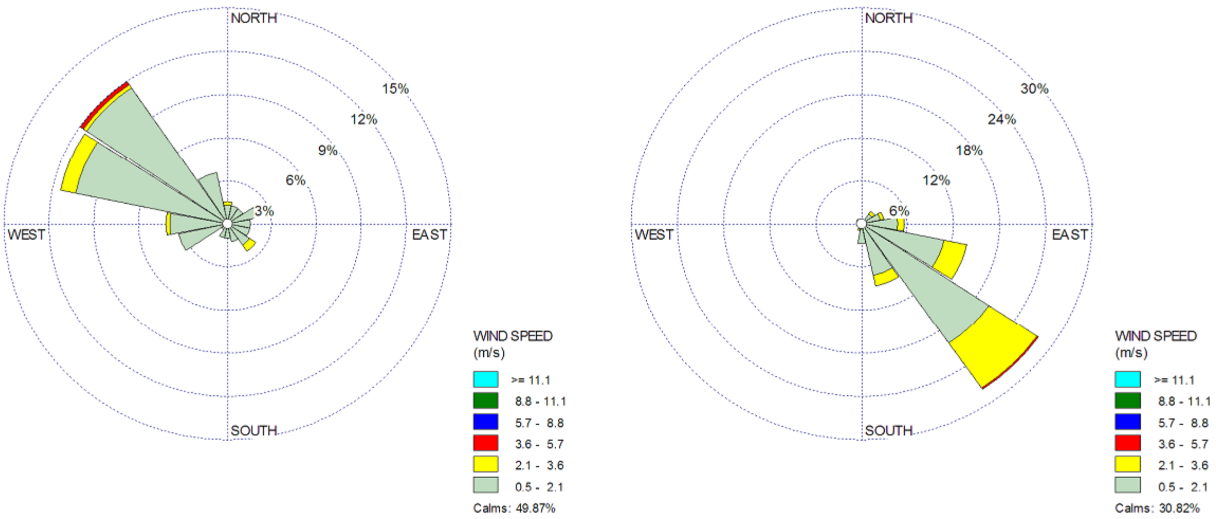

(a) (b)

FIGURE 4. Wind rose plot in (a) Dry period and (b) Wet Period.

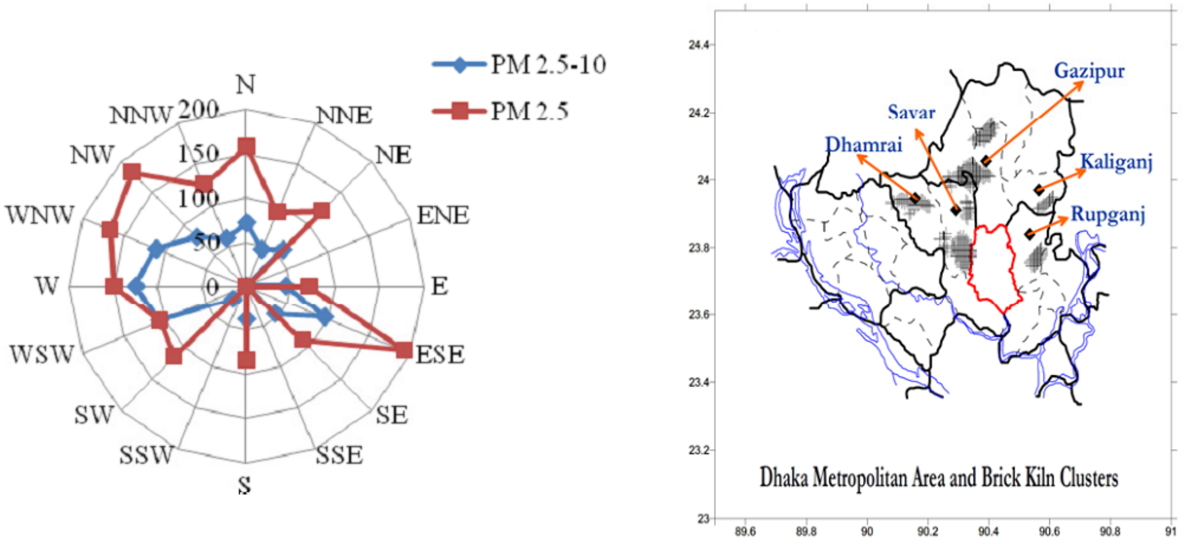

FIGURE 5. (a) Radar plot showing the concentration of $PM_{2.5}$ and $PM_{2.5-10}$ corresponding to different wind directions during the dry period and (b) Brick clusters around Dhaka City [5]

of air pollution potential. Figure 2 also suggests that the high concentration of PM during the dry season cannot be explained by lack of precipitation during the dry season; extrapolating the trend of PM variation (with number of rainy days) to days without precipitation (i.e., zero rainy days) yields PM concentrations far below those actually observed during the dry season (see Fig. 1).

The residence of pollutants in the atmosphere and transport are controlled not only by the rate of emission/formation but also by certain physical parameters such as wind speed and direction. The direction and speed of the prevailing wind may significantly affect the concentration, distribution and translocation of the particles [14, 15]. Wind speed and direction provide real-time information on pollutant transport in a region and can be used to assess the relationships between sources and pollutant levels. The two wind rose plots for Dhaka city in Fig. 4 shows that the predominant wind direction for dry and wet periods are north-west (NW) and south-east (SE), respectively. In order to study the effect of wind speed and direction on PM concentrations, the dry period dataset during October 2002 – May 2004 has been used. The wet period was not considered in the analysis because the major pollution sources located outside the city boundary (i.e., the brick kilns) remain closed during that period. Winds coming from different directions are grouped into 16 categories such as N, NNE, NE, ENE, E etc. and for each specific direction, the days on which winds were coming from that direction have been identified and the concentrations of PM for those particular days have been averaged. The radar plot in Fig. 5a shows the average PM concentrations of each of these categories for the dry period. Both $PM_{2.5}$ and $PM_{2.5-10}$ show higher concentrations when winds come from north-west direction (Fig. 5a). This is expected as the major brick clusters of Gazipur, Savar and Dhamrai are situated along the northwestern periphery of Dhaka city (Fig. 5a), and wind blowing from those directions will likely to carry the particulate pollution load. There is a slight confounding factor of increased concentration due to southeastern wind direction because there are no known brick kiln clusters in that direction. This indicates that there might be industries in that direction other than brick kilns that might contribute higher particulate concentrations. The likely contributors are the industrial installations in Narayanganj which are mostly located along the banks of the Sitalakhya River. The degraded airshed in that region is documented in several reports [16]. The strong association between wind blowing from the north and northwestern direction and PM concentrations supports the hypothesis that during the dry period brick clusters of Gazipur, Savar and Dhamrai significantly dominate the air quality of Dhaka city and closure of kilns during the wet period is the major reason of seasonal variation of PM in Dhaka.

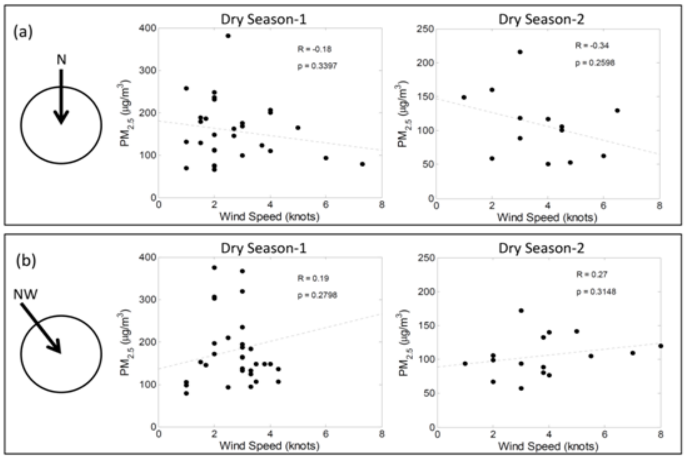

FIGURE 6. Scatter plot showing the relationship between PM2.5 and wind speed in dry season for two different wind directions: (a) north, and (b) and northwest

In order to understand whether wind speed has any bearing on the PM concentrations of Dhaka city, the dry season data was further filtered and PM data associated with N and NW wind directions were considered. The wind from North (N) and Northwestern (NW) directions were correlated with the corresponding daily $PM_{2.5}$ concentrations and the scatter plots are shown in Fig. 6. For winds blowing from the north (N) direction, a weak negative correlation was found between wind speed and $PM_{2.5}$ concentration for both dry period-1 (r = -0.18) and dry period-2 (r = -0.34). A weak positive correlation was found corresponding to wind blowing from north-west (NW) (r = 0.19 and 0.27 for dry period-1 and dry period-2 respectively). However, all of these correlations were found to be insignificant ($p>0.05$) indicating that wind speed does not appear to have a significant influence on PM concentration in Dhaka.

CONCLUSION

In this study, the probable association between brick kilns, some meteorological parameters and particulate matter (PM) pollution dynamics in Dhaka city has been explored. Daily precipitation appears to have trivial influence on PM reduction through wet deposition, though the number of rainy days in a month showed significant negative correlation with PM concentration. Analysis of wind direction suggests that brick-kilns located to the north-west direction of

Dhaka city are major contributors to PM concentration in Dhaka air during dry season (October to March). These observations provide strong indication that closure of brick kilns during wet period is the main reason behind the seasonal variation of PM in Dhaka. This type of study can be useful in suggesting mitigation measures to control ambient PM concentrations. Such mitigation measures may include relocating the brick kiln clusters to a location which will cause the minimum impact on Dhaka city under the prevailing meteorological conditions.

REFERENCE

1. Environmental Performance Index, Yale Centre for Environmental Law & Policy, Yale University, Centre for International Earth Science Information Network, Columbia University, 2014
2. World Health Organization (WHO) air quality guidelines, A working Group meeting, Bonn, Germany, Copenhagen, WHO Regional office for Europe, 18–20 October, 2005. Available online at http://www.euro.who.int/Document/E87950.pdf, accessed in April 2010.
3. United Nations Human Settlements Programme (UN HABITAT) State of the world's cities 2008/2009—harmoniouscities. Nairobi, 2008.
4. WHO, Outdoor air pollution in the world cities. World Health Organization, Geneva, 2011.
5. S. Guttikunda, "Impact Analysis of Brick Kilns on the Air Quality in Dhaka, Bangladesh", *SIM-air Working Paper Series: 21-2009*, available online at:www.urbanemissions.info/simair.
6. B. A. Begum, E. Kim, S. K. Biswas, and P. K. Hopke, *Atmospheric Environment* 38 (19), 3025-3038 (2004).
7. World Bank, Small study on air quality of impacts of the North Dhaka brickfield cluster by modeling of emissions and suggestions for mitigation measures including financing models. Consultant report prepared by Bangladesh University of Engineering and Technology for the World Bank, Washington DC, 2007.
8. United National Development Program (UNDP), Improving kiln efficiency in the brick making industry. GEF-United National Development Program, Dhaka, 2011
9. B. A. Begum, S. K. Biswas, P. K. Hopke, and D. D. Cohen, "Multi-element analysis and characterization of atmospheric particulate pollution in Dhaka," *Aerosol and Air Quality Research* 6 (4), 2006, pp. 334-359
10. B. A. Begum, S. K. Biswas, and P. K. Hopke, "Assessment of trends and present ambient concentrations of $PM_{2.2}$ and PM_{10} in Dhaka, Bangladesh," *Air quality. Atmos Health* 1, 2008, pp. 125–133
11. B. A. Begum, S. K. Biswas, and P. K. Hopke, "Key issues in controlling air pollutants in Dhaka, Bangladesh," *Atmos Environ* 45, 2011, pp. 7705–7713.
12. Government of Bangladesh (GoB), Revision of the Environment Conservation Rules 1997. SRO No. 220-Rule/2005, Ministry of Environment and Forest, Government of the People's Republic of Bangladesh, Dhaka, 2005.
13. Clean Air & Sustainable Environment (CASE) Project, Department of Environment (DoE), Ministry of Environment & Forest, Government of the Peoples Republic of Bangadesh, available online at: http://www.case-moef.gov.bd/
14. D. Giri, K. V. Murthy, and P. R. Adhikary, "The Influence of Meteorological Conditions on PM_{10} Concentrations in Kathmandu Valley," *Int. J. Environ. Res.*, **2(1),** 49-60(2008).
15. J. T. Van der Wal, and L. H. J. M. Janssen, "How contribute emission of PM10 and meteorology to concentrations of fine particles in the Netherlands," *J. Aerosol Sci.*, **27**, 681–682 (1996).
16. Bureau of Research, Testing & Consultation (BRTC), Environmental Impact Assessment of the World Bank financed 335 MW power plant at Siddhirganj, Narayanganj. Department of Civil Engineering, BUET, 2012

International Conference on Mechanical Engineering 2015
(ICME 2015) 18 – 20 December, 2015, Dhaka, Bangladesh

Paper ID : 053

Design of an Air Superiority Fighter

Md Saifuddin Ahmed Atique[1, a)], Shuvrodeb Barman[1, b)] , Asif Shahriar Nafi[1, c)],
Masum Bellah[1, d)] and Md. Abdus Salam [1, a)]

[1]*Department of Aeronautical Engineering, Military Institute of Science & Technology (MIST), Mirpur Cantonment, Dhaka, Bangladesh*

[a)]Corresponding author: saif.atique16@gmail.com
[b)] shuvrodebbarman@gmail.com

Abstract. Air Superiority Fighter is considered to be an effective dogfighter which is stealthy & highly maneuverable to surprise enemy along with improve survivability against the missile fire. This new generation fighter aircraft requires fantastic aerodynamics design, low wing loading (W/S), high thrust to weight ratio (T/W) with super cruise ability. Conceptual design is the first step to design an aircraft. In this paper conceptual design of an Air Superiority Fighter Aircraft is proposed to carry 1 crew member (pilot) that can fly at maximum Mach No of 2.3 covering a range of 1500 km with maximum ceiling of 61,000 ft. Payload capacity of this proposed aircraft is 6000 lb that covers two advanced missiles and one advanced gun. The Air Superiority Fighter Aircraft was designed to undertake all the following missions like: combat air petrol, air to air combat, maritime attack, close air support, suppression, destruction of enemy air defense and reconnaissance.

INTRODUCTION

Air Superiority Fighters are designed with a view to entering and seizing control of enemy airspace. Generally, an air Superiority fighter is blesses with long range and beyond visual range (BVR). These dogfighters generally require more time to make them prepared to go for mission. These class of aircraft claims high maintenance cost. Being expensive, the number of production of air superiority fighters is less. Few examples of air superiority fighters are: F-15, F-22, SU-30 MKI, Euro fighter etc.

Air superiority fighters are capable of engaging enemy fighters than compared to others type of aircraft (i.e. Multirole Fighters). Aerospace vehicle design is a prominent branch of engineering design. Engineering design refers to the procedure or technique of devising a system component or process to meet desired requirements.

Conceptual design is the very first thing approach of designing an aircraft when it covers size, weight and configurations and performance parameters of different components. Maximum take-off weight, thrust to weight ratio and Wing Loading are determined at preliminary stage. A solid foundation is provided by the conceptual design and preliminary design of each of the component or parts of the aircraft i.e. wing, tail, fuselage, landing gear, propulsion systems etc.

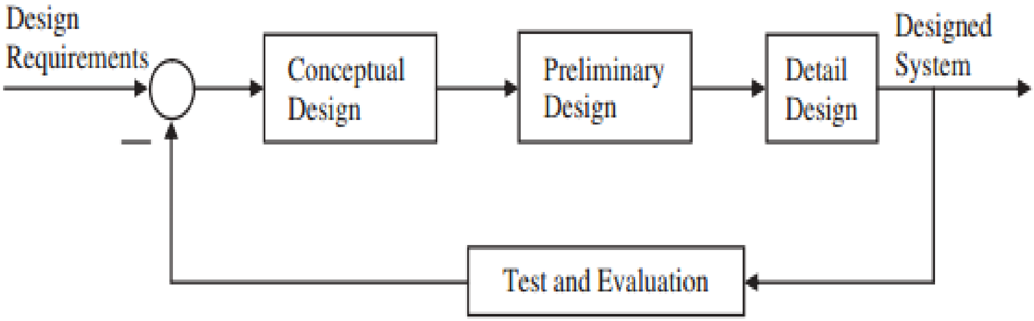

FIGURE 1. Relationship among four major design activities

Nomenclature

V_H	Horizontal Tail Volume Coefficient
V_V	Vertical tail Volume Coefficient
S_h/S	Ratio of horizontal tail area to wing reference area
AR_h	Aspect ratio of the horizontal tail
AR_v	Aspect ratio of the Vertical tail
λ_h	Taper ratio of the horizontal tail
λ_v	Taper ratio of the Vertical tail
Λ_h	Sweep angle of Horizontal tail
Λ_v	Sweep angle of vertical tail
Γ_h	Dihedral angle of horizontal tail
$(t/c)_{max}$	Thickness to chord ratio

Mission Profile

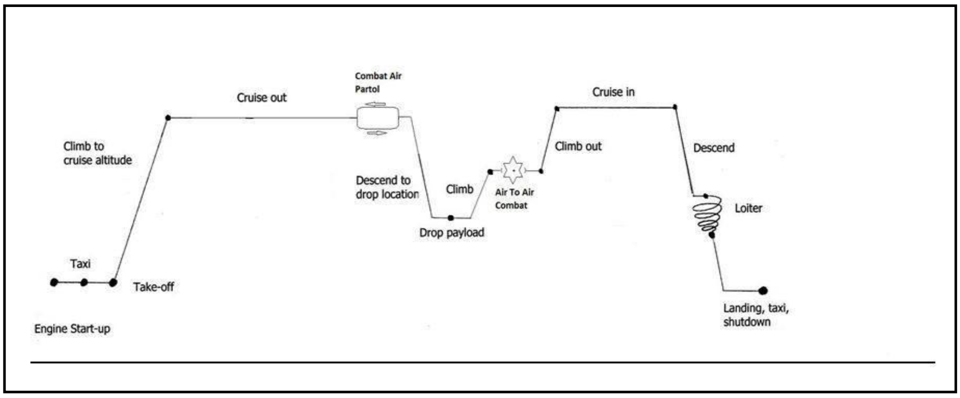

FIGURE 2. Mission Profile

CONCEPTUAL DESIGN

Conceptual Design is an umbrella term given to all forms of non-aesthetic design management disciplines.

Selection of Wing

Monoplane, mid wing, swept back, plain flap, Fixed Wing with fixed shape was selected. The reason for selecting mid wing is that it is more attractive compared to low wing or high wing. For the reinforcement of the wing structure, a strut is not usually used. Having aerodynamically streamlined the mid wing configuration has less interference drag compared to low wing or high wing.

Selection of Landing Gear

Retractable, Tricycle landing gear is selected. Tricycle landing gear is selected for safety reason though it Increase manufacturing, operation & maintenance cost.

Selection of Propulsion System

Twin engine turbofan buried inside the rear fuselage was selected for designed Air Superiority Fighter.

PRELIMINARY DESIGN

The preliminary design phase tends to employ the outcomes of a calculation procedure. As the name implies, at the preliminary design phase, the parameters determined are not final and will be altered later. Three primary aircraft parameters of WTO, S, and T (or P) form the output of the preliminary design phase. These three parameters will govern the aircraft size, the manufacturing cost, and the complexity of calculations.

Maximum Takeoff Weight

To determine maximum take-off weight the following equation was used. We used the following equation for that purpose.

$$W_{TO} = \frac{W_P}{1 - \left(\frac{W}{W_T}\right.}$$

We calculate maximum take-off weight (W_{TO}) = 56391.022 lb. (25578.9675 kg)

Thrust to weight Ratio

From the relation of thrust to weight ratio with wing loading in case of stall speed, maximum speed, take-off run, rate of climb and service ceiling the value of thrust to weight ratio we got is 1.273.

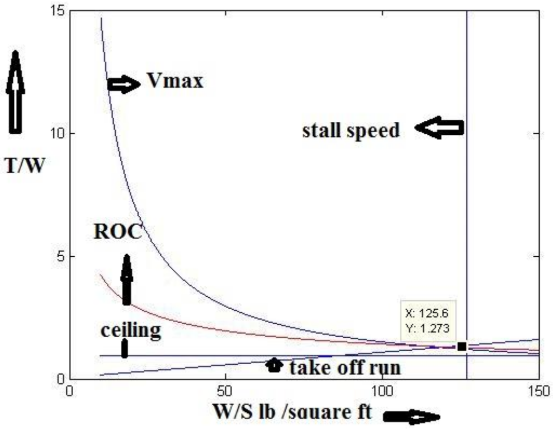

FIGURE 3. Matching Plot for Air superiority Fighter

Determination of Wing Surface Area Engine Thrust

Wing Area, S = $\frac{W_{TO}}{(\frac{W}{S})_d} = \frac{56391.022\, lb}{125.6\, \frac{lb}{ft^2}}$ = 448.97 ft^2 =41.71 m^2

Engine Thrust, T = $W_{TO} \times (\frac{T}{W})_d$ = 56391.022 × 1.273 lb.
= 71785.77 lb.

DETAIL DESIGN

Details design means the elaborate design of the aircraft component like: wing, fuselage, propulsion systems, landing gear, tail etc.

Wing Design

The wing is used to generate aerodynamic force mainly known as lift to keep the aircraft airborne. We calculate Sweep angle as 67 degree and taper ratio as 0.3. Calculated value of wing span is 10.22 m, flap span 6.645 m, flap area 9.1983 m2 and flap chord 1.3837 m. Wing chord was found as 4.089 m. This criteria was fulfilled by NASA SC (2)-0414 AIRFOIL (sc20414-il). The selected airfoil has maximum thickness of 14% that is located at 36% of chord where maximum camber of 1.5% was found at 83% of chord.

Tail Design

By analyzing both historical data and different jet aircraft some parameters were selected for horizontal tail as got: $V_H = 0.24$, $S_h / S = 0.183$, $AR_h = 2.30$, $\lambda_h = 0.36$, $\Lambda_h = 48$, $\Gamma_h = 0$ *and for vertical tail:* $V_V = 0.06$, $S_v / S = 0.346$, $(t/c)_{max} = 7\%$, $\lambda_v = 0.22$. The plan form area of the is determined as 6.82 m^2. Wing/fuselage aerodynamic pitching moment co-efficient is calculated as -0.028. The horizontal tail lift co-efficient at cruise is -0.1461.

Propulsion System

Calculated thrust requirement is 71842.162 lb. We selected the engine from manufacturing catalogue. We select 2 × NPO Saturn izdeliye 117 (AL-41F1) for initial production, izdeliye 30 for later production thrust vectoring turbofan.

Fuselage Design

Fuselage design is accomplished according to Federal Aviation Rules, FAR-25. Length and diameter of the fuselage was taken 19.8 m (64.96 ft.) & 2.08 m (6.84 ft.).

Landing Gear Selection

Calculated landing gear height is 2.1938 m. The distance between main gear and aircraft forward c.g is 0.8869m.

HIGH LIFT DEVICE SELECTION

Plain flap was selected as the high lift device for the trailing edge because of its simplicity. Even though it was simple one but many modern aircrafts such as F-15E Eagle and MIG-29 employ plain flaps.

Final Model

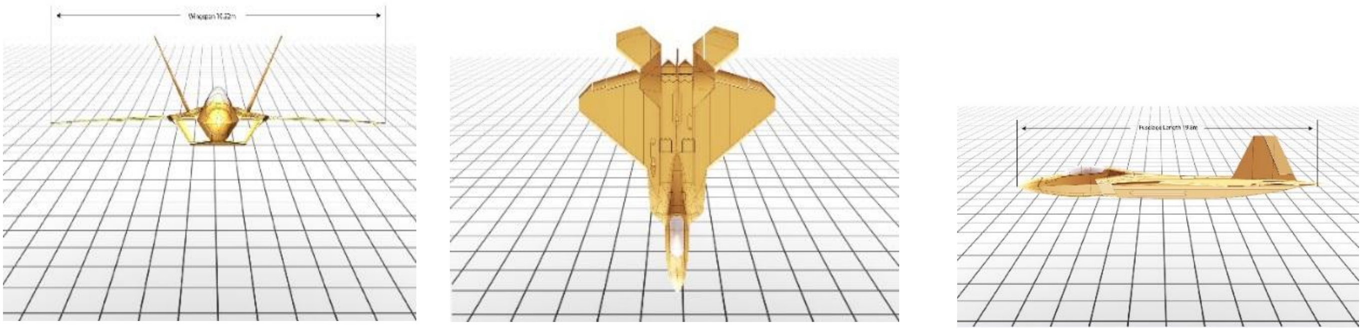

(a) (b) (c)

FIGURE 4. Three view of designed Air Superiority Fighter (a) front view (b) top view (c) side view

Comparison with Similar Aircraft

TABLE 1. A comparison between F-22 Raptor & our own designed aircraft

Parameters	**F-22 Raptor**	**Designed Aircraft**
No. of crew	1	1
Length	18.92 m	19.80 m
Wing span	13.56 m	10.22 m
Take-off weight	83,500 lb.	56391.022 lb.
Engine	Pratt & Whitney F119	2 × NPO Saturn izdeliye 117 (AL-41F1)
Maximum Range	2960 km	1500 km 810 NM
Maximum Speed	1.82 Mach	2.3 Mach
Thrust to Weight Ratio (T/W)	1.08	1.273
Wing Loading (W/S)	377 kg / m^2	619.86 kg/m^2
Ceiling	20 km	18.59 km
Wing Area (S)	78.04 m^2	41.81 m^2
Rate of Climb (ROC_{max})	350 m / sec.	272 m/sec.
Stall Speed (V_{stall})	56.54 m/sec. (184.42 ft./sec.)	61.74 m/sec. 202.56 ft./sec.

CONCLUSION

Air Superiority Fighter is a very advanced next generation fighter aircraft which is highly controllable and considered as a queen of air to air combat and dogfight. As the aircraft is used for military purposes so it was very difficult and sometimes impossible for us as designers to find out the proper aeronautical information for an aircraft like this. As a result lots of assumptions were made which hampers the design accuracy a little bit. As budding aircraft designers we wish if proper data and information were available the design could be more accurate.

ACKNOWLEDGEMENT

We are grateful to our head of department, Md. Abdus Salam for supervising this design analysis. The authors would also like to thank M A Taher Ali, Sheikh Reaz who carefully read the manuscript and gave valuable suggestions for further improvement.

REFERENCES

1. J. Nawar, N. N. Probha, A. Shahriar, A. Wahid and S. R. Bakaul, “Conceptual Design of a Business Jet Aircraft”, *International Conference on Mechanical, Industrial and Energy Engineering,* Khulna, Bangladesh, December 25-26,2014.
2. D. P. Raymer, *Aircraft Design: A Conceptual Approach,* Fourth Edition, (American Institute of Aeronautics and Astronautics, Inc., Virginia, 2006).
3. M. H. Sadraey, *Aircraft Design - A Systems Engineering Approach* (John Wiley & Sons Ltd., United Kingdom, 2013).
4. J. D. Anderson, Jr., *Aircraft Performance and Design* (The McGraw-Hill Companies, Inc., New York, 1999).
5. T. H. G. Megson, *Aircraft Structures,* Fourth Edition, (Elsevier Ltd.).
6. J. Cutler, J. Liber, *Understanding aircraft structures*.

International Conference on Mechanical Engineering 2015
(ICME 2015) 18 – 20 December, 2015, Dhaka, Bangladesh

Paper ID : 079

Studies of Electrical Conductivity and Complex Initial Permeability of Multiferroic $xBa_{0.95}Sr_{0.05}TiO_3$-(1– x) $BiFe_{0.90}Gd_{0.10}O_3$ Ceramics

Mohammad J. Miah[1, 3, a)], M. N. I. Khan[2] and A. K. M. Akther Hossain[1]

[1]Department of Physics, Bangladesh University of Engineering & Technology, Dhaka
[2]Materials Science Division, Atomic Energy Center, Dhaka
[3]Department of Physics, Comilla University, Comilla

[a)] Corresponding author: mmjulhash@yahoo.com

Abstract. Multiferroic $xBa_{0.95}Sr_{0.05}TiO_3$-(1–x)$BiFe_{0.90}Gd_{0.10}O_3$ [xBST-(1–x)BFGO] (x = 0.00, 0.10 and 0.20) ceramics were prepared by the standard solid-state reaction technique. Crystal structure of the ceramics was determined by X-ray diffraction pattern. All the compositions exhibited rhombohedral crystal structure. The tolerance factor 't' varied from 0.847 to 0.864. The AC conductivity spectrum followed the Jonscher's power law. The Nyquist plots indicated that only grains have the contribution to the resistance in this material and the values of grain resistance (R_g) increased with BST content. The real part of complex initial permeability decreased with the increase in frequency and increased with increasing BST content. Magnetoelectric coefficient was determined for all compositions. The maximum value of magnetoelectric coefficient was found to be 1.467 $mV.cm^{-1}.Oe^{-1}$ for x = 0.20.

Keywords: Multiferroic; Electric properties; Magnetic properties; Magnetoelectric coefficient.

INTRODUCTION

Conductivity is a vital issue in the research of material science and polymer science. Electrical conductivityreveals the essential electrical characteristics of electroceramics and hence clarification of electrical conductivity mechanism is of primary importance. Materials that exhibit ferromagnetic/antiferromagetic and ferroelectric orders simultaneously are known as multiferroics [1]. $BiFeO_3$ (BFO) is one of the most extensively studied multiferroic compound which exhibits electric as well as magnetic properties at room temperature. Conductivity plays a crucial role in BFO. BFO can easily be incorporated into functional microelectronic devices and it is also an environment friendly material. But the applications of BFO have been restricted because of its large leakage current, difficulty in fabricating single phase and high difference in ferroic transition temperatures (T_C = 370°C and T_N = 830°C [2]) etc.

Researchers all over the world are working to improve the properties of BFO by the incorporation of other materials. To improve magnetic as well as electric properties, recent work has been focused on the solid solutions of BFO with other perovskite materials. Among perovskite materials, BT is the most common and exhibits high dielectric properties. Although there is an improvement of magnetic properties and disappearance of secondary phases due to the formation of solid solution between BFO and BT, there are still some serious problems (e. g. poor electrical insulation, large coercive fields, high leakage current etc.) those hinder the practical applications of these materials. As a result the magnetoelectric property is not improved significantly.The conductivity in BT-BFO solid solution has been studied over last few decades [3-5]. Moreover, the magnetic properties of the above mentioned ceramics have been reported by several authors [6, 7]. But the effect of $Ba_{0.95}Sr_{0.05}TiO_3$ (BST) on electrical and magnetic properties of $xBa_{0.95}Sr_{0.05}TiO_3$-(1–x)$BiFe_{0.90}Gd_{0.10}O_3$ [xBST-(1–x)BFGO] ceramics has not been investigated so far. In the present work, perovskite xBST-(1–x)BFGO (x = 0.00, 0.10, and 0.20) ceramics are prepared by the conventional solid-state reaction technique and their electric properties, magnetic properties and magnetoelectric coefficient have been reported.

EXPERIMENTAL

$xBa_{0.95}Sr_{0.05}TiO_3$-(1–x)$BiFe_{0.90}Gd_{0.10}O_3$ (x = 0.00, 0.10, and 0.20) ceramics were prepared by the conventional solid-state reaction method. Dried raw materials of $BaCO_3$(99.9%), $SrCO_3$(99.9%), TiO_2(99.9%), Bi_2O_3(99.9%), Fe_2O_3(99.9%) and Gd_2O_3(99.95%) were mixed according to the stoichiometric formula and ball-milled in distilled water for 24 h to increase the degree of mixing. Mixed powders were calcined at 850 °C for 1 h. To obtain a homogeneous mixture the calcined powders were ground thoroughly and ball-milled again. Then the mixture was mixed with 10% polyvinyl alcohol (PVA) as a binder for granulation. From these powders disk- and toroid-shaped samples were prepared using a uniaxial press at 45 MPa pressure. Finally, the green pellets were sintered at 950 °C.

Crystal structure of the samples were characterized by using an X-ray diffractometer (Model D8 Advanced Bruker Gobel Mirror) with a Cu anode (Cu-K_α radiation source with λ = 1.541Å) at room temperature. The electrical and magnetic properties were carried out at room temperature in the frequency range 20 HZ to 120 MHz by using a Wayne Kerr 6500B Impedance Analyzer. For electrical measurement the samples were painted by conducting silver paste on both sides to ensure good electrical contacts. The dielectric constant (ε') was calculated by using the formula: $\varepsilon' = Cd/\varepsilon_0 A$, where, C is the capacitance of the pellet, d is the thickness, A is the cross-sectional area of the electrode and ε_0 is the permittivity in free space. The AC conductivity, σ_{AC}, of the samples was calculated using the relation: $\sigma_{AC} = \omega\varepsilon'\varepsilon_0\tan\delta$, where, ω is the angular frequency and $\tan\delta$ is the dielectric loss. The real part (μ_i') and imaginary part (μ_i'') of the complex initial permeability were measured as a function of frequency using the relations: $\mu_i' = L_S/L_0$ and $\mu_i'' = \mu_i'\tan\delta$, where, L_S is the self inductance of the sample core and L_0 is the inductance of the winding of the coil without the sample and $\tan\delta$ is the magnetic loss. L_0 is derived from the geometrical relations, $L_0 = \mu_0 N^2 S/\pi\bar{d}$, where, μ_0 is the permeability in vacuum, N is the number of turns of the coil (N = 5), S is the cross-sectional area and $\bar{d} = (d_1+d_2)/2$ is the mean diameter of the toroidal sample, where, d_1 and d_2 are the inner and outer diameter of the toroidal sample, respectively. The magnetoelectric properties of the prepared samples were carried out by dynamic method using a magnetoelectric (ME) coefficient measurement system following the relation, $\alpha_{ME} = V/d.H_{AC}$, where, V is the ME voltage developed across the sample, d is the effective thickness of the sample and H_{AC} is the amplitude of applied AC field.

RESULTS AND DISCUSSION

X-Ray Diffraction Analysis

Fig. 1 shows the X-ray diffraction (XRD) pattern of xBST-(1–x)BFGO ceramics at room temperature. All the compositions exhibit pure perovskite structure. The peaks have been indexed following rhombohedrally distorted perosvkite structure. No peak of $Ba_{0.95}Sr_{0.05}TiO_3$ is observed confirming its substitution in the host material $BiFe_{0.90}Gd_{0.10}O_3$. The lattice parameters ‘a’ and ‘c’ are calculated following the formula of hexagonal equivalent [8] and using the intense peaks (012) and (110). The lattice parameters a’ and ‘c’ are listed in Table 1. It is observed that the value of lattice parameter ‘a’ is increasing with the increase in BST content. The results are well consistent with previous reports of BT-BFO system [9].

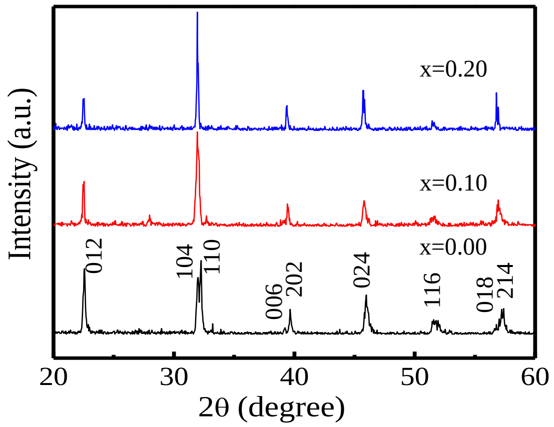

FIGURE 1. X-ray diffraction pattern of various xBST-(1–x)BFGO ceramics.

Tolerance factor

Mismatch in ionic radius and also in valence states between the A and B–site atoms causes distortions in the perovskite structure. Goldschmidit [10] introduced a parameter called tolerance factor (t) to describe the stability of perovskite structure. The tolerance factor ‘t’ is defined as [10],

$$t = \frac{R_A + R_O}{\sqrt{2}(R_B + R_O)} \qquad (1)$$

Where, R_A, R_B and R_O are the ionic radius of A-site atom, B-site atom and oxygen respectively. For $xBa_{0.95}Sr_{0.05}TiO_3$-(1–x)$BiFe_{0.90}Gd_{0.10}O_3$ compound the above equation can be written as :

$$t = \frac{(x)0.95.R_{Ba^{2+}} + (x)0.05.R_{Sr^{2+}} + (1-x)R_{Bi^{3+}} + R_{O^{2-}}}{\sqrt{2}[(x)R_{Ti^{4+}} + (1-x)0.9.R_{Fe^{3+}} + (1-x)0.1.R_{Gd^{3+}} + R_{O^{2-}}]} \qquad (2)$$

Where, $R_{Ba}{}^{2+}$, $R_{Sr}{}^{2+}$, $R_{Bi}{}^{3+}$, $R_{Ti}{}^{4+}$, $R_{Fe}{}^{3+}$, $R_{Gd}{}^{3+}$ and $R_O{}^{2-}$ are the ionic radius of Ba^{2+}, Sr^{2+}, Bi^{3+}, Ti^{4+}, Fe^{3+}, Gd^{3+} and O^{2-} respectively. The calculated value of 't' for xBST-(1–x)BFGO ceramics is shown in Table 1. The value of 't' varies from 0.847 to 0.864. It is noticed that 't' increases with increasing BST content, which indicates the perovskite structure of xBST-(1–x)BFGO ceramics becomes more stable as BST content increases.

AC Conductivity

The variation of AC conductivity (σ_{AC}) as a function of frequency at room temperature is shown in Fig. 2(a). It is seen that the spectrum exhibit two different regions. In low frequency region (region I) which corresponds to DC conductivity (σ_{DC}), the conductivity is almost frequency independent because the resistive grain boundaries are more active at low frequencies according to the Maxell-Wagner double layer model for dielectrics [11]. On the other hand, in the high frequency region (region II), which is known as hopping region, AC conductivity increases rapidly because at higher frequencies the conductive grains become more active thereby increasing hopping of charge carriers and contribute to rise conductivity. This frequency dependence of conductivity can be described by Jonscher's power law [12]: $\sigma_{AC}(\omega) = \sigma_{DC} + A\omega^n$, where, σ_{DC} is the frequency independent DC conductivity, A is the temperature dependent pre-exponential factor and 'n' is the frequency exponent. The exponent 'n' represents the degree of interaction between mobile ions and the lattice around them.

The conductivity of the ceramics can also be explained on the basis of polaron hopping mechanism. In large polaron model, σ_{AC} decreases with the increase of frequency while in small polaron hopping mechanism, the σ_{AC} increases with the increase of frequency [13]. Fig. 2(b) shows the variation of log (σ_{AC}) as a function of log (f) and it is seen that σ_{AC} increases with increasing frequency. This confirms that the conduction phenomenon in this material is due to small polaron hopping. Similar results are also reported by other researchers [14, 15]. Nature of non linear curve is also observed above certain frequency which indicates mixed polaron (small and large) conduction as reported by Kadam et al. [15]. The value of frequency exponent 'n' is determined from the slope of log (σ_{AC}) vs log (f) curves and the values of 'n' for the present solid solution are presented in Table 1. One may notice that the values of 'n' are less than unity (0.61<'n'<0.83) and increase with the increase in BST content. Das et al. [16] and Sahni et al. [17] have reported the similar results for Ba^{2+} and Gd^{+3} doped BFO and Mn-doped BT-BFO ceramics respectively.

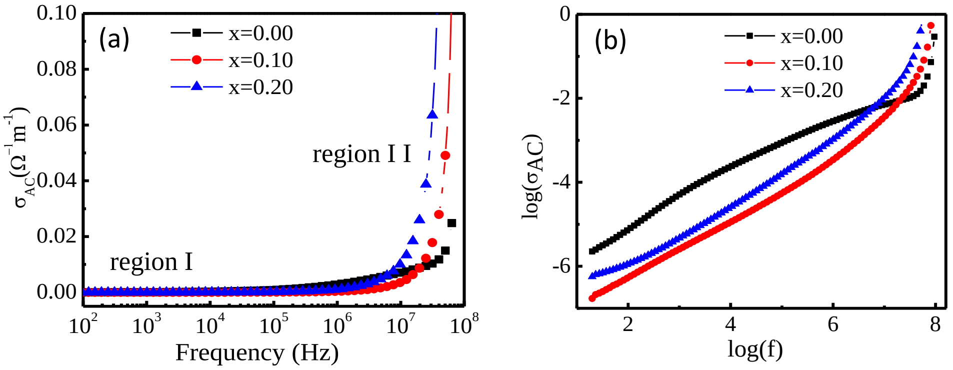

FIGURE 2. (a) Frequency dependence of σ_{AC} and (b) plot of log (σ_{AC}) versus log(f) of various xBST-(1–x)BFGO ceramics.

Complex impedance spectroscopy

Polycrystalline ceramics consist of grains and grain boundaries. Complex impedance spectroscopy is a powerful tool that separates the contributions of grain and grain boundary to the electrical properties of dielectric materials following the brick-layer model [18]. For this, the sample is represented by an equivalent

TABLE 1. Lattice parameters, tolerance factor (t), frequency exponent (n) and grain resistance (R_g) for various xBST -(1−x)BFGO ceramics.

Compositions x	Lattice parameters a (Å)	c (Å)	Tolerance factor t	Frequency Exponent ‘n’	Grain resistance R_g (MΩ)
0.00	5.55	13.70	0.847	0.61	26
0.10	5.58	13.60	0.855	0.82	30
0.20	5.59	13.57	0.864	0.83	60

circuit as shown Fig. 3(a). The equivalent circuit consists of three RC circuits (R_g & C_g; R_{gb} & C_{gb}; and R_s & L_s) connected in series. These RC elements correspond to grains, grain boundaries and electrode-specimen interface in order of decreasing frequency. Each RC element of the equivalent circuit gives rise to a semicircle. A single semicircle in the real part (Z´) of total impedance vs imaginary part (Z´´) plot indicates grain effects and the second semicircle indicates the presence of grain boundary effects. If a third semicircle is present, it indicates the electrode effects. Fig. 3(b) shows the complex impedance spectra (Z´ vs Z´´ plot known as Nyquist diagram) for different compositions taken over a wide range of frequency range (20 Hz-120 MHz) at room. All composites exhibit a single semicircular arc starting from the origin, indicating the materials have grain effect and the grain boundary does not contribute to the conductivity mechanism in this system. On the other hand, the electrode used in the present research provides a good electrical contact and the resistance for interface can be negligible. The values of resistance for the grains (R_g) are determined from the intercepts on the Z´ axis of Z´ vs Z´´ plots (Fig. 3(b)) and the values are listed in Table 1. It has been observed that the values of R_g increases with BST content because of the better dielectric properties of BST.

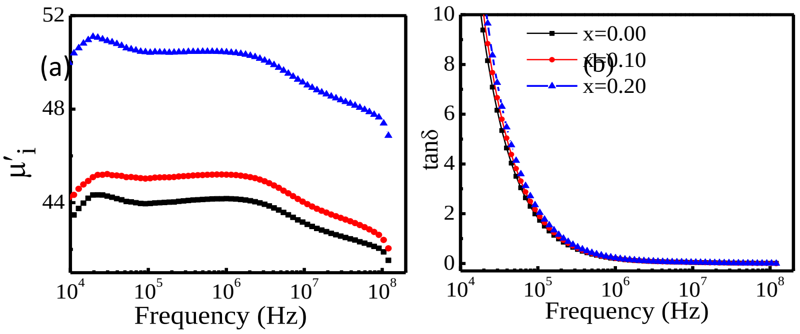

FIGURE 3. (a) Equivalent circuit and (b) complex impedance spectra (Z´ vs Z´´ curve) of various xBST-(1−x)BFGO ceramics.

Complex initial permeability

The variation of real part of complex initial permeability (μ_i´) with frequency is shown in Fig. 4(a). The

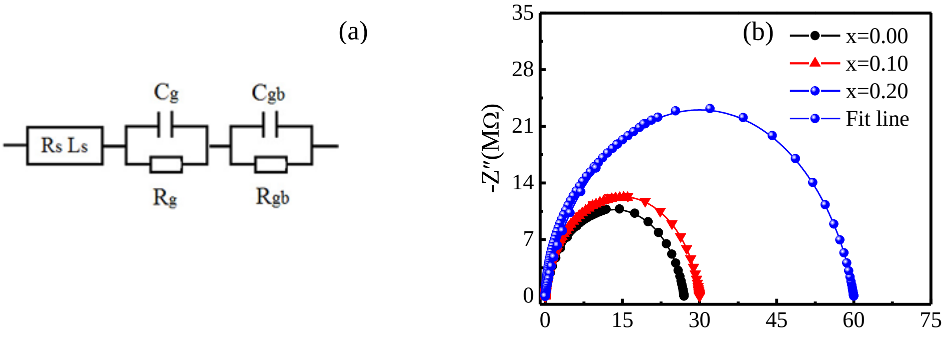

FIGURE 4. Variation of (a) μ_i´ and (b) tanδ with frequency of xBST-(1−x)BFGO ceramics.

value of μ_i' is found to decrease with frequency because the domain wall motion cannot follow the AC field at higher frequencies. On the other hand, at higher frequencies, impurities between grains and intragranular pores act as pinning points and obstruct the motion of spin and domain walls thereby decreasing their contribution to the permeability [19]. It is also observed that the value of μ_i' increases with the addition of BST. Pure BFO has spiral spin structure and due to this structure it has antiferromagnetic ordering. The substitution of larger ions Ba^{2+}(1.35 Å) and Sr^{+2}(1.18Å) on A-site and Ti^{4+}(0.68Å) and Gd^{3+} (0.94Å) on B-site of BFO make a change in Fe–O–Fe bond angle and also create a distortion in the spiral spin structure of BFO. This helps to release the macroscopic magnetization and consequently leading to enhance magnetic order [20].

Fig. 4(b) shows the variation of magnetic loss (tanδ) with frequency. It is observed that tanδ is decreasing with frequency and has very low value at high frequency. It is also noticed that tanδ is decreasing with BST content because of the reducing imperfections (defects, voids etc) with the addition of BST.

Magnetoelectric Coefficient

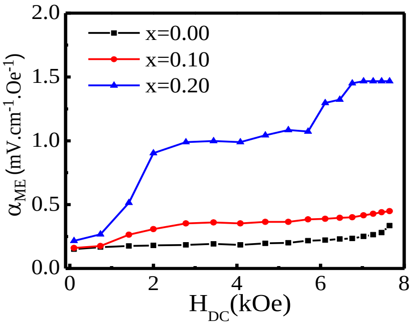

FIGURE.5. Variation of α_{ME} with magnetic field.

The variation of Magnetoelectric coefficient (α_{ME}) with applied DC magnetic field for various compositions of xBST-(1–x)BFGO ceramics is shown in Fig. 5. The value of α_{ME} is found increasing with magnetic field and then remains constant at higher field which indicates that the magnetostriction reaches at a saturation state after a certain magnetic field and produces a constant electric field in ferroelectric domain. Similar type behavior is also observed in $BiFeO_3$-$BaTiO_3$ [21] solid solution. It is clearly seen that the value of α_{ME} is significantly enhanced compared to that of the undoped BFGO. Highest value of ME coefficient is found to be 1.467 mV.cm^{-1}.Oe^{-1} for x=0.20.

CONCLUSIONS

Multiferroic xBST-(1–x)BFGO (x = 0.00, 0.10 and 0.20) ceramics have been fabricated by the conventional solid- state reaction method. Crystal structure, electric properties, magnetic properties and magnetoelectric coefficient of the cramics have been investigated. All compositions exhibit pure perovskite structure with rhombohedral unit cell. The σ_{AC} increases with increasing frequency due to electron hopping at the higher frequency. The value of frequency exponent ‘n’ is found to increase with BST content. R_g is found to increase with BST content and equivalent circuit is used to explain the phenomena. It is also observed that the value of μ_i' increases with increasing BST content. The value of α_{ME} increases with increasing BST content and highest value of α_{ME} is found for x = 0.20. The studied multiferroic ceramic is a lead free compound and it is expected to be environment friendly.

ACKNOWLEDGEMENTS

The authors greatly acknowledge the CASR Grant No. 253(21), Bangladesh University of Engineering and Technology (BUET), Dhaka, Bangladesh to provide financial support for this research.

REFERENCES

1. H. Schmid, Ferroelectrics **162**, 317 (1994).
2. J. Moreau, C. Michel, R. Gerson, and W. James, J. Phys. Chem. Solids **32**, 1315 (1971).
3. M. M. Kumar, A. Shrinivas, and S. V.Suryanarayana, J. Appl. Phys. **87**, 855 (2000).
4. M. Kuamr, S. Shankar, R. K. Kotnala and Om Parkash, J. Alloys and Comp. **577**, 577 (2013).

5. B. Wodecka-Dus and D. Czekaj, Archives of Metallury and Mater. **56**, 1127 (2011).
6. Y. Wei, X. Wang, J. Zhu, X. Wang and J. Jia, J. Am. Ceram. Soc. **96**, 2163 (2013).
7. H. Zhang, W. Jo, K. Wang, and K. G. Webber, Ceram. Intern. **40**, 4759 (2014).
8. P. Uniyal, G. S. Lotey, A. Gautam, N. K. Verma and K. L.Yadav, J. Supercond. Novel Magn. **27**, 569(2014).
9. Zhang H, Jo W, K. Wang and K. G. Webber , Ceram. Int. **40**, 4759 (2014).
10. V. M. Godschmidt, Naturwissenschafen **14**, 477 (1926).
11. K. Wagner, J. Ann. Phys. **40**, 817 (1913).
12. A. K. Jonscher, J. Mater. Sci. **16**, 2037 (1981).
13. D. Adler, J. Feinleib, J. Phys. Review **2**, 41(1969).
14. R. P. Mahajan, K. K. Patankar, N. M. Borange, S. C. Choudhari, A. Ghatage, and S. A. Patil, Indian J. of Pure and Appl. Phys. **38**, 615 (2008).
15. S. L. Kadam, K. K. Patankar, C. M. Kanamodi, B. K. Chougule, Mater. Res. Bull. **39**, 2265 (2004).
16. R. Das, T. Sarkar and K. Mandal, J. Phys. D: Appl. Phys. **45**, 455002 (2012).
17. M. Sahni, N. Kumar, S. Singh, Ashis Jha, S. Chaubey, M. Kumar and M. K. Sharma, J. Mater. Sci: Mater. Electron. **25**, 2199 (2014).
18. J. R. MacDonald, Impedance spectroscopy, Willey, New York, 1987.
19. A. Globus, P. Duplex, M. Guyot, IEEE Trans. Magn. **7**, 617 (1971).
20. R. A. M. Gotardo, D. S. F. Dionysio, S. D. Garcia, J. A. Eiras, M. F. S. Alves, L. F. Cotica, I. A. Santos, A. A. Coelho, J. Appl. Phys. **112**, 104112 (2012).
21. R. Gupta, J. Shah, S. Chaudwhary, S. Singh and R.K. Kotnala,. J. NanopartRe **15**, 2004 (2013).

International Conference on Mechanical Engineering 2015
(ICME 2015) 18 – 20 December, 2015, Dhaka, Bangladesh

Paper ID : 096

Controlling an Industrial Robotic Arm Using Light Dependent Gesture Recognition

Nahiduzzaman[1, a)], Sanzida Hossain[1, b)] and Altab Hossain[2, c)]

[1]*Mechanical Engineering Department, Military Institute of Science and Technology, Dhaka-1216, Bangladesh.*
[2] *Nuclear Science & Engineering Department, Military Institute of Science and Technology, Dhaka-1216, Bangladesh.*

a) Corresponding author:eefat92@gmail.com
b)sanzi_hoss@yahoo.com
c)altab76@gmail.com

Abstract. Gesture control is a method of Human Machine Interfacing (HMI) using motion of the human body parts. This paper presents the construction of a model industrial robotic arm and controlling it with light dependent gesture recognition. In a fixed lighted environment, the hand will cast a shadow of a fixed darkness which will move along with the moving hand. This phenomenon is used in our gesture control system which is comprised of low cost Light-Dependent Resistor (LDR) sensors and a Microcontroller which are used to track the consecutive positions of the shadow of the hand and guess the pattern indicated by the operator. Identifying different patterns indicated by the operator the Microcontroller commands the robotic arm to execute certain operations. The robotic arm has three types of movement which are rotation about a vertical axis, lifting up and down and opening and closing of the grip.

INTRODUCTION

In the present world machines have become an essential part of human life. A huge challenge of using these machines is communicating with these machines efficiently. The methods of communicating with machines are known as Human Machine Interface (HMI) [1]. There are various methods of HMI for passing commands to machine, which are mechanical switches, electronic remote, voice control [2], mind control [3], gesture control etc. The term “natural user interface” is becoming commonly used to describe interface systems like voice control, mind control and gesture control, reflecting the general lack of any intermediate devices between the user and the system. Gesture control is the ability to recognize and interpret movements of the human body in order to interact with and control a computer system without direct physical contact [4]. An efficient gesture control is the easiest to handle because this requires minimum effort and even disabled people can use this method.

Gesture control system can be done by image processing [5,6] ultrasonic sensor [7,8] and other various methods. Here we attempted a different approach to detect gesture indication by detecting the variation of light intensity over a sensor while a hand moves over it. Light intensity varia00tion is measured by LDR sensors’ voltage fluctuations. These LDR sensors come at a cheap price and are quiet available. That’s why using these sensors make the construction of these gesture control system very low cost.

CONSTRUCTION AND MECHANISM

Final actuation of the system is the different movements of a robotic arm. To complete this action the system depends on some input and output signal conditioning and mechanical actuation procedure. Thus the whole construction has two major parts, electrical circuitry and mechanical structure. The electric circuitry deals with sensors and all other equipment and mechanical structure includes motor and physical construction.

Arrangement of sensors

The gesture of the hand is detected in a few patterns over the sensors at various positions. Our construction demonstrates the simplest form of this method. We used four sensors for detecting those patterns. Positions of the sensors are shown in figure 1.

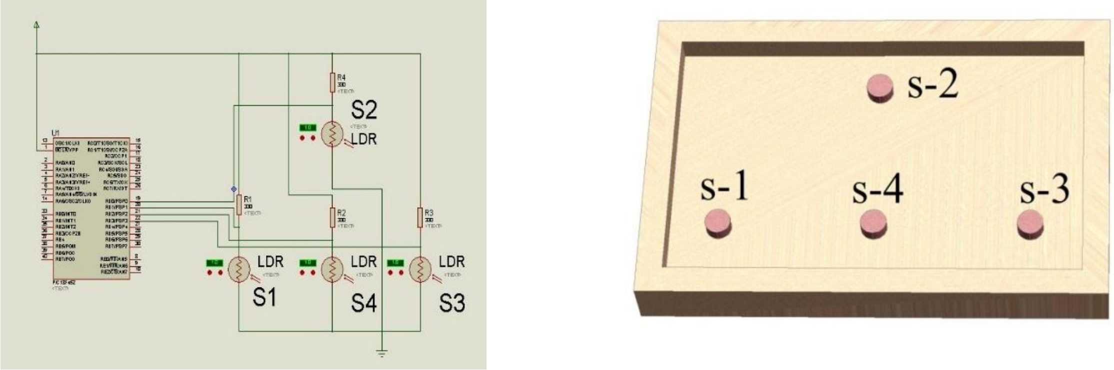

(a) (b)

FIGURE 1. Positions and connections of the LDR sensors (a) circuit connection (b) on the control panel

Mechanical Structure and motor arrangement

The mechanical structure of the robotic arm has three motors located at three different places to give the arm three different motions. The schematic diagram of mechanical structure of the robotic arm is shown in figure 2.

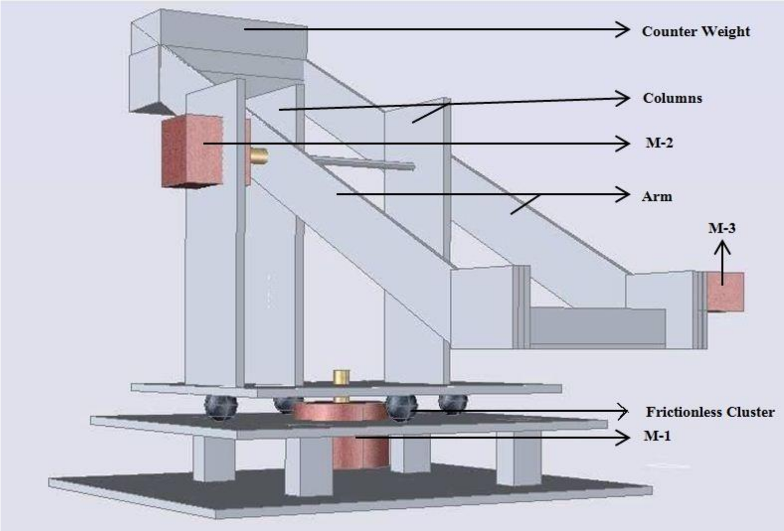

FIGURE 2. Arm Structures and Motor Positions.

Where motor m-1 gives rotational motion, motor m-2 gives up-down motion and motor m-3 opens and closes the grip of the arm by a driving a rack and pinion through a belt drive. There are two push buttons to give signal to micro controller indicating the arm has reached the top and bottom position. A counter weight is placed in the opposite of the grip to reduce the required torque during up and down movement. The effective length of the columns is reduced by adding bar in the lowest portion of the column. This reduces columns' buckling effect.

Command execution according to gesture pattern

Our system deals with six different patterns to execute six commands.

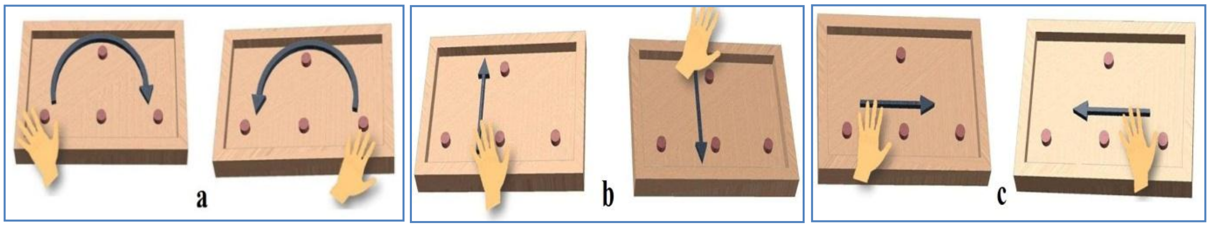

(a) (b) (c)

FIGURE 3. (a) Turning of arm (b) Up-down movement (c) Opening and closing of grip

As shown in figure 3 when the operator moves his hand in a clockwise and anti-clockwise circular motion on x-y plane motor M-1 will cause the arm to move clockwise and anti-clockwise direction respectively. The motor will continue to transmit mechanical power until the operator stops gesture pattern indication. When the operator moves his hand along y-axis in negative and positive direction motor M-2 will cause the arm to move up and down respectively. When operator moves his hand in a translatory motion along x-axis in negative and positive direction motor M-3 will cause the grip to open and close respectively.

METHOD OF OPERATION OF THE SENSORS

When light is incident on the LDR sensor its resistance decreases. At a fixed lighting environment the darkness of the shadow varies with the distance of the hand from the sensor. The relationship between output voltage of the sensor (V) and distance of hand (d) is as follows:

$$\mathrm{v} \propto \frac{1}{d} \qquad (1)$$

This phenomenon is used to locate the position of the hand. When there is nothing upside the sensor the output voltage is low and operator moves hand upside the sensor the voltage increases due to change in resistance. Thus for a certain reference value the position of hand can be detected.

RESULTS AND DISCUSSIONS

The experiment is performed in outdoor (day light) and indoor lighting conditions to determine the suitable environment for the better performance of the system. The output voltage is the main parameter that serves to detect presence of hand of the operator. As the output voltage varies with the varying distance of the hand, it is important to learn the variation of voltage with varying distance of hand in different lighting conditions.

The following results were found while doing the experiment, which represent output voltage of the sensor with different distance of the hand from the sensor:

TABLE 1. Output voltage for different distance at different lighting condition

Distance of hand (inch)	**Output voltage of sensor(V) at Daylight (outdoor)**	**Output voltage of sensor(V) at fixed light (indoor)**
No Hand	0.45	1.7
5	0.5	3.1
4	0.65	3.95
3	0.75	4.2
2	0.9	4.7
1	1.15	4.95

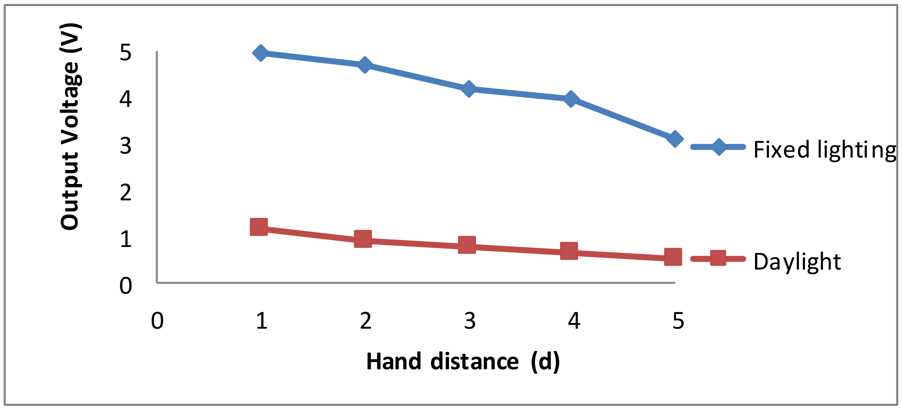

FIGURE 4. Output voltage vs. Hand distance graph for different lighting conditions

As we can see from above experimental results, the distribution of the voltage in daylight is less (0.5V-1.15V) than that of indoor fixed lighting condition (3.1V-4.95V). Also the difference of free sensor output to least hand distance output is low for daylight condition. This makes the indoor operation more suitable for the system, because the large distribution reduces operational difficulties of the operator. The reference voltage can be selected easily with a good expected accuracy. On the other hand for the day light condition it is very difficult to deal with quite small voltage range. This means the operator needs to move his hand very precisely and accurately to operate within the range of reference voltage.

When light source is not perpendicular to the control panel and light incidents at an angle from the source to the sensors, it causes the operating performance of the system to reduce. The following results were experienced for varying the incident angle of light on the sensor.

TABLE 2. Output voltage for different incident angle for indoor lighting

Distance of hand (inch)	**Output voltage of sensor(V) at 0°**	**Output voltage of sensor(V) at 30°**	**Output voltage of sensor(V) at 60°**
No hand	1.7	1.7	1.7
5	3.1	2.65	2.01
4	3.95	3.25	2.34
3	4.2	3.91	2.66
2	4.7	4.41	3.08
1	4.95	4.69	3.75

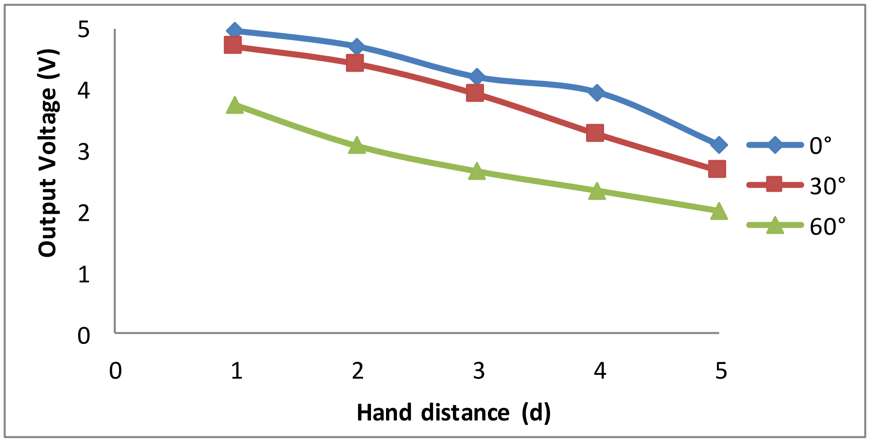

FIGURE 5. Output Voltage vs. Hand distance graph for different light inclination

If the light incidents on the sensors in an inclined manner, the movement of hand will have very less effect on the sensors and the sensor output voltage will vary within a very small range. This will make it difficult for the system to decide whether any gesture pattern is indicated or not. And the system may fail to take gesture as input at the exact time. This can cause output actuation to take place a little earlier or later which is not desired. From the above results it is seen that the more the incident angle increases the more is the performance reduced.

POSSIBILITIES AND LIMITATIONS

Same construction can be obtained by using more number of LDRs. But that will require a higher capacity microcontroller, which will increase the manufacturing cost. But using four LDRs as the system we mentioned above also capable of performing same tasks with acceptable efficiency. However system with more sensors can be constructed for much more efficient and precise gesture control which can be controlled from a longer distance. Arranging the LDRs in a 3 dimensional arrangement can be set up to identify motion in any direction and thus can take any gesture command as small as a finger movement. But LDR can react on motion only if the LDR is placed in the opposite side of the light. So if LDR is used in a three dimensional arrangement it can receive data only from one surface. However this problem can be solved by using a LASER-LDR pair. For each LDR one LASER will be set up in opposite direction. This will make the LDR work even more precisely. Thus the system can be made more accurate by using laser LDR pairs. Then the system will not depend on ambient light and the system can be used in outdoor conditions as well.

The same construction can be made by using ultrasonic sensor instead of LDRs. Ultrasonic sensors are not dependent of light. So they can also be used in outdoor applications unlike LDR sensor. This adds a major advantage to the system. However Ultrasonic sensors are more expensive than LDR, which will increase the manufacturing cost. Also these sensors receive signal from a conical region, making it difficult to use higher number of sensors in a single system and may require specially made sensors.

CONCLUSION

Gesture control system is beneficial for old and physically disabled people while communicating with machines. Nowadays gesture control is used in military purpose and also in so many home appliances. Though our system is shown for industrial purpose only it can also be used in domestic and outdoor environment with some improvements like using sensors in a 3D matrix, using LASER-LDR pairs etc. as described earlier. With the advancement of science the physical interaction of human with machines are lessening day by day. Our finding can be used to further eliminate the need for interacting media to communicate with machines in a low cost because of using cheap LDR sensors. This will help to reduce cost in manufacturing, maintaining and repairing such system. A specially made robotic arm with good mechanical design as shown in this paper can be used for industrial purpose and which can be useful in transporting industrial goods from one place to another. Controlling such robotic arm with gesture pattern as discussed earlier will make it easier and efficient to handle.

ACKNOWLEDGEMENTS

The authors sincerely acknowledge the support of Department of Mechanical Engineering, Military Institute of Science and Technology (MIST), Dhaka-1216.

REFERENCES

1. C. Fillyaw, J. Friedman, and S. M. Prabhu, Testing Human Machine Interface (HMI) Rich Designs using Model-Based Design, The MathWorks, Inc.
2. A. Q. AL-Thahab, Journal of Babylon University, Pure and Applied Sciences **19(3),**1123-1139 (2011).
3. L. Thunuguntla, R.N.V. Mohan, P. Mounika, Int. Journal of Engineering Research and Applications **4, 195-198 (**2014).
4. N. Petersen, D. Stricker, Continuous Natural User Interface: Reducing the Gap Between Real and Digital World, IEEE International Symposium on Mixed and Augmented Reality, Science and Technology Proceedings, Orlando, Florida, USA, 2009.

5. H.K. Kaura, V. Honrao, S. Patil, P. Shetty, Gesture Controlled Robot using Image Processing, International Journal of Advanced Research in Artificial Intelligence**2(5)**,(2013).
6. M. Becker, E. Kefalea, E. Macel, C.V.D. Malsburg, M. Pagel, J. Triesch, J.C.V. Uggen, R.P.W. Urtz and S. Zadel, A Gesture-controlled Robot for Object Perception and Manipulation, Autonomous Robots, **6,** 203-221 (1999), Kluwer Academic Publishers, Boston.
7. N. Gupta, R. Singh, S. Bhatia, Hand Gesture Recognition Uning Ultrasonic Sensor and ATMEGA128 Microcontroller, IJRET: International Journal of Research in Engineering and Technology eISSN: 2319-1163.
8. G.S. Rao, D. Bhattacharya, A. Pandey, A. Tiwari, Dual Sensor Based Gesture Robot Control Using Minimal Hardware System, International Journal of Scientific and Research Publications **3(5),** (2013).

International Conference on Mechanical Engineering 2015
(ICME 2015) 18 – 20 December, 2015, Dhaka, Bangladesh

Paper ID : 105

Irradiation Effect on Parasitic Resistance of Monocrystalline Photovoltaic Solar Cell

Md. Nazrul Islam[1,a)], Md.Arifur Kabir[2], S.M Sifat Morshed Chowdhury[3,b)], Sharif Mohammad Mominuzzaman[4]

[1,2] Research & Technical Services, Bangladesh National Power Grid, Dhaka, Bangladesh
[3,4] Department. of Electrical & Electronic Engineering, Bangladesh University of Engineering and Technology (BUET), Dhaka, Bangladesh

a)Corresponding author:nazrul@pgcb.org.bd.
b)sifat04@gmail.com

Abstract. Resistive effects in solar cells reduce the efficiency of the solar cell by dissipating power in the resistances. The most common parasitic resistances are series resistance and shunt resistance. The key impact of parasitic resistance is to reduce the fill factor. Both the magnitude and impact of series and shunt resistance depend on the geometry of the solar cell, at the operating point of the solar cell. This paper gives an idea about how the solar cell performance changes with the change in irradiance in reality and the result is shown by conducting a number of experiments. In this paper authors have developed a empirical equation for the irradiation effect on series resistance of solar cell by using experimental data and try to show that parasitic resistance of the solar cell be a function of irradiance that was not considered in any PV model. All effects are observed from 105 W/m^2 to 602 W/m^2 in this experiment.

1. INTRODUCTION

Solar PV cells are electronic devices that use P-N junctions to directly convert sunlight into electrical power. A complex relationship between voltage and current is exhibited by the P-N junction in the solar cell.

Solar cells capture slow-moving low energy electrons. These effects are saturated and cause a fixed energy loss under bright light condition. However, on an overcast day i.e. at lower insolation levels these mechanisms show an increasing percentage of the total power generated. Too much insolation causes saturation of cells, and the number of free electrons or their mobility decreases greatly. Characterization and performance evaluation of photovoltaic modules under a natural insolation play a very important role in photovoltaic research and is essential in realizing the scope of new technologies on the horizon [1]. The specifications given by the manufacturers of different types of silicon PV modules are usually for standard test conditions (STC i.e. 1000 W/m^2 irradiance, 25^{0}C cell temperature and AM 1.5 global spectrum) [2]-[5].

This paper is organized as follows: Section II presents characteristics of PV solar cell. Experimental setup and results are presented in Section III and Section IV respectively. In this section it is shown that series resistance gradually decreases with increasing irradiation. Conclusion of this work is given in Section V. Finally, References of this work are given.

Nomenclature

I_{sc}	Short circuit current	A	Ideal factor
V_{oc}	Open circuit voltage	R_s	Series resistance
MPP	Maximum power point	R_{sh}	Shunt resistance
FF	Fill factor	I_{PH}	Photo current
P_{max}	Maximum power	T_C	Cell working temperature

G	Solar irradiation	I_S	Cell saturation of dark current

2. CHARACTERISTICS OF SOLAR CELL

The fundamental parameters related to solar cell characteristics are Short circuit current (ISC), Open circuit voltage (VOC), Maximum power point (MPP) and Fill factor [6]. A general mathematical description of I-V output characteristics for a PV cell has been studied for over the past four decades. Such an equivalent circuit-based model is mainly used for the MPPT technologies. The simplest equivalent circuit of the general model which consists of a photo current, a diode, a parallel resistor expressing a leakage current, and a series resistor describing an internal resistance to the current flow, is shown in Fig. 1.

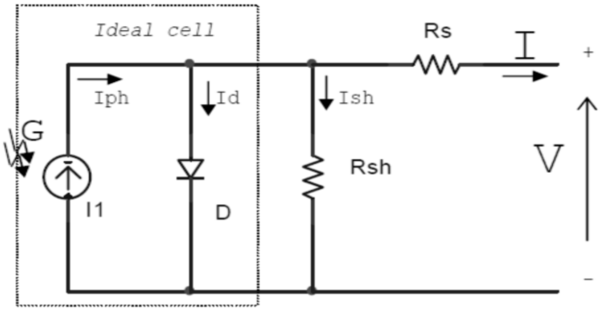

FIGURE 1. PV Cell Equivalent Circuit Model

The voltage-current characteristic equation of a solar cell is given as $I = I_{PH} - I_S\,[\exp\,(\,q(V + IR_s) / KT_CA) - 1] - (V + IR_s)/R_{sh}$, where I_{PH} is a light-generated current or photocurrent, I_S is the cell saturation of dark current, q (= 1.6 $\times 10^{-19}$C) is an electron charge, k (= 1.38 $\times 10^{-23}$J/K) is a Boltzmann's constant, T_C is the cell's working temperature, A is an ideal factor, R_{sh} is a shunt resistance, and R_s is a series resistance. The photocurrent mainly depends on the solar insolation and cell's working temperature, which is described as $I_{PH} = [I_{SC} + K_I\,(T_C - T_{Ref}\,)]G$, where I_{SC} is the cell's short-circuit current at a 25°C and 1000W/m^2, K_I is the cell's short-circuit current temperature coefficient, T_{Ref} is the cell's reference temperature, and G is the solar irradiation in W/m^2.

On the other hand, the cell's saturation current varies with the cell temperature, which is described as $I_S = I_{RS}\,(T_C / T_{Ref}\,)^3 \exp[qE_G\,(1/T_{Ref} - 1/T_C\,)/\,kA]$, where I_{RS} is the cell's reverse saturation current at a reference temperature and a solar radiation, E_G is the bang-gap energy of the semiconductor used in the cell [7].

3. EXPERIMENTAL SETUP

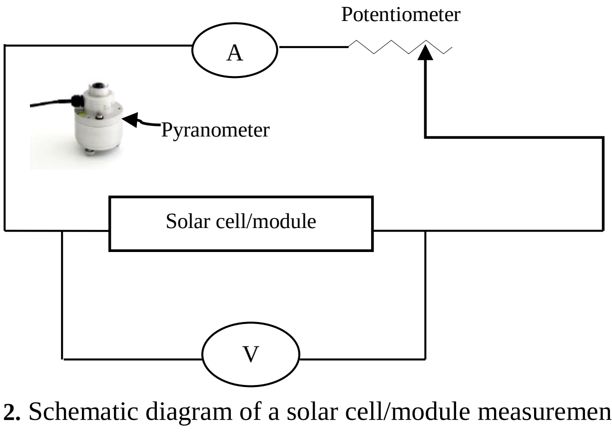

FIGURE 2. Schematic diagram of a solar cell/module measurement system

In this study, the block diagram of the experimental set up is shown in Fig. 2. It consists of a rheostat, a Pyranometer to measure the solar radiation, two digital multi-meters and a solar panel that has the key specifications listed in table1.

TABLE 1. Major specifications of the experimental module

Shinew XH SERIES,Model:XH-36M-5	
Maximum power (V_{mp})	5w
Open circuitVoltage (V_{oc})	21.47V
Short circuit current (I_{sc})	310m A
Voltage at P_{max}	17.40 V
Current at P_{max}	290 mA
Module dimensions	342×160×25mm
Module weight	0.8kg
Cell type	Mono crystalline
No.of cells	36 in series
Data measured in standard condition(STC):Irradiation 1000 W/m^2,AM1.5,cell temperature 25^0C,Tested according to:IEC 61215 and IEC 61730	

4. EXPERIMENTAL RESULT

The term Irradiance is defined as the measure of power density of sunlight received at a location on the earth and is measured in watt per metre square whereas irradiation is the measure of energy density of sunlight. The term Irradiance and Irradiation are related to solar components. As the solar irradiation keeps on changing throughout the day similarly I-V and P-V characteristics varies with the increasing solar irradiance both the open circuit voltage and the short circuit current increases and hence the maximum power point varies which shows in Fig. 3 and Fig. 4.

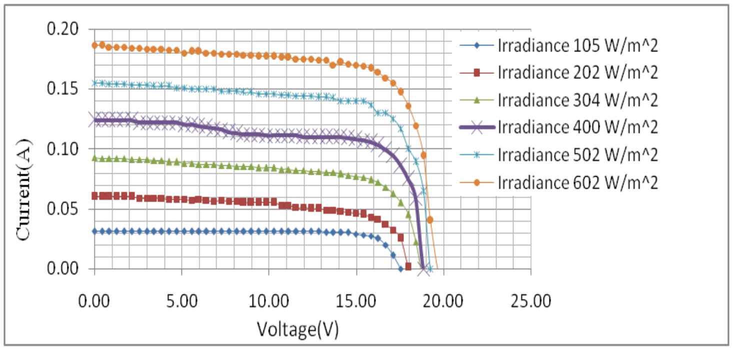

FIGURE 3. Current- voltage characteristics at six various irradiance levels

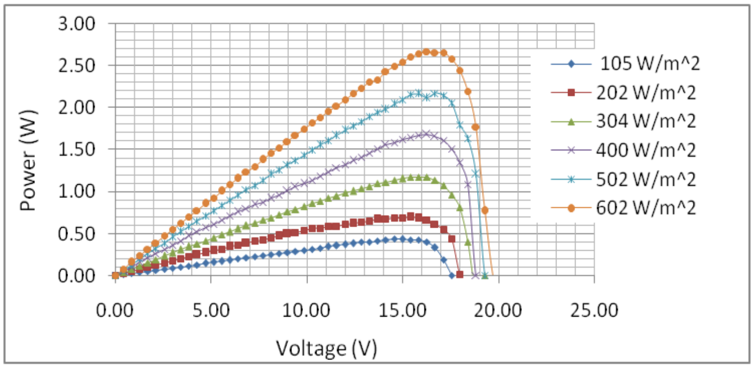

FIGURE 4. Power versus voltage characteristics at six different irradiance levels

In Fig. 3 shows the I-V characteristics at six different irradiation levels. It is observed that the value I_{SC} which is minimum (0.03A) at irradiation, 105 W/m^2 and it is maximum (0.19A) at irradiation, 602 W/m^2. In Fig. 4 shows the P-V characteristics at six different irradiation levels. It is observed that the value P_{max} which is minimum (0.226w) at irradiation, 105 W/m^2 and it is maximum (2.6 w) at irradiation, 602 W/m^2.

Series resistance in a solar cell has three causes: firstly, the movement of current through the emitter and base of the solar cell; secondly, the contact resistance between the metal contact and the silicon; and finally the resistance of the top and rear metal contacts. The main impact of series resistance is to reduce the fill factor, although excessively high values may also reduce the short-circuit current. Practically Series resistance is highly affected by irradiation but no model consider this effect. In Fig.5, the effect of irradiation on series resistance is shown. The raise of the series resistance is rapid for small illumination levels. This resistance varies from 116.25 ohms to 14.35 ohms between 105 W/m^2 to 602 W/m^2.

It is possible to approximate the series and shunt resistances, R_S and R_{SH}, from the slopes of the I-V curve at V_{OC} and I_{SC}, respectively. The resistance at Voc, however, is at best proportional to the series resistance but it is larger than the series resistance. R_{SH} is represented by the slope at I_{SC}. Typically, the resistances at I_{SC} and at V_{OC} will be measured and noted, as shown in Fig. 4.

Where

$$Rsh = \frac{\Delta Vsc}{\Delta Isc} \quad and \quad Rs = \frac{\Delta Voc}{\Delta Ioc}$$

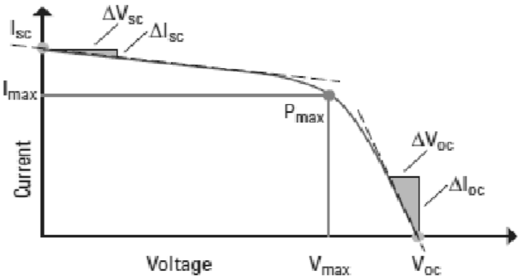

FIGURE 5. Obtaining Resistances from the I-V Curve

From Fig. 3, we found the value of R_s and R_{sh} by using method that is described in Fig. 5. In table 2, it is shown that the value of series and shunt resistance is varying with solar irradiance variation.

TABLE 2. Datasheet of series and shunt resistance w.r.t solar irradiance

Solar Irradiation(W/m^2)	100.00	200.00	300.00	400.00	500.00	600.00
R_s (Ω)	116.25	46.41	30.60	22.69	16.17	14.35
R_{sh} (Ω)	1071.20	1070.79	1070.79	1070.57	1070.36	1070.13

The authors have developed an empirical equation for the irradiation effect on series resistance of solar cell by using experimental data.

$$R_s(measured) = R_s(ref)\left[\mathrm{k1}\frac{\exp\left(\frac{\mathrm{k2}}{\mathrm{G}}\right)}{\sinh(\mathrm{k3}\times\mathrm{G})} \right] \tag{1}$$

Where

R_s (ref) =Value of series resistance at reference irradiation 1000 w/m^2, k1, k2 and k3 are constant [k1=1.5714, k2=27 and k3=0.001255], G=measured solar irradiance.

The experimental series resistance value and equation series resistance value are shown in table 3.

TABLE 3. Compare series resistance between experimental and developed equation value

Solar Irradiation(W/m^2)	100.00	200.00	300.00	400.00	500.00	600.00
R_s (Ω) (Experimental value)	116.25	46.41	30.60	22.69	16.17	14.35
R_s (Ω) (Equation Value)	114.47	49.62	31.21	22.48	17.33	13.92
Deviation error (%)	1.53%	6.91%	1.99%	0.92%	7.17%	2.99%

It is observed that Fig.6 follows this equation. The author could not able to measure the series resistance over 600 W/m^2 due to weather conditions of Bangladesh. But that value of series resistance is found by using the equation which is shown in Fig .6. It is observed that the experimental value and equation value are approximately same for all irradiance levels. In Fig. 7, It is described that how efficiency varying with varying series resistance of the solar cell. It is observed that efficiency is rising up with decreasing series resistance. Efficiency varies from 7.7% to 13.6% between 128.15 ohms to 14.35 ohms.

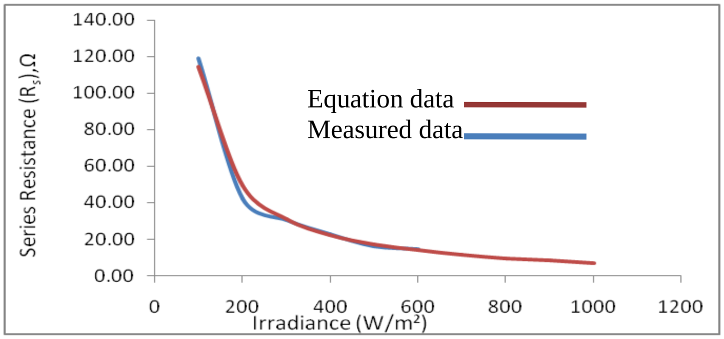

FIGURE 6. Series resistance as a function of solar Irradiance (compare between equation and measured value)

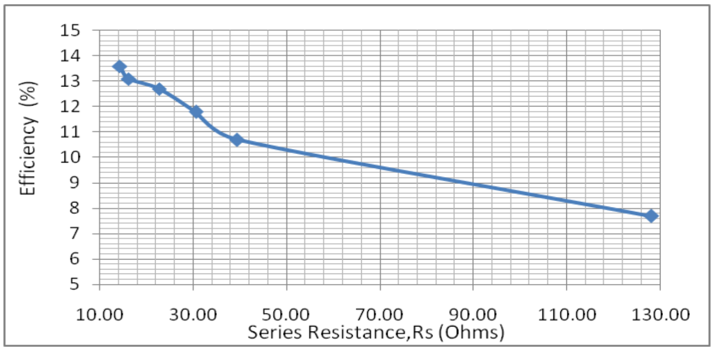

FIGURE 7. Efficiency as a function series resistance

Low shunt resistance causes power losses in solar cells by providing an alternate current path for the light-generated current. In Fig. 8, the effect of irradiation on shunt resistance is shown in below. The shunt resistance shows a marked dependence on the irradiance in this curve. It is observed from this curve, R_{sh} decreases with increasing irradiance. The change of shunt resistance, R_{sh} is not large. It is varied from 1071.2 ohms to 1070.13 between 105 W/m^2 to 602 W/m^2.

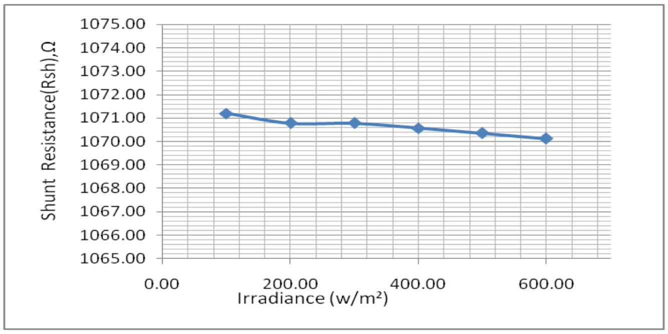

FIGURE 8. Shunt resistance as a function of solar irradiance

5. CONCLUSION

Parasitic resistance is the important parameters for solar cell but it is not given in nameplate by the manufacturers. The resistive behaviour tends to change the curve of the diode, resulting the above case as a decline in both the power and fill factor, regardless of I_{SC} and V_{OC} not change. In this paper, it is represented that how parasitic resistance affected by solar irradiation varying. It is observed that series resistance decreases largely with increasing irradiance and the change of shunt resistance is very small with increasing irradiance. Both are decreasing with increasing irradiance but it is improved efficiency for the change of series resistance and decreases efficiency for the change of shunt resistance. No PV model considers the effect of irradiation on parasitic resistance of solar cell/module. In future, it will be possible to develop a complete solar PV system model which considers the irradiation effect on parasitic resistance.

ACKNOWLEDGEMENTS

The authors would like to thank Department of Electrical & Electronic Engineering, Bangladesh University of Engineering & Technology for providing necessary experimental platform for research and analysis for the completion of the paper.

REFERENCES

1. T. Esram and P. L. Chapman, "Comparison of Photovoltaic Array Maximum Power Point Tracking Techniques," IEEE Transactions on Energy Conversion, **22(2),**439 – 449(2007).
2. Tariq salmi, Mounir Bouzguenda and Adel Gastil, International Journal of renewable energy research **2(2),** 2012
3. N. D. Benavides and P. L. Chapman, “Modeling the effect of voltage ripple on the power output of photovoltaic modules,” IEEE Trans. Ind.Electron. **55(7),** 2638–2643(2008).
4. Huan-Liang Tsai, Ci-Siang Tu and Yi-Jie Su, “Development of Photovoltaic Model Using MATLAB/SIMULINK”, Proceedings of the World Congress on Engineering and Computer Science WCECS, San Francisco, USA, 2008.
5. Jeyraj Selvaraj and Nasrudin A. Rahim, “Multilevel Inverter For Grid-Connected PV System Employing Digital PI Controller”, IEEE Transactions On Industrial Electronics **56(1),** 149-158 ,(2009).
6. S. Rustemli and F. Dincer, “Modeling of Photovoltaic Panel and Examining Effects of Temperature in Matlab/Simulink”, Electronics and Electrical Engineering, **109(3),** 35-40 (2011).
7. Kinal Kachhiya, Makarand Lokhande and Mukesh Patel, “Model of Solar PV Module and MPPT Algorithm”, Proceedings of the National Conference on Recent Trends in Engineering and Technology, 2011.

International Conference on Mechanical Engineering 2015
(ICME 2015) 18 – 20 December, 2015, Dhaka, Bangladesh

Paper ID : 124

Extraction of Fat From Cowhide Fleshings of Tannery: An Approach to Produce Byproduct

Md. Abul Hashem[a] , Md. Shahruk Nur-A-Tomal

Department of Leather Engineering, Khulna University of Engineering & Technology (KUET), Khulna-9203, Bangladesh

[a]Corresponding author: mahashem96@yahoo.com, mahashem@mail.kuet.ac.bd

Abstract. An investigation was carried out to estimate the extraction of fat from cowhide fleshings. In leather processing, just after liming, swollen pelts (lime treated hide/skin) have to pass through an operation to improve the diffusion of chemicals into pelt from the flesh side known as fleshing. Fleshing is the indispensable mechanical operations in leather processing where substantial amounts of inevitable solid waste (termed as fleshings) is produced. Generally fleshings' is kept indiscriminately inside or outside the industrial area as green, which has negative effect on the environment including human health. It contains a considerable amount of fat, which could be a great source for the production of byproduct: soap, glycerine, biogas, biodiesel etc. To extract fat, collected fleshing was delimed with boric acid and hydrochloric acid for 5-6 hrs. The delimed fleshings' was then heated with water bath (water: fleshings =1:1). After clearly separated fat from the fleshings, finally fat was collected from the aqueous phase. Assays were carried out to optimize the extraction parameters: water bath temperature, extraction time and agitation. The optimized extraction conditions were temperature 75°C, extraction time 3 h without agitation. It was calculated 6.2% fats were extractable from the fleshings and yearly 638.6 MT fat could be extracted only from cowhide fleshings.

INTRODUCTION

Leather sector is one of the most export-oriented sectors of Bangladesh, which plays an important role in the national economy. According to the Export Promotion Bureau (EPB), in the fiscal year 2013-14 leather sector earned US$1.29 billion by exporting leather, leather products and footwear [1]. But due to generating vigorous amount of environmental pollutants, Department of Environment (DoE), Bangladesh has been categorized tannery as '**red**' category industry.

Tannery waste generation, disposal and management are causing serious problems to survive tannery especially in Bangladesh.Tannery produces a huge amount of environmental pollutants in the form of solid, liquid and gaseous besides it consumes substantial amounts of energy. The approaches of tannery waste management applied are not sufficient; considerable portions of such solid waste are used for landfills [2]. Cleaner and waste-free production is the prime requisite for the tanneries in terms of waste management.

Tanning is an essential operation to shield the raw hide/skin against microbiological degradation as well as to stabilize collagen with defined tanning agents. Leather processing (tanning) is a complex procedure comprising of several technological steps which produce a significant amount of waste. A group of researchers reported that every 10 kg of raw hide/skin processing converts only 2 kg of raw materials into leather and more than 6 kg is generated as solid wastes [3]. Of course, generation of solid waste is related to the characteristics of raw material and manufacturing process of hide/skin. There are 220 tanneries in Bangladesh; most of them are located at Hazaribagh, Dhaka. Daily 100 tons solid waste is produced from the tannery in the form of trimmings of finished leather, shaving dust, hairs, trimmed animal flesh skin/hide which contaminate the soil and water [4]. Most of the tannery solid wastes are generated in beamhouse especially in fleshing operation.

In tannery, firstly raw hide/skin undergoes the operation so-called unhairing and liming (commonly known as liming). In conventional liming operation, sodium sulphide (Na_2S) and lime (CaO) are used to remove keratinous substances (hair, wool, epidermis, etc.), interfibrillary proteins (albumins, globulins etc.) [5]. After liming, pelt (lime treated hide/skin) has to pass through an operation known as 'Fleshing'. Fleshing is one of the most indispensable mechanical operations in leather processing where substantial amounts of inevitable solid waste (termed as fleshings) is produced. The fleshing operation involves cutting or removing of unwanted part from the flesh side of pelt to improve the diffusion of tanning agents and chemical uptake into pelt from the flesh side. It is not possible to omit the fleshing operation as skipping it causes chemical wastage as well as good quality leather could not be produced. It is reported that fleshings' is the 50-60% of total solid wastes generated in the tanning industry [6].

FIGURE. 1. General dumping site view of fleshings near DND dam, Hazaribang.

In Bangladesh, yearly 33.80 thousand tons wet salted cowhide and 24.80 thousand tons wet salted goatskin are taken for leather production in which 10.3×10^3 MT fleshings from wet salted cowhide and 9.8×10^3MT fleshings from wet salted goatskin are generated during fleshing operation [7]. The produced a huge amount of fleshings' is kept indiscriminately inside or outside the industrial area as green (without treatment). Generally tanneries collect fleshings in wheelbarrow and dump nearby tannery area. In Fig. 1 shows the fleshings dumped at the western part of Hazaribagh near Dhaka-Narayanganj-Demra (DND) dam. As stated, fleshings' contains proteinaceous substances that are hydrolysed to amino acids through proteolytic bacteria; amino acids are further hydrolysed by bacteria, which liberate gaseous ammonia (NH_3), hydrogen (H_2), carbon dioxide (CO_2), volatile fatty acids (VFAs) etc., that are directly merged to the air [8]. The VFAs help to generate toxic hydrogen sulphide (H_2S) gas from the fleshings as equation (1). Individuals of the tannery area are frequently inhaled the liberated gaseous substances and suffering in difficulties. Fleshings' also has a negative effect on water and soil.

$$HS^{-}/S^{2-} + H^{+} \rightarrow H_2S \tag{1}$$

Fleshings' contains subcutaneous tissue, fat and flesh. It is composed of various constituents among them fat content is 4-18% [9]; fat content varies according to the type of animal, feeding and climate.

Many researchers have accounted to minimize the tannery wastes: reuse of liming liquor [10], enzymatic hair saving unhairing instead of hair burning liming [11, 12], recycling of spent chrome liquor [13, 14], chrome recovery from shaving dust [15], leather board from shaving dust [16], composite from buffing dust [17] etc. Fleshings' does not bargain important usage to extract fat to produce any byproduct although it contains a considerable amount of fat [18].

An attempt was made to extract fat from the fleshings of cowhide which could be used as raw material in byproduct production. The approach could also contribute a significant reduction in the environmental impact of inevitable solid waste and decrease the costs associated with disposal.

MATERIALS AND METHODS

Sampling

Cowhide fleshings' was collected from SAF Leather Industries Ltd., Jessore, Bangladesh just after fleshing operation in polyethylene bag and brought back to the laboratory immediately for experimentation.

Materials

Chemicals were used for the experiments, which are generally used in the tannery. Boric acid (commercial grade) hydrochloric acid (commercial grade) was used to obtain different action. Reagents (ethanol and potassium hydroxide) were used to determine total fat and acid value which was purchased from Merck Limited (India).

Characterization Of Fleshings

pH, moisture and total fat content of the collected fleshings were quantified in the laboratory. Moisture content (%) and total fat (%) was determined using standard methods as described in [19].

pH of the fleshings was measured with pH (UPH-314, UNILAB, USA) meter. Before measuring pH, the meter was calibrated.

To determine moisture content of the fleshings, about 5 g fleshings were heated at 103±2°C in drying oven until constant weight was obtained. The weight of dried fleshings was subtracted from weight of wet fleshings to obtain moisture content.

To determine the total fat content of the fleshings firstly the fat was extracted from it using a Soxhlet extractor. The weight of the conditioned distillation flask was measured. After extraction of fat from fleshings, mixture of fat and ethanol was transferred into distillation flask. The ethanol was evaporated from the distillation flask by heating at drying oven until constant weight was obtained. The dry weight of total fat was calculated by following equation (2).

$$\text{Total fat (\%)} = \frac{\text{Wt. of flask with extracted fat} - \text{Wt. of blank flask (conditioned)}}{\text{Dry wt. of fleshings}} \times 100 \tag{2}$$

Deliming Of Fleshings

The collected fleshings' was washed with water to remove unbound/free lime. Fleshing was chopped into small size to facilitate the next operations. The fleshings' was delimed with 2% (w/w) boric acid for about 5-6 hours to remove chemically bound lime. The pH of delimed fleshings was adjusted to 6-7 by treating with dilute hydrochloric acid and further washed with water.

Fat Extraction From Fleshings

The delimed fleshings were subjected to heating at water bath in a beaker with water (water: fleshings = 1:1) for several hours. After clearly separated fat from fleshings, the mixture was then transferred to the separating funnel and finally fat was separated from the aqueous phase. The residual water in fat was then distilled off. The extracted fat is shown in Fig. 2.

FIGURE. 2. Extracted cowhide fat.

Optimization Of Extraction Process

Assays were carried out to optimize the extraction parameters like water bath temperature, extraction time and agitation, so that higher amount along with better quality fat could be attained for large scale extraction. The experiments were performed for optimization is shown in Table 1. The optimized conditions were established by investigating the percentage of fat and acid value of the extracted fat from the fleshings. To optimize the parameters 100 g delimed fleshings was taken in each experiment.

TABLE 1. Factors of fat extraction from fleshings and its experimental levels.

Temperature (°C)	Time (hour)	Agitation
55	1	Yes
65	2	No
75	3	
85	4	
95	5	

Analysis For Process Optimization

The amount of extracting fat (%) was determined as discussed in section 2.3. The weight of the conditioned evaporating dish was first measured using an analytical balance. After extraction of fat from fleshings, mixture of fat and water was transferred into the evaporating dish and heated at drying oven until constant weight was obtained. The percentage of extracting fat (dry weight) was calculated by following equation (3).

$$\text{Extracted fat (\%)} = \frac{\text{Wt. of evp. dish with extracted fat} - \text{Wt. of blank evp. dish (conditioned)}}{\text{Total fat in fleshings}} \times 100 \qquad (3)$$

The acid value of extracted fat was determined by following ISO EN 3682 standard method. A standard acid-base titration with a standard solution of 1.0 M potassium hydroxide solution was performed to measure the acid value.

RESULTS AND DISCUSSION

Characteristics Of Fleshings

In Table 2 shows the characteristics of the collected fleshings. It seems that pH (>12) was highly alkaline because of introduction of lime and sodium sulphide in liming operation. Therefore, it was necessary to neutralize fleshing by means deliming to eliminate sodium sulphide and lime. Fleshing was contained 9.1% fat, which designates that it would be used as raw material for other industries as a source of fat. Simple technique could be employed to extract fat from the fleshings.

Table 2. Characteristics of untreated fleshings.

Parameter	Value
pH	12.2 ± 0.1
Total fat (%)	9.1 ± 0.2
Moisture content (%)	66.3 ± 0.4

Optimization Of Extraction Process

The results obtained from assays to determine the effect of agitation to extract fat from fleshings is represented in Fig. 3. Negative result was perceived with agitation. Agitation increased the percentage of extracted fat, but contrarily increased the acid value, i.e. contributed contamination of free fatty acid which was undesirable. With agitation leads to degrade fat, thus significantly acid value was increased. The best extraction of fat was attained without agitation.

Experiments were carried out to determine the optimum time for extraction of fat. Fig. 4 discloses the effect of extraction time, which indicates that with the increase of time the percentage of extracted fat was increased significantly to a certain level beyond this small increase, was encountered and acid value of extracted fat was increased expressively. As beyond certain extraction time actual little amount of fat was extracted oppositely the extracted fats get degraded consequently acid value was increased. According to the analysis outcomes, 3 hours was selected as the optimal extraction time.

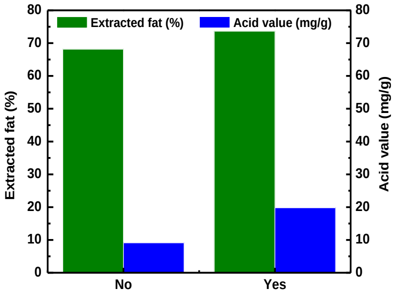

FIGURE. 3. Effect of agitation.

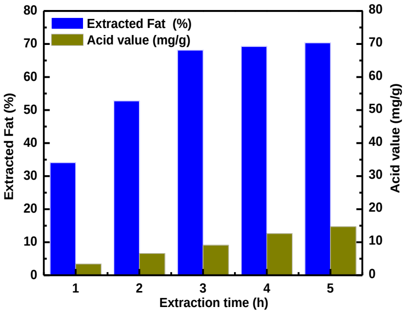

FIGURE 4. Effect of extraction time.

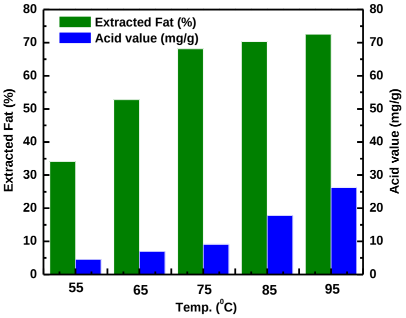

FIGURE. 5. Effect of temperature.

The water bath temperature had a significant effect on extraction of fat, which is represented in Fig. 5. It is observed that the acid value of extracting fat was increased noticeably in elevated temperature, which indicates degradation of fat is more at higher temperature. At the same time with increasing temperature, percentage of extracting fat was increased extensively to a certain level; beyond this level slight increase in percentage of extracting fat was observed. Based on the experimental data, temperature 75°C was considered as optimal extraction time.

Since the observations, it could be concluded that the best extraction conditions were found: temperature 75°C and extraction time 3 hours without agitation.

Estimation Of Extracted Fat

It was calculated that 6.2% (dry weight) fats were extractable at the optimized conditions. It was estimated that yearly 638.6 MT fat could be extracted only from cowhide fleshings. Extraction of fats from the fleshings could be a potential source for byproduct production.

Simple technologies could allow extracting fat as input for other processing industries in the form of raw material, which will consent producing useful end products. Researches on this issue could contribute a significant reduction the environmental impact of the inevitable solid wastes besides decreases the costs associated with disposal of the wastes.

CONCLUSION

An attempt was carried out to extract fat from fleshings for using in byproduct production. The characteristics of collecting fleshings disclose that obviously fleshing is a source of fatty substance. It was estimated yearly 638.6 MT fat could be extracted only from cowhide fleshings. The huge amount of extracted fat from the fleshings could be a great source for the production of byproduct such as soap, glycerin, biogas, biodiesel etc. The attempt could be enable the production of valuable products from the inevitable waste from tannery consecutively reduction of environmental pollution.

REFERENCES

[1] Export Promotion Bureau (EPB), Ministry of Commerce, Bangladesh, 2014.

[2] K. Wieczorek-Ciurowa, S. Famielec, K. Fela, The process of waste incineration in the tanning industry, CHEMIK 65 (2011) 917–922.

[3] R. Boopathy, S. Karthikeyan, A. Mandal, G. Sekaran, Characterisation and recovery of sodium chloride from salt-laden solid waste generated from leather industry, Clean Tech. Environ. Policy 15 (2013) 117–118.

[4] Accountants and Business Advisers (PKF), Technical report: leather sector includes a value chain analysis and proposed action plans, Bangladesh INSPIRED, Dhaka, 2013.

[5] S. Jian, T. Wenyi, C. Wuyong C, Kinetics of enzymatic unhairing by protease in leather industry, Journal of Cleaner Production 19 (2011) 325–331.

[6] J. Kanagaraj, K.C. Velappan, N.K. Chandra Babu, S. Sadulla, Solid wastes generation in the leather industry and its utilization for cleaner environment-A review, Journal of Scientific and Industrial Research 65 (2006) 541–548.

[7] M.A. Hashem, M.S. Nur-A-Tomal, B.K. Mondal, Solid waste generation during fleshing operation from tannery and its environmental impact: Bangladesh perspective, Proc. of the 2nd International Conference on Advances in Civil Engineering (ICACE-2014), CUET, Chittagong, Bangladesh, December 26–28, 2014, 32–37.

[8] P. Shanmugam, N.J. Horan, Optimising the biogas production from leather fleshing waste by co-digestion with MSW, Bioresource Technology 100 (2009) 4117–4120.

[9] R. Lupo, Fleshing treatment and compacting, Proc. of the IULTCS II. Euro Congress, Istanbul, Turkey, May 24–27, 2006.

[10] C.A. Money, Adminis, U. Recycling of lime-sulfide unhairing liquors I. Smallscale trials, J. Soc. Leather Technol. Chem. 58, 35–40, 1974.

[11] V. Valeika, K. Beleska, V. Valeikiene, V. Kolodzeiskis, An approach to cleaner production: from hair burning to hair saving using a lime-free unhairing system, Journal of Cleaner Production 17 (2009) 214–221.

[12] A. Dettmer, É. Cavalli, M.A.Z. Ayub, M. Gutterres, Environmentally friendly hide unhairing: enzymatic hide processing for the replacement of sodium sulfide and deliming, Journal of Cleaner Production 47 (2013) 11–18.

[13] A.D. Covington, R.L. Sykes, J.R. Barlow, E.T. White, A practical chrome recovery system using magnesium oxide. J. Soc. Leather Technol. Chem. 67 (1983) 5–12.

[14] K.J. Sreeram, J.R. Rao, R. Sundaram, B.U. Nair, T. Ramasami, Semi-continuous recovery of chromium from wastewater, Green Chem. 2 (2000) 37–41.

[15] M. Erdem, Chromium recovery from chrome shaving generated in tanning process, Journal of Hazardous Materials B129 (2006) 143–146.

[16] A. Crispim, M. Mota, Leather shavings treatment: An enzymatic approach. J. Soc. Leather Technol. Chem. 87 (2003) 203–207.

[17] M.A. Hashem, M.S. Nur-A-Tomal, Fabrication of composite from leather buffing dust for using in footwear and leather products industry, Proc. of the 3rd International Leather Engineering Congress: Innovative Aspects for Leather Industry 2015 (IAFLI-2015), Izmir, Turkey, 21–22 May 2015.

[18] S. Çolak, G. Zengin, H. Özgünay, Ö. Sari, A new and environmental friendly method for utilization of leather industry fleshings: Biodiesel, Proc. of the IULTCS II. Euro Congress, Istanbul, Turkey, May 24–27, 2006.

[19] C. Carpenter, Determination of fat content, Food Analysis Laboratory Manual: Food Science Texts Series, Springer US, 2010, 29–37.

International Conference on Mechanical Engineering 2015
(ICME 2015) 18 – 20 December, 2015, Dhaka, Bangladesh

Paper ID : 134

Development of A Two Wheeled Self Balancing Robot with Speech Recognition and Navigation Algorithm

Md. Muhaimin Rahman [a], Ashik-E-Rasul[b], Nowab. Md. Aminul Haq[c], Mehedi Hassan[d], Irfan Mohammad Al Hasib[e] and KM. Rafidh Hassan[f]

Department of Mechanical Engineering, Bangladesh University Engineering and Technology, Dhaka-1000, Bangladesh

[a]Corresponding author: sezan92@gmail.com
[b] akif.extra@gmail.com
[c] aminulhaq.buet@gmail.com
[d] buetmehedi10@gmail.com
[e]irfanmohammadalhasib@gmail.com
[f] rafidh.06@gmail.com

Abstract. This paper is aimed to discuss modeling, construction and development of navigation algorithm of a two wheeled self balancing mobile robot in an enclosure. In this paper, we have discussed the design of two of the main controller algorithms, namely PID algorithms, on the robot model. Simulation is performed in the SIMULINK environment. The controller is developed primarily for self-balancing of the robot and also it's positioning. As for the navigation in an enclosure, template matching algorithm is proposed for precise measurement of the robot position. The navigation system needs to be calibrated before navigation process starts. Almost all of the earlier template matching algorithms that can be found in the open literature can only trace the robot. But the proposed algorithm here can also locate the position of other objects in an enclosure, like furniture, tables etc. This will enable the robot to know the exact location of every stationary object in the enclosure. Moreover, some additional features, such as Speech Recognition and Object Detection, are added. For Object Detection, the single board Computer Raspberry Pi is used. The system is programmed to analyze images captured via the camera, which are then processed through background subtraction, followed by active noise reduction.

INTRODUCTION

Two wheeled Self Balancing Robots are one of the most widely discussed robots in the modern world and academia. Some reviews and previous works are at [1],[2],[3]. In this paper, the movement, the positioning system and navigation of the robot have been discussed. For navigation, a unique internal positioning system (IPS) has been developed. Previously, various IPS were developed like Wireless Indoor Positioning System [6] Ultrasonic Indoor Positioning System [7, 8]. But the common problem with those methods is that, those systems only could detect the robot in an enclosure. To locate other objects, wireless receivers with micro processors must be embedded on them. That will make the process more time-consuming. Also, the robot has to process huge amount of data from three Ultrasonic transmitters to get location, namely using the "Trilateration" technique. This process makes whole system slower. In this project, "Object tracking" method is proposed as a simple but effective solution for positioning. Because Object tracking method will allow not only to locate other objects in the enclosure but also it will take less time because the robot microprocessor will not need to do extra work. Another approach that makes this system unique is that, another PID controller [4] [5] is developed. There are various types of Methods for Object tracking. Such as Point tracking [9, 10], Kernel Tracking [11] and Silhouette Tracking [12, 13].In this project Point Tracking method is used. Because the Camera will be on much higher level than the robot, so Point Tracking will cause negligible error. Moreover, if Kernel or Silhouette tracking were used they will consume more time for processing signals which will make the system inefficient. In case of object detection methods there are also various methods [14]. Like Color Detection, Edge detection or Canny Edge Detector [15] etc. But these methods have some problems. Like Color Detection is too much simple and less accurate to specify the robot only. But Edge detection and Canny edge detectors are more time consuming. That is why the combination of the above three methods, Template Matching [16] is used in this project. For Vocal and visual information that can be used as communication media to allow machines to interact with people has attracted considerable attention in the development of intelligent human-machine interaction devices [17]. Speech processing has been one of the most exciting areas of the signal processing which has made it possible for machine to follow human voice commands and understand human languages. Automatic speech recognition (ASR) techniques have been widely used in numerous practical applications in recent years [18]. With the improvement of modern technology in case of smart phone devices and its device applications, the ASR function is attracting much attention to the people who has the fascination of communicating with the machine. The hidden Markov model (HMM) [19], artificial neural network (ANN) [20], and support vector machine (SVM) [21] are frequently used computational models for performing speech recognition tasks.

SELF BALANCING

Mathematical Modeling

The Basic Transfer Function that is used for this system is taken from Control tutorials of Prof. Bill Messner and Prof. Dawn Tilbury which are available at [23]. The Transfer Function is given below,

$$\phi(s) = \frac{\frac{ml}{s}}{s^3 + \frac{b(I+ml^2)}{q}s^2 - \frac{(M+m)mgl}{q}s - \frac{bmgl}{q}} f(s) \tag{1}$$

Where ϕ = yaw angle, M = Mass of Lower Base, m = Mass of Upper Part, I = Moment of Inertia b = Damping Coefficient and $q = [(M+m)(I+ml^2) - (ml)^2]$. Here *f*(s) is the Laplace Transformation of the Force Required, F(t). This force, is directly connected to the Torque of the Motor, τ.

$$\mathrm{F} = 2\tau r \tag{2}$$

Again, we can show that torque τ, is dependant on The Input Voltage of the Motor.

$$I = mr^2 \tag{3}$$

$$\tau = I\alpha \tag{4}$$

From [22], we know the relation between Input Voltage and Angular Displacement of the Motor,

$$\frac{\theta(s)}{E(s)} = \frac{\frac{K_t}{R_a J_m}}{s\left[s + \frac{1}{J_m\left(D_m + \frac{K_t K_b}{R_a}\right)}\right]} \tag{5}$$

Here, the value of $K_t R_a$ and K_b can be obtained from the Relationship between the Torque, τ and angular velocity ω [22],

$$T_m = -\frac{K_b K_m}{R_a}\omega_m + \frac{K_t}{R_a}e_a \tag{6}$$

We know that,

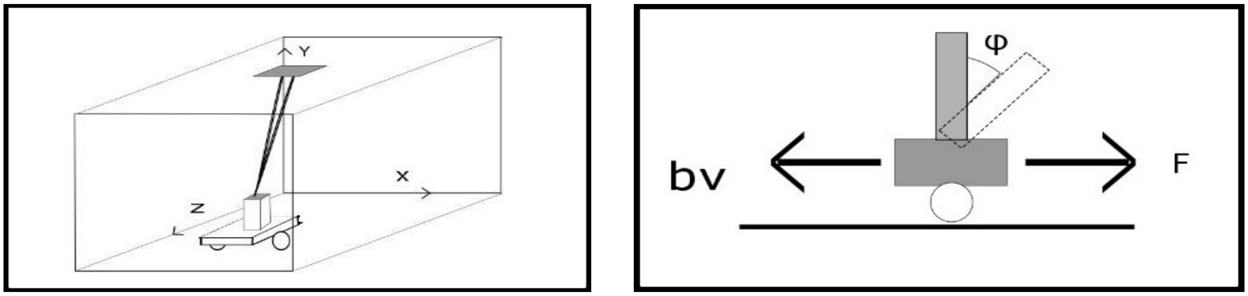

(a) (b)

FIGURE 1. (a) Free Body Diagram of The Positioning System , (b) Free Body Diagram of The Self Balancing.

$$\alpha(s) = s^2\theta(s) \tag{7}$$

So, the equation (5) will become,

$$\frac{\alpha(s)}{E(s)} = s\frac{\frac{K_j}{R_aJ_m}}{[s+\frac{1}{J_m}\left(D_m+\frac{K_jK_m}{R_a}\right)]} \tag{8}$$

Now, from equation (1),(2) ,(4) and (8) the final Equation will become ,

$$\phi(s) = AE(s) \tag{9}$$

Where,

$$A = \frac{ml}{s^3+\frac{b(I+ml^2)}{q}s^2-\frac{(M+m)mgl}{q}s-\frac{bmgl}{q}}\frac{1}{2mr^3}\frac{\frac{K_t}{R_aJ_m}}{[s+\frac{1}{J_m}\left(D_m+\frac{K_tK_b}{R_a}\right)]} \tag{10}$$

This is the Required relation between input voltage and yaw angle, ϕ.

Controller Design

By definition, the Formula for PID controller is

$$E = K_pe(t) + K_j\int e(t) + \frac{d}{dt}e(t) \tag{11}$$

Where,

$$e(t) = S_p - \phi(t) \tag{12}$$

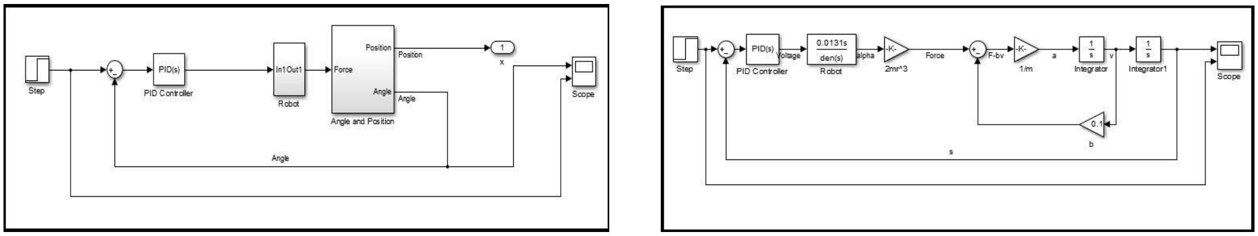

(a) (b)

FIGURE 2. SIMULINK Model of (a) Self Balancing Robot and (b) Navigation System

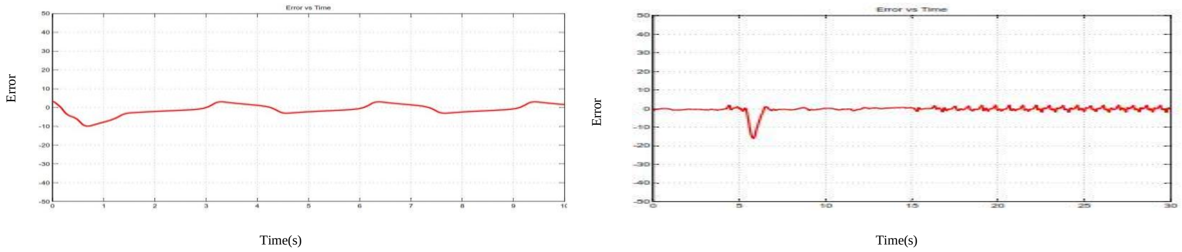

(a) (b)

FIGURE 3. (a) Simulation and (b) Practical Results

The Free body Diagrams of the project is shown in Fig. 1**.**

Simulation

A SIMULINK Model has been developed for the Self Balancing of the Robot (Fig. 2(a)). By trial and error the PID gains, K_p, K_d and K_i are determined . They are 113,1.38 and 0.13 respectively. Fig 3 shows the simulation results.

NAVIGATION SYSTEM

Algorithm

The Algorithm Used for Navigation System is given below,

1. Load the template and convert it to grayscale image.
2. Measure the Height and width of the template.
3. Start Capturing Images.
4. Convert Every Image into a Grayscale Image.
5. Match Template Using Squared Difference Method.
6. Search for the Minimum value in the resultant Probability Matrix.
7. If the Minimum Value is equal to Desired Calibrated Minimum Value, then the location of the minimum in the resultant matrix is the location of the top left corner of the template matrix.
8. Determine the Bottom Right Corner of the Resultant Template Matched Area. Then Derive the Center of the template averaging the points.
9. Else there is no robot in the room.
10. Go to Step 3.

Mathematical Model

For modeling the navigation system, we have to start again from equation (12). Using Newton's Second Law,

$$ma = f - bv \tag{13}$$

Where, b is the Damping Coefficient, which is assumed to be 0.1 and v is the linear velocity. m and a are mass of the robot and linear acceleration respectively. Now,

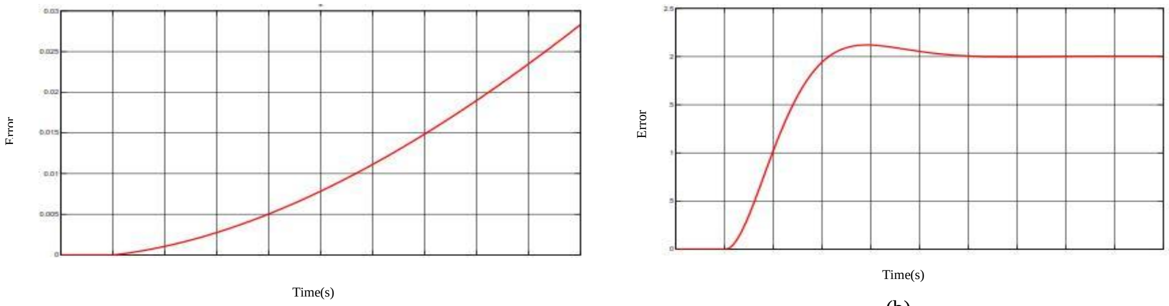

(a) (b)

FIGURE 4. Navigation System Simulation Results (a) Without Controller and (b) With Controller

$$x = \int\int a = \int\int \left[\frac{F-bv}{m}\right] \tag{14}$$

$$E = K_p e(t) + K_i \int e(t) + K_d \frac{d}{dt} e(t) \tag{15}$$

Where,

$$e(t) = S_p - x \tag{16}$$

The SIMULINK Block Diagram for the Navigation system is shown in Fig. 2(b) with PID controller block.

Simulation and Practical Results

Using SIMULINK PID controller block, the Correct PID parameters are determined using PID tuning. The gains are K_p = 2696, K_i=259 and K_d = -1321. The Simulation result using controller is shown in Fig. 4(b). We can observe from Fig. 4(a) that the position goes to infinite without the controller. Which won't happen if we use the controller. In Fig. 4 the Positioning of the Robot is shown. From the Image processing, the Location is shown to be x=693, y=1354. Which Corresponds to x = 18 and y = 44. The Real Position was x = 20, y=44 cm.

(a) (b) (c)

FIGURE 5. (a) Template (b) Detected Object (c) Prototype

OBJECT DETECTION

Algorithm

1. Capture Image.
2. Subtract Background using Template Matching.
3. Sharpen Noisy Images
4. Convert to Binary Images.

(a) (b) (c) (d)

FIGURE 6. (a) Prototype (b) Current Frame (c) Subtracted Background (d) Shape and Centroid Detection

5. Detect Shapes of the Object using Contour Detection Algorithm.
6. Determine Centroid of the Object by drawing Rectangles where ever Contours are Matched.
7. Go To Step 1. The Whole Process is shown in Fig. 6

SPEECH RECOGNITION

Algorithm

1. Take Voice Input
2. Filter the Signal Using Kalman Filtering. Original Voice Signal and High pass filtered signal is shown in Fig. 7
3. Translate the filtered signal to text Command.
4. Search Object according to the text
5. If No Object Name is stored in the memory surf through Internet to find the Object
6. Do Job according to the Voice Command
7. Go to Step 1.

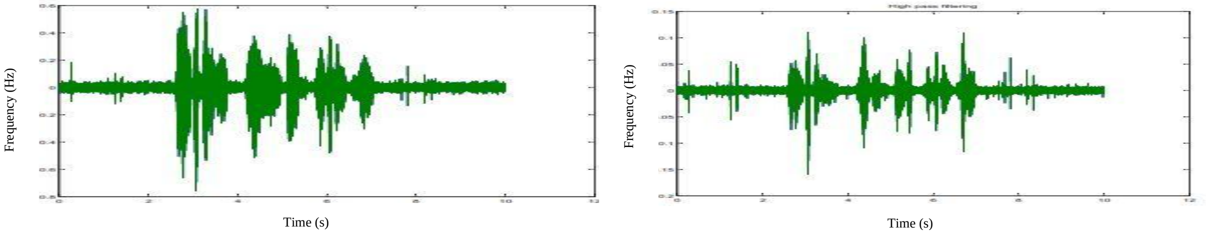

(a) (b)

FIGURE 7. (a) Original Voice Command (b) Filtered Voice Command.

CONCLUSION

The Prototype of the Robot is shown in Fig. 5(c). We have developed a mathematical model of the robot. Here, the input is Voltage supplied to the motors and the output is the yaw angle of the robot. Existing works on inverted pendulum always have force as input not voltage of the actuator. Also mathematical model has been developed for the navigation system. Controllers for both of the systems had been developed and the practical experiments' results match quite perfectly with the simulation results. The Use of Object tracking technique as Navigation system makes the robot move more accurately and smoothly. Here the Speed of the Image processing for Object tracking is increased using OpenCV platform. Again, the use of the "Raspberry Pi" makes the robot work fast for object detecting and sound processing. For processing the sound signal, "Kalman filtering" technique has been used. Still there are some areas of development and future work of the Robot. As the System is a Nonlinear System, we need to develop a non linear controller for best result. For navigation we need to devise algorithms for multi room enclosure. With all of these constraints the robot gave us best result.

REFERENCE

1. Junfeng Wu, Wanying Zhang and Shengda Wang, “A Two-Wheeled Self-Balancing Robot with the Fuzzy PD Control Method”, *Mathematical Problems in Engineering*, Volume 2012, Article ID 469491
2. Liang Sun and Jiafei Gan. “ Researching of Two-Wheeled Self-Balancing Robot Base on LQR Combined with PID”, *Intelligent Systems and Applications (ISA), 2010 2nd International Workshop* , 2010.
3. Rich Chi Ooi, “Balancing a Two-Wheeled Autonomous Robot”, The University of Western Australia, 2003.
4. Stuart Bennet, “Development of The PID Controller”
5. J. C. Basilio and S. R. Matos, “Design of PI and PID Controllers With Transient Performance Specification”, *IEEE TRANSACTIONS ON EDUCATION*, VOL. 45, NO. 4, NOVEMBER 2002.
6. Hui Liu, Pat Banerjee and Jing Liu. “Survey of Wireless Indoor Positioning Techniques and Systems”, *IEEE TRANS- ACTIONS ON SYSTEMS, MAN, AND CYBERNETICSPART C: APPLICATIONS AND REVIEWS*, VOL. 37, NO. 6, NOVEMBER 2007.
7. Khalid Hasnan , Said A. Elshayeb, Saparuddin Arin and Luhur Budi Saesar. “A REVIEW ON INDOOR GPS FOR MOBILE ROBOT POSITIONING USING ULTRASONIC” ,*World Engineering Congress 2010*, Malaysia Conference on Engineering and Technology Education, 2 nd 5th August 2010, Kuching, Sarawak, .
8. Carlos Medina, Jose Carlos Segura and Angel De la Torre. “Sensors 2013”, 13, 3501-3526; doi:10.3390/s130303501.
9. Trishan Esram and Patrick L. Chapman, “Comparison of Photovoltaic Array Maximum Power Point Tracking Techniques”, *IEEE TRANSACTIONS ON ENERGY CONVERSION*, VOL. 22, NO. 2, JUNE 2007.
10. Hohm, D.P., Ropp, ME, “Comparative study of maximum power point tracking algorithms using an experimental, programmable, maximum power point tracking test bed”, Photovoltaic Specialists Conference, 2000. *Conference Record of the Twenty-Eighth IEEE*, Page 1699 - 1702.
11. Dorin Comaniciu, Visvanathan Ramesh and Peter Meer. “Kernel-Based Object Tracking”
12. Nicholas R. Howe , “Silhouette Lookup for Automatic Pose Tracking”.
13. Li Guan, Jean-Sebastien Franco and Marc Pollefeys, “Multi-Object Shape Estimation and Tracking from Silhouette Cues”.
14. Omar Javed and Alper Yilmaz, “Mubarak Shah, Object Tracking: A Survey”, *ACM Computing Surveys*, Vol. 38, No. 4, Article 13, Publication date: December 2006.
15. Canny and John , “A Computational Approach to Edge Detection”, *IEEE Transactions on Pattern Analysis and Machine Intelligence* (Volume:PAMI-8 , Issue: 6), Page 679 - 698, Nov. 1986
16. Roger M. Dufour, Eric L. Miller, Nikolas P. Galatsanos, “Template Matching Based Object Recognition With Unknown Geometric Parameters”, *IEEE TRANSACTIONS ON IMAGE PROCESSING*, VOL. 11, NO. 12, DECEMBER 2002.
17. F.Harashima and S. Suzuki, “State-of-the-art intelligent mechatronics in human-machine interaction”, *IEEE Industrial Electronics Magazine*, vol. 4, no. 2, pp. 913, 2010.
18. S. K. Gaikwad, B. W. Gawali, and P. Yannawar, “A review on speech recognition technique”, *International Journal of Computer Applications*, vol. 10, no. 3, pp. 1624, 2010.
19. L. R. Rabiner, “A Tutorial on hidden Markov models and selected applications in speech recognition”, *Proceedings of the IEEE*, vol. 77, no. 2, pp. 257286, 1989.
20. A.K. Paul, D. Das, and M. M. Kamal, “Bangla speech recognition system using LPC and ANN”, in Proceedings of the IEEE 7th International Conference on Advances in Pattern Recognition (ICAPR 09), pp. 171174, Kolkata, India, February 2009.
21. A. Ganapathiraju, J. E. Hamaker, and J. Picone, “Applications of support vector machines to speech recognition”, *IEEE Transactions on Signal Processing*, vol. 52, no. 8, pp. 23482355, 2004.
22. Prof. Bill Messner and Prof. Dawn Tilbury, *Control Tutorials For MATLAB and SIMULINK*, University of Michigan, http://ctms.engin.umich.edu/CTMS/index.php?aux=Home
23. Norman S. Nise, *Control Systems Engineering*, 6th Edition, Page 8

International Conference on Mechanical Engineering 2015
(ICME 2015) 18 – 20 December, 2015, Dhaka, Bangladesh

Paper ID :138

Optimization of Machining Parameters for Minimizing Surface Roughness in Turning GFRP Composite Using ANN and PSO Methodology

Md. Shafiul Alam [1, a)], Ahmed Yusuf [1, b)], Abir Rahman [1, c)], Inzamam-ul-haq [1, d)], NR Dhar [2, e)]

[1] *Department of Mechanical and Production Engineering, Ahsanullah University of Science and Technology, Dhaka-1208, Bangladesh*
[2] *Department of Industrial and Production Engineering, Bangladesh University of Engineering and Technology, Dhaka-1000, Bangladesh*

a) Corresponding author: shafiul078.aust@gmail.com
b) ahmedyusuf91@gmail.com
c) rahmanabir85@gmail.com
d) inzi.ipe61@gmail.com
e) nrdhar@ipe.buet.ac.bd

Abstract. The influence of surface roughness in determining the quality of finished products in any industrial application has an enormous impact on gaining competitive edge and establishing superiority. Thus, recognizing and understanding the factors influencing the resulted surface roughness are the crucial issues helping to achieve the desired goal in any competitive industrial environment. Fact is that machining process parameters are major factors affecting the outcome. This research is focused on determining the optimum machining parameters (cutting speed, feed rate, depth of cut) which result in minimizing the surface roughness in turning glass fiber reinforced polymer (GFRP) matrix composite using coated carbide insert. To understand the effects of machining parameters on surface roughness and to determine relationship between them; Particle Swarm Optimization (PSO) has been employed. A multiple regression equation is used as objective function to determine the optimum values of inputs (cutting speed, feed, and depth of cut) using PSO formula and it yields an optimum value of surface roughness of 0.6252 µm. Artificial Neural Network (ANN) has also been implemented to predict various level of surface roughness for different machining parameters. To predict the surface roughness (R_a), standard multilayer feed-forward back-propagation hierarchical neural network has been applied and the findings provide an overall value of coefficient of determination of 0.88881. These investigations of turning operation provide optimal process parameters for a certain level of surface roughness resulting in gaining competitive edge in any industrial application.

INTRODUCTION

Through the history of our race-the human race, it is observed as well as understood that we are an ever burgeoning and blooming species evolving at every instance in the field of science, engineering and technology. A major key aspect of this era of modern engineering and technology brought by this evolution is the ability of recognizing the appropriate use of any material in various and discrete field of engineering and technology. In such cases getting the desired material for those particular engineering purpose is done by utilizing the proper use of composite material. The capability of composites for specific purposes has been one of their more advantages and also one of the greater challenges to adopting them as alternative to conventional materials [1-2].

When it comes to machining of glass fibre reinforced polymer matrix composite material (GFRP), it differs from the conventional material due to the anisotropic structure of this material. Furthermore, due to the reinforcement of fiber in polymer matrix the machining of composite materials exhibits some problem which is not the case for other conventional materials such as metals [3]. The users of FRP are facing so many difficulties when machining it, because technical back ground acquired for conventional materials cannot be applied for such new materials, whose ability to machining is different from that of conventional materials, thus it is desirable to experimentally investigate the behaviour of FRPs during the machining process[4]. Thus ensuring the desired level of quality in turning GFRP is much more difficult than the conventional materials. Surface Roughness and dimensional accuracy are the major factors needed to predict the machining performances of any machining operation [5]. Thus recognizing and understanding the required machining parameters for optimum surface roughness is crucial in determining the quality of the machining operation. Davimetal [6] studied the influence of cutting parameters on surface roughness in turning glass-fiber reinforced plastics using statistical analysis. Machining of composite materials depends on the type of fiber inserted in the composites, particularly by the mechanical properties. For optimization of the machining parameters, several quantitative methods have been developed to achieve the desired objectives. For the process of single objective optimization, several different techniques have been proposed such as geometric and stochastic programming [7], regression analysis [8], and Taguchi method and analysis of variance (ANOVA) technique [9].

In recent times Artificial intelligence based modelling approaches are becoming popular and thus advisable for real time applications out of which Artificial Neural Network (ANN) was found to be reliable, viable, and attractive [10]. An ANN based model was developed by O¨zel and Karpat to predict surface roughness and tool flank wear during finish dry hard turning of AISI H13 steel [11]. Leo and Varadarajan developed a model using ANN approach with fluid application parameters to simulate surface milling of hardened AISI4340 steel with minimal fluid application [12]. On the other hand, PSO technique was introduced by Kennedy and Eberhart [13] to solve continuous optimization problems Li et al. [14]. The optimization of process parameters for constant cutting force was discussed based-on virtual machining by Zhao et al. [15]. The framework of virtual machining based cutting parameters optimization was established by applying PSO methodology. Then two controlled experiments were conducted and the results of experiment showed that machining process with constant cutting force can be achieved via cutting parameters optimization based on virtual machining.

In this present research, PSO has been implemented to analyse and understand the effects of various process parameters on surface roughness in turning GFRP composite material. Factors considered in this experiment are cutting speed, feed rate and depth of cut. ANN has also been implemented to predict the data of machining process parameters. This investigation of turning operation provides optimal process parameters for any desired value of surface roughness which results in gaining a competitive edge over others in any industrial application.

EXPERIMENTAL STUDY

According to the objective of this research work stated earlier, a set of experimental data is to be generated by executing a first-hand experiment on effects of machining parameters in turning GFRP Composite. The experimental data is utilized to build a mathematical model using PSO formula. The data is also used to predict more conditions of possible machining process parameters by using ANN. Table 1 is provided stating the experimental conditions.

TABLE 1. Experimental Conditions

Process Parameters	**RPM, N**	**Feed Rate, So (mm/rev)**	**Depth of Cut, t (mm)**
	320	0.10	0.5
	500	0.14	1.0
	630	0.17	1.5
	800	0.20	2.0
Cutting tool	Coated Carbide Insert		
Environment	Dry		

A FORMAL STATEMENT OF ANN

Artificial Neural Networks (ANN) are a genre of statistically adaptive mathematical model inspired by biological neural network which are used for the purpose of approximation and estimation of functions of various individual fields that depend on a considerable number of inputs which are generally unknown. To design artificial neural networks, basic configuration and elements which are required have been presented in the Fig. 1. The formal neuron 'i' has an input function 'x' that corresponds to the incoming activity (synaptic input) of the biological neuron, the effective magnitude of information transmission between neurons (determined by synapses) is represented by weight w, the main computation performed by a biological neuron is described by the activation function $z_i = f(x, w_i)$ and the overall activity transmitted is corresponded to the next neuron in the processing stream by the output function $y_i = f(z_i)$. The term transfer function is the summation of activation function $z_i = f(x, w_i)$ and the output function $y_i = f(z_i)$

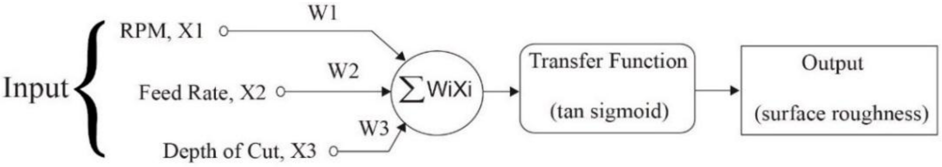

FIGURE 1. A single ANN neuron with its elements

Model of ANN

An Artificial Neural Network (ANN) model is developed for the purpose of determining surface roughness (Ra) for this research. For this model input parameters are considered as RPM, Feed (So) and Depth of Cut (d) and the only output parameter is surface roughness (Ra). To design the network for this research, each of the three input cutting parameters has three neurons in the input layer and the only output has a single neuron in the output layer. Tangent of sigmoid transfer function 'tan sig' has been employed to design an optimal network architecture. The ANN configuration is represented as 3-20-1. The hidden layer consists of twenty neurons and output layer consisting of one output neuron.

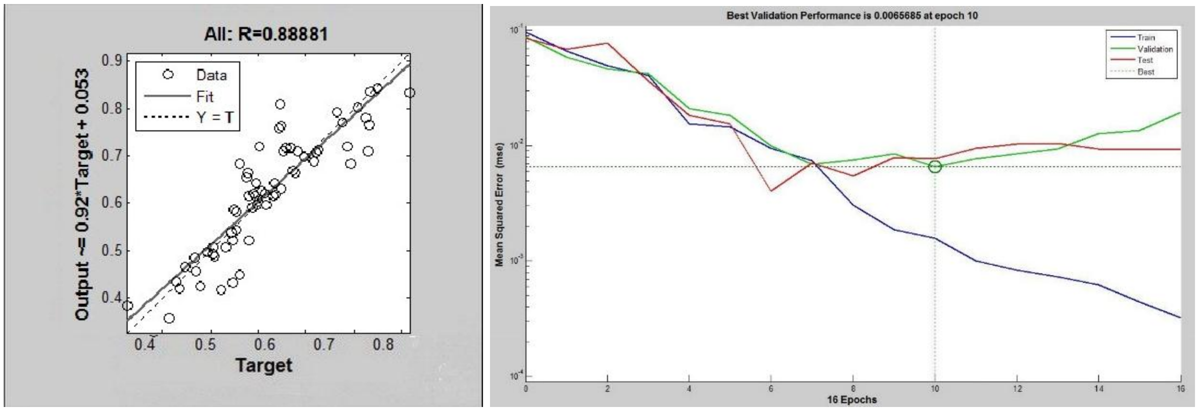

(a) (b)

FIGURE 2. (a) Neural Network Training Regression (plot regression), Epoch 16, Validation Stop and (b) Neural Network Training Performance (plot perform), Epoch 16, Validation Stop

To predict the surface roughness (Ra), standard multilayer feed-forward back-propagation hierarchical neural network has been considered for this research. The accuracy of prediction of the ANN model depends on how well the data are fitted. From Fig. 2(a), the overall R^2 value is 0.88881. It can be observed from Fig. 2(b) that the best validation performance gain at epoch. The Test and Validation curve is near to the best line. After performing the ANN the predicted value is stored and compared with actual value in Fig. 3

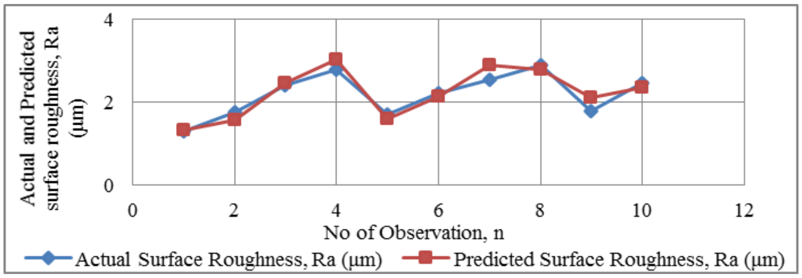

FIGURE 3. Comparison between actual and predicted value of surface roughness

PARTICLE SWARM OPTIMIZATION (PSO)

Particle swarm optimization (PSO) is a stochastic optimization technique based on population which is developed by Dr. Eberhart and Dr. Kennedy in 1995. As a modern artificial intelligence technique, PSO has many similarities with evolutionary computation techniques such as Genetic Algorithms (GA). However, PSO has no evolution operators unlike GA such as crossover and mutation. A population of random solutions are compiled to initiate the system of problem space and generations are continuously updated for the purpose of searching the optima. Then each particle of problem space is updated by following two "best" values in every iteration. The first one is the best solution (fitness) that has been achieved so far (The fitness value is also stored.) which is called pbest. Another "best" value tracked in the population by the particle swarm optimizer is the best value obtained so far by any particle in the problem space. This best value is a global best and called gbest. After finding the two best values, the particle updates its velocity and positions with following Eqn. (1) and (2),

$$v_i = v_i + c_1 rand()(p_i - x_i) + c_2 Rand()(p_g - x_i) \tag{1}$$

$$x_i = x_i + v_i \tag{2}$$

PSO Model Analysis

The algorithm PSO Model Analysis is written in MATLAB. The algorithm is conducted in the following regression equation to find the optimum parameter. In this equation, the dependent variable is surface roughness and the independent variable is RPM, feed rate, depth of cut and their interactions.

$$\begin{aligned} Y = {} & 0.0008005476256077 \times x_1 + 13.6660720244177 \times x_2 + 0.558837696743011 \times x_3 + -0.00263547253858943 \times x_1 x_2 \\ & + 0.000369293511218919 \times x_1 x_3 + -2.07837899954338 \times x_2 x_3 + -0.0830911444271629 \end{aligned} \tag{3}$$

The PSO algorithm contains following parameters:

- Number of swarm particle: 50
- Number of maximum iteration:50
- Particle size: 6 & Learning factor $c_1 = c_2 = 0.7$

To determine the desired optimum output of surface roughness (Ra); a set of data (input) are fed in to the PSO formula. A set of random data are generated from this data to find the required value for inputs to achieve the optimum output. Now the required inputs for independent variables (x_1, x_2, x_3, x_1x_2, x_1x_3, x_2x_3) are obtained by assigning the random values (data) into independent variable and continuing the iteration process till the calculation reaches at saturation. At the optimum surface roughness, each particle reach a certain saturation point. Now from this analysis; x_1,

x_2, x_3, x_1x_2, x_1x_3, x_2x_3 (Cutting speed, Feed rate, DOC, Cutting speed*Feed rate, Cutting speed*DOC, DOC*Feed rate) has number of iteration of respectively 5,5,6,7,4,4 to reach at saturation meaning that optimum value of output is achieved.

RESULT AND DISCUSSION

In this research, two types of artificial intelligent models are used to investigate and understand the effect of different machining parameters in optimizing and predicting the surface roughness in turning GFRP composite. A feed-forward back-propagation algorithm is used to conduct this prediction. The ANN is set on 1000 epochs and the program is stopped at 16 epochs. The comparison demonstrates a good agreement between the actual and the predicted value of surface roughness. PSO is applied to optimize the machining parameters in turning the GFRP composite. A regression equation is constructed using the input parameter. The PSO model optimizes this regression equation and finds out the optimum surface roughness which is 0.6252 µm, where the Cutting speed is 100.53 m/min, feed 0.1 mm/rev and DOC is 0.5 mm. The interaction of the input parameter also influence the output parameter. The interaction between the parameter are Cutting speed & Feed rate; Cutting speed & DOC; Feed rate & DOC and the value is 160, 160, 0.4 respectively for obtaining this desired output. Fig. 4 shows that the fitness data has a number of iteration of 6 to reach at saturation meaning that optimum value of output is achieved. PSO model helps to find out the crucial parameter that effects the surface roughness and ANN model helps to anticipate the outcome of the surface roughness.

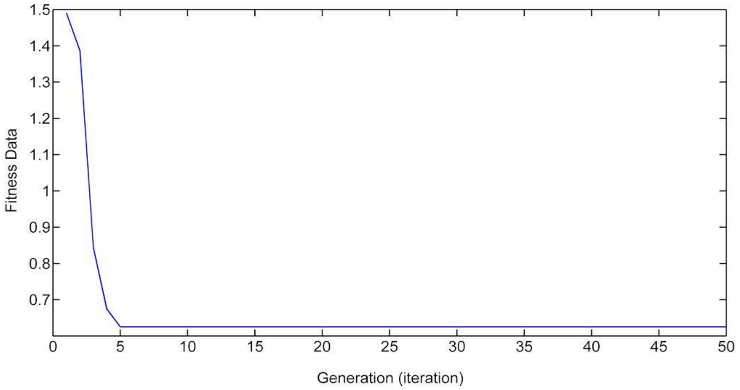

FIGURE 4. Fitness graph

CONCLUDING REMARKS

A primary objectives in machining operation is to produce product with low cost while maintaining high quality. In such a case, machining economics can be a significant consideration. It involves with the optimum selection of machining parameters. These parameters directly affect the cost, productivity and quality of products. A better prediction model can help as to choose the optimum machining parameters before performing machining operation.

- The data generated from the experiment shows that surface roughness increase with the increase in feed as well as depth of cut. The data also shows that with the increase of cutting speed there is a decrease in surface roughness.
- An Artificial Neural Network (ANN) model is developed to predict surface roughness (Ra) for this research. The accuracy of prediction of the ANN model depends on accuracy of data training. The training value of R^2 in this model is 0.95487 and overall R^2 value is 0.88881which indicates that it predicts with good level of accuracy.
- The multiple regression equation helps understanding the relationship between the machining parameters and the surface roughness. Particle Swarm Optimization (PSO) has been employed to optimize process parameters yielding an optimum value of surface roughness of 0.6252 µm, where the Cutting speed is 100.53, feed rate 0.1 and Depth of cut is 0.5. This analysis does show what level of quality is achievable in turning GFRP composites.

REFERENCES

1. M. Bannister, App. Sci. Manufacturing **32**, 901-910 (2001).
2. R. A Kishore and R. Tiwari and I. Singh, Advance. Product. Engg. Management **4**, 37-46 (2009).
3. N. S. Hu and L. C. Zhang, J. Mater. Proc. Technology **152**, 333-338 (2004).
4. G. Santhanakrishnan and R. Krishnamurthy and S. K. Malhotra, J. Mech. Work. Technology **17**, 195-204 (1988).
5. A. Mital and M. Mehta, Int. J. Product. Research **26**, 1861-1876 (1988).
6. J. P. Davim and F. Mata, Int. Lub. Tribology **56**, 270-274 (2004).
7. D. T. Phillips and C.S. Beightler, AIIE Transaction **2**, 355-360 (1970).
8. F. Čuš and J. Balič, J. Mater. Proc. Technology **118**, 485-489 (2001).
9. M. S. Alam and A. Yusuf and A. Rahman and Inzamam-ul-haq, Int. J. Sci. Eng. Research **6**, 892-896 (2015).
10. G. Chryssolouris and M. Guillot, ASME J. Engg. Industry **112,** 122–131 (1990).
11. T. O¨zel and Y. Karpat, Int. J. Mach. Tools Manufacture **45**, 467–479 (2005).
12. K. L. D. Wins and A. S. Varadarajan, Int. J. Advance. Product. Engg. Management **7**, 51- 60 (2012).
13. J. Kennedy and C. Eberhart, Proceedings of IEEE International Conference on Neural Network. (1995).
14. J. G. Li and Y. X. Yao and D. Gao and C. Q. Liu and Z. J. Yuan, App. Mech. Materials **10**, 879-883 (2008).
15. H. Zhao and J. G. Li and Y. X. Yao and C. Q. Liu, App. Mech. Materials **10**, 483 (2008).

International Conference on Mechanical Engineering 2015
(ICME 2015) 18 – 20 December, 2015, Dhaka, Bangladesh

Paper ID : 172

Design and Construction of an Automatic System for Minimizing the Risk of Sinking of Water Vehicle

Amit Sutradhar[1,a)], Md. Mahbubur Rashid[1,b)], Md. Helal-An-Nahiyan[1,c)] and
Manash Kumar Mandal[2,d)]

[1]*Department of Mechanical Engineering, Khulna University of Engineering & Technology, Khulna-9203, Bangladesh*
[2]*Department of Electrical &Electronic Engineering, Khulna University of Engineering & Technology, Khulna-9203, Bangladesh*

a)Corresponding author: amitndc12@gmail.com
b)mahbubrashid12@yahoo.com
c)nahiyan.me@gmail.com
d)manashmndl@gmail.com

Abstract. This paper focuses on the reduction of the risk of water vehicle like launch, ferry, ship and boat from sinking which is a burning problem of Bangladesh now-a-days. Every year death toll is rising by leaps and bounds due to this unexpected phenomenon. The sinking mostly occurs due to overloading and lack of consciousness. That's why, an automated system is introduced here to make the travelers warned about the overloading situation through raising alarm before the vehicle starts to move on. The tolerance limit of the vehicle is determined based on the theory of buoyancy and floatation. Moreover, while moving on the water, the vehicle may get victim of sinking due to rough weather, low visibility or machineries breakdown. So water level indicator is used to determine the safe level of water. When water level rises up to the safe limit or just before crossing the safe limit, another alarm will warn the passengers which will sound quite different from the first alarm as stated before. And at once the on board GPS sensor will record the current position of the vehicle and transmit the location to the nearest rescue authority via GSM module in the form of text message which will help them to take necessary steps for the rescue of the passengers as soon as possible. Effective implementation of this method can reduce the accident as well as this research can also be a helpful tool to organize further researches in this field for the sake of humanity.

INTRODUCTION

Bangladesh is a riverine country and waterways are very important means of communication in this region. Every year around 87.80 million passengers are carried through this route (Bangladesh Inland Water Transport Authority). This important mode of transport is ridden with tragic disasters every year, incurring a heavy toll of human lives as like as shown in Fig. 1(a). According to official statistics of Department of Shipping, 3,869 people have died and 279 gone missing in 458 launch disasters since 1976. Certainly the independent surveys will give much higher figures on this [1]. It has been found that collision is the main cause of accidents having maximum share of 55%. The second contributor of the accidents is overloading. Overloading has 26% share of total number of accidents since 1975. Most of the accidents due to overloading indicate that vessels were found to be overloaded as many as 5 times of their capacity as shown in Fig. 1(b) [1,2].


(a) (b)

FIGURE 1. (a). Scores are killed each year from ferry disasters, (b) Overcrowding increases the top weight making the vessel unstable and accident prone.

Response and recovery is the utmost requirement of any emergency. Unfortunately this concept is totally neglected in IWT sector. The relevant authority (BIWTA) has very limited capacity and outdated instruments for carrying out rescue operations. In the study it has been found that, rescue operations are always at dilemma. In so many cases, rescue mechanism of BIWTA could not reach the spot within two to three days after the occurrence [1].

Though the maximum possible safe load that a vehicle can carry is written in the front side of some vehicle, people care a little about this. Also it is not that much easier to count the number of passengers entering to or leaving the vehicle. That's why, our primary target is to reduce the overloading by implementing an alarming system to warn the passengers and others and instructing them to unload. Moreover, water level indicator has been used at different portions of the vehicle to detect the safe level of water. When water level rises up to the safe limit or just before crossing the safe limit, another alarm will warn the passengers which will sound quite different from the first alarm as stated before. At once the on board GPS (Global Positioning System) sensor will record the current position of the ship and transmit the location to the nearest rescue center via GSM (Global System for Mobile communication) module in the form of text message. The outcome is that, getting message, the authority in the nearest distance can take effective steps as soon as possible. As a result, a heavy toll of life can be saved along with the detection of the vehicle.

BACKGROUND CONCERNING OUR DESIGN

Modern ships have an automatic system control which includes control, alarm and monitoring system that have access to all process control station and can monitor them. M. S. Zaghloul developed ship control system using Supervisory Control and Data Acquisition (SCADA) which includes alarm system controlling data recorder, GPS, radar and many other things [3,4]. S.M. K. Reza et al. designed microcontroller based automatic system for water level sensing and controlling in a wired and wireless environment [5]. Neena et al. designed an automated water level indicator using liquid level sensor to detect the level of water or any liquid and buzzer for beeping when water level is full [6] . Ayob Johari et al. developed water level monitoring system with an integration of GSM module to alert the person-in-charge through Short Message Service (SMS) [7]. Khondker Shajadul Hasan et al. proposed cost effective GPS-GPRS based object tracking system to view present and the past positions recorded of a target object on Google Map through the internet [8].

But there is no application of these type of automation in the passenger carrying water vehicle like launch, ferry. So in this paper we have combined these type of technologies but in other ways considering the feasibility, low cost and efficiency and implemented these for other purposes which are quite different from the above stated purposes. In this paper, we have worked for a small prototype. Here the load capacity limit of a water vehicle is determined by the theory of buoyancy and floatation that is usually used in the design of ship, launch all over the world [9]. There are wide range of applications of weight measurement which have been executed by load sensors. But here force sensitive resistors have been used for detecting load for a small prototype. Water level indicator is constructed taking the cost and feasibility into account. Here the GPS system with GSM module is implemented using adafruit fona module which is used numerously now–a-days.

THEORY

Conditions of Stability of Floating Body

When a floating body is given a small displacement it will rotate about a point, so the point at which the body rotates is called as the Metacenter (M) as shown in Fig.2. The intersection of the lines passing through the original center of buoyancy (B) and center of gravity (G) of the body and the vertical line through the new center of buoyancy. The distance between center of gravity of a floating body and Metacenter is called as Metacentric height (GM) as shown in Fig 2. It is necessary for the stability of a floating body, if metacenter is above center of gravity body will be in stable equilibrium as shown in Fig. 2(a) because the restoring couple produced will shift the body to its original position. Otherwise it will be in unstable equilibrium as shown in Fig. 2(b). Metacentric height is very important to determine the safe loading of a vehicle [10,11,12].

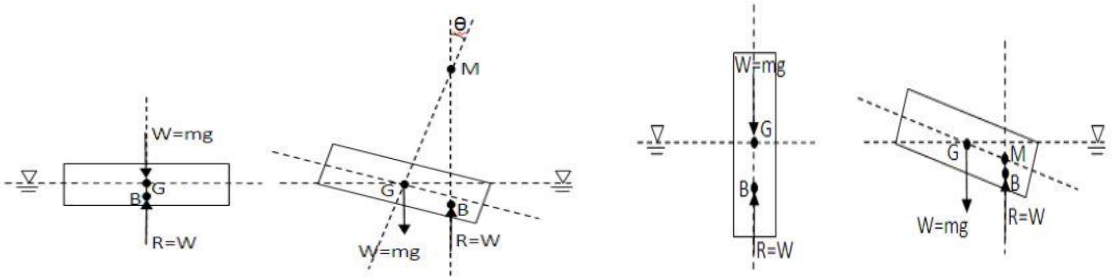

(a) (b)

FIGURE 2. (a) Stable Equilibrium M is above G, (b) Unstable Equilibrium M is below G.

Buoyant force $= F_B = W =$ weight of volume of liquid displaced by the body.
Hence, Metacenter must be above the center of gravity.

Determination of Metacentric Height as well as Safe Load and Safe Water Level

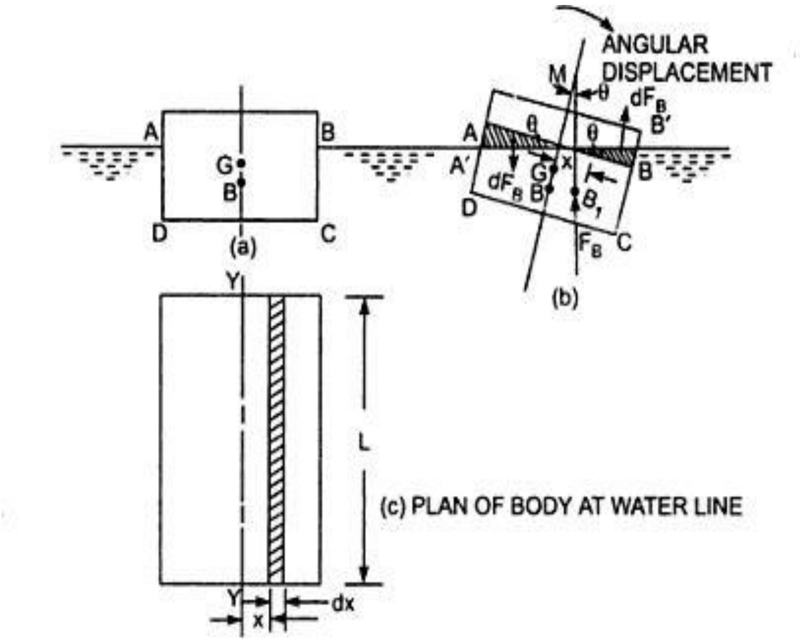

FIGURE 3. Analytical method for meta-centric height

Figure 3 (a) shows the position of a floating body in equilibrium. The floating body is given a small angular displacement (θ) in the clockwise direction. This is shown in Fig. 3(b). A small strip of thickness dx at a distance x from O towards the left of the axis is considered. Plane of body at water line is shown in Fig. 3(c).

$$\begin{aligned}
&W \times BM = \rho g I \\
&\Rightarrow BM = \frac{\rho g I}{W}[I = 2\int x^2 dA] \\
&\because W = \rho g \times \forall \\
&\therefore BM = \frac{I}{\forall} \\
&\therefore GM = BM - BG = \frac{I}{\forall} - BG
\end{aligned} \tag{1}$$

Here ρ is the density of water, $\forall$ is the volume of submerged body in the water and GM is the required meta-centric height.

There is another method for the determination of meta-centric height which is described below:

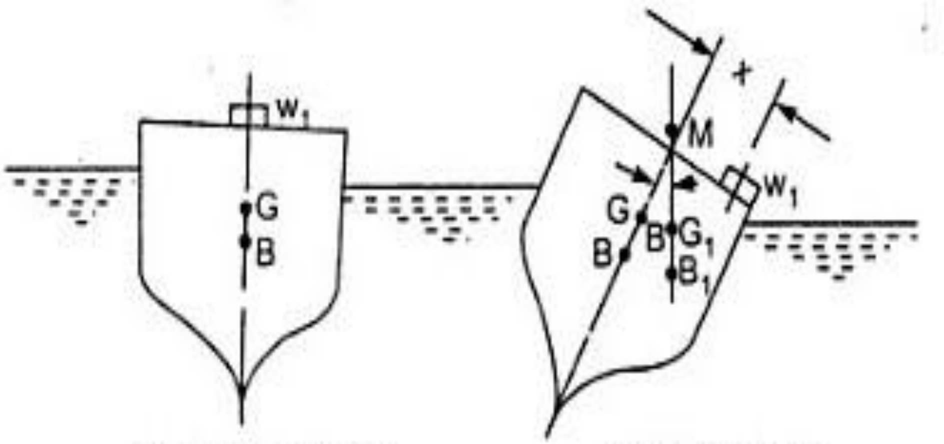

(a) Floating body (b) Tilted body

FIGURE 4. Experimental method of determination of meta-centric height

In this method, center of gravity of the floating vessel must be known. Here w_1 is a known weight placed over the center of vessel as shown in Fig. 4(a). The weight w_1 is moved across the vessel towards right through a distance x as shown in Fig. 4(b).Hence the new center of gravity of the vessel will shift to G_1 .The moment due to change of G is

$$\begin{aligned}
&GG_1 \times W = W \times GM \tan\theta \\
&w_1 x = WGM \tan\theta \\
&\Rightarrow GM = \frac{w_1 x}{W \tan\theta}
\end{aligned} \tag{2}$$

By using the above governing equations (1) and (2), we can find the meta-centric height. Then the meta-center and the center of gravity of the vehicle are calculated with respect to different loads and thus considering their relative positions, the tolerance limit and the safe level of water is determined for safety [9,10,11,12].

EXPERIMENTAL METHOD

Equipment List

Equipment used in this experiment are listed below:

- **Infrared (IR) sensors:** For activating Force Sensitive Resistor to measure weight. And another pair to detect tilt.
- **Force Sensitive Resistor (FSR):** For measuring weight within small range.
- **Arduino UNO:** Microcontroller board which collects sensor data, calculate total weight, shows warning via Liquid Crystal Display and alarm system consisting of LED and Piezo Buzzer.
- **Liquid Crystal Display (LCD):** For showing necessary information.
- **Light Emitting Diode (LED):** It is used as a part of the alarm system which will show visible red light to show warning.
- **Piezo Buzzer:** It is also used as a part of the alarm system which will sound an alarm if there is tilting detected.
- **HC-SR04 Ultrasonic:** Ultrasonic sonar sensor to detect height of the water level from the vehicle.
- **Adafruit Fona 808 Cellular Plus GPS Shield for Arduino**: A hardware module capable of sending Short Message Service (SMS) and pinpoint the location of the vehicle via GPS.

Weight Measurement System

There are a pair of IR sensors. RX and TX are situated in the entry point facing opposite direction pointing to each other keeping their line of action identical. The action of these IR pair is to detect person and make the Force Sensitive Resistor active to take the value of weight. When the Force Sensitive Resistor detects a reading more than some threshold value then it records the reading and add it to the total existing load of the water vehicle. There are another pair of RX Tx Ir at the exit point to detect the departure of person. When the exit IRs are triggered another Force Sensitive Resistor becomes active and it records the weight of the exiting person and subtracts from the total existing load weight of the water vehicle. The calculated total weight, entry point weight and exit point weights will be displayed in a Liquid Crystal Display.

Alarm and Warning System

If the total dead load weight of the water vehicle becomes greater than the safe weight limit then the piezo buzzer will produce a warning tone. And a red LED will start blinking. The control algorithm of weight measurement and alarming is shown below in Fig.5.

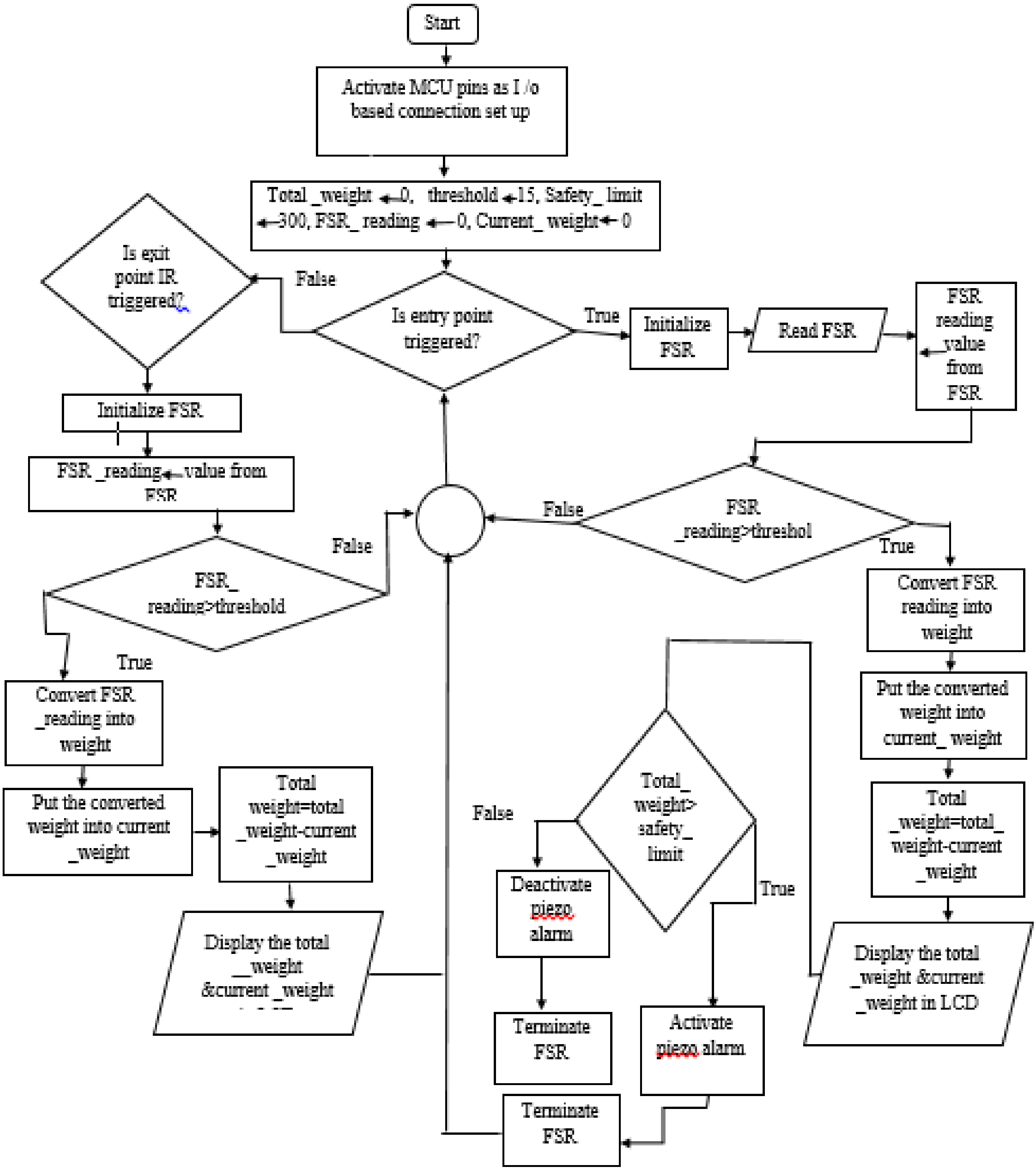

FIGURE 5. Flow chart of control algorithm of weight measurement and alarming

Description of Circuit Configuration and Circuit Diagram

Figure 6 shows the circuit arrangement for measuring weight, weight updates in LCD and alarm system. The IR receivers are connected with the Analog to Digital Converter Pin of arduino A0 and A1 since analog values of sensors are needed. Two 10k Ω resistances are used as a pull up resistance in this case. Same condition goes to Force Sensitive Resistor as well, and again a 10K Ω resistance is used as a pull up resistance and it is connected to A2 of arduino. Two IR LED is connected with the +5VDC with safety resistance of value 220Ohm. A Piezo Buzzer is connected to the digital pin D8 of the microcontroller since only alarm on or off are needed. A Liquid Crystal Display of 2 rows and 16 columns is added to view the weight information on it. The LCD RS, EN, DB4, DB5, DB6, DB7 pins are connected to the D2, D3, D4, D5, D6, D7 of the arduino respectively

.

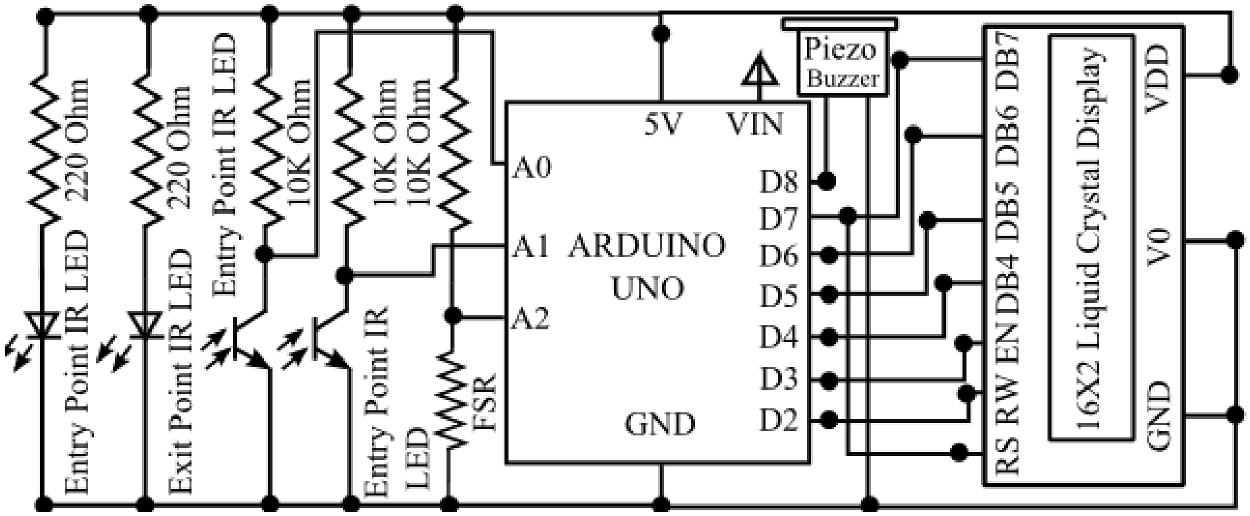

FIGURE 6. Circuit Diagram for weight measurement, weight updates in LCD and alarm system

Water Level Indication for Detecting Tilt

There are two HC-SR04 Ultrasonic sensors along with two IR sensors. The condition for detecting tilt is the distance reading from one sensor will be greater than the other one. Another pair of IRs have been used to strengthen the probability of tilt. Figure 7 represents the control algorithm of water level indication and alarming.

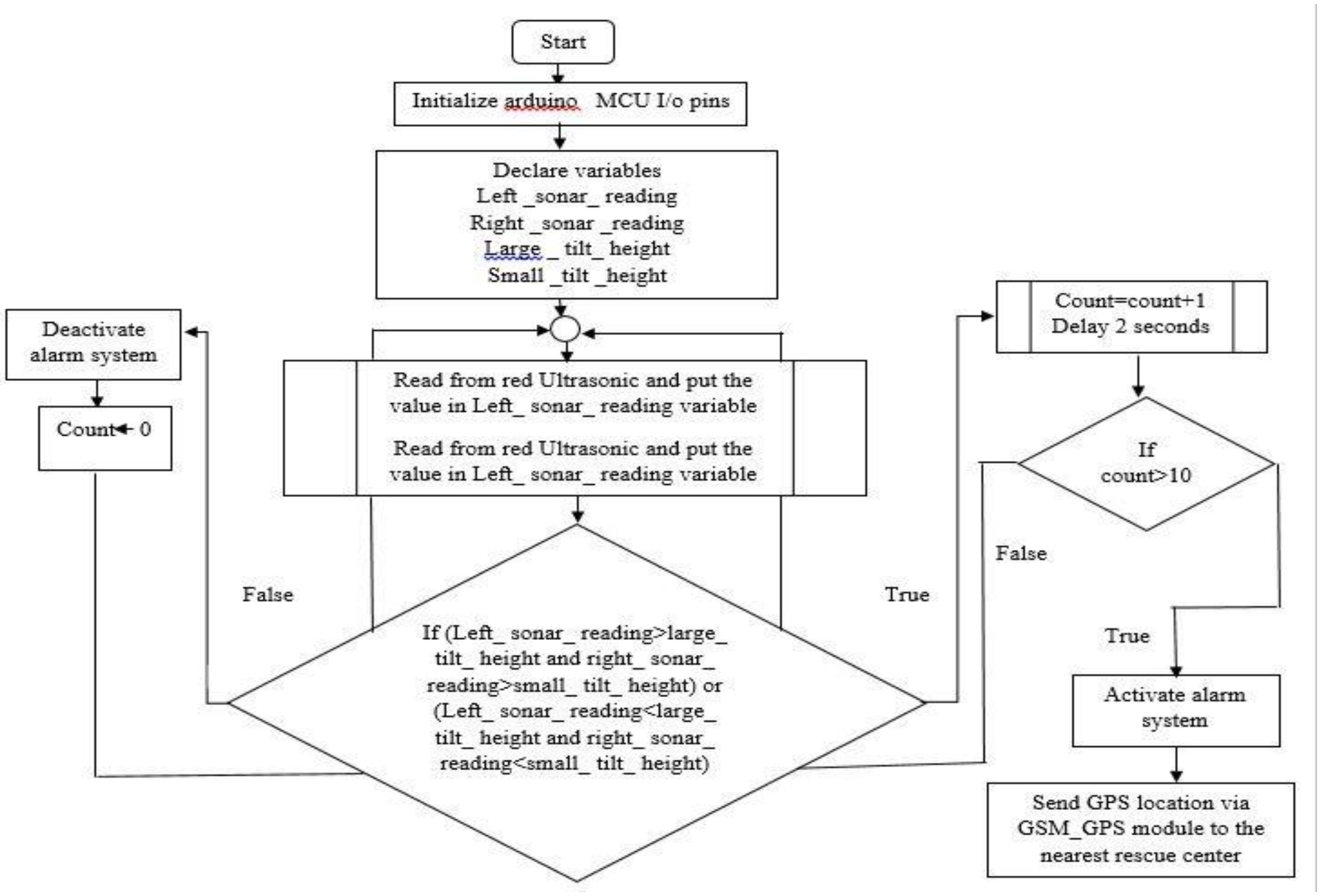

FIGURE 7. Flow chart of control algorithm of water level indication and alarming

Description of Circuit Configuration and Circuit Diagram

Two Ultrasonic Sonar (HC-SR04) is connected with the digital i/o pin D9, D10, D11, D12. There are two IR LED connected with the +5VDC with safety resistance of 220Ω. Two analog IR Receiver are connected with the ADC pin of arduino A3 and A4 with 10k pull up resistor for each one. Circuit arrangement is shown in Fig.8.

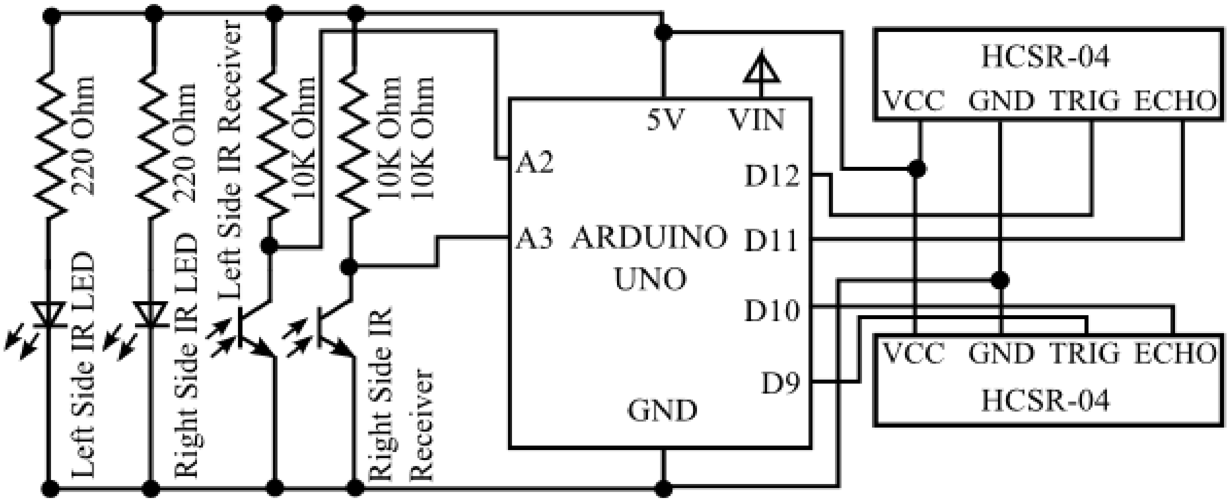

FIGURE 8. Circuit Diagram for Water Level Indicator

Location Tracker and SOS [Save Our Souls] Message Sending System

Whenever the symptom of tilt of the vehicle is detected for about a certain period of time, then the on board GPS sensor will record the current position of the ship and transmit the location to the nearest rescue center via GSM module in the form of text message performed by adafruit –fona module as shown in Fig.9.

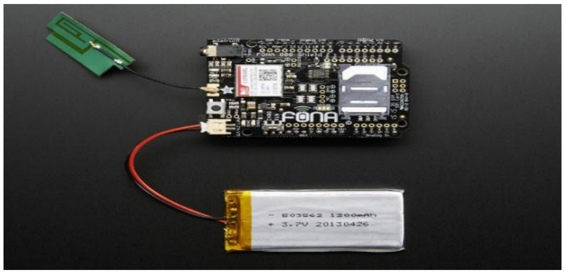

FIGURE 9. Adafruit- Fona Module

RESULTS & DISCUSSION

A small boat shaped prototype was built as shown in Fig.10 and it was tested in water. Safe loading was calculated 300gm for this prototype. When the prototype starts getting loaded, the force sensitive resistor (FSR) becomes active. Also the current weight and total weight are shown on liquid crystal display (LCD) along with the danger level as shown in Fig.11 (a) and (b). And it is observed that if the total weight exceeds the safe limit (i.e. 300gm), the piezo alarm starts instantly and continues until it reaches the safe tolerance limit.

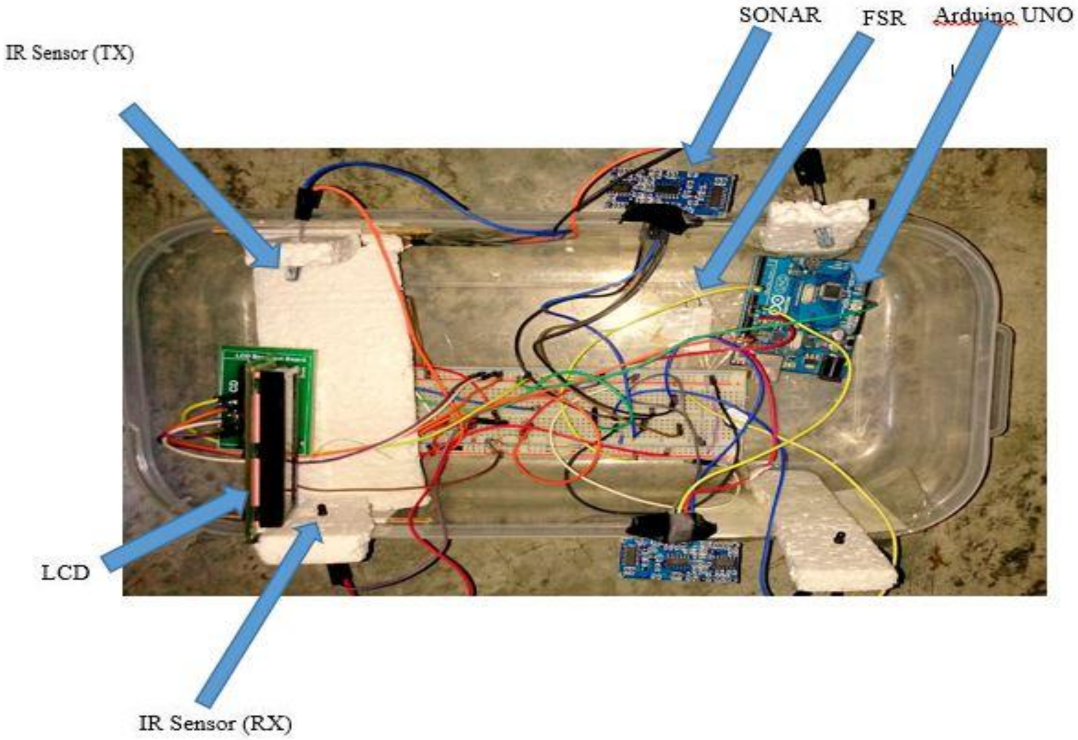

Figure 10. Prototype of the experiment

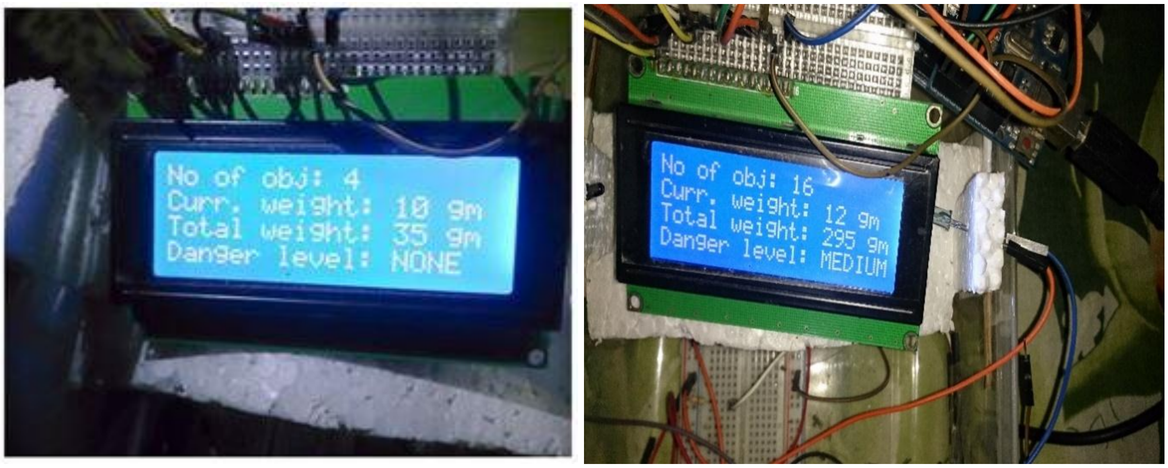

(a) (b)

Figure 11. Weight update in LCD (a)safe level, (b)medium danger level.

It can be noted that FSR can only measure between small ranges of weight. And if the size of the load exceeds the area of the FSR then the deviation appears in measured values. In practical, industrial load sensors can be used.

Also the water level indicator can sense the water level and can detect tilt .It can distinguish the safe and dangerous level of water. Whenever the water level goes beyond safe level, it starts raising alarm. As the IR sensors are not water resistive, a medium is used between IR sensors and water to determine the water level. It is to mention that the detection of tilt depends on the thickness of the medium. The reading of IR varies with the thickness of the material forming the medium (e.g. Glass, plastic etc.). It is observed that the thinner is the medium, the larger is the difference of the measured IR value between air and water and the greater is the accuracy in the detection of tilt.

Due to small prototype, here single entry and exit point has been taken into consideration. But in case of the practical water vehicle, the weight measuring process can be performed efficiently and quickly by the insertion of multiple entry and exit point. If multiple exit and entry point are used, then there will be a master arduino connected to the according slave arduinos in those entry/exit points. Data transfer between the slave arduinos and master one can either be executed by Serial Peripheral Interface (SPI) or by Inter-Integrated Circuit (I2C) Bus.

As the water level reaches unsafe level, at once a message is sent to mobile by GSM-GPS system within 15 seconds automatically. There will be a database containing the contact numbers along with the approximate GPS location, so when there is an alarm, MCU will cross check the current position of the water vehicle with the database and send distress signal according to the location.

Hence it can be noted that all the purposes of this research stated above have been fulfilled successfully.

CONCLUSION

In a riverine country like Bangladesh, this technology is very much effective to pave the way of communication through waterways. During any vehicle accident in waterway, almost all the time most of the victims can't be rescued and are subjected to unnatural death. Even sometimes the vehicle can't be identified as the rescue authority gets the news of sinking after 2-3 hours of the accident. That's why, the technology proposed in this paper will be fruitful to a great extent. It is to mention that extra features may also be added i.e. sonars can be used in several portions of the water vehicle to detect the presence of another vehicle within a certain region with a view to avoiding collision. After all, it can be concluded that this technology is quite feasible enough to implement in this country.

ACKNOWLEDGEMENTS

The authors are highly grateful to BIWTC, Aricha Ferry Service Unit, Shibalaya, Manikgonj for providing information and assuring the feasibility of this research work.

REFERENCES

1. A. K. Azad, “Riverine passenger vessel disaster in Bangladesh: options for mitigation and safety”, Fall2009, Postgraduate Programs in Disaster Management (PPDM), BRAC University, Dhaka, Bangladesh.
2. N. A. Huq and A. M. Dewan, “Launch disaster in Bangladesh: A geographical study”, Geografia Vol.1, Issue 2 (14-25).
3. M. S. Zaghloul, *Online Ship Control System Using Supervisory Control and Data Acquisition (SCADA),* Int. J. Computer Sci. and Application (IJCSA), Vol. 3, Issue 1, February 2014.
4. M. S. Zaghloul, *Design of Open Architecture Ship Alarm, Monitoring and Control System*, Int. J. Research in Eng. & Tech. (IMPACT: IJRET) ISSN (E): 2321-8843; ISSN (P): 2347-4599, Vol. 2, Issue 1, Jan 2014, pp. 69-86.
5. S. M. K Reza, S. Ahsanuzzaman, M. Tariq, S.M. M. Reza, *Microcontroller Based Automated Water Level Sensing and Controlling: Design and Implementation Issue*, Proc. of the W. Cong. on Eng. and Computer Sci., Vol I, San Francisco, USA,2010.
6. N. Mani, Sudheesh T.P, V. Joseph, Titto V.D, Shamnas P.S, *Design and Implementation of a Fully Automated Water Level Indicator*, Int. J. Adv. Research in Electrical, Electronic and Instrumentation Eng., Vol. 3, Issue 2, February 2014.
7. A. Johari, M. Helmy, A. Wahab, N.Suryani, A. Latif, M. E. Ayob, M. I. Ayob, M. A.Ayob, M. N.H. Mohd, *Tank Water Level Monitoring System Using GSM Network*, Int. J. Computer Sci. and Info. Tech., Vol. 2 (3), 2011, pp.1114-1120.
8. K. S. Hasan, M. Rahman, A. L. Haque, M A. Rahman, T. Rahman and M. Rasheed, *Cost Effective GPS-GPRS Based Object Tracking System*, Proce. of the Int. MultiConference of Engineers and Computer Scientists , Vol I , Hong Kong 2009.
9. J. Megel and J. Kliava, “Metacenter and ship stability”, American Journal of Physics, American Association of Physics Teachers, 2010, 78 (7), pp.738-747.
10. Dr. R.K. Bansal, “Buoyancy and Floatation”, in *A Textbook of Fluid Mechanics and Hydraulic Machines*, ninth ed., (Laxmi Publications (P) LTD, New Delhi-110002), pp.131-162.
11. Dr. P.N. Modi and Dr. S.M. Seth, “Buoyancy and Floatation”, in *Hydraulics and Fluid Mechanics Including Hydraulic Machines*, fourteenth ed., (R.K. Jain, Standard Book House, Delhi-110 006), pp.145-175.
12. Dr. K.R. Arora, “Buoyancy and Floatation”, in *Fluid Mechanics, Hydraulics and Hydraulic Machines*, ninth ed., (A.K. Jain, Standard Publishers Distributors, Delhi-110006), pp.85-111.

International Conference on Mechanical Engineering 2015
(ICME 2015) 18 – 20 December, 2015, Dhaka, Bangladesh

Paper ID : 176

Design, Fabrication & Performance Analysis of an Unmanned Aerial Vehicle

M. I. Khan [1, a)], M. A. Salam [1, b)], M. R. Afsar [1, c)], M. N. Huda [1, d)] and
T. Mahmud [1, e)]

[1]*Department of Aeronautical Engineering, Military Institute of Science and Technology (MIST), Mirpur Cantonment, Dhaka-1216, Bangladesh*

a)Corresponding author: inzamimkhan@gmail.com ,
b)head@ae.mist.ac.bd,
c)rayhan@ae.mist.ac.bd,
d)toyon153@gmail.com,
e)sonon619@gmail.com

Abstract. An Unmanned Aerial Vehicle was designed, analyzed and fabricated to meet design requirements and perform the entire mission for an international aircraft design competition. The goal was to have a balanced design possessing, good demonstrated flight handling qualities, practical and affordable manufacturing requirements while providing a high vehicle performance. The UAV had to complete total three missions named ferry flight (1st mission), maximum load mission (2nd mission) and emergency medical mission (3rd mission). The requirement of ferry flight mission was to fly as many as laps as possible within 4 minutes. The maximum load mission consists of flying 3 laps while carrying two wooden blocks which simulate cargo. The requirement of emergency medical mission was complete 3 laps as soon as possible while carrying two attendances and two patients. A careful analysis revealed lowest rated aircraft cost (RAC) as the primary design objective. So, the challenge was to build an aircraft with minimum RAC that can fly fast, fly with maximum payload, and fly fast with all the possible configurations. The aircraft design was reached by first generating numerous design concepts capable of completing the mission requirements. In conceptual design phase, Figure of Merit (FOM) analysis was carried out to select initial aircraft configuration, propulsion, empennage and landing gear. After completion of the conceptual design, preliminary design was carried out. The preliminary design iterations had a low wing loading, high lift coefficient, and a high thrust to weight ratio. To make the aircraft capable of Rough Field Taxi; springs were added in the landing gears for absorbing shock. An airfoil shaped fuselage was designed to allowed sufficient space for payload and generate less drag to make the aircraft fly fast. The final design was a high wing monoplane with conventional tail, single tractor propulsion system and a tail dragger landing gear. Payload was stored in undercarriage box for maximum load mission and emergency medical mission. The aircraft structure, weights 5.6 lb., constructed by balsa wood, depron and covering film was the only feasible match for the given requirements set by the competition organizers. The defined final aircraft was capable of: Completing 3 laps within 4 minutes at the first mission; flying 3 laps with 4 internal payloads at the second mission; flying 3 laps with all possible payload configurations at the third mission.

INTRODUCTION

The UAV is an acronym for Unmanned Aerial Vehicle. According to Federal Aviation Administration (FAA) [1], UAV is defined as a device used or intended to be used for flight in the air that has no on-board pilot. This device excludes missiles, weapons, or exploding warheads, but includes all classes of airplanes, helicopters, airships, and power-lift aircraft without an on-board pilot. UAVs are currently used for a number of missions, including reconnaissance and attack search and rescue operations, inspecting power lines and pipelines, delivering medical supplies. This UAV is designed to be deployed when medical emergency service is needed. Unconstrained by local traffic and roads, it, in theory, could arrive at the scene faster than an ambulance. It can deliver medical supplies to local remote or otherwise inaccessible regions because it’s designed to land on rough fields where runway is absent. It can also be used for disaster relief by delivering aid, including water and medical supplies in the time of local natural disaster to affected areas.

CONCEPTUAL DESIGN

To begin determining aircraft configuration, a variety of aircraft concepts were generated. A Figure of Merit (FOM) analysis was used to select competitive configurations to satisfy the given aircraft and given mission requirements [2]. To represent importance of various factors different configurations were given Weight of Factor. Then different configurations were scored for a specific factor. Total score was calculated by eqn. (1).and a configuration with highest total score was selected [3].

$$\text{Total Score} = \sum \text{Weight of Factor} * \text{Score of Factor} \quad (1)$$

The final configuration selected was an aerofoil shaped fuselage with a high wing, conventional tail and tri-cycle landing gear. For the purpose of propulsion single tractor DC motor was chosen.

PRELIMINARY DESIGN

After completing a conceptual sketch, now it was time to define, iterate critical design variable for each discipline and optimize them to maximize total flight score. Aerodynamics, propulsion, stability and control and structure were evaluated for each evaluated for each of the individual design Iterations.Every Iteration and final Optimization was driven to maximize overall score.

Design and analysis methodology

The Preliminary design was done iteratively and was optimized for all the missions to assume highest possible score .Individual design parameters were used as an input and the performance result in each iteration was monitored to explore any further improvements in those parameters. If improvement were monitored at any point the next iteration was started from that point.

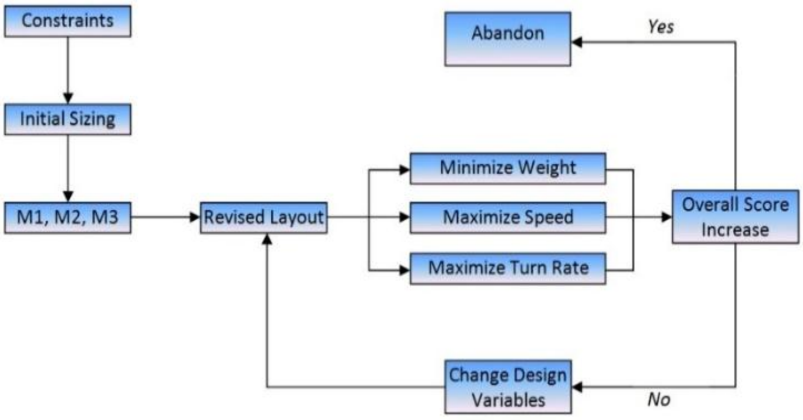

FIGURE 1. A closed loop optimization process flow chart

Design and sizing trades

Raymer's [4] method was utilized to determine thrust to Weight ratio (T/W) as a function of wing loading for critical design cases. In the analytic equations of the function the aspect ratio, Oswald efficiency, parasite drag and co efficient of lift was taken as 5, 0.90, 0.02, 1.8 respectively. The equation was than graphed by MATLAB® [5] and the design point was selected.

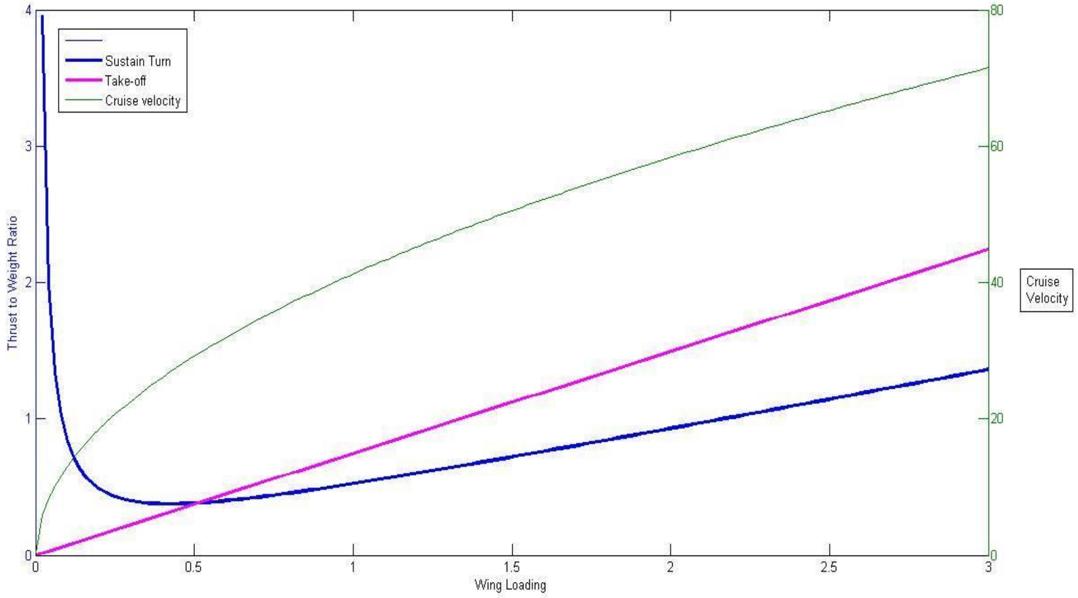

FIGURE 2. Thrust to Weight ratio (T/W) Vs. Wing loading curve

Wing and empennage airfoil selection

Some important factors like-maximum lift coefficient, drag polar, stall characteristics, pitching moment coefficient, manufacturability were considered during wing aerofoil selection [6]. Four aerofoils were selected [7] for detailed analysis and XFLR5 [8] was used to analyse those aerofoils.

TABLE 1. Wing aerofoil selection

Parameters	**Weight**	**E423**	**MH80**	**NACA23012**	**SD7062**
C_{lmax}	5	5	3	4	4
(L/D)	5	5	3	3	4
Stall	3	4	3	2	2
Manufacturability	3	4	4	4	4
-(dCm/dα)	2	5	3	3	2
Total		84	57	59	62

Finally the table showed E423 was the best aerofoil for the wing which will be able to generate desired amount of lift with good aerodynamic performance. To have reduced weight and avoid complexity flat plates were used as empennage aerofoil.

STABILITY CHARACTERISTICS

To meet performance goals, the UAV was designed to have excellent static and dynamic stability characteristics allowing it to remain stable even when payloads shift in flight. To ensure required stability, the aircraft aerodynamics were analysed according to the following standard design principles suggested by Etkin [9].

- Centre of gravity was placed ahead of the aerodynamic centre with a static margin of 10%.
- Payload compartment was near the centre of gravity to reduce centre of gravity travel.
- Propeller centreline was collinear with the centre of gravity preventing pitch moment.

Static margin was calculated using Etkin [9].For mission-1 it was 8% and for mission-2&3 10% of Mean Aerodynamic Chord (MAC).

DETAIL DESIGN

The prime consideration during detail design was to design a simple, light but strong structure which can be manufactured fast and within a reasonable cost. Dimensional parameters were calculated using Raymer's [4] method which had a fuselage of 23in.×10in.×10in. and other important parameters are presented by the following table:

TABLE 2. Dimensional parameters of the aircraft

Parameters	Wing	Horizontal Stabilizer	Vertical Stabilizer	Aileron	Rudder	Elevator
Span	4.70 ft.	18.68 in.	7.73 in.	23 in.	6.6 in.	18.68 in.
Chord / % of chord	0.94 ft.	5.3 in.	5.3 in.	20%	30%	30%
Area	4.42 ft.^{2}	99.715 in.^{2}	39.88 in.^{2}	-	-	-
Max. Deflection	-	-	-	±25^0	±25^0	±25^0
Aerofoil	E423	Flat plates	Flat plates	-	-	-
Aspect Ratio	5	3.5	1.5	10.2	6.2	17.6

Structural characteristics

Structural arrangement of wing mainly focused on sustaining a 3.42g load during mission, which is equivalent to 3.25g for mission 2 and 3.Spars were designed [10] to sustain the bending and twisting moment during maximum load condition**.** V-n diagram for three different missions is provided.

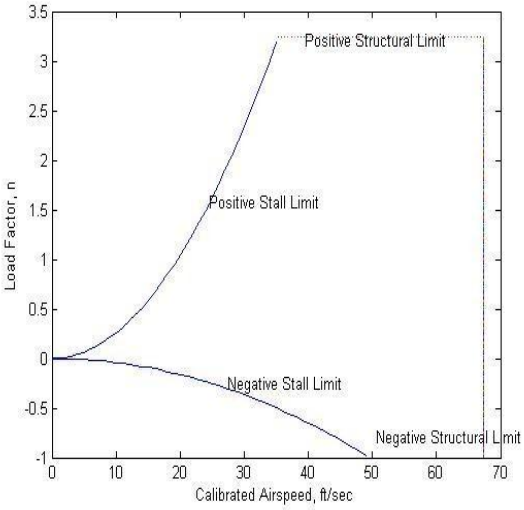

FIGURE 3.V-n diagram for mission-1

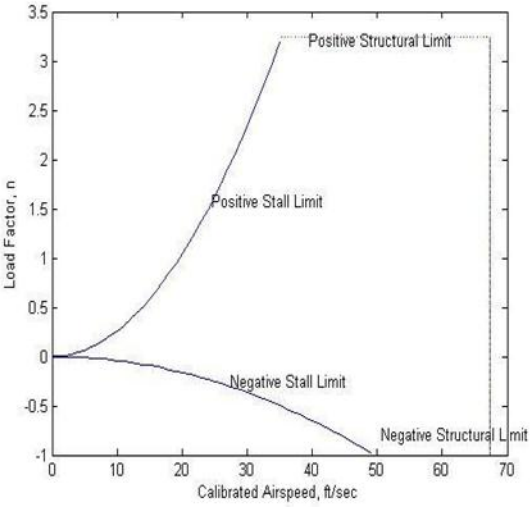

FIGURE 4.V-n diagram for mission -2 & 3

Detail drawing

SolidWorks 2013 [11] was used as CAD tool. The detail drawings of the designed aircraft are presented below.

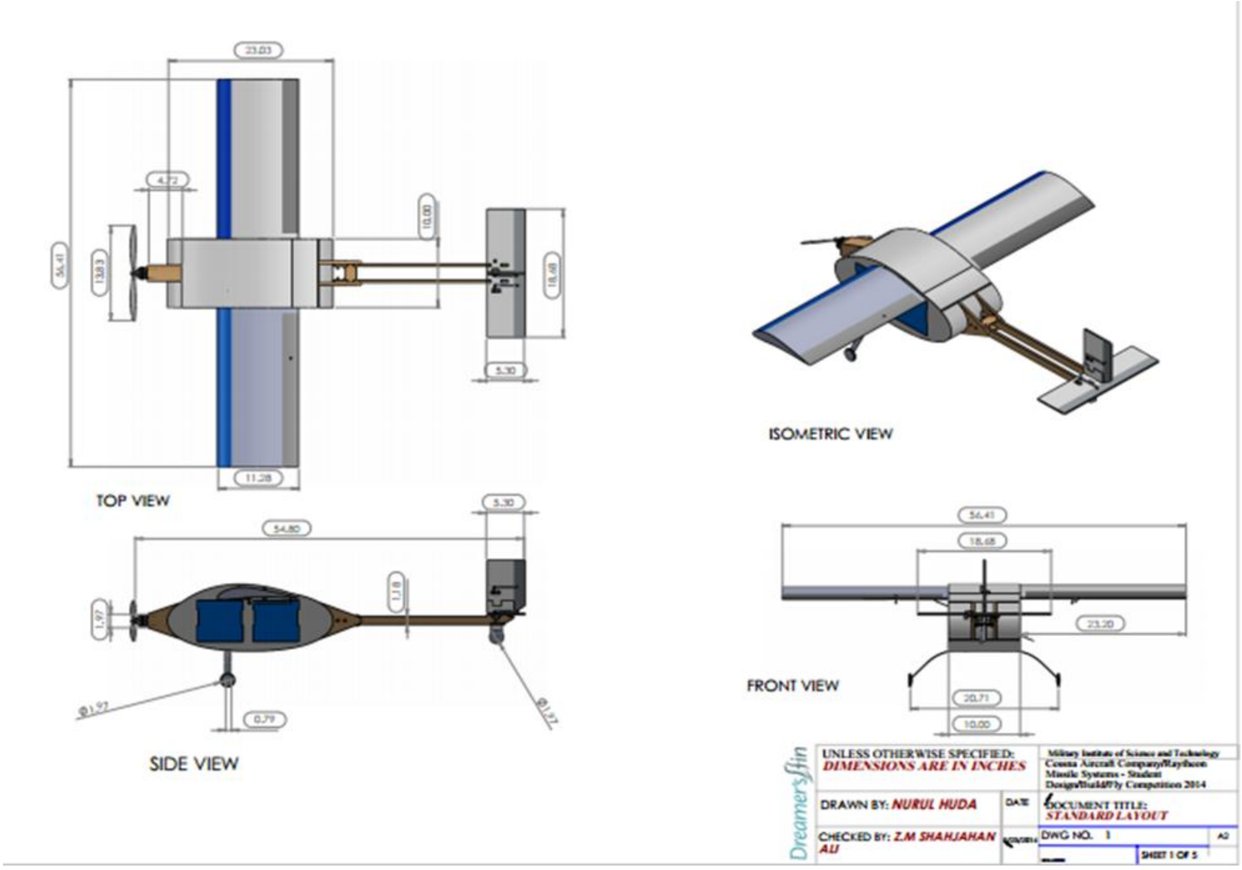

FIGURE 5. CAD drawing of the designed aircraft

Centre of Gravity estimation

As per FAA regulation [12] datum was considered ten cm. ahead of the motor mount. Centre of Gravity position for mission 1, 2 & 3 was estimated at 16.9598(in.), 17.3373(in.) & 16.9535(in.) from the datum using the same.

FABRICATION PROCESS

Total two prototypes were built during this process. First one was built of solid foam and several tests were done on it. But it was not strong enough to carry desired payload. To make the structure strong and light enough laser cut balsa was used for the production of final prototype's major components.

FLIGHT TEST & PERFORMANCE PARAMETERS

All three missions were completed by the final prototype. Flight test results were measured using conventional way like- weight by digital weight machine, distance by measuring tape, time by stopwatch and velocity by speed gun.

TABLE 3. Flight performance parameters

Mission	Parameter	Expectation	Test Result
1	Max speed	36 ft./s	40 ft./s
	Stall speed	18ft./s	19 ft./s
	Turn time	4s	9s
	No. of Laps	3	2
	Lap time	216s	300s
	RAC Weight	3	3.6
2	Take-off weight	5lb	5.6lb
	Max speed	43ft./s	40ft/s
	Stall speed	25ft/s	20ft/s
	Loading time	4min	2min
	Take-off distance	35ft	37ft
	RAC weight	3lb	3.6lb
3	Take-off weight	5lb	5.6lb
	Take-off distance	35ft	31ft
	3 Laps time	195s	203s

FIGURE 6. Flight test

CONCLUSION AND RECOMMENDATIONS

For the evaluation of flight performance all the missions were performed with final prototypes, simulating all the requirements. And the performance of flight was satisfactory.

In case of further development and improvement in performance author's recommendations are listed below.

- System engineering was followed for the design of this particular UAV. A single design solution is impractical for an aircraft. So some other approach like conceptual design can be followed to find out a better design solution.
- Throughout the design process weight plays an important role which affects the design parameters the most. So for effective and cost efficient design a light weight material for UAV like carbon fibre, composite material can be used for the fabrication process.

- Different wind models like-cross wind, head wind, gust etc. affect the performance and stability of UAV, so study on wing modelling must be taken into consideration for further development in design process.
- More attention in designing tail of an aircraft can result in reduced weight and drag and increase aerodynamic efficiency of the overall aircraft.

REFERENCES

1. "Integration of Civil Unmanned Aircraft Systems in the National Airspace System (NAS) Roadmap''-1st edition, (Federal Aviation Administration (FAA), 2013), page 47- 48.
2. Design/Build/Fly (DBF) Competition Rules, (AIAA, Wichita, 2013-14).
3. Abu Horaira Banna, M.; Afsar, M.R.; Ali, Z.M.S.; Abdus Salam, M., "Design, analysis & optimization of a small unmanned aircraft," in *Aerospace Conference, IEEE* (IEEE, Big Sky, MT, 2015), pp.1-18.
4. Raymer, D.P, "Aircraft Design: A Conceptual Approach''-4th edition, (AIAA, Washington, dc, 2006).
5. MATLAB ® Software.
6. Michael S. Selig, James J. Guglielmo, Andy P.Broeren and Philippe Giguere, "Summary of Low Speed Airfoil Data,"-Vol. 1, (SoarTech Publications, Virginia Beach, Virginia, 1995).
7. UIUC Airfoil Co-ordinate Database.
8. XFLR5 Airfoil Analysis Software.
9. Bernard Etkin, Lloyd Duff Reid, "Dynamics of Flight: Stability and Control''-3rd edition, (Wiley, 1995).
10. T.H.G. Megson, "Aircraft Structures for Engineering Students" -5th edition, (Elsevier, 2013).
11. SolidWorks 2013 Software.
12. "Aircraft Weight and Balance Handbook: FAA-H-8083-1A''-Vol. 1, (Aviation Supplies & Academics, 2007).

International Conference on Mechanical Engineering 2015
(ICME 2015) 18 – 20 December, 2015, Dhaka, Bangladesh

Paper ID :177

Thermal Comfort Analysis: A Case Study of LIG Housing in Chhattisgarh

Nisha Netam[1, b)], S. Sanyal[1, c)], S. Bhowmick[1, a)]

[1]*Department of Mechanical Engineering, NIT Raipur, Chhattisgarh, 492010, India*

a) Corresponding Author: sbhowmick.mech@nitrr.ac.in
b)nishane.me@nitrr.ac.in
c) ssanyal.mech@nitrr.ac.in

Abstract. The present work reports the evaluation of temperature distribution inside an Low Income Group (LIG) house located in the city of Raipur, Chhattisgarh, using a Agros2D which is multi-platform C++ application capable of higher-order finite element formulation with ***h***, ***p*** and ***hp*** adaptivity for the solution of differential equations based on the Hermes library. Variation of room air temperature along the length (x) of the house is calculated at different altitudes viz. 0.5m, 1m, 1.5m, 2m, 2.5m, and 3m. 2D model is generated for all the respective altitudes which show the temperature distribution inside the building.

INTRODUCTION

Low Income Group (LIG) houses are constructed by Chhattisgarh Housing board and major part of the middle class family resides in these houses. Raipur region (21.14ºN, 81.38ºE) climate is hot and dry in summer with temperature variation of 48º C maximum and 23ºC minimum. Thermal comfort is an important parameter for design of any building and it has been observed that LIG houses do not fulfill the comfort requirement under extreme weather conditions. Indoor air temperature is also an important parameter to determine thermal comfort.

The aim of this study is to investigate indoor air temperature to determine thermal performance of LIG house. This opens an interesting area of investigation wherein the temperature distribution inside the building can be computed to identify and classify different thermal zones and suggest solutions in the form of design modifications to moderate the thermal conditions naturally and cost effectively. As artificial moderation is costly and not environment friendly, identification of parameters of building design that could affect the moderation of thermal environment thereby enhancing thermal comfort is always a welcome opportunity.

The thermal design of buildings depends on many parameters indoor conditions required, the outdoor climatic conditions, building construction materials and insulation. Thermal performance of six different roof structure used in building construction in Saudi Arabia has been investigated by Al-Sanea [3], and it is reported that the effect of solar radiation on building envelope component is two times higher than that of effect of conduction and convection heat transfer on building envelope. Various analyses to predict the thermal performance of a whole building has been reported by many researchers. Chel et al. [5] investigated thermal performance of a mud-house located at Solar Energy Park of IIT Delhi, New Delhi (India). Based on energy balance equations a thermal model of the house consisting of six interconnected rooms was developed. Florides et al [9] used the TRNSYS computer program for the modeling and simulation of the energy flow inside the modern houses of Cyprus and presented energy consumption analysis. Mendes et al. [6] developed mathematical model for thermal performance analysis of building using MATLAB /SIMULINK. Due to environmental concern eco-friendly and innovative buildings are being introduced by many researchers. Pollard et al [8] investigated the effect of solar radiation on room air temperature of building to minimize the use of electrical energy by utilizing effectively solar radiation.

SIMULATION METHODOLOGY

In this paper, a powerful open source software Agros2D has used to predict room air temperature distribution of LIG house. Agros2D is a multi-platform C++ application capable of higher-order finite element formulation with ***h***, ***p*** and ***hp*** adaptivity for the solution of differential equations using Hermes library. Analysis has been carried out for a particular day of 21st June 2015 at noon 12.00 pm. Schematic plan of LIG house situated at Raipur region is shown in Fig. 1 and the thermal performance analysis has been carried out on this geometry. In order to determine temperature distributions in the room at different altitude, different boundary conditions have been considered. Although the building is a three dimensional structure, however, the analysis is simplified by reducing this complexity into 2 dimensions by distributing the roof solar radiation on the surrounding vertical walls. The distribution on these vertical walls is assumed to be a linear mathematical function with largest contribution at the roof altitude and least contribution near the ground. This implicates that the PLAN of the house has been simulated at different altitudes and the results have been compiled to get a 3 dimensional solution using a 2 dimensional algorithm. Agros2D simulates this in a convenient manner.

Designed details and properties of material have given in Table 1. These properties are used in mathematical model and simulation model for calculating room air temperature of LIG house.

TABLE 1. Material properties and their values considered in mathematical model**.**

Material	Property	Value
Outer Wall	Thermal Conductivity	2.224 W/mK
Inner Wall	Thermal Conductivity	2.602 W/mK
Roof	Thermal Conductivity	3.212 W/mK
Door	Thermal Conductivity	0.174 W/mK
Glass	Thermal Conductivity	0.814 W/mK
Air	Thermal Conductivity	0.024 W/mK
Inside Wall	Convective heat transfer coefficient	8.3 W/m^{2}K
Outside Wall	Convective heat transfer coefficient	22.7 W/m^{2}K

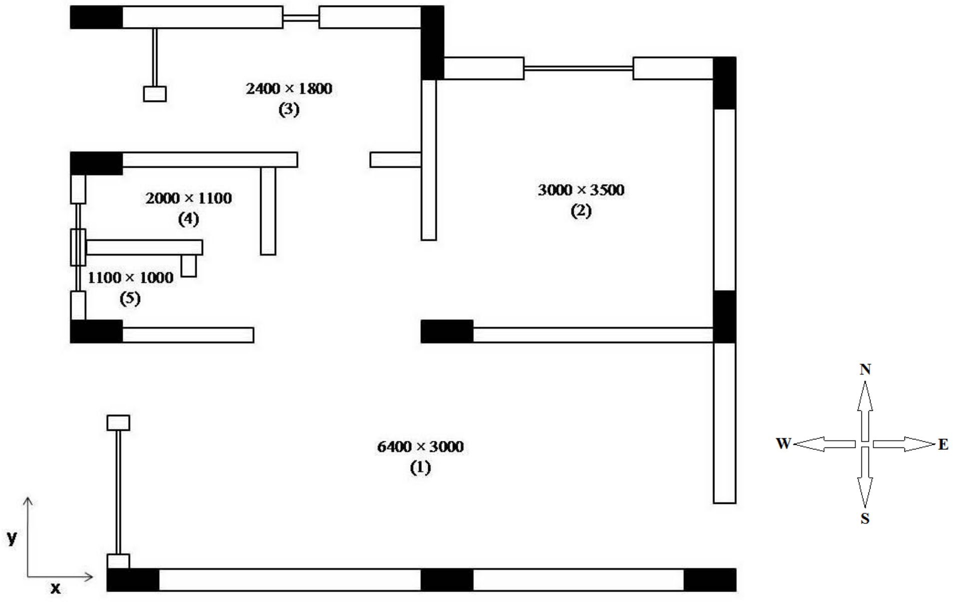

FIGURE 1. The layout of LIG house in C.G. prepared by housing board. (All dimensions are in mm)

Living Room 2. Bed Room 3. Kitchen 4. Bathroom 5. Toilet

MATHEMATICAL MODEL

Assumptions involved for developing mathematical model are

1. Solar radiation is constant for one hour duration.
2. Thermal properties of material are constant. It does not vary with temperature.
3. Convection heat transfer coefficient is assumed to be constant.
4. There is no heat loss/gain through ground.
5. Heat transfer is one directional along the wall and roof.
6. Inside and outside convective heat transfer coefficient is constant.
7. Doors and windows are closed.

Applying the energy conservation for each room and mathematical equation can be written as:

$$m_a c_a \sum \frac{dT_r}{dt} = Q_{gain} - Q_{loss} \tag{1}$$

Q_{gain}= heat gain through wall, window, door, roof and internal sources.

$$Q_{gain} = Q_{wall} + Q_{roof} + Q_{window} + Q_{door} + Q_{internal} \tag{2}$$

Q_{loss}= heat loss due to ventilation and ground

$$Q_{loss} = Q_{ventilation} + Q_{ground} \tag{3}$$

Heat balance equation for rooms can be written as:

$$\Sigma m_a c_a \frac{dT_r}{dr} = \sum_{i=1}^{4} (UA)_{wall}(T_{sol} - T_r) + (UA)_{roof}(T_{roof} - T_{r1}) + [A_{win} U_{win}(T_{sol} - T_r) + \mathrm{A}_{win}\, \tau I] + (UA)_{door}(T_{sol} - T_r) + Q_{internal} - \frac{\rho VCN(T_r - T_a)}{3600} - (UA)_{ground}(T_{r1} - T_o) \tag{4}$$

The overall heat transfer coefficient (U) of wall can be calculated from

$$U_{wall} = \left(\frac{1}{h_i} + \frac{l_1}{K_1} + \frac{l_2}{K_2} + \dots + \frac{1}{h_o}\right) \tag{5}$$

Total solar radiation incidence on wall/ roof can be calculated by given equation:

$$I_t = (I_{DN} \cos\theta + I_d + I_r) \tag{6}$$

Where, I_{DN} = Direct solar radiation is

$$I_{DN} = A.\exp\left(-\frac{B}{\sin\beta}\right) \qquad (\mathrm{W/m^2}) \tag{7}$$

I_d = Diffuse solar radiation from the sky

$$I_d = C I_{DN} F_{ws} \qquad (\mathrm{W/m^2}) \tag{8}$$

I_r = Solar radiation reflected from ground onto surface

$$I_r = (I_{DN} + I_D)\rho_g F_{WG} \qquad (\text{W/m}^2) \tag{9}$$

θ = Angle of incidence. The angle of incidence for wall is

$$\theta_{wall} = \cos^{-1}(\cos\beta.\cos\alpha) \tag{10}$$

Angle of incidence for roof is

$$\theta_{roof} = 90 - \beta \tag{11}$$

Where A is the apparent solar irradiation, B is atmospheric extinction coefficient, C can be taken as 0.135 for mid-summer and as 0.058 for winter, F_{WS} is view factor or configuration factor, ρ_g reflectivity of horizontal surface and F_{WG} is the angle factor.

RESULTS AND DISCUSSION

The effect of solar radiation on room temperature has been estimated for the LIG house. The ambient temperature data has been collected from the metrological department and the simulations of effect of solar radiation on the LIG house plan has been carried out using Agros 2D.

Lengthwise distribution of temperature at different altitudes is shown in Fig. 2. The figure reports the room air temperature distribution at different altitudes of 0.5m, 1m, 1.5m, 2m, 2.5m, and 3m respectively. To quantify the effect of solar radiation, contour plots of the temperature distribution inside the living room is plotted in Figure 3(a-f) for different altitudes. It can be observed that with the increase in altitude of living room, the temperature increases. Also, for each particular altitude, the temperature of the room near the door is very low as compared to other parts of the room due to lower thermal conductivity of the wood. The results show that with in the room the temperature is not constant due to the variable solar radiation values at different outside walls existing at different orientations.

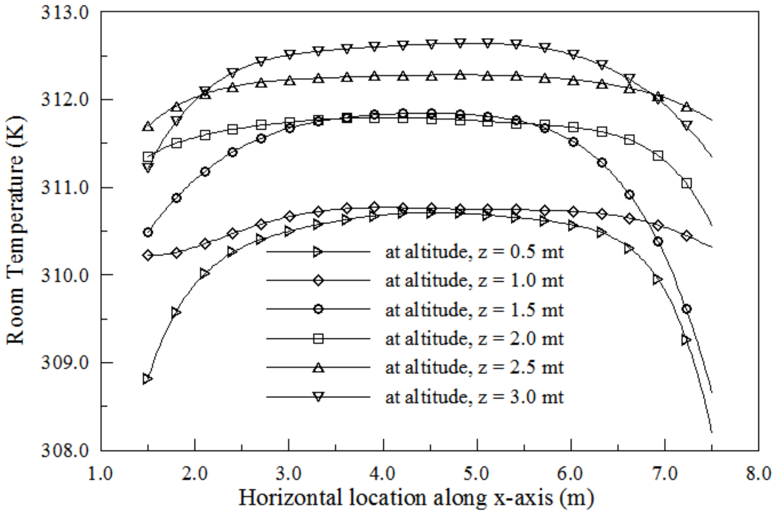

FIGURE 2. Temperature distribution inside the living room at different altitudes.

CONCLUSIONS

In the present work, thermal performance analysis has been done for LIG house of Chhattisgarh at different altitudes of building. With the results obtained from the simulation it is observed that temperature distribution inside the building is depend on the altitude of the building, solar radiation and material properties. The computations were carried out in order to find the accurate results in the shortest time possible. The results help to identify and classify different thermal zones that are transient throughout the day and lays proper foundation for identification and modification of design parameters for enhancing thermal comfort.

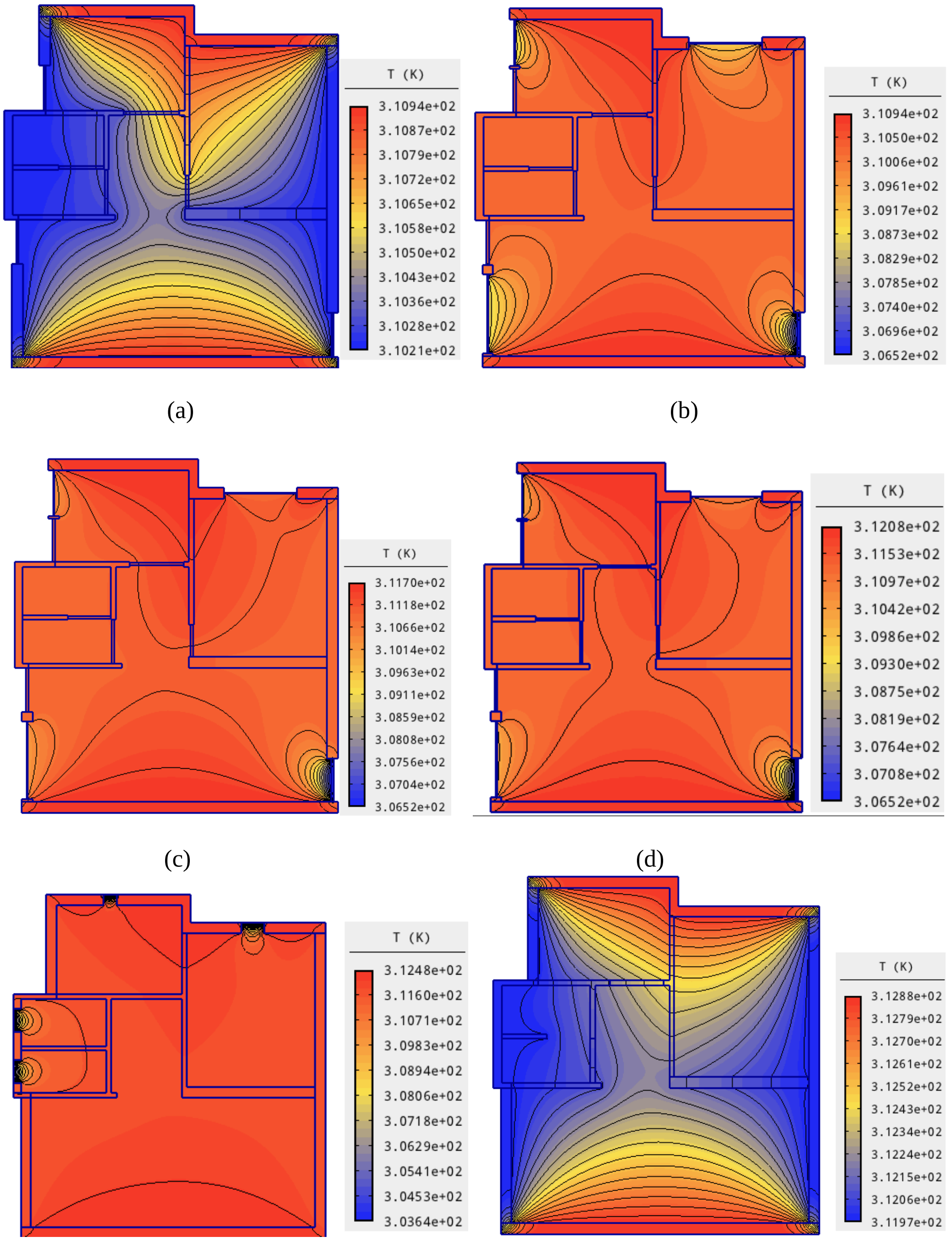

(a) (b)

(c) (d)

(e) (f)

FIGURE 3. Room air temperature distribution of LIG house at altitudes (a) 0.5 m (b) 1m (c) 1.5m (d) 2m (e) 2.5 m (f) 3 m.

NOMENCLATURE

Ma	Air mass (kg)
Ca	Specific heat of air (J/KgK)
Tr	Room temperature (K)
Tsol	Sol-air temperature (K)
A	Area (m2)
U	Overall heat transfer coefficient (W/m2K)
T	Transmissivity
I	Solar Radiation (W/m2)
V	Volume (m3)
ρ	Density (kg/m3)
N	Air change rate (h-1)
L	Thickness of material layer (m)
K	Thermal conductivity (W/mK)
hi	Inside heat transfer coefficient
ho	Outside heat transfer coefficient
α	Wall solar azimuth angle
β	Altitude angle
To	Earth temperature (25ºC)

REFERENCES

1. R. J. de Dear, G. S. Brager, ASHRAE Trans. **104**, 145-167 (1998).
2. N. Mendes, G. H.C. Oliveira and H. X. de Araújo, “Building Thermal performance analysis by using Matlab/Simulink” in proceedings of *Seventh International IBPSA Conference* Rio de Janeiro, Brazil (2001), August pp. 13-15.
3. S. A. Al-Sanea, Build. and Envirn. **38**, 1039 – 1049 (2003).
4. J. A. Duffie, W. A. Beckman, *Solar Engineering of Thermal Processes* (John Wiley & Sons , New Jersey, 2006)
5. A. Chel, G. N.Tiwari, Energy and Build. **41**, 56–66 (2009).
6. J. Morrissey, T. Moore, R. E. Horne, Renewable Energy. **36**, 568-577 (2011).
7. N. Ahmed M. Al-Tamimi, S. F. Syed Fadzil, W. M. Wan Harun, J. Sust. Develop. **4**, (2011).
8. A.Pollard, R. O. Driscoll and D. N. Pinder, “The impact of solar radiation on the air temperature within a residential building’’ in International solar energy society Solar World Congress, Adelaide (2001).
9. G. A. Florides, S. A. Kalogirou, S. A. Tassou and L. C. Wrobel, Energy **25**, 915–937 (2000).

International Conference on Mechanical Engineering 2015
(ICME 2015) 18 – 20 December, 2015, Dhaka, Bangladesh

Paper ID :189

Heavy Metal Speciation and Toxicity Characteristics of Tannery Sludge

Md. Ariful Islam Juel[1, a],Zia Uddin Md. Chowdhury[1, b] andTanvir Ahmed[2, c]

[1]*Department of Leather Engineering, Khulna University of Engineering and Technology, Khulna-9203, Bangladesh*
[2]*Department of Civil EngineeringBangladesh University of Engineering and Technology, Dhaka-1000, Bangladesh*

[a)]Corresponding author: juelbclt@gmail.com
[b)]zia1.chowdhury@yahoo.co.uk
[c)]tanvirahmed@ce.buet.ac.bd

Abstract. Heavy metals present in tannery sludge can get mobilized in the environment in various forms and can be a cause for concern for the natural ecosystem and human health. The speciation of metals in sludge provides valuable information regarding their toxicity in the environment and determines their suitability for land application or disposal in landfills. Concentrations of seven heavy metals (Cr, Pb, Cd, Ni, Zn, As and Cu) in tannery sludge were determined to evaluate their toxicity levels. Metal contents ranged over the following intervals: As: 1.52-2.07 mg/kg; Pb: 57.5-67 mg/kg; Cr: 15339-26501 mg/kg; Cu: 261.3- 579.5 mg/kg; Zn: 210.2-329.1 mg/kg and Ni: 137.5-141.3 mg/kg (dry weight basis).The concentrations of all heavy metals in the sludge samples were lower compared to EPA guidelines except chromium which was found to be several orders of magnitude higher than the guideline value. Toxicity Characteristics Leaching Procedure (TCLP) test indicated that the leaching potential of chromium was higher compared to the other heavy metals and exceeded the EPA land disposal restriction limits. To quantitatively assess the environmental burden of the chromium associated with tannery sludge, the IMPACT 2002+ methodology was adopted under the SimaPro software environment. Considering the USEPA limit for chromium as the baseline scenario, it was found that chromium in the tannery sludge had 6.41 times higher impact than the baseline in the categories of aquatic ecotoxicity, terrestrial ecotoxicity and non-carcinogens. Chromium has the highest contribution to toxicity in the category of aquatic ecotoxicity while copper is the major contributor to the category of terrestrial ecotoxicity in the tannery sludge.

INTRODUCTION

Leather industry plays a significance role in the economy of Bangladesh. Bangladesh earned $1.29 billion from exports of leather, leather goods and footwear in the 2013-14 fiscal which accounts for 4.2 percent of the country's total exports[1]. There are reportedly around 220 tanneries in Bangladesh but, in fact 113 tanneries are in effective operation which are mostly situated at Hazaribagh area [2]. Although the tanning industry is environmentally important as a principal user of meat industry waste, the industry is perceived as a consumer of resources and a producer of pollutants. Annually about 85000 tons of raw material are processed in Bangladesh [2]. Processing one metric ton of raw hide generates 200 kg of final leather product, 250 kg of non-tanned solid waste, 200 kg of tanned waste, and 45-50 m3 of wastewater containing 2500-12500 mg/l suspended solid[3]. In wastewater treatment process, different chemicals are added and most of the chemicals get settled out during the process. Finally they end up in the sludge. Tannery sludge is an unwanted residual solid generated in the tannery wastewater treatment plant and its management is a critical environmental issue. In Bangladesh, there is no set method for tannery sludge disposal, and the sludge are disposed in landfill sites haphazardly or openly, leading to soil, surface water and groundwater contamination, and can pose a threat to natural resources, the environment and residents living within the immediate vicinity of the sludge disposal locations [4]. Very common heavy metals like As, Cr, Co, Ni, Cu, Zn, Fe, Cd may be prevalent in the tannery sludge due to use of basic chromium salt, different syntans, dyes, pigments, retanning agents etc. in the tanning process. These heavy metals are very harmful because of their non-biodegradable nature, long biological half-lives and their potential to accumulate in different body parts [5][6][7]. Metal-containing sludge application in agricultural land is risky, because these metals may be taken up by the crop roots and incorporated into the plant tissue. Ultimately, these toxic metals can get entrance into the human body and lead to bio-accumulation and bio-magnification. So excessive accumulation of heavy metals in agricultural soils through wastewater irrigation and sludge disposal may not only result in soil contamination, but also affect food quality and safety [8]. Health effects of these metals include kidney malfunction, the possibility of DNA damage or cancer development, damage to the central nervous system, reproductive failure and possibly even infertility. [5][9][10][11]. Heavy metal concentration in tannery sludge and their mobilization potential are therefore of great interest.Here we determine the various heavy metal contents in sludge generated from the Effluent Treatment Plant of a leather manufacturing industry in Bangladesh. The heavy metal leaching potentialfrom the sludge and its toxicity effect on the environmentare also assessed.

MATERIALS AND METHOD

Sludge samples were collected from Apex Tannery Ltd, unit-2, Gazipur, Bangladesh in January, 2015. One month, 6 month and 12 month aged sludge were collected from the sludge drying beds and dump sites to assess the temporal variation of sludge constituents. The samples were stored and conveyed using polythene bags. After collection, some portion of sludge samples were dried in a vacuum oven at 105°C until constant weight, lightly ground for homogenization and prepared for the analysis of selected heavy metals, moisture content and organic content. For heavy metal analysis, 5 gm. of dried sample was digested with acid (HNO3: HCl =1:3 volume ratio) to prepare a 500 ml solution. Finally, concentration of seven heavy metals (As, Pb, Cd, Cr, Ni, Cu, and Zn) was determined in the environmental engineering laboratory, BUET by using Atomic Absorption Spectrophotometer (AAS). Toxicity characteristics leaching procedure (TCLP) test for sludge samples were performed according to USEPA 1311 method to determine the immediate toxicity level of heavy metals [12]. The environmental impact assessment was conducted based on impact 2002+ methodology using SimaPro, a commonly used Life Cycle Analysis (LCA) software. This software is integrated with various databases and impact assessment methods [13].

RESULT AND DISCUSSION

Physical characteristics of sludge

The pH of sludge samples ranged between 7.4-7.8 and therefore, the sludge can be regarded as neutral. The moisture content of the sludge samples ranged between 60% - 76%. The organic contents of one month, six month and twelve month aged sludge were 33.53%, 27.11% and 24.75% respectively. This indicated that with the increasing the age of sludge the organic content reduced gradually due to degradation of organic substances.

Heavy metal content in sludge

The selected heavy metal concentrations for each sample found in the sludge in this study are shown in Table 1 where sample 1, sample 2 and sample 3 represent one-month, six-month and twelve-month aged sludge respectively. Metal contents ranged over the following intervals: As: 1.52-2.07 mg/kg; Pb: 57.5-67 mg/kg; Cd: < 0.01 mg/kg; Cr: 15339-26501 mg/kg; Cu: 261.3- 579.5 mg/kg; Zn: 210.2-329.1 mg/kg and Ni: 137.5-141.3 mg/kg (dry weight basis). Mean concentration of the metals were: As: 1,769 mg/kg; Pb: 63.77 mg/kg; Cd: BDL; Cr: 19229 mg/kg; Cu: 385.73 mg/kg; Zn: 250.6 mg/kg; Ni: 139.5mg/kg, allowing to arrange the metals from higher to lower mean content in this sludge as: Cr > Cu > Zn> Ni >Pb> As > Cd.

The total heavy metals content found in the sludge were compared to several international regulatory limits of heavy metal content for sludge utilization.The present study found that the average concentration of arsenic, cadmium, lead, nickel and zinc except chromium and copper were well below the India, China and USA Land Disposal Restriction Limits. When compared with recommended limits, Cr showed more than 75 times higher than SEPAC (State Environmental Protection Administration of China) limit and about 7 times higher than USEPA limit

(Table1) [14]. Usually tannery sludge contains high levels of chromium as most of hides and skins are tanned with basic chromium salt and more than 60% of the chromium is wasted and ultimately transferred to sludge through wastewater treatment processes [15]. Due to high chromium content the sludge will not be suitable for soil amendment applications in agricultural land or home vegetation. The average concentration of copper in the sample was 385.73 mg/kg which exceeded the India (270 mg/kg) and China (100 mg/kg) land disposal restriction limit but was below the USEPA (4300 mg/kg) limit.

TABLE 1. Concentration of heavy metals in tannery sludge and different legislations for sludge utilization

Parameter	**Heavy metals in the sample (mg/kg)**						
	As	**Cr**	**Pb**	**Cd**	**Ni**	**Cu**	**Zn**
Sample 1	1.7	15339	57.3	BDL	139.7	579.5	210.2
Sample 2	2.1	26501	67.0	BDL	137.5	261.3	212.5
Sample 3	1.5	15847	67.0	BDL	141.3	316.4	329.1
Average	1.8	19229	63.8	-	139.5	385.7	250.6
Standard Deviation	0.3	6303	5.6	-	1.91	170.1	68.0
Permissible limit in India[a]	-	-	250-500	3-6	-	135-270	300-600
SEPAC limit in China[b]	-	250	350	0.6	26600	100	300
USEPA limit[c]	75	3000	840	85	420	4300	7500

NA: Not Available, [a] Source: Awashthi (2000), [b] Source: SEPA (1995), [c] Source: USEPA Clean Water Act, Title 40, section 503.13, BDL: Below Detection Limit. (Detection limit for Cd is 0.01 mg/l)

Toxicity Characteristics Leaching Procedure (TCLP) Test

The Toxicity Characteristics Leaching Procedure (TCLP) test is designed to identify wastes that are likely to leach hazardous concentrations of particular toxic constituents into the groundwater. During the TCLP test, constituents are extracted from the waste to simulate leaching actions that occur in landfills. If the concentration of the toxic constituents exceeds the regulatory limit, the waste is classified as hazardous.

TABLE 2. Results of concentrations of As, Cr, Pb, Ni, Cu and Zn in Standard TCLP leaching test of leachates from raw sludge

Parameter	**Leached as mg/l**					
	As	**Cr**	**Pb**	**Ni**	**Cu**	**Zn**
Sample 1	0.013	2.75	0.082	0.32	0.055	0.044
Sample 2	0.015	0.453	0.033	0.088	BDL	0.01
Sample 3	0.019	0.407	0.018	0.147	BDL	0.002
Average	0.016	1.203	0.044	0.185	0.055	0.019
Standard Deviation	0.003	1.340	0.033	0.121	-	0.022

Note: BDL: Below Detection Limit(Detection limit for Cu is 0.01 mg/l)

The result of mean concentrations of As, Cr, Pb, Ni, Cu and Zn in TCLP test is given in Table 2. When the TCLP result is compared with the EPA Land Disposal Restrictions Limits (LDR) [16] (Figure 1), the mean concentration of As, Pb, Ni, Cu and Zn were found to be under the prescribed limit but the mean concentration of chromium exceeded the EPA standard. This indicates that there is a potential risk of ground water contamination by chromium.

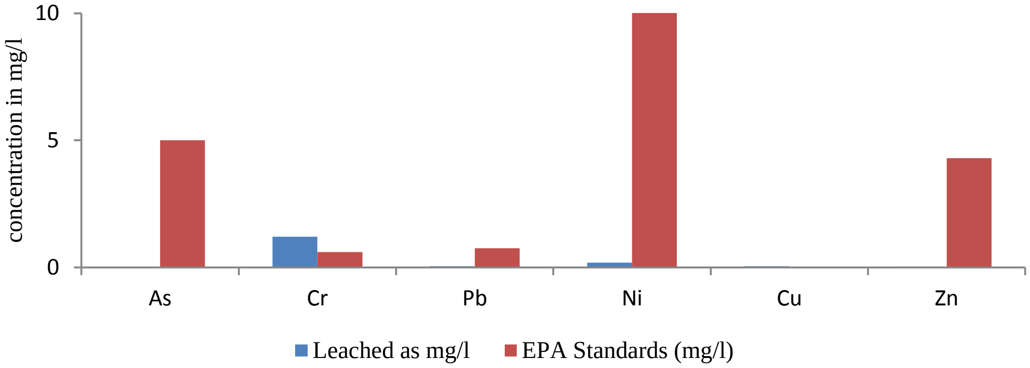

FIGURE 1. Results of average concentrations of As, Cr, Pb, Ni, Cu and Zn in Standard TCLP leaching test of leachates from raw sludge and their EPA Standards

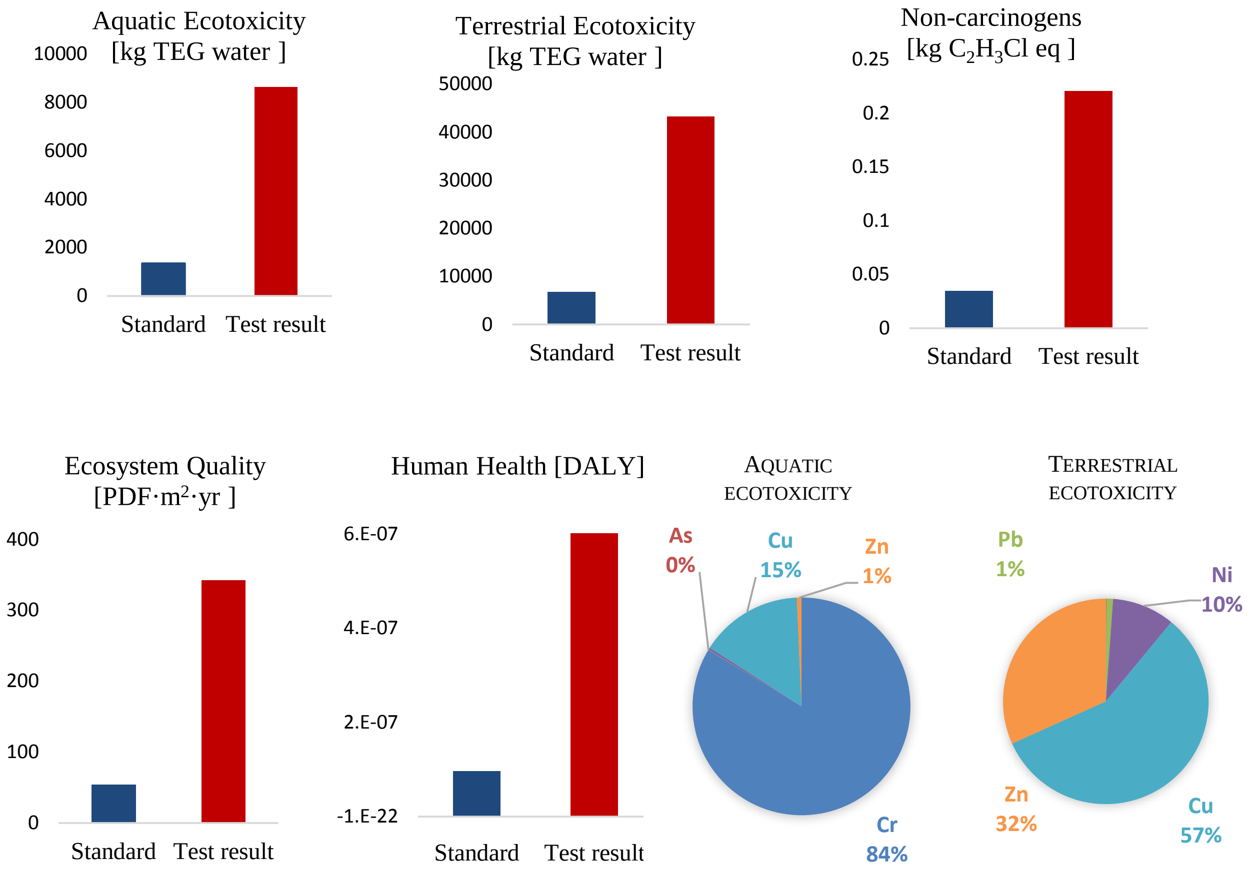

FIGURE 2. The environmental impact (aquatic ecotoxicity and terrestrial ecotoxicity) and damage assessment (ecosystem quality and human health) of chromium obtained from total extraction. Pie charts indicate the relative contribution of heavy metals over impact categories aquatic ecotoxicity and terrestrial ecotoxicity.

Impact assessment

Impact assessment is a technical quantitative, and/or qualitative process to characterize and assess the effects of the environmental burdens. The impact assessment of tannery sludge containing chromium was conducted based on impact 2002+ methodology [17]. This method links all types of results via several midpoint categories like carcinogens, non-carcinogens, aquatic ecotoxicity, terrestrial ecotoxicity, aquatic acidification, aquatic eutrophication, terrestrial acidification/nitrification, land occupation, global warming, non-renewable energy consumption and mineral extraction to four damage categories (human health, ecosystem quality, climate change and resources). Linking to midpoint is associated with certain conversion factors for each pollutant and conversion to damage categories is also associated with damage factors. SimaPro was used to analyze the impact of heavy metal measured from total extraction. It has been found that only chromium goes beyond the USEPA standard limit (Table1) which has impact in terms of aquatic and terrestrial ecotoxicity (contributing to the damage category of ecosystem quality) and non-carcinogens (contributing to the damage category of human health). The extent of impact with respect to the USEPA standard for all impacts and damage categories is shown in Figure 2. Assessment has been done based on the leachate of heavy metals per kg of tannery sludge released into the agricultural area. It can be seen that the impact of heavy metals in the sludge is estimated to be about 6-7 times higher than that corresponding to the permissible standards stated in USEPA over all the damage categories. This is mainly due to the toxic effect of heavy metals on the ecosystem (both aquatic and terrestrial) and human health.InFigure 2, Kg equivalent of a reference substance expresses the amount of a reference substance that equals the impact of the considered pollutant (e.g. TEG-Triethylene glycol) in the midpoint categories. PDF·m^2·y (Potentially Disappeared Fraction of species disappeared on 1 m^2 of earth surface during one year) is the unit to measure the impacts on ecosystems. DALY (Disability-Adjusted Life Years) characterizes the disease severity, accounting for both mortality (years of life lost due to premature death) and morbidity (the time of life with lower quality due to an illness, e.g., at hospital)[18].

The relative contribution of heavy metals over these damage categories has also been assessed. It has been estimated that chromium has higher order of toxicity (84%) in the aquatic ecotoxicity category followed by copper (15%) for tannery sludge. On the other hand copper contributes the maximum (57%) to terrestrial ecotoxicity followed by Zinc (32%) and Nickel (10%). This assessment has only been done based on the total heavy metal content of the sludge samples.

CONCLUSION

Tannery sludge management in Bangladesh is a challenging task for the industries, which are producing wastewater treatment residues. The traditional means of disposal of sludge has been either by open dumping (sometimes near the rivers) or by land filling which are all uncontrolled processes. This may lead to serious soil and ground water pollution through leaching of heavy metals. Results presented in this study show that Chromium is the principal heavy metal contaminant in tannery sludge that has potential to be released in the environment leading to soil and groundwater pollution. High chromium concentrations in the sludge from tanneries may also render the sludge unsafe for agricultural and home vegetation applications. TCLP tests confirmed that the sludge can be classified as hazardous as per EPA standards. The impact assessment using SimaPro showed that the release of toxic sludge in the environment has high potential for environmental degradation. In order to reduce the environmental burden of tannery sludge or promote its beneficial uses as compost or soil conditioner, chromium recovery is essential in the effluent treatment process.

REFERENCES

1. M. A. Hashem, A. Islam, S. Mohsin and N. Tomal, Sustain. Water Resour. Manag. **1**, 343–347 (2015).
2. H. L. Paul, A. P. M. Antunes, A. D. Covington, P. Evans, and P. S. Phillips, J. Soci. Leather Tech. Chemist **97**, 25–32 (2013).
3. S. Hüffer and T. Taeger,J. Am. Leather Chem. Association, **99**, 424–428 (2004).
4. J.C. Thompson, J. Azariah and A. G. R. Viji,Environ. Monit. Assessment, **18**, 359–368 (1999).
5. S. E. Manahan, *Environmental Chemistry*, 8th edition (Lewis Publisher,Boca Raton, Florida, 2005).

6. B. Wilson and F. B. Pyatt, UK. Ecotoxico. Environ. Safety,**66**, 224–231 (2007).
7. K.P. Singh, D. Mohan, S. Sinha and R. Dalwani, Chemosphere**55**, 227–255 (2004).
8. M. Muchuweti, J. W. Birkett, E. Chinyanga,R.Zvauya, M. D. Scrimshaw, J. N. Lester, Agri. Ecosyst. Environment **112**, 41–48 (2006).
9. G. S. Senesi, G. Baldassarre, N. Senesi and B. Radina, Chemosphere **39**, 343–377 (1999).
10. M. K. Türkdoğan, F. Kilicel, K. Kara, I. Tuncer and I. Uygan, Environ. Toxicol. Pharmacology **13**, 175–179 (2002).
11. G. Kocasoy and V. Sahin, J. Environ. Sci. Health**42**, 2139–2146 (1999).
12. USEPA, *Toxicity Characteristic Leaching Procedure (TCLP).* (USEPA Method 1311, Publication SW846, 1992) available at: https://www.epa.gov/epaoswer/hazwaste/test/pdfs/1311.pdf.
13. M. Goedkoop, M. Oele, J. Leijting, T. Ponsioen and E. Meijer, *Introduction to LCA with SimaPro*. available at: https://www.pre-sustainability.com/download/SimaPro8IntroductionToLCA.pdf
14. USEPA, *Land Application of Sewage Sludge*. Available at http://www3.epa.gov/npdes/pubs/sludge.pdf
15. K. Kolomaznik, M. Adamek, I. Andel and M. Uhlirova, J. Hazard. Materials **160**, 514–520 (2008).
16. USEPA, *Land Disposal Restriction*. Available at: http://www.gpo.gov/fdsys/pkg/CFR-2012-title40-vol28/xml/CFR-2012-title40-vol28-sec268-40.xml
17. O. Jolliet, M. Margni, R. Charles, S. Humbert, J. Payet, G. Rebitzer and R. Rosenbaum, Int. J. Life Cycle Assessment **8**, 324–330 (2003).
18. S. Humbert, M. Margni, and O. Jolliet, *IMPACT 2002+ User Guide Draft for version 2.1* (Switzerland, 2011)

International Conference on Mechanical Engineering 2015
(ICME 2015) 18 – 20 December, 2015, Dhaka, Bangladesh

Paper ID : 199

Biogas Production from Tannery Wastage Using Mesophilic Anaerobic Digestion Process

Md. Naim Jahangir[1, a)], Siduzzaman Khan[1], Ayesha Kabir Mila[1], Mohidus Samad Khan[2, b)], Mohammad Arif Hasan Mamun[1]

[1]Department of Mechanical Engineering, Bangladesh University of Engineering and Technology, Dhaka 1000, Bangladesh, 2Department of Chemical Engineering, Bangladesh University of Engineering and Technology, Dhaka 1000, Bangladesh.

a) Corresponding author: naim.buet09@gmail.com
b) mohid@buet.ac.bd

Abstract. Tannery industries in the recent times have become a major source of fetid fleshy wastage. The tanning process, which includes fleshing, splitting and liming-reliming leaves fleshy wastage and shaving wastage. Production of biogas from tannery wastage not only reduces the use of fossil fuel but also ensures faster and safer degradability of harmful wastage. Biogas production by anaerobic digestion process applying mesophilic condition leads to microbial conversion of organic matter to methane. For biogas production, filtering flasks of 1.5-4 liter capacity were used as preheater and digester. A carbon to nitrogen ratio of 23:1 is optimal for methane gas production. To keep the continuous process within the optimal range, nitrogen gas was flushed at 6 to 8 psi pressure in the preheater. After that the raw material was kept at 47°C to 57°C in the furnace for 3-5 hours to make the process mesophilic. For biogas production a mixture was prepared containing fleshy tannery wastage, thioglycollate broth as anaerobic culture media, and water solution of carbohydrate and protein. Mesophilic digestion process takes 18 to 24 days to produce biogas. Here three different methods have been applied and 14.14% of methane gas obtained using the 3rd method. Further research can be done to identify the value added options of solid digested waste as fertilizer after biogas production from anaerobic digestion of tannery wastage. Using biogas, both electricity and heat can be produced with the help of gas powered generator and it can also be used in cooking and power plants when gas turbine reaches its peak speed.

INTRODUCTION

Tannery wastage in the recent past has become a major source of environmental imbalance. Different health problems such as skin diseases like itch, rash, cough, fever, diarrhea, headache, asthma, dizziness etc are increasing due to unplanned tannery waste disposal. In the tanning process many chemicals such as chromium oxide, ammonium sulfate, formic acid, sulfuric acid, sodium chloride etc are used which causes solid and liquid wastes [1]. İn the processing of raw hide and skin the sulphuric acid and salt are used and then they are treated with the solutions of chromium salts. In the tannery, chromium waste, HCl, sulphuric acid, sodium arsenate, arsenic sulphite etc are used for different tanning process such as soaking, liming, deliming, tanning etc [2]. Tannery wastage mainly contains fetid raw flesh which is a major concern for environment because it takes a lot of time to degrade. On the other hand, the consumption of energy is rapidly increasing and the related environmental pollution and climate change are approaching critical stage requiring sustainable solution. The human population worldwide uses 220 EJ energy per year, 78% of this being supplied by fossil energy carriers.

The European Union has remarked a joint effort to reduce the emission of greenhouse gases by 20%. It also advised that 20% of the energy produced should be supplied from sustainable energy by 2020 [3]. Biogas is environmental friendly. Biogas is mainly a gas mixture of CH_4 and CO_2 which is produced by micro-organisms under anaerobic conditions. The digested wastage after biogas production from the digestion process contains nutrients and can be used as soil conditioner [4]. Anaerobic digestion is the most widely used method of organic waste disposal due to its high performance in volume reduction and stabilization and the production of biogas that makes the process profitable [5]. It is divided into four steps: hydrolysis, acidogenesis, acetogenesis and methanogenesis. In each stage, different group of micro-organisms works. Three major group of micro-organisms are primary fermenting bacteria, anaerobic oxidizing bacteria and methanoginic archea [4-6]. Conditions and variables influencing anaerobic digestion are total solid content, temperature, retention time, pH, carbon to nitrogen ratio, mixing property.

Anaerobic digestion process can be classified as mesophilic and thermophilic process. In mesophilic process, temperature is kept within 30°C-40°C and in thermophillic process temperature is kept above 55°C. Wastage mixture was preheated at 47°C-55°C so that decompose may occur at a faster rate. Digester was kept at 35°C for 18-24 days. The relationship between the amount of carbon and nitrogen present in organic materials is represented by the C: N ratio. Optimum C: N ratios in anaerobic digesters are in between 20 to 30. A high ratio is an indication of a rapid consumption of nitrogen by the methanogenesis and results in a lower gas production [8].

METHODOLOGY

Methodology used in that research consists of three basic parts: preheater, digester and gas chromatography. At first, tannery wastage was cut into small pieces and then Sodium Bicarbonate was mixed with the pieces. Necessary amount of distill water and milk were added with the samples. Then nitrogen gas was flushed at 6-10 psi pressure. It was kept in the furnace at 50°C for about an hour for faster decomposition. The content of biogas varies with the material being decomposed and the environmental conditions involved [9]. Potentially all organic waste materials contains adequate quantities of the nutrients essential for the growth and metabolism of the anaerobic bacteria in biogas production. However, the chemical composition and biological availability of the nutrients contained in this materials varied with species, factors affecting growth and age of the animal or plant [9]. Various waste have been utilized for biogas production and they include amongst others; animal waste [10-12], industrial waste [13], food producing waste [14], plant residues [15, 16] etc. After proper decomposition, produced gas was released through the opening of the valve and broth was applied to ensure proper bacterial growth. Considering the fact of the necessity of high carbohydrate, lipid and protein for proper culturing media, thioglycollate broth was used. Nitrogen was flushed at 2-4 psi pressure after ensuring all the valves were closed. Then the digestion stage starts and the whole setup was kept for another 20-24 days. 1st and 2nd sample didn't show any comprehensive result. In the 3rd sample, we tried to control pH in the optimal range and final result showed that increased amount of methane at the gas chamber. It is obvious that biogas as well as methane gas yield is increased as the temperature increased from 20°C-30°C [17]. The final part of design was gas collection and measurement of gas percentages using gas chromatogram. Tedlar bag was used to collect gas. Bag size varied from 1 liter to 1.5 liter. Silica gel bed used during gas collection to ensure that no moisture can enter into the gas chromatogram. In that part of gas chromatography, inert gases such as He, Ne, N2 were used as carrier gases. Our obtained result and standard result were compared to identify the percentage of produced gas.

SAMPLE PREPARATION & EXPERIMENTAL SETUP

Sample Preparation

Preparation of samples for the 1st and 2nd setup were almost same. The solution contained distilled water, milk and broth. About 280 gram of tannery wastage was cut into small pieces. Equal amount of water was mixed with it. 200 ml milk was mixed with the broth and this solution was mixed with main wastage solution. Nitrogen was flushed in the leak proof chamber at 8 psi. The sample was kept inside the furnace for about 2 hours at 47°C. It was the preheating stage which helps proper decomposition of samples. Gas pressure inside increased too high and thus CO_2 dominated gas were blown out from the chamber through the valve. Again nitrogen was flushed at about 4-5 psi pressure. Generally it takes 18 days to produce biogas. This is the digesting part of the samples. Mesophilic condition was maintained during those 18 days. It was done to ensure proper growth of microorganisms. In the 2nd sample, preheating wasn't applied to check the wastage property in atmospheric temperature and pressure and the change in biogas production percentage. The 3rd sample contained 105 gram tannery raw fleshy wastage, 105 gram distilled water and 105 gram of milk. About 10 gram of broth was mixed with the sample solution. Then it was kept in the furnace at 45°C for 1 hour. Internal pressure raises to about 28 psi and pressure was released. Some basic compounds were mixed into the chamber because excess CO_2 made the chamber acidic. Keeping the pH in the optimal range was the main objective of it.

Experimental Setup

A 2 liter filtering flask was used for the 1st sample (FIGURE1 (a)). The flask had two openings. One in the upper side and the other is at the right side. The upper part was sealed using rubber gasket. Araldite was used to seal the flask with the gasket. Valves with special fitting was attached at the opening of the side portion. Valve size was universal to assure easy gas transfer system. After flushing nitrogen, soapy water was used to check if there was any leakage. Gas was leaking from the spacing between the chamber and the cork. Fetid smell was emitting from the chamber. The major problem we faced was gas leakage and then we used positive-negative gum instead of araldite. Positive-negative gum has the advantages of being sealed within one or two hour whereas araldite takes 6 or 7 hours. This time, nitrogen was flushed and there was no additional smell. Using soapy water, we didn't find any bubbles. Thus we got our first leak proof setup. Our 2nd setup was very similar to the 1st one. This time we used normal flask of 4 liter instead of filtering flask (FIGURE 1(b)). Generally filtering flask are more resistant to heat. Here flask's thickness was less than the filtering flask. Both setup were used for mesophilic anaerobic digestion but in the first sample preheating was done at 45°C.

In the 2nd setup, after flushing nitrogen, gas flask was kept at atmospheric temperature. We tried to check how the temperature property changes with production of gas. Our main purpose was to maintain the anaerobic media in an optimal condition. For proper culturing and bacteria growth, it is very important to maintain optimal condition [18]. The flask had one openings in the upper surface. Fittings were prepared and sealed with the upper portion of the rubber cork. Universal port size was engaged everywhere. That made our work easier to find appropriate joints. Cork was sealed with the flask using positive-negative gum. Keeping pH in the optimal range, was a challenge. To keep the solution within the optimal range of pH, $NaHCO_3$ was used. Addition of $NaHCO_3$, made the solution pH within the optimal range. But with the production of CO_2 and increasing pressure, pH and pressure were hard to control. CH_4 doesn't produce at a great quantity even though the internal gas pressure was near about 30 psi.

(a) (b) (c)

FIGURE 1. Experimental Setups for biogas production

According to the Doerr er al biogas production process works best at neutral pH values or slightly above neutral value (7-8.5). For that reason, releasing CO_2 was very important which makes the chamber acidic. After the preheating stage the last sample was poured in the flux with increased amount of $NaHCO_3$ and gas was released twice from the production chamber (FIGURE 1(c)). That was done for two purpose. First one is to decrease gas pressure inside the chamber and the 2nd one is to remove CO_2.

RESULT & DISCUSSION

TABLE 1 shows the percentage of gas produced in the experiment. Three different process were applied and thus it can clearly be observed that production of biogas production varied a lot depending on the culturing condition. The first sample was kept in air tight chamber with chemicals for 22 days. The result shows 52.1 % of CO_2, and less than 1% of CH_4. The pressure was measured 28 psi. To develop the procedure, the second sample was flushed with N_2 without any preheating stage. It was kept for 20 days in the digester to digest properly. These results 49.76% of CO_2. But the CH_4 content was still less than 1%. Increased CO_2 made the gas chamber more acidic and optimal pH range wasn't existed in the chamber. Inside the gas flux chamber, pressure was about 20 psi. The optimal pH condition wasn't maintained properly.

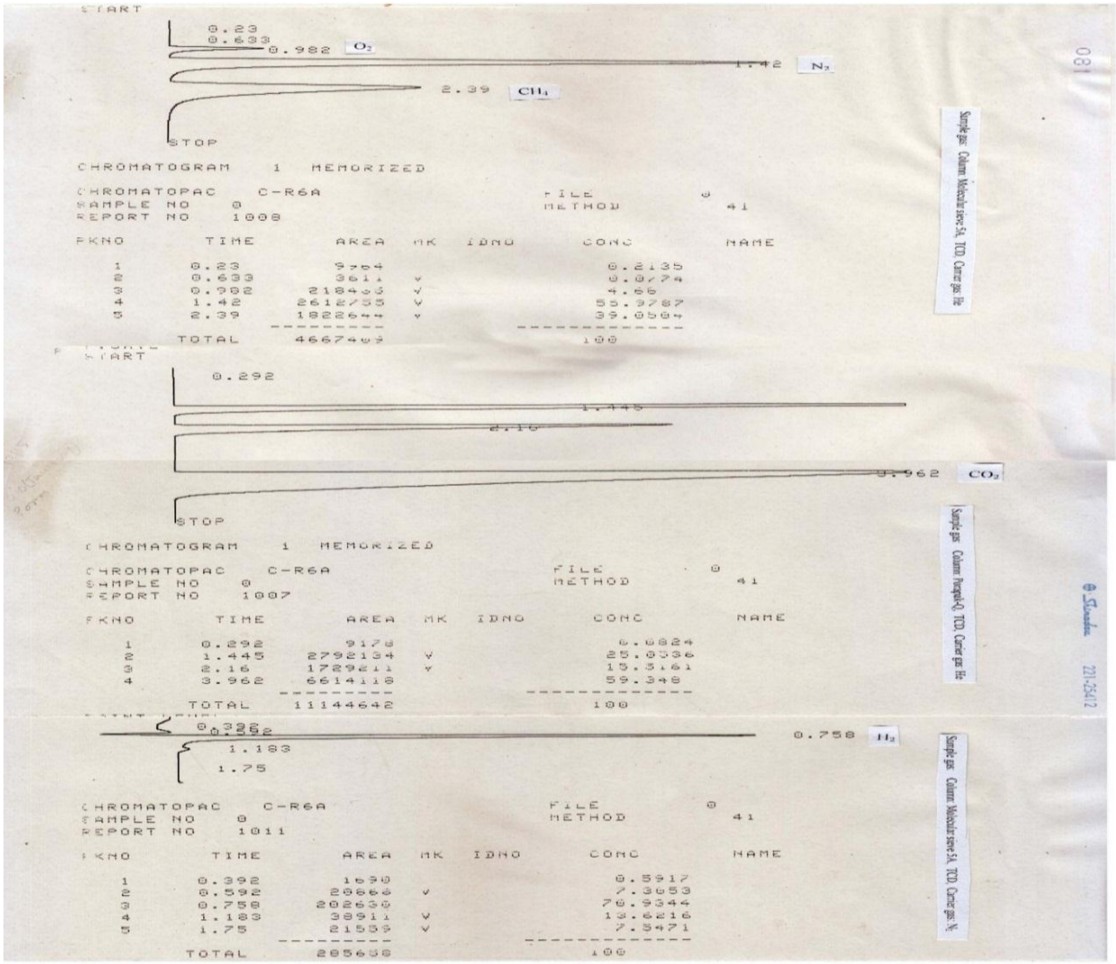

```
CHROMATOGRAM     1   MEMORIZED

CHROMATOPAC     C-R6A                       FILE           0
SAMPLE  NO      0                           METHOD          41
REPORT  NO      1008

PKNO       TIME         AREA   MK   IDNO       CONC          NAME

  1        0.23          9764                   0.2135
  2        0.633         3611   V               0.0774
  3        0.982       218433   V               4.66
  4        1.42       2612755   V              55.9787
  5        2.39       1822644   V              39.0584
                    ---------              -------------
         TOTAL        4667409                 100
```

```
CHROMATOGRAM     1   MEMORIZED

CHROMATOPAC     C-R6A                       FILE           0
SAMPLE  NO      0                           METHOD          41
REPORT  NO      1007

PKNO       TIME         AREA   MK   IDNO       CONC          NAME

  1        0.292         9178                   0.0824
  2        1.445      2792134   V              25.0536
  3        2.16       1729211   V              15.5161
  4        3.962      6614118                  59.348
                    ---------              -------------
         TOTAL       11144642                 100
```

```
CHROMATOPAC     C-R6A                       FILE           0
SAMPLE  NO      0                           METHOD          41
REPORT  NO      1011

PKNO       TIME         AREA   MK   IDNO       CONC          NAME

  1        0.392         1690                   0.5917
  2        0.592        20668   V               7.3653
  3        0.758       202630                  76.9344
  4        1.183        38911   V              13.6216
  5        1.75         21559   V               7.5471
                    ---------              -------------
         TOTAL         285658                 100
```

FIGURE 2: Results obtained after gas chromatography for sample 3. It is a dry basis analysis where gas detection tubes (GASTEC, Japan) have been used for H2S and NH3 detection

In the 3rd setup (FIGURE 1(c)), all the procedures were same. But $NaHCO_3$ was used after preheating and after 26 days, we found about 14.14% of methane with increased amount of CO_2. H_2S level was above 160 ppm and it was more than the measuring capacity of used gas chromatograph (GC-14B, Shimadzu, Japan). In order to produce high amount of biogas there is a need for microorganism to access the substrate. Because the substrate act as a food for the microorganism, the lack of it will reduce biogas production [20]. That is why increased amount of carbohydrate, lipid and protein were used in the container. Controlling temperature and pH are very important for the growth of microorganism. FIGURE 2 shows the gas chromatography results obtained after producing biogas for sample 3. Model of used gas chromatography was GC-14B, Shimadzu, Japan. Gas detection tubes (GASTEC, JAPAN) have been used for H_2S and NH_3 detection. At standard condition, known volume percentage (8.37) of CH_4 covered 1159342 unit square area. CH_4 of sample 3 covered 1822644 unit square area that gives 13.15% CH_4 in 92.95% volume. This is further converted to dry basis 100% analysis which gives 14.14 % of CH_4.

TABLE 1: Percentage of gas produced (dry basis mole percentage)

Analysis	**CH_4**	**CO_2**	**O_2**	**N_2**	**H_2**	**NH_3**	**H_2S**
Sample-1 (mole%)	0.0032	52.10	3.78	34.09	4.60	-	-
Sample-2 (mole%)	0.0011	49.76	4.18	46.06	-	-	More than 160 PPM
Sample-3 (mole%)	14.14	58.68	1.99	23.81	1.38	-	More than 160 PPM

Pressure gauge was not used directly with the setup. It was connected with the valve of the fitting as shown in the figure in the experimental setup section. Because of the fitting, each time some gases were leaking from the main chamber. Thus we got some reduced percentage of biogas. Silica bed was prepared using a bottle and rubber cork with two holes. 2 pipes with fitting were applied in those holes. Inside the bottle, silica was applied. Gas from the chamber passed through this bed and becomes moisture less. Then moisture free gas was collected in tedlar bag and was set for gas chromatography operation.

CONCLUSION

Special types of water solution containing carbohydrate, lipid, protein and other chemicals were used. Appropriate broth wasn't available and we selected broth according to the needs for culture media from the available resources. Controlling pH in the optimal range was a major issue as production of CO_2 made the solution acidic. Higher percentage of CH_4 produces at relatively lower pressure. That's why, there was a vast improvement of CH_4 production in the 3rd sample. Controlling pH in a more organized way should produce higher percentage of CH_4. Mesophilic anaerobic digestion process is used where temperature range is about 30°C -40°C.

Leakage problem is one of the major obstacles for biogas production. Here 8 experimental setups were made. 5 of which were beset with leakage problems. Special types of positive-negative gum were used here. There should be new ideas to make air tight chamber which can withstand high temperature for both mesophilic and thermophilic anaerobic digestion process. Protein rich compounds can produce 50-54% biogas. Tannery wastage consists of protein, lipid, carbohydrate etc. By adding compounds to increase its protein percentage may produce higher percentage of methane gas. But optimal pH range and temperature should be maintained for proper microorganism growth.

Further researches can be done to identify the value added options of solid waste as fertilizer after biogas production from anaerobic digestion of tannery wastages. That would reduce a lot of cost and that would allow the full use of tannery wastage. Using biogas, both electricity and heat can be produced and it can also be used in cooking.

ACKNOWLEDGEMENT

The author wants to acknowledge Md. Shamsur Rahman for his kind assistance during gas analysis and setup preparation.

REFERENCES

1. P. Gain, “Bangladesh Environment: Facing the 21st century,” SEHD proceedings, (Society for Environment and Human Development, Dhaka, 2002), pp. 12-18.
2. Tinni, S. Hoque, et al., Journal of Environmental Science and Natural Resources **7.1**, 149-156 (2015).
3. Kovács, Etelka, "Augmented biogas production from protein-rich substrates and associated metagenomic changes", Bioresource technology-178, (Bioresource technology, Tainnan, 2015), pp. 254-261.
4. Bayr, Suvi. “Biogas production from meat and pulp and paper industry by products,” (Jyväskylä studies in biological and environmental science, Jyvaskyla, 2014) pp. 280-286.
5. P. Vindis, et al., Journal of Achievements in Materials and Manufacturing Engineering **36.2,** 192-198 (2009).
6. Wieczorek, Nils, Mehmet Ali Kucuker, and Kerstin Kuchta. "Microalgae-bacteria flocs (MaB-Flocs) as a substrate for fermentative biogas production," Bioresource technology-194, (Bioresource technology, Tanian, 2015), pp. 130-136.
7. Abdollahi, Hamid, Mohammadreza Atashzar, and Maryam Amini. Journal of Medical Hypotheses and Ideas **9.2,** 67-71 (2015).
8. Verma, Shefali, "Anaerobic digestion of biodegradable organics in municipal solid wastes," PhD Thesis, Columbia University, 2002.
9. Manyi-Loh, E. Christy, Sampson N. Mamphweli, Edson L. Meyer, Anthony I. Okoh, Golden Makaka, and Michael Simon, International journal of environmental research and public health **11.7**, 7184-7194 (2014).
10. E.O. Uzodinma, and A. U. Ofoefule, International Journal of the Physical Sciences **4.2**, 91-95 (2009).
11. Ofoefule, U. Akuzuo, Joseph I. Nwankwo, and Cynthia N. Ibeto. Journal of Advances in Applied Science Research **1.2**, 1-8 (2010).
12. A.U. Ofoefule, et al. International Journal of the Physical Sciences **4.34**, 7811-7815 (2011).
13. A.U. Ofoefule, E. O. Uzodinma, and O. D. Onukwuli, Trends apple. Sci. Res. **2(6)**, pp. 554-558 (2007).
14. Arvanitoyannis, Ioannis S., and Theodoros H. Varzakas. "Vegetable waste treatment: comparison and critical presentation of methodologies." Critical Reviews in Food Science and Nutrition 48, no. 3 (2008), pp. 205-247.
15. Ofoefule, A. U., E. O. Uzodinma, and O. D. Onukwuli. International Journal of Physical Sciences **4.8**, 535-539 (2009).
16. C. Mondal, G. Biswas. International Journal of Engineering and Science. ISSN – 2778-4721, **l1.6**, 01-06, (2012).
17. Wu, Jinfeng, Jinbo Xiong, Changju Hu, Yu Shi, Kai Wang, and Demin Zhang. "Temperature sensitivity of soil bacterial community along contrasting warming gradient." Applied Soil Ecology 94 (2015), pp. 40-48.
18. J. Imu, D.M Samuel, “Biogas production potential from municipal organic wastes in Dhaka city,” IJRET ISSN 2319-116 (Research India Publication, Delhi, 2012), pp. 13-18.

International Conference on Mechanical Engineering 2015
(ICME 2015) 18 – 20 December, 2015, Dhaka, Bangladesh

Paper ID : 203

A Mathematical Model of Extremely Low Frequency Ocean Induced Electromagnetic Noise

Manik Dautta[1,a),b)], Rumana Binte Faruque[1,c)] and Rakibul Islam[1,d)]

[1]*Research & Development Engineer, Anyeshan Limited, Dhaka.*

[a)]Corresponding author: manik.dautta@anyeshan.com
[b)]URL: http://www.anyeshan.com
[c)]rumana.faruque@anyeshan.com
[d)]rakibul.islam@anyeshan.com

Abstract. Magnetic Anomaly Detection (MAD) system uses the principle that ferromagnetic objects disturb the magnetic lines of force of the earth. These lines of force are able to pass through both water and air in similar manners. A MAD system, usually mounted on an aerial vehicle, is thus often employed to confirm the detection and accomplish localization of large ferromagnetic objects submerged in a sea-water environment. However, the total magnetic signal encountered by a MAD system includes contributions from a myriad of low to Extremely Low Frequency (ELF) sources. The goal of the MAD system is to detect small anomaly signals in the midst of these low-frequency interfering signals. Both the Range of Detection (R_d) and the Probability of Detection (P_d) are limited by the ratio of anomaly signal strength to the interfering magnetic noise.In this paper, we report a generic mathematical model to estimate the signal-to-noise ratio or SNR. Since time-variant electro-magnetic signals are affected by conduction losses due to sea-water conductivity and the presence of air-water interface, we employ the general formulation of dipole induced electromagnetic field propagation in stratified media [1]. As a first step we employ a vol-umetric distribution of isolated elementary magnetic dipoles, each having its own dipole strength and orientation, to estimate the magnetic noise observed by a MAD system. Numerical results are presented for a few realizations out of an ensemble of possible realizations of elementary dipole source distributions.

INTRODUCTION

An aerial platform equipped with a MAD system is primarily used to detect, localize, and possibly track large ferromagnetic object submerged in a vast body of water. The performance of the system, as measured by P_d and False Alarm Rate (FAR), is governed by the complexity of underlying electromagnetic processes. A MAD sensor responds to temporally- and spatially-varying earth's magnetic field, magnetic noise generated by the aerial platform, ocean-induced magnetic noise, geomagnetic noise, magnetic noise caused by local geological features, and magnetic signals generated by ferromagnetic objects of interest [2, 3, 4, 5]. The desired magnetic signature is produced by the target object's ferromagnetism, motion-induced eddy currents, and corrosion-related sources [6].

Predicting the effectiveness of an aerial vehicle-based MAD system to detect the target of interest is a challenging task. To evaluate the MAD sensor's performance, presence of noisy DC-like and ELF magnetic signals in the search environment must be taken into consideration. Knowledge of extraneous noise-like signals in a typical search environment is usually obtained from field measurements, which in general depend on the time of the day and are accompanied by seasonal variations. Collection of these signals also is a time consuming and expensive process. The purpose of this paper, is therefore, to simulate dominant components of magnetic noise signals in a given ocean environment. Specifically, we present a mathematical frame-work for modeling magnetic noise in an ocean environment. Simple illustrations of the application of the frame-work to estimate magnetic noise and their adverse effects on target induced signal are also presented.

MATHEMATICAL FORMULATION

The main objective of this work is to calculate SNR for successful detection by MAD system. Below detailed mathematical procedure for calculating signal and noise power will be presented.

Magnetic Fields due to Dipoles Embedded in Stratified Media

Closed form equations of EM fields due to magnetic and electric dipoles are known through [7]. In this paper calculation for magnetic fields will be presented only. For a magnetic dipole, magnetic flux density in a uniform medium is given as,

$$\tilde{\mathbf{B}}_{mdip}(\mathbf{r},\omega) = \frac{\mu}{4\pi}\left[\frac{k^2(\hat{r}\times\tilde{\mathbf{m}})\times\hat{r}}{r} + \{3\hat{r}(\hat{r}\cdot\tilde{\mathbf{m}}) - \tilde{\mathbf{m}}\}\left\{\frac{1}{r^3} - \frac{ik}{r^2}\right\}\right]e^{ikr} \tag{1}$$

Here, time dependence $e^{-i\omega t}$ was assumed. $\tilde{\mathbf{B}}$ and $\tilde{\mathbf{m}}$ denotes phasor representation of magnetic field density and magnetic moment vector respectively. It is noted that throughout the paper bold letters denote vector field and tilde at the top of letters denote phasor quantity. $\mathbf{r}$ is the position vector of the observation point and $\hat{r}$ denotes unit vector along that direction. μ is the relative permeability and ε is the permittivity of the medium. $k = \omega\sqrt{\mu\varepsilon}$ is the wave number which denotes phase change per meter for a wave. In case of a stratified anisotropic media, a method is presented for calculating EM fields by Tang in Ref. [1]. The geometric configuration of that method for three different regions are described in Fig. 1a. Here for sea-water environment region (0) is sea-water, region (1) is air and region (-1) is sea-bed region. The dipole source is located in region (0) at the origin. Here the source can be horizontal electric dipole, horizontal magnetic dipole, vertical magnetic dipole, or vertical electric dipole. The magnetic field intensity is expressed in TE and TM mode formulation as

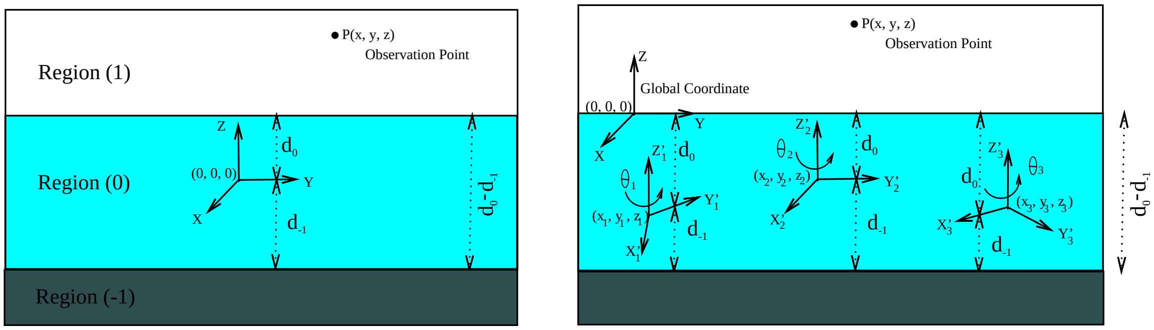

(a) Geometric representation given by Tang in Ref. [1]. (b) Proposed geometry considering multiple sources.

FIGURE 1. $d_0 - d_{-1}$ represents width of region (0) which was kept fixed at $200m$. Point P is the observation point and considered stable at $10m$ above the interface. Global coordinate is at air-water interface. Different dipoles are placed at (x_l, y_l, z_l) where l identifies dipole number. Each dipole is considered to be in the origin of respective local coordinates to match the equations for single dipole of Fig. 1a. For each dipole $d_0 = |z_l|$, hence $d_{-1} = d_0 - 200m$. θ_l represents orientation of l^{th} dipole and each dipole is assumed to have an initial phase constant of ψ_l.

$$\tilde{\mathbf{H}} = \tilde{\mathbf{H}}^{TM} + \tilde{\mathbf{H}}^{TE} \tag{2}$$

In region (j) the general solutions for waves outgoing in the $\hat{r}$ direction and traveling in the $\hat{z}$ direction are listed below. TM components are:

$$\begin{bmatrix} H_j^{TM}(r) \\ H_j^{TM}(\phi) \\ H_j^{TM}(z) \end{bmatrix} = \begin{bmatrix} \int_{-\infty}^{+\infty} d\lambda \left(\frac{-i\omega\varepsilon'_j}{\lambda^2 r}\alpha_j^+(\lambda,z)\,H_n^{(1)}(r\lambda)\,S_n^{TM'}(\phi)\right) \\ \int_{-\infty}^{+\infty} d\lambda \left(\frac{i\omega\varepsilon'_j}{\lambda}\alpha_j^+(\lambda,z)H_n^{(1)'}(r\lambda)\,S_n^{TM}(\phi)\right) \\ 0 \end{bmatrix} \tag{3}$$

Whereas TE components are:

$$\begin{bmatrix} H_j^{TE}(r) \\ H_j^{TE}(\phi) \\ H_j^{TE}(z) \end{bmatrix} = \begin{bmatrix} \int_{-\infty}^{+\infty} d\lambda \left(\frac{-\gamma_j{}^{(m)}}{\lambda} \beta_j^{-}(\lambda, z) H_n^{(1)'}(r\lambda)\, S_n^{TE}(\phi) \right) \\ \int_{-\infty}^{+\infty} d\lambda \left(\frac{-\gamma_j{}^{(m)}}{\lambda^2 r} \beta_j^{-}(\lambda, z) H_n^{(1)}(r\lambda)\, S_n^{TE'}(\phi) \right) \\ \int_{-\infty}^{+\infty} d\lambda \left(\beta_j^{+}(\lambda, z) H_n^{(1)}(r\lambda)\, S_n^{TE}(\phi) \right) \end{bmatrix} \tag{4}$$

Here $k_j{}^2 = \omega^2 \mu_j \varepsilon_j{}'$, $\gamma_j{}^{(e)} = \sqrt{\lambda^2 - k_j^2}$, $\gamma_j{}^{(m)} = \sqrt{\lambda^2 - k_j^2}$, $\alpha_j{}^{\pm}(\lambda, z) = \pm A_j(\lambda)\, e^{\gamma_j{}^{(e)} z} + B_j(\lambda)\, e^{-\gamma_j{}^{(e)} z}$ and $\beta_j^{\pm}(\lambda, z) = \pm C_j(\lambda)\, e^{\gamma_j{}^{(m)} z} + D_j(\lambda)\, e^{-\gamma_j{}^{(m)} z}$. From Equations 3 and 4, the first, second and third elements of the column matrices are the $\hat{r}$, $\hat{\phi}$ and $\hat{z}$ components of the field respectively. $H_n^{(1)}$ is the Hankel function of the first kind and order n. $S_n^{TM}(\phi)$ and $S_n^{TE}(\phi)$ stand for sinusoidal functions of ϕ depending on the dipole source. Primes on any term denotes differentiation with respect to the arguments. Here, $H_n^{(1)'}(r\lambda) = {nH_n^{(1)}(r\lambda)}/{(r\lambda)} - H_{n+1}^{(1)}(r\lambda)$ is the derivative of Hankel function of the first kind. $A,\ B,\ C,\ D$ are functions of λ , and they are obtained by the application of boundary conditions which are used for our case given by Tang in Ref. [1]. For the elementary dipoles under consideration, field values derived by Kong in Ref. [8] are used.

Signal Power Calculation

The value of magnetic field, $\mathbf{B}_{signal}$ at region $(j = 1)$ i.e. air region can be obtained using Equations 3 and 4 where a single dipole source was placed in region $(j = 0)$ i.e. in sea-water. Target source is assumed to be a large vertical magnetic dipole having $k \to 0$. Source power, P_{signal} can be written as,

$$P_{signal} \propto \left| \tilde{\mathbf{B}}_{signal} \right|^2 \tag{5}$$

Noise Power Calculation

For noise modelling, concept of multiple dipole sources come into consideration. To illustrate the hypothetical concept of multiple sources a geometrical representation is presented in Fig. 1b. Here observation point $P(x,\ y,\ z)$, different dipoles position (x_l, y_l, z_l), their respective orientation θ_l and initial phases ψ_l will be considered random in nature. The net field $\tilde{\mathbf{B}}(r, \phi, z)$ is known for a geometric configuration given in Fig. 1a with the help of Equations 3 and 4 for cylindrical coordinate system. For convenience all the values are converted into Cartesian coordinate system. In Fig. 1b each dipole can be viewed in a local frame of reference. So a transformation matrix governing the translation and rotation can be used in this regard to map the global coordinates to local frame of references so that identical equations can be used to determine the field values. Therefore time-varying noise signal can be obtained using Equation 6.

$$\mathbf{B}_{noise}(x, y, z, t) = \mathrm{Re}\left\{ \sum_{l=1}^{N} \mu_j \tilde{\mathbf{H}}_j (x'_l, y'_l, z'_l)\, e^{-i(\omega_l t + \psi_l)} \right\} \tag{6}$$

Here N is the total number of dipoles and $\mathrm{Re}\{\}$ represents real value of the argument. The position of observation point with reference to local coordinate system is obtained for individual dipoles using the following transformation:

$$\begin{bmatrix} x'_l \\ y'_l \\ z'_l \end{bmatrix} = [R_{z'}(\theta_l)]^{-1} \begin{bmatrix} x - x_l \\ y - y_l \\ z - z_l \end{bmatrix}$$

Where $R_{z'}(\theta_l) = \begin{bmatrix} \cos\theta_l & -\sin\theta_l & 0 \\ \sin\theta_l & \cos\theta_l & 0 \\ 0 & 0 & 1 \end{bmatrix}$ is the rotation matrix with respect to z' axis. It is noted that prime coordinates refer to positions with respect to local frame of reference. Finally noise power is obtained using Equation 7.

$$P_{noise} \propto \left| \mathbf{B}_{noise,RMS} \right|^2 = \sum_{l=1}^{N} \left(\frac{B_{jl}}{\sqrt{2}} \right)^2 \tag{7}$$

Here $B_{jl} = \mu_j H_j (x'_l, y'_l, z'_l)$ is the amplitude of magnetic flux density at region j due to l^{th} dipole.

Signal-to-Noise Ratio (SNR) Calculation

Signal-to-noise ratio is defined as the ratio of the power of a signal (meaningful information) and the power of background noise (unwanted signal). In dB scale SNR is calculated as:

$$SNR_{dB} = 10\log_{10}\left(\frac{P_{signal}}{P_{noise}}\right) = 20\log_{10}\left(\frac{B_{signal}}{B_{noise,RMS}}\right) \tag{8}$$

Where P_{signal} and P_{noise} will be calculated using Equations 5 and 7 respectively.

RESULTS AND DISCUSSIONS

For a static magnetic dipole ($k \rightarrow 0$) its magnetization is static in nature i.e. it doesn't have any propagation of wave like feature. Again magnetic permeability of sea-water and air are same. Therefore considered static magnetic dipole field will not be altered at air-water interface as their magnetic properties are same. Closed form Equation 1 is valid for uniform medium. Since air and sea-water have identical magnetic property, field value from Equation 1 and from Tang Equations 3 and 4 should exactly match. It is found that for a dipole placed $50m$ below the interface and field value observed $10m$ above the interface for a dipole of strength $1000Am^2$ is $0.9259nT$ which is same from both set of equations. In this paper above mentioned dipole is considered as target signal. To consider the effect of distributed wave, ocean current etc. sea-water nature can be modeled as sources of low frequency electromagnetic induced noise.

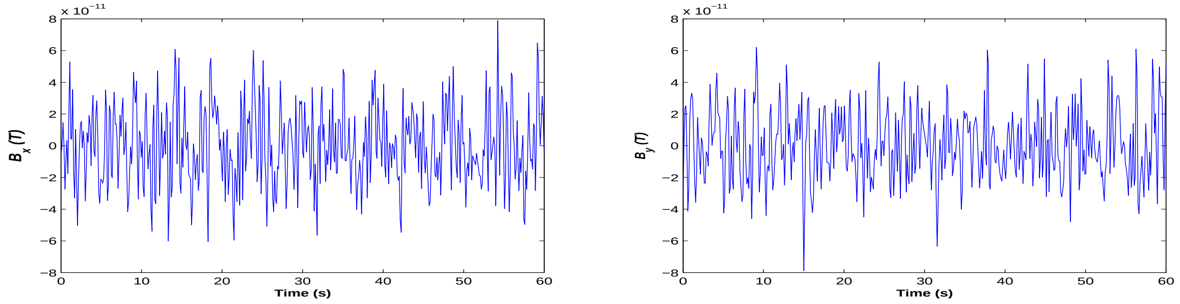

(a) Noise Magnetic Field: $x-$component (B_x).

(b) Noise Magnetic Field: $y-$component (B_y).

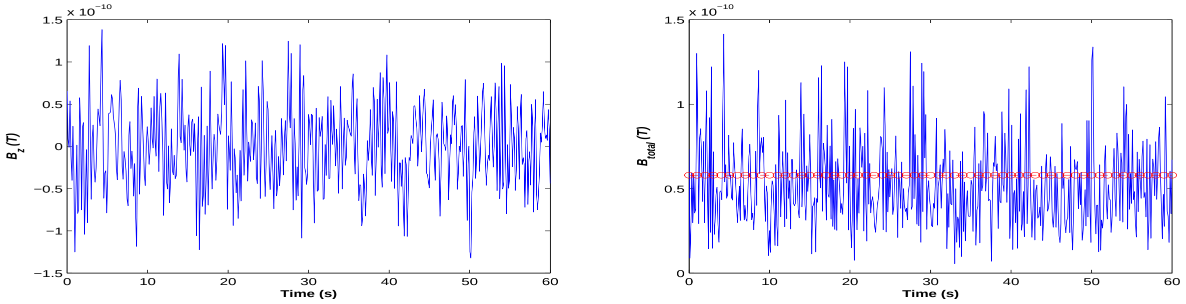

(c) Noise Magnetic Field: $z-$component (B_z).

(d) B_{total}(Noise).

FIGURE 2. Here Fig. 2a to Fig. 2c provide three-axis components of time-varying noise magnetic field observed at $10m$ above the air-water interface. Two types of magnetic dipole (horizontal & vertical) are considered. In this paper total number of dipoles are 100. Time varying signals are observed within a time frame of $[0, 60s]$. The parameter for dipoles are: $m = rand[0.1, 0.2]Am^2$, $f = rand[0.1, 3]Hz$, $\theta = rand[0, 360^0]$ and $\psi = rand[0, 2\pi]$. Dipoles are assumed to be placed within $3-4m$ below air-water interface randomly. The parameters for air medium (region 0) are: $\sigma = 0\mho$, $\mu = 1\mu_0$, $\epsilon = 1\epsilon_0$ and for sea-water medium (region (1)) are: $\sigma = 5\mho$, $\mu = 1\mu_0$, $\epsilon = 78\epsilon_0$. Fig. 2d plots absolute value of three axis components termed as B_{total}. Red circled line denotes RMS value of the obtained flux density.

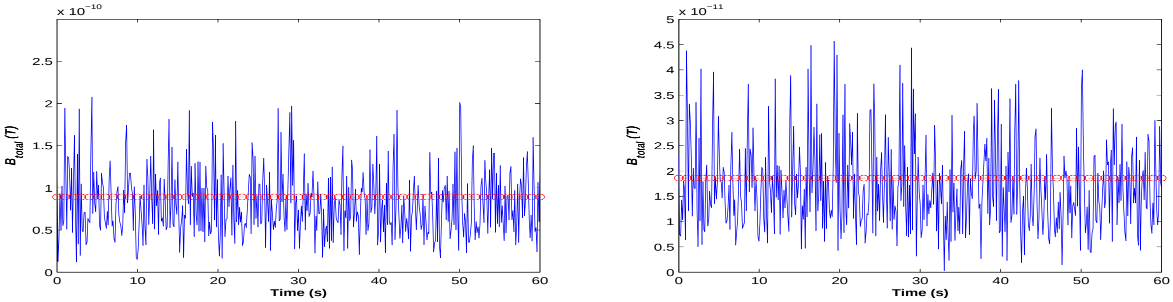

(a) B_{total} for dipoles placed within $1-2m$.

(b) B_{total} for dipoles placed within $9-12m$.

FIGURE 3. Time-varying noise contribution from different layers.

Here two types of dipoles are considered as sources of noise namely horizontal magnetic dipole along $x-$direction and vertical magnetic dipole [1]. A mathematical model for noise calculation was developed and time varying noise signal in Fig. 2 is observed for 100 dipoles. The dipoles are placed within $3-4m$ below the interface where placings are performed following random gaussian distribution. Again dipole moments m, dipole frequencies f, orientations θ and initial phases ψ are also considered random in nature. In Fig. 2a to Fig. 2c time-varying noise along three axes are plotted to correspond with detection technique of Three-Axis Magnetometer [9]. From Fig. 2d it is clear that for 100 dipoles placed randomly within $3-4m$ below the interface noise contribution lies within $0.02nT$ to $0.12nT$ approximately with a RMS value of $0.05797nT$ and SNR of $24.07dB$. If dipole positions are varied keeping other parameters constant, a change in noise value is obtained and that value will diminish significantly if dipoles are far below the interface. For example, in Fig. 3a RMS value of noise is approximately at $0.08927nT$ which is greater than the noise obtained at Fig. 2d and SNR is reduced to $20.31dB$. Again for dipoles within $9-12m$ noise value decreases to around $0.01861nT$ and hence SNR improves to $33.94dB$. Therefore noise contribution gradually diminishes with the increase in layer depth from the interface and exactly opposite case for SNR. It is noted that red markers in total field plots denote RMS value line.

MAD systems detect signal which is composed of target signal and noise signal. At Fig. 4 results are shown for a target source of $1000Am^2$ placed at $50m$ below the interface and 100 dipoles as noise sources placed within $3-4m$ layer below the interface. In Fig. 4a to Fig. 4c time-varying target signal corrupted by noise along three axes are plotted to correspond with detection technique of Three-Axis Magnetometer [9]. From Fig. 4d it is clear that RMS value (shown with red marker) of noisy target signal is around $0.9277nT$. From dipoles, RMS noise contribution is around $0.05797nT$ which gives SNR of $24.07dB$. Target source may be at any depth in the ocean. The average depth of the ocean is about $14,000ft(=4267.2m)$. In this paper, sea environment is considered to be $200m$ deep. As the target moves further from the interface SNR decreases which impedes the detection of MAD system. It is known that, for a successful detection noise contribution should be atleast 2 to $3dB$ below the the target signal strength. The authors proposes that in case of deep ocean environment MAD system range can be increased to around $500m$ if the target strength is sufficient enough (e.g. $4000Am^2$).

CONCLUSION

Variation of magnetic field sensed by MAD systems may occur due to temporal and spatial variation in earth magnetic field, magnetic noise generated by aerial platform, ocean-induced magnetic noise, geomagnetic noise etc. In this paper a noble mathematical approach was presented to calculate noise contribution due to ocean induced electromagnetic field considering arbitrary randomly distributed magnetic dipoles having random strengths, orientations, frequencies and initial phases. A method to calculate signal-to-noise ratio was also be presented. It is noted that all of the simulation results and their interpretations are proposed considering shallow sea environment.

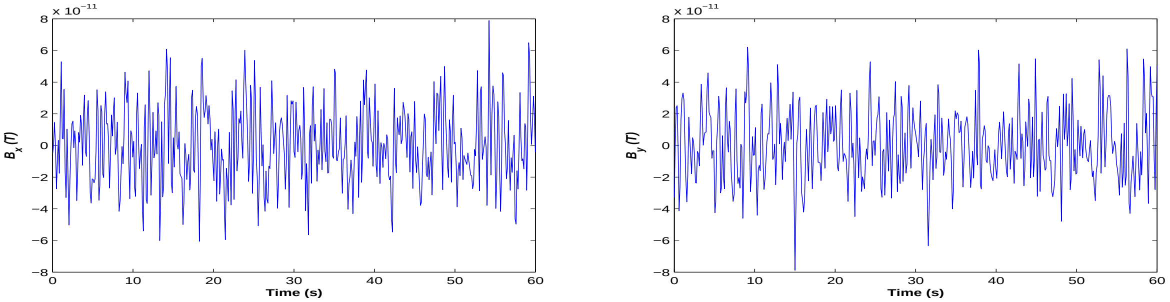

(a) Noise Magnetic Field: $x-$component (B_x).

(b) Noise Magnetic Field: $y-$component (B_y).

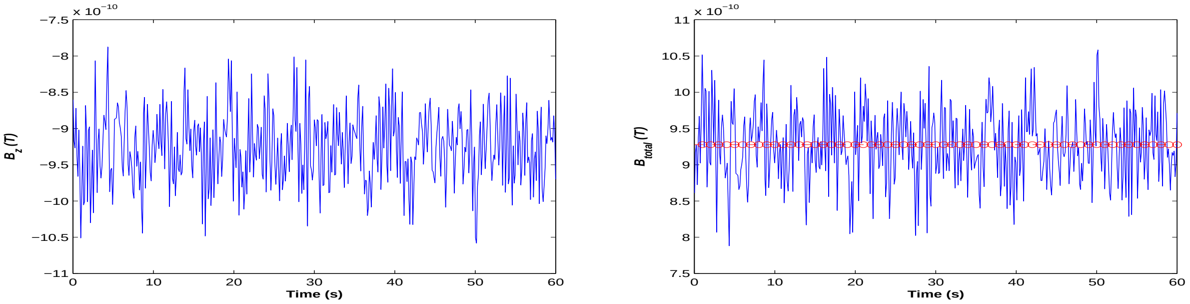

(c) Noise Magnetic Field: $z-$component (B_z).

(d) B_{total}(Noise).

FIGURE 4. Time varying signal obtained by MAD system where noise signal of Fig. 2 is superimposed with target or desired signal. Here source is considered as vertical magnetic dipole of strength $m = 1000Am^2$ and of very low frequency such that $k \rightarrow 0$. Source position is $50m$ below the air-water interface.

REFERENCES

1. C.-M. Tang, Antennas and Propagation, IEEE Transactions on **27**, 665–670Sep (1979).
2. T. B. Sanford, Journal of Geophysical Research **76**, 3476–3492 (1971).
3. W. Podney, Journal of Geophysical Research **80**, 2977–2990 (1975).
4. C. Manoj, A. Kuvshinov, S. Maus, and H. Lhr, Earth, Planets and Space **58**, 429–437 (2006).
5. J. J. Holmes, Synthesis Lectures on Computational Electromagnetics **1**, 1–78 (2006).
6. J. J. Holmes, Synthesis Lectures on Computational Electromagnetics **3**, 1–68 (2008).
7. S. J. Orfanidis, *Electromagnetic Waves and Antennas* (Rutgers University, 2008), 718–723.
8. J. A. Kong, Geophysics **37**, 985–996 (1972).
9. A. Sheinker, L. Frumkis, B. Ginzburg, N. Salomonski, and B.-Z. Kaplan, Magnetics, IEEE Transactions on **45**, 160–167 (2009).

International Conference on Mechanical Engineering 2015
(ICME 2015) 18 – 20 December, 2015, Dhaka, Bangladesh

Paper ID :228

Recovery of Zinc and Manganese with Sulfuric Acid-Glucose System from Spent Zn-C Batteries: A Hydrometallurgical Approach

Muhammad Raisul Abedin[1,2], Shamsul Abedin[1,2], Md. Hasib Al Mahbub[1], Nandini Deb[1]
and Mohidus Samad Khan[1, a)]

[1] *Department of Chemical engineering, Bangladesh of Engineering and Technology (BUET), Dhaka-1000, Bangladesh*
[2] *Equally first author: both authors contributed equally*

[a)] Corresponding author: mohid@buet.ac.bd

Abstract. The global consumption of Zn-C dry cell batteries is significant. The metal contents of Zn-C dry cells are not environmentally hazardous. However, higher amount of Zinc (Zn) and Manganese (Mn) present in Zn-C dry cells shows an industrial interest in recycling and recovering Zn and Mn. The study proposes a hydrometallurgical process for recovering Zn and Mn from spent dry cell (Zn-C battery) batteries. Dry cells were manually dismantled to collect the battery paste. Neutral leaching was carried out to remove potassium and non-metal contents. The battery powder was leached in sulfuric acid medium with glucose as reducing agent. The experiments were conducted according to '2^4 full factorial design'. The purpose of the design was to identify the most effective and optimum condition for Zn and Mn recovery from spent Zn-C batteries. In this experiment battery powder concentration, glucose concentration, sulfuric acid concentration and temperature were considered as the key variables. In this study 86.54 % of Mn and 82.19% of Zn were recovered from the original battery powder. The best operating condition for this highest recovery was at 80^0 C with 100 gm/L of battery powder, 45 gm/L of glucose and 1.0 M sulfuric acid. The leached liquor was then precipitated as hydroxide salts of Zn and Mn with 1 N NaOH solution.

INTRODUCTION

Zn-C dry cells are used worldwide as a popular power source of electric appliances and the electromagnetic devices. They have gained popularity due to their low price and favorable electrical properties. In 2003, 30.5% of the total annual sales of batteries in Eastern and Western Europe were Zn-C batteries and 60.3% was alkaline batteries [1]. After their shelf life, these batteries containing metals are disposed to the environment; therefore, these large quantities of batteries become a serious threat to the environment. A number of studies have been conducted for extracting and recycling of heavy metals from these spent batteries which can also be seen as a secondary source of raw materials [2, 3].

Several methods to economically extract valuable heavy metals present in the waste dry cells have been proposed.A number of hydrometallurgical and pyrometallurgical techniques have been developed by researchers over the years [4, 5]. Pyrometallurgical method is energy consuming since it requires selective volatilization at a very high temperature and releases toxic gaseous effluents [3]. Hydrometallurgical process may utilize alkaline or acidic leaching medium [3, 6, 7]. Reductive acidic leaching processes includes reducing agents such as H_2O_2 [3, 6, 7], SO_2 [7], oxalate [9] or carbohydrates [10] for higher yield of Mn. Liquid-liquid extraction, electro-deposition and precipitation can also be utilized for selective separation of Zn and Mn [3].

This paper focuses on leaching with sulfuric acid and glucose (dextrose) as reducing reagent through hydrometallurgical route. Experimental conditions were planned according to 2^4 full factorial design. The objective was to find an optimum leaching condition for highest simultaneous recovery of Zn and Mn and studying the effects of the factors involved. This study will also be useful to model, design and critically analyze the industrial process of metal recovery from the spent dry cells.

PRETREATMENT OF ZINC-CARBON DRY CELLS AND POWDER CHARACTERIZATION

Spent D-type Zinc-Carbon dry cells were collected from Olympic Industries Limited Bangladesh. Manual dismantling of the batteries was carried out to accommodate separation of black battery paste from other components. Fine particles of the battery powder were obtained using a laboratory grinder. The powders were dried in a laboratory oven for 24 h at 110ºC to ensure complete removal of moisture. The moisture content in the wet battery powder was found to be about 8% of the total weight of the battery paste. Dry battery powder was washed with deionized water keeping a solid/liquid ratio of 1:10 under constant stirring at 450 rpm for 3 hours using a hot plate equipped with a magnetic stirrer (Phoenix Instrument RSM-05-H). This neutral leaching process was carried out at a constant temperature of 80ºC. The filtrate was analyzed with an Atomic Absorption Spectrophotometer (Shimadzu AA-6800). The analysis revealed that no Zinc and Manganese ions were removed from the powder in this step. The neutral leached powder was dried in a laboratory oven for 24 h at 110ºC. All the experiments in this study were performed using these neutral leached powders. Semi-quantitative analyses of the dry powder and the neutral leached powder were carried out using a X-Ray Fluorescence Spectrometer (Shimadzu XRF-1800). Elemental compositions found from the analyses are given in Table 1.

Table 1. Elemental Composition of Dry and Washed Battery Powders

Element	Weight Percentage (%)	
	Dry Battery Powder	Washed Battery Powder
C	30.65	21.04
Mn	39.14	54.41
Zn	21.90	16.66
Fe	3.97	4.02
Si	1.40	1.49
Al	1.13	1.42
K	0.58	0.71
Ca	0.20	0.08
Cr	0.13	0.13
P	0.11	0.12
S	0.10	0.10
Co	0.09	0.08
Ni	0.60	0.05

METHODS AND MATERIALS

Acidic Leaching

In acidic leaching step zinc oxide (ZnO) and manganese oxide (MnO) can fully be dissolved in sulfuric acid solution. Both the oxides form soluble sulfates according to the following reactions [8]

$$ZnO + H_2SO_4 \rightarrow ZnSO_4 + H_2O$$
$$MnO + H_2SO_4 \rightarrow MnSO_4 + H_2O$$

However, Mn_2O_3 and Mn_3O_4 are partially soluble due to the formation of insoluble MnO_2 [11].

$$Mn_2O_3 + H_2SO_4 \rightarrow MnO_2 + MnSO_4 + H_2O$$
$$Mn_3O_4 + 2H_2SO_4 \rightarrow MnO_2 + 2MnSO_4 + 2H_2O$$

In this study glucose (dextrose) is used as reducing agent to enhance the dissolution of MnO_2 which results in higher recovery of Mn. The dissolution occurs according to the following reaction [10]:

$$12MnO_2 + C_6H_{12}O_6 + 12\ H_2SO_4 \rightarrow 6CO_2 + 18\ H_2O + 12MnSO_4$$

Factorial Design

The experiments were designed according to a 2^4 full factorial design. Factorial designs are widely adopted in experimental studies with different materials and experimental conditions for recovery of valuable metals [8, 9]. In this study four factors: battery powder concentration, glucose concentration, sulfuric acid concentration, and temperature, were chosen for the experiments and each factor had two levels (high and low). So, there were 16 different experimental conditions in this study to find the optimum experimental conditions for highest simultaneous recovery of Zinc and Manganese. This experimental model allows us to analyze the interactions among the factors and their effect on recovery.

Experimental

All the tests were performed in a 500 ml closed Erlenmeyer flask set on a hot plate equipped with a magnetic stirrer (Phoenix Instrument RSM-05-H). The experimental conditions are shown in Table 2.

Two battery powder concentrations were used for the experimental study: 100 gm/L and 200 gm/L. The solution mixture was prepared by dissolving neutral leached battery powder and glucose (Merck) of varying concentrations of 45 gm/L, 90 gm/L,135 gm/L and 270 gm/L in 50 ml sulfuric acid. The following sulfuric acid concentrations were used: 1.0 M, 1.5 M, 1.8 M and 2.0 M. The mixture was continuously stirred for 3 hours at 450 rpm with the hot plate magnetic stirrer at varying temperatures of 40^0C and 80^0C. The final solution was filtered with Whatman No.42 filter paper. The amount of Zn and Mn dissolved in the filtered solution was measured by Atomic Absorption Spectrophotometer (AAS) using AA-6800(Shimadzu).

The filtered solution from the acidic leaching step was chemically precipitated by 1N NaOH solution. The solution was precipitated as $Zn(OH)_2$ and $Mn(OH)_2$ by increasing the pH slowly. Complete precipitation of Zinc and Manganese hydroxides occurred at pH value of 8 and 12 respectively.

Table 2. Experimental Condition for 2^4 Full Factorial Design

Serial No. (N)	Treatment	A (Battery Powder)	B (Glucose Concentration)	C (Sulfuric Acid Concentration)	D (Temperature)	A (g L^{-1})	B (g L^{-1})	C (M)	D (◦C)
1	(1)	−	−	−	−	100	45	1	40
2	a	+	−	−	−	200	90	1.8	40
3	b	−	+	−	−	100	135	1	40
4	ab	+	+	−	−	200	270	1.8	40
5	c	−	−	+	−	100	45	1.5	40
6	ac	+	−	+	−	200	90	2	40
7	bc	−	+	+	−	100	135	1.5	40
8	abc	+	+	+	−	200	270	2	40
9	d	−	−	−	+	100	45	1	80
10	ad	+	−	−	+	200	90	1.8	80
11	bd	−	+	−	+	100	135	1	80
12	abd	+	+	−	+	200	270	1.8	80
13	cd	−	−	+	+	100	45	1.5	80
14	acd	+	−	+	+	200	90	2	80
15	bcd	−	+	+	+	100	135	1.5	80
16	abcd	+	+	+	+	200	270	2	80

RESULTS AND DISCUSSION

The results of all the experimental runs are shown in Table 3 and plotted in Figure 1. The results show that recovery of Zn was higher with lower concentrations of acid. Very high concentration of glucose showed a negative impact on simultaneous recovery of Zn and Mn. Glucose concentrations of 90 gm/L and 135 gm/L showed higher simultaneous recovery at 40^0C temperature. Lower temperature was found to be more effective for recovery of Zn. Battery concentration did not show significant impact on recovery of Zn and Mn. The results from Table 3 and Figure 1 show that maximum 86.54 % of Mn and 82.19% of Zn was recovered with 100 gm/L of battery powder, 45 gm/L of glucose and 1.0 M sulfuric acid at 80^oC.

Table 3. Recovery Percentages of Zn and Mn

N	Treatment	Zinc Recovery (%)	Manganese Recovery (%)
1	(1)	41.10	65.38
2	a	40.33	60.06
3	b	77.15	59.08
4	ab	32.88	32.49
5	c	46.67	39.31
6	ac	37.67	68.27
7	bc	66.67	67.38
8	abc	23.97	48.08
9	d	82.19	86.54
10	ad	38.04	57.97
11	bd	3.62	67.31
12	abd	13.39	35.74
13	cd	6.67	56.15
14	acd	3.62	64.08
15	bcd	6.67	74.87
16	abcd	3.62	63.06

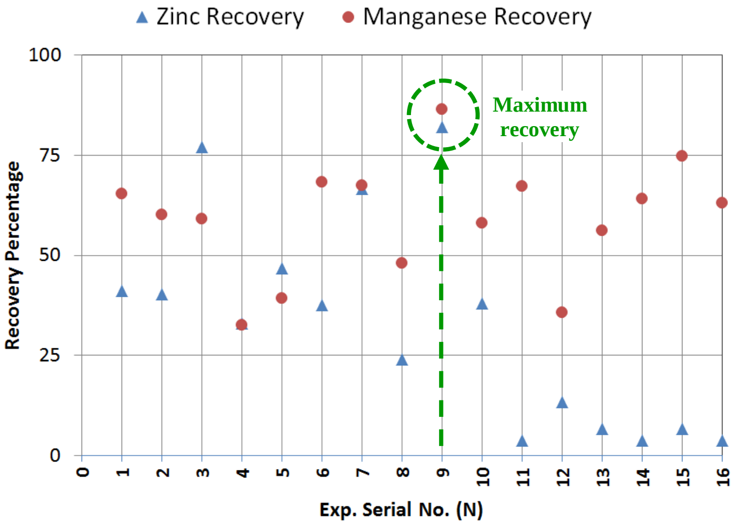

Figure 1. Recovery percentages of Zn and Mn using 2^4 full factorial design.

CONCLUSION

To accommodate the need of the increasing population, usage of different types of batteries is increasing all over the world. Disposal of waste dry cells have become an important issue due to strict environmental regulations imposed by different countries and international organizations. In this study, we have proposed a hydrometallurgical process and a 2^4 full factorial design to extract Zinc and Manganese from spent dry cell batteries and explored the viability of glucose as a suitable reducing agent for this process. Highest simultaneous recovery of Zinc and Manganese was found to be 82.19% and 86.54% respectively; leaching conditions for the highest recovery were 1 M H_2SO_4, 45 gm/L glucose, 100 gm/L battery powder at 80^{o}C under constant stirring. Using glucose as the reducing agent makes this process attractive because of its low cost and non-hazardous nature. The future research will address scaling up the recovery process to an industrial scale and to study its economic feasibility.

ACKNOWLEDGEMENTS

The authors acknowledge Mr. Nazrul Islam of Olympic Battery Ltd. Bangladesh for providing spent Zn-C batteries, Professor Rowshan Mamtaz of the Department of Civil Engineering, BUET for helping with AAS experiment, and Department of Glass and Ceramics Engineering, BUET for XRF analysis.

REFERENCES

1. L. Toro et al., CHEMICAL ENGINEERING **11**, 173-178 (2007).
2. L. R. S. Veloso et al., Journal of Power Sources **152**, 295-302 (2005).
3. E. Sayilgan et al., Hydrometallurgy **97,** 158-166 (2009).
4. D. C. R. Espinosa, A. M. Bernardes and J. A. S. Tenório, Journal of Power Sources **135,** 311-319 (2004).
5. A. M. Bernardes, D. C. R. Espinosa and J .A. S. Tenório, Journal of Power Sources **130**, 291-298 (2004).
6. T. H. Kim et al., Metals and Materials International **14**, 655-658 (2008).
7. J. Avraamides, G. Senanayake and R. Clegg, Journal of Power Sources **159**, 1488-1493 (2006).
8. E. Sayilgan et al., Hydrometallurgy **97**, 73-79 (2009).
9. I. De Michelis et al., Journal of Power Sources **172**, 975-983 (2007).
10. G.Furlani , F. Pagnanelli,F. Ferella, F. Vegliò and F. L. Toro, Hydrometallurgy **99**, 115-118 (2009).
11. F. Ferella et al., International Journal of Chemical Engineering , (2010).

International Conference on Mechanical Engineering 2015
(ICME 2015) 18 – 20 December, 2015, Dhaka, Bangladesh

Paper ID : 233

Removal of Heavy Metal from Industrial Effluents Using Baker's Yeast

Anika Ferdous, Nuzhat Maisha, Nayer Sultana and Shoeb Ahmed[a)]

Department of Chemical Engineering, Bangladesh University of Engineering and Technology, Dhaka 1000, Bangladesh

[a)]Corresponding author: shoebahmed@che.buet.ac.bd

Abstract. Bioremediation of wastewater containing heavy metals is one of the major challenges in environmental biotechnology. Heavy metals are not degraded and as a result they remain in the ecosystem, and pose serious health hazards as it comes in contact with human due to anthropogenic activities. Biological treatment with various microorganisms has been practiced widely in recent past, however, accessing and maintaining the microorganisms have always been a challenge. Microorganisms like Baker's yeast can be very promising biosorbents as they offer high surface to volume ratio, large availability, rapid kinetics of adsorption and desorption and low cost. The main aim of this study is to evaluate the applicability of the biosorption process using baker's yeast. Here we present an experimental investigation of biosorption of Chromium (Cr) from water using commercial Baker's Yeast. It was envisaged that yeast, dead or alive, would adsorb heavy metals, however, operating parameters could play vital roles in determining the removal efficiency. Parameters, such as incubation time, pH, amount of biosorbent and heavy metal concentration were varied to investigate the impacts of those parameters on removal efficiency. Rate of removal was found to be inversely proportional to the initial Cr (+6) concentrations but the removal rate per unit biomass was a weakly dependent on initial Cr(+6) concentrations. Biosorption process was found to be more efficient at lower pH and it exhibited lower removal with the increase in solution pH. The optimum incubation time was found to be between 6-8 hours and optimum pH for the metal ion solution was 2. The effluents produced in leather industries are the major source of chromium pollution in Bangladesh and this study has presented a very cost effective yet efficient heavy metal removal approach that can be adopted for such kind of wastewater.

INTRODUCTION

Water pollution is the contamination of water bodies. This form of environmental degradation occurs when pollutants are directly or indirectly discharged into water bodies without adequate treatment to remove harmful compounds. The specific contaminants leading to pollution in water include a wide spectrum of chemicals, pathogens, and physical changes such as elevated temperature and discoloration. Many of the chemical substances are toxic and include organic and inorganic substances. Organic water pollutants include detergents, disinfection by-products found in chemically disinfected drinking water, such as chloroform, food processing waste, which can include oxygen-demanding substances, fats and grease, insecticides and herbicides, a huge range of organohalides and other chemical compounds, petroleum hydrocarbons [1], including fuels (gasoline, diesel fuel, jet fuels, and fuel oil) and lubricants (motor oil), and fuel combustion byproducts from storm water runoff. Inorganic water pollutants include acidity caused by industrial discharges (especially sulfur dioxide from power plants), ammonia from food processing waste, chemical waste as industrial by-products, fertilizers containing nutrients--nitrates and phosphates found in storm water runoff from agriculture, as well as commercial and residential use, heavy metals from motor vehicles (via urban storm water runoff) and acid mine drainage [1, 2]. With the rapid development of various industries, different waste materials are directly or indirectly discharged into the environment. This situation is severe in the developing countries, causing serious environmental pollution, and threatened biolife [3].

Among different types of heavy metals, Chromium and its compounds have been proved to be highly toxic, which are being mixed with natural water from a variety of industrial effluents. The major sources are: textile dyeing, leather tanning, electroplating and metal finishing industries [4]. Conventional methods for removing dissolved heavy metal ions from waste waters include chemical precipitation, chemical oxidation and reduction, ion exchange, filtration, electrochemical treatment and evaporative recovery. Precipitation is the most common method for removing toxic heavy metals up to parts per million (ppm) levels from water. Electro-winning is widely used in the mining and metallurgical industrial operations for heap leaching and acid mine drainage. Electro-coagulation is an electrochemical approach, which uses an electrical current to remove metals from solution. Reverse osmosis and electro-dialysis involve the use of semi-permeable membranes for the recovery of metal ions from dilute wastewater. These techniques have significant disadvantages including incomplete metal removal, the need for expensive equipment and monitoring systems, high reagent or energy requirements or generation of toxic sludge or other waste products that require disposal [5].

On the other hand, Biosorption, a property of certain types of inactive, dead microbial biomass to bind and concentrate heavy metals from even very dilute aqueous solutions, is one of the most promising technologies involved in the removal of toxic metals from industrial waste streams and natural waters [6, 7]. Heavy metals considered in the field of biosorption are usually classified as the following three categories: toxic metals (Hg, Cr, Pb, Cu, Ni, Cd, As etc.), precious metals (Pd, Pt, Ag, Au etc.) and radionuclides (U, Th, Ra, Am etc.), whose specific weight is usually more than 5.0 g/cm^3 [3]. Biosorption can be considered a collective term for a number of passive, metabolism independent, accumulation processes and may include physical and/or chemical adsorption, ion exchange, coordination, complexation, chelation and microprecipitation [6]. The biosorption of heavy metal ions using microorganisms is affected by several factors. These factors include the specific surface properties of the organism (biosorbent) and the physicochemical parameters of the solution such as temperature, pH, initial metal ion concentration and biomass concentration [8]. *Saccharomyces cerevisiae* is an inexpensive, readily available source of biomass for heavy metal removal from waste water. Yeast cell wall consists mainly of polysaccharides, proteins and lipids. The functional groups that help in surface accumulation of heavy metal in yeast mainly are: carboxyl, amino, amide, hydroxyl, sulphydril and phosphate groups. Though this had been utilized before, the optimum condition for maximum removal efficiency is not known yet. This study investigates the removal performance by varying possible parameters to find an optimum condition for Chromium-Yeast biosorption system.

CHROMIUM POLLUTION AND POTENTIAL BIOSORBENT

Due to the increased use of different types of heavy metals and their harmful effects, the heavy metal pollution has become one of the most serious environmental problems these days. Two stable oxidation states of Chromium persist in the environment, Chromium (+3) and Chromium (+6), which have contrasting toxicities, mobility and bioavailability [9]. Chromium (+6) is known to be a highly toxic metal and one of the sources that drives to many cancers namely, cancer of lung, oesophagus, and liver [10]. Due to severe toxicity of Cr (+6), World Health Organization (WHO) and United States Environmental Protection Agency (USEPA) have set the guideline for drinking water with upper limit of 50 µg L^{-1} [11]. Tannery is one of the oldest and fastest growing industries in Bangladesh. Chromium salts used during tanning generates two types of chrome- hexavalent and trivalent chromium. However, the hexavalent form is 500 times more toxic than the trivalent [12]. The release of untreated tannery effluent affects the natural water bodies' flora and fauna of the ecosystem and hence causes harmful effects on human health and environment [13].

The removal of heavy metals can be achieved by different procedures, but each of these has their own drawbacks. Since most of these engineering technologies have failed in effluent treatment process in terms of extent of removal, as alternatives, slowly, biological tools are being substituted in pollution abatement programs [14]. The use of microbial cells as biosorbents for heavy metal offers a potentially inexpensive alternative compared to conventional methods of heavy metal decontamination from a variety of industrial aqueous process streams. The major advantages of biosorption over conventional treatments include- low cost, high efficiency of metal removal from dilute solutions minimization of chemical and/or biological sludge, no additional nutrient requirement, regeneration of biosorbent and possibility of metal recovery [6]. Many microbial species such as bacteria, fungi, yeast and algae are known to be capable of adsorbing heavy metal on their surface and/or accumulating within the structure [15]. Among various biosorbents, *Saccharomyces cerevisiae* has a viable proposition due to its availability from classical food and fermentation industries (e.g. breweries) [16]. Both living and dead yeast cells have been used as biosorbents in the removal of toxic metal species [17]. These cells have the potential to accumulate a broad range of heavy metal ions.

They are thus considered to be economically attractive biosorbents for the treatment of a wide variety of metal-containing industrial effluents. Biosorption using yeast has thus emerged as an efficient, simple, eco-friendly, and cost effective promising technology for the management of heavy metal pollution [18].

MATERIALS AND METHODS

Metal solutions

All the reagents used were of analytical reagent grade and solutions were prepared in distilled water. An aqueous stock solution of known concentration of Cr (+6) ions was prepared using Potassium dichromate ($K_2Cr_2O_7$) salt. This was used as the source of Cr (+6) in synthetic wastewater. The pH of the solution was adjusted using 0.1 N H_2SO_4.

Preparation of biomass

Baker's yeast was initially dried to remove moisture by heating in an oven at 100°C for 10 minutes.

Biosorption studies

Batch biosorption studies were carried out using a certain amount of yeast biomass and 100 ml of Cr (+6) solution in a conical flask with constant stirring using PHOENIX RSM – 05H magnetic stirrer operated at 150 rpm. A medium sized magnetic bead was used for the stirring purpose. The change in the following operating conditions- pH, contact time and metal concentration were investigated to observe the change in absorption rate. For each of the experiment the mixture was stirred at 150 rpm followed by filtration with Whatman filter paper. No. 40. Then the concentration of the filtrate containing residual Cr (+6) was determined spectrophotometrically.

Cr (+6) ion determination

The initial and final concentration of the Cr(+6) solution was determined using HACH DR/4000U spectrophotometer following the standard method [19]. The percentage of Cr removal due to bioadsorption was calculated as % Cr removal = $[(C_i - C_f) / C_i] \times 100$ %, where C_i and C_f are initial and final concentration of Cr (+6) solution (mg/L), respectively [20].

RESULTS AND DISCUSSION

Each Sample solution containing heavy metal ions were incubated under constant agitation at 150 rpm and the effects of incubation time, change in initial concentration and pH were observed. The results calculated were the amount of Cr (+6) removed by per gram of yeast and rate of uptake, which is percentage of Cr (+6) removed in each experimental run.

$$\text{Rate of removal} = \frac{(Initial\ amount\ of\ Cr(+6) - Final\ amount\ of\ \ Cr(+6))(in\ mg)}{Amount\ of\ yeast\ taken\ (in\ grams)} \tag{1}$$

$$\text{Rate of uptake} = \frac{(Initial\ amount\ of\ Cr(+6) - Final\ amount\ of\ \ Cr(+6))}{Initial\ amount\ of\ Cr(+6)} \times 100\ \% \tag{2}$$

Initial incubation experiments were performed at different agitation speeds, and it was found that 150 rpm was the highest speed that could be applied without breaking the yeast cells.

Effect of Incubation Time

The sample solutions were kept under agitation for 3, 6 and 16 hours at 150 rpm. It was observed that in case of chromium (+6) ions, the heavy metal removal efficiency increases with incubation time, however after a certain time, the removal rate does not increase as it did initially. As seen from Fig. 1(a), incremental rate of uptake after 6 hr is not as high as the earlier period.

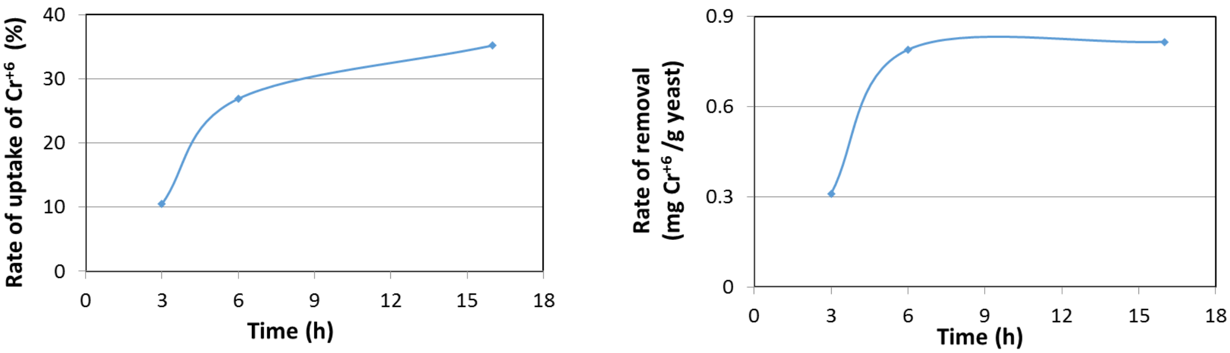

(a) (b)

FIGURE 1. (a) Rate of uptake of Cr^{+6} vs. incubation time; (b) Rate of removal of Cr^{+6} vs. incubation time

Effect of Initial Concentration of Sample Solution

Sample solutions of Cr^{+6} of different known concentrations were prepared and incubated under agitation for 3 hours at 150 rpm. Increased initial concentration results in increased amount of Cr^{+6} removal per gram of yeast (Fig.2(a)).

However, removal efficiency decreases with an increase in initial concentration showing an inverse relationship (Fig. 2(b)). Each gram of yeast has a certain adsorption capacity and thus, for a certain amount of yeast total amount of metal removal remains similar. Accordingly, the rate of uptake decreases with the increase in initial chromium concentration. Interestingly, despite being the amount of yeast same, higher initial concentration helped the yeast to adsorb slightly higher amount and the value slightly increases with the increase in the concentration of the initial solution as evident from Fig. 2(a).

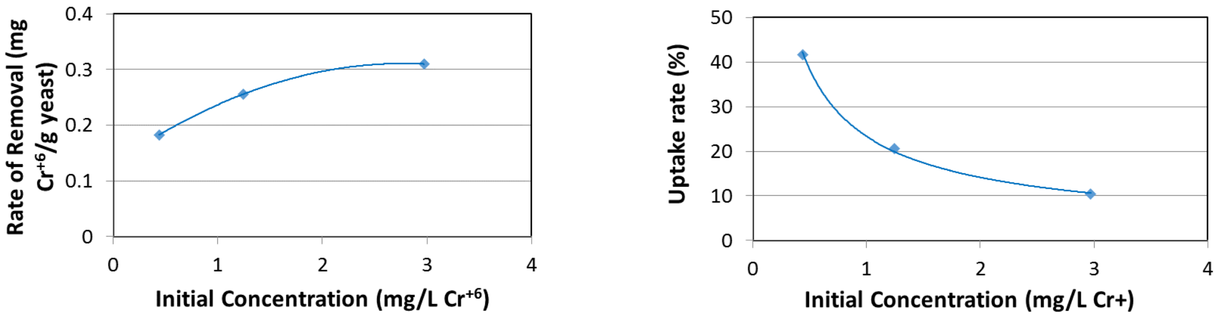

(a) (b)

FIGURE 2. (a) Rate of removal of Cr^{+6} vs. initial concentration of sample solution; (b) Rate of Uptake of Cr^{+6} vs. initial concentration

Effect of pH of Sample Solution

It was anticipated that pH of the solution might have an effect on the removal rate and uptake rate. To investigate that, same sample solution in different pH (2, 3 and 6.4) was incubated for 3 hours and 6 hours under agitation at 150 rpm. A decrease in pH resulted in an increase in amount of Cr^{+6} adsorbed by per gram of yeast. Based on obtained values, optimum pH was found to be around 2 for 6 hours incubation time. This indicates the requirement of pH control during wastewater treatment containing heavy metals.

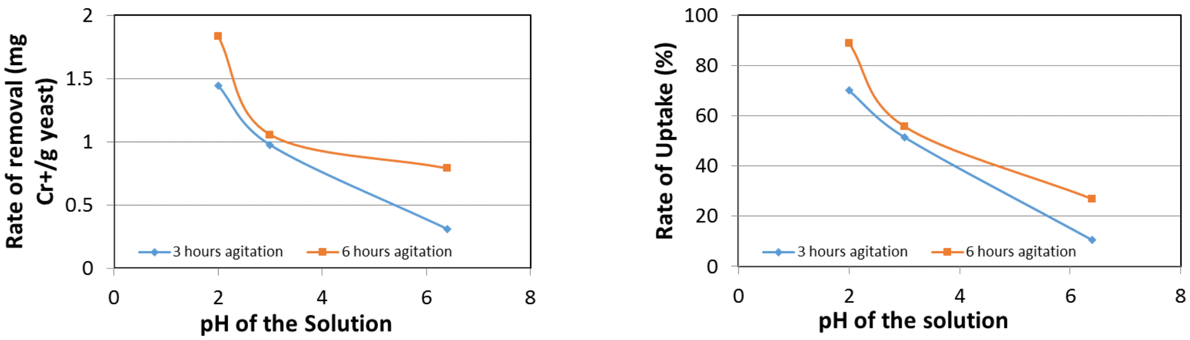

(a) (b)

FIGURE 3. (a) Rate of removal of Cr^{+6} vs. pH of sample solution; (b) Rate of Uptake of Cr^{+6} vs. pH of sample solution

CONCLUSION

Biosorption offers an economically feasible technology for efficient removal and recovery of metal(s) from aqueous solution. The process of biosorption has many attractive features including the selective removal of metals over a broad range of pH and temperature, its rapid kinetics of adsorption and desorption and low capital and operation cost. Biosorbents can easily be produced using inexpensive growth media or obtained as a by-product from industry. It is desirable to develop biosorbents with a wide range of metal affinities that can remove a variety of metal cations. These will be particularly useful for industrial effluents, which carry more than one type of metals. Biosorption processes are applicable to effluents containing low concentrations of heavy metals for an extended period. This aspect makes it even more attractive for treatment of dilute effluent that originates either from an industrial plant or from the primary wastewater treatment facility. Thus biomass-based technologies need not necessarily replace the conventional treatment routes but may complement them. In this study, *S. cerevisiae* has been used as a biosorbing agent for the removal of chromium ions. The effects of incubation time, initial concentration and pH were observed. The results calculated were the amount of Cr^{+6} removed by per gram of yeast and rate of uptake, which is percentage of Cr^{+6} removed in each experimental run. Both removal rate and uptake rate increased with incubation time. Optimum agitation time for yeast removal was found to be around 6-8 hours. Removal rate increased but uptake rate decreased with increased initial concentration of Cr^{+6}. Removal rate and uptake rate increased with decrease in pH. Based on obtained values, optimum pH was found to be around 2 for 6 hours agitation time. This study provides with a preliminary range of parameter values for efficient heavy metal removal. This can be further optimized with more stringent control and additional parameter optimization. This will be very useful for the industries with wastewater treatment facilities, financially and technically.

REFERENCES

[1] R. P. G.Allen Burton Jr., "Chapter 2," in *Water pollution is the contamination of water bodies of water bodies. This form of environmental degradation occurs when pollutants are directly or indirectly discharged into water bodies without adequate treatment to remove harmful compounds. The specifi*, New York, CRC/Lewis Publshers, 2001.

[2] T. R. Schueler, "Cars Are Leading Source of Metal Lowad in California," The Practice of Watershed Protection, Elicott City, 2000.

[3] P. L. Bishop, Pollution prevention: fundamentals and practice, Waveland Press, 2004.

[4] S. Siraj, "Removal of Chromium From Tannery Effluent Using Chitosan-Charcoal Composite," vol. 25, no. 1, 2012.

[5] E. G. K. T. Aksu Z., "A comperative study for the biosorption characteristic of Chromium (VI) on Ca- alginate, agarose and immobilized C. vulgaris in a continuous packed bed column, 295-316," vol. 34, no. 2, 1999.

[6] B. F. G. Veglio F., "A biosorption of toxic metals : an equilibrium study using free cells of Anthrobacter sp.," vol. 32, 1997.

[7] V. B., "Biosorption for the next century," El Escorial, Spain, 1999.

[8] K. T. Sag Y., "The Selective Biosorption of Chromium (VI) and Copper (II) ions from binary metal mixtures by R. arrhizus," vol. 31, 1991.

[9] R. C. a. T. Anirudhan, "Chromium VI adsorption by sawdust: kinetics and equilibrium, 228-236," vol. 4, 1997.

[10] M. Prasad, Trace elements as contaminats and nutrients - consequences in ecosystems and human health, pp 511, USA: John Wiley and Sons, Inc. , 2008.

[11] N. J. M. M. I. S. D. Srivastava, "Application of genetic engineering for Chromium removal from industrial wastewater, 434-439," vol. 48, 2010.

[12] L. A. M. S. Xavier M., "Removal of Chromium from Real Tannery Effluent by Using Bio-adsorbent," vol. 2, no. 7, 2013.

[13] D. D. M. S. D. S. Mandal T, "Treatment of leather industry wastewater by aerobic biological and Fenton oxidation process 2014-211," vol. 180, 2010.

[14] S. M. R. N. K.M.S. Sumathi, "Use of low cost biloogical-waste and vermiculite for removal of chromium from tannery waste," vol. 96, no. 3, 2005 Feb.

[15] R. a. M. M. Campbell, "Continuous flow fermentation to purify waste water by the removal of cadmium, pg. 398-407," vol. 50, 1990.

[16] E. W. Yongming Lu, "Heavy metal removal by caustic-treated yeast immobilized in alginate," Vols. Journal of Hazerdous Materials, 49, 1996.

[17] H. M.-P. B. Volesky, "Biosorption of heavy meal by Saccharomyces cerevisiae," Vols. 42, pg.797-806, 1995.

[18] S. S. Z. B. B. K. Ashok V. Bankar, "Management of Heavy Metal Pollution by Using Yeast Biomass," in *Micororganisms in Environmental Management : Microbes and Environment*, Springer, 2012.

[19] HACH, *DR/4000 SPECTROPHOTOMETER MODELS 48000 and 48100 USER MANUAL 08/04 3ed*, USA: Hach Company, 1995-1999,2004.

[20] N. L. a. K. Joshi, "Biosorption of heavy metal (chromium) using biomass," Vols. Global Journal of Environmental Research, 3, no. 1, 29-35, 2009.

International Conference on Mechanical Engineering 2015
(ICME 2015) 18 – 20 December, 2015, Dhaka, Bangladesh

Paper ID : 234

Health Hazard of Food Adulteration: Diffusivity Analysis of Formaldehyde in Formalin Treated Fish Samples

Sadat Kamal Amit[1, 2], Md. Mezbah Uddin[1, 2], Shawly Samira[1], Rizwanur Rahman[1], SM Rezwanul Islam[1] and Mohidus Samad Khan[1, a)]

[1]*Department of Chemical Engineering, Bangladesh University of Engineering and Technology (BUET), Dhaka-1000, Bangladesh*
[2] *Equally first author: both authors contributed equally.*

a) Corresponding author: mohid@buet.ac.bd

Abstract. Health risk regarding indiscriminate use of chemical preservatives in foods has become a matter of major concern in Bangladesh. Although many of the chemical preservatives are considered to be safe, but several have negative and potentially life threatening side effects. It is reported that formalin, a 37 to 40 per cent solution of formaldehyde, is widely used to increase the shelf-life of fishes. Direct consumption of formalin is harmful. However, the effect of consuming formalin dosed fish and the effect of formalin on fish nutrition value is less understood. No data exists about the diffusivity of formaldehyde in fish flesh. Besides, detecting formalin or formaldehyde in fishes and other food items is rather challenging since formaldehyde in food items can be interfered by the presence of other aldehyde, ketone or alcohol groups in foods. Formaldehyde can also be naturally produced in fish and other food items during the ageing and deterioration. This experimental research aims to measure the effect of formalin on key nutritional parameters: protein and lipid, of fish sample (Rohu fish; labeo rohita). The time dynamic behavior of residual HCHO concentration in fish sample is also analyzed. Natural occurring formaldehyde concentration profile is also obtained at different temperature. To analyze time and temperature effect on the formaldehyde diffusion in fish flesh, experiments are conducted at different temperature (4°C, 8°C and 12°C) for up to 54 hours. This systematic approach and methodology can also be applied to analyze other chemically preserved food items and corresponding health hazards.

INTRODUCTION

Fish and fishery products have been recognized as one of the major nutrition sources due to their high protein and unsaturated fatty acid contents [1]. Fish contains fat, free amino acids and water, which are susceptible to spoilage by microorganisms and biochemical reactions during post-mortem process [2]. During storage, many fish species exhibit changes in textural properties, long before they are spoilt [3]. This may result in flesh softening and gaping and trimming losses, resulting in reduced fillet yield. In addition, products may have a poorer appearance, therefore, downgraded and/or returned to the producer, with accompanying loss of reputation and economical losses [4]. Fish and seafood are very perishable and can only be kept fresh in ice for 8 to 14 days depending on the species. In order to keep the freshness of fish and seafood, fishermen and fish vendors often tend to use formaldehyde solution as chemical preservative [5]. Besides, formaldehyde is one of the most effective and widely used compounds in fish culture for therapeutic and prophylactic treatment of fungal infection and external parasites of fish egg [9]. Formaldehyde is also known as methanal and its chemical formula is HCHO. At room temperature, formaldehyde is a colorless gas with a pungent, irritating odour. [6]. Formalin is a generic term which describes a solution of 37 to 40 per cent formaldehyde gas dissolved in water [7]. Recently, International Agency for Research on Cancer (IARC) has classified formaldehyde as a Group 1 carcinogenic to humans [5]. Epidemiological studies have examined the cancer mortality among persons with occupational and residential exposure to formaldehyde [8]. As consumption of formaldehyde is hazardous to human body, it is important to investigate the content and effect of formaldehyde in fish and seafood [5]. In Bangladesh using formalin as chemical preservative is illegal; however, it is reported that fish vendors often use formalin to increase shelf-life of fish in spite of knowing this practice illegal. Therefore, analyzing the effects of formalin on fish nutrition value is more relevant for Bangladeshi context. This research work aims at detecting and quantifying formaldehyde in fresh and formalin treated fish samples, and analysing the effects of formalin on major nutritional parameters of fish samples: protein and fat. Alongside, it also reports the time dynamic concentration behaviour of formaldehyde in the dosed samples. To analyze time and temperature effect on the formaldehyde diffusion in fish flesh, experiments were conducted at different temperatures (4°C, 8°C and 12°C) for up to 54 hours. Naturally occurring formaldehyde concentration profile was also obtained at different temperature.

MATERIALS AND METHODS

Materials

Formalin free Rohu fish (*Labeo rohita*) was collected from different locations of Dhaka. 800ppm formaldehyde solution was prepared by diluting formalin (40% w/w formaldehyde). Nash reagent was used as an indicator which was prepared by adding 2ml of acetyl acetone and 3ml of acetic acid with 150g of ammonium acetate in an Erlenmeyer flask and the volume was adjusted to 500ml to prepare concentrated Nash reagent. Trichloroacetic acid (10 w/w %) was used to extract formalin from fish fillet. Sodium hydroxide, NaOH (1 N, 5N) sulfuric acid, H_2SO_4 (1N) was used to adjust the pH of the distillate to be in range of 6.0 to 6.5 [12]. 160 ml methanol, CH_3OH and 160 ml chloroform, $CHCl_3$ were used during blending 50 g of fish sample for lipid extraction. Anhydrous Sodium Sulfate was used for removing water from bottom layer after blending process.

For digestion concentrated sulfuric acid, H_2SO_4 was used. Digestion salt mixture was prepared by mixing potassium sulfate, K_2SO_4 and copper sulfate $CuSO_4$ in a ratio of 31.25: 1. In order to liberate ammonia 40% sodium hydroxide, NaOH solution was added to digested solution. Indicator solution was prepared by mixing 0.033% methyl red and 0.1% bromocresol green in 95% ethanol. Distillation product ammonia was collected in a mixture of standardized H_2SO_4, indicator solution and distilled water. The mixture was titrated with standardized sodium hydroxide, NaOH [13].

Method for Crude Lipid Determination

Formalin free fish was cut into pieces. Single piece of fish was dipped into 2 liters of 800 ppm formalin solutions for 15 minutes and kept below 4^0C for 1 hour. 160 ml Methanol and 80 ml Chloroform were added to 50 g sample fish. Water, chloroform and methanol ratio was maintained at 4:5:10 by adding water. The blended content was filtered through Buchner funnel and transferred to a separating funnel for settling into an upper aqueous and a lower chloroform layer. The chloroform layer was taken to a round bottom flask and heated at 100^0C. After being consistent the weight of the flask was taken.

Method for Protein Determination

Formalin free fish sample was dipped into 2 litres 800 ppm formalin solutions for 15 minutes. 0.5g sample, 5 g digestion salt mixture and 10 ml of concentrated sulfuric acid were taken into a 500 ml Kjeldahl flask. The mixture was digested until it became a clear solution. After cooling, 250 ml of distilled water and 28g of 40% sodium hydroxide solution were added and connected to a distillation apparatus. The distillate was collected in an Erlenmeyer flask containing a mixture of 10 ml standardized sulfuric acid, 10 drops of indicator solution and 100 ml distilled water. 150 ml distillate was collected and titrated with standardized sodium hydroxide to greenish-blue endpoint. A reagent blank was run using the same process [13].

Residual Concentration and Degree of Diffusivity Determination of Formaldehyde in Formalin Treated Fish Samples

Formalin free fish sample was dipped into 800ppm formalin solution or 15 minutes. Samples were stored at a temperature of 4°C, 8°C and 12°C. Fish sample was blended with equal weight of water. Trichloroacetic acid was added with blend and filtered. Distilled water was added with 5ml of filtrate. pH was adjusted in between 6 to 6.5.

Volume of the extract was made up to 25ml by adding water. 5ml of this extract was taken and Nash was added. Solution was kept at 60°C water bath for 5min and then cooled to room temperature. Optical density (absorbance) was measured at 415nm by using UV mini-1240 spectrophotometer [12]. A calibration curve was prepared for the spectrophotometer to determine the residual concentration.

RESULTS AND DISCUSSION

Comparison of Nutritional Value between Normal and Formaldehyde Dosed Sample

Lipid includes fat, oils and waxes. Lipid content varies more widely than protein, moisture and mineral contents. However, there is considerable seasonal variation in the fat content of fatty fish. Chemical evidence indicates that formaldehyde combines with unsaturated lipids at the double bond. The resulting complex contains a free carbonyl group which probably originates from the formaldehyde. The reaction occurs over a wide pH range, and takes place in the absence of oxygen or moisture.

Formalin or formaldehyde acts as a cross-linker to protein which tends to 'freeze' the native state of tissues and cells. Crosslinking is the process of chemically joining two or more molecules by covalent bond. Cross-linked reagents are molecules that contain two or more reactive ends capable of chemically attaching to specific functional groups. Attachment between two groups on a single protein results in intra-molecular crosslinks that stabilize the protein as a tertiary or quaternary structure. Thus, protein content gets reduced by protein fixation by formaldehyde. Table 01 enlists the effect of 800ppm formaldehyde on fish lipid and protein.

From the experimental results, the change of fat content was found very little (Table 1, Figure 1a). It may have appeared as no reaction took place between formalin and lipid in presence of moisture and oxygen (general condition). Variation in fat content may result due to non-homogenize flesh sample. Also fat content may vary from one sample to another and due to their age, gender

TABLE 1. Effect of 800ppm formaldehyde on lipid and protein content

Nutritional Parameter	**Fresh Sample**	**800 ppm Dosed Sample**
Crude Lipid (%)	1.22	1.24
Protein (%)	26.67	23.9

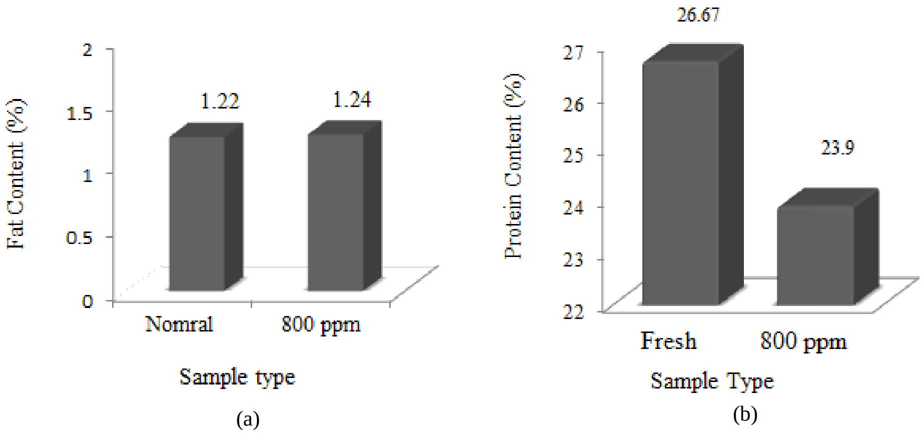

(a)

(b)

FIGURE 1. Effect of Formaldehyde on (a) Crude lipid (b) Protein

The protein content got reduced by dosing of formalin (Table 1, Figure 1b). In normal fish sample protein content is around 26.67 per cent whereas due to dosage of 800ppm formalin it reduces to 23.9 per cent. Protein content gets reduced as formaldehyde acts as a fixative agent to form bridge of protein molecules and increases shelf life by prohibiting enzymatic breakdown.

Concentration Profile of Residual HCHO for 800 ppm Dosed Fish Sample at Different Temperature

Figure 2 was generated for residual formalin exists in 800ppm dosed fish flesh after specific time interval. Diffusion occurs due to concentration gradient. Usually diffusion of liquids increases with increment of temperature. Diffusion of HCHO in fish flesh is a complex phenomenon and evaluating direct relation with temperature is difficult to determine. Residual concentration of HCHO is also dependent on reaction rate of HCHO with protein considering that HCHO is not reacting with lipid due to presence of moisture and oxygen. The complex formation reaction is enhanced with increment of temperature. Therefore, the residual amounts deduced in various time intervals are function of these two occurring. From Figure 2, it is seen that residual HCHO decreases with increasing temperature. At higher temperature, diffusion proceeds at a higher rate, which causes low residual HCHO. All the curves giving a steady state value after a certain period which does not change further for longer retention time.

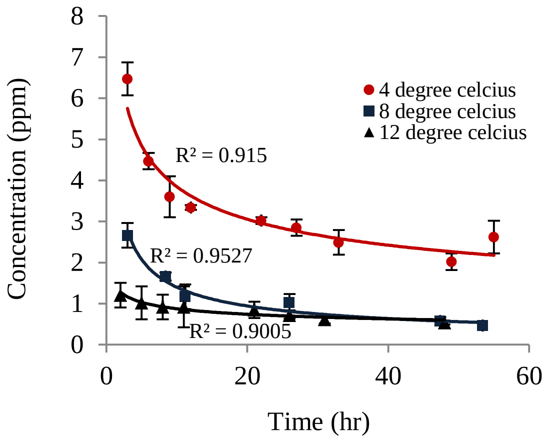

FIGURE 2. Residual HCHO concentration profile in fish flesh with respect to time at different temperature

Concentration Profile of Naturally Occurring HCHO for Fresh Fish Sample at Different Temperature

Fish is a perishable substance. It is subjected to spoilage due to autolytic enzymatic reaction, oxidative reaction or microbial attack. During these spoilage processes formaldehyde can be produced. Experimental results showed that small amount of formaldehyde exist in fish naturally (Figure 3). Formaldehyde amount increases with time as the extent of spoilage increases. The rate of HCHO formation is higher at high temperature (Figure 3d). At high temperature microbial activity is increased and hence spoilage got increased. At low temperature, enzymatic break down and microbial activity got slower.

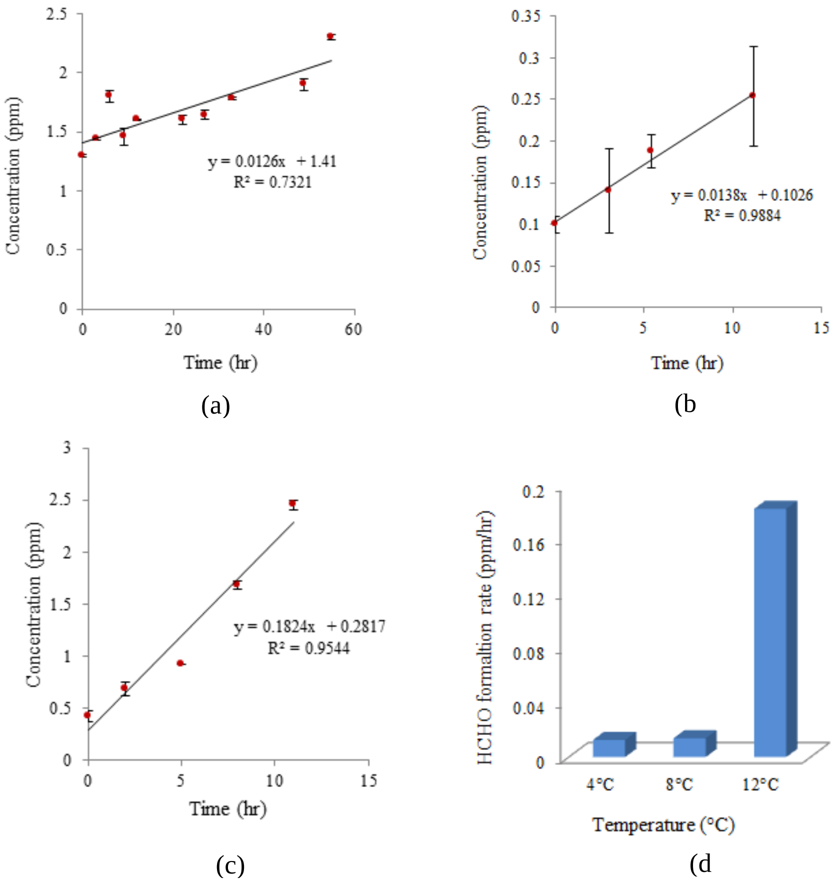

(a) (b

(c) (d

FIGURE 3. Concentration of HCHO with respect to time for fresh fish sample at (a) 4°C (b) 8°C (c) 12°C and (d) comparison of HCHO formation rate at different temperature

CONCLUSION

This study reports the time dynamic concentration of naturally producing formaldehyde in fresh fish samples, residual formaldehyde in formalin treated fish sample and the change in nutritional parameters due to formaldehyde (800 ppm) dosing. The concentration of naturally occurring formaldehyde increased slowly in fresh fish sample with respect to time. The concentrations of residual formaldehyde in fresh fish samples were found very low (< 4 ppm) comparing to samples treated with 800 ppm formaldehyde solution. Experimental results also showed that protein content reduced as a result of treatment with formalin. The protein content of fresh fish and formaldehyde (800ppm) treated fish were found 26.67 and 23.90%, respectively. On the other hand, the effect of formalin on the fat content is almost insignificant. The results indicate that only a fraction of the applied formaldehyde was adsorbed by fish protein. The residual HCHO amount can be greater than 2µg (maximum consumption limit per day declared by EPA), and regular consumption may have a harmful effect on human health.

ACKNOWLEDGEMENTS

This research was supported by BCEF Academic Research Fund, CASR Research Fund, and financial support from the Department of Chemical Engineering, BUET.

REFERENCES

1. P. Masniyom, O. Benjama and J. Maneesri, International Food Research Journal **20,** 1401-1408 (2013).
2. J. T. V. Gabriel Fernandes, Nutrition Research, 1993. 13(1): p. S19-S45.
3. H. A. Bremner, *Fish flesh structure and the role of collagen - its post-mortem aspects and implications for fish processing.*, in *1991 International Conference on Quality Assurance in the Fish Industry*. 1992, Elsevier Science and Technology Books: Copenhagen, Denmark.
4. L. Hultmann, *Endogenous proteolytic enzymes - Studies of their impact on fish muscle proteins and texture*, in *Faculty of Natural Sciences and Technology, Department of Biotechnology*. 2003, Norwegian University of Science and Technology: Norway.
5. N. Noordiana, A. B. Fatimah and Y. C. B. Farhana, International Food Research Journal **18**, 125-136 (2011).
6. R. G. Liteplo, R.B., M.E. Meek, R. Chénier, *FORMALDEHYDE*. 2002, World Health Organization: Geneva.
7. M. M. Rahman, S. A., M. M. Hosen and A. K. Talukder, Bangladesh Research Publications Journal **7,** 161-169 (2012).
8. M. Lippmann, *Environmental Toxicants: Human Exposures and Their Health Effects*. March 26, 2009, Hoboken, New Jersy: John Wiley and Sons, Inc. 1200.
9. M. M. Rahman, S.A.A., M. M. Hosen, A. K. Talukdar, *Detection of formalin and quality characteristics of selected fish from wet markets at sylhet city in Bangladesh.* Bangladesh Res Pub J, 2012. 7(2): p. 161-169.
10. F. N. Tsuda M, Sato S and T. Sugimura, *Marked increase in the urinary level of N-nitrosothioproline after ingestion of cod with vegetables.* Cancer Research **48**, 4049-4052 (1988).
11. H. H. H. Lone Gram, International Journal of Food Microbiology **33,** 121-137 (1996).
12. S. CHCaB, *Measurement of formaldehyde in fish muscle using TCA extraction and Nash* Measurement of formaldehyde in fish muscle using TCA extraction and Nash 1973. 30: p. 91-98.
13. L. A. Romero, and F. G. Yost, Journal of Fluid Mechanics **322**, 109-129 (1996).

International Conference on Mechanical Engineering 2015
(ICME 2015) 18 – 20 December, 2015, Dhaka, Bangladesh

Paper ID : 248

Experimental Investigation of the Electrical Conductivity of MWNT Filled HDPE Composites

Al Basir$^{1, 2, a)}$

[1]School of Engineering and Materials Science, Queen Mary University of London, Mile End Road, London,
E1 4NS, United Kingdom.
[2]Department of Mechanical and Chemical Engineering, Islamic University of Technology, Board Bazar, Gazipur,
Bangladesh.

a) Corresponding author: al.basir005@yahoo.com

Abstract. Multi-walled carbon nanotubes (MWNT) filled high density polyethylene (HDPE) composites were fabricated by conventional melt mixing method. The melt flow index of the used HDPE was 1.2g/10 min which can be said as polymer matrix with low melt flow index (LMFI). The percolation behaviour and positive temperature co-efficient (PTC) effect of HDPE (LMFI)/MWNT conductive polymer composites were examined. It was observed that HDPE (LMFI)/MWNT composites displayed percolated behaviour. The percolation threshold for HDPE (LMFI)/MWNT composites was found to be approximately 1.9 wt. % of MWNT. It was found that MWNT filled HDPE (LMFI) composites showed PTC effect that occurred around the melting temperature of composites due to expansion of polymer matrix. Moreover, HDPE (LMFI)/MWNT composites also displayed negative temperature coefficient (NTC) effect that occurred after the melting temperature of polymer matrix.

INTRODUCTION

Now-a-days conductive polymer composites (CPC) are extensively using in variety of applications, such as: electromagnetic interference shielding, sensing, electrostatic dissipation etc [1-6]. CPCs are made of polymer matrix and conductive fillers. Conventionally in conductive polymer composite, conductive fillers are dispersed in an insulating polymer matrix. The average distance between the conductive fillers is large when the filler fraction is very low and thus the conductivity throughout the composite is negligible. When the amount of filler is increased sufficiently then the mean distance between the conductive fillers decreases and the consequence is the linkages between conductive fillers and formation of initial conductive path through the entire material [7,8]. The corresponding filler content required to form the initial conductive path is designated as percolation threshold [7,8]. After the percolation threshold, conductivity of polymer composite can change dramatically for small variation of filler content [7,8]. At high filler concentration, the number of conductive paths increases significantly which forms a three dimensional network and in this state the conductivity of the material is remarkably high and minimum change in the conductance of polymer composite is observed for further increase in conductive filler [7,8]. Disruption of these conductive paths initiate when the temperature of CPC reaches close to the melting temperature of polymer matrix and the consequence is the increase in resistivity in CPC which is known as positive temperature coefficient (PTC) effect. A PTC effect result from break up of conductive paths is an excellent property of conductive polymer composites that make them immensely acceptable to use in self-regulated heaters and circuit protection devices.

The paper is focused on research of the percolation behaviour of multi-walled carbon nanotubes (MWNT) filled high density polyethylene (HDPE) composites where the melt flow index of used HDPE is low. Low melt flow index HDPE has been designated as HDPE (LMFI). Research has also been carried out to show that HDPE

(LMFI)/MWNT composites display not only positive temperature co-efficient (PTC) effect but also negative temperature co-efficient (NTC) effect.

EXPERIMENTAL SECTION

Materials

HDPE with melt flow index of 1.2g/10 min was used as polymer matrix which was supplied by Total Petrochemical under the name of M5510EP. The density and the melting temperature of M5510EP were 0.955 g/cm^3 and 134^o C respectively. Multi-walled carbon nanotubes (MWNT) were used as conductive fillers were supplied by Nanocyl with the trade name NC7000. The average diameter of MWNT was about 9.5 nm whereas the average length was about 1.5μm.

Preparation of Nanocomposite Specimens

In order to prepare HDPE (LMFI)/MWNT composites, at first a masterbatch containing 5 wt% MWNT was made by extrusion in a twin screw mini extruder (DSM Micro 15) using screw speed of 50 rpm at 210^{o}C for 5 minutes. After that, the prepared masterbatch was diluted by adding HDPE (LMFI) to make the concentrations required for the experiment. The blended mixtures were cut into pellets, placed into a mould and then hot pressed to get a definite form of samples having 23.90 mm × 3.80 mm × 1.63 mm dimensions. In this experiment, blended mixtures were hot pressed using temperature 200^o C and pressure of 60 bars for 3 minutes after holding for 5 minutes by employing Collin P 300 E hot press. Water cooling system of hot press was applied to cool down the hot pressed samples to room temperature.

Measurements and Observations

In order to investigate the electrical properties, silver paste was applied at the ends of each sample surface and the reason of doing so was to reduce the contact resistance between sample and electrodes. Keithleypicoammeter and multimeter was used to measure the resistance along the sample length. An applied voltage of 2V was employed in steps of 0.2V to conduct electrical tests at room temperature. The electrical resistivity of each sample was calculated by employing equation (1).

Resistivity,

$$\rho = \mathrm{R}\frac{\mathrm{A}}{\mathrm{L}}(\Omega.cm) \tag{1}$$

Where,

R = Electrical resistance along the sample length (Ω)
A = Cross sectional Area of sample (cm^2) and
L = Distance between electrodes after clamping to the ends of the sample (cm)

The volume resistivity of the samples was measured as a function of temperature by placing the samples in a heating chamber and then clamping the copper electrodes to their ends. In order to reduce the contact resistance between sample and the electrodes, silver paint was applied at ends of the samples before clamping them with electrodes. The technique followed to investigate the PTC characteristics was to employ applied voltage 2V while continuously measuring the current of heated specimen from room temperature to maximum 200^{o}C. Whenever temperature reached the desired value, the voltage was switched off and the tested samples were allowed to cool to room temperature. The PTC intensity of the samples was calculated by the formula given in equation (2).

PTC intensity,

$$\mathrm{I}_{\mathrm{PTC}} = \log\left(\frac{\rho_{\max}}{\rho_{\mathrm{rt}}}\right) \tag{2}$$

Here, $\rho_{\max}$ =Maximum resistivity (Ω.cm)

ρ_{rt} =Resistivity at room temperature (Ω.cm)

The scanning electron microscope (FEI Inspector-F, Netherlands) was used to study the morphology of the samples. The samples were carefully fractured at liquid nitrogen atmosphere and then the fractured surface was coated with a thin layer of gold in order to prevent charging before doing the imaging.

RESULTS AND DISCUSSION

Electrical Properties of HDPE (LMFI)/MWNT Composites

HDPE (LMFI) with MWNT conductive filler loading level of 1.8, 1.9, 2, 3 and 5 wt. % were prepared to investigate the percolation behavior. Figure 1 represents the volume resistivity as a function of the MWNT content for HDPE (LMFI)/MWNT composites. The change in resistivity with increasing MWNT content indicated percolation behavior of composites. The reason of reduction in resistivity of HDPE (LMFI)/MWNT composites with increasing MWNT content is the increase in conductive paths within polymer matrix. The addition of more MWNT conductive fillers within polymer system reduces the average distance between nanotubes which facilitate to cause the direct contact between nanotubes or the electron tunneling and the consequence is the decrease in resistivity. Figure 1 shows a dramatic change in resistivity between polymer composites with 1.8 wt. % MWNT and 3 wt. % MWNT. Figure 1 also represents a minimum change in resistivity between composites with 3 wt. % MWNT and 5 wt. % MWNT which indicates that high loading of MWNT conductive filler causes the polymer matrix to reach its saturation point and the consequence is the small change in resistivity with increasing filler concentration.

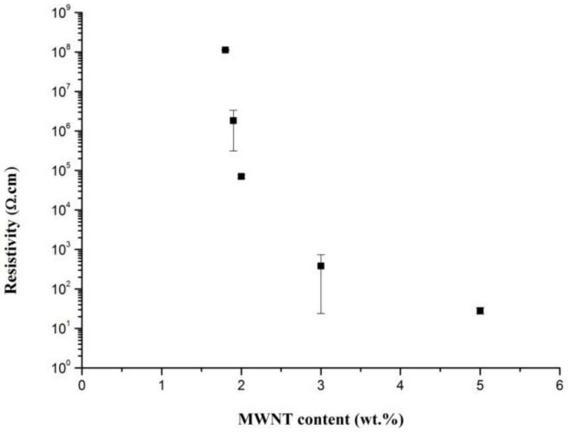

FIGURE 1. Electrical volume resistivity of HDPE (LMFI) containing different weight percentages of MWNT

Percolation scaling law: $\sigma \propto (P - P_c)^t$ was implemented to analyze the conductivity of composite containing conductive fillers in an insulating polymer matrix where σ denotes the conductivity of the polymer composite, P is the volume fraction, $P_c$is the percolation threshold and t represents the conductivity exponent [2,3]. The result found from Fig. 2 and Fig. 3 exhibited the percolation threshold for HDPE (LMFI)/MWNT composites to be approximately 1.9 wt. % of MWNT content. The value of conductivity exponent t was also found from the slope of the line of Fig. 3 which was 2.3. Two dimensional network form by the conductive fillers when the values of t is within the range of 1-1.33 but for the three dimensional network the range of t values change to 1.6-2 [3]. It is expected that the network formed by MWNT conductive fillers within HDPE (LMFI) is three dimensional as the obtained value of t for HDPE (LMFI)/MWNT composite is close to the range of t values for three dimensional networks. The value of$t$ was 4.47while investigation was carried out on HDPE/MWNT composites [2]. The variation in t values was obtained for MWNT filled HDPE composite while different techniques were applied [3].

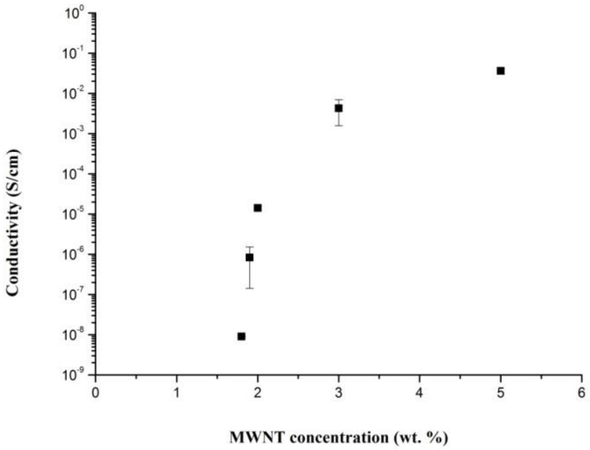

FIGURE 2. Conductivity against different concentrations of MWNT for HDPE (LMFI)/MWNT polymer composites

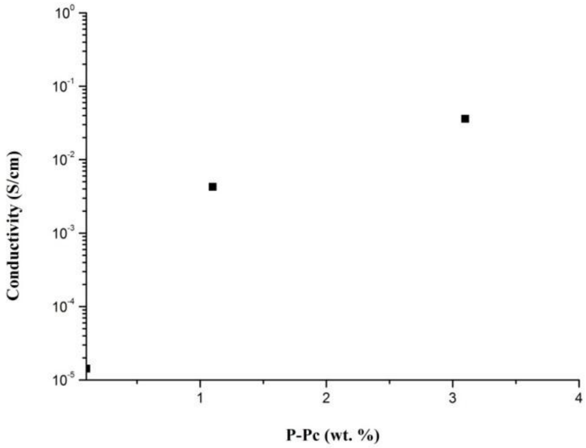

FIGURE 3. Plot of conductivity against (P-P_c) for HDPE (LMFI)/MWNT polymer composites

PTC Behaviour of HDPE (LMFI)/MWNT Composites

HDPE (LMFI) filled with 2 wt. % MWNT was employed to investigate the positive temperature coefficient (PTC) effect of composite. In order to investigate the effect of temperature on resistivity of sample, HDPE (LMFI)/2 wt. % MWNT composite was heated from room temperature to about 160^{o}C. Resistivity versus temperature plot for composite containing 2 wt. % MWNT is presented in Fig. 4.

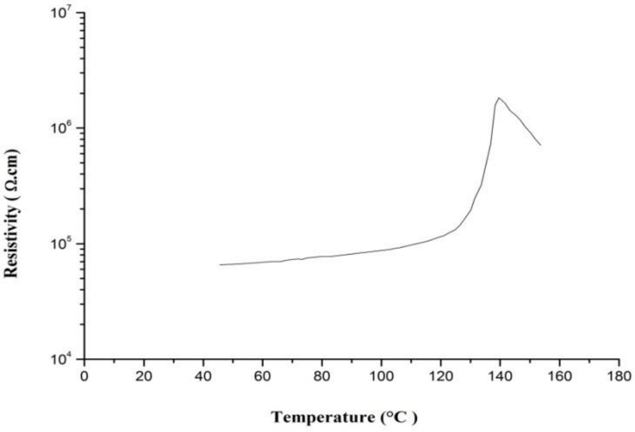

FIGURE 4. PTC curve for HDPE (LMFI) containing 2 wt. % MWNT

It was found from Fig. 4 that tested polymer composite exhibits both PTC and NTC effect. Basically expansion of polymer matrix occurs around the melting temperature of composite which is 134°C for this case. Such expansion disrupts the conductive network constructed by MWNT and the consequence is the increase in resistivity. This is the phenomena for the PTC effect of the composite. However, after the melting temperature, a rapid drop in resistivity of HDPE (LMFI)/2 wt. % MWNT composite was also observed due to reorganization of MWNT to form new conductive pathways. This phenomenon is known as negative temperature coefficient (NTC) effect. Moreover, the PTC intensity (I_{PTC}) is calculated from the logarithm ratio of maximum resistivity (ρ_{max}) and resistivity at room temperature (ρ_{rt}) as given in equation (2) and the calculated value of PTC intensity for HDPE (LMFI)/2 wt.% MWNT composite was 1.4.

Morphology of HDPE (LMFI)/MWNT Composite

The morphology of pristine MWNT is bundle-like or entangled. The SEM image of cross-section of composite containing 2.5 wt. % MWNT is shown in Fig. 5. It is observable that composite shows isolated MWNT (detectable as small bright contrasts) dispersed in HDPE (LMFI) matrix and a few agglomerations of MWNT as well. Basically the stronger interaction between MWNTs in comparison to interaction between HDPE and MWNT lead MWNTs to agglomerates.

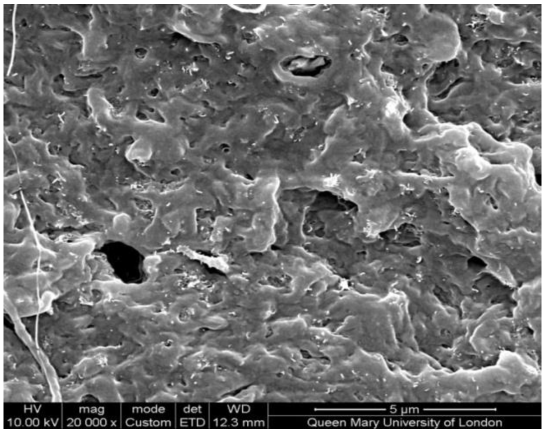

FIGURE 5. SEM image of HDPE (LMFI) filled with 2.5 wt. % MWNT, at 20000x magnification

CONCLUSION

HDPE (LMFI)/MWNT composites made by melt mixing method perfectly displayed percolated behaviour while the percolation threshold was about 1.9 wt. % of MWNT. PTC effect was displayed by HDPE (LMFI)/MWNT composites which occurred around the melting temperature (134ºC) of composites because of expansion of polymer matrix. Basically this expansion of polymer matrix disrupted the conductive network formed by conductive fillers and consequently increased the resistivity. NTC effect was also observed for MWNT filled HDPE (LMFI) composites and the reason behind this was beyond the melting point, MWNT fillers reorganized them to form new conductive pathways within polymer matrix and the consequence was the sharp reduction of resistivity of HDPE (LMFI)/MWNT composites.

REFERENCES

1. M. K. Seo, K. Y. Rhee and S. J. Park, Current Applied Physics **11**, 428-433 (2011).
2. F. Liu, X. Zhang, W. Li, J. Cheng, X. Tao, Y. Li and L. Sheng, Composites Part A: Applied Science and Manufacturing **40**, 1717-1721 (2009).
3. W. Bauhofer and J. Z. Kovacs, Composites Science and Technology **69**, 1486-1498 (2009).
4. A. Kono, K. Shimizu, H. Nakano, Y. Goto, Y. Kobayashi, T. Ougizawa and H. Horibe, Polymer **53**, 1760-1764 (2012).
5. Lee Joong-Hee, S. K. Kim and N. H. Kim, Scripta Materialia **55**, 1119-1122 (2006).
6. A. Rybak, G. Boiteux, F. Melis and G. Seytre, Composites Science and Technology **70**, 410-416 (2010).
7. R. Stru¨mpler and J. Glatz-Reichenbach, Journal of Electroceramics **3**, 329-346 (1999).
8. M. O. Lisunova, Y. P. Mamunya, N. I. Lebovka and A. V. Melezhyk, European Polymer Journal **43**, 949-958 (2007).

International Conference on Mechanical Engineering 2015
(ICME 2015) 18 – 20 December, 2015, Dhaka, Bangladesh

Paper ID : 261

Structural Modification of Silica on Addition of P_2O_5

A. H. M. Azadur Rahman[1,a)], Md. ArifurRahman Khan[1,b)], AnikaBenozir Asha[1,c)], Manzila Islam Tuheen[1,d)], Md. Miftaur Rahman[1,e)]

[1]*Department of Materials and Metallurgical Engienering, Bangladesh University of Engineering and Technology, Dhaka-1000, Bangladesh*

a)Corresponding author: zisan.037@gmail.com
b)arifurrahman.mme@gmail.com
c) anikabenozir.033@gmail.com
d) manzilaislam@yahoo.com
e) miftaurrahman@mme.buet.ac.bd

Abstract.P_2O_5 is added to SiO_2 to reduce its softening temperature which occurs by the breaking of strong Si-O-Si bridging bonds. The aim of this work was to observe this structural change of SiO_2 with the addition of P_2O_5, varying its amount and varying the sintering temperature and holding time at that temperature. In this work, SiO_2 was doped with 5 weight per cent and 10 weight per cent of P_2O_5 by mixing SiO_2 powder with $(NH_4)_2HPO_4$, heating the mix at 500^0 C to remove NH_3 and after pelletisation, the pellets were sintered at 1100^0 C for 2 hours and 1200^0 C for 8 hours. The sintered pellets were then characterized by Fourier Transform Infrared (FTIR) spectroscopy to determine the effect of P_2O_5 addition on the structure of SiO_2. FTIR spectra reveals that addition of P_2O_5 causes new peaks to emerge at about 500-550 cm^{-1} and 794 cm^{-1} after sintering at 1100^0 C for 2 hours with a decrease in the per cent absorbance of Si-O-Si stretching, bending and rocking vibration modes. After sintering at 1200^0 C for 8 hours bands at 1020-1040 cm^{-1} for Si-O-NBO (Non Bridging Oxygen) have appeared which reveals the breaking of Si-O-Si bridging bonds. This is the indication of the degradation of crystalline structure and formation of amorphous structure.

Keywords:P_2O_5; SiO_2; Sintering; FTIR Spectroscopy; Non bridging Oxygen; Amorphous Structure

INTRODUCTION

SiO_2 has wide application in the microelectric devices as a gate and as field effect oxides in metal-oxide semiconductor field-effect-transistors (MOSFETs), as passivation layers because of its high electrical resistivity that can be as high as 1018 ohm-cm [1,2]. Also, the structure of SiO_2 consists of interconnected SiO_4tetrahedra that are connected by highly flexible Si-O-Si bridging bonds. This flexibility results in many possible crystalline structures of SiO_2 to transform into amorphous structure which does not crystallize upon annealing at normal temperatures. This amorphous SiO_2 gets sufficiently flowable at higher temperature which is a requirement for planarization in IC processing. This makes SiO_2 suitable for integrated circuit application. But the temperature to achieve this flowability is about $1300\text{-}1400^0$C for pure SiO_2 which is too hot for other features on the wafer to tolerate [3]. Moreover, small positive ions like Na^+ and K^+ ions can migrate through the open structure of the amorphous SiO_2 under the influence of electric field which is detrimental to microelectronic devices [3,4]. That is why, dopants like phosphorus, boron or a combination of the two is added to SiO_2. Phosphorus after doping into SiO_2, getters these alkali ions [4,5] and makes SiO_2 to soften and flow at 950^0C to 1150^0C [3]. This phosphorous doped silicate glass is used as a premetal dielectric layer between polysilicon and metal in logic devices. Also, they have potential applications in Raman fiber lasers and amplifiers [6], biomedical research, catalysis, drug delivery and imaging [7-9].

Many processes for producing phosphosilicate glasses have been used like sol gel processing [7, 10], modified chemical vapor deposition [6] and plasma enhanced chemical vapor deposition [11]. Sol gel processing possesses a disadvantage of large volume changes during fluid removal, pyrolysis, and/or densification. Columnar grain growth and uneconomical deposition rates are some major disadvantages of vapor condensation methods [12]. In this present study we have used a facile route of powder processing which is more economical than the other processing routes and the most widely used processing techniques for the processing of ceramic powder. This powder processing technique includes the following steps - powder manufacture, powder preparation for consolidation, consolidation of powder to an engineering shape and sintering. In this work, we have added 5 weight percent and 10 weight percent of P_2O_5 into high purity SiO_2 powder by the powder processing technique. Due to the highly hygroscopic nature of P_2O_5, we have used Di-ammonium Hydrogen Phosphate, $(NH_4)_2HPO_4$ powder as the source of P_2O_5 which dissociates into P_2O_5 according to the following reaction [13]:

$2(NH_4)_2HPO_4 = P_2O_5 + 4NH_3 + 3H_2O$

Our main aim is to observe the structural modifications of SiO_2 by varying the amount of P_2O_5, the sintering temperature and the holding time at that temperature by using the Fourier Transform Infrared Spectroscopy (FTIR) technique and then obtain an optimum sintering temperature at low cost.

EXPERIMENTAL PROCEDURES

Powder preparation

Powder mixing in ball mill

HDPE(High density Poly Ethylene) container, ZrO_2 balls, beaker and sieve all were first washed with detergent and then cleaned ultrasonically. Then Calculated amounts of diammoniumhydrogenphosphate, $(NH_4)_2HPO_4$ and SiO_2 were weighed to produce 10 gm sample of SiO_2 doped with 5% P_2O_5 and SiO_2 doped with 10% P_2O_5 each. These were then mixed inside the HDPE container by ball milling process using ZrO_2 balls in the acetone for 24 hrs. Mixed powder was then collected in a beaker with acetone and dried in a drying oven at about 100^0 C. Sample was then preserved in an air tight container.

Heat treatment for the removal of ammonia

Powders prepared from both of these processes were then put inside a furnace. These were then heated up to 500^0C at rate of about 4^0 C/min. At 500^0 C temperature, these samples were then held for about 7 hours. Samples were then furnace cooled.

Powder compaction to produce pellets:

Heat treated powder was then mixed with 2.5% binder in an agate mortar to produce a powder mixture of 1 gram to produce a pellet of 1 gram weight for each of the compositions. The binder composition is 81% C, 13.5% H, 2.9% O, and 2.6% N. This 1 gram of binder mixed powder is then poured into the die cavity of the pressing machine. Compaction pressure is kept at 40KN and was held for about 1 minute. The compact was then ejected from the die using the lower punch. This process was repeated to produce required numbers of pellets.

Sintering of the pellets

Pellets sintered at about 1100^0 C and 1200^0C. The sintering cycle constitutes first heating the pellets to about 500^0 C at a heating rate of about 2^0 C per minute, holding there for about one hour to remove the binder content, then again heating at the rate of 5^0 C per minute to two sets of temperatures with different holding time. Holding time for sintering at 1100^0C was 2 hours and 1200^0C was 8 hours After that the samples were furnace cooled.

Fourier Transform Infrared Spectroscopy (FTIR)

Fourier Transform Infrared Spectroscopy of pure silica powder and SiO_2 doped with 5% and 10% P_2O_5 and sintered at 1100^0 c for about two hours in the wave number range of 400 -1400 cm^{-1} and 1200^0 C for about eight hours in the wave number range of 400 -4000 cm^{-1}, were performed in the Nicolet 380 FTIR machine. Potassium bromide (KBr) powder was used as a standard material to measure the background.

RESULTS AND DISCUSSION

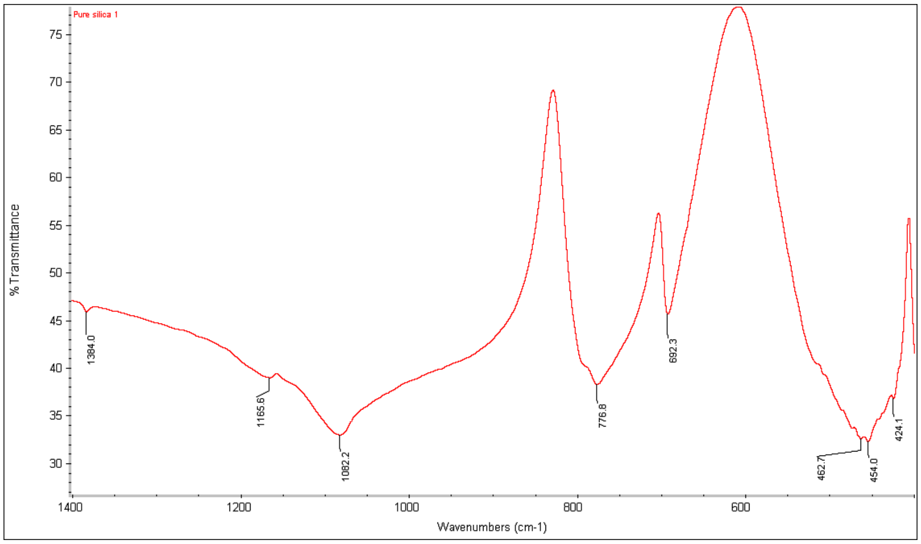

FIGURE 1.FTIR spectra of pure SiO_2

Figure 1 shows the FTIR spectra of pure SiO_2. In this figure, band located at 1082.2 cm^{-1}, represents the Si-O-Si stretching vibration [14] in pure SiO_2. Band located at 454 cm^{-1} [14], represents the Si-O-Si rocking vibration and band at 776.8 cm^{-1} represents the Si-O-Si bending vibration [14,15].

After addition of P_2O_5 and by sintering at 1100^0 C for two hours,some strong peaks were observed from figure 2 and figure 3 other than those observed for pure SiO_2. Some peaks of low intensity in the range of 500-550 cm^{-1} were observed for 5% P_2O_5 addition and for 10% P_2O_5 some strong peaks were also observed at 500.3 and 513.7 cm^{-1}. These peaks between 500-600 cm^{-1}represent the PO_4^{3-} bending vibration [14].

The strong peaks at 794.8 cm^{-1} for 5% P_2O_5 and 793.6 cm^{-1} for 10% P_2O_5 represent the P-O-P asymmetric stretching of the bridging oxygen atoms bonded to a phosphorus atom in a phosphate tetrahedron [16]

The comparison of % Transmittances for the Si-O-Si stretching, Si–O–Si bending and Si-O-Si rocking vibrations of pure silica, 5% P_2O_5 and 10% P_2O_5 added silica are tabulated and plotted in Table 1 and Fig 4 respectively.

TABLE 1: Comparison of % transmittances for various vibrational modes

Vibrational Mode	**Pure SiO_2**	**SiO_2-5%P_2O_5**	**SiO_2-10%P_2O_5**
Si-O-Si stretching	28	34	36
Si-O-Si bending	33	51	51
Si-O-Si rocking	26	40	40

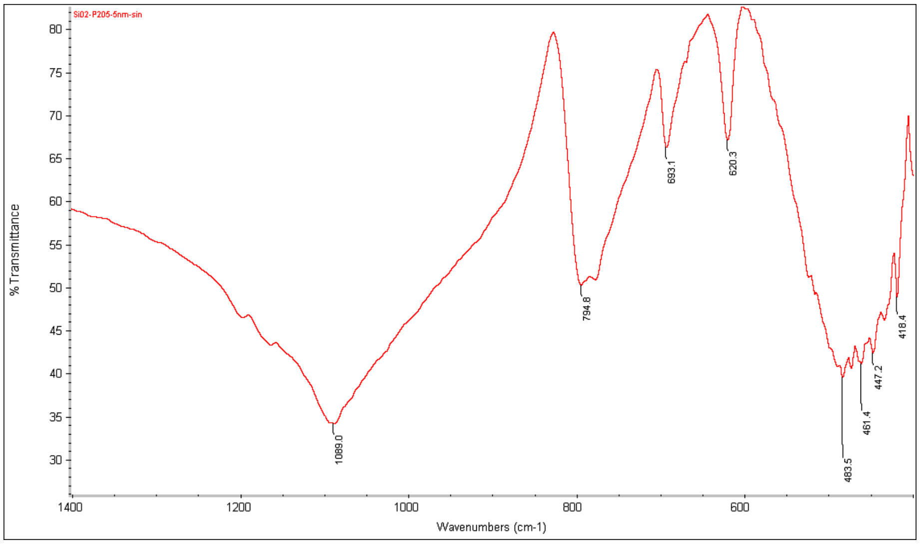

FIGURE 2.FTIR spectra of SiO_2-5% P_2O_5 after sintering at 1100^0 C for two hours

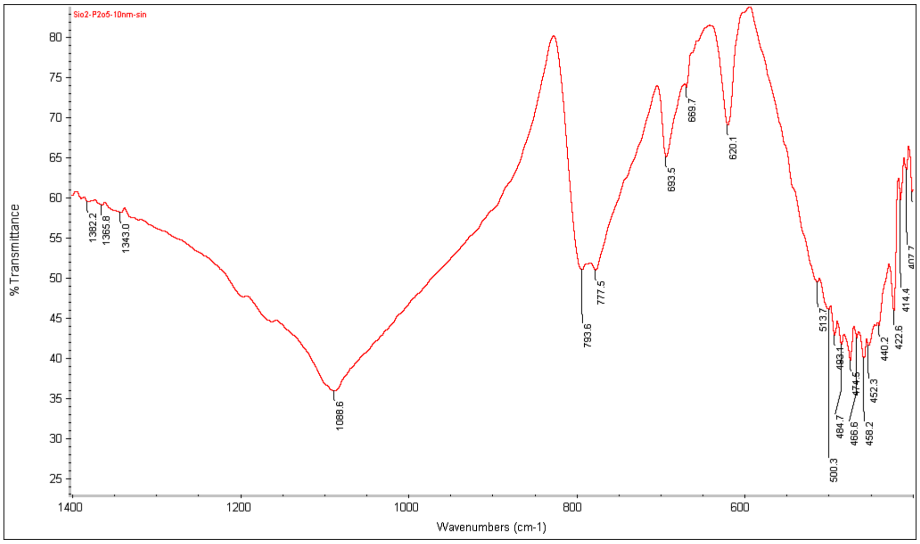

FIGURE 3.FTIR spectra of SiO_2-10% P_2O_5 after sintering at 1100^0 C for two hours

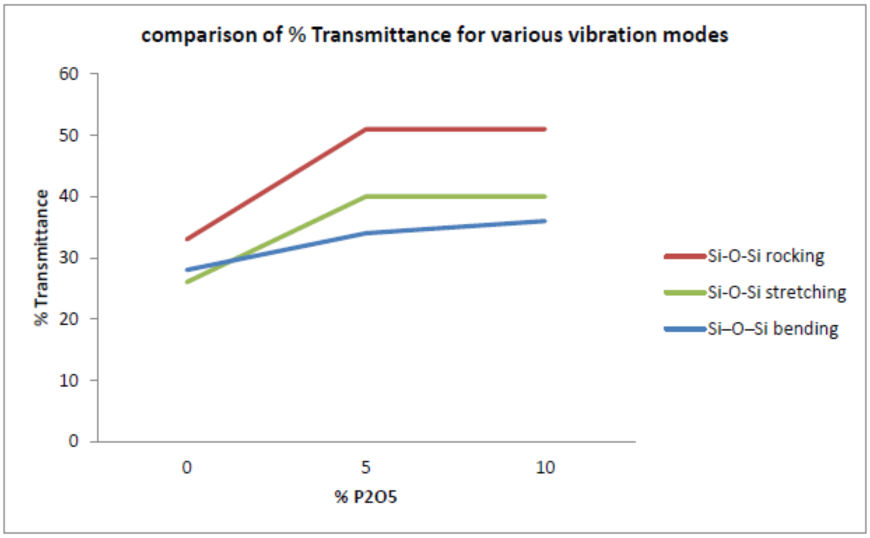

FIGURE 4. Comparison of % Transmittance with addition of P_2O_5 for various Si-O-Si vibration modes

This shows that % transmittance increases which means % absorbance decreases as P_2O_5 is added. Breaking of some bridging oxygen bonds due to P_2O_5addition may attribute to this increment.

FTIR spectra of the SiO_2-10% P_2O_5 after sintering at 1200^0 C for about 8 hours is shown in the figure 5.

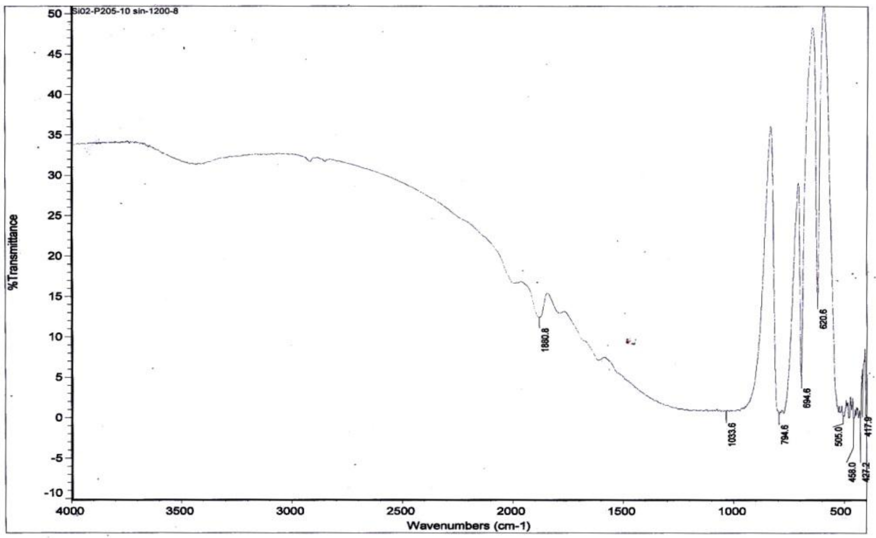

FIGURE 5.FTIR spectra of SiO_2-10% P_2O_5 after sintering at 1200^0C for eight hours

In this figure, a broaden peak ranging from 900 – 1300 cm^{-1} were observed with very low transmittance value. This is due to the formation of PO_4^{3-} symmetric stretching, Si-O-NBO Stretching, PO_4^{3-} asymmetric stretching vibration modes which causes the breakage of bridging oxygen bonds of Si-O-Si stretching to transform into non-bridging oxygen. The presence of Si-O-NBO Stretching causes a great amount of distortion in the crystallinity pure silica and the formation of amorphous phase in the sintered product. The reference regions of these special interests in FTIR spectra are listed in Table 2

TABLE 2: IR frequencies of some functional groups

Vibration Mode	**Reference wavenumbers (cm^{-1})**
PO_4^{3-} symmetric stretching	900-970 [14,17]
Si-O-Si stretch	1080 [14]
Si-O-NBO stretching	1020 to 1040[14,18]
PO_4^{3-} asymmetric stretching	1000-1100 [19]

This broaden peak was not appeared at previous figures for different sintering programs. So previous heating schedules in this work was unable to make sufficient breakage of giant crystalline structure of pure silica as we got no peak in the range of 1020-1040cm^{-1} wavenumber showing the evidence of presence of Si-O-NBO stretching except for sintering at 1200^0C for 8hrs.

CONCLUSIONS

This work investigated the structure modification of SiO_2 after addition of P_2O_5 in its network structure. Varying the amount of P_2O_5 addition, the sintering temperature and the holding time we got the alluring result of the first appearance of Si-O-NBO (Non Bridging Oxygen) for sintering at 1200^0 C temperature for 8hours from the FTIR spectroscopy. The appearance of this Si-O-NBO (Non Bridging Oxygen) band proves the crystal distortion of SiO_2 which leads to the formation of amorphous phase. This degradation in crystallinity increases the flowability of SiO_2 which is highly required in integrated circuit processing.

ACKNOWLEDGEMENTS

The authors sincerely thank Dr. Md. Fakhrul Islam, Professor and Head, Dept of Glass & Ceramic Engineering, (GCE, BUET) for allowing us to perform the entire work in GCE, BUET.

REFERENCES

1. C. W. Nam and S. I. Woo,Thin Solid Films **237**,314-319 (1994)
2. R. F. Pierret, Semiconductor Device Fundamental, Addsion-Wesley Publishing Company, 1996.
3. D.Dobkin, M.K. Zuraw, Principles of Chemical Vapor Deposition, first ed., Kluwer Academic Publishers, 2003
4. W. C. Hsiao, C. P. Liu, Y. L. Wang, Journal of Vacuum Science & TechnologyB **23**, 2146-2150 (2005)
5. A. Modelli and S. Manzini, Journal of Applied Physics**71**, 5123-5129 (1992)
6. V.G. Plotnichenko , V.O. Sokolov, V.V. Koltashev, E. M. Dianov, Journal of Non-Crystalline Solids**306**, 209–226 (2002)
7. A. M. Elnahrawy, A. I. Ali, New Journal of Glass and Ceramics 4, 42-47 (2014)
8. H. Portales, M. Mattarelli , M. Montagna , A. Chiasera , M. Ferrari, A. Martucci , P. Mazzoldi , S. Pelli , G.C. Righini, Journal of Non-Crystalline Solids **351**, 1738-1742 (2005)
9. C.Anderson, and A.J. Bard, Journal of Physical Chemistry **99**, 9882-9885 (1995)
10. A. G. Kannan, N. R. Choudhury, N. K. Dutta, Journal of Electroanalytical Chemistry **641**, 28-34 (2010)
11. Y. Shioya, M. Maeda, K. Takasaki, M. Takagi, Patent US4394401(1983)
12. F. F. Lunge, Journal of the American Ceramic Society**72**, 3-15 (1989)
13. S.C. Odinma, N.H. Okoyeand V.E. Okoro, International Journal of Engineering Science Invention **2**, 56-60 (2013)
14. H. Aguiar , J. Serra, P. González, B. León, Journal of Non-Crystalline Solids **355,** 475-480 (2009)
15. J. Serra, P. Gonzalez, S. Liste, C. Serra, S. Chiussi, B. Leon, M. Perez-Amor , H.O. Ylanen , M. Hupa, Journal of Non-Crystalline Solids **332,**20–27 (2003)
16. I. Battisha, A. E.Nahrawy, New Journal of Glass and Ceramics **2**, 17-22 (2012)
17. D. Carta, J. C. Knowles, M. E. Smith, R. J. Newport, Journal of Non-Crystalline Solids**353**, 1141-1149 (2007)
18. M. Kawashita, F. Miyaji, T. Kokubo, G. H. Takaoka, I. Yamada, Y. Suzuki, and M. Inoue, Journal of Non-Crystalline Solids **255,** 140-148 (1999)
19. R. S. Pryce, L. L. Hench, Journal of Materials Chemistry**14**, 2303-2310 (2004)

Electrodeposition of p-type Cuprous Oxide Thin Film for Solar Application

Sadi Md. Shahriar [a], Safayet Jamil[b] and Kazi Md. Shorowordi[c]

Department of Materials and Metallurgical Engineering, Bangladesh University of Engineering & Technology (BUET), Dhaka-1000, Bangladesh

[a]Corresponding author: sdshahriar@gmail.com
[b]safayetjamil038@gmail.com
[c]kmshorowordi@mme.buet.ac.bd

Abstract. The Cuprous oxides are being considered as p-type semiconductor materials for its photovoltaic properties and used in solar cell manufacturing. Electrodeposition process is the cheapest process to deposit cuprous oxide thin film on substrate materials. In the present study, an attempt has been taken to deposit p-type cuprous oxide on copper substrate at different electrodeposition parameters. A potentiostat with silver electrode (Ag/AgCl) as a reference electrode in a bath containing cupric sulfate solution, lactic acid and sodium hydroxide is used for electrodeposition. Voltage applied during deposition is from -0.40V to -0.55V. The concentration of cupric sulfate is varied from 0.20M to 0.40M and concentration of lactic acid is kept at 3M. During deposition pH of the bath is maintained at 11.9 to 13.0. The deposited films have been characterized by FE Scanning Electron Microscope (SEM) equipped with Energy Dispersive Spectroscopy (EDS), X-ray diffractometer (XRD) and UV spectroscopy. It is found that different color thin films are deposited at different processing conditions. From the visual investigation and characterization, it is observed that good cuprous oxide thin film is deposited when deposition voltage was -0.5V and bath pH was 12.5 at 65^{o}C. The average film thickness is found to be in the range of 2.3 to 7.9 µm. The structure, grain size and preferred orientation of deposited cuprous oxide and their band gap for solar application have also been discussed.

INTRODUCTION

The world's major energy sources are non-renewable, and are faced with ever increasing demand, thus are not expected to last long. These non-renewable sources are mainly of fossil fuels and contribute tremendously to the perennial problem of global warming. The eminent depletion and pollution problems of non-renewable energy sources make the international community focus attention on alternative sources of energy [1].

There are many different renewable resources from which electricity can be generated. Prime examples include wind, tidal, geothermal, bio-fuels, hydroelectric, solar thermal and photovoltaic. All of these renewable resources (excluding geothermal) are driven by solar radiation as the fundamental energy input [2].

The requirements of solar cells are high efficiency, low-cost and a short payback time. The current commercial market for solar cells is dominated by cells made of crystalline silicon, accounting for around 80% of the market share [3]. Making the production process cheaper or developing solar cells that require less material to make will reduce costs. One of the alternatives using less material is the thin film solar cell. The downside of this technology, however, is that most of the thin film solar cells are made of rare (and thus expensive) and/or toxic materials. Examples include rare tellurium or indium and the toxic cadmium or selenium [4].

Cuprous oxide (Cu_2O) is highly a desirable semiconductor oxide for use in solar energy conversion due to its direct band gab (E_g=1.9-2.2eV) and a high absorption coefficient. Cu_2O has several advantages such as non-toxicity and low cost, and can be prepared with simple and cheap methods on large scale. Its outstanding excitonic properties including a large exciton binding energy (~140 meV) have been the target of much research efforts during the past decades [5].

Electrodeposition is a versatile and low-cost technique for preparing thin films of oxide semiconductors on conductive substrates. Electrodeposition is a particularly attractive method because of its simplicity, scalability, economy, and used to synthesis various structures of semiconductor at low temperatures with good control over growth parameters [6]. Thus, the present study has been carried out to deposit and characterize p-type Cu_2O thin film on copper (Cu) substrate.

EXPERIMENTAL

Preparation of Substrates (cathode)

Rectangular Cu sheets (about 1 mm thick) were used as the substrates and were polished using different grades of emery papers. The polished sheets were washed with water followed by rinsing in 10% nitric acid (HNO_3) solution for the removal of foreign particles. After that, they were quickly transferred to the deposition bath to avoid contamination from contact with the environment.

Electrolytic Solution Composition

The electrolytic solution contained $CuSO_4.5H_2O$, lactic acid ($C_3H_6O_3$) and sodium hydroxide (NaOH). The concentration of lactic acid solution was always kept 3 M while concentrations of $CuSO_4.5H_2O$ and NaOH were varied from 0.20 M to 0.40 M and 3.2 to 3.5 M respectively.

Electrodeposition of Cuprous Oxide

Electrodeposition of cuprous oxide was carried out using a three electrode system in potentiostatic mode. An Ag/AgCl electrode was used as the reference electrode. Copper plates were used as both working electrode and counter (auxiliary) electrode. The pH of the bath was kept in between 11.9-13.0 by adjusting the concentration of NaOH. Deposition potential and bath temperature were varied from -0.40 to -0.60 V and from 45-75^{0}C respectively. The deposition time was 40 minutes for all the parameters used. Effects of the variation of these parameters were observed on the properties of the deposited films.

Characterization

JEOL JSM-7600F, Field Emission Scanning Electron Microscope (FESEM) was used to characterize the surface morphology of the deposited films. Energy Dispersive Spectroscopy (EDS) mode of FESEM was used to determine weight percentage of elements present in the films. D8 Advance model XRD machine was used to reveal the phases present in the deposited films. CuKα radiation was used as the source of X-ray. Pharmaspec UV-Vis spectrophotometer was used to determine the absorbance of the deposited films at the wavelength range of both UV and visible part of the electromagnetic spectrum. From the UV-Vis absorbance spectra, absorption coefficient α was calculated. Using this value, $(\alpha h\nu)^2$vs. $h\nu$ curve was plotted where $h\nu$ is the photon energy. From this plot, band gap was measured. Thicknesses of the deposited films were measured using a Fischer, Durlscope mPoR machine.

RESULTS AND DISCUSSION

Scanning Electron Microscopy (SEM)

Scanning electron microscopy was used to examine the surface morphology and grain size of the deposited films. Effect of voltage on grain size of the deposited films is shown in Fig 1. From this figure it is seen that as the voltage increases grain size decreases. The reason for smaller grains with higher voltage may be attributed to increase in deposition rate since the change in voltage to a higher value increases the steady state current [5]. For randomly generated charge carriers, the average diffusion time from bulk to surface in inversely proportional to the grain diameter. If the grain radius is reduced from micrometer dimensions to nanometer dimensions, the opportunities for recombination can be dramatically reduced [6].

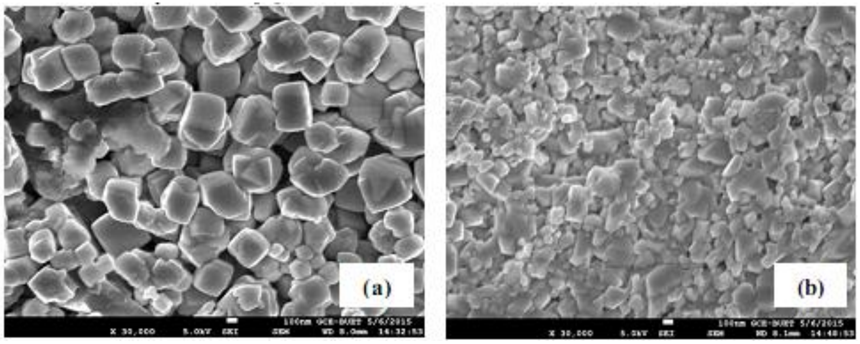

FIGURE 1. SEM images for films deposited at (a) -40V; (b) -0.55V.

Energy Dispersive Spectroscopy (EDS)

EDS analysis was performed to make sure primarily whether Cu_2O was present in the films. For the films deposited at -0.55V, 0.2M $CuSO_4.5H_2O$, 65^0C; at -0.4V, 0.3M $CuSO_4.5H_2O$, 60^0C and at -0.5V, 0.2M $CuSO_4.5H_2O$, 45^0C, mass% of O present are 10.46, 10.02 and 11.03, respectively. In stoichiometric Cu_2O, the ratio of number of copper (Cu) atoms to that of oxygen (O) atoms is 2:1 i.e. the mass percentages of oxygen and copper are 11.18 and 82.82 respectively. However, in crystalline Cu_2O this ratio is not maintained generally due to O vacancies [7]. From these results, it is seen that mass% of oxygen is close to the stoichiometric value of mass% of O in Cu_2O. The slight deviation from the stoichiometric value of 11.18% is due to presence of oxygen vacancies. In Fig 2, a typical result for EDS analysis is shown.

.

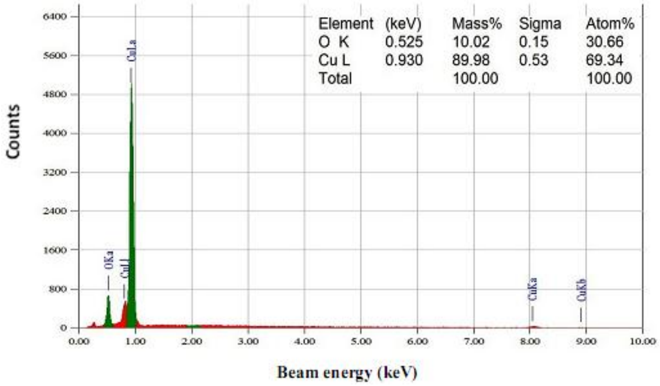

Element	(keV)	Mass%	Sigma	Atom%
O K	0.525	10.02	0.15	30.66
Cu L	0.930	89.98	0.53	69.34
Total		100.00		100.00

FIGURE 2. EDS analysis for film deposited at-0.40V, 0.3M $CuSO_4.5H_2O$ and 65^0C.

XRD Study-Peak Indexing

For the film deposited at -0.55V and 0.2M $CuSO_4.5H_2O$ (Fig 3), the XRD spectra show three peaks. According to JCPDS card no. 5-667 the first peak indicates the presence of cuprous oxide grown with (111) orientation and JCPDS card no. 4-836 specifies the next two peaks to be of copper with orientation along (111) and (200) planes. Comparing the relative intensities we find that relative amount of cuprous oxide shown in the spectra is small compared to that of copper. The reason for obtaining very small cuprous oxide peaks may be due to the fact that the deposited films are very thin which has caused the X-ray beams to penetrate through the film to the substrate; hence, the larger copper peaks are those of the copper of the substrate.

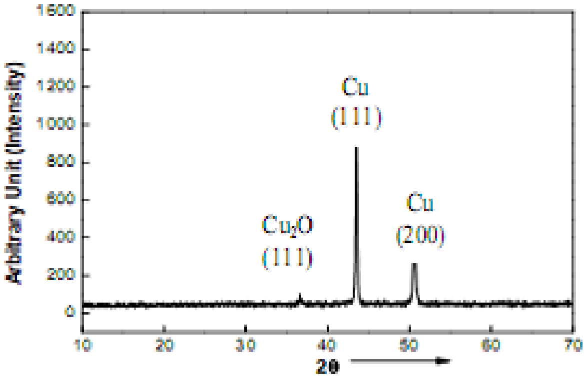

FIGURE 3. XRD spectra for film deposited at -0.55V and 0.2M $CuSO_4.5H_2O$.

UV-Vis Spectrometry

To measure the optical absorption profile of the deposited films UV-Vis spectrometry was used. Effects of deposition voltage and temperature on absorption peaks of the deposited film were studied. The variation in absorbance due to change in voltage is shown in Fig 4a and 4b. It is observed that when the voltage changes from a higher value to a lower one, the absorption intensity increases. This intensity increase might be attributed to the decrease in grain size with increasing potential which leads to faster electron transfers between orbitals. In Fig 5a and 5b, the variation in absorbance with change in temperature is shown. It is evident that increase in temperature increases the absorption intensity. This phenomenon might be due to the increase in film thickness with increasing temperature because higher temperature increase the limiting current density of concentration polarization which in turn increases the deposition rate and hence, the film thickness.

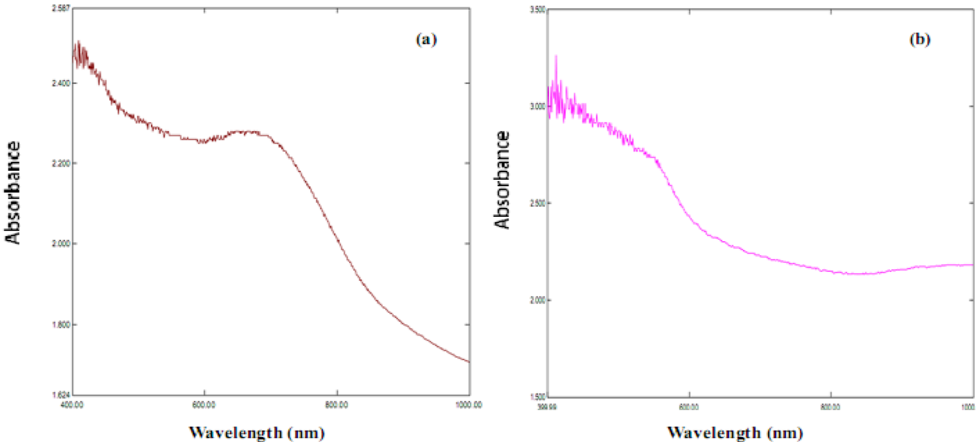

FIGURE 4. Absorbance spectra for films deposited at different voltages (a) -0.55V; (b) -0.50V.

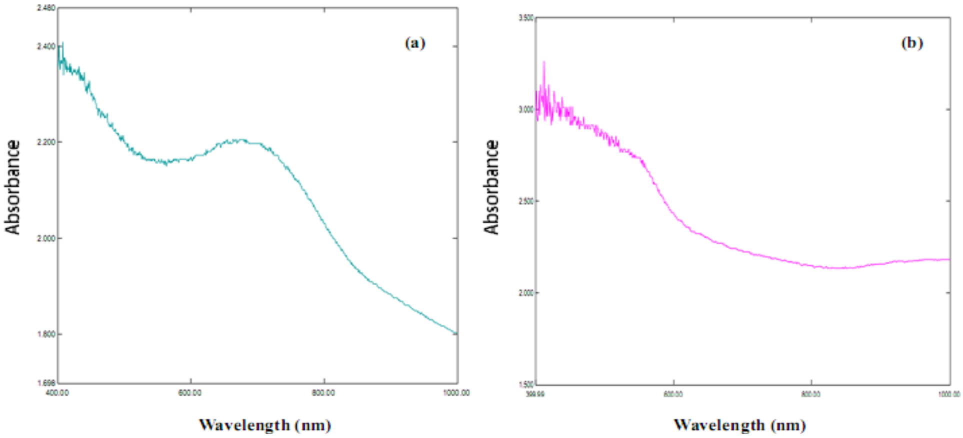

FIGURE 5. Absorbance spectra for films deposited at different temperatures (a) 45°C; (b) 75°C.

Band Gap of Deposited Film

From the UV-Vis spectra previously shown, optical band gap of the deposited films were calculated. In this work, XRD analysis shows presence of cuprous oxide for films deposited at -0.55V, 0.2M $CuSO_4.5H_2O$. Hence, band gap was measured for films deposited at these parameters. From Fig. 6, band gap is measured to be 1.40 eV for the aforementioned parameters. The band gap of Cu_2O is in the range of 1.9-2.2 eV [5]. In this work, there is however, a deviation from this ideal value. The reason for this might be due to the penetration of the UV-Vis radiation through the Cu_2O film to the Cu substrate which caused the band gaps of Cu_2O and Cu to overlap.

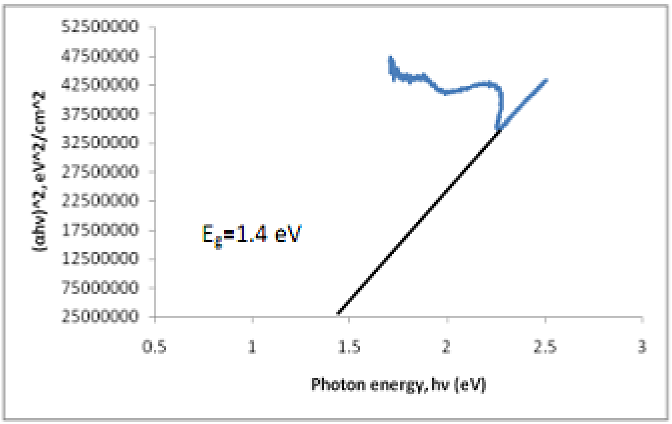

FIGURE 6. Band gap measurement for film deposited at -0.55V and 0.2M $CuSO_4$.

CONCLUSIONS

The major findings from this work are summarized as follows:

- From SEM images it was revealed that shifting the deposition voltage to a higher value decreased the grain size which is better for solar applications.
- From EDS analysis and XRD analysis evidence of Cu_2O was found in the deposited films.
- Analyzing the UV-Vis spectra, it was found that at a lower voltage absorbance increased compared to that at a higher voltage. The shift in bath temperature to a higher value increased the absorbance of the film.
- Band gap closest to the ideal value of Cu_2O was measured to be 1.4 eV.

ACKNOWLEDGEMENTS

The authors express their deepest gratitude to Bangladesh Atomic Energy Commission for conduction of XRD and Department of Physics, BUET for aiding in the band gap measurement. The authors are also very thankful to the department of Glass and Ceramic Engineering (GCE), BUET for the performance of SEM and EDS analysis.

REFERENCES

1. Y. Abdu, A.O. Musa, Bayero Journal of Pure and Applied Sciences, **2(2):** 8–12.
2. A. Cass, G. Davis, G. Francis, H. Hill, W. Aston, I. Higgins, E. Plotkin, L. Scott, A. Turner, Anal. Chem., **56** ,667(1984).
3. G. Adiboina, Thin film photovoltaic (PV) cells market analysis to 2020, The Alternative Energy eMagazine (published online), 2010.
4. K.L. Chopra, P.D. Paulson, V. Dutta, Progress in Photovoltaics Research and Applications **12**, 69-92(2004).

5. Abdelhamid El-Shaer, Abeer Ramadan Abdelwahed, Abdelraouf Tawfik, Mohsen Mossad, Dalal Hemada, International Journal of Emerging Technology and Advanced Engineering, **4(12**),(2014)
6. Y.Tang, , Z. Chen, , Z. Jia, L. Zhang, J. Li, Materials Letters, **59(4),**434-438(2005).
7. W. M. Sears and E. Fortin, Solar Energy Materials, 10, 93-103(1984).

International Conference on Mechanical Engineering 2015
(ICME 2015) 18 – 20 December, 2015, Dhaka, Bangladesh

Paper ID : 345

Effects of Cutting Fluid on Roundness and Taperness in Drilling Deep-Hole by Twist Drills

F.K.Majlish[1,a)] and N.R.Dhar[2,b)]

[1]*Post-Graduate Student, Dept. of Production and Engineering, BUET, Dhaka-1000*
[2] *Professor, Dept. of Industrial & Production Engineering, BUET, Dhaka-1000*

[b)]Corresponding author: nrdhar@ipe.buet.ac.bd
[a)]fariha.khan.majlish@gmail.com

Abstract. High production machining, grinding and drilling inherently generates large amount of heat leads to high cutting zone temperature for its higher cutting velocity, feed and depth of cut. Such high cutting temperature if not reduced impairs surface integrity of the product and reduce dimensional accuracy as well as tool life. Application of cutting fluids changes the performance of machining operations because of their lubrication, cooling, and chip flushing functions. However, the conventional cutting fluids are not that effective in such high production drilling. Low boiling temperature causes vaporization of cutting fluid and prevents it to enter into cutting interface making a barrier to flow. In addition, flowing chips through drill flute prevent the fluid to enter into the cutting zone. Further, they also deteriorate the working environment and lead to general environmental pollution. Presence of cutting fluids have a viable alternative role for drilling with respect to heat dissipation, roundness deviation and taper of the hole, chip formation mode and tool wear. This paper compares the mechanical performance of different cutting fluids to completely dry lubrication for the drilling of AISI 1040 steel based on experimental measurement of roundness deviation and taper of the hole, chip formation mode and tool wear. Results indicated that the use of cutting fluids lead to lower roundness deviation and taper of the hole, favorable chip-tool interaction and reduced tool wear.

Keywords: Drilling, AISI 1040 steel, roundness deviation, taper, chip, tool wear

INTRODUCTION

In the present days, production industries are concerned with high productivity and superior quality. As in macro scale-machining world, drilling is the most-if not the most-frequently performed operation. In the metal cutting operation, temperature is the apprehensive element. Temperature can be reduced in different ways like flood cooling, near dry cooling or micro lubrication, MQL cooling, cryogenic cooling and high-pressure jet cooling. MQL is same in fashion of dry. Flood cooling reduces temperature to some extent by bulk cooling but is not very much effective because it cools only the top surface of the job and the tool due to its overhead application [1]. Nowadays Minimum Quantity Lubrication is minimum lubricants that used together with the compressed air. This new technique is really environmental friendly because the usage of the coolant is in the small quantity [2-3].

Although modern metal cutting methods have improved in the manufacturing industry, like electron beam machining, ultrasonic machining, electrolytic machining, and abrasive jet machining, conventional drilling is still the most common machining processes [4]. The use of cutting fluid allows minimizing or eliminating the burr formation but deteriorates the surface roughness [5].The value of surface roughness is mostly influenced by spindle speed & feed rate. Dimensional accuracy will decrease if drill diameter, feed rate, spindle speed increases [6].

The main objectives of the present work are to make an experimental investigation on the role of cutting fluids (conventional cutting fluid, straight cutting oil and vegetable oil) on roundness and taperness in drilling AISI-1040 steel using HSS drill bit and overall benefits in respect of (i) Chip formation mechanism, (ii) Roundness deviation of the hole, (iii) Taperness of the hole and (iv) Tool wear. This paper will also find the good surface finish in drilling hole and the optimum condition of cutting temperature and overall benefits in respect of chip formation mechanism, roundness and taperness of the hole and tool wear that will be a guide to other people when they want to drill hole.

EXPERIMENTAL INVESTIGATION

A drilling machine is called a drill press is used to cut holes into or through metal, wood or other materials. Drilling is the operation of producing circular hole in the work piece by using a rotating cutter called drill. The most common drill used is the twist drill. Drilling machines use a drilling tool that has cutting edges at its point. The cutting tool is hold in the drill press by a chuck and is rotated and feed into the work at variable speed.

Table-1 Experimental Conditions

Machine tool	:	Z3032 X 10/1, Radial Drill Machine, China (Power 2.2 KW)
Work material	:	AISI-1040 steel
Cutting tool	:	High Speed Steel(HSS) (Φ=8 mm)
Cutting oil	:	VG-68 straight cutting oil, Vegetable oil (olive oil)
Process parameters		
Cutting velocity, Vc	:	40 m/min
In feed, So	:	0.16 mm/rev
Depth of cut, t	:	31 mm
Environment	:	i) Dry ii) Flood coolant iii) VG-68 straight cut iv) Vegetable oil (Olive oil)

For dry condition, clamping the work piece with the vice and started to drill without using any kind of cutting fluid. Before starting drilling, the job was aligned as perfectly as possible. Though there was a small error about ±0.004mm. In Fig.1 (a) shows the photographic view of making hole (in dry condition). For flood coolant condition, the built in coolant system of the drill machine is using. Using this condition it is possible for reduction of heat and to get better result from dry condition. Fig.1 (b) shows the photographic view of making hole in wet condition (Flood Coolant). For the third time, using straight cut cutting oil VG-68 as coolant. VG-68 is high quality anti-wear hydraulic oil developed for the use in a wide variety of industrial application. It provides highest anti-wear performance, long service life due to high oxidation stability, hydrolytic stability and filterability characteristics which shows in Fig.1(c). Finally, using vegetable oil (olive oil) as coolant is again followed the same procedure as VG-68. It provides the best lubrication and the poorest cooling characteristics. Similarly Fig.1 (d) shows the photographic view of making in wet condition (Olive oil).

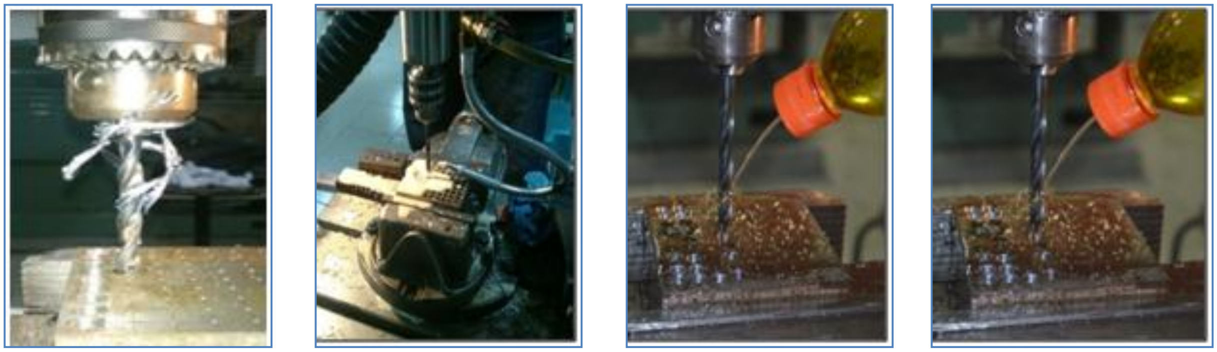

(a) Dry Condition (b) Flood Coolant (c) VG 68 Straight Cut Cutting Oil (d) Olive Oil

FIGURE 1. Photographic view of making hole under different environment

The cooling capacity of the cutting oil (Flood coolant, VG 68 straight cut cutting oil, Olive oil) at different pressure and flow rate used in this experiment is important. After heating, the work pieces were submitted to cooling condition similar to the experiments. The temperature was measured by a K-type (cromel-alumel) thermocouple for about 7 minutes. By heating the work piece for four times up to 400ºC. Each time measured temperature reduction by air, flood coolant, VG-68 and Olive oil respectively. In Fig.3 shows the temperature curve against time. For air cooling, it reduces the temperature up to 249 ºC in about 7 minutes. Whereas with VG-68, it reduces the temperature up to 51 ºC with flood coolant up to 59 ºC respectively. But with olive oil, it reduces the temperature up to 99 ºC which was better than air cooling but not as good as VG-68 or Flood coolant. In Fig.2 shows the photographic view of the heating process. In Fig.3 shows the cooling capacity of air and other cutting fluids used in the experiment.

FIGURE 2. Photographic view of heating procedure

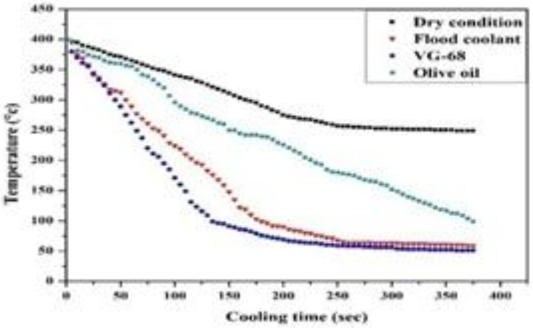

FIGURE 3. Cooling capacity of air and different cutting fluids

EXPERIMENTAL RESULTS AND DISCUSSIONS

Number of hole in drilling operation is a major concern. During drilling huge amount of heat is produced due to shearing of metal, friction between chips and flute and rubbing the flank with newly cleaved surface. During the experiment in dry condition, drill bit becomes burnt blue in color and after completing 18 holes on AISI-1040 steel, the drill bit was broken and melt with the hole. While drilling 19th hole, catastrophic (sudden and total failure of a system from which recovery is impossible) failure occurs and the drill bit was broken and melt with the whole due to high temperature and high rubbing with the wall, which makes the hole incomplete shows in Fig.4(a). On the other hand in flood coolant condition drill bit remains its original color and without any burning 18 holes are drilled on AISI-1040 with metallic blue color chips shows in Fig.4 (b). In VG-68 straight cut condition, the drill bit remains its original color after completing 18 holes and deviation was lesser than the previous two shows in Fig.4 (c). In terms of vegetable oil, the diameter of the hole was in the acceptable limit. But in this condition just drilled 12 complete holes. At 13thhole, drill bit was melted due to high temperature as shown in Fig.4 (d). In compare to other cooling method, vegetable oil does not provide better cooling action.

(a) Dry Condition (b) Flood Coolant (c) VG-68 Straight Cut Oil (d) Vegetable Oil

FIGURE 4. Photographic view of number of hole under different conditions

Chip formation during drilling operation is greatly influenced by the cutting parameters such as cutting speed, feed rate, and drill geometry. Under dry condition, the shape of the chip produced were spiral, serrated and continuous with burnt blue color when drilling AISI-1040 steel shows in Fig.5 (a). In flood coolant condition, the shape of the chips produced under flood coolant become spiral and continuous with color of metallic and light blue to burnt blue. Continuous chips with complete metallic color was found shows in Fig.5(b) while drilling with VG-68 straight cut oil shows in Fig.5(c) which resembles much reduction in temperature. But because of poor cooling characteristics of olive oil, continuous chips with metallic, brown and even brunt color chips were found shows in Fig. 5(d). So, chips produced in different wet conditions is smooth due to proper cooling and lubrication in drilling AISI-1040 steel which creates a lubricant film that protects the tool face from rubbing with the work material and pretend sharp edge of the drill bit. On the other hand saw toothed chips are produced in dry condition due absence of lubrication and serration of chips.

(a) Dry Condition (b) Flood Coolant (c) VG-68 Straight Cut Oil (d) Vegetable Oil

FIGURE 5. Photographic view of chips under different conditions

In other words, these parameters presented no tendency as feed length increased. Standard deviation of the average diameter obtained under different wet conditions is lower than that obtained using dry condition, which means that the different wet conditions presented a better quality with presence of adequate cooling and lubrication at the chip-tool interface. The roundness of the holes close to the entrance of AISI-1040 did not change very much from the beginning to the end of the holes under different wet conditions in compare to dry condition this result can be attributed to the lower cutting force and the shorter diameters. In dry condition due to excessive heating, scarcity of coolant and lubricant, rubbing the tool face with work material and commencement of tool wear, the deviation is very large as shown in Fig.6 and Fig.7.

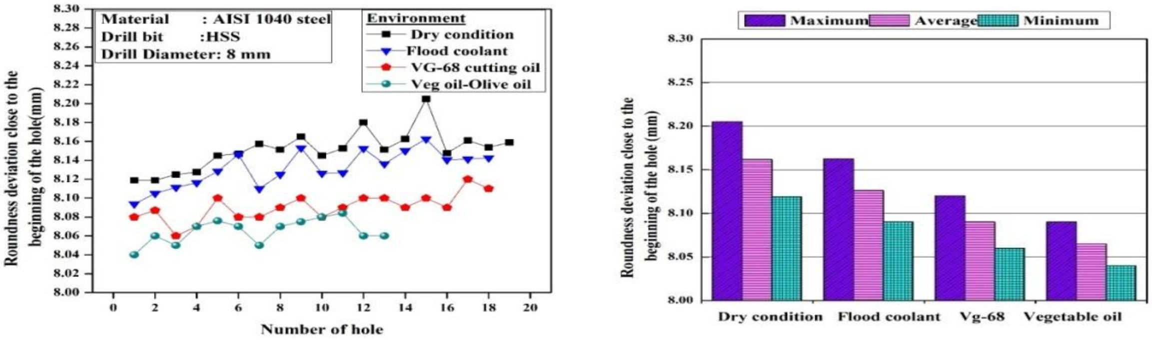

FIGURE. 6 Roundness deviation close to entrance of the hole under different conditions

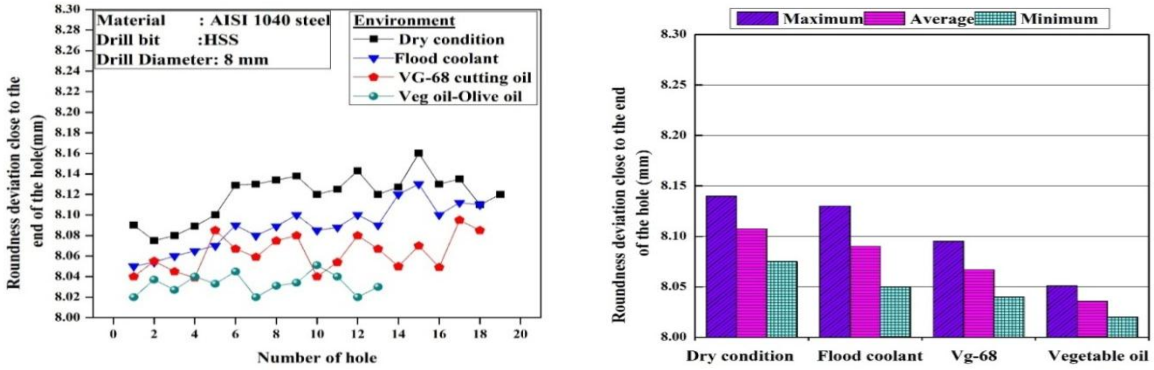

FIGURE. 7 Roundness deviation close to end of the hole under different conditions

Bottom surface roundness deviation has influential role to make taper value. Taper value was appeared in both dry and different wet conditions for AISI-1040 steel. But bad results found for holes made under dry condition are due lack of lubrication action. Variation of diameter deviation with number of the holes under different conditions shows in Fig.8.

Tool wear causes poor quality of holes surface, irregularity of roundness and unacceptable diameter deviation. Drilling under dry condition tool wear is evident for the AISI-1040 steel shows in Fig. 9(a) but no significant wear is found under wet conditions shows in Fig.9 (b), Fig. 9(c) and Fig. 9(d). Different wet condition reduces cutting temperature and provide lubrication entering into chip-tool interface making a lubrication film at high pressure, thus reduces tool wear as a result tool life is increased.

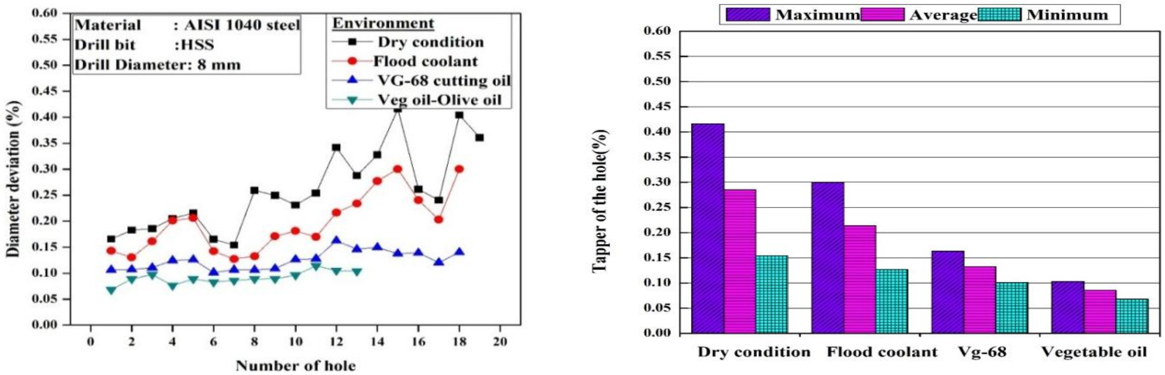

FIGURE. 8 Variation of diameter deviation with number of the holes under different conditions

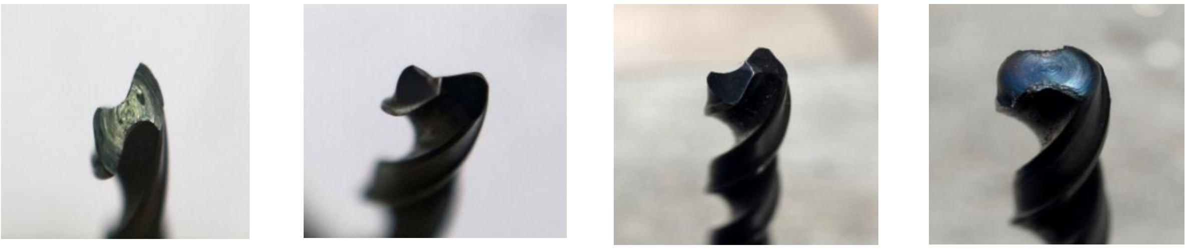

(a) Dry Condition (b) Flood Coolant (c) VG-68 Straight Cut Oil (d) Vegetable Oil

FIGURE. 9 Photographic view of tool wear under different conditions

CONCLUSIONS

Based on the experimental results the following conclusions can be drawn:

- Cooling capacity of VG-68 has the better effect among the entire environment used in this investigation.
- The quality of the holes obtained using flood coolant, VG-68 and vegetable oil are much better than that obtained in dry cutting. Roundness deviation was very small both at the entrance and end of the holes under Flood coolant, VG-68 and vegetable oil conditions in compare to dry condition, because of high cooling capacity of lubricant.
- Taper values were also smaller under wet condition in compare to dry condition for the AISI-1040 steel because of high lubrication capability of the cutting oil.
- In wet condition the chips were long in shape and continuous, so it was not stocked in the holes. This indicates that lubrication effects under wet condition in compare to dry condition is much better, because the cutting fluid effectively works here in lubrication and cooling. On the other hand in dry condition the chips were short in size and not continuous, so it stocked in the holes.
- The beneficial effects of wet condition may be attributed to effective and efficient lubrication action, which prevents the chip sticking on the tool and makes the operation easier. To carry out the operation with dry cutting is very much difficult, because the chip sticks to the spiral channels of the drill.
- Cutting fluid improves tool wear and results smaller diameter deviation and taper deviation.

ACKNOWLEDGEMENTS

The authors are deeply indebted to their thesis supervisor Dr. N. R. Dhar, Professor, Department of Industrial and Production Engineering, BUET, Dhaka for his unremitting help and encouragement throughout the progress of the project work. The authors offer their sincere thanks to all those who either directly or indirectly helped them in various ways to complete this thesis work, especially to their friends for providing courage.

REFERENCES

1. U. Heisel, M. Lutz, “Pesquisa de fluido de refrigeração e de lubrificação,Máquinas e Metais”, Vol. 388 (1998), pp.40-49.
2. N. R. Dhar, K.M. Rahman, S. Islam and M. Hossain,” Using MQL and a carbide tool in the drilling of AISI-1060 steel”, Journal of Mechanical Engineering, IEB Vol. ME 33, (June & Dec. 2004), pp. 22- 31.
3. K. M. Rahman, “Effect of MQL in Drilling Commercially Used Steels”, M. Eng. Dissertation, BUET, Dhaka, Bangladesh, (2004).
4. D. U. Braga, A.E. Diniz, G.W.A. Miranda, & N.L. Coppini, Using a MQL and a Diamond Coated Tool in the Drilling of Aluminum-Silicon Alloys, Journal of Materials Processing and Technology, **122**, 127-138(2002).
5. Z. Y. Wang and G. Petrescu, “Stress Analyses of CBN Insert in Hybrid Machining of RBSN Ceramic,” Machining Science and Technology, **8(1),**1-19 (2004).
6. Cassin C. and Boothroyed. G., “Lubrication Action of Cutting Fluid”, J. of Mechanical Engineering Science, **7(1)**,67-81(1965).

International Conference on Mechanical Engineering 2015
(ICME 2015) 18 – 20 December, 2015, Dhaka, Bangladesh

Paper ID : 349

Effects of Cutting Parameters and Machining Environments on Surface Roughness in Hard Turning using Design of Experiment

Mozammel Mia[1,a], Mahmood Al Bashir[1] and Nikhil Ranjan Dhar[2, b]

[1]*Mechanical and Production Engineering, Ahsanullah University of Science and Technology, Dhaka 1208, Bangladesh*
[2]*Industrial and Production Engineering, Bangladesh University of Engineering and Technology, Dhaka 1000, Bangladesh*

a)Corresponding author: arif_ipe@yahoo.com
b)nrdhar@ipe.buet.ac.bd

Abstract. Hard turning is gradually replacing the time consuming conventional turning process, which is typically followed by grinding, by producing surface quality compatible to grinding. The hard turned surface roughness depends on the cutting parameters, machining environments and tool insert configurations. In this article the variation of the surface roughness of the produced surfaces with the changes in tool insert configuration, use of coolant and different cutting parameters (cutting speed, feed rate) has been investigated. This investigation was performed in machining AISI 1060 steel, hardened to 56 HRC by heat treatment, using coated carbide inserts under two different machining environments. The depth of cut, fluid pressure and material hardness were kept constant. The Design of Experiment (DOE) was performed to determine the number and combination sets of different cutting parameters. A full factorial analysis has been performed to examine the effect of main factors as well as interaction effect of factors on surface roughness. A statistical analysis of variance (ANOVA) was employed to determine the combined effect of cutting parameters, environment and tool configuration. The result of this analysis reveals that environment has the most significant impact on surface roughness followed by feed rate and tool configuration respectively.

Keywords: Hard turning, Surface roughness, Design of experiment, Analysis of variance, High pressure coolant

INTRODUCTION

The hard turning process is used by the manufacturer, around the world, to produce a part that requires close dimensional accuracy, instead of producing by conventional turning process which is followed by low material removal rated grinding process. The hard turning process is accomplished by turning a hardened part that is already heat treated to the desired hardness. But turning of high hardness material (38-65 HRC) requires even higher hardness (45-70 HRC) of a cutting tool. In recent years, development of new cutting tools has facilitated the turning of high hardness work materials. Carbide tools have found its way in metal cutting industry, especially in turning highly hardened steels. Coating on the carbide tools are employed to increase the lubrication, to reduce the friction and temperature, and consequently, improve the surface finish. Coated tools, when used to turn hard materials to fabricate complex parts and shapes, reduce the manufacturing cost by up to 30 times [1].

Surface roughness is found to be significantly affected by feed rate [2, 3], followed by cutting speed and depth of cut, and the prediction of surface roughness was more accurately done by random forest regression compared to multiple regression [2]. The similar result was also found by Pal et al. [4] with an extended remark that the increase of workpiece hardness decreases R_a. Hessainia et al. [5] claimed 67.32% influence is of feed while only 22.02% is of cutting speed and no significant effect of tool vibration and depth of cut on surface finish. Feed rate and workpiece hardness are two important statistically influential factors due to their main effect as well as interaction effect on surface roughness, concluded by Aouici et al. [6]. They said to have minimal roughness at lower feed and higher cutting speed. Whereas, ANOVA showed the depth of cut has the highest impact on R_a, followed by feed and cutting speed while machining AISI 52100 by CBN tool [7]. Another ANOVA used research showed that cutting edge geometry has a significant role on surface roughness, especially honed edge geometry and lower workpiece hardness results in better surface [8]. It was also concluded while using RSM technique that the linear model is better, in predicting R_a in machining HSLA steel using coated carbide tools, as the prediction accuracy is higher [3]. Use of RSM by Bouacha et al. [9] claimed that R_a is highly, negatively and negligibly affected by the feed rate, cutting speed and depth of cut respectively. Feed rate is the most powerful among all the cutting parameters in determining the effect on surface roughness [10, 11]. In addition to cutting parameters, the machining environment also plays a significant role in surface integrity due to its cooling and lubrication effect. High pressure coolant application is a viable technique to achieve better surface finish [12].

It can be seen from the literature review that none of the studies has attempted to explore the effect of coolant application on the surface roughness. Very few studies focused on the effect of tool configuration on surface roughness. The objective of this study is to obtain the effect of cutting speed, feed rate, tool insert configuration and high pressure coolant on surface roughness in hard turning of AISI 1060 steel hardened to HRC 56 using full factorial analysis. The design of experiment (DOE) is adopted to create the number of machining runs and corresponding machining conditions. Furthermore, a statistical analysis (ANOVA) is performed to determine which parameters are statistically significant and which interaction effect is the most prominent on surface roughness.

MATERIAL AND METHOD

In this study, a workpiece made of AISI 1060 grade steel was heat treated to get the desired hardness of HRC 56±2. The dimension of the workpiece, which was a hollow cylindrical bar, was length 200 mm with external and internal diameters of 120 mm and 45 mm respectively. As thermal treatment, an electric furnace of high heating element was used to raise the temperature to 900°C in three hours and then the material was soaked at that temperature for one and half hour in the heating chamber. A quench tank, containing bluta oil (Grade-27), of capacity 600 litres was used for quenching the work material. Tempering was done, to reduce the excess hardness and brittleness, by heating the workpiece to 300^0C then cooling it in still air for two hours.

To measure the hardness value, a Rockwell hardness tester was employed and sixteen readings were taken along the radius then plotted to ensure the hardness within HRC 56±2. To skin out the outer surface, a rough cut of 2.0 mm was performed to prepare the workpiece for actual machining tests. The experiments were conducted under dry and high pressure coolant conditions. The cutting tool inserts, SNMM 120804 (Widia) and SNMG 120408 (Widia), used for the experimental test, were held by tool holder PSBNR 2525 M12 (ISO specification). The conditions under which the machining tests have been carried out are briefly given in Table-1.

TABLE 1 Experimental condition.

Machine tool	Lathe (China), 7.5 kW
Work materials	AISI 1060 (56 HRC)
Cutting tool	SNMM 120408, Widia; SNMG 120408, Widia
Coating	TiCN, WC, Co
Tool holder	PSBNR 2525 M12, Widia
High pressure coolant	80 bar, Coolant: 6.0 L/min through external nozzle
Coolant type	VG-68 (ISO grade)
Environment	Dry and HPC condition

The surface roughness, after machining by SNMM and SNMG inserts at different V_c-S_o combinations under both dry and HPC conditions, was measured by a Talysurf (Surtronic 3+). The selection of independent factors and allocation of levels are shown in Table-2. Two quantitative factors (V_c, S_o) are attributed into three levels (low-mean-high) while two qualitative factors (T, E) are taken as two levels (low-high) to see their effects.

The design of experiment is a systematic technique to matrix the possible combinations among the machining conditions so that the corresponding responses can be collected in an organized manner. The analysis is based on two 3-levels and two 2-levels factors, a total of 36 sets of machining conditions and responses as shown in Table-3.

TABLE 2 Attribution of the levels to the factors.

Symbol	Factors	Level 1	Level 2	Level 3
V_c	Cutting speed	58	81	115
S_o	Feed rate	0.10	0.12	0.14
T	Tool configuration	SNMM	SNMG	-
E	Environment	Dry	HPC	-

TABLE 3 Machining conditions and response.

Exp. No.	V_c	S_o	T	E	Ra	Exp. No.	V_c	S_o	T	E	Ra
1	58	0.1	SNMM	DRY	1.28	19	81	0.12	SNMG	DRY	1.33
2	58	0.1	SNMM	HPC	1.34	20	81	0.12	SNMG	HPC	0.74
3	58	0.1	SNMG	DRY	0.96	21	81	0.14	SNMM	DRY	1.52
4	58	0.1	SNMG	HPC	0.90	22	81	0.14	SNMM	HPC	1.42
5	58	0.12	SNMM	DRY	1.38	23	81	0.14	SNMG	DRY	1.64
6	58	0.12	SNMM	HPC	1.28	24	81	0.14	SNMG	HPC	1.16
7	58	0.12	SNMG	DRY	1.32	25	115	0.1	SNMM	DRY	1.28
8	58	0.12	SNMG	HPC	0.94	26	115	0.1	SNMM	HPC	0.96
9	58	0.14	SNMM	DRY	1.52	27	115	0.1	SNMG	DRY	1.30
10	58	0.14	SNMM	HPC	1.60	28	115	0.1	SNMG	HPC	0.74
11	58	0.14	SNMG	DRY	1.60	29	115	0.12	SNMM	DRY	1.18
12	58	0.14	SNMG	HPC	1.20	30	115	0.12	SNMM	HPC	0.72
13	81	0.1	SNMM	DRY	1.02	31	115	0.12	SNMG	DRY	1.46
14	81	0.1	SNMM	HPC	1.34	32	115	0.12	SNMG	HPC	0.80
15	81	0.1	SNMG	DRY	1.12	33	115	0.14	SNMM	DRY	1.62
16	81	0.1	SNMG	HPC	0.68	34	115	0.14	SNMM	HPC	1.00
17	81	0.12	SNMM	DRY	1.34	35	115	0.14	SNMG	DRY	1.88
18	81	0.12	SNMM	HPC	1.50	36	115	0.14	SNMG	HPC	0.86

RESULTS AND DISCUSSIONS

Analysis of variance (ANOVA)

An analysis of variance was conducted to identify the statistically significant trends in the measured response data. The results of ANOVA for the surface roughness are shown in Table-4. The analysis was carried out for a confidence level of 95% (significance level, $\alpha = 0.05$). The Table-4, scrutinizing F- and P- value, shows that the main effect of environment, feed rate, and tool configuration is of highest statistical significance, whereas, interaction between cutting speed-environment and tool configuration-machining environment are the two statistically significant effects.

Machining environment has F-value = 71.02, P-value = 0.0 and C = 26.490%, and all these three statistical indicators establish the environment as the most significant factor. It is justified by the application of high pressure coolant on the chip-tool contact point, which reduces the cutting temperature and friction between the chip-tool and tool-workpiece, and also provides sufficient lubrication for the movement of tool over the workpiece surface that creates better surface roughness than dry machining. Feed rate has F-value = 31.06, P-value = 0.0 and C = 23.169%, and all these three values clearly establish the position of feed rate as the second most statistically significant factor. A similar result is also derived from theoretical analysis, as the theoretical surface roughness is proportional to the square of the feed rate if the nose radius is considered fixed, associated with experimental results of R_a. Tool insert configuration is statistically the third most important factor among the four main effects, leaving cutting speed as the statistically least significant factor.

TABLE 4 Analysis of variance for surface roughness.

Source	DF	Seq. SS	Adj. SS	Adj. MS	F	P	C (%)
V_c	2	0.09974	0.09974	0.04987	4.11	0.036	3.066
S_o	2	0.75377	0.75377	0.37689	31.06	0.000	23.169
T	1	0.19803	0.19803	0.19803	16.32	0.001	6.087
E	1	0.86180	0.86180	0.86180	71.02	0.000	26.490
$V_c \times S_o$	4	0.04921	0.04921	0.01230	1.01	0.430	1.513
$V_c \times T$	2	0.17112	0.17112	0.08556	7.05	0.006	5.259
$V_c \times E$	2	0.40207	0.40207	0.20104	16.57	0.000	12.359
$S_o \times T$	2	0.05882	0.05882	0.02941	2.42	0.120	1.808
$S_o \times E$	2	0.10257	0.10257	0.05129	4.23	0.034	3.153
T×E	1	0.36200	0.36200	0.36200	29.83	0.000	11.127
Error	16	0.19417	0.19417	0.01214			5.968
Total	35	3.25330					100

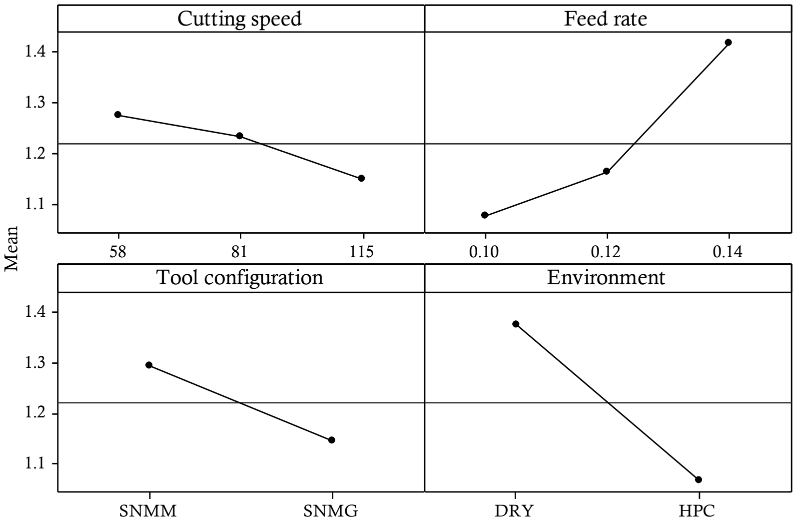

FIGURE 1. Main effects plot for surface roughness, R_a (μm).

As interaction effects investigation, the interaction between tool configuration and machining environment was found with F-value = 29.83, P-value = 0.0 and C = 11.127%. On the other hand, the interaction effect between cutting speed and machining environment has F-value = 16.57, P-value = 0.0 and C = 12.359%. Another statistically significant interaction is found between cutting speed and tool configuration with F-value = 7.05, P-value = 0.006 and C = 5.259. As the percentage contribution of error C = 5.968% it reflects that neither any important factor is neglected from the calculation nor any high measurement error was taken into account.

Therefore, the ANOVA shows, the most significant main effect comes from the environment, feed rate, tool configuration respectively while the most important interaction effects come from environment-tool configuration and cutting speed-environment respectively.

Main effect on surface roughness

The main effect of four factors i.e. cutting speed, feed rate, tool configuration and environment on the surface roughness is plotted in Fig. 1. In Fig. 1, the horizontal line reflects the mean value of the responses. The plot shows that with the increase in cutting speed mean roughness value decreases. At cutting speed 115 m/min, minimal roughness is produced and at cutting speed 58 m/min, maximum roughness is produced. On the other hand, little increase in feed rate causes a greater increase in roughness. As a result, the highest roughness is produced at 0.14 mm/rev feed and surprisingly, the lowest roughness is produced at lowest feed rate i.e. 0.10 mm/rev. At the same time, use of SNMG insert produces lower roughness value than that would be produced by SNMM insert. And, finally application of high pressure coolant ensures a drastic reduction in surface roughness over dry machining.

Residual analysis

The normal probability plot of the residuals, residual histogram, residuals versus fits and residuals versus order are plotted in Fig. 2. From Fig. 2(a) it is evident that most of the points lie reasonably close to the straight line which represents that errors are normally and independently distributed. The normality assumptions are considered valid for this curve. The residual histogram of Fig. 2(b) shows even distribution of the residuals, with no sign of skewness. The maximum frequency is expanded over (-0.05 to +0.05) leaving the rest frequency over both the tails. A clear random plot of the residuals over the fitted values is shown in the Fig. 2(c). There is no sign of any increasing/decreasing pattern to nullify the assumption of constant variance. Fig. 2(d) illustrates the residuals plot over observation order, and as it is seen that there is sudden ups and downs, indicating the residuals are uncorrelated to each other.

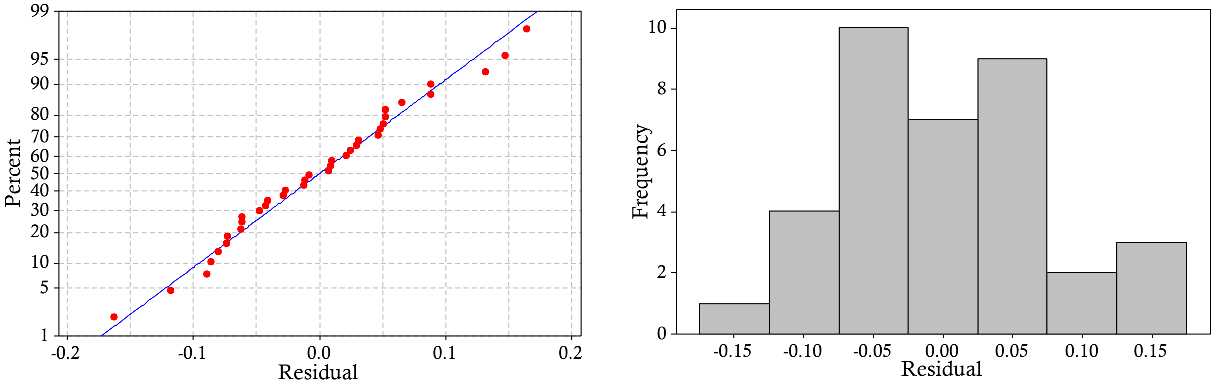

a. Normal plot of residuals for R_a.

b. Residual histogram for R_a.

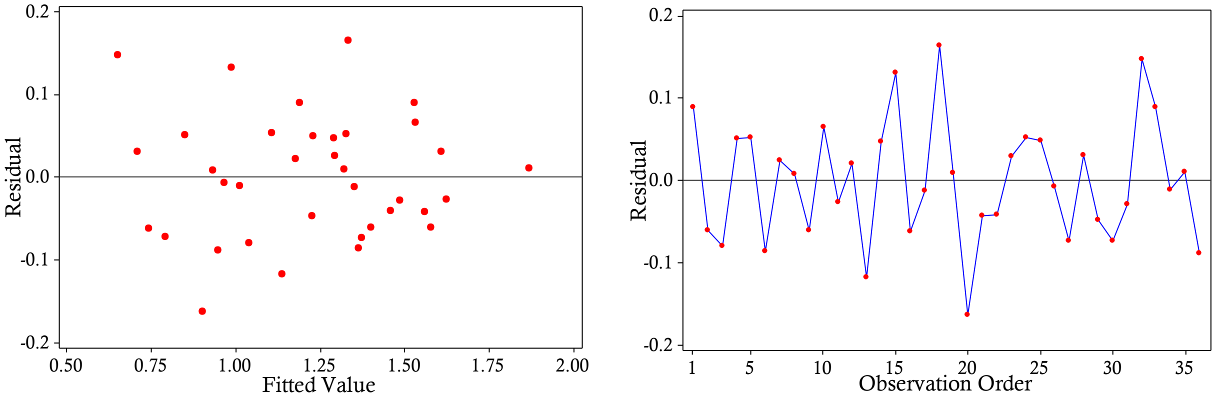

c. Residuals vs fits for R_a.

d. Residuals vs order for R_a.

FIGURE 2. Residual analysis.

3-D response surface plot

The three-dimensional surface roughness plot is shown in Fig. 3(a). The increase in feed rate and decrease in cutting speed increase surface roughness. A clear indication of interaction effect is discernible by the wrinkle along the mid-area of the curve. The contour plot of R_a versus V_c and S_o is an important tool to optimize the cutting parameters for desired surface roughness, as shown in Fig. 3(b). The curve, created by the contrast of two colours, indicates the boundary region of the optimal cutting condition values. It also indicates the trade-off of the cutting speed and feed rate for optimal roughness values. For example, although high feed rate produces higher roughness but, low roughness (1.0 ~ 1.2 µm) can be produced if the cutting speed is kept higher along with higher feed rate. At highest feed rate, the worst possible roughness begins to occur with cutting speed as low as ~92 m/min.

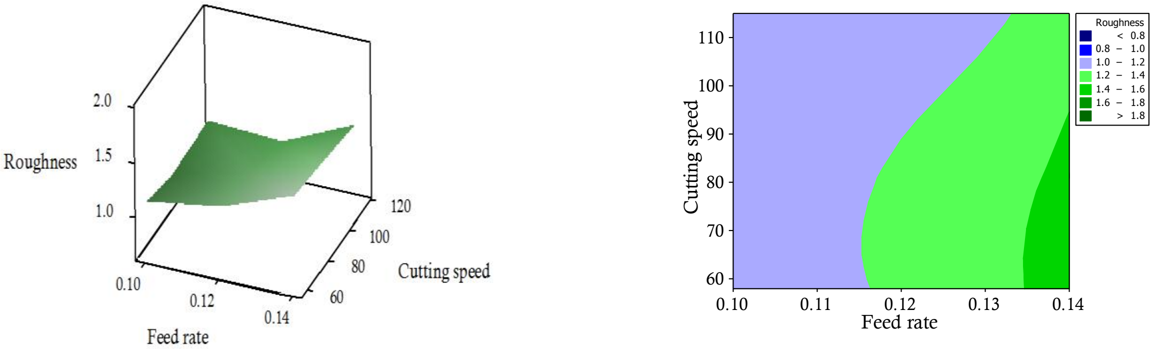

(a) 3D surface plot of surface roughness

(b) Contour plot of surface roughness.

FIGURE 3. 3D response surface plot of roughness versus cutting speed and feed rate.

CONCLUSIONS

The full factorial analysis was used to determine the effects of cutting tool, machining environment, cutting speed and feed rate in hard turning of AISI 1060 steel. The experimental results were analyzed by ANOVA. The followings are the findings drawn from the experiment and the subsequent analysis:

- The performed design of experiment involved the quantitative and qualitative factors and their effects on surface roughness. The ANOVA analysis supported the findings of full factorial analysis with sufficient statistical significance.
- The full factorial analysis shows that the environment is the most significant factor followed by feed rate and tool configuration. The high pressure coolant application reduces surface roughness with sufficient statistical significance.
- Trade-off between cutting speed and feed rate provides better surface finish i.e. lower feed and higher cutting speed tend to reduce surface roughness.

REFERENCES

1. Y. Huang, Y. K. Chou, and S. Y. Liang, International Journal of Advanced Manufacturing Technology, **443-453**, 35 (2007).
2. A. Agrawal, S. Goel, W. B. Rashid, and M. Price, Applied Soft Computing, **279-286**, 30 (2015).
3. M. Azam, M. Jahanzaib, A. Wasim, and S. Hussain, International Journal of Advanced Manufacturing Technology, **1031-1041**, 78 (2014).
4. A. Pal, S. Choudhury, and S. Chinchanikar, Procedia Materials Science, **80-91**, 6 (2014).
5. Z. Hessainia, A. Belbah, M. A. Yallese, T. Mabrouki, and J-. F. Rigal, Measurement, **1671-1681**, 46 (2013).
6. H. Aouici, M. A. Yallese, K. Chaoui, T. Mabrouki, and J-. F. Rigal, Measurement, **344-353**, 45 (2012).
7. G. Bartarya, and S. K. Choudhury, Proceedings of the Institution of Mechanical Engineers, Part B: Journal of Engineering Manufacture, **1068-1080**, 228 (2014).
8. T. Özel, T.-K. Hsu, and E. Zeren, International Journal of Advanced Manufacturing Technology, **262-269**, 25 (2005).
9. K. Bouacha, M. A. Yallese, T. Mabrouki, and J-. F. Rigal, International Journal of Refractory Metals and Hard Materials, **349-361**, 28 (2010).
10. Y. Sahin, and A. Motorcu, International Journal of Refractory Metals and Hard Materials, **84-90**, 26 (2008).
11. D. Lalwani, N. Mehta, and P. Jain, Journal of Materials Processing Technology, **167-179**, 206 (2008).
12. C. Courbon, D. Kramar, P. Krajnik, F. Pusavec, J. Rech, and J. Kopac., International Journal of Macchine Tools and Manufacture, **1114-1125**, 49 (2009).

International Conference on Mechanical Engineering 2015
(ICME 2015) 18 – 20 December, 2015, Dhaka, Bangladesh

Paper ID : 351

Optimization of Biodiesel Production from Non-Edible Pithraj Oil

Anjan Deb[1, a)], M.S. Hasan[1, b)], S.H. Chowdhury[1, c)], M. Jahangir Alam[1, d)],
Jannatul Rumky[2, e)] and Maksudur R. Khan[2, 3, f)]

[1]*Department of Chemical Engineering, Jessore University of Science & Technology, Jessore-7408, Bangladesh*
[2]*Department of Chemical Engineering & Polymer Science, Shahjalal University of Science & Technology, Sylhet-3114, Bangladesh*
[3]*Faculty of Chemical and Natural Resources Engineering, University Malaysia Pahang, 26300 Gambang, Kuantan, Pahang, Malaysia*

[a)]Corresponding author: deb_ce@yahoo.com; [b)]shuvo100519@gmail.com; [c)]shaonche10@gmail.com;
[d)]jahangirche@gmail.com; [e)]rumkyjannat@gmail.com; [f)]mrkhancep@yahoo.com

Abstract. Current research focuses the optimization of biodiesel production from non-edible pithraj oil (Aphanamixis Polystachya) using response surface methodology (RSM). Pithraj oil was extracted from the seed by mechanical press method and maximum oil content was found as 33.3%. FFA content of the oil was found as 13.8% that restricts the widely used base catalyzed transesterification method for biodiesel production. To make the oil suitable for base catalyzed transesterification; pretreatment of crude oil was carried out to reduce the FFA content by acid catalyzed esterification. Acid catalyzed esterification was conducted at 65°C with a catalyst (sulfuric acid) concentration of 15 wt% of FFA. Optimum FFA to methanol molar ratio was found as 1:30. After esterification the FFA content of the oil reduces to 1.8% and then base catalyzed transesterification was applied to produce biodiesel. Various reaction parameters such as oil to methanol molar ratio, catalyst concentration, reaction time and temperature were optimized using response surface methodology. ^{1}H NMR of crude pithraj oil and pithraj biodiesel was studied and analyzed that confirms the complete conversion of pithraj oil to biodiesel. Finally the biodiesel, produced at optimum condition, was characterized under various standard method and found comparable with petro-diesel and biodiesel standard.

INTRODUCTION

The rising population, rapid economic growth and industrialization have incessantly increased the demand of energy in developing countries like Bangladesh. The current demand of energy in Bangladesh is mostly met from non-renewable sources such as natural gas and coal[1]. Since these sources are non-renewable in nature, the reserve will be depleted one day. In addition, burning of these fossil fuels has serious detrimental environmental consequences. For this reason scientists are focusing their view on the alternative renewable energy resources that is technically feasible, economically competitive, environmentally acceptable and readily available[2]. In this context, biodiesel is gaining more and more importance as an attractive fuel due to its renewable and biodegradable nature and low emission profiles as compared to petroleum diesel[3, 4].

Biodiesel is a mono alkyl ester of long chain fatty acids produced from vegetable oils or animal fats. In other words, when a vegetable oil or animal fat chemically reacts with an alcohol, it can produce Fatty Acid Methyl Ester (FAME)[5]. Commercial production of methyl ester first began in Europe in 1990. More than 2.7 million tones biodiesel was produced in Europe in 2003, but their target is around 20% total diesel market in 2020. In addition, the USA future plan for biodiesel production is around 3.3 million tons in 2016[6].

Depending upon the climate and soil conditions, different countries are looking for different types of vegetable oils as substitutes for diesel fuels. For example, soyabean oil in the US, rapeseed and sunflower oils in Europe, palm oil in South-east Asia (mainly Malaysia and Indonesia) and coconut oil in the Philippines are being considered[7].

Currently, most of the biodiesel is produced from edible oils which are easily available on large scale from the agricultural industry. However, continuous and large-scale production of biodiesel from edible oils has recently been of great concern because they compete with food materials – the food versus fuel dispute[8]. Many researchers have recommended that non-edible vegetable oils such as Pongamia pinnata (karanja)[9], Maduca indica (mahua)[10], Hevea brasiliensis (rubber seed)[7], Jatropha curcas (Jatropha)[11] and Aphanamixis Polystachya (Pithraj)[12] have high potential for biodiesel production.

Recently, Ferdous et al.[13] studied the production of biodiesel from Pithraj oil which had FFA content of 7.5%. Higher FFA content of the crude oil restricts the widely accepted base catalyzed transesterification method for biodiesel production. However, Pretreatment of the crude oil was carried out by acid catalyzed esterification. Esterified oil was then subjected to base catalyzed transesterification for the complete conversion of triglyceride to fatty acid methyl ester.

In the present study an attempt was made to optimize the production of biodiesel from esterified oil using Response Surface Methodology (RSM). RSM is a collection of statistical and mathematical techniques that has been using for optimizing processes in which a response of interest is influenced by several process variables[14, 15]. Analyzing the effect of all independent variables and their interactions a model was developed to find out the optimum conditions. Finally various properties of biodiesel produced at optimum condition were measured and compared with biodiesel standard and pertodiesel.

MATERIALS AND METHODS

Chemicals

Methanol (99-100%), ethanol (99-100%), sodium hydroxide pellets (96%), potassium hydroxide pellets (>84%), phenolphthalein (pH 8.2 - 9.8), starch, acetone (99%), n-Hexane(96%), hydrochloric acid (37%), isopropanol, iodine, sodium iodide, glacial acetic acid, bromine, carbon tetrachloride etc. were purchased from Merck, Germany. All the chemicals used were analytical reagent grade.

Extraction of Oil

Pithraj seeds were collected from the local forests in Bangladesh. Oil from the seed was extracted by mechanical press extraction method. A vertical, manual operated, cylindrical (4.3 cm ID) mechanical press was constructed which have a spiral screw that conveys the mass from the hoper to pressure raising area. Slow and continuous rotation of the press allows raising sufficient pressure for the extraction of oil. After oil extraction it was filtered and stored at room temperature for further use.

Preparation of Biodiesel

Biodiesel was prepared from pithraj oil by base catalyzed transesterification. Before that crude pithraj oil was esterified to reduce the FFA content below 2wt%. Esterification was carried out at 65°C and atmospheric pressure. Typically, 100 ml oil was taken in a three necked 500 ml round bottomed flask equipped with a reflux condenser. The flask was placed on an electric heater with a temperature controller and magnetic stirrer. Sulfuric acid (15 wt% of FFA) was mixed with required amount of methanol and transferred into the reaction medium. The reaction continued until the FFA of oil reduces below 2%. After that the reaction contents were cooled to room temperature and reaction product was washed with hot water until clear water found. The organic phase was collected and dried under vacuum at 100°C for 30 min. The dried sample (50 ml) was then put into a three-necked 500 ml round bottomed flask, equipped with a reflux condenser, for base catalyzed transesterification. Sodium hydroxide pellets were mixed with required amount of methanol. The flask was placed on an electric heater with a temperature controller and magnetic stirrer. The transesterification reaction was performed under vigorous stirring at 60°C. After a certain period reaction was stopped by adding stoichiometric amount of HCl. Then contents were cooled to room temperature and reaction product was washed with hot water until clear water found. The organic phase (biodiesel) was collected and dried under vacuum at 100°C for half an hour and stored for characterization.

Experimental Design for Optimization

There are four factors (FFA to methanol molar ratio, catalyst concentration, temperature and reaction time) that affect the transesterification reaction to produce biodiesel from esterified oil. In order to study the effect of all variables on the yield of Biodiesel, 2^{4-1} factorial experimentations were carried out in two levels. The real and coded values of these variables are presented in table 1:

TABLE 1. Factors and levels of independent variables used in the experimental design

Factors	**Code**	**Low (-1)**	**High (+1)**
Methanol molar ratio	X_1	3	6
Catalyst concentration	X_2	0.5	1
Temperature (°C)	X_3	40	60
Time (min)	X_4	30	60

This fractional factorial design results in eight experimental points and all experiments were conducted in triplicate to reduce variability in the data collection, are presented in table 3. The complete regression equation that describes the contribution of all the factors on the biodiesel production is as follows:

$$Y = b_o + b_1X_1 + b_2X_2 + b_3X_3 + b_4X_4 + b_{12}X_{12} + b_{13}X_{13} + b_{23}X_{23}$$

Where Y is the response (yield of biodiesel) and X_i values (i = 1, 2, 3, 4) indicate the corresponding parameters in their coded forms. Estimation of the regression coefficients that caused the model to best fit a set of collected response variable data was carried out by the least squares method. A reduced regression model, which involved only the significant variables, was produced after examining the significance of each individual regression coefficient by Student's t-test at 5% significance level. ANOVA evaluates the significance of regression by determining if there is a relationship between the response variable and a subset of the regressor variables via the Fisher's statistical test (F-test)[16]. All analysis was performed with the Minitab software (Minitab Statistical Software, Release 15 for Windows, State College, Pennsylvania).

Analytical Methods for Oil and Biodiesel

FFA content in the oil and biodiesel samples was analyzed by the method described in AOCS Aa 6-38[17]. Saponification value (SV) was determined by standard method[18]. Typically, 1 g sample was taken with 25 mL alcoholic KOH solution, heated for 1 h in a steam bath with occasional shaking and titrated the excess KOH with the 0.5 M hydrochloric acid solution.

Physical properties such as moisture content, density and calorific value of the oil were determined by following ASTM D 1744 (Karl Fisher method), ASTM D 1480/81 and ASTM D 240 respectively. Viscosity, flash point, pour point and cloud point were determined by standards ASTM D 445, ASTM D 93 (Pensky–Martens Flashpoint Apparatus, Lazer Scientific Inc., Germany), ASTM D 2500, and ASTM D 97 respectively.

^{1}H nuclear magnetic resonance (NMR) spectra were recorded at 293 K on a 400 MHz spectrometer (Burker Biospin DPX-400, Fallean, Switzerland), with chemical shifts being referenced to the residual peaks of $CHCl_3$ in $CDCl_3$ (in parts per million).

RESULT AND DISCUSSION

Characterization of Crude Oil

TABLE 2. Properties of crude pithraj oil

Property name	**Value**
Color	Dark green
Specific gravity @ 25°C	0.92
Viscosity (mm^2/s) @ 25°C	79.69
FFA Content, wt%	13.8
Saponification value (mg KOH/gm oil)	248.2
Average molecular weight*	870.5

* Molecular weight was determined from the composition of the oil[12]

Oil was extracted from the seed by mechanical press method and the oil content of the seed was found as 33.3% (vol. /wt). Extracted oil was filtered and stored at room temperature for further use. Characterization of the crude oil was carried out under standard methods and the results are represented in table 2.

Pretreatment of Crude Oil

The most important factor that limits the direct transesterification of crude vegetable oil is the FFA content of the oil. To overcome this problem acid catalyzed esterification was conducted. In that case alcohol reacts with FFA of the oil in presence of an acid catalyst and produce ester with water; where water inhibits the transesterification of glycerides[19]. Two important factors that persuade the esterification reaction are FFA to methanol molar ratio and the concentration of acid catalyst. Figure 1 represents the effect of methanol molar ratio on esterification reaction. All the reaction was carried out at 15wt% catalyst concentration at a temperature of 60°C for 60 min. from this figure it is clear that FFA content reduces below 2wt% at 1:30 FFA to methanol molar ratio. Further increase in the amount of methanol has no significant effect on FFA reduction.

Figure 2 represents the effect of catalyst concentration on esterification reaction. From this figure it is seen that 15wt% of catalyst is optimum for the reduction of FFA below 2wt% within 45 min. All the oil was then esterified at 1:30 oil to methanol molar ratio and 15wt% of catalyst concentration at 60°C for one hour to ensure the reduction of FFA below 2wt%.

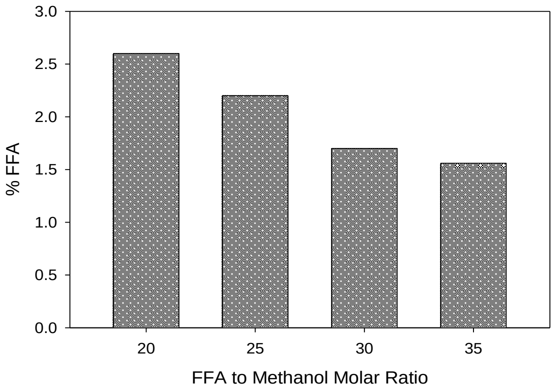

FIGURE 1. Effect of FFA to Methanol molar ratio on esterification reaction

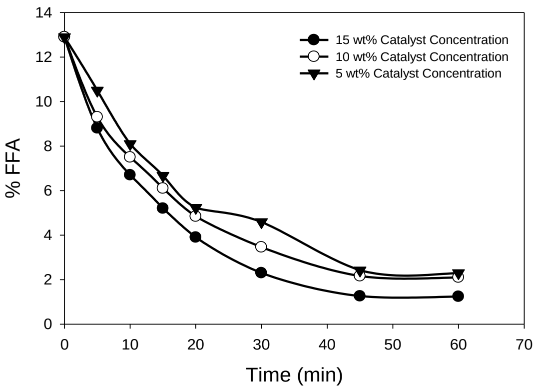

FIGURE 2. effect of catalyst concentration on esterification reaction

Preparation of Biodiesel from PO

Biodiesel was prepared from the esterified oil by base catalyzed transesterification. There are four major reaction parameters that affect the transesterification reaction named oil to methanol molar ratio, catalyst concentration, reaction time and temperature. All the parameters were optimized and the results are presented below.

Effect of Methanol Molar Ratio

The methanol/ oil molar ratio is one of the important variables that affect the yield of biodiesel. From the reaction stoichiometry it is evident that 3 mole methanol is required for 1mole of oil to convert biodiesel. Since the reaction is reversible, the excess amount of alcohol is used in order to shift the reaction equilibrium, to avoid the reverse reactions and to accelerate the process. The reaction was carried out at three different FFA to methanol molar ratio with a catalyst concentration of 1wt% of oil at 60°C for 1 hour and the results are represented in figure 3. From figure 3 it was observed that, the yield of biodiesel increases as the molar ratio of methanol/oil increases.

Effect of Catalyst Concentration

Figure 4 represents the effect of catalyst (NaOH) concentration on the yield of biodiesel. Generally, catalyst enhances the rate of a reaction by reducing the activation energy. To investigate the effect of catalyst concentration transesterification reaction was carried out at four different amount of catalyst. All the reactions were conducted at 1/6 oil to methanol molar ratio at 60°C for 30 minute. Best result was obtained at a catalyst concentration of 1wt% of oil. Further increase in the concentration of catalyst reduces the yield of biodiesel due to loss for soap formation during washing.

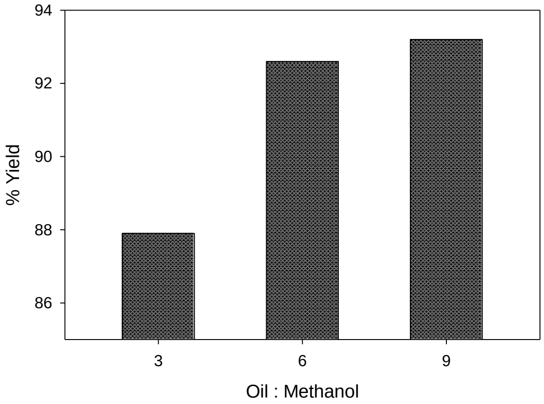

FIGURE 3. Effect of methanol molar ratio on transesterification reaction

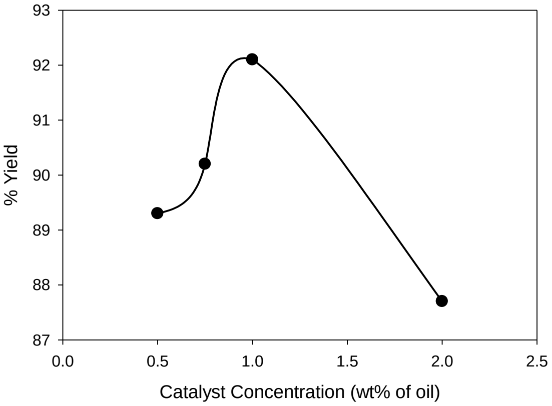

FIGURE 4. Effect of catalyst concentration on transesterification

Optimization Study of PO Biodiesel

Optimization study was carried out by the factorial design of the experiment. The fractional factorial design is the simplified form of full factorial design that is used to reduce the number of experiments when there are many factors included in the study[20]. Eight sets of experiment were run to investigate the effect of all independent variables and their interactions and the results are shown in table 3. All experiments were conducted in triplicate to reduce variability in the data collection.

TABLE 3. Experimental design and result of experiment

Run	X_1	X_2	X_3	X_4	% FFA conversion			
					Y_1	Y_2	Y_3	Y_{avg}
1	-1	-1	-1	-1	85.8	86.6	87.1	86.5
2	+1	-1	-1	+1	88.7	89.7	89.2	89.2
3	-1	+1	-1	+1	87.5	88.3	87.2	87.7
4	+1	+1	-1	-1	90.7	90.5	91.2	90.8
5	-1	-1	+1	+1	87.2	87.1	87.5	87.3
6	+1	-1	+1	-1	90.2	89.5	89.7	89.8
7	-1	+1	+1	-1	88.4	88.6	87.5	88.2
8	+1	+1	+1	+1	93.0	92.5	92.2	92.6

Table 4 represents the estimated effects and regression coefficients, along with the corresponding standard deviation and t-statistics (T) values for the main effects and second-order interaction terms. The main regression equation, after putting values of all coefficients, is as follows:

$$Y = 88.99 + 1.59X_1 + 0.08X_2 + 0.45X_3 + 0.18X_4 + 0.29X_1X_2 + 0.14X_1X_3 + 0.11X_1X_4 \cdots\cdots(1)$$

TABLE 4. Estimated effects and coefficients of the regression model

Term	Effect	Coefficient	SD_{Coefficient}	T-Value
Constant		88.9958	0.0972	915.76
Molar Ratio	3.1917	1.5958	0.0972	16.42
Catalyst Concentration	1.6083	0.8042	0.0972	8.27
Temp	0.9083	0.4542	0.0972	4.67
Time	0.3583	0.1792	0.0972	1.84
Molar Ratio*Cat. Conc.	0.5750	0.2875	0.0972	2.96
Molar Ratio*Temp	0.2750	0.1375	0.0972	1.41
Molar Ratio*Time	0.2250	0.1125	0.0972	1.16

The estimations of main effects of the variables, together with their interaction terms, are shown on a Pareto chart (Fig.5). The vertical line in the Pareto chart specifies the minimum statistically significant magnitude of effect for 5% significance level, while the horizontal column lengths are proportional to the degree of significance for each effect. Any effect or interaction that exceeds the vertical line is considered significant. From this analysis, it was found that the insignificant parameters are the D, AC and AD interaction. After neglecting the insignificant terms at 5% significance level, a reduced model of Eq. (1) was produced:

$$Y = 88.99 + 1.59X_1 + 0.08X_2 + 0.45X_3 + 0.29X_1X_2 \cdots\cdots\cdots (2)$$

In Eq. (2), the size of regression coefficients denotes the degree of significance of each independent variable on Yield of Biodiesel.

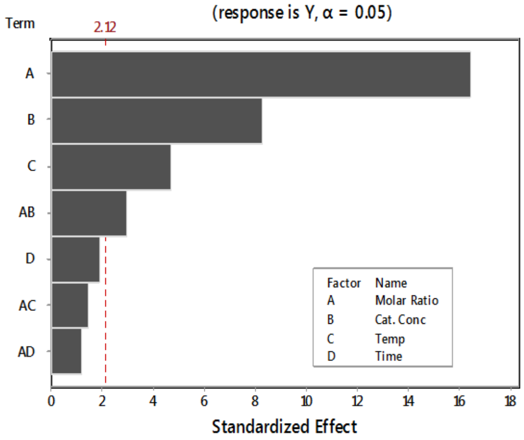

FIGURE 5. Pareto chart of the standardized effect

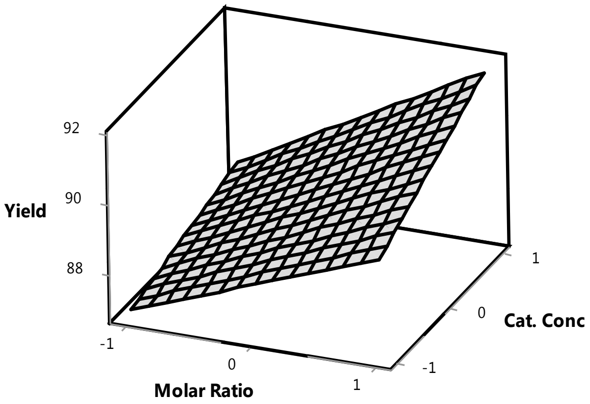

FIGURE 6. Interaction plot of significant parameters

TABLE 5. Analysis of variance (ANOVA)

Source	DF	Sum of squares	Mean square	F-value	P-value
Model	7	85.10	12.16	53.64	0.00
X1	1	61.12	61.12	269.65	0.00
X2	1	15.52	15.52	68.47	0.00
X3	1	4.95	4.95	21.84	0.00
X4	1	0.77	0.77	3.40	0.08
X1X2	1	1.98	1.98	8.75	0.01
X1X3	1	0.45	0.45	2.00	0.18
X1X4	1	0.30	0.30	1.34	0.26
Pure Error	16	3.63	0.23		
Cor. Total	23	88.73			

R^2 = 95.91%, Adjusted R^2 = 94.12%, Predicted R^2 = 90.80%, DF = Degree of freedom

The adequacy of fit of the reduced regression model for %Yield (Eq. (2)) was analyzed by ANOVA at 5% significance level (Table 5). From Table 5, the high F and low P values of the main effects and the two-way interactions suggest that they contribute significantly to the response (%Yield). The R^2 value of the model obtained is 95.91% (Table 5). This denotes that only 4.09% of the total variability is not explained by the regressor in the model. The small difference between the R^2 and R^2 (adj) values, that is 1.79%, implies that there is a least chance that insignificant terms have been included in the model[16]. Hence, the reduced model (Eq. (2)) can be used as a predictive tool to obtain %Yield of Biodiesel over the entire uncertainty range of the studied variables. The response surface corresponding to the regression equation (Fig. 6) indicates that for maximum catalyst concentration a high yield of biodiesel is obtained for higher molar ratio.

Characterization of Biodiesel

^{1}NMR Study:

^{1}H NMR spectroscopy was studied to investigate the presence of triglyceride (TG) backbone and methyl ester in the oil and biodiesel sample and its spectrum is shown in Fig.7. Glyceridic protons of triglycerides are assigned in the range of 4–4.5 ppm[7]. From the spectrum of raw oil it is seen that two distinct peaks are available in that region but in the biodiesel spectrum it is totally absent. In addition the characteristic peak of methoxy protons was observed at 3.62 ppm and peaks of α-CH_2 protons at 2.26 ppm in the biodiesel sample. These two peaks are the distinct peaks for the confirmation of methyl esters present in biodiesel.

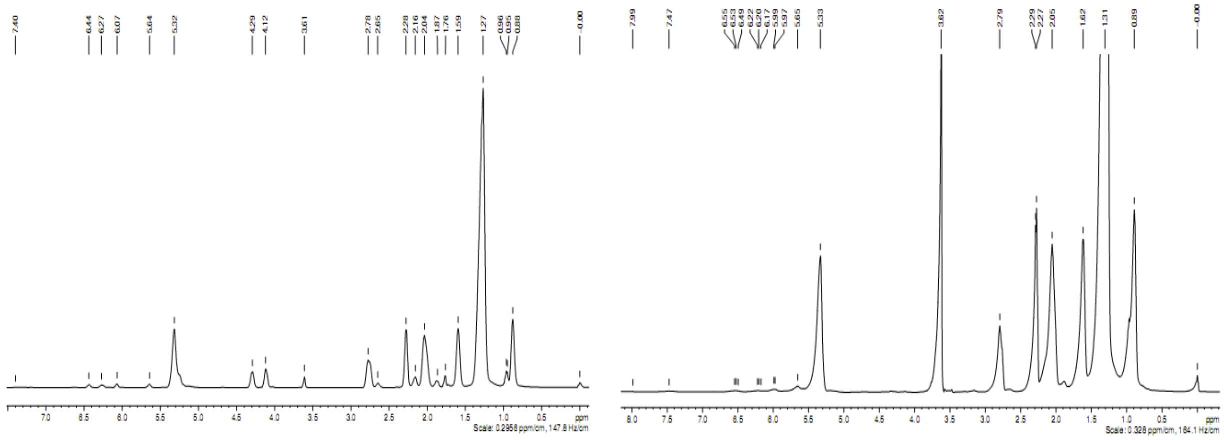

(a) (b)

FIGURE 7. ^{1}NMR of (a) Crude Pithraj Oil and (b) POME

Properties of biodiesel

Biodiesel produced at optimum conditions are subjected to characterization for comparison with biodiesel standard and petro-diesel standards and are presented in Table 6. Most of the physicochemical properties of Pithraj oil methyl ester are comparable to those of biodiesel standard and petro-diesel[19].

CONCLUSION

Biodiesel was prepared from non-edible pithraj oil by base catalyzed transesterification. Due to high FFA content of the crude oil it was first subjected to acid catalyzed esterification to reduce the FFA content suitable for base catalyzed transesterification. Optimization of the transesterification reaction was studied using response surface methodology and a regression equation was developed for biodiesel yield from pithraj oil. ^{1}H NMR study confirms the removal of TG backbone and the presence of methyl ester in the biodiesel. This product can be successfully used as diesel in diesel engine.

TABLE 6. Properties of biodiesel

Property	POME	Biodiesel Standards	Petro-Diesel Standards
Color	Reddish	-	-
Specific Gravity @ 15.5°C	0.89	0.88	0.85
FFA content (wt %)	0.78	0.80 (max)	-
Kinematic Viscosity (mm^2/s) @ 40°C	4.2	1.9 – 6.0	1.3 - 4.1
Flash Point (°C)	150	130 (min)	60 - 80
Cloud Point (°C)	3	Not Specified	-15 to 5
Sulfur Content	Nil	0.05% w/w (max)	-
Saponification value (mg KOH/gm Oil)	212.2	-	-
Iodine value	74.5	-	-
Cetane Index	55.3	47 (min)	-

ACKNOWLEDGMENTS

The authors acknowledge the Ministry of Science and Technology for financial support (Project No: 39.012.002.02.01.017.2014/R&D 57/131).

REFERENCES

1. M. Z. Baten, E. M. Amin, A. Sharin, R. Islam and S. Chowdhury, presented at the Developments in Renewable Energy Technology (ICDRET), 2009 1st International Conference on the, 2009 (unpublished).
2. L. Meher, D. V. Sagar and S. Naik, Renewable and sustainable energy reviews **10** (3), 248-268 (2006).
3. A. Ashraful, H. Masjuki, M. Kalam, I. R. Fattah, S. Imtenan, S. Shahir and H. Mobarak, Energy Conversion and Management **80**, 202-228 (2014).
4. F. Ma and M. A. Hanna, Bioresource technology **70** (1), 1-15 (1999).
5. C. Öner and Ş. Altun, Applied Energy **86** (10), 2114-2120 (2009).
6. A. Talebian-Kiakalaieh, N. A. S. Amin and H. Mazaheri, Applied Energy **104**, 683-710 (2013).
7. M. Morshed, K. Ferdous, M. R. Khan, M. Mazumder, M. Islam and M. T. Uddin, Fuel **90** (10), 2981-2986 (2011).
8. A. Atabani, I. A. Badruddin, A. Badarudin, M. Khayoon and S. Triwahyono, Renewable and Sustainable Energy Reviews **37**, 840-851 (2014).
9. M. N. Nabi, S. N. Hoque and M. S. Akhter, Fuel Processing Technology **90** (9), 1080-1086 (2009).
10. S. V. Ghadge and H. Raheman, Biomass and Bioenergy **28** (6), 601-605 (2005).
11. H. J. Berchmans and S. Hirata, Bioresource technology **99** (6), 1716-1721 (2008).
12. S. Palash, H. Masjuki, M. Kalam, A. Atabani, I. R. Fattah and A. Sanjid, Energy Conversion and Management **91**, 149-157 (2015).
13. K. Ferdous, A. Deb, J. Ferdous, M. R. Uddin, M. R. Khan and M. Islam, Journal of Chemical Engineering **28** (1), 45-49 (2014).
14. D. Baş and İ. H. Boyacı, Journal of Food Engineering **78** (3), 836-845 (2007).
15. M. A. Bezerra, R. E. Santelli, E. P. Oliveira, L. S. Villar and L. A. Escaleira, Talanta **76** (5), 965-977 (2008).
16. R. H. Myers, D. C. Montgomery and C. M. Anderson-Cook, *Response surface methodology: process and product optimization using designed experiments*. (John Wiley & Sons, 2009).
17. *Official Methods and Recommended Practices of the American Oil Chemists' Society*, 5 th ed. (Champaign: AOCS Press, 1998).
18. J. B. G.H. Jeffery, J. Mendham, R.C. Denney, *Vogel's Textbook of Quantitative Chemical Analysis*, 5th ed. (Longman Scientific & Technical, UK, England, 1989).
19. Y. Sharma, B. Singh and S. Upadhyay, Fuel **87** (12), 2355-2373 (2008).
20. K. Hinkelmann and O. Kempthorne, *Design and Analysis of Experiments, Special Designs and Applications*. (John Wiley & Sons, 2012).

International Conference on Mechanical Engineering 2015
(ICME 2015) 18 – 20 December, 2015, Dhaka, Bangladesh

Paper ID : 366

Effects of Cutting Parameters and Flow Rate on Cutting Force and Surface Roughness in Surface Milling of Hardened AISI 4140 Steel

Mahmood Al Bashir[1, a)], Mozammel Mia[1] and Nikhil Ranjan Dhar[2, b)]

[1]*Mechanical and Production Engineering, Ahsanullah University of Science and Technology, Dhaka 1208, Bangladesh*
[2]*Industrial and Production Engineering, Bangladesh University of Engineering and Technology, Dhaka 1000, Bangladesh*

[a)]Corresponding author: shoishobtheone@gmail.com
[b)]nrdhar@ipe.buet.ac.bd

Abstract. The present research article analyses the effect of cutting parameters and flow rate of pulsed jet minimum quantity lubricant on the two most important machining responses, cutting force and surface roughness. During the time of experiment and subsequent analysis; the depth of cut, material and its hardness, tool sharpness and machine vibration are assumed constant. The investigated material for this surface milling operation is AISI 4140 steel, heat treated to get a hardness of 40 HRC, whereas, the cutting tool is four flute end mill cutter made of carbide material. The pulsed-MQL system was used to direct the lubricant spray towards the tool-workpiece contact point for lubrication in addition to cooling purpose. Design of experiment was employed with three factors (cutting speed, table feed rate, pulse flow rate), each of which are of three levels (low-medium-high) to determine the number of experimental runs. Two different responses, cutting force and surface roughness, were considered for a full factorial analysis which has been performed to examine the effect of main factors as well as interaction effect of factors on the responses. Analysis of variance was employed to determine the acceptability of the full factorial analysis and its statistical significance. The result of this analysis reveals that the feed rate has the highest impact, on both cutting force and surface roughness, followed by cutting speed, whereas, the pulse jet flow rate has a very insignificant effect.

INTRODUCTION

The use of cutting fluid has been a common practice in manufacturing industries to reduce the heat, facilitate chip removal and lubrication process. But the use of coolants is restricted due to the probable health hazard [1], environmental issues and high cost. An alternate approach, to reduce the usage of cutting fluid, is the application of cutting fluid as minimum as possible.

Minimum quantity lubrication (MQL) presents itself as a viable alternative for hard machining with respect to tool wear, heat dissertation and machined surface quality. Using this technology, a little amount of environmentally compatible fluid [2], when properly selected and applied, can make a substantial difference in the effectiveness of tool performance. In MQL, lubrication is obtained via the lubricant while a minimum cooling action is achieved by the pressurized air that reaches the tool/work interface. Further, MQL reduces induced thermal shock and helps to increase the workpiece surface integrity in situations of high tool pressure [3]. Varadarajan et al. [4] have introduced a new MQL application technique which overcomes the problems caused by mist. In this method, small quantities of cutting fluid were applied in the form of high velocity, narrow, pulsed jet.

Yan et al. [5] investigated the significance of the MQL injection parameters on the milling of 50CrMnMo steel. The increase in air flow rate led to a reduction in tool wear, reportedly due to better chip removal and the improved penetration of the flow to the cutting zone. Hwang et al. [6] evaluated the machinability of Aluminum in milling using MQL and flood. ANOVA analysis showed that the cutting forces were largely dependent on the cutting parameters, as opposed to the mode of lubrication, whereas, the surface roughness values were dependent on all the cutting conditions.

To attain a better surface finish of the milled components the optimal machining parameters and tool geometry are to be selected. Suresh et al. [7] developed a response surface model for surface roughness in terms of speed, feed, depth of cut and nose radius and optimized using the genetic algorithm. Oktem et al. [8] developed a mathematical model for surface roughness using feed rate, cutting speed, axial depth of cut, radial depth of cut and machining tolerance. Other studies showed, surface roughness is mostly influenced by cutting speed [9], feed rate and nose radius [10] and the cutting force is impacted largely by feed rate [11].

Most of the literature review presented here emphasised on finding the relationship of cutting velocity, feed rate and depth of cut with the surface roughness and cutting force under flood cooling and dry milling condition. MQL flow rate also affects the surface roughness and cutting force of the machined material, which is attained in a few pieces of research. The objective of this study is to obtain the effect on cutting speed, feed rate and MQL flow rate on surface roughness and cutting force in milling of AISI 4140 steel. The design of experiment and statistical analysis by ANOVA is performed to determine which parameters are significant along with prominent interactions on two machining responses i.e. cutting force and surface roughness.

MACHINE, MATERIAL AND METHOD

AISI 4140 has many applications such as forgings for the aerospace and oil and gas industries, along with myriad uses in the automotive, agricultural and defence industries. The AISI 4140 used in the research was a plate of 200 mm length, 100 mm width and 40 mm thickness. AISI 4140 was heated using an electric furnace to attain preferred hardness level. It took three hours to raise the temperature to 900°C and the material was kept at the heating chamber for one and a half hour. For quenching the material, a tank of 600-liter capacity was used. To relieve the internal stresses and reduce brittleness, tempering was done by heating the workpiece to 300^0C, holding it at that temperature for two hours, and then cooling it, in the natural air.

A four flute end mill cutter, with 12 mm diameter and 30º helix angle, was used. The machining test has been carried out by milling of hardened steel in a column and knee type vertical milling machine by four flute carbide milling cutter at different cutting velocities and feeds under dry and MQL cutting condition. The conditions under which the machining tests have been carried out are briefly given in Table-1. Cutting force was measured using a dynamometer. It consists of a load cell type dynamometer with charge amplifier. The surface roughness of the machined surface after each operation was measured by a Talysurf roughness checker (Surtronic 3^+, Rank Hobson, UK) using a sampling length of 0.8 mm. The experimental arrangement, a milling machine connected with pulse jet minimal quantity lubricant applicator, is shown in Fig. 1.

TABLE 1. Experimental conditions

Machine Tool : Vertical Knee and Column type Milling Machine, China
Work Materials : AISI-4140 Hardened steel (dimension: 200x100x40 mm)
Hardness : 40 HRC
Cutting Tool : Carbide End Milling Cutter (Ø12 mm)
Cutting Fluid : VG 68 Straight cut cutting oil
Environment : Dry and MQL

TABLE 2. Independent factors and their levels

Symbol	Factors	Level 1	Level 2	Level 3
V_c	Cutting Speed (m/min)	12	22	32
S_0	Feed Rate (mm/min)	22	44	68
Q	MQL Flow rate (ml/hr)	50	100	150

The selection of the cutting speed and feed rate combination was chosen as per the industrial practice and requirements. The selection of the independent factors and allocation of levels are shown in Table-2. Three quantitative factors are attributed into three levels (low-medium-high) to investigate the effects.

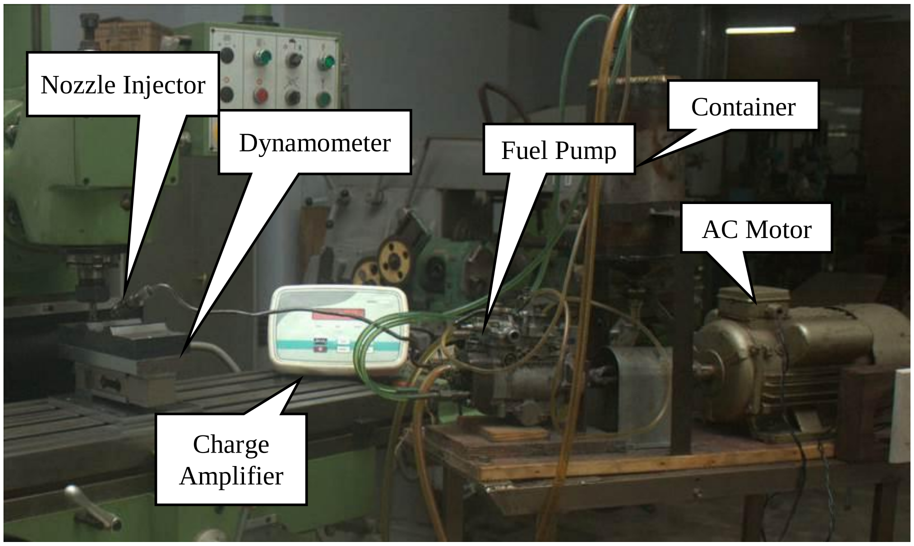

FIGURE 1. Photographic view of the machining set-up with pulse jet applicator.

FULL FACTORIAL ANALYSIS

The design of experiment is a systematic approach in arranging the possible combinations during any machining process to find out the responses in an organized manner. The analysis that is performed here is based on three 3-level factors, attaining a total of $3^3 = 27$ sets of machining conditions and responses as shown in Table-3.

The full factorial analysis composed of determining the main and/or interaction effect of independent parameters on the dependent parameter(s). In this article, a full factorial analysis was conducted to examine the effect of cutting speed, feed rate and MQL flow rate in respect of cutting force and surface finish of the produced parts. The outcome of the full factorial analysis is supported by statistical intervention.

TABLE 3. Machining conditions and response

Ex. no.	V_c	S_o	Q	F	R_a	Ex. no.	V_c	S_o	Q	F	R_a
1	12	22	50	12.0	1.38	15	16	34	100	13.2	1.39
2	12	22	75	10.4	1.29	16	16	44	50	17	1.47
3	12	22	100	11.6	1.37	17	16	44	75	13.8	1.38
4	12	34	50	15.8	1.52	18	16	44	100	15.5	1.46
5	12	34	75	12.5	1.43	19	22	22	50	9.2	1.21
6	12	34	100	14	1.52	20	22	22	75	8.2	1.12
7	12	44	50	19	1.61	21	22	22	100	9.2	1.19
8	12	44	75	15	1.52	22	22	34	50	12.2	1.38
9	12	44	100	16.8	1.61	23	22	34	75	10.5	1.29
10	16	22	50	10.8	1.31	24	22	34	100	11.8	1.37
11	16	22	75	9.8	1.22	25	22	44	50	15	1.41
12	16	22	100	11	1.3	26	22	44	75	12.1	1.32
13	16	34	50	13.8	1.4	27	22	44	100	13.6	1.4
14	16	34	75	11.8	1.31						

RESULTS AND DISCUSSIONS

Effects on surface roughness and cutting force

The effects of cutting speed, table feed rate and flow rate of pulse jet lubricant, on surface roughness and cutting force, are shown in Fig. 2. The horizontal straight line in Fig. 2 represents the mean values of the responses. The change of mean surface roughness with respect to cutting speed, feed rate and flow rate is shown in Fig. 2(a), and that of cutting force is shown in Fig. 2(b).

It is visible from Fig. 2(a) that the cutting speed has negative effect on surface roughness, whereas, the feed has positive effect. The mean R_a decreases with the increase of cutting speed while mean R_a increases with increasing table feed. But, the flow rate of MQL pulse jet reveals that the mean R_a is minimal at medium flow rate (=75 ml/hr). The minimal mean surface roughness is attainable, as suggested by Fig. 2(a), at cutting speed of 22 m/min, table feed of 22 mm/min, and flow rate of 75 ml/hr.

Similar effects are, also, discernible from Fig. 2(b) for the contributions of speed, feed and flow rate on cutting force. The average value of the cutting force, corresponding to the level-2 magnitude of cutting speed and table feed, lies very close to the horizontal line, whereas, that of flow rate is situated little below the mean value. It is also exhibited that the dispersion region of mean cutting force, about the mean line, is narrow compared to that of table feed. The cutting force corresponding to the extreme values of the table feed possesses lowest and highest mean values of cutting force. The minimal cutting force is found at the highest cutting speed (=22 m/min), lowest table feed (=22 m/min) and a flow rate of 75 ml/hr.

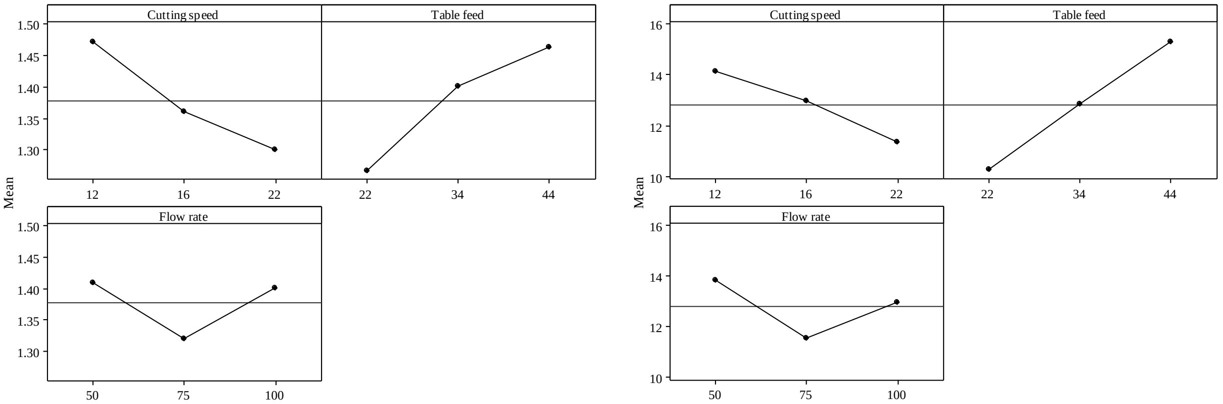

(a) Surface roughness, µm (b) Cutting force, N

FIGURE 2. Main effects plot for (a) surface roughness (b) cutting force.

Statistical analysis

The statistical analysis of the full factorial technique is performed by employing analysis of variance (ANOVA) at the significance level α=0.05 (confidence level 95%). The ANOVA for both cutting force and surface roughness is shown in Table 4. The F-value and P-value determine the statistical significance of the independent variables and of the interaction effects among the factors while the percentage contribution accounts for the effects of any factors on the response characteristics.

In case of cutting force, from the Table 4(a), it is visible that the cutting speed, table feed rate and flow rate all are statistically significant for the specified significance level ($P<0.05$). The table feed has P-value = 0.0, F-value = 2536.39 and C = 63.60%. All these three indicators make the feed rate as the statistically most significant factor when the response is cutting force. The cutting speed follows the table feed and holds the second position for being statistically significant with P-value = 0.0, F-value = 788.83 and C = 19.78%. The least significant factor is the flow rate of the pulse jet minimal lubrication.

As listed under Table 4(b), table feed rate remains the most dominant factor followed by cutting speed and flow rate. The feed rate possess a P-value = 0.0, F-value = 25087.00 and C = 49.17% which makes it the most statistically significant contributor. The cutting speed, with P-value = 0.0, F-value = 18781.00 and C = 36.95%, is the second most effective input element leaving flow rate as the least significant factor. For both cutting force and surface roughness, the percentage contribution due to error is less than 0.1% which is a clear indication that the entire important factors are accounted for and the calculation is free from high measurement errors. The table feed-flow rate interaction for cutting force and cutting speed-feed rate interaction for surface roughness are the most effective interactions with statistical significance.

Therefore, the ANOVA analysis reveals that, the table feed is the most effectual contributor for both cutting force and surface roughness. The second and third significant factors are the cutting speed and flow rate respectively. Although, the all three interactions are statistically significant to the confidence level but table feed-flow rate and cutting speed-table feed are the most effective factors for cutting force and roughness respectively.

TABLE 4. Analysis of variance

(a) For cutting force						(b) For surface roughness					
Source	DF	Seq. SS	F	P	C (%)	Source	DF	Seq. SS	F	P	C (%)
V_c	2	35.94	788.83	0.0	19.78	V_c	2	0.139	18781.00	0.0	36.95
S_o	2	115.55	2536.39	0.0	63.60	S_o	2	0.185	25087.00	0.0	49.17
Q	2	24.18	530.78	0.0	13.31	Q	2	0.044	5977.00	0.0	11.70
$V_c \times S_o$	4	0.81	8.90	0.005	0.445	$V_c \times S_o$	4	0.008	550.00	0.0	2.13
$V_c \times Q$	4	1.2	13.15	0.001	0.660	$V_c \times Q$	4	0.000104	7.00	0.010	0.027
$S_o \times Q$	4	3.83	42.0	0.0	2.106	$S_o \times Q$	4	0.000059	4.00	0.045	0.015
Error	8	0.18			0.099	Error	8	0.00003			0.008
Total	26	181.69			100	Total	26	0.376193			100

3-D contour plot

The contour plot of cutting force F versus cutting speed V_c and table feed S_0 is shown in Fig. 3(a). The different colours indicate separate regions of surface roughness for a range of cutting speed and feed rate. The lowest roughness ($R_a < 1.2\mu m$) is attainable for the cutting speed close to the highest value ($V_c > 19.6$ m/min) and the table feed close to the lowest value ($S_0 < 22$ mm/min). The worst quality surface, in terms of roughness ($R_a > 1.6\mu m$), is produced for higher table feed ($S_0 > 22$ mm/min) and lower cutting speed ($V_c < 13.6$ m/min). The mediocre surface roughness ($R_a = 1.3 – 1.4$ μm) is achieved at a strategic selection of cutting speed ranging of 12 – 22 m/min and table feed ranging from 21 – 45 mm/min.

The contour plot of cutting force F versus cutting speed V_c and table feed S_0 is illustrated in Fig. 3(b). The Fig. 3(b) reveals that the cutting force is dependent on the cutting speed and table feed, according to the different bands which are formed and displayed by different colours. The cutting force can be lower than 10 N if the cutting speed is selected from 18 m/min to 22 m/min and the table feed is maintained approximately at 21 mm/min to 27 mm/min. In contrary, the higher range of cutting force ($F > 18$ N) can be achieved with higher table feed ($S_0 > 41$ mm/min) and lower cutting speed ($V_c < 14.3$ m/min).

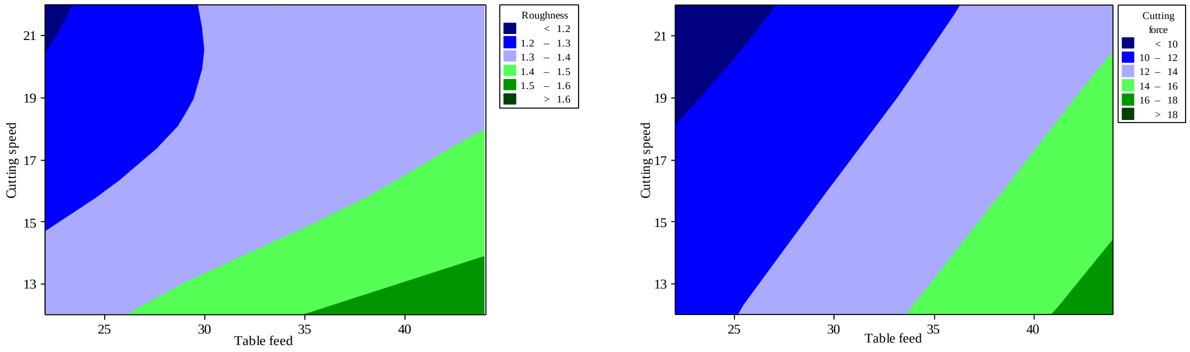

(a) Surface roughness

(b) Cutting force

FIGURE 3. Contour plot of (a) surface roughness (b) cutting force vs. cutting speed, table feed.

Hence, from the contour plot of surface roughness and cutting force (shown in Fig. 3), it is concluded that the optimal setting, for both surface roughness and cutting is lower the better for table feed and higher the better for cutting speed.

CONCLUSIONS

The effects of cutting parameter viz. cutting speed, table feed and the flow rate of the minimal quantity lubricant in the form of pulse jet application, on two responses i.e. surface roughness and cutting force, is evaluated using full factorial analysis which is supported by analysis of variance. A total of 27 experimental runs, in end milling of AISI 4140 steels, were carried out to perform the analysis. The experiment and succeeding analysis reveals the following conclusions:

- The performed end milling operation was carried out using a sophisticated pulse jet applicator by varying the flow rate of the lubricant. For each step, three data were recorded and the mean value was used for the analysis. Any unusual data was considered as outliers and excluded from further processing.
- The ANOVA supported the full factorial analysis and marked the statistical significant factors and the interactions among the factors.
- The cutting speed and feed rate has negative and positive effect on surface roughness, respectively. Pulse jet flow rate was found as the least dominant factor.
- The feed rate is the most significant factor with a contribution of 63.6% and 49.17% for cutting force and surface roughness respectively. The cutting speed, which is also statistically significant, is the second most effective factors in determining the quantity of cutting force and surface roughness with 19.78% and 36.95% contribution successively.

REFERENCES

1. Y. Ding, and S. Hong, J. of Manuf. Sci. and Eng., **76-83**, 120 (1998).
2. T. Wakabayashi, I. Inasaki, and S. Suda, Machining science and technology, **59-85**, 20 (2006).
3. A. Attanasio, M. Gelfi, C. Giardini, and C. Remino, Wear, **333-338**, 260 (2006).
4. A. Varadarajan, P. Philip, and B. Ramamoorthy, Int. J. of Mac. Tools and Manuf., **193-200**, 42 (2002).
5. L. Yan, S. Yuan, and Q. Liu, Chinese J. of Mechanical Engineering, **419-429**, 25 (2012).
6. Y.-K. Hwang, C.-M. Lee, and S.-H. Park, Int. J. of Precision Eng. and Manuf., **65-73**, 10 (2009).
7. P. Suresh, P. V. Rao, and S. Deshmukh, Int. J. of Mac. Tools and Manuf., **675-680**, 42 (2002).
8. H. Öktem, T. Erzurumlu, and H. Kurtaran, J. of Mat. Proc. Tech., **11-16**, 170 (2005).
9. B. M. Gopalsamy, B. Mondal, and S. Ghosh, J. of Sci. & Ind. Research, **686-695**, 68 (2009).
10. M. Kaladhar, K. V. Subbaiah, and C. S. Rao, Int. J. of lean thinking, **1-19**, 3 (2012).
11. A. F. Ibraheem, S. K. Shather, and K. A. Khalaf, Eng. &Tech, **11**, 26 (2008).

International Conference on Mechanical Engineering 2015
(ICME 2015) 18 – 20 December, 2015, Dhaka, Bangladesh

Paper ID : 376

Particle Mass and Gaseous Emissions from Residential Wood Stoves under Standard Laboratory Conditions

M. Obaidullah[1, a)], M. A. R. Sarkar[2], S. Bram[3] and J. De Ruyck[4]

[1]*Centre for Energy Studies, Bangladesh University of Engineering and Technology, Dhaka 1000, Bangladesh*
[2]*Department of Mech. Engg., Bangladesh University of Engineering and Technology, Dhaka 1000, Bangladesh*
[3]*Department of Mechanical Engineering, Vrije Universiteit Brussel, 1050 Brussels, Belgium*
[4]*Department of Engineering Technology, Vrije Universiteit Brussel, 1050 Brussels, Belgium*

[a)]Corresponding author: mdobaidullah@ces.buet.ac.bd

Abstract. Biomass fuels are widely available across the globe and provide a major share of renewable energy in most countries. Biomass combustion produces large quantities of particulate matter (PM) that have a negative impact on ambient air quality. This could be harmful especially in densely populated areas. The objectives of the paper were to evaluate particle mass concentrations in two size fractions of PM_1 (size <1 µm) and $PM_{2.5}$ (size <2.5 µm), and CO emissions under standard laboratory conditions obtained from two commercially available Belgian made modern residential wood stoves with capacity 10 kW and 20 kW. Four combustion batches with minor modification of primary air flows into the combustion chamber for each stove were conducted to get a clear picture of the emission results. Particle mass concentrations were measured in real time using an Electrical Low Pressure Impactor Plus (ELPI+) instrument from Dekati Ltd., Finland, which measures particles with a fast response time in a wide particle size range from 6 nm to 10 µm aerodynamic diameter. Gaseous concentrations of O_2 and CO_2 were measured continuously using a Horiba PG-250 analyzer and CO emissions were measured using a Siemens Ultramat 6 gas analyzer. The measurement protocols of each combustion test were conducted according to the European standard EN 13229. The combustion experiments were conducted in a laboratory of a stove manufacturing plant in Namur, Belgium. PM_1 and $PM_{2.5}$ fractions of all the batches of both stoves varied from 108 to 327 mg/Nm^3 and 130 to 420 mg/Nm^3 respectively in the combustion cycle. The CO emissions from all the batches varied from 450 to 1050 mg/Nm^3 for the 10 kW stove and 690 to 1400 mg/Nm^3 for the 20 kW stove. The results of particle mass concentrations and CO emissions from this study could be useful for the improvement of the combustion process in o reducing emissions from these appliances. No correlations were observed between the emissions results and the minor modifications of primary air flows into the combustion chamber.

INTRODUCTION

Biomass meets approximately 14% of the world's energy demand. The European Union (EU) has set a target to produce at least 20% of energy from renewable sources by 2020 [1]. The Belgium government has also set a target to meet 13% of energy from renewable sources by 2020 [2]. A significant quantity of this energy will be generated by the combustion of biomass fuels. The combustion of biomass fuels leads to the formation of broad range of pollutants and can be classified into two groups, which are gaseous emissions and particle emissions [2]. The gaseous emissions are the main gas compounds (CO_2, H_2O and O_2), the flue gas also contains CO, partially combusted hydrocarbons (CxHy or OGC), sulphur dioxide (SO_2), nitrogen oxides (NOx), hydrogen chloride (HCl) and different solid or liquid particles. Besides gaseous emissions, particle emissions are always observed during biomass combustion. Particle emissions originate from several sources. Particles can be divided into two groups under this category [3]. These are fine particles and coarse particles. Particles smaller than 1 µm (micro meter) in diameter are often called fine particles. These fine particles are generally formed from elements that are vaporized during combustion, which later saturate and form fine particles by nucleation. The nucleated particles grow further by coagulation, agglomeration, condensation and surface reaction. Particles larger than 1 µm in diameter are often called coarse particles, forming mainly from char or ash species with low vapour pressures which do not vaporize during combustion [4, 5]. PM_1, $PM_{2.5}$ and PM_{10} fractions refer to mass concentrations of particles smaller than 1, 2.5 and 10 µm. PM_1 and $PM_{2.5}$ are the most harmful for people as the particles can penetrate deep into the lungs. These particle sizes are always related to the aerodynamic diameter which represents the diameter of a spherical particle with a density of 1000 kg/m^3 having the same drag in air as the particle of interest [6, 7].

There is lack of information regarding the characterization of particulate and gaseous emissions from small scale biomass combustion appliances. Several studies on particle emissions from biomass stoves were carried out in EU countries. For example, Boman et al. [8] investigated six types of different pellet fuels in three different commercial pellet burners (10–15 kW) and observed that fine particles (< 1 µm) contain a significant amount of the total PM emissions. Bäfver et al. [9] experimentally studied particle and CO emissions from modern and old type residential stoves of various heat capacity fired with wood logs and wood pellets. Measurements were performed using a DLPI for mass size distributions while an ELPI was used for number size distributions. Modern pellets stoves showed lower mass concentration of particles as well as lower CO concentration than the old type wood stoves. They found that in all cases, the particle mass emitted was dominated by fine particles and there was only a small fraction of coarse particles. Qie et al. [10] studied particle emissions in a small scale pellet boiler (50 kW) using a Dust Tank-II Handheld Aerosol Monitor from 100 nm to 10 µm. Three types of biomass pellets, i.e. wood pellets, Miscanthus pellets and straw pellets were combusted. $PM_{0.1-10}$ concentrations of wood pellets, Miscanthus pellets and straw pellets were 72.7 mg/Nm^3, 100 mg/Nm^3 and 150 mg/Nm^3 respectively. PM concentration results show that wood pellets as biomass fuel are better than Miscanthus and straw pellets. However, limited information regarding particle and gaseous emissions from small scale combustion appliances is found in the literature.

There is a need for more knowledge of particulate matter and gaseous emissions from small scale application of wood stoves. The objectives of the present work were to experimentally evaluate particle mass emissions and gaseous emissions from two commercially available Belgian made modern wood stoves with a capacity 10 kW and 20 kW respectively. The work includes particle mass concentration in two size fractions PM_1 and $PM_{2.5}$, and CO emissions from the combustion cycle as well as comparison with previously reported data. The stoves were operated in several batches with minor modification of primary air flows into the combustion chamber to obtain a clear picture of the emission results.

MATERIALS AND METHODS

Fuel Characteristics

The dimension of the wood logs was about 33 cm in length and 10 cm in diameter and the mass of each wood logs fuel was about 1.15 kg. The wood logs are Beech species available in the Belgian forest. The chemical composition of the fuels was tested in the laboratory of SGS Environmental Services, Arnhem, the Netherlands. The elemental composition of the wood log fuel used in the combustion experiments was 43.8% carbon, 4.8% hydrogen, 38.3% oxygen, moisture 13% and lower heating value was 16.2 MJ/kg.

Combustion Wood Stoves

The combustion appliances used in the experiments were two different commercially available Belgian made modern wood stoves of 10 kW and 20 kW heat output respectively. The volume of the combustion chamber is 0.090 m^3 for the 10 kW stove and 0.175 m^3 for the 20 kW stove. The flame is directed upwards and can be seen from the outside of the stoves, since the front side of the stoves has a transparent glass window. The top surface of the combustion chamber is equipped with a baffle plate made of vermiculite (high temperature insulation material). The other sides of the combustion chamber are insulated with refractory ceramic bricks made of calcium silicate. Both stoves have the advantages of two staged combustion with supplying of primary and secondary air.

Experimental Setup

The schematic of the experimental setup for the gaseous and particle emission measurements is shown in Figure 1. The measurement protocols of each combustion test were conducted according to the European standard EN 13229 [11]. For each stove, measurements were repeated for several batches with minor medication of primary air flows into the combustion chamber to get a clear picture of the emissions results.

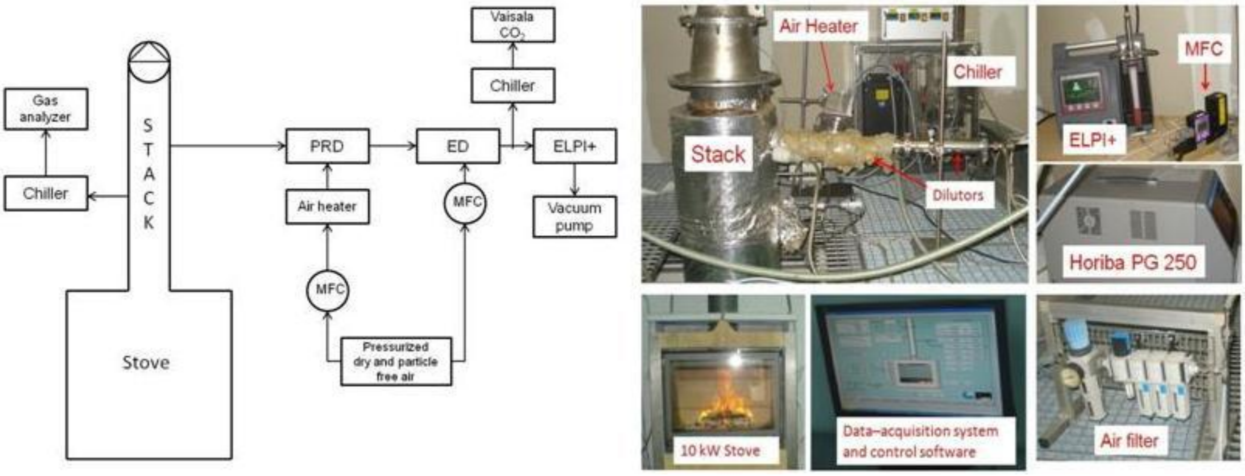

(a) (b)

FIGURE 1. Experimental setup for emission measurements from wood stoves, (a) schematic of the setup, (b) some photos of the measurements

Particle Emissions Measurements

Particle mass concentrations were measured in real time using an Electrical Low Pressure Impactor Plus (ELPI+) from Dekati Ltd., Finland. It measures particles with a fast response time in a wide particle size range from 6 nm to 10 µm aerodynamic diameter. A partial flow from the stack about 1.8 m above the wood stoves was led through an externally insulated bent tube probe which was made of 12 mm (diameter) stainless steel. The flue gases were passed through a partial flow dilution tunnel before reaching the particle measuring instrument, the ELPI+. The dilution tunnel consists of a porous tube diluter (PRD), an ejector diluter (ED) and an air heater. The working principle of the ELPI+, the measurement procedures of dilution air flows and the calculation of dilution ratio (DR) are discussed in the work [2, 12, 13].

Gaseous Emissions Measurements

Gaseous concentrations of O_2 and CO_2 were measured continuously using a Horiba PG-250 analyzer and CO emissions were measured using a Siemens Ultramat 6 gas analyzer. The measurement principles of the gas analysers were galvanic analyzer for O_2 and non-dispersive infrared for CO and CO_2. The raw flue gases were sampled by the steel probes from the stack at about 1.8 m above the stoves.

RESULTS AND DISCUSSIONS

The combustion process in stoves is characterized by three combustion phases: the startup (ignition) phase, the combustion phase and the burnout (ash cooking) phase. The emission measurements of the burnout phase were not performed according to the testing procedure of the standard EN 13229. The emission results of CO, PM_1 and $PM_{2.5}$ are defined as the amount of emission produced from the startup to the end of combustion phase.

Gaseous Emissions

Generally, gaseous emissions from manually batch fired stoves are highly variable. Combustion behaviour is affected by different factors such as fuel properties, appliance type and operational practice, etc. The NOx emissions were not performed from the stoves because these emissions were measured by the manufacturer once during the formal pass-test. The following values were obtained 88 mg/Nm³ for the 10 kW stove and 105 mg/Nm³ for the 20 kW stove, which satisfy the European norms (240 mg/Nm^3). Besides, the NOx cell of the Horiba PG 250 analyzer was not operational. For those reasons, NOx emission measurements were not performed.

Time Series of CO_2, CO and O_2 Concentrations

Figure 2 shows the variations of the concentration of CO, CO2, O2 and temperature of the flue gases over the measurement time during the combustion cycles of the 20 kW stove. The time for supplying a new batch of logwood was defined from the moment when no visible flames were observed and CO2 concentration reached about 5 %. Then, a batch of wood logs was supplied on the glow bed of the previous fire. It can be seen that at the startup phase, the highest concentrations of CO and significant variations of temperature of the flue gas occur. During the combustion phase, the CO concentrations are sufficiently lower and the stack temperature is higher. In figure 2, it is also observed that O2 concentrations increase and CO2 concentrations decrease during the combustion phases. This might be explained by the combustion of volatiles at the start of the combustion phase followed by a combustion slowdown as the fuel amount decreases.

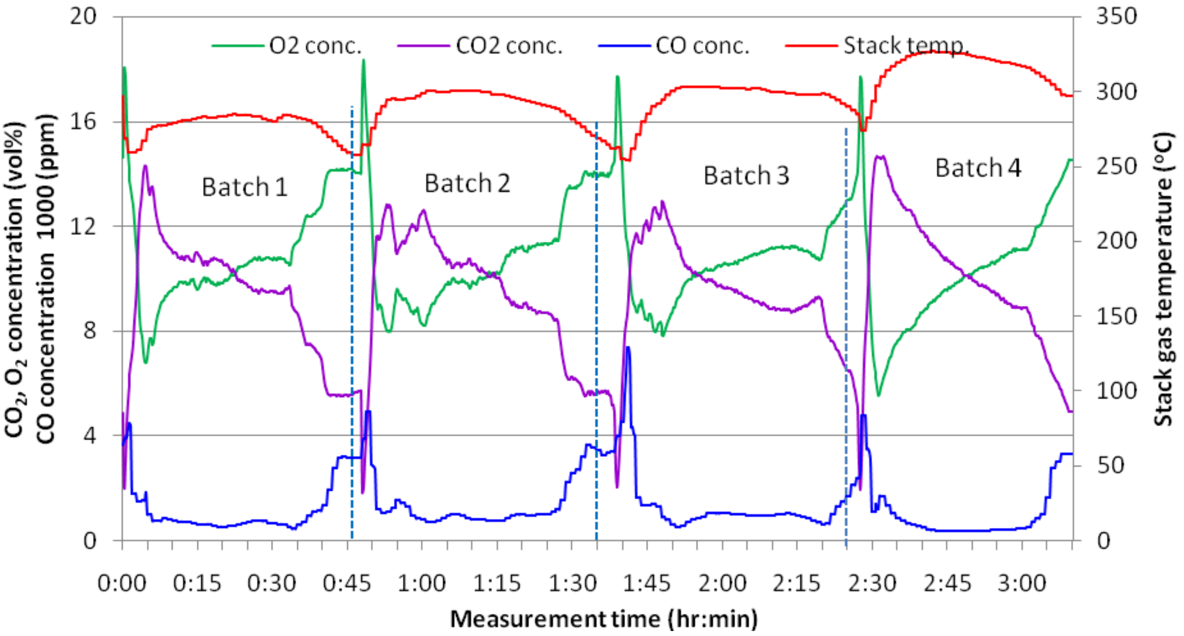

FIGURE 2. Variation of gas concentrations of CO, CO2, O2 and stack temperature measured for t he 20 kW stove

CO Emissions

CO emissions are observed in the combustion of all carbonaceous fuels, as an intermediate product of the combustion process. It is the most important intermediate product of fuel conversion to CO_2. It is oxidized to CO_2 under appropriate temperature and oxygen availability and sufficient presence of OH radicals. Figure 3 compares the CO emissions from all the measurements from both stoves with the required limit value (for Belgium) of standard NBN EN 13229 [14]. The CO emission values presented here are normalized to 13 vol % dry oxygen content. The error bars present the uncertainties of measurements calculated as the square root of the sum of the square of the standard error of mean (SEM) and the instruments' error. Both stoves (except batch 1 of the 20 kW stove) satisfied the required limit value of the standard. The results show that the CO emissions from all the batches varied from 450 to 1050 mg/Nm^3 for the 10 kW stove and 690 to 1400 mg/Nm^3 for the 20 kW stove.

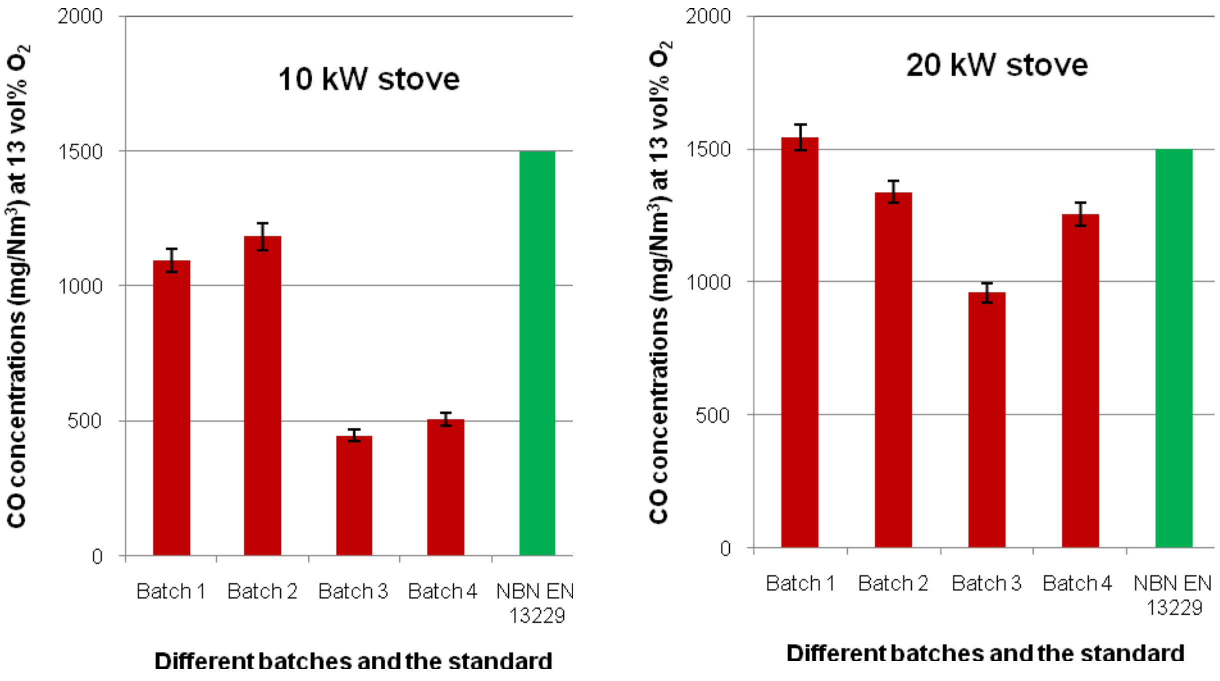

(a) (b)

FIGURE 3. Comparison of CO emissions with the Standard NBN EN 13329, (a) for the 10 kW stove, (b) for the 20 kW stove

It is observed that the CO emissions with the 20 kW stove were higher than the 10 kW stove due to the differences in combustion chamber volume, fuel consumption and heat output. The average fuel load for each batch of the 20 kW stove (4.37 kg/batch) was about 2 times higher than the 10 kW stove (2.19 kg/batch). This can also be discussed in other ways. The higher air excess factor (λ=2.1) obtained in the 20 kW stove might have caused lower combustion temperature, leading to high CO emissions. On the other hand, a correctly matched air excess factor (λ=1.8) for the 10 kW stove created favorable combustion conditions leading to less CO emissions. No correlation was observed between CO emissions and minor modification of primary air flows into the combustion chamber. The higher CO emissions indicate poorer combustion conditions since these are related with incomplete combustion. Present results of the total CO emission are close to those reported in another study of a residential modern wood stove [15], while quite lower than those reported in other studies of wood modern stoves [9, 16-18].

Particle Mass Emissions

Particle emission measurements were conducted for a total of 8 batches from two modern Belgian made modern wood stoves under standard laboratory condition. The flue gas velocities in the stack of the 10 kW and 20 kW wood stoves were 0.47 m/s and 0.65 m/s respectively. The flue gas velocity in the nozzle was about 0.29 m/s. This means that the PM measurements are sub-isokinetic and therefore PM_{10} fractions, are not included in this paper as the present work puts emphasizing on the very small particles.

Figure 4 compares the particle mass concentrations of PM_1 and $PM_{2.5}$ fractions obtained from different batches of the 10 kW stove and 20 kW stove respectively. The error bars present the uncertainty of the measurements. It is observed from the Figure 3 that PM_1 fractions of all the batches of both stoves varied from 106 to 327 mg/Nm^3 while and $PM_{2.5}$ fractions varied between 138-413 mg/Nm^3. Batch 4 for the 10 kW stove and Batch 1 for the 10 kW stove emitted the lower PM emissions in the both fractions. The mass concentrations results obtained from the combustion experiments are little high when compared to the literature [8, 10], which may be due to the difference of the combustion technologies, the measurement protocols and the instruments used.

The obtained results demonstrate quite some variation in the measured PM_1 and $PM_{2.5}$ values over time for the different batches, which is typical for the combustion of wood log stoves. PM_1 concentrations of all the batches of the 10 kW stove accounted for 76.8 % of the PM2.5 concentrations, while 75.6% of the 20 kW stove, which are little lower values than the literature [8].

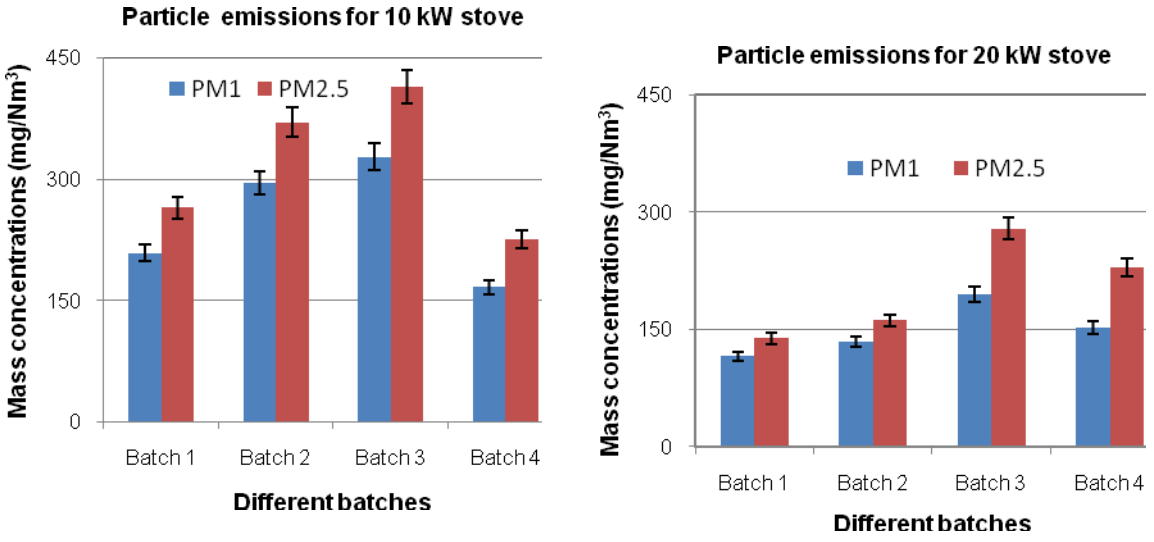
Particle emissions for 10 kW stove

Particle emissions for 20 kW stove

(a)

(b)

FIGURE 4. PM_1 and $PM_{2.5}$ emissions from different batches, (a) for the 10 kW stove, (b) for the 20 kW stove

The PM_1 and $PM_{2.5}$ emissions from the 20 kW stove are much lower than the 10 kW stove. The average fuel consumption for each batch of the 10 kW stove is about one-half lower than the 20 kW stove, which might impact on particle emissions. Besides, the particle formation and emissions are related to various aspects such as combustion conditions, fuel properties, combustion appliances, air fuel ratio and combustion processes, etc. [2-5, 13].

CONCLUSIONS

The results presented in this paper show the CO and particle emissions from several batches of two commercially available Belgian made modern wood stoves. The combustion experiments were conducted in a laboratory of a stove manufacturing plant in Namur, Belgium. The following conclusions can be made from this study.

- The CO emissions from all the batches varied from 450 to 1050 mg/Nm^3 for the 10 kW stove and 690 to 1400 mg/Nm^3 for the 20 kW stove. The CO emissions from all batches of both stoves (with exception for the Batch 1 of 20 kW) satisfied the required limit value of the standard.
- The results of CO emissions from the different combustion phases of the wood stoves demonstrate that detailing characterization of certain parameters could be useful for the improvement of the entire combustion process. CO emissions from small scale biomass combustion appliances can be reduced using flue gas cleaning technologies such as catalytic combustors.
- PM_1 fractions of all the batches of both stoves varied from 106 to 327 mg/Nm^3 while and $PM_{2.5}$ fractions varied between 138-413 mg/Nm^3. The obtained results demonstrate quite some variation in the measured PM_1 and $PM_{2.5}$ values over time for the different batches, which is typical for the combustion of wood log stoves.
- The results of our particle mass emissions were higher compared to similar work in the literature. Particle mass emissions can be reduced by installing electrostatic precipitators (ESPs) units in the stack. These systems have higher particle separation efficiency than the cyclones and wet scrubbers and use in the EU countries. However, such particle removal technologies are quite expensive for small scale applications.

ACKNOWLEDGEMENTS

The author gratefully acknowledges the support of the Erasmus Mundus External Cooperation Window (EM ECW) of the European Commission, grant agreement number 2009-1663/001-001-ECW and the European Regional Development Fund (ERDF/EFRO), project P12-05 EMOVO. The experiments presented in this paper were conducted at the combustion laboratory of Stûv, Namur, Belgium. The author would like to express sincere thanks to the entire department for their help and support. Constant help of Dr. Igor Dyakov, Mr. Thomas Duquesne and Mr. Jean Dominique Thomassin made those days of measurements to be very productive.

REFERENCES

1. M. F. Demirbas, M. Balat, H. Balat, Energy Conversion and Management **50**, 1746-60 (2009).
2. Obaidullah M. Particle Emissions from Small Scale Combustion Appliances. Brussel, Belgium: Vrije Universiteit Brussel (VUB); Ph.D. thesis, November 2014.
3. M. Obaidullah, S. Bram, V. Verma, J. De Ruyck, International Journal of Renewable Energy Research **2**, 147-59 (2012).
4. Obernberger I, Brunner T, Barnthaler G. Fine particle emissions from Modern Austrian small scale biomass combustion plants. 15th European biomass conference and exhibition. Germany7-11 May 2007. p. 1546-57.
5. O. Sippula, J. Hokkinen, H. Puustinen, P. Yli-Pirila, J. Jokiniemi, Atmospheric Environment **43**, 4855-64 (2009).
6. Nussbaumer T, Klippel N, Johansson L. Survey on measurements and emission factors on particulate matter from biomass combustion in IEA countries. Proc 16 th European Biomass Conference and Exhibition2008. p. 2-6.
7. J. D. McDonald, B. Zielinska, E. M. Fujita, J. C. Sagebiel, J. C. Chow, J. G. Watson, Environmental Science & Technology **34**, 2080-91 (2000).
8. C. Boman, A. Nordin, D. Bostrom, M. Ohman, Energy & Fuels **18**, 338-48 (2004).
9. L. S. Bäfver, B. Leckner, C. Tullin, M. Berntsen, Biomass and Bioenergy **35**, 3648-55 (2011).
10. G. Qiu, Renewable Energy **50**, 94-102 (2013).
11. EN-13229. Open fires and inserts solid fuel - Requirements and test methods. French Association Standardization; June 2002.
12. M. Obaidullah, I. Dyakov, L. Peeters, S. Bram, J. De Ruyck, Comparison of particle emissions from enclosed parking garages and streets. GNEST **15**, 457-65 (2013).
13. Obaidullah M, Dyakov I, Bram S, Ruyck DE J. Particle Emissions from Domestic Wood Stoves under Laboratory Conditions. Global Nest **17**, 637-52 (2015).
14. Royal-Decree, Belgium. Regulating the minimum efficiency requirements and emission levels of pollutants heaters with solid fuels. October 2010, (available at http://environnement.wallonie.be/legis/air/air064.htm).
15. Roy MM, Corscadden KW. Applied Energy **99**, 206-12 (2012).
16. Pettersson Er, Boman C, Westerholm R, Bostrom D, Nordin A. Energy & Fuels **25**, 315-23 (2011).
17. Schmidl C, Luisser M, Padouvas E, Lasselsberger L, Rzaca M, Ramirez-Santa Cruz C, et al. Atmospheric Environment **45**, 7443-54 (2011).
18. Koyuncu T, Pinar Y. Biomass and Bioenergy **31**, 73-9 (2007).

International Conference on Mechanical Engineering 2015
(ICME 2015) 18 – 20 December, 2015, Dhaka, Bangladesh

Paper ID : 379

A High Performance Neutron Powder Diffractometer at 3MW Triga Mark-II Research Reactor in Bangladesh

I. Kamal[1, a)], S. M. Yunus[1, b)], T. K. Datta[1, c)] , A. K. M. Zakaria[1] A. K. Das[1], S. Aktar[1], S. Hossain[1], R. Berliner[2, e)] and W. B. Yelon[3, f)]

[1]*Institute of Nuclear Science and Technology, Atomic Energy Research Establishment, Ganakbari, Savar, Dhaka*
[2]*Instrumentation Associates, Durham, North Carolina, USA*
[3]*Oak Ridge National Laboratory, Oak Ridge, Tennessee, USA*

[a)] Corresponding authors: imtiaz_kamal26@yahoo.com
[b)]yunussm11@yahoo.com
[c)]tk_datta4@yahoo.com
[e)] RB@instrumentationAssociates.com
[f)]yelonwb@hotmail.com

Abstract.A high performance neutron diffractometer called Savar Neutron Diffractometer (SAND) was built and installed at radial beam port-2 of TRIGA Mark II research reactor at AERE, Savar, Dhaka, Bangladesh. Structural studies of materials are being done by this technique to characterize materials crystallograpohically and magnetically. The micro-structural information obtainable by neutron scattering method is very essential for determining its technological applications. This technique is unique for understanding the magnetic behavior in magnetic materials. Ceramic, steel, electronic and electric industries can be benefited from this facility for improving their products and fabrication process.This instrument consists of a Popovicimonochromator with a large linear position sensitive detector array. The monochromator consists of nine blades of perfect single crystal of silicon with 6mm thickness each. The monochromator design was optimized to provide maximum flux on 3mm diameter cylindrical sample with a relatively flat angular dependence of resolution. Five different wave lengths can be selected by orienting the crystal at various angles. A sapphire filter was used before the primary collimator to minimize the first neutron. The detector assembly is composed of 15 linear position sensitive proportional counters placed at either 1.1 m or 1.6 m from the sample position and enclosed in a air pad supported high density polythene shield. Position sensing is obtained by charge division using 1-wide NIM position encoding modules (PEM). The PEMs communicate with the host computer via USB. The detector when placed at 1.1 m, subtends 30˚ (2θ) at each step and covers 120˚ in 4 steps. When the detector is placed at 1.6 m it subtends 20˚ at each step and covers 120˚ in 6 steps. The instrument supports both low and high temperature sample environment. The instrument supports both low and high temperature sample environment. The diffractometer is a state-of-the art technology for diffraction study in our country.

INTRODUCTION

The Savar Neutron Diffractometer (SAND) is a High-resolution Position Sensitive Detector based Neutron Powder Diffractometer. The special features of SAND are as follows. It is equipped with- i) Primary Collimator and Fast Neutron Filter, ii) Monochromator Shield, iii) Monochromator Goniometer and Monochromator, iv) Monochromatic Beam Selector and Collimator, v) Monochromatic Beam Shutter and Neutron Monitor, vi) Diffractometer Arm and Sample Rotation Stages, vii) Position Sensitive Detector and Detector Shield, and viii) Air Pad Floor. These components are supported by the specially built electronic controls for the stepper motors that drive the monochromator goniometer and diffractometer movement on an air-pad floor. All of the devices are controlled by the Neutron Diffractometer Control System (NDCS) software supplied by IA that is hosted on the system control computer. The NDCS has tools for the analysis and display of diffractometer data, for the maintenance and alignment of the position sensitive detectors array, and for the maintenance of the diffractometer data archive.

SAND is additionally equipped with a helium cryo-refrigerator for carrying out experiments between room temperature to ~ 10 K. High temperatures (up to 600 °C) measurement facility is also available in the SANDSystem. The major components of the SAND are described below.

INSTRUMENT SYSTEMS

Primary Collimator and Neutron filter

Fig. 3 below contains a drawing of the primary collimator. It consists of and 8″ OD outer aluminum tube which is welded to a 5.5″ OD inner tube. The inner tube has welded flanges at each end and top and bottom Swagelok fittings that can be used to fill and drain the inner volume with deionized water. The windows at each end of the inner volume have been thinned to 0.1″ to suppress absorption of thermal neutrons. A 5″ diameter, 6″ long single crystal sapphire crystal is mounted in the tapered section at the front (upstream) end of the collimator as a fast neutron filter.

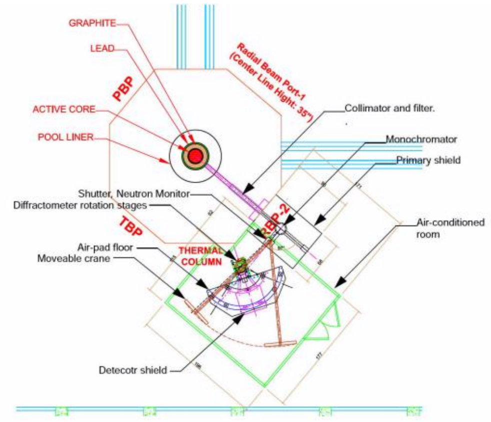

FIGURE 1. The principal components of SAND in relationto the reactor bay and an air conditioned control room

FIGURE 2. Electronic System of SAND

The space between the outer (8″OD) and inner (5.5″ OD) tubes is filled with RX277 neutron absorbing grout. The inner (5.5″ OD) volume can be filled with deionized water to provide an effective beam port shutter when the reactor is shut down.

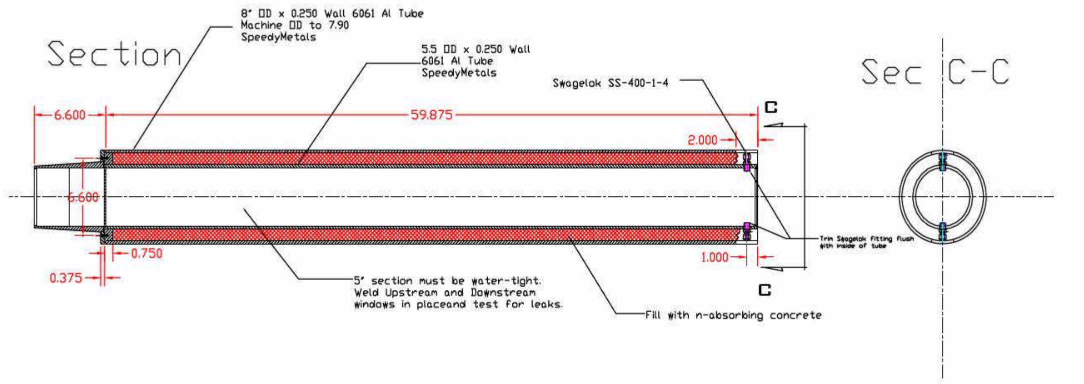

FIGURE 3. Layout of the primary (in pile) collimator.

Primary Shield

The primary shield for SAND consists of 7 steel jacketed, internally reinforced, heavy concrete filled blocks having appropriate sizes. The center block has a cavity that fits the Monochromator Mushroom (400

Lbs). The shield assembly is placed against a 68 x 68 x 1 in^3 steel plate that is bolted to the reactor face leaving a 1 in space behind that is filled with RX277 neutron absorbing grout. The plate provides a surface reliably square and perpendicular to the primary beam tube.

Monochromator and Monochromator Goniometer

The monochromator is fabricated from 9 single crystal silicon slabs 0.570 x 0.210 x 7.5 in^3 that have been cut from the same 6 mm thick wafer of silicon. These blades are bent horizontally by a 4-point bending apparatus to a radius of 11.8 m. In the vertical direction, the blades are arranged in a polygonal approximation to the surface of a sphere of radius 1.76 m. Fig. 4 shows the monochromator and the monochromator goniometer. The monochromator is positioned with the bending screw at the top, appropriate for use of the (115), (113) and (335) reflections. The thickness, offset angle and bending radius of the silicon slabs have been calculated to optimize the intensity and diffractometer resolution for the (115) reflection of the monochromator at 97º take-off angle and a sample-monochromator distance of 1.90 m yielding a wavelength of 1.5656 A.

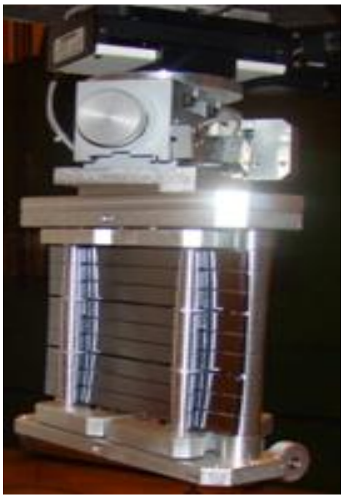

FIGURE 4.Monochromator assembly.

FIGURE 5. The complete setup of the SAND at the reactor beam port.

Diffractometer and Air-Pad Floor

The diffractometer is composed of two coaxially mounted Huber rotation stages mounted on a screw-jack leveled base. A Huber 430 400 mm diameter stepper motor controlled stage is used for the Detector Arm (2Q) motion and a Huber 420 200 mm diameter stage for the sample rotation. Each of these is equipped with ROD1020 incremental optical encoder with 2500 increments per revolution and a Vexta stepper motor.The air-pad floor consists of a screw-jack leveled slab of aluminum, 1.25″ thick covered by a 0.050″ thick layer of high pressure plastic laminate. The diffractometer base and air-pad floor are bolted together with heavy aluminum gussets and each of these must be leveled individually in order to fit properly together. The diffractometer base assembly also provides for the support of the arc-shield and the monochromatic beam line tubing. The arrangement of the diffractometer base and its connection to the air-pad floor is seen in Fig. 5.

Sample Mounting Devices

The SAND diffractometer is equipped with two systems for mounting samples on the diffractometer table. The first uses a collet chuck mounted Huber sample table to hold the sample rotator or other device for supporting samples at room temperature.This device is attached to the diffractometer table using two large Allen head screws. After starting the screws (but before tightening), the centering post, found in the tool cabinet inside a cardboard tube, is inserted through the open collet chuck and the base is moved around gently until the post slides into the table beneath. Also the accessories for mounting the sample in high temperature (600°C) and very low temperature (10K) environments the necessary attachments are being supplied. Figs. 6 showthe available sample mounting devices for room temperature, low temperature and for high temperature in SAND. A vacuum pump is needed for creating vacuum environment for high and low temperature studies, is also available as an attachment.

FIGURE 4.(a) Huber sample table **(b)** Cryo refrigerator **(c)** Vacuum pump **(d)** High temp. furnace

EXPERIMENTAL METHODS

Calibration

For testing the performance of the diffractometer, first of all calibration of the instrument has been done by adjusting its various components and parameters. Finally diffraction measurement on standard ploy crystalline Ni powder was done to verify the diffraction pattern. Figs. 6(a-d) show the different steps of calibration.

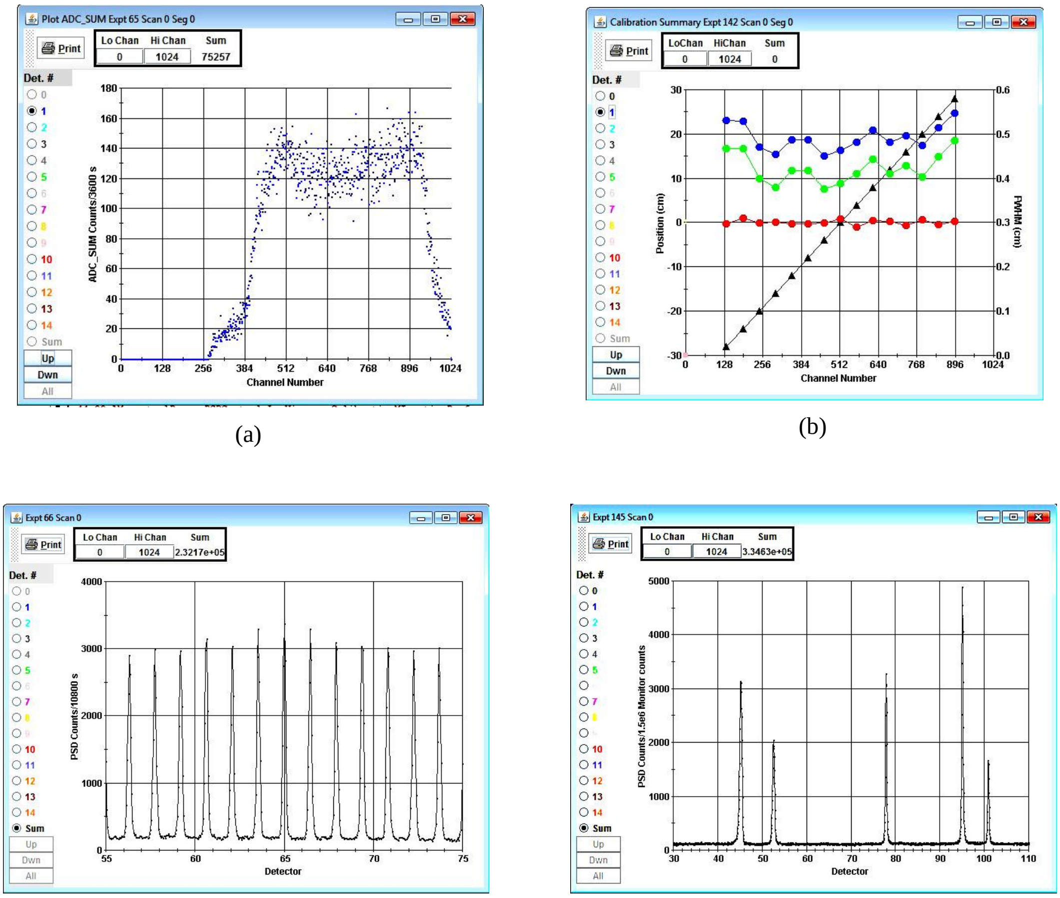

(a) (b)

(c) (d)

FIGURE 6. (a) Pulse Height Spectra, (b) Deviation curve fordetectortuning, (c) Cd mask pattern of detector tuning, (d) ND Pattern taken from standard Ni powder.

Case study-1: Neutron Diffraction Study of $MgCr_xFe_{1-x}O_4$ (x=0, 0.2, 0.4, 0.6, 0.8 &1.0) Powder at Room Temperature

As a case study,structural and magnetic characterizations of the spinel ferrite $MgCrFeO_4$ (for x=0) has been carried out at room temperature. The samples were prepared by conventional solid state sintering method in air at 1300°C. X-ray diffraction experiments were carried out on all the samples in order to verify the crystalline form of the samples and to check whether it is in single phase or not. After confirming the crystalline and single phased sample Neutron diffraction study has been performed. The neutron diffraction patterns have been taken keeping the detector in both of the positions at 1.1 m and 1.6m from the sample position of SAND. Reactor power was kept constant at 2.4 MW which provided the beam of thermal neutronshaving the wave length λ =1.5656 Å. Different crystallographic and magnetic parameters of the sample have been determined by Rietveld data refinement program adopting FullProf and Rietan-2000 computer code [1-3]. The sample was found to be ferrimagnetic with spinel structure at room temperature. Here the data for only one sample, $MgCr_xFe_{1-x}O_4$ (x=0), has been presented.The diffraction patterns obtained from the sample are shown in Fig.7 andFig. 8.

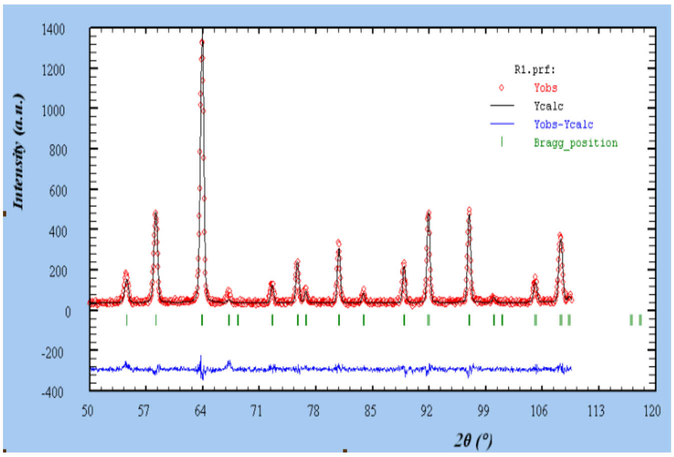

FIGURE 7. Fitted neutron diffraction pattern of $MgCr_xFe_{2-x}O_4$ (x=0.0) at nearer position.

Analysis of the Results

Rietveld refinement of the neutron diffraction data [1, 2] reveals that the sample possesses cubic symmetry corresponding to the space group Fd3m. The different crystallographic parameters and distribution of cations Mg, Cr and Fe on the tetrahedral (A site) and octahedral (B site) sites have been determined from the analysis of the neutron diffraction data in the Rietveld method. The fractional co-ordinates of oxygen (u) and the lattice parameter a, b, c, α, β and γ have been determined. The measured values of oxygen position parameter u = 0.2577(8), lattice parameter a = b = c = 8.339960 Å and $\alpha = \beta = \gamma = 90^o$. The magnetic structure of the sample has been found to be ferromagnetic. The moment distributions in the A and B sub lattices have been determined. The A site and B site moments were found to be 4.8476 and 3.3582 Bohr magneton respectively. The fitted neutron diffraction patterns are shown in Fig. 7 and Fig. 8. Figures showed an excellent agreement between the observed (circles) and calculated (continuous line) profiles [4, 5]. The reliability (agreement) factors of the refinement were also very reasonable. They are: R_p(profile) = 17.4, R_{wp}(weighted) = 18.8, R_e(expected) = 18.1 and $\chi^2 = R_{wp}/R_p$= 1.082 for Fig. 7. And those for the Fig. 8 were R_p(profile)= 20.1 R_{wp}(weighted) = 20.3 R_e(expected) = 19.1 and $\chi^2 = R_{wp}/R_p$= 1.134

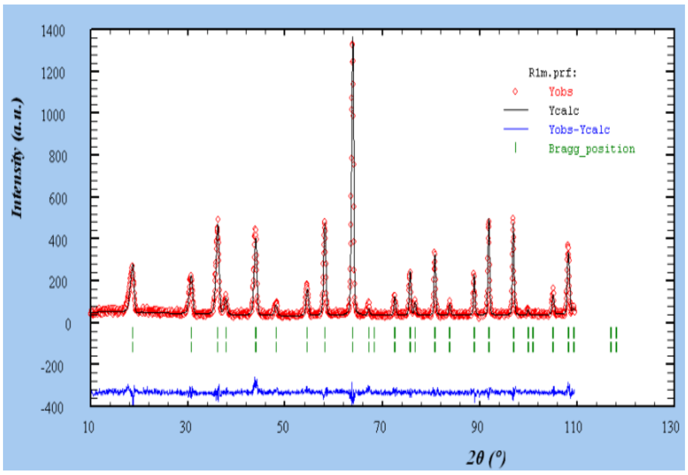

FIGURE 8. Fitted neutron diffraction pattern of $MgCr_xFe_{2-x}O_4$ (x=0.0) at distant position.

CONCLUSIONS

The performance of the SAND has been found quite satisfactory since it well-reproduced the diffraction data from standard Ni sample. All the components of SAND work very effectively and give the diffraction data in shorter time. Neutron diffraction data have been taken for the sample $MgCr_xFe_{1-x}O_4$ (x=0) at nearer (1.1m) and distant positions (1.6m), respectively. Time consumed for taking one set of data at nearer position was ~4 hours and that for the distant position was ~6 hrs. The obtained data were analyzed using Rietveld method. The well-known spinel structure with cubic symmetry was found in the specimen. At nearer position of the detectors the intensity is higher than that of the distant position but the resolution of the peak profile is better in the distant position. The SAND is completely fit for neutron diffraction study for different kind of samples such as- metal, metallic alloys, ceramic and other composite materials.

REFERENCES

1. H. M. Rietveld, A profile Refinement Method, Journal of Applied Crystallography **2,** 65-71 (1969).
2. H. M. Rietveld, ActaCryst.,**22** 151 (1967).
3. Juan Rodrigues Carvajal program: FullProf, Version 3.1c January 96 LLB JRC Laboratorie, Leon Billouin (CEA-CNRS).
4. A. K. M. Zakaria, M. A. Asgar, S-G. Eriksson, F. U. Ahmed, S. M. Yunus and H.Rundlof, The Study of Magnetic Ordering in the Spinel System $Zn_xMg_{0.8-x}Ni_{0.2}Fe_2O_4$ by Neutron Diffraction, Journal of Magnetism and Magnetic Materials **265,** 311-320 (2003)
5. S. M. Yunus, J. A. Fernandez-Beca, M. A. Asgar, F. U. Ahmed, M. A. Hakim, Neutron Diffraction Study of Magnetic Disorder in $Zn_xMg_{0.8-x}Ni_{0.2}Fe_2O_4$ Ferrite with x= 0.0, 0.2, 0.4 and 0.6, Physica B **262,** 112-124 (1999)

International Conference on Mechanical Engineering 2015
(ICME 2015) 18 – 20 December, 2015, Dhaka, Bangladesh

Paper ID : 380

Statistical analysis of the effects of Wire EDM machining parameters on Material Removal Rate and Kerf Width of commercially available Tool steel

N.G. Roy[1], A. Pramanick[1], P. P. Dey[1] and M. Ghosh[2]

Department of Mechanical Engineering, IIEST Shibpur, West Bengal, India.
Department of Metallurgy & Materials Engineering, IIEST Shibpur, West Bengal, India.

[a)]Corresponding author: ngroywedm@gmail.com

Abstract. In the present study the parametric analysis of Wire EDM was performed on material removal rate (MRR) and kerf width of tool steel by using response surface method (RSM) and analysis of variance (ANOVA) technique. This work studies the effect on MRR (mm^3/min.) and kerf width (mm) by changing the machining parameters like pulse peak current (*IP*), pulse–on time (T_{on}), pulse-off time (T_{off}) and servo voltage (*SV*). Square and interaction effects of mathematical models have been found between the machining parameters and the output responses like MRR and kerf width. Response surfaces are found to be close to the experimental values.

INTRODUCTION

There has been multitudinous progress over the decades in the field of materials science and non conventional machining, innovation of new technologies as well as need for better performances of existing technologies demands much more from the material-machining-characterization. These materials are either traditional materials with enhanced properties or newly developed materials with high-performance capabilities. Today's manufacturing industry has been facing challenges from these advanced and modern 'difficult-to-machine' high precision, high surface quality, complex shaped materials and very high machining cost. Some materials play a vital role in modern manufacturing industries like aircraft, automobile, tool, die-punch, and mould making industries [1]. The improved physical, chemical, and mechanical properties of these materials have yielded enormous economic benefit to the manufacturing industries through improved product performance and design. Traditional machining processes has been failed to machine such materials economically therefore they are increasingly being replaced by nonconventional machining process. WEDM is an important process, effectively applied for the machining of such materials, precisely and cost-effectively. The main mechanism of metal removal in WEDM constitutes the erosion due to spark generated between tool and work-piece submerged in a liquid dielectric medium. The sparks generated between the gap of tool and work-piece removes the material with the help of de-ionized water, which flushes all the debris of eroded material [2, 3]. Since no cutting forces are present, WEDM is ideal for delicate parts. There has been no mechanical contact between the wire and work-piece. WEDM is a process of machining electrically conductive materials by using preciously controlled sparks that occurs between an electrode and a work-piece in presence of a dielectric fluid [4].

WEDM has been well established technique used in modern manufacturing industry to produce high quality machining of all types of electrically conductive materials, alloys and even ceramic materials, of any hardness with intricate shape, and profile which would have been difficult to manufacture by conventional machining [5]. The efficiency of any non-conventional machining considered less in comparison to conventional machining performances of any process is characterized by its product quality and productivity i.e material removal amount. MRR is expressed as the material removal rate resulted from various machining operations. WEDM process has been employed as quite demanding machining but the mechanism of process is complex and far from completely understood. Therefore, it is hard to establish a model that can accurately predict the responses (MRR, kerf width etc) by correlating the process parameter, though several attempts have been already employed. The important concern is the optimization of the process parameters such as pulse peak current intensity (*IP*), pulse on duration (T_{on}), pulse-off time (T_{off}) and servo voltage (*SV*) to minimize kerf width and simultaneously improving MRR. Many attempts had been made for modelling of WEDM process and investigation of the process performance to improve the surface quality and MRR are still challenging problems, which restrict the expanded application of the technology [6]. Kerf width (cutting width) is one of the important performance measures in WEDM. It determines the dimensional accuracy of the finishing part. Kerf width depends mainly on the machining parameters. Kerf width is the measure of actual gap between two sides of the wire i.e. diameter of the EDM wire plus the overcut. The wire–workpiece gap usually ranges from 0.025 to 0.075 mm and is constantly maintained by a computer controlled positioning system. The outcome of this study would add to the database of the WEDM machinability of this particular steel and also would be extremely useful for the machinist as the technology charts for WEDM being difficult to available. Pradhan and Biswas [6] presented a neuro-fuzzy model to predict MRR of AISI D2 tool steel with IP, T_{on} and duty cycle (τ) as process parameter. The model predictions were found to be in good agreement with the experimental results. Kanagarajan et al. [7] had chosen IP, T_{on}, electrode rotation, and flushing pressure as design factor to study the EDM process performance such as SR and MRR on Tungsten carbide/cobalt cemented carbide. The most influential parameters for minimizing the SR have been identified using the RSM and experimentally verified by conducting confirmation experiments. Jaharah et al. [8] investigated the machining performance such as SR, electrode wear rate and MRR with copper electrode and AISI H3 tool steel workpiece and the input parameters taken are IP, T_{on}, and T_{off}. The optimum condition for R_a was obtained at low IP, low T_{on} and T_{off} and concluded that the IP was the major factor effecting both the responses, MRR and R_a.

The prime advantage of employing RSM is the reduced number of experimental runs required to generate sufficient information for a statistically adequate result. Many researchers have applied RSM successfully to manufacturing environments. Kuppan et al. [9] derived mathematical model for MRR and average R_a of deep hole drilling of Inconel 718. The experiments were planned using CCD and RSM was used to model the same. It revealed that MRR has been more influenced by pulse peak current and duty factor, and the parameters were optimized for maximum MRR with the desired Ra value using desirability function approach. Chiang [10] had explained the influences of IP, T_{on}, τ and voltage on the responses; MRR, electrodes wear ratio, and R_a. The experiments were planned according to a CCD and the influence of parameters and their interactions were investigated using ANOVA. Erzurumlu et al. [11] have developed a RSM model and compared with the artificial neural network model. Pradhan et. al. [12] however applied RSM model to estimate the influence of process parameters on material removal rate.

From the above researches, it can be seen that very few works has been reported yet relating to modeling of kerf width and MRR on the experimented sample of which chemical composition is shown in Table 1. The modeling done after machining the sample by WEDM using RSM and CCD which make it possible to explain the variability associated with each of the technological variables studied.

Table 1: Chemical composition of experimented steel sample (wt.%)

Material	C	Cr	Mn	Ni	Mo	W	Si	V
Tool Steel	**0.96**	**1.54**	**0.43**	**0.09**	**0.05**	**0.14**	**0.12**	**0.01**

RESPONSE SURFACE METHODOLOGY (RSM)

RSM has been considered as a collection of mathematical and statistical techniques that are useful for modelling and analysis of problems in which output or response has been influenced by several input variables at different levels depicted in Table 2. The objective is to find the correlation between the Design of Experiments (DOE) methods used to approximate an unknown function for which only a few values are computed as in Table 3. These relations are then modelled by using least square error fitting of the response surface. A Central Composite Design (CCD) is used since it gives a comparatively accurate prediction of all response variable averages related to quantities measured during experimentation [13]. CCD offers the advantage of those certain level adjustments which have been acceptable. In CCD, the limits of the experimental domain to be the response and the variables investigated [14]. It is one of explored and are made as wide as possible to obtain a clear response from the model. The T_{on} (the first digit of the three digit value used as machine control prefix), T_{off}, Ip, and SV are the machining variables selected for this investigation.

Table 2: Different process variables with their levels

Variable Parameters (Units)	Level 1	Level 2	Level 3	Level 4	Level 5
T_{on} (μs)	104	110	116	122	128
T_{off} (μs)	50	53	56	59	62
IP (A)	90	120	150	180	210
SV (V)	10	15	20	25	30

TABLE 3. DOE by RSM with Machine Inputs and Response parameters

Sl. No.	T_{on}	T_{off}	IP	SV	MRR	Kerf Width
1	116	62	150	20	0.8795	0.2715
2	110	59	180	25	0.6284	0.3558
3	122	53	120	15	1.4371	0.3312
4	116	56	150	20	0.8663	0.2964
5	116	56	210	20	1.0365	0.3432
6	116	56	150	20	0.8288	0.2991
7	116	56	90	20	0.8943	0.2997
8	110	59	120	15	0.5345	0.2820
9	116	56	150	30	0.6672	0.2982
10	122	53	180	25	0.9821	0.2661
11	122	53	180	15	1.3918	0.3009
12	116	56	150	20	0.7563	0.2883
13	110	59	120	25	0.5480	0.3030
14	116	56	150	20	0.7383	0.2925
15	116	56	150	20	0.7812	0.3066
16	116	56	150	10	0.9703	0.3306
17	122	59	180	15	1.0975	0.2916
18	122	59	120	15	0.9907	0.2814
19	122	59	120	25	0.9191	0.2706
20	110	53	120	25	0.5695	0.2751
21	110	59	180	15	0.5318	0.3222
22	122	59	180	25	0.9019	0.2955
23	116	56	150	20	0.8037	0.2895
24	110	53	180	15	0.5475	0.2844
25	110	53	180	25	0.5417	0.2889
26	110	53	120	15	0.5754	0.2768
27	116	56	150	20	0.7686	0.3081
28	122	53	120	25	0.9885	0.2709
29	128	56	150	20	1.1164	0.2734
30	116	50	150	20	0.9105	0.2676
31	104	56	150	20	0.2444	0.2766

REGRESSION ANALYSIS

The second-order model is normally used when the response function is not known or nonlinear. In the present study, a second-order model has been utilized. The experimental values are analyzed and the mathematical model is then developed that illustrate the relationship between the process variable and response. The second-order model in equation 1 explains the behaviour of the system.

$$Y = \beta_0 + \sum_{i=1}^{k} \beta_i x_i + \sum_{i=1}^{k} \beta_{ii} x_i{}^2 + \sum_{i=1}^{k-1} \sum_{j=2}^{k} \beta_{ij} x_i x_j + \varepsilon \qquad (1)$$

where, Y used as the corresponding response, X_i as input variables, X_i^2 and X_iX_j are the squares and interaction terms, respectively, of these input variables. The unknown regression coefficients are β_o, β_i, β_{ij} and β_{ii} and the error in the model is depicted as ε.

Regression Model of MRR

Based on the experimental data gathered, statistical regression analysis enabled to study the correlation of process parameters with the MRR. Both linear and non-linear regression models were examined; acceptance was based on high to very high coefficients of correlation (R) calculated. In this study, for four variables under consideration, a polynomial regression has been used for modeling. For simplicity, a quadratic model of MRR is proposed and can be written as shown in Equation 2.

$$MRR = -26.51 + 0.4630 * T_{on} - 0.027 * T_{off} - 0.0244 * IP + 0.1094 * SV - 0.000847 * T_{on} * T_{on} + 0.00257 * T_{off} * T_{off} + 0.000045 * IP * IP + 0.000164 * SV * SV + 0.003121 * T_{on} * T_{off} + 0.000006 * T_{on} * IP - 0.002550 * T_{on} * SV + 0.000191 * T_{off} * IP + 0.00297 * T_{off} * SV - 0.000001 * IP * SV \qquad (2)$$

Regression Model of Kerf Width

The second order quadratic fit model of Kerf Width proposed has been shown in equation 3.

$$Kerf\ Width = -7.90479 + T_{on} * 0.0821091 + T_{off} * 0.132088 - IP * 0.00305075 - SV * 0.005198 - T_{on} * T_{on} * 1.61558E - 04 - T_{off} * T_{off} * 7.97619E - 04 + IP * IP * 6.44048E - 06 + SV * SV * 0.000161357 - T_{on} * T_{off} * 5.82639E - 04 - T_{on} * IP * 3.97222E - 05 - T_{on} * SV * 3.32083E - 04 + T_{off} * IP * 9.84722E - 05 + T_{off} * SV * 0.000583 + IP * SV * 2.45833E - 05 \qquad (3)$$

The coefficients of regression model can be estimated from the experimental results by regression analysis with the software MINITAB (ver.16). The interaction and square effects have been presented in the Table 4, 5 and the mathematical relationship between the output response and the input parameters has been established by the equations 2, 3.

Table 4: Analysis of Variance for Kerf Width

Source	DF	Adj SS	Adj MS	P- Value
Model	14	0.014223	0.001016	0.000
Linear	4	0.003057	0.000764	0.000
T_{on}	1	0.000311	0.000311	0.041
T_{off}	1	0.000557	0.000557	0.009
IP	1	0.001690	0.001690	0.000
SV	1	0.000499	0.000499	0.013
Square	4	0.004302	0.001075	0.000
T_{on}*T_{on}	1	0.000967	0.000967	0.001
T_{off}*T_{off}	1	0.001474	0.001474	0.000
IP*IP	1	0.000961	0.000961	0.001
SV*SV	1	0.000465	0.000465	0.015
Interaction	6	0.006865	0.001144	0.000
T_{on}*T_{off}	1	0.001760	0.001760	0.000
T_{on}*IP	1	0.000818	0.000818	0.002
T_{on}*SV	1	0.001588	0.001588	0.000
T_{off}*IP	1	0.001257	0.001257	0.000
T_{off}*SV	1	0.001225	0.001225	0.000
IP*SV	1	0.000218	0.000218	0.082*

Table 5: Analysis of Variance MRR

Source	DF	Adj SS	Adj MS	P- Value
Model	14	1.91877	0.13705	0.000
Linear	4	1.64116	0.41029	0.000
T_{on}	1	1.48793	1.48793	0.000
T_{off}	1	0.03712	0.03712	0.007
IP	1	0.00494	0.00494	0.277*
SV	1	0.11116	0.11116	0.000
Square	4	0.09696	0.02424	0.003
T_{on}*T_{on}	1	0.02660	0.02660	0.019
T_{off}*T_{off}	1	0.01532	0.01532	0.065*
IP*IP	1	0.04749	0.04749	0.003
SV*SV	1	0.00048	0.00048	0.730*
Interaction	6	0.18064	0.03011	0.001
T_{on}*T_{off}	1	0.05050	0.05050	0.002
T_{on}*IP	1	0.00002	0.00002	0.950*
T_{on}*SV	1	0.09365	0.09365	0.000
T_{off}*IP	1	0.00471	0.00471	0.288*
T_{off}*SV	1	0.03177	0.03177	0.012
IP*SV	1	0.00000	0.00000	0.994*

RESULTS AND DISCUSIONS

The standard errors on estimation of the coefficients has been tabulated in the column 'SE coefficient'. The factors having p-value more than 0.05 are considered insignificant (shown with '*'symbol in p-column). The mathematical model made to represent MRR depicts that linear terms of *IP*, T_{on}, T_{off}, *SV* alongwith square and interaction terms of inputs have been the most influencing parameters in order of significance except the interaction plot *IP*SV* (p-value 0.082*).

The ANOVA coefficient as in Table 6 for the quadratic model depicts the value of Coefficient of determination R^2 as 96.85%, which shows significant value that how much variation in the response is explained by the model. The higher of R^2, indicates the better fitting of the model with the data. However, for kerf width R^2 is 93.36%, which accounts for the number of predictors in the model describes the significance of the relationship. It is important to check the adequacy of the fitted model, because an incorrect or under-specified model can lead to misleading conclusions. By checking the fit of the model one can check whether the model is under specified. The model adequacy checking includes the test for significance of the regression model, model coefficients, and lack of fit, which is carried out subsequently using ANOVA on the model. The fit summary recommended by the R^2-adjusted that the quadratic model is statistically significant for analysis of MRR and kerf width both.

Table 6: ANOVA coefficients and sum of error

Responses	S	R-sq(%)	R-sq(adj) (%)	Total Error
MRR	0.0625	96.85	94.09%	16
Kerf Width	0.0079	93.36%	87.54%	16

The effect of the machining parameters *(Ip,* T_{on} T_{off} *and SV)* on the response variables SR have been evaluated by conducting experiments as described in the previous section and analysed by using MINITAB 16. ANOVA has been employed to check the sufficiency of the second-order model. Since all the points on plot come close to form a straight line, it implies that the data are normal. It can be seen that the regression model is reasonably well fitted with the observed values. In addition figure 1 (a) and (b) depicted the trend analysis plot of the MRR and Kerf Width illustrates that the increase in T_{on}, discharge energy produced will be higher; this results in increased MRR and minimizes kerf width. Increasing the pulse-on time and peak current increases the number of electrons striking the work surface thus eroding out more material from the work surface per discharge.

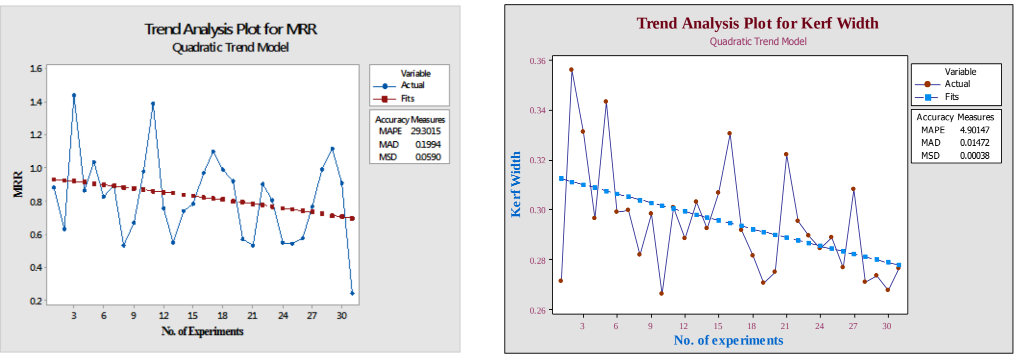

FIGURE 1. (a) Trend analysis plot of MRR vs No. of experiments, (b) Trend analysis plot of Kerf width vs No. of experiments

The main effect plots figure 2 (a) and (b) show the relation to the process parameters of *IP*, T_{on}, T_{off} and *SV* with MRR and kerf width. It can be seen from the figure 2(a) MRR tends to increase significantly with the increase in T_{on} and similar rate of decreased value of *SV*. From this observation it can be concluded that the T_{on} is directly and *SV* is inversely proportional to MRR for the given range of experiment conducted. In case of *IP* and T_{off} the values acted indifferently for any value of MRR. In figure 2(a) the main effect plot has been shown that the However, the MRR tends to increase with increase in T_{on}, especially at higher *IP*. It can be noted from the main effect plot figure 2 (b) that the kerf width increased with increase of T_{on} first then decresed abruptly and reached maximum value at 128 µm. It has been observed that kerf width is low at T_{on} =104 µS and T_{off} = 50 µS, followed by gradual increase in kerf width and then decrease maximum at the highest level of T_{on} and T_{off}. The *IP* characteristics acted exactly opposite in nature of the T_{off} characteristics. kerf width observed maximum at minimum value of *SV*=10 V then reached minimum value of kerf width at *SV*=25 V and finally the slope of curve shown increasing in nature.

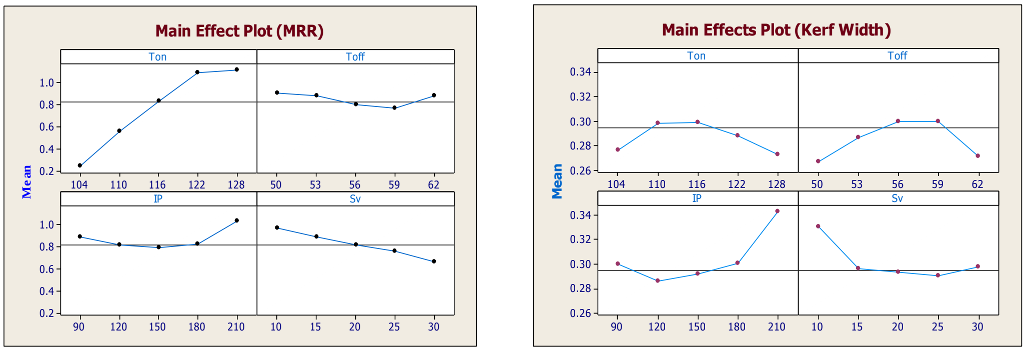

Fig. 2 (a) Main effect plot of MRR (in Y – axis), (b) Main effect plot of Kerf Width (in Y - axis) with the input parameters (in X –axis)

CONCLUSIONS

In the present study, the process parameters with significant influence on MRR and Kerf Width were determined by using RSM. A second order response model of these parameters are developed and found that T_{on}, T_{off} *and SV* significantly affect the MRR compared to the pulse peak current. The response model of the input parameters developed for Kerf width found quite significant except only one interaction term *IP*SV* (P- value 0.137). The most high value of MRR has been achieved at T_{on}=128 µS, T_{off}= 50 µS, *IP*= 210 A and *SV*=10 V. The lowest value of kerf width achieved at T_{on}=128 µS, T_{off}= 50 µS, *IP*= 120 A and *SV*=25 V within the experimental domain. The research findings of the present study based on RSM models can be used effectively in machining of the commercially available tool steel in order to obtain best possible WEDM efficiency.

REFERENCES

1. G. Selvakumar, G. Sornalatha, S. Sarkar, S. Mitra, "Experimental investigation and multi-objective optimization of wire electrical discharge machining (WEDM) of 5083 aluminum alloy", Trans. Nonferrous Met. Soc. China **24**, 373_379, (2014)
2. M. Durairaj, D. Sudharsun, N. Swamynathan, "Analysis of Process Parameters in Wire EDM with Stainless Steel using Single Objective Taguchi Method and Multi Objective Grey Relational Grade", International Conference on Design and Manufacturing, IConDM 2013, Procedia Engineering **64,** 868 – 877, (2013)
3. Neeraj Sharma, Ajit Singh, Renu Sharma, Deepak, "Modelling the WEDM Process Parameters for Cryogenic Treated D-2 Tool Steel by integrated RSM and GA" Procedia Engineering **97**, 1609 – 1617, (2014)
4. K.H. Ho, S.T. Newman, S. Rahimifard, R.D. Allen, State of the art in wire electrical discharge machining (WEDM), Int. J. Machine Tools Manuf. **44** ,1247-1259, (2004)
5. Brajesh Kumar Lodhi, Sanjay Agarwal, "Optimization of machining parameters in WEDM of AISI D3 Steel using Taguchi Technique", Procedia, CIRP **14** , 194 – 199,(2014)
6. M. K. Pradhan, R. Das, and C. K. Biswas, "Comparisons of neural network models on surface roughness in electrical discharge machining," *Proceedings of the Institution of Mechanical Engineers, Part B: Journal of Engg Manufacture*, vol. **223**, JEM1367 , (2009)
7. D. Kanagarajan, R. Karthikeyan, K. Palanikumar, and P. Sivaraj, "Influence of process parameters on electric discharge machining of WC/30%Co composites," *Proceedings of the Institution of Mechanical Engineers, Part B: Journal of Engineering Manufacture*, vol. **222**, no. 7, pp. 807–815, (2008).
8. A. Jaharah, C. Liang, A. Wahid, S.Z., M. Rahman, and C. Che Hassan, "Performance of copper electrode in electical discharge machining (edm) of AISI H13 harden steel," *Int. Journal of Mechanical and Materials Engineering*, vol. **3**, no. 1, pp. 25 -29, (2008).
9. P. Kuppan, A. Rajadurai, and S. Narayanan, "Influence of EDM process parameters in deep hole drilling of Inconel 718," *International Journal of Advance Manufacturing Technology*, vol. **38**, pp. 74–84, (2007).
10. K. Chiang, "Modeling and analysis of the effects of machining parameters on the performance characteristics in the edm process of Al_2O_3+TiC mixed ceramic," *International Journal of Advanced Manufacturing Technology*, vol**. 37**, no. 5-6, pp. 523–533, (2008)
11. O. H. Erzurumlu, T., "Comparison of response surface model with neural network in determining the surface quality of moulded parts," *Materials and Design*, vol. **28**, no. **2**, pp. 459–465, (2007).
12. Mohan K Pradhan*, Chandan K. Biswas, "Investigations into the effect of process parameters on MRR in EDM of AISI D2 steel by response surface methodology", Journal of Mechatronics and Intelligent Manufacturing (JoMIM), Vol. **1**, Issue No.3-4, , Sp. Issue , (2010).
13. R. L. Mason, R. F., D. Gunst, Texas, and J. L. Hess., "*Statistical Design and Analysis of Experiments With Applications to Engineering and Science"*, 2nd Edition, A John Wiley & sons publication, pp. 582-585(2003).
14. D. C. Montgomery, "Design and analysis of experiments," 8th Edition, *John willy and Sons Inc.*, pp. 501-510 (2013).

International Conference on Mechanical Engineering 2015
(ICME 2015) 18 – 20 December, 2015, Dhaka, Bangladesh

Paper ID : 398

Investigation On The Properties Of Denim Garment Treated With Indigofear Tinctoria And Natural Reducing Agent

Delwar Hossain[1,a)] , Mashiur Rahman Khan[2] and Zulhash Uddin [3]

[1]*Department of Textile Engineering, Dhaka University of Engineering and Technology, Bangladesh*
[2]*Department of Apparel Manufacturing Engineering, Bangladesh University of Textiles, Bangladesh*
[3]*Faculty of Textile Chemical Processing Engineering and Applied Science, Bangladesh University of Textiles, Bangladesh*

[a)]Corresponding author: delwar@duet.ac.bd

Abstract. The durability is one of the most important properties of denim garment demanded by user and consumer. The durability is directly influenced by the mechanical properties of denim garment. The aim of this work is to study the effects of dyeing denim with natural indigo dye (Indigofear tinctoria) reduced by natural reducing agent (Date palm) compare to conventional dyeing process. Denim garment properties such as seam performance, stiffness, strength and drapability of denim is measured and evaluated. The results showed that the denim samples dyed with indigofear tinctoria reduced by natural reducing agent has higher mechanical properties than denim dyed with conventional process. The morphological changes of the fibres in the denim garment were studied by using Scanning Electron Microscope (SEM). Chemical analysis also done through Fourier Transform Infrared Spectroscopy (FTIR).

INTRODUCTION

The growing public awareness has been expressed through an expanding premium market for goods & services that carry “Natural” or Eco-safe or “Green” or similar labels [1, 2]. Considerable chemical load in the wastewater results from the dyeing step, where dyestuff and specific chemicals are used to fix the dyestuff on textiles. For this reason, the use of eco-friendly natural dyes is getting more interests [3-5] and the use of low environmental impact biotechnology [6] gives rise to new sustainable technology. In case of indigo dye, the released dye bath contains reducing agents, alkali and other auxiliaries. Strong reducing agents are required to convert the indigo dye into the alkali soluble leuco-form to enable adsorption and diffusion into the fiber. The most widely used reducing agent for industrial indigo dyeing is sodium dithionite ($Na_2S_2O_4$) due to its powerful reduction power. However, the generation of non-renewable oxidation products such as sulfite and sulfate causes various problems in the disposal of the dyeing bath and the washing water. It is not possible to regenerate dithionite up to now, so the used dye bath has to be discharged into the wastewater [7]. Indigo is one of most important vat dyes in textile industry, with the current annual world consumption including other vat dyes, 33 million kilograms. It is used extensively today for dyeing cotton yarn in the manufacture of denims and blue jeans. It is a challenging task to develop cleaner processes for indigo dyeing due to the global trend of sustainability and the environmental concerns. The improvement of indigo dyeing process by eliminating or minimizing the production of inorganic waste from chemical reducing agents, can be made by many methods, such as the use of iron (II) complexes (gluconic acid complexes) [8], organic reducing agents [9], biological reduction [10], and electrochemical reduction [11,12,13]. However, most of these methods are not deemed satisfactory because of technical and economic limitations. Considering high starch content of banana peel we explored to use banana peel, extract as a biodegradable reducing agent to replace sodium dithionite for developing a greener indigo dyeing process [14].Like this only few research has been carried out. The modification in the process of application of natural indigo dyes to replace the reduction by sodium dithionite with natural, eco-friendly reducing system that should give similar color value with better durability of garments. In this paper it was aimed to apply locally available sweetened fruit Date palm as a reducing agent on natural indigo dye (Indigofear Tinctoria) & examined their performance in comparison with traditional sodium dithionite based indigo dyeing on the basis of different mechanical properties. In addition we tried to analyze the morphological changes of fiber in the fabric by using Scanning Electron Microscope(SEM).Also analyze the reduction agent solution by chemical analysis through Fourier Transform Infrared Spectroscopy (FTIR).

EXPERIMENTAL

Materials

Indigo Dyes & reducing agents

The commercially available natural indigo used in this study was extracted from Indigofera tinctoria, Brand-Living blue. The synthetic vat dye was collected from BASF. Natural reducing agent (Date) collected from a joydebpur fruit market.

Fabric Specification

TABLE-1. Fabric specification

Characteristics		Cotton
Yarn count (Tex)	Warp	12
	Weft	08
Ends per inch		120
Picks per inch		62
Weave		3/1 (Twill)

Methods

Extraction of Reducing Agents

At first natural reducing agent(Date palm) was collected from a local fruit market and chopping into small pieces. One liter natural reducing agent can produce of synthesis from 200 gram fruits peel. The fruit peels were boiled for 30 min to obtain extracts. The extract was filtered and preserves the extract as a liquid form in a suitable jar in a room temperature.

Dyeing

Conventional process

Pretreated samples were treated using fixed amount of natural indigo dye of 10 gm/l. This dyeing process conducted in dyeing solution containing Ethanol-8gm/l,$Na_2S_2O_4$-10 gm/l,Na_2CO_3-10gm/l and material to liquor ratio 1 :25 in laboratory scale. The process was carried out at temperature 50C for 30 min.

Experimental process

Pretreated samples were treated using fixed amount of natural indigo dye of 10 gm/l.This dyeing process coducted in dyeing solution containing Ca(OH)2-15 gm/l,Natural Reducing agent -10gm/l and material to liquor ratio

1 :25 in laboratory scale.The process was carried out at temperature 30°C for 30 min.

Depth of Shed (K/S value)

The K/S value at 650 nm was determined by Data Color spectrophotometer. The dyed samples using reducing agents such as sodium dithionite ,natural reducing agent (Date palm)were folded four times & after calibration of Data Color spectrophotometer was exposed and the values of samples was taken.

SEM study

Scanning electron microscopic studies were carried out for the natural indigo dyed samples with different reducing agents like, sodium dithionite & natural reducing agent (date palm) using JEOL 6360 microscope,Japan.It has operated in the range of different wave lengths & magnitude dimensions(35x,500x,1000x,2000x)

Testing and Analysis

To obtain and analysis the results treated samples were tested using Universal testing machine (Brand: Testometric, Model-M250-3CT, Origin: India);Fabric drape tester(Model M213, Brand –SDL ATLAS, Origin-UK),Fabric stiffness tester (Model-M003B,Brand:mesdan,Origin-UK). Tensile strength and elongation at break was determined by using fabric strength tester according to ASTM-D-5034 test method. Fabric stiffness measured according to ASTM D1388 method using cantilever stiffness process also fabric drapeibility was tested according to Cusick Drape test (BS 5058) method .Seam performance was analyzed according to ASTM-D1083-04.

RESULT AND DISCUSSION

Depth of Shade

The depth of shade of cotton fabric dyed with natural indigo dye using sodium dithionite and natural reducing agent (date palm) is shown in Table. 2 The k/S value at 650 nm for indigo dyed fabric using sodium dithionite is 13.2(strength 50.36), for dyed fabric using natural reducing agent(Date Palm) is 13.9 (strength 104.67).Hence the depth of shade of cotton fabric dye with natural indigo dye using natural reducing agent shows deeper shade then dyed samples using sodium dithionite.

TABLE 2: Colour measurement of different sample

Samples	K/S value	Color strength difference	F%	W% (100-F%)
Conventional Process	13.2	50.36	59.75	40.25
Experimental Process	13.9	104.67	52.56	47.44

3.2. Effect of reducing agents on the mechanical properties of dyed samples

3.2.1. Analysis of Fabric strength

By analysis the beheviour under stress the sample treated with natural indigo dye with naturul reducing agent shows significal strength properties in both warp and weft direction relate to samples dyed by natural indigo dye with sodium dithionite.Warp strength is better in case of sample NN,where as in SS sample the strength shows same results (Fig.2 a).The elongation is higher in both warp and weft yarn for sample which is treated with natural reducing agent reather then the sample treated with sodium dithionite during dyeing as areducing agent (Fig.2 b).In case of NN sample the value of elongation at breake is higher in weft side then the warp side. During weaving cotton fabrics were subjected to considerable tensions, particularly in the warp direction. In subsequent finishing processes such as calendaring this stretch was increased and temporarily set in the fabric. The fabric is then in a state of dimensional instability [15]. Subsequently when the denim garment was thoroughly wetted in dyeing solution, it tended to revert its more stable dimensions which results in the contraction of the yarns. This effect is usually greater in the warp direction than in the weft direction. This is known as relaxation shrinkage [15]. Due to relaxation shrinkage, PPI (picks per inch) was increased than untreated samples, as a result fabric elongation can be more. But in NS sample during dyeing the set of weft yarn may be effected by dyeing solution which containe strong alkali sodium dithionite as a result its hydrolyse the weft yarn and shows less strength compare to NN sample.

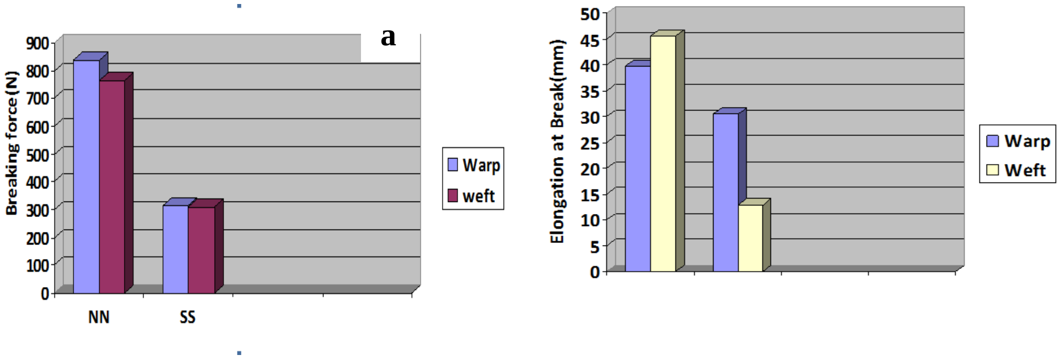

** NN= Dyed sample using natural indigo dye with natural reducing agent(date palm); NS= Dyed sample using natural indigo dye with sodium dithionite.

FIGURE. 2. a) Strength of of dyed fabric using different reducing agents b) Elongation of dyed samples

Seam performance analysis

Seam performance is a major indicator of garments durability. The seam performance was analyse by identifying the seam strength and unseam strength .The results(Table. 3) shows that the NN samples shows better and higher result compare to NS sample.

TABLE.3 Determination of seam strength

Test no.	Process	Width (mm)	Seamed strength (kgf)	Unseamed strength (kgf)
1	Natural indigo dye +Natural reducing agent (NN)	6	20.98	94.47
2	Natural indigo dye +Sodium dithionite (NS)	6	19.55	55.01

Analysis of Mechanical Properties

To determine the mechanical properties, Fabric stiffness and fabric drapebility were tested. In both case its seems that bending length (CMS) valued low for NN samples 1.36 where as for NS sample it is 1.51.Its indicates that the NN sample is more softer then NS sample. For drapeibility, the drape co-efficient is 91.20% for NS sample and 89.50% for NN sample. This results(Table. 4) disclosed that the sample dyed with natural indigo dye using natural reducing agent impart higher drapeibility compare to sample dyed with natural indigo dye using sodium dithionite.

TABLE .4 Determination of fabric stiffness and fabric drapeibility

Mechanical Properties	Unit	With Natural Reducing agent(NN)	With Sodium dithionite(NS)
Fabric Stiffness	Bending Length(CMS)	1.36	1.51
Fabric drapeibility	Drape Co-efficient (%)	89.50	91.20

3.2.4. Elemental analysis by FTIR

An intense C-S stretching mode can be observed at 1027 cm-1 confirming the presence of carbon-sulfur compound as a result sodium dithionite produce hazardous organic residual wastes(fig.3 a).[16] where as -N-H and O-H stretching mode were observed at 1636.62, 3450.01 & 2943.25 cm-1 in date palm reducing agent (fig.3. b) as more

prominent with some other waves as 2062.19 and 1079.48 evident the presence of =C-H,-C=O. So it is clear that date palm is more eco-friendly then sodium dithionite as a reducing agent for natural indigo dye.

FIGURE.3. a) FTIR analysis of Date palm reducing agent ; b) FTIR analysis sodium dithionite

SEM analysis

Effect of Natural indigo dye reduction with natural reducing agent (Date palm): The morphological of the dyed cotton fabric was examined by scanning electron microscopy (SEM) on the samples using Date palm and sodium dithionite as a reducing agents.Fig.4. A); B); C) and Fig.5. A); B); C) reveal the SEM images of grey control sample at magnification of 35X and 1000X and 2000X respectively, which were the cotton sample treating with natural reducing agent and sodium dithionite. The SEM results showed the convolution of the dyed samples in Fig.4.C) is more round and smooth where as in Fig.5.C) its show ribbon like structure with less uniform shape. The Fig.4 A) shows parallel ridges and less fibrils (projecting fibers) and ruptures visible in the images, because yarns are treated with natural reducing agent during dyeing process.

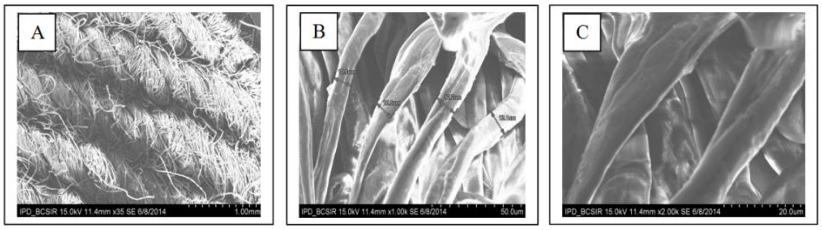

FIGURE.4. A) SEM analysis of date palm reduced sample at 35X ; B) SEM analysis of date palm reduced sample at 1000X C) SEM analysis of date palm reduced sample at 2000X

Fig. 5. shows loosened, disoriented and wrinkled surfaces due to fiber degradation by sodium dithionite which is strong alkali. due to presence of alkali crystal on the fiber internal structure it also weaken the fabric structure.From Fig 4. B) and Fig.5. B) it can be easily comparable the average uniformity of fiber in the fabric structure is presence in NN sample to NS samples.

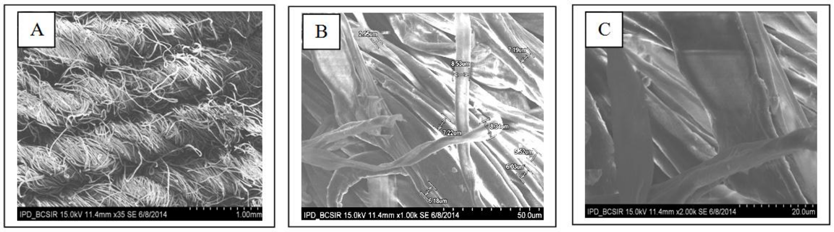

FIGURE.5. A) SEM analysis of sodium dithionite reduced sample at 35X ; B) SEM analysis of sodium dithionite reduced sample at 1000X C) SEM analysis of sodium dithionite reduced sample at 2000X

CONCLUSION:

From the various results obtained in this research work and the discussions carried out, the conclusions arrived are summarized below:

From this study it has been learned that use of natural indigo with natural reducing agent instead of synthetic reducing agent as sodium dithionite make more eco-friendly and cost effective way .
The objective measurements and evaluation affirmed that the mechanical properties of the sample treated by natural indigo dye with natural reducing agent is relatively better in comparison with natural dye with synthetic sodium dithionite so that posses higher durability and lifetime of garments. The depth of shade of natural indigo dyed fabric using natural reducing agent (date palm) is showed higher K/S value as 13.9 and obtained deeper shade leading to quality dying. The effectiveness of natural indigo dye using date palm on experimental samples is confirmed by SEM photography & FTIR analysis.

REFERENCE :

1. Bansal, P., & Roth, K.. Why companies go green: a model of ecological responsiveness. Academy of management journal, 43(4), 717-736(2000).
2. Esty, D., & Winston, A. Green to gold: How smart companies use environmental strategy to innovate, create value, and build competitive advantage. John Wiley & Sons. (2009)
3. R. Mansour, B. Ezzili, and M. Farouk, Fiber. Polym., 14, 786 (2013).
4. O. Avine, A. Celik, G. Geduk, and A. Yavas, Fiber. Polym., 14, 866 (2013).
5. K. H. Prabhu, M. D. Teli, and N. G. Waghmare, Fiber. Polym., 12, 753 (2011).
6. 4. R. Zhang and Z. Cai, Fiber. Polym., 12, 478 (2011).
7. T. Bechtold and A. Turcanu, J. Cleaner Production, 17, 1669 (2009).
8. B. Semet, B. Säckingen, G.E. Grüningen, Melliand Textilber. 76 (1995)161-164.
9. R.B. Chavan, Indian J. Fibre Text. 26 (2001) 93-100.
10. A.N. Padden, P. John, M.D. Collins, R. Hutson, A.R., Hall, J. Archaeol. Sci. 27 (2000) 953-956.
11. A. Roessler, X. Jin, DYES PIGMENTS. 59. (2003) 223-235.
12. M. Božič, V. Kokol, DYES PIGMENTS. 76. (2008) 299-309.
13. A. Roessler, D. Crettenand, Dyes Pigments 63. (2004) 29-37.
14. Shin, Younsook, Min Choi, and Dong Il Yoo. "Utilization of fruit by-products for organic reducing agent in indigo dyeing." Fibers and Polymers 14.12 (**2013**): 2027-2031.
15. Cookson, P. G., 1992, “Relationships between Hygral Expansion, Relaxation Shrinkage, and Extensibility in Woven Fabrics”, Textile Res. J. 62: 44.
16. Shang, Jiwu, et al. "Analysis of hazardous organic residues from sodium hydrosulfite industry and utilization as raw materials in a novel solid lubricant production." *Journal of hazardous materials* 198 (2011): 65-69.

International Conference on Mechanical Engineering 2015
(ICME 2015) 18 – 20 December, 2015, Dhaka, Bangladesh

Paper ID : 419

Fabrication Characteristics and Mechanical Properties of Rice Husk Ash Reinforced A380 Alloy Composites

Sheikh Jaber Nurani[1,a)], Chandan Kumar Saha[1, b)], Farzana Ferdous[1, c)], and M. N. Haque[1, d)]

[1]*Department of Materials and Metallurgical Engineering, Bangladesh University of Engineering and Technology, Dhaka 1000, Bangladesh*

[a)]Corresponding author: sheikh.jaber.nurani@gmail.com
[b)]chandan.buet08@gmail.com.
[c)]ffj025@gmail.com
[d)]nhaque@mme.buet.ac.bd

Abstract. Aluminium metal matrix composites reinforced with ceramic particles are widely used in aerospace and automobile industries due to their better mechanical properties than aluminium alloys. In this work scrap Aluminum piston is used as the matrix material and rice husk ash (RHA) which is common waste from burnt rice husk used as fuel in Bangladesh, is used as reinforcement. This creates an opportunity of waste management and alloy strength improvement at an affordable cost. Particle size ranges from 53 to 74 µm in 3, 6, 9 and 12% by weight was used as reinforcement with the aluminium alloy using stir casting method. For each composite samples, RHA particles were preheated to the temperature of 750 degree centigrade and held at this temperature for 2 hours. Then, these preheated alumina particles were added gradually into the molten matrix alloy and was stirred for 5 minutes. Gradual addition of particles in such way improves wettability and uniform distribution. Finally, the molten composites were poured into a permanent metallic molds at a temperature of 650 degree centigrade. The mechanical properties and microstructural characterization of the fabricated composites were investigated. The result reveal that tensile strength, compressive strength and hardness of the aluminium alloy-RHA composites increases with increase in RHA particles because the highly dispersed RHA particles severely limits the movement of dislocation through the metal matrix. But increase in the weight fractions of RHA particles slightly decreases the ductility of the composites. Density of the composites decreases with addition of RHA particles hence increases the specific strength. Microstructural study shows the fine dispersion of RHA particles in composites.

INTRODUCTION

The metal matrix composites (MMCs) have higher physical and mechanical properties such as superior strength to weight ratio, high modulus, strength and excellent wear resistance [1]. Aluminum metal matrix composites are extensively used in aerospace, automobile and electric power industries owing to its better mechanical properties [2]. Aluminium and magnesium alloys are used comprehensively for MMCs due to their light weight, excellent mechanical properties, easily availability and corrosion resistance [3]. Al_2O_3, SiC, TiC and RHA particles are widely used as reinforcement in aluminium alloy to improve mechanical properties and wear resistance [4-5]. In present work piston alloy containing higher amount of silicon has been used as master alloy because of its better mechanical properties and cast ability [5-6]. This work is a reward to efforts aimed at the development of recyclable piston alloy matrix composites with high performance indices at lower price. It is found that, ashes which is obtained from controlled burning of agro-wastes such as rice husk, baggase, bamboo leaf, ground nut shell and coconut shell can be used as reinforcement to improve the properties of AMCs and minimize the ecological burden of these wastes [6-7].

Now a day, more and more efforts have been given to use recycled wastes in composite materials as reinforcing fillers [8]. One of the agriculture waste by-products is Rice Husk Ash (RHA) which is abundantly available. It is found that high percentages of silica (SiO_2) as well as other refractory oxides such as aluminium oxide (Al_2O_3) and hematite (Fe_2O_3) are present in rice husk ashes [9-10]. Amorphous silica with ultra-fine size, very good reactivity and huge surface area can be produced under controlled burning conditions. Therefore, rice husk ash to reinforce aluminium metal as a source of silica particulate will produce a material that exhibits combination of physical and mechanical characteristics of both the metal matrix and the silica from the ashes [11]. Usman et al [12] observed better mechanical properties when RHA is used as reinforcement in aluminum alloy. There are different routes by which a metal-matrix composite can be manufactured e.g. solid phase, liquid phase and vapour phase production techniques. In this work stir casting process has adopted because of its important advantages than other techniques e.g. the wide selection of materials, better matrix particle bonding, easier control mixer structure, simple and inexpensive processing, flexibility components and applicability of large quantity production, excellent productivity for near net shaped [9-12].

In current research it is focused to make use of the rice husk ash (3%, 6%, 9% and 12%) to produce aluminium alloy matrix composites by dispersing it through stir cast route into matrix. Mechanical properties, Microstructural study both optical and scanning electron microscope (SEM) shows the fine dispersion of RHA particles in matrix.

EXPERIMENTAL

The scrap piston was bought from local market was melted in a pit furnace at 750^{0}C. Degasser was used before pouring to remove dissolved gasses and then poured in sand mould at 650^{0}C. Rectangular shaped bar was produced which was used as master alloy. Table 1 shows the composition of the master alloy, which is alloy grade A 380 –

TABLE 1. Composition of matrix alloy

Si	**Cu**	**Mg**	**Mn**	**Fe**	**Ni**	**Zn**	**Cr**	**Al**
9.78	3.20	0.58	0.56	0.36	0.21	0.12	0.02	Bal

A perforated metallic sheet was used to carry combustion of the rice husk. Perforations provides air circulations which aids combustion. Dry rice husks were placed on the perforated metallic sheet and rice husks were left to cool at room temperature after complete burning. Then RHA was heated at temperature 700ºC for 4 hours to reduce the volatile and carbonaceous matters of the rice husk ash. The sieve analysis was performed to separate rice hush ash particles size of 53-74 µm. The chemical composition of the rice husk ash is given in the table 2.

TABLE 2. Composition of RHA particle

SiO_2	**Al_2O_3**	**MgO**	**Fe_2O_3**	**Others**
97.10	1.12	0.83	0.32	Bal

The desired composites were produced by the. One kg of master alloy placed in graphite crucible in a pit furnace and melted at 750°C. After complete melting, degasser is used to remove dissolved gasses. After that master alloy melt was transferred to holding furnace of the stir casting machine to hold the temperature. Then the alumina particle size of 53-74µm was gradually added into the molten alloy which was continuously stirred at 500 rpm. The particle was preheated at about 750°C for 2 hours before adding in order to improve its wettability. The particle was added in the vortex which was produced due to stirring and after adding all the particle, the stirring was continued for 5 minutes in order to get a homogeneous distribution of the reinforced particle. Four different composites were produced by adding 3%, 6%, 9% and 12% RHA in matrix alloy respectively. Finally the composite was poured into permanent cast iron mould at 650°C. After cooling to room temperature three tensile samples were prepared by following ASTM E8 standard. Compression tests are carried out as per ASTM-E9-95. Hardness of the samples was tested by Rockwell hardness tester using B scale. Charpy impact tests were conducted on notched specimens. Test specimens measured 75 mm length with diameter of 10 mm. The notch had a depth of 2 mm and a notch tip radius of 0. 02 mm at an angle of 45 Degree. The measured experimental density was used to estimate the porosity levels in the composites. This was achieved by comparing the experimental and theoretical densities of each weight ratio of RHA reinforced composite produced.

RESULT AND DISCUSSION

Effect of Reinforcement on Hardness

The relation between hardness and percentage of reinforcement is shown in fig. 1 and it is seen that hardness increases linearly with the addition of RHA particles. Because RHA increases the surface area by reducing the grain size of matrix. The presence of such large surface area and hard particle SiO_2 (RHA) provides higher resistance to plastic deformation, hence increase the hardness [13-14].

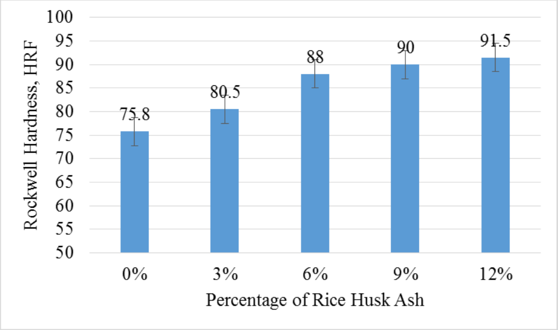

FIGURE 1. Variations of hardness with addition of RHA in matrix alloy

Effect of Reinforcement on Tensile Strength and Compressive Strength

All the composite has higher strength than matrix alloy which is shown in figure 2(a). When load is applied, RHA particle acts as dislocation barrier and increases tensile properties [11]. It is also observed that tensile strength increases with addition of RHA particle upto 9% because more the particle, more the resistance to dislocation and improvement in tensile strength. Adhesion between matrix and particle is good when amount of reinforcement is lower. With the increment of particle addition, agglomeration of particle and poor wettability between matrix and particle happens. This is why decrease in tensile strength of the composite containing 12% RHA than that of composite containing 9% RHA.

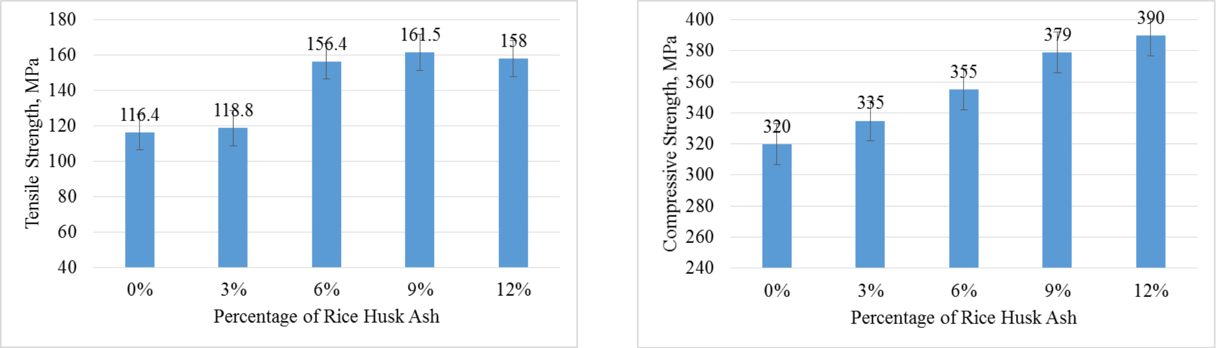

(a) (b)

FIGURE 2. Variation of (a) tensile strength, (b) compressive strength, with addition of RHA particle in matrix alloy

Variation of compressive strength with addition of RHA is shown in 2(b). Compressive strength increases with addition of RHA as hardening is occurred of the matrix alloy by the help of RHA particle.

Effect of Reinforcement on Ductility

Relation between elongation and RHA is presented in Fig. 3(a). Elongation decrease with addition of RHA due to hardening of the matrix by RHA particle. Clustering of particle also responsible for that reduction of elongation [15]. Impact strength shown in Fig. 3(b) also decreases as expected with addition of RHA particle. Because increment of the hardness with addition of RHA particle decreases the load bearing capacity.

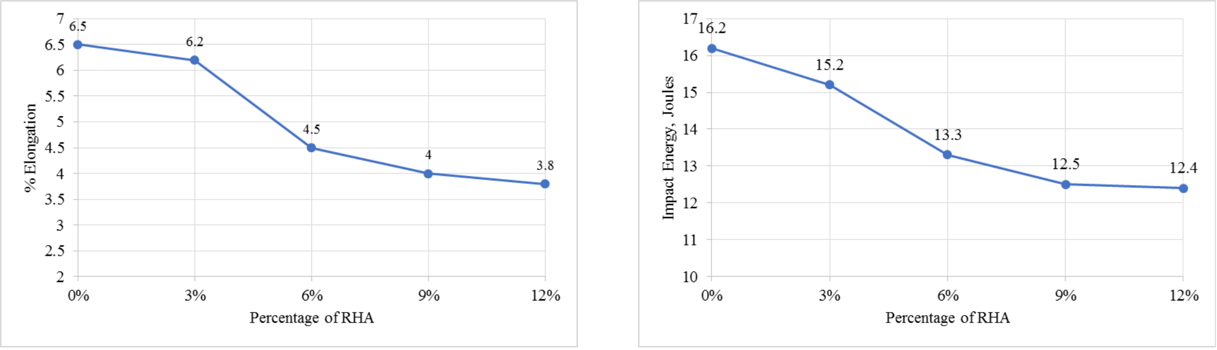

(a) (b)

FIGURE 3. Variation of (a) Elongation, (b) Impact Energy, with addition of RHA particle in matrix alloy.

Effect of Reinforcement on Density and Porosity

The effect reinforcement of RHA on the density and percent porosity of the composites is illustrated in fig. 4 as a function of reinforcement content. Technically, porosity is inversely proportional to density, i.e. higher porosity and lower density leads to poor mechanical properties.

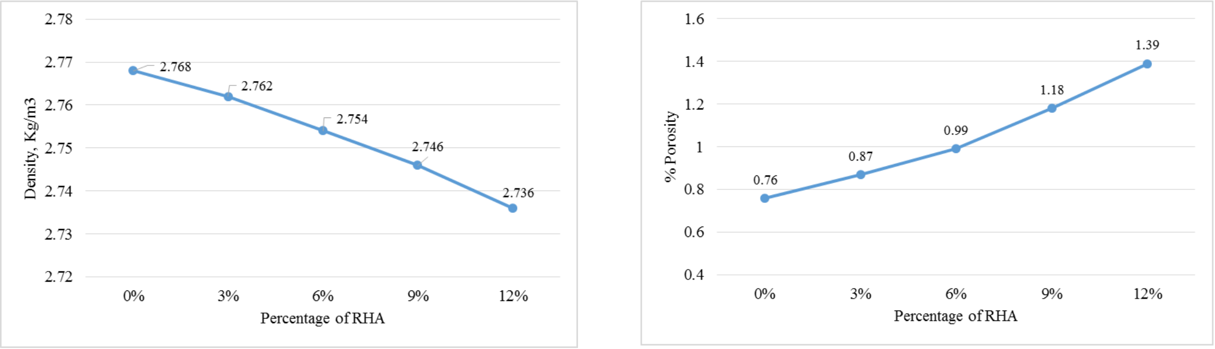

(a) (b)

FIGURE 4. Variation of (a) Density, (b) Porosity, with addition of RHA particle in matrix alloy.

It is observed from the fig. 4 that there’s existence of porosities in the produced composites and porosities increases with addition of RHA particles. Poor adhesion between particle and matrix due to poor wettability causes increase in porosity and decrease density of the composite [16]. Also specific weight of RHA is lower than aluminium alloy hence decrease density. It is however a positive sign that the percent porosities are between 0.76 – 1.39% which is within the acceptable range of 4% in cast metal matrix composites.

Microstructure

Fabrication of metal matrix composites reinforced with RHA particles by casting processes is usually challenging because of the very low wettability of RHA particles along with the agglomeration phenomena which results in non-uniform distribution, casting defects like porosity and hence results in poor mechanical properties [15].

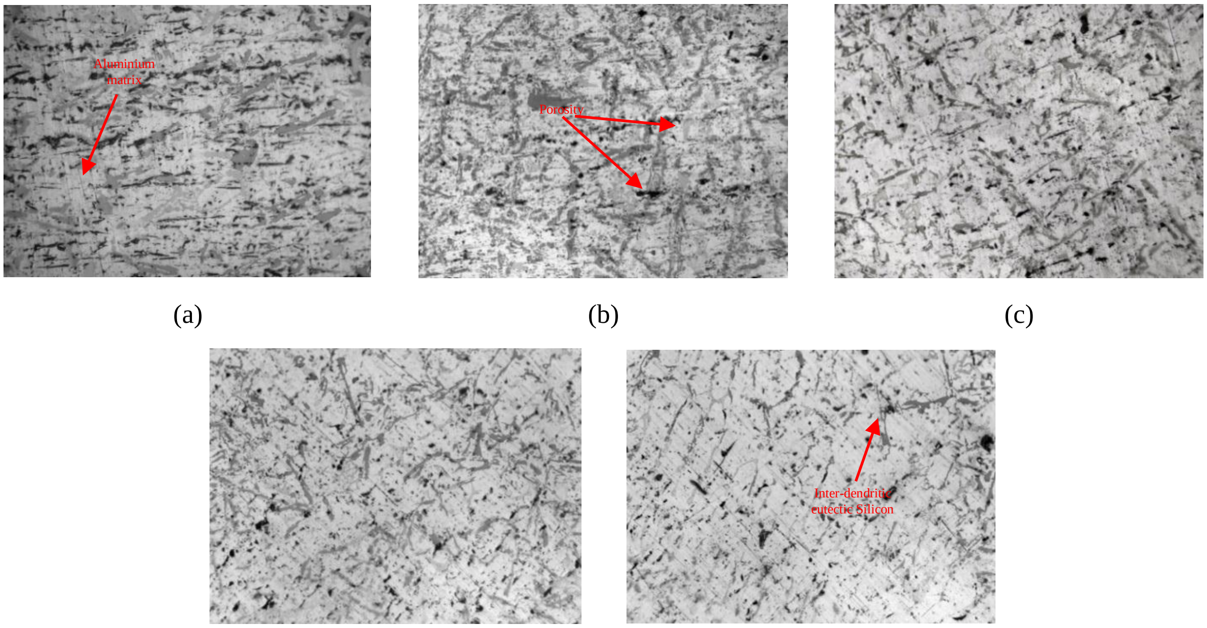

(a) (b) (c)

(d) (e)

FIGURE 5.200X optical micrograph showing the microstructure of the a) matrix alloy, b) Composite containing 3% RHA, c) Composite containing 6% RHA and d) Composite containing 9% RHA particles, e) Composite containing 12% RHA particle

The microstructures in fig.5 indicates that grain size of the alumina particle reinforced composite is smaller than the matrix alloy without alumina particles because the particles act as heterogeneous nucleation sites during solidification [17]. Islands of well dispersed silicon in an alpha matrix. The microstructure consists of alpha plus fine eutectic. The prepared composites microstructure contains primary α-Al dendrites, eutectic silicon and primary silicon and alumina particle. Primary silicon has a blocky appearance but intermetallic and eutectic are flaky which is shown in fig. 5 [18]. We observe islands of well dispersed silicon in an alpha matrix in fig 5. Examination of the composite microstructures shows that the distribution of particles in the matrix alloy is uniform. It is observed from the fig that porosity increases with addition of RHA particle. When the composite is reinforced with 5% alumina (Fig. 5) three is low agglomeration at the matrix and comparatively good adhesion between matrix and particle, while the further addition (10% and 15% RHA) of particles increases the agglomeration of particles at places and poor adhesion between matrix and particle (Fig.5). For this reason micrographs shows an increasing trend in porosity with increasing RHA particles.

CONCLUSION

All Composites were prepared by the less expensive stir-casting method using mechanical mixing of the molten alloy.The result showed increase in both tensile and compressive strength with increasing RHA particle. The increase in tensile strength is due to the addition of hard particles which hinders dislocation motion.The effect of hard alumina particles in aluminium alloy was studied with respect to hardness value and increasing trend in hardness was observed. This increase in hardness can be explained by work hardening which occurred as a result of particle addition, whereas ductility decreased with the addition of particles.The study of microstructure of the composite specimen revealed that grain size became finer with the increasing alumina particles which contributed to improved mechanical properties. Wettability of the particles within the molten matrix had been decreased by increasing the reinforcement particles which resulted in agglomeration phenomena and porosity increased due to agglomerated reinforcement particles.

ACKNOWLEDGMENTS

We acknowledge the careful supervision and constant guidance of Dr. M.N. Haque and the assistance of Dr. Ahmed Sharif in our project. The authors also acknowledge with thanks to the Department of Materials and Metallurgical Engineering of Bangladesh University of Engineering and Technology for giving us the opportunity and funding for our project. We are also thankful to other lab coordinators for their help throughout the whole project related works.

REFERENCES

1. S.A. Sajjadi, H.R. Ezatpour, and H. Beygi, Mat Sci Eng A **528**, 8765-8771(2011).
2. Y. Sahin, and M. Acilar, Compos Part A **34**, 709-718 (2003).
3. S.V. Prasad, and R. Asthana **17**, 3445-453 (2004).
4. U. Rattanasak, P. Chindaprasirt, and P. Suwanvitaya, International Journal of Minerals **17**, 654 (2010).
5. S.J. Nurani, C.K. Saha, and M. N. Haque, International Journal of Innovative Science and Modern Engineering (IJISME) **3**, 75-79 (2015).
6. V.S.Aigbodion, S.B. Hassan, E.T. Dauda, and R.A. Mohammed, Tribology in industry **33**, 28-35 (2011).
7. K. Katsuyoshi, O. Hideki, U. Junko, and U. Takateru, Material transactions **46**, 2586-2591 (2005).
8. M. K. Surappa, Sadhana **28**, 319–334 (2003).
9. P.B. Madakson, D.S. Yawas, and A. Apasi, Int. J. of Engg. Sci. & Tech. **4**, 1190-1198(2012).
10. H. Zhang, X. Zhao, X. Ding, H. Lei, X. Chen, and Z. Wang, Bio resource Technology **101**, 1263–1267(2010).
11. A. M. USMAN, A. Raji, N. H. Waziri, and M. A. Hassan, Leonardo Electronic Journal of Practices and Technologies **25**, 84-98 (2014).
12. A. M. Usman, A. Raji, M. A. Hassan, and N. H. Waziri, the International Journal of Engineering and Science **3**, 2319–1805 (2014).
13. P.K. Rohatgi, R.Q. Guo, H. Iksan, E.J. Borchelt, and R. Asthana, Metallurgical & Materials Transaction A **244**, 22 – 30 (1997).
14. S.Basvarajappa., G.Chandramohan., A.Mahadevan.,R.Subramanian., and P. Gopalakrishnan, Wear, 262, 1007–1012 (2007).
15. M.K.Surappa, Materials Science and Engineering: A **480**, 117-124 (2008).
16. D. S Prasad,and A. R.,Krishna, International journal of engineering science and technology **12**,7603-7608 (2010).
17. S. Nagarajan,B. Dutta, and M. K. Surappa, Compos Sci. Technol. **59**, 897–902 (1999).
18. A.J. Moffat, S. Barnes, B.G. Mellor, and P.A.S. Reed, International Journal of Fatigue **27**, 1564–1570(2005).

International Conference on Mechanical Engineering 2015
(ICME 2015) 18 – 20 December, 2015, Dhaka, Bangladesh

Paper ID : 438

Effect Of Zr And Ti On Microstructures And Mechanical Properties Of As-Cast Al-Mg Alloys

Sanjidah Akter Urmi[1], Fahmida Gulshan[a)], Abdullah Al Shafe, A. H. M. Azadur Rahman and ASW Kurny

Department of Materials and Metallurgical Engineering, Bangladesh University of Engineering and Technology, Dhaka-1000, Bangladesh.

[a)] fahmidagulshan@mme.buet.ac.bd

Abstract. The influence of Zirconium and Titanium on the structure and mehanical properties of Al-5Mg alloy was investigated. 2% Zirconium and 2% Titanium individually and combined 2wt% Zirconium and 2wt% Titanium was added to Al-5Mg alloy by melt processing technique. The microstructure of the cast alloys was observed under optical microscope and its relation tensile properties and microhardness was investigated. The addition of Zr and Ti was found to refine the grains of Al-Mg alloys. This occurs due to the precipitation of Al3Zr and Al3Ti intermetallics which pin dislocations and hinder grain boundary motion. This also caused , increase in yield strength, ultimate tensile strength, hardness and decrease in percent elongation . Maximum yield strength and minimum percent elongation were observed for Al-5Mg-2Zr alloy and Al-5Mg-2Ti alloy respectively. Al-5Mg-2Zr-2Ti alloy gave maximum hardness and maximum tensile strength9 point font.

INTRODUCTION

Aluminium alloys containing magnesium as the primary alloying element are a group of non-heat treatable alloys possessing high ductility, excellent corrosion resistance, medium strength and weldability. Wrought Al-Mg alloys have aerospace, automotive, marine and cryogenic applications whereas cast alloys are mainly used for their corrosion resistance, food processing, dairy and chemical processing applications [1, 2]. Alloys with low Mg content possess good formability whereas the high Mg alloys have superior castability and high strength [3]. Strengthening in these alloys is primarily achieved by the solid solution strengthening by Mg, which has a substantial solid solubility in Al. But to achieve strength level analogous to the precipitation hardening alloys, high Mg levels are required. But this high level of Mg poses processing challenges and makes these alloys prone to stress corrosion cracking [3,4].

In 1971, Wiley first proposed an effective way of enhancing the strength of Al alloys which involves the addition of alloying element [5]. These alloys often contain small additions of transition elements such as scandium, manganese, zirconium or titanium to improve the strength of the alloy by grain refinement [6]. Addition of these transition metals form tri-aluminides having low solubilities and diffusion coefficient and control evolution of grain, sub-grain structure and grain coarsening during subsequent processing operations. [7- 9]. Addition of Zr results in the precipitation of Al_3Zr particles in the Al matrix [10]. Due to their high melting points compared with that of Al matrix, these particles are coherent and have good thermal stability. Additionally, their stability against coarsening and re-dissolution cause a more even distribution of dislocations and pin grain boundaries. More than 0.1% addition of Zr causes Al_3Zr particles to form as a primary phase from the melt during rapid solidification which act as nuclei for the solidification of Al. Thus Zr causes grain refining operation of Al [7, 11-13]. Addition of Ti during thermal processing causes Al_3Ti intermetallic phase to form in situ which is intrinsically stable with a melting point of 1623 K [14,15]. This high melting point along with low density of about 3.3 Mg/m^3 and slowest diffusivity in Al (e.g.

diffusivity 3.0×10^{-19} m^2s^{-1} and 3.2×10^{-17} m^2s^{-1} at 500°C and 600°C respectively) make these strengthening dispersoids particularly suitable and resistant to coarsening which is a very important for strength retention at high temperature [14].

The main aim of this study was to observe the microstructural changes of as-cast Al-5 weight% Mg alloy due to the addition of 2 weight% Zr and 2 weight% Ti both individually and jointly and then relate the microstructural changes to the changes in mechanical properties.

EXPERIMENTAL PROCEDURES

Casting Procedure:

Alloys with chemical compositions given in the table 1 were used in this paper. Aluminum was introduced as a precursor bar form and magnesium was taken in ribbon form. Zirconium and titanium were taken in as nano-powder.

TABLE 1: Alloy Compositions (balance Al) wt%

Alloy	**Mg**	**Zr**	**Ti**
Alloy 1	5		
Alloy 2	5	2	
Alloy 3	5		2
Alloy 4	5	2	2

The alloys were melted in a natural gas fired clay-graphite crucible furnace using fluxing agent. The melt temperature was monitored with a chromel-alumel (type K) thermocouple. The temperature of the melt was raised to 800-900oC and kept at that temperature for some time and the melt was stirred with an alumina rod for about 30 seconds. During this time, sufficient amount of degasser, comprised mainly/mostly of ammonium chloride (NH4Cl), was added to the melt. After the skimming the impurities off, the melt was poured in to a metal mold preheated to almost 2000C. Cast samples were then allowed to cool to room temperature and were cut by a hacksaw to a size of 1/2'' x 1/2" x 1/2" size for hardness measurement and optical microscopic analysis.

Microstructural Analysis:

For microstructural analysis, a small piece of sample was cut near from the corner. It was then grounded, fine polished with emery papers, further polished in a velvet paper by using alumina powder and then etched using etching reagent that contains 25 ml CH_3OH, 25 ml HCl, 25 ml HNO_3 and 1 drop HF. Microstructures of the samples were then observed using an optical microscope (OPTIKA, ITALY, B-600 MET).

Tensile Test:

Tensile test was conducted at room temperature using INSTRON 3369 universal testing machine. Samples were cut according to the DIN standard and tested using a common strain rate of 10^{-3} S^{-1}. In each alloy at least 3 samples were tested and then average values were taken. Three parameters were extracted from the recorded curves: the ultimate tensile strength (UTS), the yield strength (YS) and the percentage elongation.

Hardness Test:

Rockwell hardness was measured using Rockwell hardness testing machine (FR-IE, Future Tech. Corporation, Tokyo, Japan) using All hardness measurements were performed on blocks of > 5 mm thickness using F scale. The blocks for hardness measurement were ground using 600 µm SiC paper prior to hardness measurements. A 1/16 inch steel ball indenter was used. A load of 60 kgf was applied for a period of 15 s.

RESULTS AND DISCUSSION

Microstructural Analysis:

Figure 1(a) shows different features of alloy 1. Upper left and bottom left of figure 1(a) show the primary dendrites which appear due to rapid solidification. Upper right of figure 1(a) shows the secondary dendrite growth from the primary dendrites. Bottom right of figure 1(a) shows clearly the secondary dendrite arm spacing (SDAS).

Figure 1(b) shows different features of alloy 2. Upper left of figure 1(b) shows the dendrite structure. Upper right of figure 1(b) shows porosity. Middle left of figure 1(b) shows the primary and secondary dendrite growth. Bottom left of figure 1(b) shows clearly the SDAS.

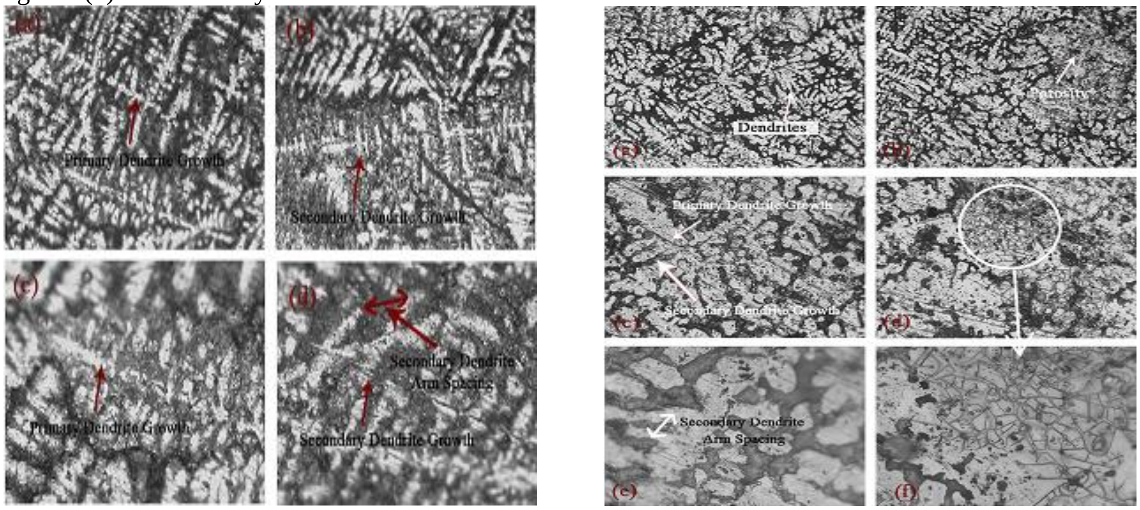

(a) (b)

FIGURE 1. (a) Microstructure of Alloy 1 (Al-Mg), Magnification: 200x. (b) Microstructure of Alloy 2 (Al-Mg-Zr), Magnification: 200x

Figure 2(a) shows different aspects of alloy 3. Upper left and upper right of figure 2(a) show the dendrite structures. Middle left and middle right of figure 2(a) reveal the primary and secondary dendrite growth respectively while Bottom right of figure 2(a) shows the SDAS.

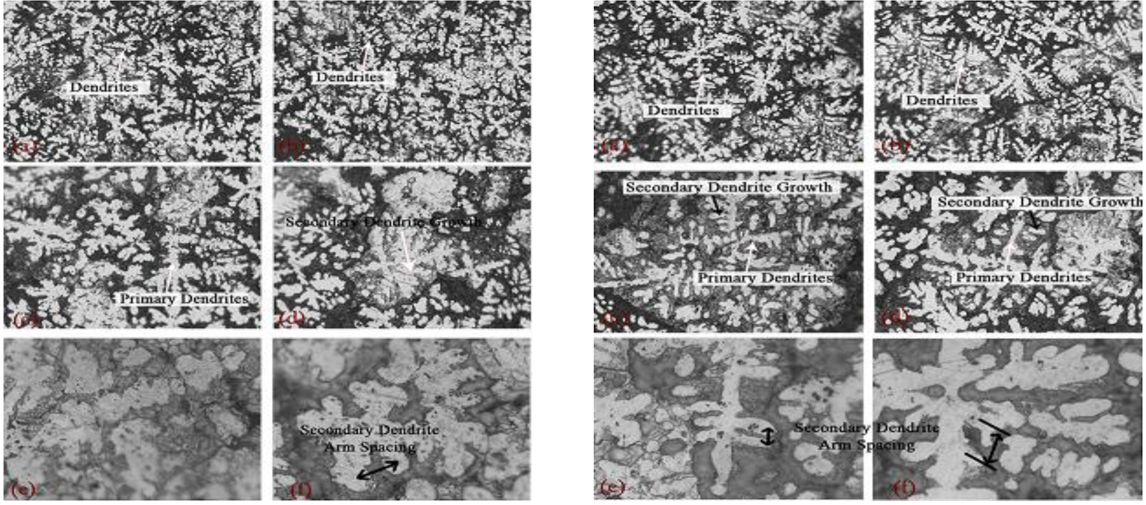

(a) (b)

FIGURE 2. (a) Microstructure of Alloy 3 (Al-Mg-Ti), Magnification: 200x. (b) Microstructure of Alloy 4 (Al-Mg-Zr-Ti), Magnification: 200x

Figure 2(b) shows the microstructures of alloy 4. In the figures, Upper left and upper right of figure 2(b) show the dendrite structure. Middle left and middle right of figure 2(b) show the primary and secondary dendrite growth. Bottom left and bottomright of figure 2(b) show the secondary dendrite arm spacing.

The calculated SDAS for alloy 1 to alloy 4 are shown in Table 2. This was calculated by measuring the distance between peak to peak or valley to valley in the secondary dendrite arms. The distance was then divided by the magnification number providing the result in centimeter (cm) unit. From the Table 2, the largest average SDAS value is for alloy 1, while the smallest value is for alloy 4 containing Zr and Ti along with Mg in pure Al. So it can be said that, grains are much smaller in alloy 4 than alloy 1 hence SDAS is lower in this alloy. Also, alloy 2 and 3 has smaller values (very close to alloy 4) of SDAS. So, alloy 2 and 3 also has very small grain sizes. Thus the combined effect of Zr and Ti in alloy 4 is not greatly increased compared to alloy 2 and 3. Overall interpretation can be standardized as, the grain refining action of third element like Zr or Ti individually is greater than combined action of them. Also, SDAS is smaller in alloy 3 than alloy 4 attributing better result of Ti than Zr.

TABLE 2. Secondary Dendrite arm spacing for alloy 1 to alloy 4

Alloy	**Measurement 1 (cm)**	**Measurement 2 (cm)**	**Measurement 3 (cm)**	**Measurement 4 (cm)**	**Average (cm)**
Alloy 1	0.0085	0.006	0.0045	0.005	0.006
Alloy 2	0.0025	0.0025	0.003	0.0025	0.002625
Alloy 3	0.0025	0.002	0.002	0.003	0.002375
Alloy 4	0.002	0.0035	0.0015	0.002	0.00225

Tensile Properties:

Figure 5(a) shows that alloy 4 has the best ultimate tensile strength (UTS) of 204.433 MPa followed by alloy 1 with ultimate tensile strength of 182.4 MPa. These values are more than the values obtained for alloy 3 and alloy 2 with ultimate tensile strengths of 181.0667 and 137 respectively. The abrupt increase of UTS in alloy 4 can be attributed due the combined effect of Zr and Ti trialuminides. Both of Al_3Zr and Al_3Ti provide grain refining by pinning effect. These particles provide obstacles against grain boundary movements. The decrease of UTS in alloy 2 and alloy 3 can be explained by the nonuniform distribution of Al_3Zr and Al_3Ti particles. From the figure it can be obtained that grain refining action of Ti is greater than Zr as Al_3Ti provide better grain refinement.

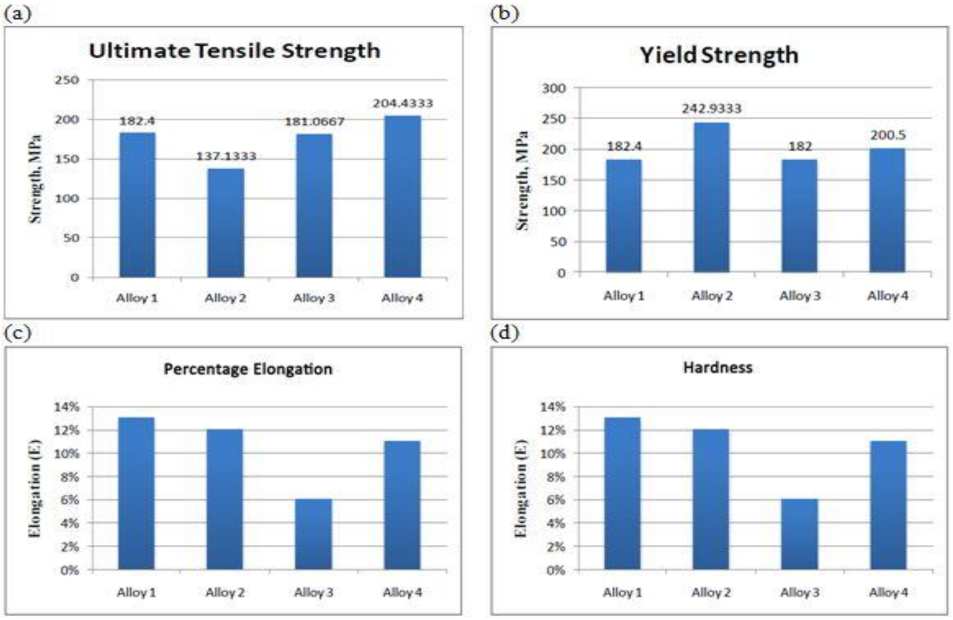

FIGURE 3. (a) variation of ultimate tensile strength for alloy 1 to alloy 4; (b) variation of yield strength for alloy 1 to alloy 4; (c) different percentage elongation (average value) for different alloys; (d) variation of hardness of alloy 1 to alloy 4.

Factors affecting UTS also affect yield strength of alloys. Yield strengths of different alloys have been shown in Figure 5(b). From the figure, yield strength is higher for alloy 2 containing Zr, followed by alloy 4, then alloy 1 and last of all alloy 3.

Figure 5(c) shows the elongation of the four alloys. Percentage elongation or ductility was the highest for alloy 1 and lowest for alloy 3. Since Zr and Ti precipitates increases the strength of alloys, it substantially also reduces the ductility. Sudden abrupt decrease in elongation for alloy 3 can be demonstrated by the defects in the testing setup along with structure of the alloy. Ti provides better grain refinement than Zr as can be stated by UTS values, but it reduces elongation as well. Al_3Ti is very coherent with Al matrix and thus provide it lower elastic energy of the coherent interface. Their smaller grain size and lower misfit also reduces elastic energy hence ductility decreases.

Hardness Test:

Figure 5(d) shows that alloy 4 has the highest hardness value followed by alloy 2. Alloy 4 has both Zr and Ti addition in the structure. Hence both Al_3Zr and Al_3Ti intermetallic compounds are present in the structure. Both of these intermetallic compounds are hard and from coherent particles with grain boundaries. They inhibit the propagation of grain boundary sliding. All of these criteria increase the hardness of alloy 4. On the other hand, unexpected large decrease of hardness in alloy 3 can be attributed to the inhomogeneous distribution of Al_3Ti particles.

CONCLUSIONS

It can be concluded that, Al-Mg alloy solidifies as a dendrite structure and the mechanical properties of the alloy depend on the extent of dendrites formed in the structure. Increase in secondary dendrite arm spacing (SDAS) decreases tensile strength and percentage elongation while decrease in SDAS increases them. Addition of both Zr and Ti refines the grains of Al-Mg alloy, refining action of Ti ~~is~~ being greater than that of Zr. Ultimate tensile strength is highest when both Zr and Ti are added. The yield strength of alloys containing both Ti and Zr is somewhat lower than alloy containing only Zr. Percentage elongation and ductility decreases with the addition of Zr or Ti or both. Ti reduces much ductility than Zr while combined action of Zr and Ti is higher than Ti alone. Combined action of Zr and Ti addition increases hardness than any other alloys tested.

The effect of Ti addition is more pronounced than when only Zr is added while combined action of Zr and Ti is higher than that of Ti alone. Combined action of Zr and Ti addition is most effective to increase hardness of Al-Mg alloys.

ACKNOWLEDGEMENTS

The authors express their thanks and gratitude to Dr. M. A. Gafur, Project Director, “Development of Materials for Tools and Biometallic implant”, PP & PDC, BCSIR for allowing access to the laboratory facilities and also for his valuable advice. They are especially indebted to Engr. Md. Rakibul Qadir (PP &PDC, BCSIR, Dhaka), for his continuous help and useful suggestions. The financial support provided by BUET is gratefully acknowledged.

REFERENCES

1. Sri Lathabai, P.G Lloyd, “*The effect of scandium on the microstructure, mechanical properties and weldability of a cast Al–Mg alloy”*, Acta Materialia, 50(2002), 4275-4292
2. S. Vijayan, R. Raju, Kumarasamy Subbaiah, N. Sridhar, Sajja Rama Koteswara Rao, *“Friction stir welding of AL-MG alloy optimization of process parameters using Taguchi method”*, Experimental Techniques 34(2009), 37–44
3. H. Watari , T. Haga, Y. Shibue, K. Davey, N. Koga, “*Twin roll casting of magnesium alloys with high aluminum contents”*, Journal of Achievements in Materials and Manufacturing Engineering 18(2006), 419-422
4. R. H. Jones, D. R. Baer, M. J. Danielson, J. s. Vetrano, “*Role of Mg in the stress corrosion cracking of an Al-Mg alloy”*, Metallurgical and Materials Transactions A 32(2001), 1699-1711.

5. Willey LA, inventor; Aluminum Company of America, assignee. Aluminum Scandium Alloy. US patent 3,619,181.(9 November 1971).
6. Anthony E Hughes, Nick Birbilis, Johannes M.C. Mol, Santiago J. Garcia, Xiaorong Zhou and George E. Thompson (2011). "*High Strength Al-Alloys: Microstructure, Corrosion and Principles of Protection, Recent Trends in Processing and Degradation of Aluminium Alloys"*, Prof. Zaki Ahmad (Ed.), ISBN: 978-953-307-734-5
7. A.E. Mahmoud, M. G. Mahfouz, H. G. Gad- Elrab, *"Influence of Zirconium on the Grain Refinement of Al 6063 alloy"*, Int. Journal of Engineering Research and Applications 4(2014), 188-194.
8. P. Cavaliere, Emanuela Cerri, Paola Leo, "*A Study of the Response of a Zr-modified 2014 Aluminium Alloy Subjected to Fatigue Loading"*, Materials Forum 28(2004), 172-177
9. Emmanuel Clouet, Alain Barbu, Ludovic La, Georges Martin, *"Precipitation kinetics of Al3Zr and Al3Sc in aluminum alloys modeled with cluster dynamics"*, Acta Mater. 53 (2005), 2313-2325.
10. Raeza Mahmudi, P. Sepehrband, Hamid M. Ghasemi, "*Improved properties of A319 aluminum casting alloy modified with Zr"*, Materials Letters, 60(2006), 2606-2610.
11. J.D Robson, , P.B Prangnell, "*Modelling Al3Zr dispersoid precipitation in multicomponent aluminium alloys"*, Materials Science and Engineering: A 352(2003), 240–250
12. Seong Ill Park, Seung Zeon Han, Si Kyung Choi, Hyuck Mo Lee, "*Phase Equilibria of Al(Ti,V,Zr) Intermetallic System"*, Scripta Materialia 34 (1996), 1697-1704.
13. P. Cavaliere "*Effect of friction stir processing on the fatigue properties of a Zr modified 2014 aluminium alloy*"Materials Characterization, 57 (2006), 100–104.
14. I. C. Barlow, H. Jones, W. M. Rainforth, "*Evolution of Microstructure and Hardening, and the Role of Al3Ti Coarsening During Extended Thermal Treatment in Mechanically Alloyed Al-Ti-O Based Materials*", Acta materialia 49 (2001), 1209–1224.
15. L.A. Dobrzański, K. Labisz , A. Olsen, "*Microstructure and mechanical properties of the Al-Ti alloy with calcium addition'*, Journal of Achievements in Materials and Manufacturing Engineering 26(2008), 183-186.

International Conference on Mechanical Engineering 2015
(ICME 2015) 18 – 20 December, 2015, Dhaka, Bangladesh

Paper ID : 497

A Simulation based Approach to Optimize Inventory Replenishment with RAND Algorithm: An Extended Study of Corrected Demand using Holt's Method for Textile Industry

Mohammad Sarwar Morshed[1, a)], Mostafa Mashnoon Kamal[1, b)] and Somaiya Islam Khan[1, c)]

[1]*Department of Mechanical & Production Engineering, Ahsanullah University of Science and Technology, Tezgaon, Dhaka, Bangladesh.*

[a)]msmorshed@hotmail.com
[b)] Corresponding author: kamal.mostafamashnoon@gmail.com
[c)]somaiyaislamkhan@gmail.com

Abstract. Inventory has been a major concern in supply chain and numerous researches have been done lately on inventory control which brought forth a number of methods that efficiently manage inventory and related overheads by reducing cost of replenishment. This research is aimed towards providing a better replenishment policy in case of multi-product, single supplier situations for chemical raw materials of textile industries in Bangladesh. It is assumed that industries currently pursue individual replenishment system. The purpose is to find out the optimum ideal cycle time and individual replenishment cycle time of each product for replenishment that will cause lowest annual holding and ordering cost, and also find the optimum ordering quantity. In this paper indirect grouping strategy has been used. It is suggested that indirect grouping Strategy outperforms direct grouping strategy when major cost is high. An algorithm by Kaspi and Rosenblatt (1991) called RAND is exercised for its simplicity and ease of application. RAND provides an ideal cycle time (T) for replenishment and integer multiplier (k_i) for individual items. Thus the replenishment cycle time for each product is found as $T \times k_i$. Firstly, based on data, a comparison between currently prevailing (individual) process and RAND is provided that uses the actual demands which presents 49% improvement in total cost of replenishment. Secondly, discrepancies in demand is corrected by using Holt's method. However, demands can only be forecasted one or two months into the future because of the demand pattern of the industry under consideration. Evidently, application of RAND with corrected demand display even greater improvement. The results of this study demonstrates that cost of replenishment can be significantly reduced by applying RAND algorithm and exponential smoothing models.

INTRODUCTION

The Study of inventory problems dates back to 1915, when F. N. Harris developed a very simple however useful model of an inventory problem [1]. Inventory is the total amount of goods or materials contained in a store or factory at any given time. The raw materials, work-in-process goods and completely finished goods that are considered to be the portion of a business's assets that are ready or will be ready for sale. Inventory represents one of the most important assets that most businesses possess.

The textile industry is primarily concerned with the production of yarn, and cloth and then the subsequent designing or manufacture of clothing and their distribution. A textile industry has a large variety of inventories that are critical to the overall profit of the firm and managing those are as a result very crucial. Inventories that are maintained by textile industries are (1) Raw materials (2) Finished fabric (3) Spare parts and (4) General store.

Inventory control involves maintaining a certain level of raw materials with safety stock for production that can response with the changing demands. For replenishing two way generally considered- (1) Independent replenishment

(2) Joint replenishment (JRP). Several algorithms have been suggested to find the solution for JRP. Kaspi and Rosenblatt in 1991, suggested a simple procedure, RAND, for determining the economic ordering quantity for items jointly replenished and their ordering frequency with respect to an ideal cycle time [2].In this research this algorithm has been followed to offer a suitable replenishment policy with replenishment cycle and ordering quantity. RAND is a mathematical programing method, with multi stage programming. A simulation based approach can provides more accuracy and less time consumption. That is why a simulation was used to run this model for determining the optimum solution.

In practice, inventory control system generally work in dynamic environment. Calculating ordering quantities, determining the appropriate reordering point, picking the accurate inventory replenishment policies and managing safety stock are not enough for rapidly changing environment. The decision maker must be able to monitor the trend and modify the replenishment strategy. From this viewpoint, this research is based on selecting an appropriate replenishing model for textile industries and demand forecasting by analyzing the trend of product demands.

LITERATURE REVIEW

Joint replenishment Problem (JRP) has been heavily researched since the early work of Starr and miller (1962), Goyal (1973) Shu (1971). Because of the major ordering cost, using group replenishment may lead to substantial cost savings. The savings from group replenishment are significant when the major ordering cost is higher. Many algorithm have been proposed to find the quality solution for JRP. Tactics to solving the JRP can be classified into two types: A direct grouping strategy (DGS) and an indirect grouping strategy (IGS). It is suggested that IGS outperforms DGS when major cost is high. This paper include the reviews of previous work on indirect grouping strategies. Goyal (1973) & Shu (1971) introduced methods to find an inventory replenishment policy which produced sub optimal solution [3, 4]. In 1974 Goyal developed an algorithm to find the optimal solution to minimize the total cost. He presented a systematic and enumerative method for determining the basic cycle time [5]. But his solution may be computationally prohibitive for large problem. In 1976 Silver introduced a simple heuristic to find the optimal or near optimal set of k_i, (frequency of ordering of product/multiple integer). His method then uses this k_i, to find the optimal or near optimal cycle time T minimal TC (total cost) [6]. Goyal & Belton (1979) published a modification of Silver's method which gave closer to optimal solution in most cases. He has given a modified formula to for getting k_i [7]. Goyal in 1988 published a method which improved upon Goyal (1974), Goyal & Belton (1979) and Silver (1976) [8]. A complete review of early work is found in Goyal & Satir (1989) [9].

Additional work by Kaspi & Rosenblatt (1991) resulted in an algorithm called RAND [2]. RAND was an improvement over Kaspi & Rosenblatt (1983) [10]. Silver (1976) heuristic became a part of new heuristic algorithm proposed by Kaspi & Rosenblatt (1983). Kaspi & Rosenblatt used the formula of determining the value of T (cycle time) from Silver's algorithm with a small modification of denoting item 1 with the lowest value of $(S+s_i)/D_iv_i$. Their algorithm may be viewed as a local improvement of Silver's in finding the ki. RAND was improvement over this algorithm by determining minimum and maximum values for T, T_{min} and T_{max}. A set of initial values of T are then determined from this range. For each values of these initial T, the 1983 algorithm is used to find the values for k_i. The authors did extensive experiment in order to compare their result with others. They concluded that RAND was an improvement over all other strategies and was almost as good as the optimal solution.

The approach to forecasting time series is to first specify a model, which is not for all case. This model is a statistical formulation of the dynamic relationships between that which we observe (i.e. the so called information set), and those variables we believe are related to that which we observe. It should thus be stated immediately that this discussion will be restricted in scope to those models which can formulated parametrically [11].

Muth was the first to suggest a statistical foundation for simple exponential smoothing (SES) by demonstrating that it provided the optimal forecasts for a random walk plus noise [12]. Further steps towards putting exponential smoothing within a statistical framework were provided by Box and Jenkins, Roberts, and Abraham and Ledolter who showed that some linear exponential smoothing forecasts arise as special cases of ARIMA models [13, 14, 15]. However, these results did not extend to any nonlinear exponential smoothing methods.

Exponential smoothing methods received a boost from paper published in 1985(Gardener) which laid the foundation for much of the subsequent work in this area [16]. Later in the same year, Snyder showed that SES could be considered as arising from an innovation state space model (i.e., a model with a single source of error) [17].Most of the work since 1980 has involved studying the empirical properties of the methods (e.g., Bartolomei and Sweet; Makridakis and Hibon) [18, 19], proposals for new methods of estimation (Ledolter and Abraham) [20] or has concerned statistical models that can be considered to underlay the methods (e.g., McKenzie) [21]. The damped multiplicative methods of Taylor gave the only genuinely new exponential smoothing methods over this period [22].

PROBLEM DEFINITION AND MODELING

The problem addressed in this article, called the inventory replenishment problem, is that of determining the replenishment cycle of ‘n’ different items that come from the same supplier as well as defining a proper demand for each item in order to minimize the total cost in due course. In these companies, the demand for each item is estimated. Then, based on these estimates, the inventory and planning department proceed to material planning. This results to two potential bad consequences, which ultimately causes increased production cost. For some cases, due to faulty or non-scientific demand forecast and replenishment policy, a large amount of excess raw material inventory is left off. On the other hand, a non-methodical forecast may also cause raw material shortage. In this study, we plan to suggest the optimal inventory replenishment strategy along with a scientific method of forecasting demand of chemical raw materials in a joint replenishment policy for the textile industry under consideration such that the current superfluous cost over chemical raw material replenishment is minimalized. The costs are (1) holding cost for on hand inventories, (2) major ordering cost (fixed cost associated with each order) and (3) minor ordering cost (variable cost incurred with each item included in the order).

The assumption that holds the most importance is that the replenishment policy currently pursued by textile industries is considered to be one which happens to be an individual replenishment for each item. This assumption is made as most of the textile industries do not follow any sort of scientific and systematic method of replenishment rather they highly depend on managerial decisions. A few other basic assumptions are – (1) Supply is readily available, (2) Demand for the each item is known and constant, (3) Holding cost is linear in the number of units held, (4) No quantity discounts, (5) No stock-outs are allowed, (6) No limit on the amount of storage available

Notations and Equations

D_i=Annual demand for product i (units/year)
h_i= Annual holding cost of product i ($/year)
s_i= The minor ordering cost incurred if product i is ordered in a replenishment ($/order)
k_i= Integer multiplier of replenish cycle time T for each product(ordering frequency)
T=Time between successive replenishment (years)
S= Major ordering cost associated with each ($/order)

For IGS the cycle time for product i is,

$$T_i = k_i T \tag{i}$$

And the ordering quantity for product i is,

$$Q_i = T_i D_i \tag{ii}$$

The total annual holding cost is,

$$C_H = \sum_{i=1}^{n} Q_i h_i / 2 = (T/2) \sum_{i-1}^{n} k_i h_i D_i \tag{iii}$$

The total annual ordering cost is,

$$Co = (S/T) + \sum_{i=1}^{n} s_i / k_i T = (1/T)(S + \sum_{i=1}^{n} s_i / k_i \tag{iv}$$

Finally the total annual cost is,

$$TC = C_O + C_H = (T/2) \sum_{i=1}^{n} k_i h_i D_i + (1/T)(S + \sum_{i=1}^{n} s_i / k_i \tag{v}$$

RAND Approach

The total annual cost is given by TC in equation (v) where T is a continuous variable and k_i (i=1, 2... n) is an integer. Initially from all products data, T_{min} and T_{max} are measured using the following two formulas,

$$T_{\min} = MIN(2si / hiDi)^{1/2} \tag{vi}$$

$$T_{\max} = [2(S+\sum_{i=1}^{n} s_i)/\sum_{i=1}^{n} h_i D_i]^{1/2} \qquad \text{(vii)}$$

Further calculation is proceeded by dividing this range with ‘*m*’ different equally spaced values of T, T_j (j=1, 2….m). For every T_j, and for all product’s (i=1, 2…, n) optimum ordering frequency, k_i^* is measured. For finding k_i, firstly k_i^2 is determined from,

$$k_i^{\,2} = (2s_i / h_i d_i T_j^{\,2} \qquad \text{(viii)}$$

This k_i^2 is compared with a condition, $L(L-1) < k_i^2 \leq L(L+1)$. Here *L* is an integer number, which will increase in iterative way, for first iteration, *L*=1. Where the above condition will be fulfilled that *L* will be the value of k_i* which means, $k_i^*=L$. By this procedure for all products (i=1, 2, 3…n) k_i^* is calculated.

In addition an optimum *T** is calculated by these k_i* using,

$$T^* = [2(S+\sum_{i=1}^{n} s_i / k_i)/\sum_{i=1}^{n} k_i h_i D_i]^{1/2} \qquad \text{(ix)}$$

This *T** is used to find the total cost using equation (v) in place of *T*. This way, varying the values of T_j, *m* number of total cost is calculated. Among which the minimum *TC* is selected. And for that *TC* corresponding values of *T** and k_i* are chosen.

EXPERIMENT AND RESULTS

Based on the data collected from a textile industry the total cost of holding for 1 year is approximately $274383.28, total minor ordering cost is $4871.00 and after totalling with major ordering cost for 12 replenishments ($282.05×12) in 1 year causes a total cost of $282,638.88 for replenishment of chemical raw materials.

Cost analysis using RAND algorithm

Following the procedure mentioned in section 3.2, RAND algorithm is applied using the collected inputs from the textile industry. Different values of ‘m’ were considered ranging from 5 to 50 as we know that a higher value of ‘m’ will provide a more precise result. However, the outcomes from m=10 was convincing. In table 1, T_8 is chosen to be the optimum cycle time for having the lowest number of replenishments among the lowest TCs (T_7 and T_8). Using this RAND algorithm the total cost of replenishment is $144,450 which is nearly half of the cost currently occurring.

TABLE 1. Total cost and optimum cycle time for different values of Tj (where, m=10)

	1	**2**	**3**	**4**	**5**	**6**	**7**	**8**	**9**	**10**
Tj	0.0086	0.0096	0.0106	0.0116	0.0127	0.0137	0.0147	0.0157	0.0167	0.0177
T*	0.0101	0.0108	0.0137	0.0141	0.0147	0.0152	0.0154	0.0157	0.0161	0.0164
TC ($)	154990	153630	147190	146250	145020	144500	144450	144450	144610	144840

The following table 2 shows the values of cycle time for few individual items, T_i ($T_i=T^*\times K_i^*$), as a fraction of year along with their replenishment quantity, Q_i ($Q_i= T^*\times K_i^*\times D_i$), in terms of kilograms in correspondence to the lowest value of TC, $144450.

TABLE 2. Individual replenishing cycle time and order quantity

	Item	**523**	**565**	**601**	**602**	**604**	**606**	**607**	**609**	**610**	**612**	**614**	**621**	**622**	**626**
***TC* = $ 144450**	***K_i****	1	1	2	1	1	3	1	1	1	1	2	1	1	1
	T*	0.016													
	T_i*	0.016	0.016	0.032	0.016	0.016	0.048	0.016	0.016	0.016	0.016	0.032	0.016	0.016	0.016
	D_i	384880	100442	34908	21975	87635	37640	156150	294450	1408000	166680	41590	101000	82490	63290
	Q_i	6043	1577	1096	345	1376	1773	2452	4623	22106	2617	1306	1586	1295	994

Cost analysis using RAND algorithm with forecasted demand

As some noteworthy anomaly is observed in the demands and consumptions, a forecast of the demand for each item is performed using Holt's method along with corresponding errors. A comparison between observed data, forecast demand and corrected demand is shown for item 523 in the fig. below.

FIGURE 1. Comparison of observed data and forecast demands of item 523

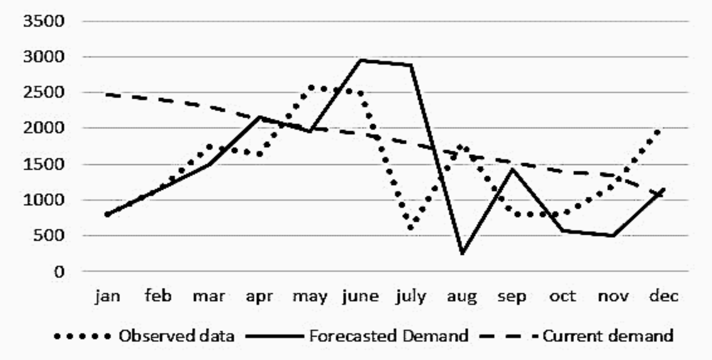

Total cost of replenishment is again calculated using the same procedure as in the previous calculation by means of RAND algorithm.

TABLE 3. Total cost and optimum cycle time for different values of Tj (where, m=10) with forecast demand

	1	**2**	**3**	**4**	**5**	**6**	**7**	**8**	**9**	**10**
Tj	0.0151	0.0163	0.0176	0.0188	0.0200	0.0213	0.0225	0.0238	0.0250	0.0262
T*	0.0199	0.0201	0.0203	0.0210	0.0214	0.0221	0.0221	0.0222	0.0229	0.0234
TC ($)	97195	96925	96736	96251	96104	95952	95952	95973	96145	96321

Here T6 and T7 presents the lowest value for TC as $95,952. Any of these two can be chosen as optimum since they both have identical values of T^*, TC and K_I^*. It is seen from repeated simulation of the RAND algorithm that this set of data for all values of m from 5 to 50 provides the same lowest value for total cost of replenishment. The values of cycle time, T_i and replenishment quantity, Q_i for few individual items are shown in the following table.

TABLE 4. Individual replenishing cycle time and order quantity

	Item	**523**	**565**	**601**	**602**	**604**	**606**	**607**	**609**	**610**	**612**	**614**	**621**	**622**	**626**	**627**
TC = $ 95952	**Ki***	3	1	1	4	1	2	1	1	1	1	2	1	1	1	2
	T*	0.022														
	Ti*	0.066	0.022	0.022	0.088	0.022	0.044	0.022	0.022	0.022	0.022	0.044	0.022	0.022	0.022	0.044
	Di	17287	75002	22616	1619	58456	32572	87420	115827	739595	29966	14831	66626	58718	37365	18639
	Qi	1146	1658	500	143	1292	1440	1932	2560	16345	685	656	1472	1302	826	812

DISCUSSION AND CONCLUSION

This research presents the inventory replenishment problems, where joint replenishment was considered as a replenishing policy. The work was done on the basis of present textile industrial environment and the purpose of this research was to minimize their annual holding and ordering costs using RAND algorithm. This actually refers that the purpose is to identifying replenishment cycle time for individual products that will generate the lower holding and ordering cost. Firstly, the total annual cost was calculated according to their current practice of replenishment and the cost was about $282,638. This cost, however, may slightly differ from the real case as there were some assumption in the calculation yet it can be considered nearly accurate. Afterwards, RAND was applied with the same demand. The total annual cost of replenishment was calculated for this procedure which was $144,450 and it was 49% lesser then actual. As an additional work, forecasting was carried out for the precision of their demand data to minimize the cost further. For forecasting, double exponential smoothing method (Holt's method) was used as there was no seasonality rather some trend in product demands was visible. With error comparison, it was proved that Holt's forecasting method provide more accurate demand. As a final work RAND was applied with these new forecasted demands to find out the total cost. The total cost was reduced by 66% from the currently pursued process and 33% from the previous RAND. Thus, this research undoubtedly exhibits this fact that application of RAND will enormously improve the replenishment policies of textile industries in Bangladesh.

REFERENCES

1. B. Shore, Operations Management (Tata McGrath-Hill, New Delhi, 1980), pp. 363.
2. M. Kaspi, M.J. Rosenblatt, International Journal of Production Research **29(1)**, 107–114 (1991).
3. F. T. Shu, Management Science **17(6)**, 406–410 (1971).
4. S.K. Goyal, Management Science **20(2)**, 232 (1973).
5. S. K. Goyal, Management Science, **21(4)**, 436–443 (1974).
6. E. A. Silver, Management Science **22(12)**, 1351–1361 (1976).
7. S. K. Goyal, A.S. Belton, Management Science **25(6)**, 604 (1979).
8. S. K. Goyal, International Journal of Production Research **26**, 1237 (1988).
9. S. K. Goyal, A.T. Satir, European Journal of Operations Research **38**, 2–13(1989).
10. M. Kaspi, M.J. Rosenblatt, IEEE Transactions **15(3)**, 264–267 (1983).
11. S.K. Prajakta, Time series forecasting using Holt-Winters Exponential Smoothing. Kanwal Rekhi School of Information Technology, 1−13 (2004).
12. Muth, Journal of the American Statistical Association **55(290)**, 297-299 (1960).
13. G. Box, G. Jenkins, Time series analysis: Forecasting and control, San Francisco: Holden-Day, 1970.
14. S. A. Roberts, Management Science **28**, 808-820 (1982).
15. F. L. Adelman, I. Adelman, Econometrica **27(4)**, 596-625 (1959).
16. E. S. Gardner Jr., Journal of Forecasting **4**, 1-28 (1985).
17. R. D. Snyder, Journal of the Royal Statistical Society. Series B **47**, 272 – 276 (1985).
18. S. M. Bartolomei, A.L. Sweet, International Journal of Forecasting **5**, 111 – 116 (1989).
19. S. Makridakis, M. Hibon, International Journal of Forecasting **7**, 317-330 (1991).
20. J. Ledolter, B. Abraham, Journal of Forecasting **3**, 79 – 84 (1984).
21. E. McKenzie, Journal of Forecasting **3**, 333 – 344(1984).
22. J. W. Taylor, International Journal of Forecasting **19**, 273 – 289 (2003).

International Conference on Mechanical Engineering 2015
(ICME 2015) 18 – 20 December, 2015, Dhaka, Bangladesh

Paper ID : 530

Analysis of Performance With Variable Stroke of a Torque Based Renewable Micro Hydro Power Generation Plant

Muhammad Mahbubul Alam[1,a)], Md Shad Rahman[2,b)], Rasel A Sultan[2,c)] and M Ahmed Naif[3,d)]

[1] *Bangladesh University of Engineering & Technology, Dhaka-1000, Bangladesh*
[2] *Graduate research student, Process Engineering (Engineering Oil and Gas), Memorial University, Newfoundland*
[3] *Military Institute of Science and Technology, Mirpur Cantonment, Dhaka-1216, Bangladesh*

b)Corresponding author: shadrahman09@gmail.com
c)raselahmed0411@yahoo.com

Abstract. The most important addition of modern science is renewable energy. And the most useful and the most cheaply renewable power generation source is Hydropower. Flowing water creates energy that can be captured and turned into electricity. This is called Hydroelectric power or Hydropower. Hydropower is considered a renewable energy resource because it uses the earth's water cycle to generate electricity. Water evaporates from the earth's surface, forms clouds, precipitates back to earth, and flows toward the ocean. As far as Bangladesh is concerned, only a small fraction of electricity is generated by hydropower. The government has set a target of meeting 5 per cent of the electricity demand by 2015 by utilizing renewable energy and 10 per cent by the year 2020. Currently, renewable energies contribute to less than 1 per cent of the country's total electricity generation .The aim of our analysis is to demonstrate and observe the hydropower of our country in micro-scale by our experimental setup which is completely new in concept .This paper consists results of our findings and we find larger the number of stroke higher the rpm correspondingly higher efficiency. We find maximum rpm for 2stroke when fixed fly wheel weight was 18Kg and water was 10liter. It might help in case of utilizing this renewable energy potential at high scale.

INTRODUCTION

From the beginning of human race human beings has been consuming energy .A world without energy cannot be imagined. At every step of life, human depends on energy. Global primary commercial energy consumption has grown at an average annual rate of about 2% per year over the last 200 years; during 1990-2000, the consumption increased by 11%. The demand for energy is increasing day by day. Hydroelectric power, or hydroelectricity, is generated by the force of falling water. (Hydro comes from the Greek word for water.) It's one of the cleanest sources of energy, and it's also the most reliable and costs the least. The hydrologic cycle–water constantly moves through a vast global cycle, in which it evaporates from lakes and oceans, forms clouds, precipitates as rain or snow, then flows back to the ocean. The energy of this water cycle, which is driven by the sun, is tapped most efficiently with hydropower [1]. There are various types of hydro power facilities like; Impoundment hydropower, Undershoot waterwheel, Overshoot waterwheel, Small hydro power etc. Hydropower, large and small, remains by far the most important of the "renewables" for electrical power production worldwide, providing 19% of the planet's electricity [2]. Small hydro is in most cases 'run-of-river'; in other words any dam or barrage is quite small, usually just a weir, and generally little or no water is stored. The civil works purely serve the function of regulating the level of the water at the intake to the hydro-plant. Therefore run-of-river installations do not have the same kinds of adverse effect on the local environment as large hydro. . Hydropower has various degrees of 'smallness'. To date there is still no internationally agreed definition of 'small' hydro; the upper limit varies between 2.5 and 25 MW. A maximum of 10 MW is the most widely accepted value worldwide, although the definition in China stands officially at 25 MW. In the jargon of the industry, 'mini' hydro typically refers to schemes below 2 MW, micro-hydro below

500 kW and Pico-hydro below 10 kW [3]. These are arbitrary divisions and many of the principals involved apply to both smaller and larger schemes. Much of the technical effort to develop small hydro in recent times has therefore focused on measures to improve cost-effectiveness of the technology [4]. A reliable bank of such field information is now growing. It exists to help spread the word about these and other technologies, lessening the dependence of the developing world on expensive and finite energy resources [5]. Using the water flow rate, head and torque motion hydro power can be produced in a micro scale without facing any problem related to cost, performance and efficiency. It can work over a range of water flow and head conditions with very simple build up and virtually no maintenance required. And it is shown in Fig.1. The overall performance of this micro hydro power plant will change by the number of stoke it will have [5]. The efficiency of this plant maximize by increasing of stroke number. The larger the stroke number larger output it will have with same amount of flow and fixed weight.

Nomenclature

1. M - Mass
2. F – Force
3. r- Radius distance
4. T- Torque
5. N- Revolution
6. Rpm- Revolution per minute
7. w- Angular velocity
8. P- Power
9. L- Length
10. W- Width
11. H- Height
12. M.W- Mega Watt
13. K.W- Kilo Watt
14. Kg- Kilogram
15. t- Time
16. g- gravity acceleration

EXPERIMENTAL METHOD

Experimental Setup

Our setup is shown in Figure1. (a) and Figure1.(b). The setup comprises of 4 basic parts: Arm, Flywheel, Frame, Shaft and bearing. Arm is basically serves as the prime mover in the setup. Weights and counter weights are places at the two ends to create the up and down motion .It consist of a wooden hub, metallic extensions, and bearings with rachet joint, buckets. We assembled the two parts of the arm by inserting CI bar in wood slots and sandwich it between two wood bars. For proper supports and to prevent movement and free ball set in the engraved gear shape and fixed by two wood bars over it. A 6 inch screw has been fitted through the wood and CI bar. A flywheel is an inertial energy-storage device. It absorbs mechanical energy and serves as a reservoir, storing energy during the period when the supply of energy is more than the requirement and releases it during the period when the requirement of energy is more than the supply. The flywheel we used is a custom made flywheel whose weight can be adjusted. This flywheel constructed by CI 2/2 inch hollow bar is cut to suitable size .They are filled with cement

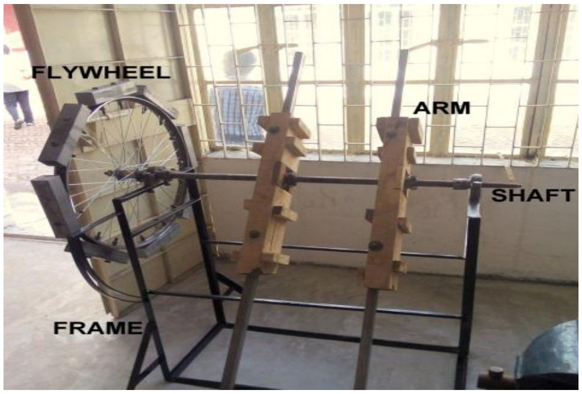

FIGURE 1 (a) The prototype Experimental Setup

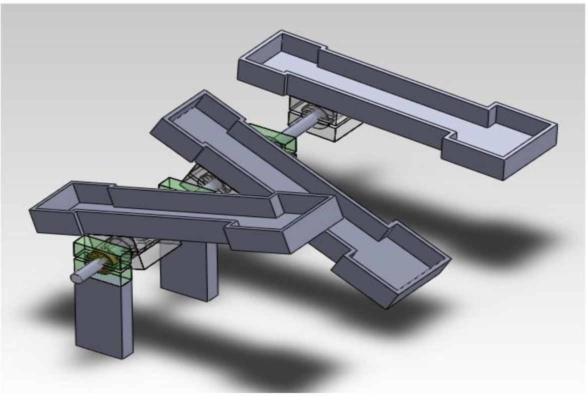

FIGURE 1 (b) Design of Experimental Setup to increase weight. 8 were made each weighing 2kg .The heavy weight bars are fixed on the circumference of a rickshaw's wheel. The frame holds all the apparatus. A cast iron frame is built using arc welding in the MIST welding shop according to the design. And set accordingly cutting by Hex Saw, Cutting by machine saw and Joining by Arc welding. The shaft connects the Flywheel and Arm .Its rotary motion is the required output motion .Bearing connects the frame and shaft. Along with bearing hub it supports the shaft.

Experimental Procedure

- At first we let the water flow from the water tank. The water then hit the water bucket linked with the arm. In our model there were only two buckets linked with two arms. As water flows into bucket and make enough torque to rotate the shaft
- Two arms are connected with the shaft perpendicularly. They are connected via bearing which helps to rotate the shaft.
- First we varied the quantity of water that was flowing into the water bucket. And we observed the "rpm" of the flywheel through a Tachometer. The Tachometer was "contact point type".
- We calculated the power output from the speed (rpm) data which were recorded during the operation of rotating shaft.
- Then again we repeated our experiment, but this time the mass of the flywheel was changed gradually and the water quantity was also changed.
- We recorded the values and calculated the power from different rpm (speed) recorded.
- After that we plotted graphs containing rpm, power for different water quantities and different flywheel.

RESULT AND DISCUSSION

The graphs were plotted, time (sec) in X direction and Speed (rpm) in the Y direction. We plotted 9 graphs in total for different amount of water quantities (Liters). We varied the amount of water and observed the results for 1 stroke and 2 stroke arrangements. The Blue color line was 2 strokes and the red color line was 1 stroke .The curve tends to set a constant value after rising sometime.

General Formula:

$$\begin{aligned}\text{POWER} &= \text{TORQUE} * \text{ANGULAR VELOCITY}\\ &= \text{FORCE} * \text{DISTANCE} * 2 * \pi * \text{RPS}\\ &= \text{MASS} * \text{ACCELATION} * \text{DISTANCE} * 2 * \pi * \text{RPS}\\ &= m * g * s * 2 * \pi * \text{RPS}\\ &= M * 9.81 * 1.22 * 2 * \pi * (\text{RPM} / 60)\end{aligned}$$

In Figure.2 (a) the 1st graph shows that the curve for 10 kg flywheel and 5 liter water. Red line steady at 23 seconds and blue in 25 seconds. Corresponding rpm and power were 28rpm 176 Watt and 38 rpm 238 watt.

In Figure.2 (b) the 2nd graph shows that the curve for 10 kg flywheel and 7 liter water. Red line becomes steady at 15 seconds and blue in 17 seconds. When rpm and power were 37 rpm 325 Watt and 50 rpm 437 Watt.

In Figure.2 (c) the 3rd graph shows that the curve for 10 kg flywheel and 10 liter water. Red line steady at 35 seconds and blue line in 40 seconds. Corresponding rpm and power were 48rpm 602Watt and 71rpm 890Watt.

In Figure.2 (d) the 4th graph shows that the curve for 14 kg flywheel and 5 liter water. Red line steady at 12 seconds and blue in 9 seconds. Corresponding rpm and power were 37rpm 232Watt and 49rpm 308watt.

In Figure.2 (e) the 5th graph shows that the curve for 14 kg flywheel and 7 liter water. Red line steady at 16 seconds and blue in 12 seconds. Corresponding rpm and power were 50rpm 437Watt and 68rpm 597watt.

In Figure.2 (f) the 6th graph shows that the curve for 14 kg flywheel and 10 liter water. Red line steady at 22 seconds and blue in 16 seconds. Corresponding rpm and power were 77rpm 965Watt and 98rpm 1228watt.

In Figure.2 (g) the 7th graph shows that the curve for 18 kg flywheel and 5 liter water. Red line steady at 22 seconds and blue in 6 seconds. Corresponding rpm and power were 40rpm 250Watt and 58rpm 363watt.

In Figure.2 (h) the 8th graph shows that the curve for 18 kg flywheel and 7 liter water. Red line steady at 28 seconds and blue in 30 seconds. Corresponding rpm and power were 59rpm 518Watt and 73rpm 640watt.

In Figure.2 (i) the 9th graph shows that the curve for 18 kg flywheel and 10 liter water. Red line steady at 26 seconds and blue in 28 seconds. Corresponding rpm and power were 80rpm 1020Watt and 103rpm 1291watt

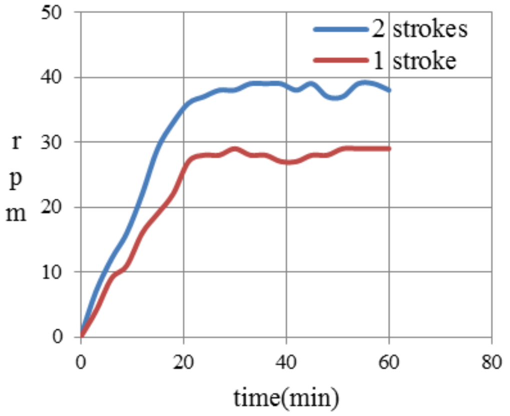

FIGURE 2 (a) Variation of speed with time for 10 kg flywheel and 5 liter water

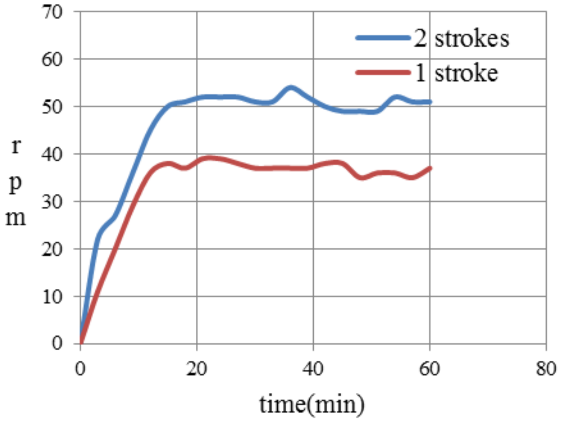

FIGURE 2 (b) Variation of speed with time for 10 kg flywheel and 7 liter water

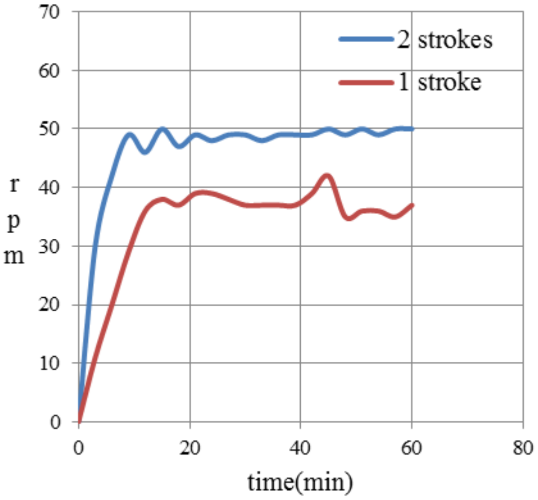

FIGURE 2 (c) Variation of speed with time for 10 kg flywheel and 10 litre water

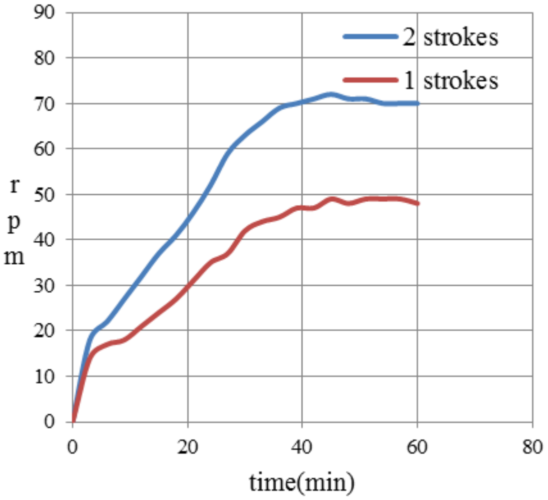

FIGURE 2 (d) Variation of speed with time for 14 kg flywheel and 5 litre water

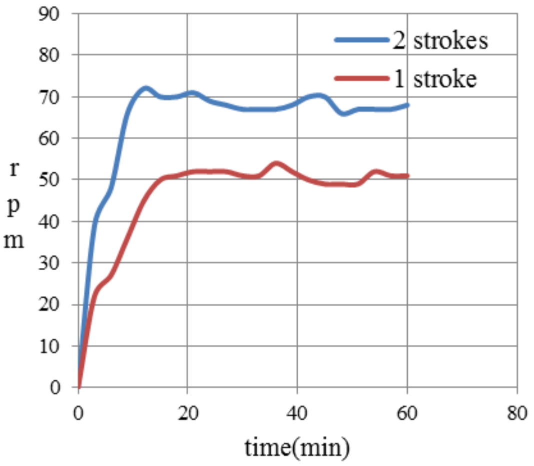

FIGURE 2 (e) Variation of speed with time for 14 kg flywheel and 7 litre water

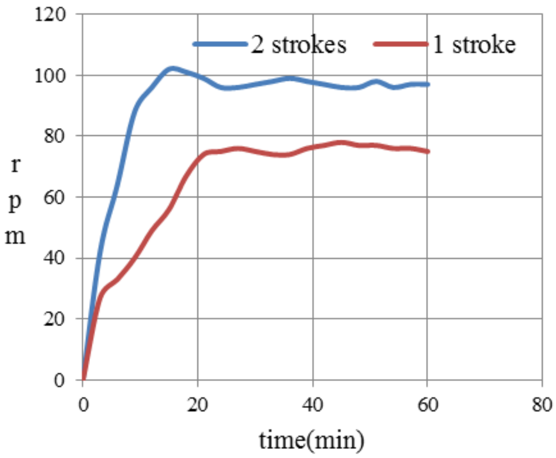

FIGURE 2 (f) Variation of speed with time for 14 kg flywheel and 10 litre water

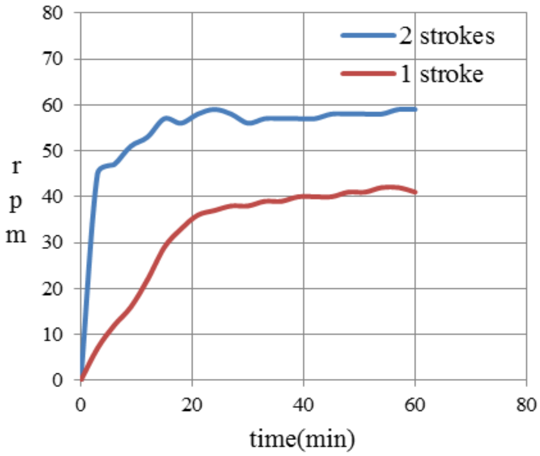

FIGURE 2 (g) Variation of speed with time for 18 kg flywheel and 5 litre water

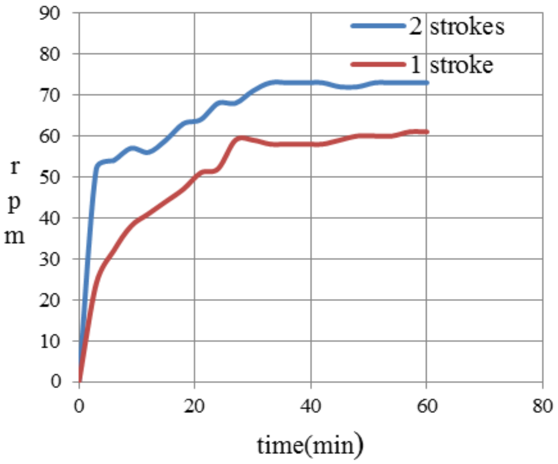

FIGURE 2 (e) Variation of speed with time for 18 kg flywheel and 7 litre water

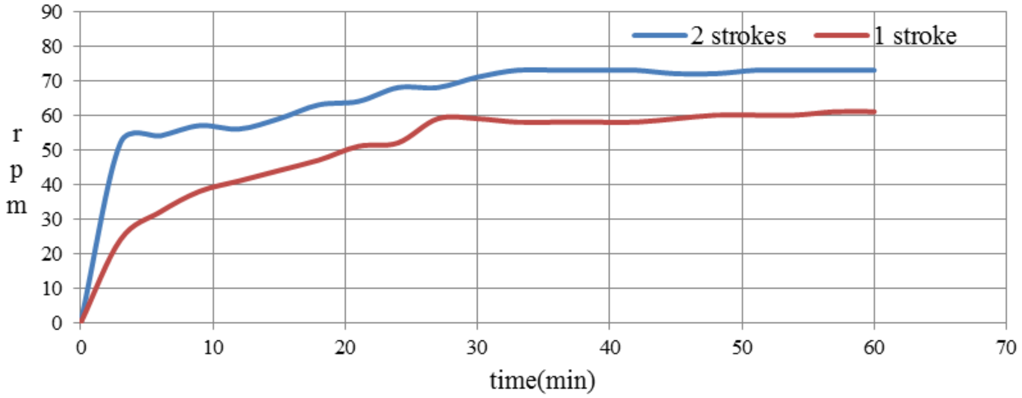

FIGURE 2 (i) Variation of speed with time for 18 kg flywheel and 10 litre water

In our experiment we varied the fixed weight fly wheel and the amount of water flow and got variable speed for 1 stroke and 2 stokes. In all the graphs 2 Strokes performance is better than 1 stroke. And also see that when the fixed weight is maximum 18kg with 10 liter water the setup produces better speed, performance and torque than others. For 2 stroke operation maximum rpm 103 and power 1291 watt and 1 stroke operation maximum rpm 80 and power 1020watt. So 2stroke provides better operation than 1 stroke. We also find maximum rpm for 2 strokes when fixed fly wheel weight was 18 Kg and water was 10 liter. And by increasing the fixed weight and water flow we can get more efficient performance.

CONCLUSION

Energy runs the civilization. The world is based on various types of energies especially renewable energy. From the graphical representation with the data of our constructed structure we saw a common trend that the shaft rpm rises steadily for a short period of time and then continues along a straight line. Increasing the flywheel weight and flow rate improves the quality of the straight line and reduces noise. We find maximum rpm for 2 strokes when fixed fly wheel weight was 18 Kg and water was 10 liters. It might help in case of utilizing this renewable energy potential at high scale. Result might vary with the parameters fixed flywheel weight, water amount and number of stroke. Most satisfactory pattern of design may vary up to some extent from case to case.

ACKNOWLEDGMENTS

The authors feel greatly honored to be able to express their earnest gratitude to the Department of Mechanical Engineering, MIST and BUET for the accomplishment of this research.

REFERENCES

1. Micro-Hydro Power. A Guide for Development Workers. 1991; Available from: http://www.sei-international.org/publications?pid=310
2. The international journal on hydropower & dams world atlas and industry guide. Available from: http://acwc.sdp.sirsi.net/client/en_US/default/search/detailnonmodal/ent:$002f$002fSD_ILS$002f0$002fSD_ILS:17871/ada/?ic=true&qf=PUBDATE%09Publication+Date%092010%092010&qu=Dams
3. Small hydropower is growing thanks to federal legislation. Available from: http://www.hydroworld.com/articles/hr/print/volume-32/issue-6/articles/agricultural-hydropower-on-the-horizon-in-colorado.html
4. DFID - Research for Development > EU-China small hydro workshop and technology guide. Available from: http://r4d.dfid.gov.uk/Project/5248/
5. Wazed MA, Ahmed S. Micro Hydro Energy Resources in Bangladesh: A Review. Aust J Basic Appl Sci;2(4). Available from: http://www.researchgate.net/publication/228210598_Micro_Hydro_Energy_Resources_in_Bangladesh_A_Review

International Conference on Mechanical Engineering 2015
(ICME 2015) 18 – 20 December, 2015, Dhaka, Bangladesh

Paper ID : 566

An Investigation on Machinability during Hard Turning with Narrow Groove Tool Insert in Different Environmental Conditions

Krishnendu Mondal [1,a)], Santanu Das [2,b)]

[1]Department of Mechanical Engineering, Bankura Unnayani Institute of Engineering, Bankura- 722146, West Bengal, India.
[2]Department of Mechanical Engineering, Kalyani Government Engineering College, Kalyani- 741235, West Bengal, India.

[a)]Krishnendu_4u@yahoo.com
[b)]Corresponding author: sdas.me@gmail.com

Abstract. 16MnCrS5 steel is applied in different structural and other industrial applications. However, it is considered to be hard and difficult-to-machine material. In this work, this steel is chosen for turning tests under different cutting conditions and machining environment (dry and wet) with narrow groove carbide tool insert. Using these diverse conditions, types of chips formed, cutting force, etc. were noted, and machinability of the tool-work combine under different conditions is explored, so that some conditions can be found out at which good machinability can be achieved. Wet condition is found to give good tool performance within a range of cutting conditions.

NOMENCLATURE

CRC	chip reduction coefficient	fc	main cutting force, N
fcn	cutting normal force, N	MRR	material removal rate
t	depth of cut, t	So	feed, mm/rev
Vc	cutting velocity, m/min		

INTRODUCTION

Traditionally, grinding is employed for finishing and semi-finishing of hard materials, but it involves low MRR, and hence, may take long manufacturing lead time. To overcome this, hard turning is being explored [1,2,3,4] to obtain benefits of fewer process steps, increased MRR, etc. This process is usually done on workpiece material hardness of 45 HRC or more. One such material, AISI D2 steel, was tested [5] to turn with different tool materials to find out suitable ones. Hard chromium plated workpiece surface was also tried [1] to turn. Hard machining was reported to have been done successfully using high toughness tools with high abrasion resistance and heat conductivity [6].

Super abrasive tools, such as PCBN and cBN, were employed for hard turning, and it could produce better surface finish than grinding with the use of right combination of insert nose radius and feed [3]. For turning of harder materials, high velocity, low feed and low depth of cut are taken for finishing operation. Many researchers chose cutting velocity, Vc between 100-250 m/min [7,8], while Yallese et al. used [9] Vc up to 350 m/min. Due to stability problem, researchers were constrained to restrict machining parameters.

Tool wear and tool life are very significant in connection with hard turning as tool wear rate is quite fast in this case. Experimental results revealed that TiN/TiCN/Al_2O_3/TiN coated inserts performed better than TiN/TiCN/ Al_2O_3/ZrCN coated carbide inserts [10]. Hard turning may or may not use coolant. Dry machining was reported to show lower tool wear rate and surface roughness than minimum quantity lubrication (MQL) [11,12] in a work.

In the present work, 16MnCrS5 steels were chosen for turning tests under varying cutting conditions and machining environment. Performance of tool insert considered is compared with respect to turning under different conditions. Tool wear tests were carried out at a cutting velocity in two environmental conditions.

MATERIALS AND METHODS

Hard turning experiments were done on a lathe with 16MnCrS5 steel rod held between a 3-jaw chuck and a revolving centre. TiC coated carbide inserts were employed. Detail of the experimental setup is given in Table 1.

Five levels of cutting velocity with three levels of feed were chosen in the 1st set of experiments. Experimental conditions are detailed in Table 2. A constant depth of cut was maintained through out the experiment. Machining tests were carried out using sharp new edges of cutting tool insert. Narrow groove inserts were used for controlled contact machining. Two environmental conditions chosen were dry and wet. Dial vernier caliper was taken for measuring chip thickness. Response variables noted were chip thickness, type and colour of chip, chip reduction co-efficient (CRC), and build-up edge formation. In experiment set II, wear tests were carried out under dry and wet conditions as detailed in Table 3.

Table 1. Experimental set-up and conditions

Machine tool	Precision lathe, Model: Turnmaster TM-35, Make- The Mysore Kiloskar Ltd., Bangalore, India
Workpiece	16MnCrS5 steel, size: ϕ80 x 300 mm
Compositions	C= 0.177%, Si= 0.283%, Mn= 0.753%, Cr= 0.854%, Mo= 0.126%, Ni= 1.186%, W= 0.161%. Ceqv= 0.583%
Cutting condition	Dry, wet (water soluble oil, Make: Burma shell, India, 1:60 ratio)
Insert type	Titanium carbide (TiC) coated carbide tool insert with narrow groove chip breaker Make: Sandvik Asia Ltd, India, Specification: SNMG 12 04 08/ 315 K 15
Tool geometry	-6º, -6º, 6º, 6º, 15º, 75º, 0.8 mm
Tool holder	Make: Sandvik Asia Ltd., India, Grade: Coromant T max-P, Specification: R174.3 2020 12

Table 2. Experimental conditions

Experiment set	Cutting velocity, Vc (m/min)	Feed, So (mm/rev)	Depth of cut, t (mm)	Environment
I a	44, 68, 109, 172, 271	0.063, 0.08, 0.1	0.5	Dry
I b				Wet

Table 3. Experimental conditions for tool wear test

Experiment set	Cutting velocity, Vc (m/min)	Feed, So (mm/rev)	Depth of cut, t (mm)	Environment
II (a)	132	0.063	1	Dry
II (b)				Wet

RESULTS AND DISCUSSION

Experiment set I a: Machining tests were conducted in dry environment, and results obtained are shown in Table 4, Fig. 1 and Fig. 2. Chip reduction coefficient (CRC) is found to be less when irregular flat continuous chips are produced at cutting velocities of 109, 172 and 271 m/min. This mostly indicates desirable machining operation involving less shear deformation of chips consuming less force. Coiled type fractured, as well as half and full round, chips are formed at a low cutting velocity of 44 m/min at the three feed values chosen, and these conditions show higher CRC.

Table 4. Experimental observations under dry condition in experiment set I a

Sl. No.	Cutting velocity (m/min)	Feed (mm/rev)	Chip form observed	Type of BUE	CRC
1	271	0.1	Blue, flat long continuous	No	1.89
2	271	0.08	Brown & blue, flat long continuous	No	1.57
3	271	0.063	Brown & blue, flat long continuous	No	1.67
4	172	0.1	Brown & blue, flat long continuous	No	1.89
5	172	0.08	Brown & blue, flat long continuous	No	1.71
6	172	0.063	Shining grey, flat long continuous	No	1.83
7	109	0.1	Brown & blue, flat long continuous	No	1.78
8	109	0.08	Brown & blue, flat long continuous	No	1.86
9	109	0.063	Brown & blue, flat long continuous	No	1.83
10	68	0.1	Shining grey, long continuous irregular, flat and open coiled	No	2.00
11	68	0.08	Blackish blue, flat long continuous	No	2.14
12	68	0.063	Blackish blue, flat long continuous	No	2.33
13	44	0.1	Brownish blue, coiled with 4-6 turns, full round & half round	Tiny loose	2.11
14	44	0.08	Brownish blue, coiled with 4-6 turns, full round & half round	Tiny loose	2.43
15	44	0.063	Brownish blue, coiled with 2-3 turns, full round & half round	Tiny loose	2.67

It is expected as coiled type chip formation needs more deformation sideway to facilitate curling [13], and narrow chip breaking groove may promote it. Fractured chips of half and full round types and coiled with few turns as obtained from these experiments are shown in Fig.1 (m-o). Higher CRC at these conditions may be due to high degree of curling over a narrow radius resulting in their breakage. Also, presence of unstable built-up-edge at this low Vc may have caused variable rake angles resulting in cutting force variation, thereby causing broken chip formation. At a low cutting velocity of 44 m/min expectedly, tiny loose built-up-edges are seen. At higher cutting velocities of 68,109, 172 and 271 m/min, expectedly, no built-up-edge is detected and long continuous chips, mostly flat type, are seen at all the feed values. Tendency of BUE formation is mostly reported at low velocities, and observations made in this work are in-line with the previous works reported [6, 13]. Figure 2 shows variation of cutting force components (Fc: main cutting force component and Fcn: cutting normal force) with cutting velocity (Vc) and feed (So). Expectedly, force values are increased with an increase in feed due to high shear area. Change in force shows a decreasing trend up to a cutting velocity of 109 m/min. There is no appreciable change in force at higher velocities. BUE formation as detected in 44 m/min Vc and formation of coiled and broken chips needing higher deformation may have resulted in higher force values at a low cutting velocity of 44 m/min. At higher Vc, there is no BUE formed, and force values are less and do not show remarkable variation. Formation of flat to irregular continuous chips needing less deformation supports less value of cutting force components. From the above discussion, it can be stated that fairly good tool performance is obtained when narrow groove coated carbide insert is employed at cutting velocities of 68, 109, 172 and 271 m/min at the chosen feeds even in dry condition.

Experiment Set I b: Observations made regarding chip and built-up edge formation as obtained from experiment set I b are detailed in Table 5 and Fig. 3.

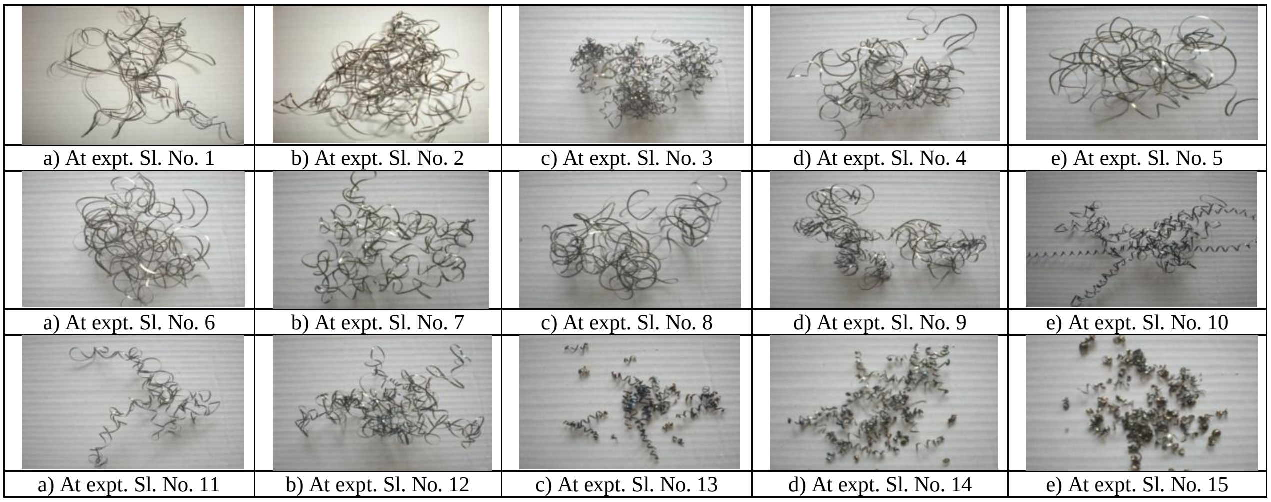

a) At expt. Sl. No. 1
b) At expt. Sl. No. 2
c) At expt. Sl. No. 3
d) At expt. Sl. No. 4
e) At expt. Sl. No. 5
a) At expt. Sl. No. 6
b) At expt. Sl. No. 7
c) At expt. Sl. No. 8
d) At expt. Sl. No. 9
e) At expt. Sl. No. 10
a) At expt. Sl. No. 11
b) At expt. Sl. No. 12
c) At expt. Sl. No. 13
d) At expt. Sl. No. 14
e) At expt. Sl. No. 15

FIGURE 1. Photographs of observed chips for experiment set I a under dry condition

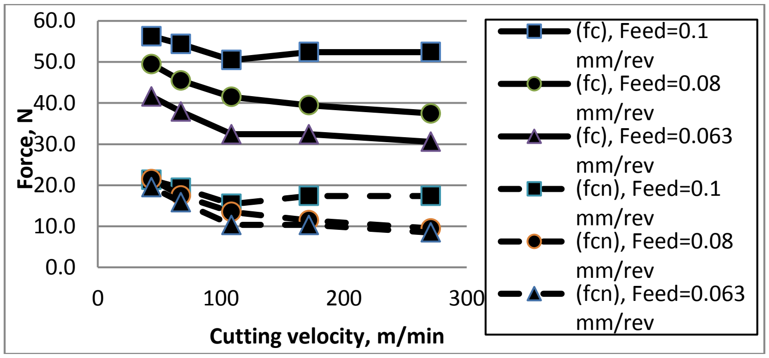

FIGURE 2. Variation of forces with cutting velocity at different feed at dry condition for experiment set Ia

Table 5. Experimental observation for experiment set I b under wet condition

Sl. No.	Cutting velocity (m/min)	Feed (mm/rev)	Chip form observed	Type of BUE	CRC
1	271	0.1	Blue, flat long continuous type	No	1.67
2	271	0.08	Blue & brown, flat long continuous type	No	1.86
3	271	0.063	Blue & brown, flat long continuous type	No	1.67
4	172	0.1	Blue & brown, flat long continuous type	No	1.56
5	172	0.08	Blue & brown, flat long continuous type	No	1.57
6	172	0.063	Shining grey, long continuous coiled type	No	1.83
7	109	0.1	Blue & brown, flat long continuous type	No	1.67
8	109	0.08	Blue & brown, flat long continuous type	No	2.00
9	109	0.063	Shining grey, long continuous coiled type	No	1.67
10	68	0.1	Shining grey, long continuous coiled type	No	1.56
11	68	0.08	Shining grey, long continuous coiled type	No	1.71
12	68	0.063	Grey, long continuous coiled type	No	1.67
13	44	0.1	Grey, coiled 8-12 turns	Tiny hard	2.22
14	44	0.08	Brownish grey, coiled 8-12 turns	Tiny hard	2.57
15	44	0.063	Brownish grey, coiled 6-8 turns	Tiny hard	2.67

At this set of experiments, at Vc 43 m/min, presence of BUE is noted similar to that in dry condition. CRC is found to be within 1.56 to 2.67. Chip forms observed (shown in Fig. 3) are mostly of flat irregular long continuous types at a cutting velocity of more than 100 m/min with a feed of 0.08 and 0.1 mm/rev. Long coiled continuous type of chips are observed at 68 m/min Vc, and at 0.063 mm/rev feed at 109 and 172 m/min Vc. Fractured coiled chips with few turns are obtained at a low cutting velocity of 44 m/min. Therefore, no clear chip breaking effect of using the narrow groove chip breaker can be noticed within the experimental domain chosen. Application of water soluble oil as the cutting fluid seems to be extending fairly good cooling and lubrication effect during machining.

Figure 4 shows the variation of cutting force components (Fc, Fcn) at different cutting velocities and feeds. Expectedly, forces increase with increase in feed due to increasing shear area. Similar to previous experiment set 1 a, in this experiment also, it is obtained that forces are high at the cutting velocity of 44 m/min. However, if force values are compared with that seen in dry condition with the same groove type insert, in some cases cutting force requirement is noted to be a bit higher in wet machining. Possible reasoning behind this may lie in the fact that in dry condition due to high heat generation, tool nose may have started micro-chipping during turning test. This may have reduced depth of cut to some extent causing lesser cutting force requirement. In wet condition, condition of the tool insert may have retained its edge sharpness under well lubricated and cooled environment. So, even if it takes more machining force than that in dry condition, it indicates better machining.

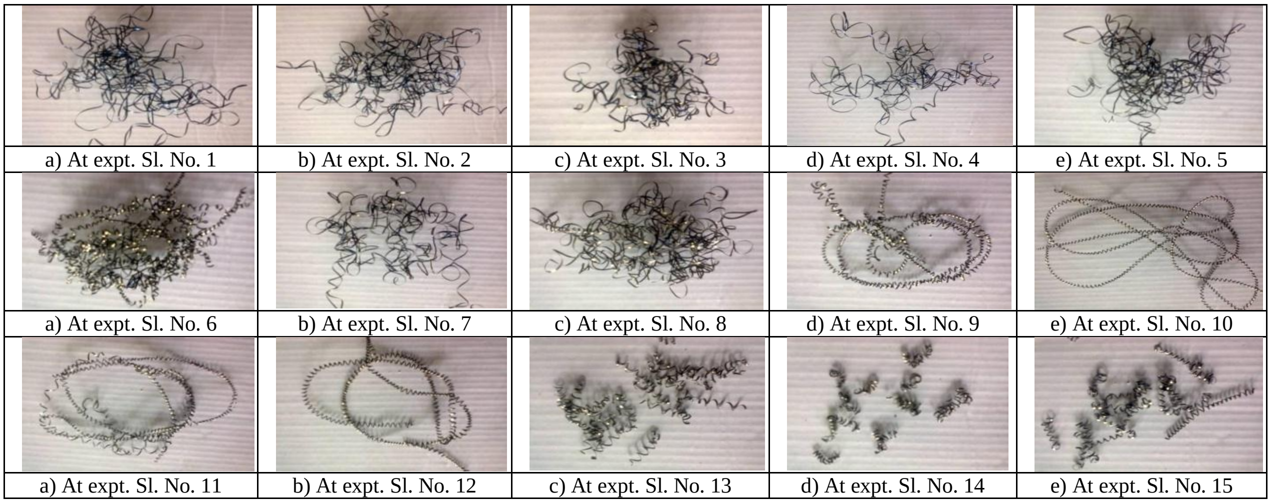

a) At expt. Sl. No. 1
b) At expt. Sl. No. 2
c) At expt. Sl. No. 3
d) At expt. Sl. No. 4
e) At expt. Sl. No. 5
a) At expt. Sl. No. 6
b) At expt. Sl. No. 7
c) At expt. Sl. No. 8
d) At expt. Sl. No. 9
e) At expt. Sl. No. 10
a) At expt. Sl. No. 11
b) At expt. Sl. No. 12
c) At expt. Sl. No. 13
d) At expt. Sl. No. 14
e) At expt. Sl. No. 15

FIGURE 3. Photographs of observed chips for experiment set I b under wet condition

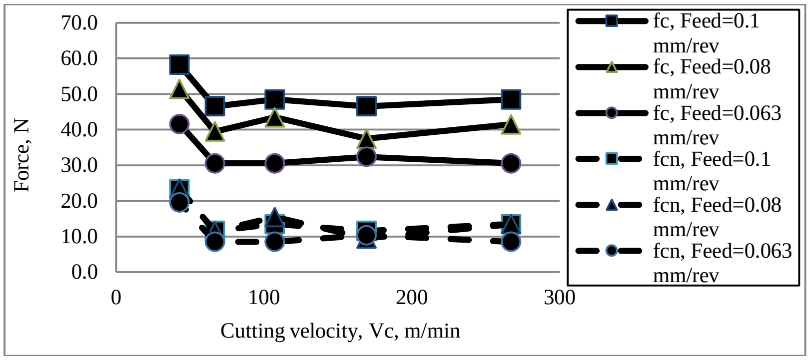

FIGURE 4. Variation of forces with cutting velocity at different feed at wet condition for experiment set I b

It may be stated that desirable tool performance can be obtained when cutting velocity chosen is from 109 m/min up to 271 m/min within the domain of experiments of the present investigation on turning of high hardness 16MnCrS5 steel with narrow groove TiC coated carbide insert.

Experiment set II: Tool Wear Test: Wear test is carried out on the insert used at a machining condition as shown in Table 3 in dry and wet environment. Growth of flank and nose wear with machining time is shown in Fig. 5. Progress of average flank wear and nose wear with machining time shows that under wet condition, wearing of both average flank wear (V_B) and nose wear (V_N) is significantly lesser than that at dry condition. After 12 minutes, dry machining gives 168 µm of average flank wear and more than 250 µm nose wear, while under wet condition, these become to be of only 94 µm and about 160 µm respectively. This indicates that dry machining for long may not be recommended with narrow groove TiC coated carbide insert for turning 16MnCrS5 steel rod.

Low tool wear rate in wet condition is quite natural as application of soluble oil reduces interfacial friction between tool, workpiece and chip, and hence, machining temperature. Thereby, thermal softening of the cutting tool becomes less probable. After 27 min. of machining, photographs of cutting tool inserts showing wear pattern under dry and wet conditions are given in

Fig. 6 and Fig. 7 respectively. High nose wear, significant notch wear and flank wear are seen clearly in dry condition. In wet condition, turning could well be done for long using the tool insert considered.

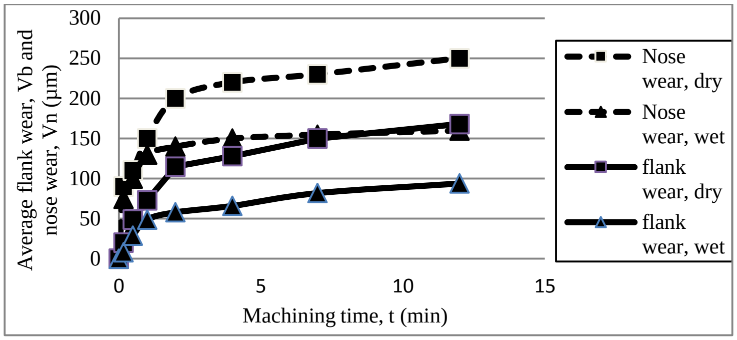

FIGURE 5. Tool wear curve in dry and wet conditions

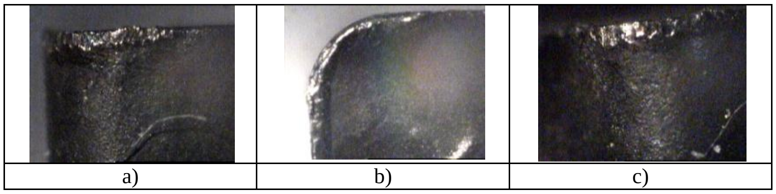
a) b) c)

FIGURE 6. View of tool at Vc= 132 m/min, So= 0.063 mm/rev in dry condition after 27 min. of machining [a) Flank, b) Crater, c) Nose wear]

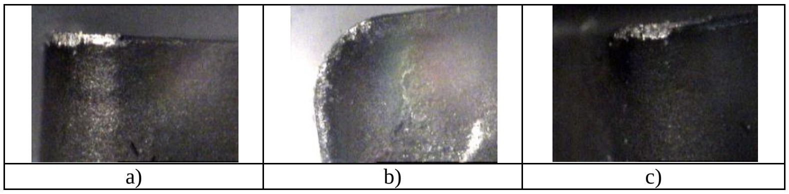
a) b) c)

FIGURE 7. View of tool at Vc= 132 m/min, So= 0.063 mm/rev in wet condition after 27 min. of machining [a) Flank, b) Crater, c) Nose wear]

CONCLUSION

From turning experiments carried out on 16MnCrS5 steel rod with narrow groove titanium coated carbide tool insert, good tool performance is observed while undertaking hard turning in wet condition giving reduced tool wearing and force requirement significantly. This may be due to reduction in friction and temperature due to cooling and lubrication action of water soluble oil in wet condition.

REFERENCES

1. K.N. Mohandas, N. Balashanmugam, C.S. Ramesh and P.V. Shashikumar, “Investigations on hard turning of hard chrome plated surfaces,” in *Proc. 3rd Int. & 24th AIMTDR Conf.*, edited by B. Satyanarayana and K. Ramji (Vishakhapatnam, India, 2010), pp.75-79.
2. M. Dogra, V.S. Sharma, A. Sachdeva and N.M. Suri, Mat. and Manuf. Processes **27**, 523-530 (2012).
3. G. Bartarya and S.K. Choudhury, J. Mat. Proc. Tech. **53**, 1-14 (2012).
4. S.B. Hosseini, R. Dahlgren, K. Ryttberg and U. Klement, Procedia CIRP **14**, 107–112 (2014).
5. M.A. Shalaby, M.A. ElHakim, M.M. Abdelhameed, J.E. Krzanowski, S.C. Veldhuis and G.K. Dosbaeva, Tribo. Int. **70**, 148–154 (2014).
6. R. Pavel, I. Marinescu, M. Deis and J. Pillar, J. Mat. Proc. Tech. **170**, 341-349 (2005).
7. W. Grezesik, Wear **265**, 327–335 (2008).
8. J. Rech and A. Moisan, Int J Mach Tools & Manuf. **43**, 543–550 (2003).
9. M.A. Yallese, K. Chaoui, N. Zeghib, L. Boulanouar and J. Rigal, J. Mat. Proc. Tech. **209**, 1092–1104 (2009).
10. A.K. Sahoo and B. Sahoo, Measurement **45**, 2153-2165 (2012).
11. C. Bruni, A. Forcellese, F. Gabrielli and M. Simoncini, J. Mat. Proc. Tech. **202**, 493–499 (2008).
12. C.H.R. Vikram Kumar and B. Ramamoorthy, J. Mat. Proc. Tech. **185**, 210–216 (2007).
13. A. Bhattacharyya, *Metal cutting: Theory and Practice* (Central Book Publishers, Kolkata, India, 1984).

International Conference on Mechanical Engineering 2015
(ICME 2015) 18 – 20 December, 2015, Dhaka, Bangladesh

Paper ID : 573

Carbon Nanotube Supported Pt-Ni Bimetallic Catalysts for Aqueous Phase Reforming of Glycerol

M. M. Rahman[1, a)], S. M. Rifat Iftekher[1, b)] and R. K. Opu[2, c)]

[1]*Department of Mechanical Engineering, CUET, Chittagong 4349, Bangladesh*
[2]*Departmrnt of Civil Engineering, RUET, Rajshahi 6204, Bangladesh*

[a)] Corresponding author: mmrahman.cuet@gmail.com
[b)] rifatiftu2@gmail.com
[c)] raihan_ruet_ce@yahoo.com

Abstract. Aqueous-phase reforming of biomass derived oxygenated hydrocarbons are expected to produce fuel cell grade (CO<300 ppm) H_2 for sustainable power generation in near future. In this work, monometallic and bimetallic catalysts of Pt and Ni, supported on multi-walled carbon nanotubes (MWNT), were prepared and tested in the aqueous-phase reforming (APR) of glycerol. Amongst the catalysts tested, bimetallic 1Pt-3Ni/MWNT catalyst gave the higher H_2 yield (93%) and selectivity (91%) than the bench mark 1Pt/MWNT catalyst. Irrespective of Pt and Ni ratio, bimetallic Pt-Ni catalysts showed two times higher activity and selectivity towards H_2 production than the monometallic Pt catalysts. Catalyst characterization by XRD, XPS showed a peak shift of Pt in bimetallic Pt-Ni catalyst than the monometallic Pt catalyst. Also the presence of Pt and Ni emission lines, in STEM EDS spectra, from both the bulk and the single crystal particles strongly suggests that Pt is present in close vicinity of Ni particle. The bimetallic interaction between Pt and Ni is thought to be responsible for the high glycerol conversion and gas phase C yield and, ultimately, the high H_2 yield observed.

INTRODUCTION

Hydrogen, a clean fuel that emits only water when combusted or used in PEM (proton exchange membrane) fuel cells, is in growing demand due to the technological advancements made in the fuel cell industry [1]. The full environmental benefit of generating power from hydrogen fuel cells is achieved when the hydrogen is produced from renewable sources such as solar power and biomass. Various renewable oxygenate compounds, such as methanol, sorbitol, glycerol, ethyleneglycol and ethanol, have been used in APR process [2]. Glycerol is produced as a by-product during biodiesel production by transesterification of vegetable oils or animal fats. One ton of biodiesel yields about 110 kg of crude glycerol or about 100 kg of pure glycerol [3]. As biodiesel production increases exponentially, the crude glycerol is also produced in a large amount. One of the promising ways to utilize this diluted crude glycerol is to produce hydrogen by APR. Glycerol can be converted into hydrogen by APR according to the following overall reaction [Eq. (1)]:

$$C_3H_8O_3 + 3H_2O \leftrightarrow 3CO_2 + 7H_2O \qquad (1)$$

Recently, several precious and non-precious metals in combination with different supports have been reported for APR of glycerol [4]. Among this variety of catalysts, the effect of the nature of the metal, as well as the nature of the support on activity, has been studied. Shabaker et al. studied Pt catalysts supported on TiO2, Al2O3, C, SiO2, Al2O3-SiO2, ZrO2, CeO2 and ZnO for the production of H2 by APR [5]; TiO2-supported Pt was the most active. However, the oxide supports are not very stable in the aqueous phase at these reaction conditions. Therefore, less reactive or inert catalyst supports are desired for APR. Wang et al [6] studied both monometallic Pt and bimetallic Pt-Ni catalysts supported on single walled carbon nanotubes (SWNT) prepared by wet-reduction method. Both of them showed higher

APR activity than the alumina supported catalyst. In addition, the catalytic activity and selectivity remained unchanged after a week of steady-state reaction. In this work, we have focused on the APR of glycerol, and have compared a Pt/MWNT catalyst with Pt-Ni/MWNT catalysts having the same Pt loading and different Ni loadings.

EXPERIMENTAL

Catalyst Preparation

The MWNT were sonicated in 1M HNO_3 at 25 °C (Branson sonifier 450) at 20 kHz for 15 min. The objectives were to obtain good dispersion of MWNT in solution and to ensure surface modification of the outer layer of the MWNT with functional groups (i.e. –COOH and –OH) to provide nucleation sites for the deposition of Pt and Ni nanoparticles. The surface modification of MWNT is necessary for metal deposition onto carbon [7, 8]. The nanotubes were then filtered and dried for further use. $[Pt(NH_3)_4](NO_3)_2$ (Strem Chemical) and $Ni(NO_3)_2\cdot 6H_2O$ (Sigma–Aldrich) were dissolved, individually or together, into ethanol to make monometallic or bimetallic catalysts, respectively. These were deposited on refluxed MWNT using a conventional impregnation technique. The mixture was then stirred overnight at room temperature, and the ethanol was allowed to evaporate. The sample was then dried in air at 100 °C for 12 h and calcined under flowing NO (1.5 vol.% with Ar) at 500 °C for 60 min (heating rate 5 °C/min). Catalysts were reduced in situ in flowing H_2 (25 vol.% with N_2) at 650 °C for 30 min (heating rate 5 °C/min) at atmospheric pressure.

Catalytic Test

The APR of glycerol was studied in a continuous flow type fixed bed reactor system. The catalyst (100mg) was loaded into a 5-mm i.d. stainless steel tubular reactor and held in position with quartz wool plugs. Reaction temperature was measured by a K-type thermocouple that was placed inside the reactor, very close to the catalyst bed. The reactor was mounted in a tube furnace (MTI GSL-1100X). A backpressure regulator (0 to 1000 psig, Swagelok) attached to a pressure gauge was used to pressurize the system with N_2, typically at 40 bar. A 1-wt% glycerol solution was introduced by a hplc digital pump (Waters 510) at a rate of 0.05 mL/min, and heating of the catalyst bed was initiated. When the reactor reached at 250 °C, N_2 flow was set at 50 sccm using a Bronkhorst mass flow controller. The system was allowed to stabilize for about 2 h before analysis of the reaction products began. Gas products were analyzed at 25-min intervals using an online gas chromatograph (Varian CP-3800) equipped with one Hayesep N, 60/80 Mesh, 5 m x 1/8″ SST column and one Molsieve 5Å, 60/80 Mesh, 1 m x 1/8" column, connected in series. Liquid products were analyzed with a Shimadzu HPLC, comprising a degasser (DGU-20A5), a pump (LC-20AD), an autosampler (SIL-20A HT), an oven (CTO-20A), and a refractive index detector (RID-10A). A Rezex RCM-Monosaccharide column (300 × 7.8 mm) was used for analyte separation. Also Shimadzu TOC-L (with auto sampler ASI-L) was used to know the total organic carbon content of the liquid phase.

RESULTS AND DISCUSSION

Catalyst Characterization

TABLE 1. N_2 physorption and H_2 chemisorption results. Unless otherwise noted, the catalysts were calcined under the flow of NO (1.5 vol.% with Ar) at 500 °C for 60 min

Catalysts	**S_{BET} (m^2/g)**	**V_{Pore} (cm^3/g)**	**D_{Pore} [nm]**	**H_2 uptake (μmol/g)**	**M_{disp} (%)**
1Pt/MWNT	296	1.6	31.9	21	38
1Pt-3Ni/MWNT	290	1.58	31.6	24	45
1Pt-6Ni/MWNT	284	1.55	31.3	26	41
1Pt-12Ni/MWNT	269	1.40	31.0	22	32
12Ni/MWNT	272	1.41	31.0	15	29

The specific surface area (Brunauer-Emmett-Teller, S_{BET}) [10], pore size (Barrett–Joyner–Halenda, BJH, adsorption branch) [11], and pore volume were measured by N_2 adsorption at liquid nitrogen temperature (−196 °C) using an Autosorb-IQ apparatus; the results are given in Table 1. Results showed that both the surface area and pore volume decreases with the increase of metal loadings. No significant change of pore diameter was observed. H_2 chemisorption was carried out using an Autosorb-IQ apparatus (Quantachrome Corporation), and measureing at water bath temperature of 60 °C. The H_2 chemisorption data is summarized in Table 1. The highest metal dispersion, 45%, was observed for the introduction of 3 wt% Ni into 1Pt/MWNT catalyst, even though metal dispersion decreased with higher Ni loading. This highest metal dispersion (45%) could be partly responsible for higher H_2 yield (Figure 3) and reaction rate (Table 2) observed by 1Pt-3Ni/MWNT catalyst.

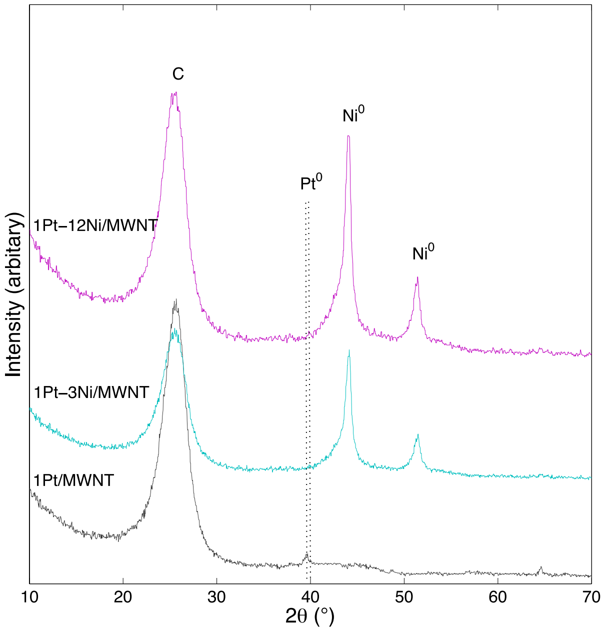

FIGURE 1. X-ray diffraction patterns of Pt and Pt-Ni catalysts. Pt catalyst was reduced at 350 °C and the Pt-Ni catalysts were reduced at 650 °C in flowing H_2 (25 vol.% with N_2) for 30 min (ramp rate of 5 °C/min).

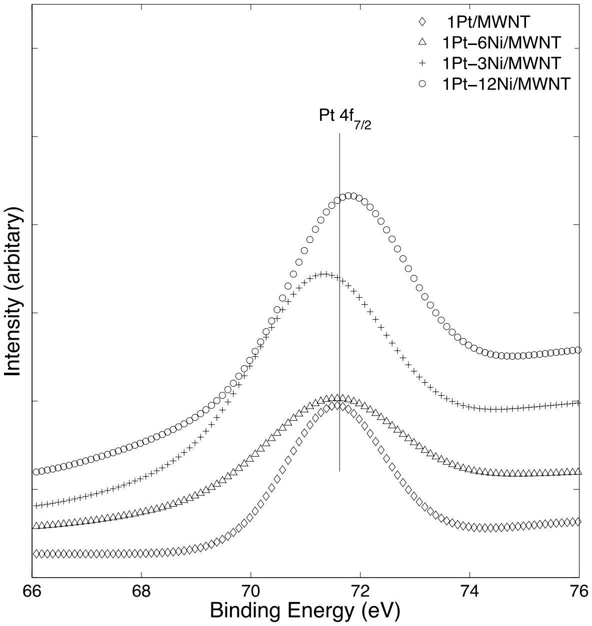

FIGURE 2. XPS patterns of Pt, Pt-Ni and Ni catalysts. Samples were calcined at 500 °C for 60 min in flowing NO (1.5 vol.% with Ar).

The crystalline structure of the supported catalysts was determined by X-ray diffractometry using Cu Kα radiation (λ = 0.1542 nm) and a graphite monochromator (model S6000, Shimadzu). Figure 1 shows that Pt (111) diffraction peak positions of bimetallic Pt-Ni catalysts slightly move to higher positions compared to monometallic Pt catalyst, indicating an interaction between Pt and Ni. The similar phenomenon of bimetallic interaction between Pt and Ni, Pt and Cu, Pt and Co were observed and confirmed in the previous reports [12]. The bimetallic interaction between Pt and Ni is thought to be responsible for the higher catalytic activity and selectivity towards H_2 production than the monometallic Pt and Ni catalysts. X-ray photoelectron spectra were recorded on an ESCALAB250Xi (Thermo Scientific, UK) using a monochromated Al Kα source (1486.68 eV) operating at 164W (10.8 mA and 15.2kV) and under a vacuum of $\leq 2 \times 10^{-9}$ mbar. Binding energies were referenced to the adventitious hydrocarbon C1*s* signal at 285.0 eV. As shown in Figure 2, the Pt 4f XPS peaks of Pt-Ni catalysts shift to low binding energy compared to pure Pt catallyst, in particular to 1Pt-3Ni sample, indicating that the electronic structure of Pt was modified when Ni was introduced. Also Ni 2p peak intensity decreases as the Pt/Ni atomic ratio increases. This result is similar to the results of Pt coated Au nanoparticles with core-shell structure [13].

Catalytic Tests

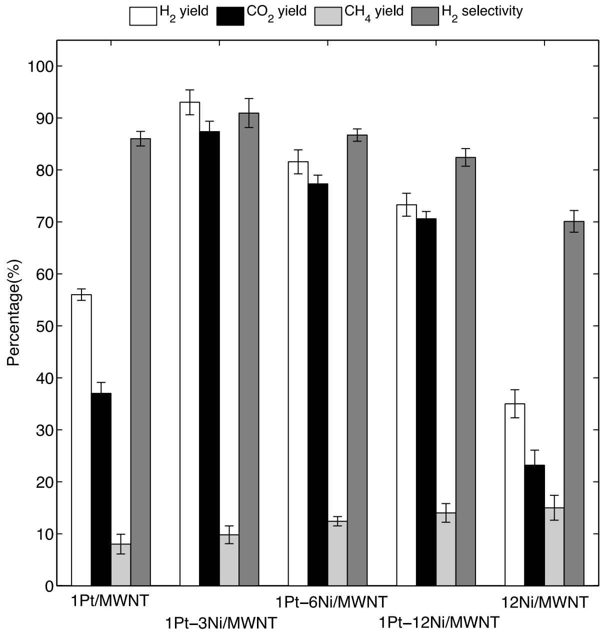

FIGURE 3. Effect of Ni addition to 1Pt/MWNT catalysts on yield and selectivity in the aqueous phase reforming of glycerol (250 °C, 40 bar, 0.05 mL/min, 100mg catalyst; data are mean values over t = 3–100 h).

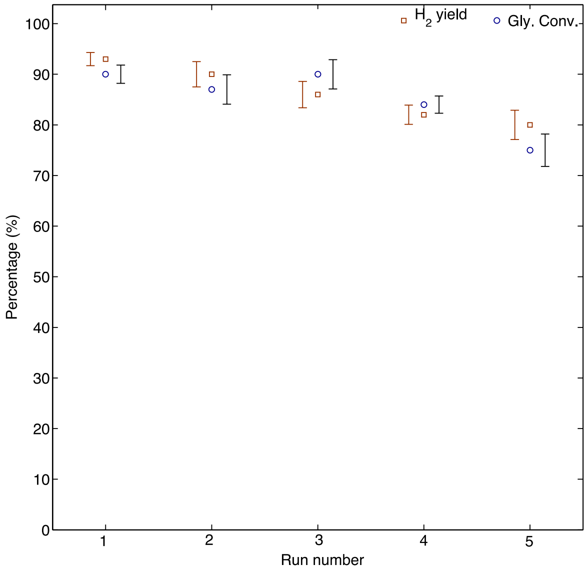

FIGURE 4. Repeated runs in the ARR of glycerol on 1Pt-3Ni/MWNT catalyst (240 °C, 40 bar, 1 wt% glycerol, 0.05 mL/min, 100 mg catalyst; data are mean values over t = 3–100 h). Error bars indicate one standard deviation; each bar is the average of ≥2 experiments.

Several bimetallic catalysts have been studied for APR of glycerol to date [6, 14-18]. We chose to study the influence of Ni as the promoter element on the performance of 1Pt/MWNT catalyst for the APR of glycerol. The effect of the Ni loading in the catalyst on the gas phase yield is presented in Figure 3. The combination of Pt and Ni increased the hydrogen yield and selectivity rather than monometallic Pt and Ni catalysts. Results shows that as the Pt:Ni ratio increases from 1:3 to 1:12, both the hydrogen yield and selectivity decreases, as the methane yield increases. The higher hydrogen yield (93%) and selectivity (91%) was achieved for 1 wt% Pt-3 wt% Ni loading than the benchmark 1Pt/MWNT catalyst. Even though, the non-novel metal catalyst, 12Ni/MWNT, showed promising results compared to highly expensive novel metal catalyst, 1Pt/MWNT, but it showed severe deactivation after 40 hours on stream, infact H_2 peak was completely disappeared after 60 h on stream. Also traces of CO and C_2H_6 was identified for 12Ni/MWNT catalyst, but were not further quantified. Among the bimetallic catalysts we tested, 1Pt-3Ni/MWNT gave the highest H_2 yield, glycerol conversion, gas phase C yield, H_2 rate and lowest CH_4 yield. So to investigate the stability of the 1Pt-3Ni/MWNT catalyst, further 4 runs were made each with 100 h on stream, the results were depicted in Figure 4. After the first run, the reactor was heated at 120 °C for 6 h and at the same time flashed with Ar to get ride of all the gaseous and liquid species trapped in the rig and the same procedure was followed before each run. As shown in Figure 4, H_2 yield was almost same for the first three runs and then decreased in 4th and 5th run. Over all after 5th run (more than 500 h on strem) H_2 yield decreased 14% and glycerol conversion decreased about 17% of the 1st run.

The liquid phase after reaction was also analyzed for all the reactions. Apart from un-reacted glycerol, traces of some other compounds were also identified, particularly ethanol, ethylene glycol, acetic acid and propylene glycol, but were not further quantified. Glycerol conversion rate, gas phase C yield, and reaction rates are shown in Table 2. Compare to monometallic Pt and Ni catalyst, all bimetallic Pt-Ni catalysts showed much higher glycerol conversion and gas phase C yield, which might be due to the interaction between Pt and Ni. Similar phenomenon has been observed by Boga et al. [19] while studying the APR of glycerol over bimetallic Pt-Cu catalysts. The highest glycerol conversion rate (>99%) and gas phase C yield (99%) was observed for 3 wt% Ni loading in 1Pt/MWNT catalyst and as the Ni loading increased to 12 wt%, glycerol conversion rate and gas phase C yield decreased to 90% and 88% respectively. The lowest glycerol conversion rate (44%) and gas phase C yield (41%) was observed for 12Ni/MWNT catalyst. The interaction between Pt and Ni greatly increased the conversion of the APR reaction, even the co-existence of individual Pt and Ni nanoparticles can greatly increase the conversion of the APR reaction, in good accordance with the literature [6].

TABLE 2. Glycerol conversion, Gas phase C yield, Reaction rate and H_2 formation rate in the aqueous-phase reforming of glycerol over MWNT supported catalysts (250 ˚C, 40 bar, 0.05 mL/min, 100mg catalyst); data are mean values over t = 3–100 h).

Catalysts	Gly. Conv. (%)	Gas phase C yield (%)	Reaction rate (mol gPt^{-1} h^{-1})	H_2 formation rate (mmol gCat^{-1} h^{-1})	C Balance, out/in (%)
1Pt/MWNT	53.6	46	0.17	1.02	97
1Pt-3Ni/MWNT	>99	99	0.32	2.12	98
1Pt-6Ni/MWNT	93.4	91	0.30	1.93	95
1Pt-12Ni/MWNT	89.7	88	0.29	1.74	103
12Ni/MWNT	44.0	41	0.11	0.78	96

Inductively coupled plasma atomic emission spectrometry (ICP–AES) analysis of the liquid effluent showed no measurable leaching of Pt and Ni. XRD pattern of spent 1P-3N/MWNT catalyst showed diffraction lines for NiO at 2θ = 37.2, 43.3, and 62.9° representing the (111), (200), and (220) planes, respectively [4, 20], means some of the Ni particles were oxidized to NiO ,which could be responsible for the deactivation of the catalyst. Also the deactivation of the catalyst might be ascribed to the carbon deposition on the catalyst [21, 22]

CONCLUSIONS

In this work, monometallic Pt and bimetallic Pt-Ni catalysts having the same Pt loading but different Ni loading, supported on multi-walled carbon nanotubes (MWNT), were prepared and tested in the aqueous-phase reforming (APR) of glycerol. Amongst the catalysts tested, bimetallic 1Pt-3Ni/MWNT catalyst gave the higher H_2 yield (93%) and selectivity (91%) than the bench mark 1Pt/MWNT catalyst. Irrespective of Pt and Ni ratio, bimetallic Pt-Ni catalysts showed two times higher activity and selectivity towards H_2 production than the monometallic Pt catalysts. To study the effect of support on the performance of monometallic Pt catalyst in APR process, two others support Al_2O_3 and MgO was also tested. MWNT support showed a positive effect on APR process, which could be due to its hydrophobic nature. Catalyst characterization by XRD, XPS showed a peak shift of Pt in bimetallic Pt-Ni catalyst than the monometallic Pt catalyst. Also the presence of Pt and Ni emission lines, in STEM EDS spectra, from both the bulk and the single crystal particles strongly suggests that Pt is present in close vicinity of Ni particle. The bimetallic interaction between Pt and Ni is thought to be responsible for the high glycerol conversion and gas phase C yield and, ultimately, the high H_2 yield observed.

REFERENCES

1. S. Dunn, Hydrogen futures: toward a sustainable energy system, Int. J. Hydrogen Energy, 27 (2002) 235-264.
2. R.D. Cortright, R.R. Davda, J.A. Dumesic, Hydrogen from catalytic reforming of biomass-derived hydrocarbons in liquid water, Nature, 418 (2002) 964-967.
3. A. Behr, J. Eilting, K. Irawadi, J. Leschinski, F. Lindner, Improved utilisation of renewable resources: New important derivatives of glycerol, Green Chem., 10 (2008) 13-30.
4. A. Iriondo, V.L. Barrio, J.F. Cambra, P.L. Arias, M.B. Güemez, R.M. Navarro, M.C. Sánchez-Sánchez, J.L.G. Fierro, Hydrogen Production from Glycerol Over Nickel Catalysts Supported on Al2O3 Modified by Mg, Zr, Ce or La, Top Catal, 49 (2008) 46-58.
5. J.W. Shabaker, G.W. Huber, R.R. Davda, R.D. Cortright, J.A. Dumesic, Aqueous-Phase Reforming of Ethylene Glycol Over Supported Platinum Catalysts, Catal. Lett., 88 (2003) 1-8.

6. X. Wang, N. Li, L.D. Pfefferle, G.L. Haller, Pt–Co bimetallic catalyst supported on single walled carbon nanotube: XAS and aqueous phase reforming activity studies, Catal. Today, 146 (2009) 160-165.
7. T.W. Ebbesen, H. Hiura, M.E. Bisher, M.M.J. Treacy, J.L. Shreeve-Keyer, R.C. Haushalter, Decoration of carbon nanotubes, Adv. Mater., 8 (1996) 155-157.
8. R. Yu, L. Chen, Q. Liu, J. Lin, K.-L. Tan, S.C. Ng, H.S.O. Chan, G.-Q. Xu, T.S.A. Hor, Platinum Deposition on Carbon Nanotubes via Chemical Modification, Chemistry of Materials, 10 (1998) 718-722.
9. M.S. Holm, Y.J. Pagan-Torres, S. Saravanamurugan, A. Riisager, J.A. Dumesic, E. Taarning, Sn-Beta catalyzed conversion of hemicellulosic sugars, Green Chem., 14 (2012) 702-706.
10. P.H.E. Stephen Brunauer, and Edward Teller, Adsorption of Gases in Multimolecular Layers, Journal of the American Chemical Society, 60 (1938) 309-319.
11. [11] L.G.J. Elliott P. Barrett, and Paul P. Halenda, The Determination of Pore Volume and Area Distributions in Porous Substances. I. Computations from Nitrogen Isotherms, Journal of the American Chemical Society, 73 (1951) 373-380.
12. A. Tegou, S. Papadimitriou, I. Mintsouli, S. Armyanov, E. Valova, G. Kokkinidis, S. Sotiropoulos, Rotating disc electrode studies of borohydride oxidation at Pt and bimetallic Pt–Ni and Pt–Co electrodes, Catal. Today, 170 (2011) 126-133.
13. D. Zhao, B.-Q. Xu, Enhancement of Pt Utilization in Electrocatalysts by Using Gold Nanoparticles, Angew. Chem. Int. Ed., 45 (2006) 4955-4959.
14. G.W. Huber, J.W. Shabaker, S.T. Evans, J.A. Dumesic, Aqueous-phase reforming of ethylene glycol over supported Pt and Pd bimetallic catalysts, Appl. Catal., B, 62 (2006) 226-235.
15. R.T.K. Baker, J.A. Dumesic, J.J. Chludzinski Jr, The effect of various bimetallics on the graphite-steam reaction, J. Catal., 101 (1986) 169-177.
16. E.L. Kunkes, D.A. Simonetti, J.A. Dumesic, W.D. Pyrz, L.E. Murillo, J.G. Chen, D.J. Buttrey, The role of rhenium in the conversion of glycerol to synthesis gas over carbon supported platinum–rhenium catalysts, J. Catal., 260 (2008) 164-177.
17. E.-Y. Ko, E. Park, K. Seo, H. Lee, D. Lee, S. Kim, Pt–Ni/γ-Al2O3 catalyst for the preferential CO oxidation in the hydrogen stream, Catal. Lett., 110 (2006) 275-279.
18. S.A. Tupy, A.M. Karim, C. Bagia, W. Deng, Y. Huang, D.G. Vlachos, J.G. Chen, Correlating Ethylene Glycol Reforming Activity with In Situ EXAFS Detection of Ni Segregation in Supported NiPt Bimetallic Catalysts, ACS Catalysis, 2 (2012) 2290-2296.
19. D.A. Boga, R. Oord, A.M. Beale, Y.-M. Chung, P.C.A. Bruijnincx, B.M. Weckhuysen, Highly Selective Bimetallic Pt-Cu/Mg(Al)O Catalysts for the Aqueous-Phase Reforming of Glycerol, CHEMCATCHEM, 5 (2013) 529-537.
20. R.L. Manfro, A.F. da Costa, N.F.P. Ribeiro, M.M.V.M. Souza, Hydrogen production by aqueous-phase reforming of glycerol over nickel catalysts supported on CeO2, Fuel Process. Technol., 92 (2011) 330-335.
21. R.R. Davda, J.A. Dumesic, Renewable hydrogen by aqueous-phase reforming of glucose, Chemical Communications, 0 (2004) 36-37.
22. T. Yoshida, Y. Oshima, Y. Matsumura, Gasification of biomass model compounds and real biomass in supercritical water, Biomass Bioenergy, 26 (2004) 71-78.

International Conference on Mechanical Engineering 2015
(ICME 2015) 18 – 20 December, 2015, Dhaka, Bangladesh

Paper ID : 582

Comparison of Oil Refining and Biodiesel Production Process between Screw press and n-hexane Techniques from Beauty Leaf Feedstock

M. M. K Bhuiya[1, a)], M. G. Rasul[1], M. M. K. Khan[1] and N. Ashwath[2]

[a]*Central Queensland University, School of Engineering and Technology*

[b]*Central Queensland University, Centre for Plant and Water Science Rockhampton, Queensland 4702, Australia*

[a)]Corresponding author: m.bhuiya@cqu.edu.au

Abstract. The Beauty Leaf Tree (*Callophylum inophyllum*) is regarded as an alternative source of energy to produce 2nd generation biodiesel due to its potentiality as well as high oil yield content in the seed kernels. The treating process is indispensable during the biodiesel production process because it can augment the yield as well as quality of the product. Oil extracted from both mechanical screw press and solvent extraction using n-hexane was refined. Five replications each of 25 gm of crude oil for screw press and five replications each of 25 gm of crude oil for n-hexane were selected for refining as well as biodiesel conversion processes. The oil refining processes consists of degumming, neutralization as well as dewaxing. The degumming, neutralization and dewaxing processes were performed to remove all the gums (phosphorous-based compounds), free fatty acids, and waxes from the fresh crude oil before the biodiesel conversion process carried out, respectively. The results indicated that up to 73% and 81% of mass conversion efficiency of the refined oil in the screw press and n-hexane refining processes were obtained, respectively. It was also found that up to 88% and 90% of biodiesel were yielded in terms of mass conversion efficiency in the transesterification process for the screw press and n-hexane techniques, respectively. While the entire processes (refining and transesterification) were considered, the conversion of beauty leaf tree (BLT) refined oil into biodiesel was yielded up to 65% and 73% of mass conversion efficiency for the screw press and n-hexane techniques, respectively. Physico-chemical properties of crude and refined oil, and biodiesel were characterized according to the ASTM standards. Overall, BLT has the potential to contribute as an alternative energy source because of high mass conversion efficiency.

INTRODUCTION

The BLT is a prospective source of non-edible vegetable oil for producing 2nd generation biodiesel due to its capability of growing in a varieties of climate conditions. It can be easily cultivated, the fruit production rate is higher as well as its seeds kernel contains high oil yield. Plenty of native species which are capable to produce biodiesel at substantial quantities have been evaluated for growth on decadent land in Australia [1]. BLT fruits are produced abundantly two times/year and seed kernels contain up to 65% of non-edible oil [2, 3] and higher than most of the general oil seed harvests such as *Jatropha curcas*- 40%, *Pongamia pinnata* – 30%, oil palm - 60% [4]. BLT accomplishes reproductive maturity in 7 years as well as can yield fruits up to 200 years [2]. Based on the fatty acid composition of BLT oil, it has been established that the fatty acid methyl esters of BLT abide by the American Society for Testing Materials (ASTM) and European Union (EN) biofuel standards [4].

However, the oil treatment process is significant as the gum, FFAs, water, phosphorous compounds as well as wax substances are contained in the crude vegetable oil which can reduce the biodiesel quality, and these should be removed prior to the biodiesel production [5]. Generally, crude oil treating process is done in order to remove the undesirable components such as dirt, moisture, proteins, gums, resins, phosphates, waxes etc. [6, 7]. Furthermore, the biodiesel produced from the refining oil affects the yield as well as quality of the biodiesel [8]. The unwanted components are removed by means of the treatments of purification, degumming, neutralization, bleaching and deodorization [7, 9]. Therefore, the purpose of the treatment process is to improve the oil quality by eradicating the undesirable compounds such as phospholipids, FFAs and pigments [7, 10].

Biodiesel is produced from vegetable oils via a transesterification process which is the most popular technology [11, 12]. Moreover, this technique has been identified as a widely accepted technique for industrialized biodiesel production due to its high conversion efficiency and low cost [13]. Transesterifictaion is the chemical reaction in which triglycerides is reacted with alcohol in the presence of appropriate catalyst. Crude glycerol and monoalkyl ester (biodiesel) are the output products of a successful transesterification process.

Therefore, the aim of this study is to accomplish a complete refining process of the BLT crude oil produced from screw press and n-hexane techniques, conduct the transesterification process to produce biodiesel and mass balances for the refining as well as biodiesel conversion processes. The American Society for Testing Materials (ASTM) standards D6751 was used to characterize the physico-chemical properties of resulting biodiesel.

MATERIALS AND METHOD

BLT oil extractions

Two methods namely mechanical oil extraction using an electric powered screw press and chemical (solvent) extraction using n-hexane as a solvent were used for oil extraction from the prepared seed kernels. The mechanical oil extraction technique was conducted using a Mini 40 Screw Press at Centre for Plant and Water science (CPWS) in Central Queensland University (CQU). Properly dried and treated BLT kernel samples were used to extract oil by this method.

In solvent extraction, the kernels were ground using a blender and coffee grinder machine to achieve a fine consistency to maximize particle surface area. Then n-hexane was added at a ratio of 2:1 (ml hexane: grams kernel) into conical flasks in which ground kernels were put. After reacting the oil mixtures were collected, filtered and decanted into aluminium foil containers for evaporating the solvent and placed under the fume hood.

Oil refining processes

Vegetable oils must be properly pre-treated prior to the transesterification process for biodiesel production. Oil refining processes consists of degumming, neutralization (deacidification) as well as dewaxing. The degumming process removes unwanted phosphorous content, whereas neutralization and dewaxing processes removes free fatty acids (FFAs) and waxes, respectively. If FFAs are not removed, it will latter convert into soap. Moreover, FFAs will reduce the conversion efficiency for the production of biodiesel as these sometimes contain some of the catalysts [14].

Degumming

The purpose of the degumming process was to remove the gums i.e. phosphorous-based compounds, primarily lecithin and cephalin from the fresh crude oil before converting it into biodiesel. First heated the filtered oil up to 60^0C about 2 hours and then added the heated (60^0C) deionized water (DI) into each replication of oil (5 for screw press and 5 for n-hexane). Acid degumming and water degumming were conducted for 4 replications and 1 replication of the crude oil, respectively. Acid degumming was performed by adding 4% (wt.) H_3PO_4 solution. The solution was heated at about 65^0C and kept for 30 minutes. After centrifugation all the hydrated gums and the oil were separated, weighted and the results were recorded.

Neutralization

In general, the crude vegetable oils contain free fatty acids from natural hydrolysis of triglycerides. The neutralization process was conducted to remove the free fatty acids before biodiesel production. In order to do this the sodium hydroxide (NaOH) aqueous solution (8% wt) was mixed with the degummed oil of each replication 5 for screw press and 5 for n-hexane techniques. After that the oil was washed with 35^0C warm tap water twice to make sure that all traces of soap were eliminated. Finally, the oil, gum and soap solution were separated by centrifugation. The oil as well as recovered gum and soap were recorded.

Dewaxing

The vegetable oil also contains large amount of waxes approach to the cloud when refrigerated or brought to lower temperatures. Therefore, the waxes have to be removed before biodiesel conversion process carried out. In order for that 5% (wt.) sodium hydroxide aqueous solution and 5% (wt.) de-ionised (DI) water were added, respectively, into the neutralized oil of each replication. The mixture was placed in a chiller at 5^0C and agitated for about 4 hours. The soapy water wetted the waxes and helped to move from oil to water phase. Finally, the oil, wax and soap were separated by centrifugation and recorded their weights.

BIODIESEL CONVERSION THROUGH TRANSESTERIFICATION PROCESS

The BLT refined oil was converted into biodiesel via transesterification process. To carry on the transesterification process sodium methoxide solution was prepared first by adding NaOH solution (1% wt.) and methanol (11.12% wt.) in a covered conical flask. The transesterification process was then conducted by adding sodium methoxide solution into the heated refined oil. The reaction temperature was maintained less than 65^0C and allowed for half an hour. After completing the reaction, the mixture was poured in the separatory funnel to separate the biodiesel and glycerin. Finally, the glycerin was removed and the biodiesel was washed with warm DI before further processing i.e. analyzing its properties.

Characterization of BLT oil and biodiesel

Physico-chemical properties of BLT crude as well as refining oil produced from screw press and n-hexane techniques were characterized according to the ASTM standards which are shown in Table1. Adhvaryu et al. [15] reported that the deposition of wax substances in oil directed to the increase in viscosity. Therefore, it is necessary to remove the wax materials which results in a lower viscosity in refined oil. Moreover, the refined oil was found to be clearer and lighter yellow colour than the crude oil. This is because of the elimination of some unwanted components through the refining process.

Biodiesel obtained through transesterification was characterized in accordance with ASTM D6751-08 standard. Physico-chemical properties of BLT biodiesel are shown in TABLE 1.

Mass balance

The mass balance for the refining oil and the biodiesel were determined in accordance with the oil input and the weights of the products.

TABLE 1. Physico-chemical properties of BLT crude and refined oil, and biodiesel.

Method	Oil Type	Property	Sample No.				
			1	2	3	4	5
Screw press	Crude	Density@ 28^0C (g/mL)	0.8905	0.8875	0.8882	0.8936	0.8953
		Viscosity@ 40^0C (poise)	0.5336	0.5277	0.5288	0.5318	0.5333
		Acid value (mg KOH/g oil)	31.42	31.19	31.3	31.86	30.24
		pH value	4.68	4.67	4.62	4.32	4.14
n-hexane	Crude	Density@ 28^0C (g/mL)	0.9011	0.8969	0.9012	0.9036	0.9057
		Viscosity@ 40^0C (poise)	0.5372	0.5426	0.5339	0.5412	0.5333
		Acid value (mg KOH/g oil)	32.65	32.87	32.71	32.58	31.96
		pH value	4.82	4.65	4.46	4.58	4.49
Screw press	Refined	Density@ 28^0C (g/mL)	0.8744	0.8666	0.8748	0.8711	0.871
		Viscosity@ 40^0C (poise)	0.4184	0.4464	0.4207	0.4248	0.4318
		Acid value (mg KOH/g oil)	6.23	6.34	5.78	6.17	6.4
		pH value	7.82	7.42	7.79	7.44	7.49
n-hexane	Refined	Density@ 28^0C (g/mL)	0.8655	0.8716	0.8682	0.8728	0.8631
		Viscosity@ 40^0C (poise)	0.4054	0.4103	0.4278	0.4156	0.4034
		Acid value (mg KOH/g oil)	3.37	3.31	4.14	3.2	3.09
		pH value	7.63	7.99	7.31	7.24	7.38
Screw press	Biodiesel	Density@ 28^0C (g/mL)	0.8631	0.8578	0.8616	0.8653	0.8625
		Viscosity@ 40^0C (poise)	0.0497	0.0489	0.0503	0.0483	0.0479
		Acid value (mg KOH/g oil)	0.79	0.67	0.73	0.61	0.56
		pH value	8.83	8.94	8.68	8.56	8.79
n-hexane	Biodiesel	Density@ 28^0C (g/mL)	0.8571	0.8548	0.8514	0.8523	0.8483
		Viscosity@ 40^0C (poise)	0.0448	0.0441	0.0453	0.0445	0.0458
		Acid value (mg KOH/g oil)	0.45	0.56	0.51	0.63	0.43
		pH value	9.55	9.4	9.48	9.57	9.64

The mass balance for a refining process was evaluated based on the weights of initial crude oil and products obtained at each step, whereas, for a transesterification process, it was obtained based on the refined oil and the biodiesel yield. The mass balance for a refining process for screw press and n-hexane techniques are shown in FIGURES. 1 and 2, respectively. And the mass balance for a transesterification process for screw press and n-hexane techniques are shown in FIGURES 3 and 4, respectively. The efficiency of BLT crude oil conversion into refined oil and then produce biodiesel and by-products (glycerin) namely “% Mass conversion” was estimated using equations 1 and 2.

$$\text{\% Mass conversion} = \frac{Wprod}{Wcrude\ oil} \times 100\% \tag{1}$$

$$\text{\% Mass losses} = 100\% - \sum(\%\ Mass\ conversion\ of\ all\ products) \tag{2}$$

Where, W_{prod} is the weight of products, kg

$W_{crude\ oil}$ is the initial weight of BLT crude oil, kg

The overall mass balance by considering the whole processes (refining and transesterification) is presented in FIGURES 5 and 6.

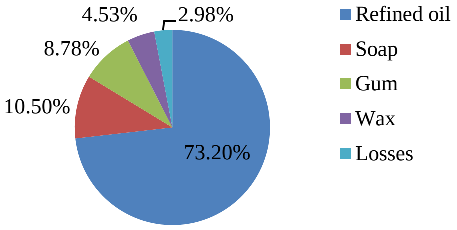

FIGURE 1. Mass balance for a refining process in screw press

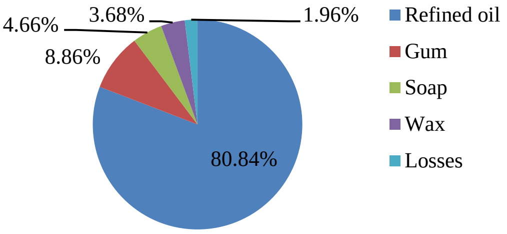

FIGURE 2. Mass balance for a refining process in n-hexane

RESULTS AND DISCUSSION

The BLT oil extracted from both a screw press and n-hexane was refined through degumming, neutralization and dewaxing processes.

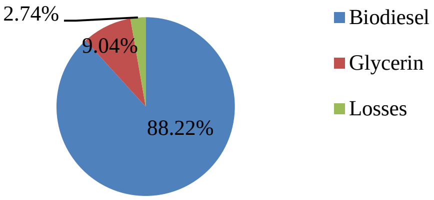

FIGURE 3. Mass balance of transesterification process in screw press

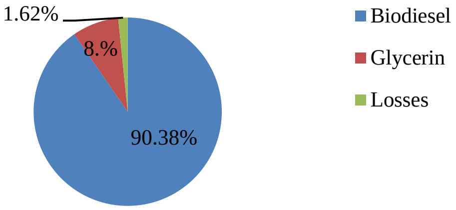

FIGURE 4. Mass balance of transesterification process in n-hexane

The degumming process was conducted for both acid degumming and water degumming. Approximately 73% of mass conversion efficiency of refined oil was obtained in screw press technique which include 8.786 % gum, 10.50% soap, 4.53% wax and 2.73% % other losses as shown in FIGURE 1. On the other hand, about 81% of mass conversion efficiency of refined oil was obtained in n-hexane method which include 8.86 % gum, 4.66% soap, 3.68% wax and 1.96% % other losses as shown in FIGURE 2. Large amount of soap by-product in neutralization process indicated high FFA composition, which reduced the yield of biodiesel conversion [16]

Refined oil was converted into biodiesel via a transesterification protocol by using a sodium methoxide solution into the oil sample. Up to 88 % (wt.) of mass conversion efficiency of biodiesel with 9% glycerine and 3% other losses was obtained in screw press method through transesterification process as shown in FIGURE 3.

The transesterification technique yielded the mass conversion efficiency up to 90 % (wt.) of biodiesel with 8% glycerine and 2% other losses in n-hexane method as shown in FIGURE 4. While the entire processes (refining and transesterification) were considered, up to 65% and 73% of mass conversion efficiency were obtained for screw press and n-hexane methods, respectively, which are shown in FIGURES 5 and 6, respectively. The ASTM characterization of obtained biodiesel was performed to confirm that the biofuel would meet the specification of standard fuels. The values of the physico-chemical properties were varied for crude and refined oil, as well as the biodiesel. All properties of BLT biodiesel met the ASTM standard specifications.

CONCLUSION

In this study, BLT oil purifying process and then conversion of refined oil into biodiesel through transesterification protocol were successfully performed. The results indicated that after treating the oil the good quality of BLT biodiesel was obtained. The properties of the BLT crude and refined oil, and BLT biodiesel were determined in accordance with the ASTM standards and the results showed that the BLT biodiesel has met the ASTM standard of fuel.

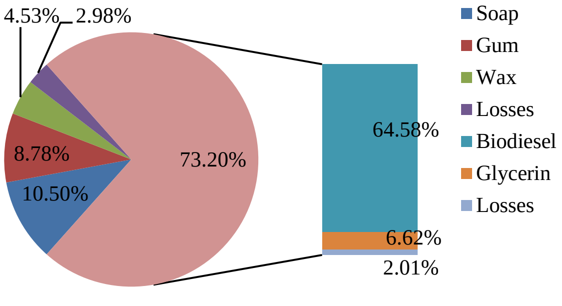

FIGURE 5. Mass balance for the complete (refining and transesterification) process in screw press

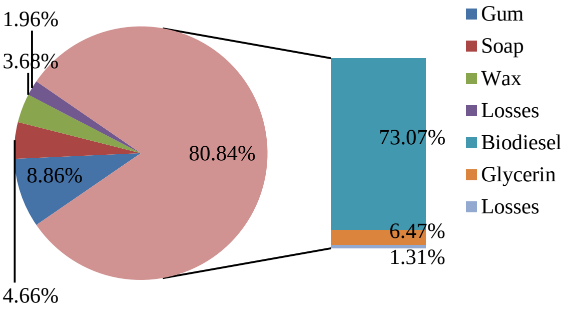

FIGURE 6. Mass balance for the complete (refining and transesterification) process in n-hexane

Approximately 73 and 81% of mass conversion efficiency was obtained through screw press and n-hexane refining processes, respectively. In biodiesel production through transesterification process, around 88% and 90% of mass conversion efficiency were yielded for screw press and n-hexane techniques, respectively. The conversion of BLT refined oil into biodiesel was yielded up to 65% and 73% of mass conversion efficiency for screw press and n-hexane techniques while the entire processes (refining and transesterification) were considered, respectively

REFERENCES

1. N. Ashwath, *Evaluating biodiesel potential of Australian native and naturalised plant species*. (Rural Industries Research and Development Corporation, 2010).
2. J. Friday and D. Okano, Traditional Tree Initiative, Hawaii (2006).
3. H. Hathurusingha and N. Ashwath, presented at the 12th international forestry symposium, Kalutara, Sri Lanka, 2007 (unpublished).
4. M. M. Azam, A. Waris and N. Nahar, Biomass and bioenergy **29** (4), 293-302 (2005).
5. C. M. Fernández, M. J. Ramos, Á. Pérez and J. F. Rodríguez, Bioresource Technology **101** (18), 7019-7024 (2010).
6. D. I. Sánchez-Machado, J. López-Cervantes, J. A. Núñez-Gastélum, G. Servín de la Mora-López, J. López-Hernández and P. Paseiro-Losada, Food Chemistry **187**, 53-57 (2015).
7. G. Santori, G. Di Nicola, M. Moglie and F. Polonara, Applied Energy **92** (0), 109-132 (2012).
8. I. M. Atadashi, M. K. Aroua, A. R. A. Aziz and N. M. N. Sulaiman, Applied Energy **88** (12), 4239-4251 (2011).
9. J. Kongkasawan and S. Capareda, International Energy Journal **13** (4), 169-176 (2012).
10. M. V. Ruiz-Méndez, G. Márquez-Ruiz and M. C. Dobarganes, Food Chemistry **60** (4), 549-554 (1997).
11. C. Verdugo, D. Luna, A. Posadillo, E. D. Sancho, S. Rodríguez, F. Bautista, R. Luque, J. M. Marinas and A. A. Romero, Catalysis Today **167** (1), 107-112 (2011).
12. J. V. Gerpen, Fuel Processing Technology **86** (10), 1097-1107 (2005).
13. L. Lin, Z. Cunshan, S. Vittayapadung, S. Xiangqian and D. Mingdong, Applied Energy **88** (4), 1020-1031 (2011).
14. S. Capareda, *Introduction to biomass energy conversions*. (CRC Press, 2013).
15. A. Adhvaryu, S. Erhan and J. Perez, Thermochimica acta **395** (1), 191-200 (2002).
16. M. Y. Koh and T. I. M. Ghazi, Renewable and Sustainable Energy Reviews **15** (5), 2240-2251 (2011).

International Conference on Mechanical Engineering 2015
(ICME 2015) 18 – 20 December, 2015, Dhaka, Bangladesh

Paper ID : 589

Electrospun Nylon 6 Microfiltration Membrane for Treatment of Brewery Wastewater

Md. Shahidul Islam[a] and Md. Saifur Rahaman[b]

Department of Building, Civil and Environmental Engineering, Concordia University, Montreal, Quebec, Canada H3G 1M8

[a]Corresponding author: shahidul@du.ac.bd
[b]saifur.rahaman@concordia.ca

Abstract. Nylon 6 microfiltration membrane, for the treatment of brewery wastewater, was fabricated using an electrospinning technique, followed by hot-pressing. The fabricated membrane was robust and demonstrated superhydrophilicity (water contact angle 0°), and higher porosity (68%) with pore sizes of 100 to 210 nm. The electrospun nylon 6 membrane showed higher pure water flux (850 LMH) at an applied pressure of 4 psi. The same membrane also demonstrated a 95% rejection rate of suspended solids (SS) in brewery wastewater treatment.

INTRODUCTION

Beer is the world's 5th most consumed beverage after tea, soft drinks, milk, and coffee. It continues to be a favorite with an average global consumption of 23 L/person each year [1]. The brewing process requires a high volume of water for both the production of beer, as well as heating and cooling, cleaning, and sanitation processes that can produce a large amount of wastewater [2]. Hence, the brewery industry is considered to be a primary source of environmental and water pollution, particularly in developing countries. This is because of the numerous organic and inorganic chemical species (suspended solids) found in brewery wastewater. The aim of this research is to fabricate a highly porous and superhydrophilic microfiltration membrane through electropsinning technique to remove suspended solids from brewery wastewater.

EXPERIMENTAL

Materials

Nylon 6 (N6) was obtained from Sigma-Aldrich, USA. Solvents, formic acid and acetic acid were received from Fisher Scientific, USA. Brewery wastewater and de-ionized (DI) water were obtained from Labatt Brasserie Quebec, Montreal, Canada and a Millipore Integral 10 water system (Millipore, Billerica, MA), respectively.

Membrane Fabrication

Nylon 6 (21% by weight) was dissolved in a formic acid and acetic acid mixture (80% formic acid and 20% acetic acid by volume) under magnetic stirring for 5 hrs at room temperature to prepare the nylon 6 solution for electrospinning. In electrospinning process, high-voltage electricity (Nanospinner NE300, Inovenso, Turkey) was applied to the prepared solutions in a syringe via an alligator clip attached to the syringe nozzle. The applied voltage was adjusted to 30 kV. The solution was delivered to the nozzle tip via a syringe pump to control the solution flow rate (0.18 mL/h). Fiber mats were collected on an electrically grounded metallic drum placed 8.8 cm abovethe nozzle tip[3-4]. Then, the fabricated nanofiber mats were pressed for 3 sec at 50 °C and 1500 psi applied pressure using a hydraulic press instrument (Model: SSI 509 E).

Characterization

Morphology and EDX spectrum analyses of the membrane were performed with field emission-scanning electron microscopy (FE-SEM) after platinum coating (QUANTA FEG 450). Water contact angle and mechanical strength of the membrane were investigated using a VCA optima instrument (AST Products, Inc.),and Chatillon (John Chatillon and Sons New York, NY), respectively.Thickness of the membrane was measured using a TMI instrument (Testing Machines, Inc.).

Porosity

The gravimetric method was used to investigate porosity of the membrane using the following equation [5]:

$$\varepsilon(\%) = [(W_w - W_d)/(\rho_w \times A \times L)] \times 100 \qquad (1)$$

where W_w and W_d are the weight of the wet and dry membranes respectively, ρ_w is the water density (0.998 g cm^{-3}), A is the effective area of the membrane, and L is the membrane thickness.

Membrane Performance Evaluation

Permeation Experiment

Water flux was measured using a dead-end stirred cell filtration device (Millipore stirred ultra-filtration cells, 8010, USA) connected to a nitrogen gas cylinder. The membrane was pre-compacted at 3 psi pressure for 30 min until constant water flux was achieved. Water flux was measured at an applied pressure of 4 psi. The equation below was used to calculate the pure water flux (J_0) for the membrane [6]:

$$J_0 = V/(A \times \Delta t) \qquad (2)$$

where V, A, and Δt are permeated water volume, membrane effective area, and measurement time, respectively. This experiment was conducted at ambient temperature.

Rejection Test

Suspended solids rejection rate for the membrane was tested using brewery wastewater. A dead-end stirred cell filtration device (Millipore stirred ultra-filtration cells, 8010, USA), connected with a nitrogen gas cylinder, was used to investigate rejection. The membrane was pre-compacted at 3 psi pressure for 30 min. Then, wastewater was allowed to permeate throughthe membrane at a stirring rate of 500 rpm and 4 psi applied pressure under nitrogen gas. The rejection of suspended solids was calculated according to the procedure outlined in the Standard Method [7].

RESULTS AND DISCUSSION

Morphology

Figure 1 demonstrates the FE-SEM images of N6 nanofibers just after electrospinning (Fig. 1A) and after hot-pressing of the electrospun nanofibers (Fig. 1B). The electrospun nanofibers were uniform in diameter (150 nm) with spider-web like structure (Fig. 1A). In fact, the ionization of N6 took place because of acidity of the N6 solution [8]. The ionization of N6 was increased at higher applied voltages throughout the electrospinning process that caused the formation of sweb-like structure of nanofibers [9]. After applying hot-press, the nanofiber mats were compacted, creating micron sized pores (100-210 nm) (Fig. 1B).

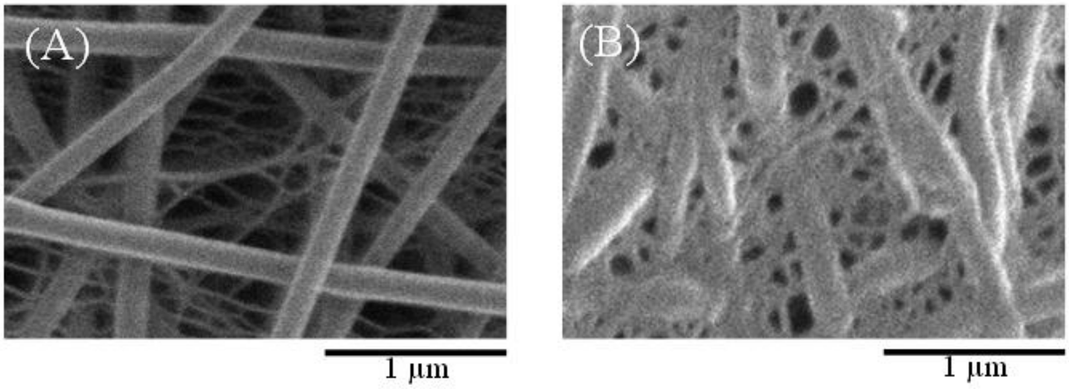

FIGURE1. FE-SEM images of electrospun nylon 6 nanofibers: (A) Before hot-pressing, and (B) After hot-pressing

The SEM-EDX spectrum of electrospun nylon 6 nanofibers is exhibited in Fig. 2. The EDX analysis clearly suggests the presence of C, N and O atoms of nylon 6. Pt was obtained in EDX spectrum due to Pt coating for conducting SEM of nylon 6 nanofibers.

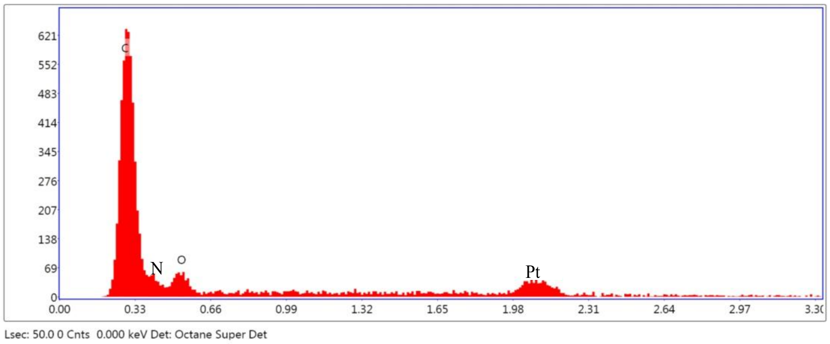

FIGURE.2. SEM-EDX spectrum of electrospun nylon 6 nanofibers (Fig. 1A).

Characteristics of the Membrane

The membrane was characterized in regard to thickness, porosity, wettability, and mechanical strength (Table 1). The thickness of the fabricated electrospun membrane was 200 μm with a porosity of 68%. The ultrahigh surface area of electrospun nanofibers was the primary phenomenon to obtain higher porosity in the electrospun membrane. The membrane was also superhydrophilic (water contact angle 0 °) and physically robust with a tensile strength of 23.75 MPa. The superhydrophilic surface was achieved due to capillary action of the highly porous electrospun membrane [10]. Higher mechanical strength was attained because of integrated effect of hydrogen bond formation and the highly interconnected spider-web-like structure of the nanofibers. The ionic species present in N6 solution can form stronger hydrogen bonds due to the more charge present on them in presence of the high voltage applied during electrospinning. The protonated amide group of ionic N6 molecules can effectively connect through hydrogen bonding with oxygen atoms of the N6 molecule in main fibers. Oxygen atoms of the ionic molecule can combine through hydrogen bonds with hydrogen atom of amides found in the main fibers as expected to form the interconnected spider-web-like fiber mats.

TABLE 1. Characteristics of electrospun nylon 6 microfiltration membrane

Thickness (μm)	Porosity (%)	Water contact angle (°)	Tensile strength (MPa)
200	68	0	23.75 ± 1.0

Filtration Performance Of The Membrane

The prepared membrane was subjected to a permeation test for pure water and an SS rejection test for brewery wastewater. The obtained results are exhibited in Table 2. At the applied pressure of 4 psi, the pure water flux for this membrane was 850 LMH, which was significantly higher than observed in the literature (200-500 LMH) [11]. Both the superhydrophilicity and higher porosity are key factors in the observed higher water flux of the membrane. In the treatment of brewery wastewater, a 95% suspended solid rejection rate was obtained using this microfiltration membrane. After filtration through this membrane, the suspended solid content in the brewery wastewater was reduced from 533 mg/L to 26 mg/L.

TABLE 2. Filtration performance of electrospun nylon 6 microfiltration membrane

Pure water flux (LMH) at 4 psi applied pressure	SS (mg/L) in brewery wastewater		SS Rejection (%) for brewery wastewater
	Effluent	Influent	
850	533	26	95

CONCLUSIONS

A nylon 6 membrane was successfully prepared for microfiltration of brewery wastewater by the integration of a facile electrospinning technique and hot-pressing. The fabricated membrane provided higher water flux (850 LMH) at very low applied pressure (4 psi). In addition, this membrane was able to remove 95% of suspended solids from the brewery wastewater. These results demonstrate that electropsun nylon 6 microfiltration membranes can satisfy both parameters (water flux and SS rejection) for the treatment of brewery wastewater.

ACKNOWLEDGEMENTS

Md. Saifur Rahaman gratefully acknowledges the Ministre de l'Agriculture, des Pêcheries et de l'Alimentation, Québec (MAPAQ) and the Natural Sciences and Engineering Research Council (NSERC) of Canada for providing funding supports for this project. Md. Shahidul Islam acknowledges the support of a doctoral-level scholarship from the Fonds de recherche du Québec – Nature et technologies (FRQNT). The authors also acknowledge ongoing support from Concordia University, Canada.

REFERENCES

1. L. Fillaudeau, P. Blanpain-Avet, G. Daufin, Water, wastewater and waste management in brewing industries, J.Clean. Prod. 14 (2006) 463-471.
2. M. B. Fakoya, H. M. Van der poll, Integrating ERP and MFCA systems for improved waste reduction decisions in a brewery in South Africa, J. Clean. Prod. 40 (2013) 136-140.
3. M.S. Islam, M. S. Rahaman, J. H. Yeum, Phosphine-functionalized electrospun poly(vinyl alcohol)/silica nanofibers as highly effective adsorbent for removal of aqueousmanganese and nickel ions, Colloid Surf. A: Phycochem. Eng. Asp. 484 (2015) 9-18.
4. J. D. Schiffman, M. A. Kiechel, A. E. Donius, U. G. Wegst, C. L. Schauer, Crosslinked poly(allylamine) fibers electrospun from basic and acidic solutions, J. Mater. Sci. 48(22) (2013) 7856-7862.
5. D. Emadzadeh, W.J. Lau, T. Matsuura, M. Rahbari-Sisakht, A.F. Ismail, A novel thin film composite forward

osmosis membrane prepared from PSf–TiO_2 nanocomposite substrate for water desalination, Chemi. Eng. J. 237 (2014) 70-80.

6. J. Ju, C. Wang, T. Wang, Q. Wang, Preparation and characterization of pH-sensitive and antifouling poly(vinylidene fluoride) microfiltration membranes blended with poly(methyl methacrylate-2-hydroxyethyl methacrylate-acrylic acid), J. Colloid Interf. Sci. 434 (2014) 175-180.
7. APHA-AWWA-WEF, Standard Methods for the Examination of Water and Wastewater, 18th ed., American Public Health Association, Washington DC, 1992.
8. R. Nirmala, K.T. Nam, S.J. Park, Y.S. Shin, R. Navamathavan, H.Y. Kim, Formation of high aspect ratio polyamide-6 nanofibers via electrically induced double layer during electrospinning, Appl. Surf. Sci. 256 (2010) 6318–6323.
9. H. R. Pant, M. P. Bajgai, C. Yi, R. Nirmala, K. T. Nam, W. Baek, H. Y. Kim, Effect of successive electrospinning and the strength of hydrogen bond on the morphology of electrospun nylon-6 nanofibers, Colloid Surf. A: Physicochem. Eng. Asp, 370 (2010) 87-94.
10. H. Dong, P. Ye, M. Zhong, J. Pietrasik, R. Drumright, K. Matyjaszewski, Superhydrophilic Surfaces via Polymer-SiO_2 Nanocomposites, Langmuir, 26 (19) (2010) 15567-15573.
11. J. Ju, C. Wang, T. Wang, Q. Wang, Preparation and characterization of pH-sensitive and antifouling poly(vinylidene fluoride) microfiltration membranes blended with poly(methyl methacrylate-2-hydroxyethyl methacrylate-acrylic acid). J. Colloid Interface Sci. 434 (2014) 175–180.

International Conference on Mechanical Engineering 2015
(ICME 2015) 18 – 20 December, 2015, Dhaka, Bangladesh

Paper ID : 596

Effect of Erodent Particles on the Erosion of Metal Specimens

M. Mahbubur Razzaque[a], M. Khorshed Alam and M. Ishak Khan[b]

Department of Mechanical Engineering
Bangladesh University of Engineering and Technology (BUET), Dhaka, Bangladesh

[a]Corresponding author: mmrazzaque@me.buet.ac.bd
[b]ishak.buet@gmail.com

Abstract. This paper presents the experimental results of the measurement of erosion rate of carbon steel specimens in sand water slurry system in a slurry pot tester. Sylhet sand has been sieved to get three sizes of erodent particles; namely, less than 250 micron, 250 to 590 micron and 590 to 1190 micron. Experiments are done with three sand concentrations (10%, 15% and 20%). The rate of erosion of the carbon steel specimens is measured as the loss of weight per unit surface area per unit time under the dynamic action of solid particles. The eroded surfaces of the specimens are examined using Scanning Electron Microscopy (SEM) to visualize the impact of the slurry of various conditions. It is seen that irrespective of the particle size the rate of erosion increases with the increase of slurry concentration. This increment of erosion rate at high concentration is high for large particles. High erosion rate is observed in case of large sand particles. In case of small and fine particles erosion rate is small because of low impact energy as well as the wastage of energy to overcome the hindrance of the finer particles before striking on the specimen surface.

INTRODUCTION

Erosion is a process of progressive removal of material from a target surface due to repeated impacts of solid particles. It is encountered in numerous industrial applications such as crude oil processing equipment, hydrotransport pipelines and coal handling plants where coal is carried by mixing it in water or oil. Solid particles suspended in a flow of solid–liquid mixture cause gradual erosion in slurry transport systems. Fig. 1 shows a hydrotransport pipeline of a river dredging system and an eroded impeller of its pump. For designing and operating a slurry transport system, a good estimate of the rate of erosion in pipes and pump components is essential. Various types of tests are conducted to understand the mechanism and rate of slurry erosion. Slurry erosion tests in a pipeline require high cost and long time. As low cost solutions, laboratory-scale test rigs such as slurry pot testers and slurry jet testers have become popular for accelerated tests on slurry erosion.

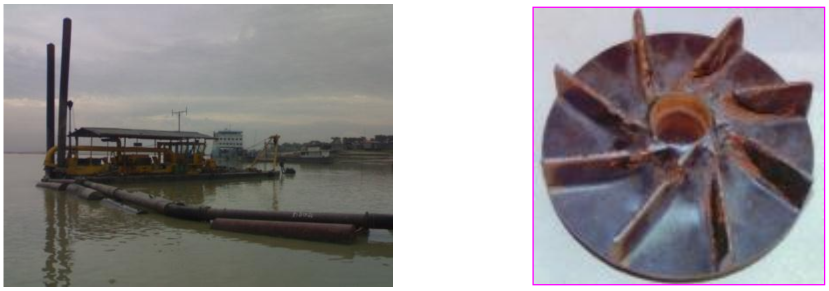

FIGURE 1. Hydrotransport pipeline of a river dredging system (left) and an eroded impeller of its pump (right).

Some researchers [1-3] carried out erosion test in pilot pipelines. Jacobs and James [2] from their experiments in a pilot plant have shown that erosion wear increases with increase in solid concentration, particle size and velocity. The rate of increase of wear with velocity is relatively much higher than that with two other parameters. Gupta et al. [3] performed experiments in both pilot pants and slurry pot testers and have shown that the pot tester results agree reasonably well with pipe line wear.

Slurry pot testers are very simple to construct and easy to operate. They provide rapid results for ranking materials based on their resistance to slurry erosion. They are widely used [9-15] to understand, characterize and model erosion resistance of materials. Lynn et al. [9] conducted experiment on steel specimens with SiC in oil slurry and reported that the erosion rate decreases with decreasing particle size for suspensions of constant solids loading. It was due to the decrease in the proportion of particles impacting the target surface as well as the decrease in impact velocity. Gandhi et al. [10] modified a slurry pot tester in order to ensure that the erosive wear on a brass wear piece is primarily due to parallel flow of a mixture prepared by mixing water with the tailing material from a zinc processing plant. They reported that the parallel flow wear increases with increase in solid concentration, particle size and velocity. The parametric dependence on velocity is comparatively much stronger as compared to that on either solid concentration or particle size. Clark and Hartwich [11] discussed the difficulties in determining the particle size effects using both pot and jet impingement testers. They observed for cylindrical wear pieces of aluminium and pyrex glass rotating in a pot with SiC in diesel oil slurry that at a nominal speed of 18.7 m/s, erosion occurred on the aluminium specimen for all SiC particle sizes while erosion occurred on the pyrex glass specimen only for large particle sizes of SiC. They have attributed this to the presence of impact energy threshold in case of pyrex glass. Desale et al. [12-15] carried out a number of experiments using a slurry pot tester to investigate the parameters affecting erosion wear of ductile materials at different impact conditions. The effects of velocity, particle size, and concentration of erodent particles in water have been investigated using different ductile materials of varying hardness. It was observed that the erosion rate of ductile materials varies with the erodent properties. The effect of erodent shape and density is more dominant at shallow impact angles.

Thus from the review of the previous studies, it may be inferred that in slurry transport pipelines, the wear of the pipe, the pump impeller and the fittings would depend on slurry composition, especially the type and size distribution of solid particles and the chemical nature of the liquid portion of the slurry. However, the current understanding is not enough to visualize the total picture of the interaction between the slurry and the pipeline that carries the slurry. Therefore, some experiments are carried out using a slurry pot tester in order to enhance the understanding of the slurry erosion mechanism. This paper presents the experimental data of erosion of carbon steel specimens by natural sand - water slurry of different sand concentrations and particle sizes.

EXPERIMENTAL SET UP AND PROCEDURE

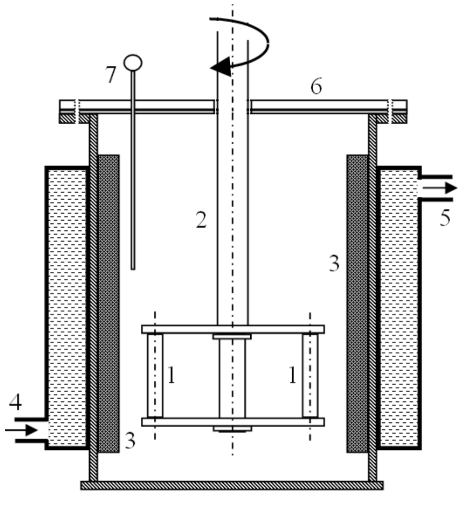

1 - carbon steel specimens
2 - spindle
3 - baffles
4 - cooling water inlet
5 - cooling water outlet
6 - slurry pot top cover
7 - thermometer

FIGURE 2. Schematic diagram of the slurry pot erosion tester.

FIGURE 3. The specimen holder attached to the spindle.

FIGURE 4. The slurry pot tester with the spindle attached a drilling machine.

Slurry Pot Tester

A schematic diagram of the slurry pot erosion tester used in the current experiments is shown in Fig. 2. The pot is made of a 252 mm long 148 mm diameter stainless steel pipe section with maximum volumetric capacity of 4.3 lit. Two 50 mm long and 8.3 mm diameter cylindrical specimens (1) of carbon steel are mounted in the specimen holder attached to a spindle (2) as shown in Fig. 3. The distance between the two specimens is 100 mm and these are securely fixed to the specimen holder so that no axial rotation takes place during the test. The spindle is then rotated by clamping it to the chuck of a drilling machine shown in Fig. 4. The slurry pot contains four vertical baffles (3) to facilitate proper mixing of the slurry.

Erodent Preparation

Golden-brown color natural Sylhet sand which is mostly silica (silicon dioxide, or SiO2) in the form of quartz is used as erodent in the present experiments. Natural sand is sieved using US standard sieves of size 16, 30 and 60 to get erodent particles graded into three different size groups. The particle size ranges of the three erodent grades and the respective average bulk densities are shown in Table 1. Because of the inside pores, the bulk density is low for the sand with coarser particles. The SEM (scanning electron microscope) images of the three grades of erodent/sand are shown in Fig 5.

TABLE 1. Sand Grading

Erodent grade	US standard sieve size	Size range (microns)	Average bulk density (gm/cm^3)
A	Passed through sieve no.60	0-250	2.59
B	Separated by sieve no. 30 and 60	250-590	2.56
C	Separated by sieve no. 14 and 30	590-1190	2.44

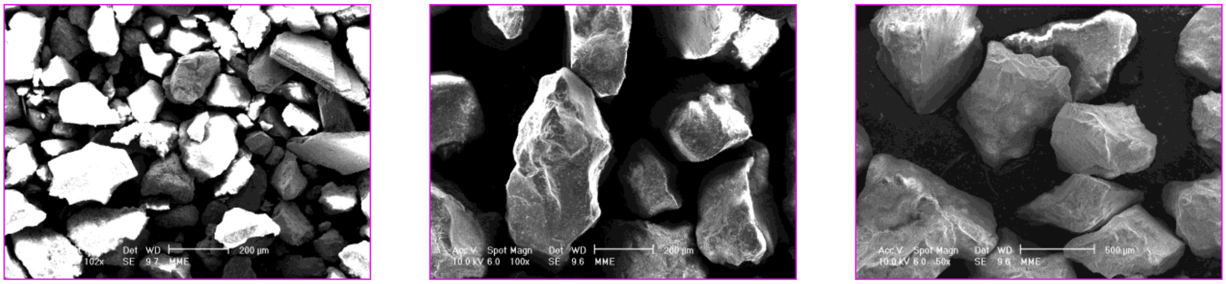

Erodent grade-A (100X magnification) Erodent grade-B (100X magnification) Erodent grade -C (50X magnification)

FIGURE 5. SEM images of the three grades of erodent particles used in the experiments.

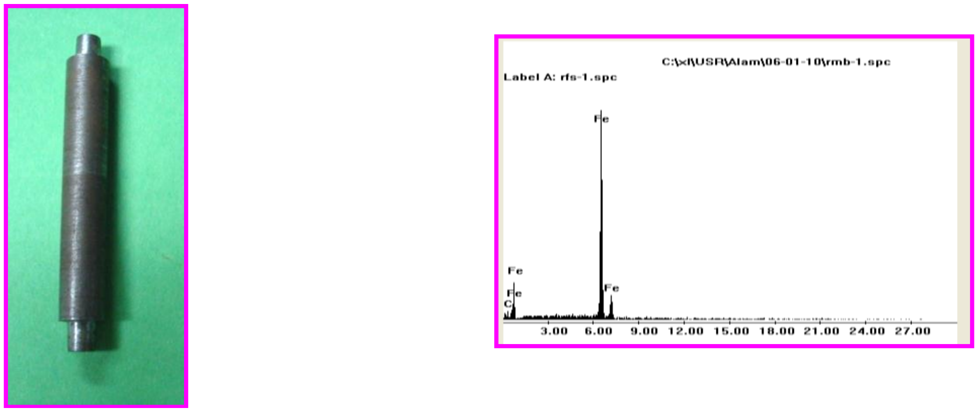

FIGURE 6. Test specimen, AISI-SAE number 1015 (left) and the energy dispersive spectrum of the specimen (right).

Target Materials

AISI-SAE 1015 grade standard Carbon steel with less than 1 % Mn is used as the target material. Cylindrical test specimens are prepared by Digital-Controlled Electrical Discharge Machining so that the surface microstructure and roughness is minimally affected. The energy dispersive spectrum of the target material is generated by Scanning Electron Microscope (SEM) to check the composition of the material and a sample is presented in Fig. 6.

Experimental Procedure

The slurry is prepared by adding sand particles into the water in the pot to get desired concentrations of sand. Before each test run, a warming up run is conducted with two dummy specimens operated in the slurry inside the pot until the temperature is raised to 35ºC. The dummy specimens are then replaced by the actual test specimens, the pot top cover is closed and the spindle is rotated in the slurry at 1230 rpm which gives a linear speed of 3.3 m/s of the specimens. Stirring of slurry at this speed has been reported [12, 13] to produce uniform concentration of throughout the slurry. Temperature of the slurry is always maintained at 35ºC using flow of cold water through the cooling water jacket surrounding the pot. At the end of each run of 60 min duration, the loss of material from the test specimen is determined by weighing and the surface roughness is observed in a Scanning Electron Microscope. The erosion rate is determined by dividing the loss of material by the surface area of a specimen and the test duration in hour. Before the next run, the inside of the pot and the interior components are thoroughly washed and dried to remove the erodent particles.

RESULTS AND DISCUSSION

For each of the three size grades of sand, the sand water slurry is prepared in three concentrations by weight; namely, 10%, 15% and 20%. Two specimens are used in each experimental run. The erosion rate presented here is the average erosion rate of the two specimens used. Table 2 summarizes the experimental data of nine experimental runs. Fig. 7 shows the variation of erosion rate as function of the sand grade (i.e. the size of the sand particles) and the slurry concentration. It is clearly visible that for all of three concentrations, the erosion rate increases with the increase of particle size. With the increase of slurry concentration, erosion rate increases for any sand grade; i.e. the particle size. This increment of erosion rate at high concentration is high for large particles.

The micrographs of the specimen surface are generated by Scanning Electron Microscope (SEM). The SEM images shown in Fig. 8 are for 20% concentration of the slurry. Examination of the images shows that in the current experiments the erosion wear occurred due to normal impact of the sand particles on the specimen surfaces. As the large particles have large impact energy, they cause more damage to the surface. So, high erosion rate is observed in case of sand particles of grade C. Grade A sands have fine particles and have less impact energy. Besides, a part of the impact energy might be wasted to overcome the hindrance of the smaller particles before striking on the specimen surface. This may have caused low erosion rate in case of sand particles of grade A.

TABLE 2. Erosion rate for different sand grades and slurry concentrations

Erodent grade	Slurry concentration (% wt.)	Slurry density (gm/cm^3)	Erosion rate (mg/cm^2/ hr)
A	10	1.0592	2.07
	15	1.0871	3.18
	20	1.1141	7.14
B	10	1.0586	4.84
	15	1.0863	6.44
	20	1.1129	12.31
C	10	1.0570	6.70
	15	1.0830	10.58
	20	1.1090	19.27

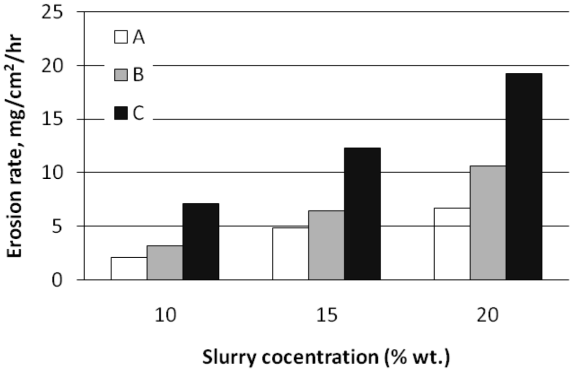

FIGURE 7. Erosion rate for different sand grades (i.e. the size of the sand particles) and slurry concentrations.

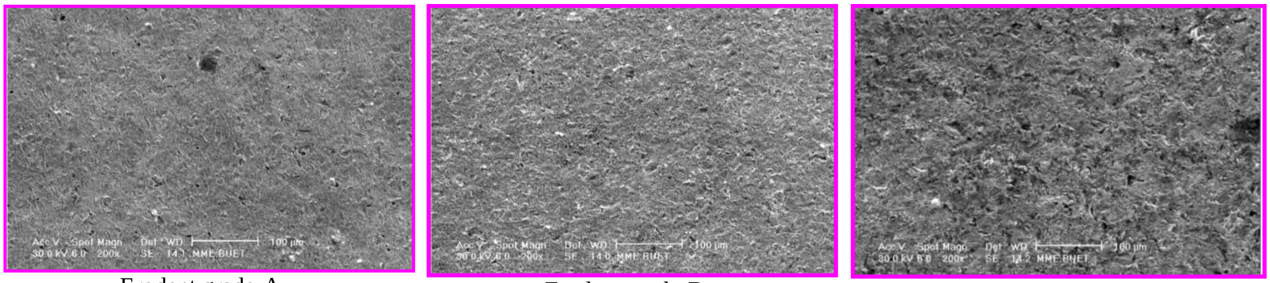

Erodent grade-A

Erodent grade-B

Erodent grade-C

FIGURE 8. SEM micrographs of the surface of the specimens after erosion experiments in sand water slurry of 20% concentration (200X magnification).

CONCLUSION

The result of slurry erosion tests of carbon steel specimens in sand water slurry system has been presented. It is seen that irrespective of the particle size the rate of erosion increases with the increase of slurry concentration. This increment of erosion rate at high concentration is high for large particles.

Close examination of the SEM images show that in the current experiments the erosion wear occurred due to normal impact of the sand particles on the specimen surfaces. As the large particles have large impact energy, they cause more damage to the surface. So, high erosion rate is observed in case of large sand particles. In case of small and fine particles erosion rate is small because of low impact energy as well as the wastage of energy to overcome the hindrance of the finer particles before striking on the specimen surface.

ACKNOWLEDGMENTS

The authors are grateful to the MME Department, BUET for granting permission to use the SEM lab to take the micrographs of the erodent particles and the metallic specimens.

REFERENCES

1. R. J. K. Wood and T. F. Jones, Wear, **255**, 206–218 (2003).
2. B. E. A. Jacobs and J. G. James, Hydrotransport 9, BHRA Fluid Engineering, Rome, Paper G3 (1984).
3. R. Gupta, S. N. Singh and V. Seshadri, Wear, **184**, 169–178 (1995).
4. B. J. Briscoe, M. J. Pickles, K. S. Julian and M. J. Adams, Wear, **203–204**, 88–97 (1997).
5. R. J. K. Wood, and D. W. Wheeler, Wear, **220**, 95–112 (1998).
6. Q. Fang, H. Xu, P. S. Sidky and M. G. Hocking, Wear, **224**, 183–193 (1999).
7. G. T. Burstein and K. Sasaki, Wear, **240**, 80–94 (2000).
8. A. Abouel-Kasem, Y. M. Abd-elrhman, K. M., Emara and S. M. Ahmed, J. Tribology, **132**, 021601.1-10 (2010).
9. R. S. Lynn, K. K. Wong and H. M. Clark, Wear, **149(1-2)**, 55-71 (1991).
10. B. K. Gandhi, S. N. Singh and V. Seshadri, Tribol. Int., **32**, 275–282 (1999).
11. H. M. Clark and R. B. Hartwich, Wear, **248**, 147–161 (2001).
12. G. R. Desale, B. K. Gandhi and S. C. Jain, Wear, **259(1–6)**, 196–202 (2005).
13. G. R. Desale, B. K. Gandhi and S. C. Jain, Wear, **261**, 914–921 (2006).
14. G. R. Desale, B. K. Gandhi and S. C. Jain, Wear, **266**, 1066–1071 (2009).
15. G. R. Desale, B. K. Gandhi and S. C. Jain, Wear, J. Tribology, **133**, 031603.1-10 (2011).

International Conference on Mechanical Engineering 2015
(ICME 2015) 18 – 20 December, 2015, Dhaka, Bangladesh

Paper ID : 600

Numerical Prediction of Heave and Pitch Motions of Ship in Waves

N. M. G. Zakaria[1, a)], Md. Al Amin Miazee[1] and Md. Masudur Rahman[1]

[1] *Department of Naval Architecture and Marine Engineering, BUET, Dhaka, Bangladesh*

[a)] Corresponding author: gzakaria@name.buet.ac.bd

Abstract. This paper contains prediction of ship motion in regular head waves. A computer program has been developed for calculating hydrodynamic coefficients and motion responses of a ship. For the validation of the result, a model of series 60 ship has been taken. Heave and pitch motion results have also been compared with experimental and other numerical results. A reasonable prediction has been found for this model. A fine form destroyer and fuller form bulk carrier have been taken to check the motion results at various Froude numbers. It has been found that the present numerical code gives very close agreement with experimental results for these two different types of hull forms.

INTRODUCTION

A ship designer may need to assess the performance of vessel in different environment including extreme weather condition. As the performance of a vessel is directly related to motion responses, so an accurate prediction of motion response is very important for designer. Motion prediction can be done either experimentally or theoretically. Experimental methods are expensive, time consuming and also not feasible at early design stage. As a result, designer depends on theoretical method mostly at least in the early stage of designing a ship.

2-D based theoretical and computational methods of ship motion computations have been under development for over the past 40 years by various researchers such as rational strip theory of Ogilvie and Tuck [1] and the new strip theory of Salvesen [2]. One main difference between the different strip theories is the dependence of the coefficients on the forward speed and the treatment of the boundary conditions. In general, all of the strip-theory calculations give satisfactory results for slender-body ships with small amplitude motions, where the nonlinear and three-dimensional effects are insignificant. Many attempts have been made to overcome some of the shortcomings of strip theory. Wang [3] combined the strip-theory approximation and the dynamic theory to derive the hydrodynamic coefficients of ship motions. The dynamic theory treats the fluid and the body together as one dynamical system. The classical dynamic theory treats the fluid as an unbounded medium, while Wang's formulation takes into account

the existence of the free surface. The results of this approach were very similar to those derived by Salvesen [2]. As a matter of fact, the two methods become identical when the interaction between the body and the free surface is neglected. Troesch [4] used the slender- body theory to derive formulae for the sway, roll, and yaw motion coefficients. Liu [5] tried to extend the strip theory and apply it to large-amplitude motions. An attempt was done to include some nonlinear effects by taking into account the instantaneous variations of the wetted hull surface during motion and its effects on the ship hydrodynamic characteristics. The method is a quasi-steady approach, which does not take into account the memory effects. Crossland [6] conducted a series of experiments to measure the heave and pitch decay-time histories of a model ship. The aim of these experiments was to explain the over prediction of the sectional damping obtained using a strip-theory program. The over prediction of the sectional damping creates poor predictions of free decay motions. This issue has not been resolved completely and it has been concluded that strip theory should be used only in low-amplitude motions when making seakeeping predictions. As mentioned before, many research works are devoted to improving strip-theory predictions, including the applicability to situations where the 3D and nonlinear effects are significant. Earlier prediction methods followed the pioneering works of Korvin-Kroukovsky [7] and were based on 2D theories. A number of 2D strip-theory based methods of computations were subsequently developed by various researchers.

In this research work 2D linear strip theory by Korvin-Korvosky and Jacobs [7] has been used to predict hydrodynamic coefficients such as added mass, damping, and exciting force. A computer program has been developed to solve the hydrodynamic coefficients. Then these coefficients were used to solve the motion equations.

NOMENCLATURE

a-e, A-E, g, G	Coefficient of equation of motion	ω_e	Frequency of encounter
Fr	Froude Number	τ	Phase angle of pitching moment
F_0	Amplitude of time-varying heaving force	$\ddot{z}$	Heaving acceleration of center of gravity of ship or model
$\overline{F}$	Complex vertical (heaving) force	z_0	Amplitude of heaving motion.
g	Gravitational acceleration	$\overline{z}$	Complex heaving motion
C_B	Block Coefficient	δ	Theoretically computed heaving phase angle
t	Time	Δ	Displacement of ship or model
ρ	Density of Water	ε	Theoretically computed pitching phase angle
L	Length of ship or model	θ	Pitching displacement
M	Total pitching moment	$\dot{\theta}$	Pitching velocity
		$\ddot{\theta}$	Pitching accelerations
M_0	Amplitude of time-varying pitching moment	θ_0	Amplitude of pitching motion
$\overline{M}$	Complex pitching moment	$\overline{\theta}$	Complex pitching motion
$N(\zeta)$	Sectional damping coefficient	λ	Wavelength
z	Heaving motion of C.G of ship or model	V	Speed of ship or model
$\dot{z}$	Heaving velocity of C.G of ship or model	σ	Phase angle of heaving force

METHODOLOGY

Strip theory given by Korvin-Korvosky and Jacobs [7] has been used for determining the parameters of the ship-motion equations. The predictions are based on 2D evaluations of the ship parameters, whereby the ship is divided into several 2D transverse sections (strips) along the ship's longitudinal axis.

The coupled set of linear differential equations can be expressed as:

$$a\ddot{z} + b\dot{z} + cz + d\ddot{\theta} + e\dot{\theta} + g\theta = \overline{F}\exp(i\omega_e t) \qquad (1)$$

$$A\ddot{\theta} + B\dot{\theta} + C\theta + D\ddot{z} + E\dot{z} + Gz = \overline{M}\exp(i\omega_e t) \qquad (2)$$

Where,
z and θ are the complex heave and pitch vectors ,
F and M are wave induced exciting force and moments,

The above equations result from equilibrium considerations of the hydrodynamic forces and moments called equation of motion, when meeting head or astern regular waves. Following the principles of classical dynamics, these forces and moments are obtained by applying Newton's Second Law of Motion to both translatory and rotational displacements of the body's center of gravity. The wave induced excitation force and moment may be defined as:

$$\overline{\boldsymbol{F}}\exp(i\omega_e t) = F_0\exp(-i\boldsymbol{\sigma})\ \exp(i\omega_e t) = F_0\exp[i(\omega_e t - \boldsymbol{\sigma})] \tag{3}$$

$$\overline{\boldsymbol{M}}\exp(i\omega_e t) = M_0\exp(-i\boldsymbol{\tau})\ \exp(i\omega_e t) = M_0\exp[i(\omega_e t - \boldsymbol{\tau})] \tag{4}$$

The differential exciting force acting on a control section distant ζ from the origin of the moving coordinate system (ship's C.G.), can be expressed in the simplified form,

$$\frac{dF}{dx} = \frac{dF_1}{dx}\cos\omega_e t + \frac{dF_2}{dx}\sin\omega_e t = [\{\phi_1 \sin\frac{2\pi\zeta}{\lambda} + \phi_2\frac{2\pi hC_w}{\lambda}\cos\frac{2\pi\zeta}{\lambda}\}\exp(-\frac{2\pi y}{\lambda})]\cos\omega_e t + [\{\phi_1\cos\frac{2\pi\zeta}{\lambda} + \phi_2\frac{2\pi hC_w}{\lambda}\sin\frac{2\pi\zeta}{\lambda}\}\exp(-\frac{2\pi y}{\lambda})]\sin\omega_e t \tag{5}$$

Where,

$$\phi_1 = h\rho g B - \frac{4\pi^2 hC_w}{\lambda^2}(\rho S k_2 k_4) \tag{6}$$

$$\phi_2 = N(\zeta) - V\frac{d(\rho S k_1 k_2)}{d\zeta} \tag{7}$$

While the differential exciting moment of this force about the C.G. is given by $\frac{dF}{d\zeta}d\zeta$. Integration of the above two quantities over the ship length results in the values of the total time-varying exciting force and moment, which are considered as the real parts of the Equation (3) and Equation (4).

Thus, $$F = F_1\cos\omega_e t + F_2\sin\omega_e t = \sqrt{{F_1}^2 + {F_2}^2}\cos[\omega_e t - \arctan\frac{F_2}{F_1}] = F_0\cos(\omega_e t - \sigma) \tag{8}$$

and , $$M = M_1\cos\omega_e t + M_2\sin\omega_e t = \sqrt{{M_1}^2 + {M_2}^2}\cos[\omega_e t - \arctan\frac{M_2}{M_1}] = M_0\cos(\omega_e t - \tau) \tag{9}$$

The analysis of the forces and moments which correspond to the ship's free oscillations in calm water yields terms which appear on the LHS of the Equation (1) and Equation (2). The final expressions for the coefficients of the equation of motion used in the computations can be found in reference Al Amin and Masudur [8].

After algebraic manipulation the complex heave and pitch amplitude becomes

$$\bar{z} = z_1 - iz_2 = \sqrt{(z_1^2 + z_2^2)}exp\left[-i\ arc\ tan\frac{z_2}{z_1}\right] \tag{10}$$

$$\bar{\theta} = \theta_1 - i\theta_2 = \sqrt{(\theta_1^2 + \theta_2^2)}exp\left[-i\ arc\ tan\frac{\theta_2}{\theta_1}\right] \tag{11}$$

Finally,

$$z = R_e\bar{z}\exp(i\omega_e t) = R_e\sqrt{(z_1^2 + z_2^2)}exp\left[i(\omega_e t - arc\ tan\frac{z_2}{z_1}\right] = z_0\cos(\omega_e t - \delta) \tag{12}$$

$$\theta = R_e\bar{\theta}\exp(i\omega_e t) = R_e\sqrt{(\theta_1^2 + \theta_2^2)}exp\left[i(\omega_e t - arc\ tan\frac{\theta_2}{\theta_1})\right] = \theta_0\cos(\omega_e t - \varepsilon) \tag{13}$$

VALIDATION

For the validation of numerical results of developed computer program, a Series 60 ship of C_B=0.7 has been taken. The principal particulars of the ship are shown in Table 1. Body plan is shown in Figure 1. Test results have been taken from Gerritsma and Beukelman [9].

Table 1. Model characteristics of series 60 ship

LWL	2.479m
LBP	2.438m
Beam	0.3481m
Draft	0.139m
LCG	0.0119m (forward of amidships)
C_B	0.70

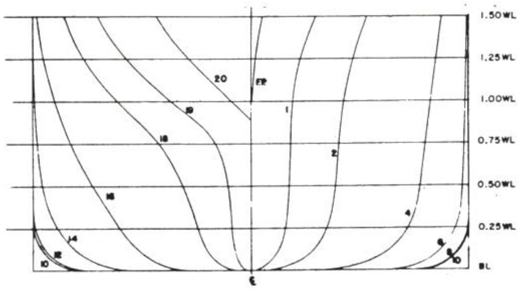

FIGURE 1. Body plan of series 60

Fig.2 shows the comparison between the calculated results with experimental and other numerical results for heave motion at Fr = 0.2. From this graph it is seen that the non-dimensional heave motion increases at a certain limit and then decreases gradually with the increase of the value of $\omega_e(L/g)^{1/2}$ and the calculated value is slightly lower from the pick of the experimental value.

Fig.3 shows the comparison between the calculated results with experimental and other numerical results for pitch motion at Fr = 0.2. From this graph it is seen that the non-dimensional pitch motion increases at a certain limit and then decreases gradually with the increase of the value of $\omega_e(L/g)^{1/2}$ and the calculated value is slightly lower from the pick of the experimental value.

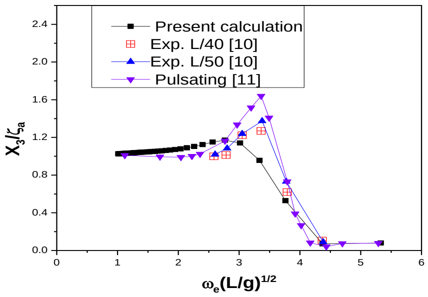

FIGURE 2. Heave motion at Fn=0.2 in head sea

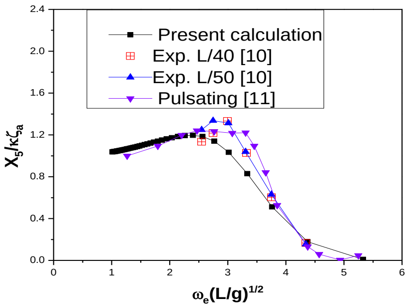

FIGURE 3. Pitch motion at Fn=0.2 in head sea

CASE STUDY

After validation, present numerical code has been applied for a high speed Destroyer of C_B=0.5374 and a slow speed Bulk Carrier of C_B=0.804. The principal particulars of these two vessels are shown in Table 2. Body plans are shown in Fig.4 and Fig.5. Test results have been taken from Salvesen [2] for the comparison.

Table 2. Model characteristics of a destroyer and a bulk carrier

Particulars	Destroyer	Bulk Carrier
LWL	5.307m	4.5m
LBP	5.307m	4.5m
Beam	0.565m	0.793m
Draft	0.194m	0.285m
LCG	0.0856m (forward of amidships)	0.144m (forward of amidships)
C_B	0.5374	0.804

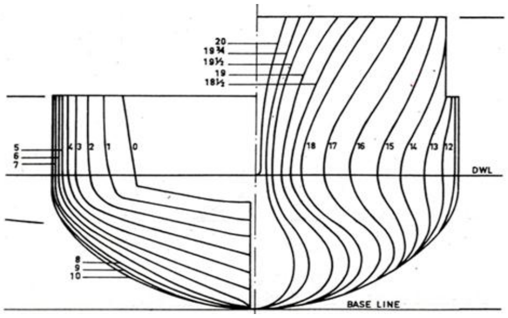

FIGURE 4. Body plan of Destroyer

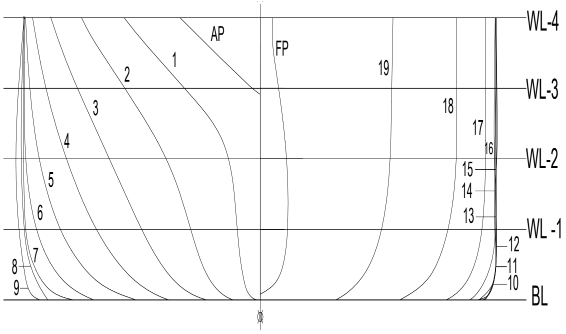

FIGURE 5. Body plan of Bulk Carrier

shows the comparison between the calculated results with experimental results for heave motion at Fr = 0.25 for the destroyer. From this graph it is seen that the non-dimensional heave motion increases at a certain limit and then decreases gradually with the increase of the value of L/λ and the calculated value is slightly lower than the pick value of the experimental one.

Fig.7 shows the comparison between the calculated results with experimental results for pitch motion at Fr = 0.25. From this graph it is seen that the non-dimensional pitch motion increases at a certain limit and then decreases gradually with the increase of the value of L/λ and the calculated value is slightly lower than the pick of the experimental value.

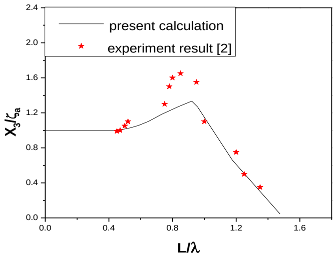

FIGURE 6. Heave motion at Fn=0.25 in head sea.

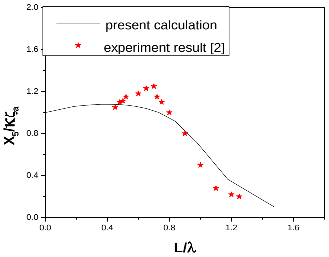

FIGURE 7. Pitch motion at Fn=0.25 in head sea.

Fig.8 shows the comparison between the calculated results with experimental results for heave motion at Fr = 0.35. Fig.9 shows the comparison between the calculated results with experimental results for pitch motion at Fr = 0.35.

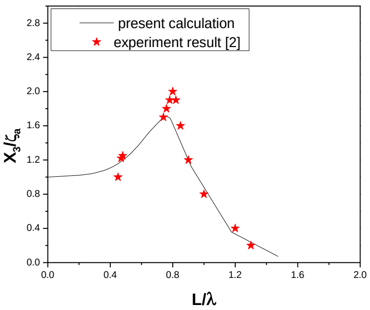

FIGURE 8. Heave motion at Fn=0.35 in head sea.

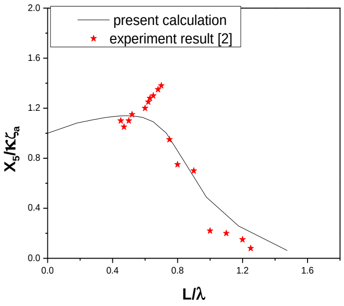

FIGURE 9. Pitch motion at Fn=0.35 in head sea.

Fig.10 shows the comparison between the calculated results with experimental results for heave motion at Fr = 0.45. Fig.11 shows the comparison between the calculated results with experimental results for pitch motion at Fr = 0.45.

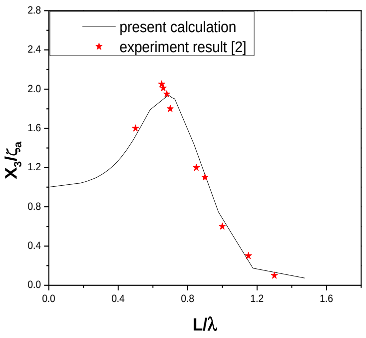

FIGURE 10. Heave motion at Fn=0.45 in head sea.

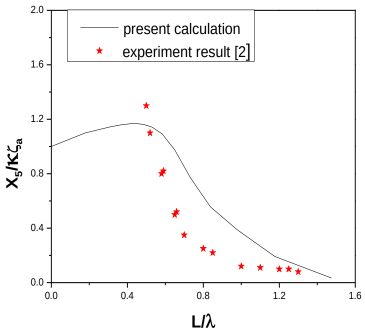

FIGURE 11. Pitch motion at Fn=0.45 in head sea.

Fig.12 shows the comparison between the calculated results with experimental and other numerical results for heave motion at Fr = 0.131 in head sea for a bulk carrier ship.

Fig.13 shows the comparison between the calculated results with experimental and numerical results for pitch motion at Fr = 0.131 in head sea from the same ship. For the compassion, NK(3D) and IRS(3D) data have been taken from Zhu et al. [12].

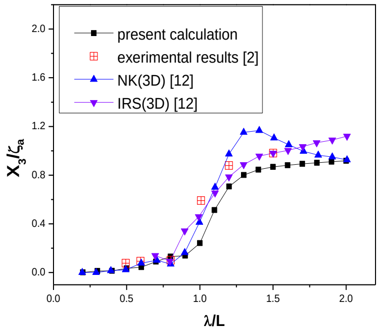

FIGURE 12. Heave motion at Fn=0.131 in head sea

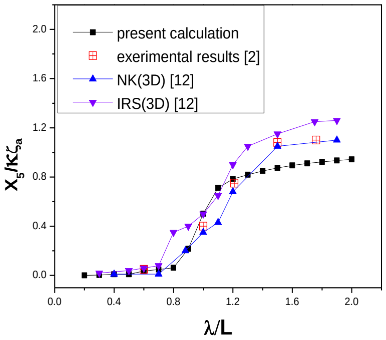

FIGURE 2. Pitch motion at Fn=0.131 in head sea.

CONCLUSION

From the numerical results calculated by the present computer code, the following conclusions may be drawn:

-The present numerical result slightly deviates from the experimental results, but overall prediction is quite reasonable.

-The program gives reasonable results for a wide range hull form (C_B = 0.50 ~ 0.80).

-As the experimental work is very costly, so this program might be useful for the prediction of ship motion at initial design stage.

REFERENCES

[1] Ogilvie, E.O. and Tuck, T.F., A Rational Strip Theory of Ship Motions, University of Michigan, 1969, Report No. 013.

[2] Salvesen, N., Tuck, E.O., Ship Motion and Ship Loads, Transactions, S.N.A.M.E., 1970.

[3] Wang., Dynamical Theory of Potential Flows with a Free Surface, A Classical Approach to Strip Theory of Ship Motions, Journal of Ship Research, September 1976.

[4] Troesch., Sway, roll and yaw motion coefficients based on a forward-speed slender-body theory-part 1, Journal of Ship Research, March 1981.

[5] Liu, Y. L. Li, and G. P. Miao, An Engineering Prediction Method for Large Amplitude Motions of Ships in Waves, In 6th International Offshore and Polar Engineering Conference, May 1997, volume III.

[6] Crossland, Wilson, P. A. and Bradburn, J. C., The Free Decay of Coupled Heave and Pitch Motions of Model Frigates, Transactions of the Royal Institution of Naval Architects, January 1993.

[7] Korvin-Kroukovsky, B.V. and Jacobs, W.R., Pitching and Heaving Motions in Regular Waves, Transactions, S.N.A.M.E., 1957.

[8] Al Amin, M., Masudur, R., Prediction of Ship Motion in Regular Head Waves, UG thesis in the Dept. of NAME, Bangladesh University of Engineering & Technology (BUET), Dhaka, Bangladesh, 2013.

[9] Gerritsma, I.J. and Beukelman, W., Analysis of the Modified Strip Theory for Calculation of Ship Motions and Wave Bending Moments, 1967, Report No. 96S.

[10] Gerritsma, J. and Beukelman, W., Comparison of calculated and measured heaving and pitching motions of a series 60, CB=0.7 ship model in regular longitudinal waves. Technische Hogeschool Delft, 1966, Report No. 139.

[11] Inglis, R. E. and Price, W. C., A Three-Dimensional Ship Motion Theory-Comparison Between Theoretical Predictions and Experimental Data of the Hydrodynamic Coefficients with Forward Speed. Trans. Roy, Inst. Nav. Arch. W2., 1981.

[12] Zhu, T., Xu, L., Singh, SP. & Ha, TB, A Comparative Study of 3-D Methods with Experimental Results for Seakeeping Analysis, ICHD Conference, Australia, 2004.

International Conference on Mechanical Engineering 2015
(ICME 2015) 18 – 20 December, 2015, Dhaka, Bangladesh

Paper ID : 601

Optimization of Bangladeshi Inland Vessels With Respect To Energy Efficiency Design Index (EEDI)

Md. Mashud Karim[a)], S.M. Rashidul Hasan[b)]
(Use the Microsoft Word template style: *Paper Author*)

Department of Naval Architecture & Marine Engineering,BUET, Dhaka-1000, Bangladesh

[a)]Corresponding author: rashed.navalarch@gmail.com

Abstract. EEDI [1] was introduced by the International Maritime organization (IMO)to stimulate innovation and technical development of all elements that increase the level of energy efficiency of a ship at design stage. The basic formulation of EEDI is based on the ratio of total CO_2 emission per tonne-mile. As CO_2 depends upon fuel consumption and fuel consumption depends upon the total power requirements, eventually this EEDI formulation has certain impact on ship design parameters and hydrodynamics. So there has a lot of scope to optimize marine vehicle in light of EEDI. Sea going ships over 400 gross tonnages are considered in the current regulation of EEDI. But there are thousands of inland ships which are not under the regulation of EEDI at this moment. Since the inland ships are not covered by current EEDI formulation there is no scope to monitor the current status of inland ship's CO_2 emission rate and thus can be optimized to reduce CO_2 emission. This optimization will reduce CO_2 and increase energy efficiency which will in turn save lot of fuel for the country. In many cases, these inland and coastal vessel designs are not optimized and energy efficient. On the other hand, since IMO or Bangladesh Inland Water Transport Authority (BIWTA) does not have any CO_2 reduction regulations for inland vessels current status is unknown. In this paper an effort was made to increase the energy efficiency level of Bangladeshi inland ships and a guideline to regulate/monitor/reduce CO_2 emission. Bangladeshi inland passenger vesselswere under consideration and their current status of EEDI was calculated to make a reference line of CO_2 emission. In the second stage, two ships (one small and one big) were selected and optimized in the light of EEDI and compared with the original one to understand how those vessels should be designed to make more energy efficient.It has been criticised [2] that EEDI regulation will force to make smaller vessels since the reference line allows higher EEDI value for small vessels. This criticism was also analyzed.

INTRODUCTION

Around 90% of global trade[3] is carried by water ways of the world due to the reason that it is the most economical and fuel efficient mode of cargo transportation. The total trade volume is increasing throughout the last century for the same reason. On the other hand, according to the 2nd Green House Gas study[4] by IMO in 1999, shipping industry in the world has emitted 1.046 million tonnes of CO_2 in 2007, which correspondsto 3.3% of the global emissions at that time. At the present trend, this percentage could go two or three times higher from the present by 2050. As a mandate to the Kyoto Protocol[5] in order to control CO_2 emission from shippingIMO has developed the first ever global CO_2 reduction index in the world, known as Energy Efficiency Design Index (EEDI). The regulations apply to all new sea going ships of 400 gross tonnages and above and entered into force on 1st January 2013. Adopted CO_2 emission control index EEDI has a target to reduce CO_2 emission from shipping by 30%[1]from phase zero (1 Jan 2013 – 31 Dec 2014) with in 1st January 2025. The purposes of IMO's EEDI are:

- To achieve a minimum energy efficiency level for new ships;
- To stimulate continued technical development of all the components influencing the fuel efficiency of a ship;
- To separate the technical and design based measures from the operational and commercial measures; and

- To enable a comparison of the energy efficiency of individual ships to similar ships of the same size which could have undertaken the same transport work (moved the same cargo).

Inland vessels are not covered by current EEDI regulations. So where do they stand in terms of energy efficiency and CO_2 emission? It has been consistently criticised about Bangladeshi inland ships that those are not stable enough, specially the passenger vessels. But are those vessels energy efficient and ready to meet the challenge of green shipping? The answer is, we do not know because we do not have any standard.

In this paper, 29 passenger vessels were investigated and with the calculated results, a regression based reference line (CO_2 emission control line) is proposed for further investigation by exact measurement. This line will be the phase zero for Bangladeshi inland vessel. After wards when this reference line values are validated with exact measurement, the CO_2 emission control standard for Bangladeshi inland passenger vessel will be established and thus emission from those vessels can be controlled.

Another aspect that has been considered in this paper is to examine two ships. Two existing passenger vessel with low efficiency has been analyzed and optimization in light of EEDI is considered. This examination will give us an opportunity how much it can be achieved to lower the EEDI (thus enhancing energy efficiency) by making some simple steps and the criteria that makes a ship efficient.

BRIEF DESCRIPTION OF EEDI

Basically EEDI is calculating the emissions of a vessel under design condition (installed power, trial speed etc.) divided with the transport work done under the same condition as per the equations below:

$$\mathrm{EEDI_{attained}} = \frac{\mathrm{CO_2 Emission}}{\text{Transport work}} \tag{1}$$

$$= \frac{\text{Power}*\text{Specific Fuel Consumption}*\mathrm{CO_2}\text{Conversion Factor}}{\text{Capacity}*\text{Speed}} \tag{2}$$

$$= \frac{\begin{array}{c}\text{Emission from Main Engine+Emission from Auxiliary Engine+Emission for running}\\ \text{shaft motor}-\text{Efficient Tech.Reduction}\end{array}}{\text{Capacity}*\text{Reference Speed}} \tag{3}$$

$$= \frac{\begin{array}{c}\text{Emission from Main Engine+Emission from Auxiliary Engine+Emission for running shaft motor}\\ -\text{Efficient Tech.Reduction}\end{array}}{\text{Capacity}*\text{Reference Speed}} \tag{4}$$

$$=\left[\left(\prod_{j=1}^{n} f_j\right) * \left(\sum_{i=1}^{nME} P_{ME(i)} * C_{FME(i)} * SFC_{ME(i)}\right) + \left(P_{AE} * C_{FAE} * SFC_{AE}\right) + \left(\left(\prod_{j=1}^{n} f_j * \sum_{i=1}^{nPTI} P_{PTI(i)} - \sum_{i=1}^{neff} * P_{AEeff(i)}\right) * C_{FAE} * SFC_{AE}\right) - \left(\sum_{i=1}^{neff} f_{eff(i)} * P_{eff(i)} * C_{FME} * SFC_{ME}\right)\right] * \frac{1}{f_i * f_c * \text{Capacity} * V_{ref} * f_w} \tag{5}$$

$$= \frac{kw * \frac{g_{fuel}}{kwh} * \frac{g_{CO2}}{g_{fuel}}}{\text{Tonne}*\text{knotical mile/h}} \tag{6}$$

$$= \frac{g_{CO2}}{\text{Tonne}*\text{knotical mile}} \tag{7}$$

The calculated EEDI for a ship will be called the attained EEDI. This attained EEDI must be less than the reference EEDI or reference line. This reference line becomes stringent at different phases.The Reference line values shall be calculated as follows:

Reference line value = $a \times b^{-c}$ (8)

Where a, b and c are the parameters given in Table 1 [6]. The reference line is based on the vessel database of Lloyd's Register Fair play [6]. Figure 1 gives a sample reference line for Container Vessels as per Lloyd's Register Fair play database. The present EEDI rules will be more stringent in different phases [6]

TABLE 1. Reference line parameter value of different types of vessel

Ship type defined in regulation	a	b	c
Bulk carrier	961.79	DWT	0.477
Gas tanker	1120	DWT	0.456
Tanker	1218.8	DWT	0.488
Container ship	174.22	DWT	0.201
General cargo ship	107.48	DWT	0.216
Refrigerated cargo carrier	227.01	DWT	0.244
Combination carrier	1219	DWT	0.488

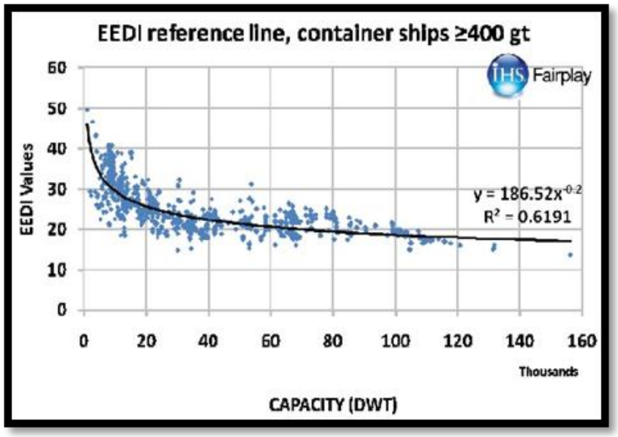

FIGURE 1. Reference line sample for Container vessel

EEDI OF INLAND PASSENGER VESSELS OF BANGLADESH

29 number of inland passenger vessels have been taken into consideration to calculate their current status of CO_2 emission per tonne.mile.Principle particulars, installed engine power, service speed, type of fuel data were considered to calculate EEDI. Figure 2 shows the scattered result of EEDI at different GRT. A regression line (Power curve) is drawn among the data points. As for equation 8, the value of a= 224.59 and c=0.174. For example, a vessel having GRT=500 will not be allowed to emit $224.59\text{X}500^{-0.174} = 76.1675$ $gmCO_2$/tonne.mile. So the vessel must be designed in such way that this would not emit 76.1675 $gmCO_2$/tonne.mile. It is possible to have more refine reference line when the number of ships under scrutiny is increased.

TABLE 2. Calculation of attained EEDI of Bangladeshi Inland Passenger Vessels

Vessel name	L WL (m)	B MLD (m)	L/B	T (m)	B/T	GRT	Speed (knot)	EEDI_att
M.L. Sharos	14.15	4.58	3.09	0.75	4.119	35.167	8	113.252
M.V. Tarika-7	41.46	7.89	5.255	1.45	3.624	240.27	11	82.2755
M.V. Eagle-2	30.8	7.8	3.949	2.2	1.795	254.68	12	104.071

M.V. Eagle-4	52.17	9.76	5.345	1.6	3.341	508.15	11	57.021
M.V. Eagle-3	67.47	10.98	6.145	1.7	3.615	807.67	11	56.8063
M.V. Bangali	74.3	12.5	5.944	1.8	3.302	1020.2	12	90.603
M.V. New Sabbir	52.2	10.37	5.034	1.8	2.797	610.99	11	71.494
M.V. Keya-1	31.45	6.71	4.687	1.2	3.906	172.62	9.5	92.4987
M.V. Anu	39.3	7.3	5.384	1.68	3.205	230.18	12	88.8741
M.V. Pubali-3	30	6.7	4.478	1.3	3.444	146.66	10	96.571
M.V. Pubali-1	45.95	9.15	5.022	1.4	3.587	302.53	11	81.8037
M.V. Swarnadip-4	31.09	6.7	**4.64**	**1.47**	3.157	150.8	11	109.115
M.V. Swarnadip-8	32.7	7	4.671	1.5	3.114	186.09	10	84.2921
M.V. Swarnadip-7	41.47	7.32	5.665	1.4	4.047	332.7	9	88.234
M.V. Prince of Russel-3	61.21	10.37	5.903	1.8	3.279	793.57	10	59.9445
M.V. Al Walid	45.4	7.31	6.211	1.33	4.67	265.05	10.5	79.1857
M.V. Shahrukh-1	58.37	10.37	5.629	1.6	3.518	533.84	12	66.2923
M.V. Reaz-2	29.3	6.9	4.246	1.4	3.033	153.09	8.8	71.1567
M.V. Kirtankhola-2	82.82	14.64	5.659	2	2.83	1485.6	13	96.3573
M.V. Farhan	40.05	9.15	4.377	1.92	2.28	328.82	11.5	72.8455
M.V. Othoy	41.46	7.89	5.255	1.45	3.624	240.27	11.5	87.7228
M.V. Manik-1	49.2	9.46	5.201	1.7	3.059	483	11	60.7343
M.V. Shahrukh	52.17	9.76	5.345	1.6	3.341	498.9	10.5	61.0476
M.V. Jaltaranga	30	6.7	4.478	1.35	3.317	151.54	10	97.6132
M.V. Jamal-3	38.51	7.4	5.204	**1.4**	3.717	217.92	11	103.568
M.V. Running Sun	34.15	6.77	5.044	1.35	3.737	248.79	9	111.984
M.V. Modern Sun	36.1	7.56	**4.775**	1.83	2.609	264.28	11	93.98
M.V. Jaltaranga-1	36.8	6.71	5.484	1.2	4.57	211.07	10	111.965

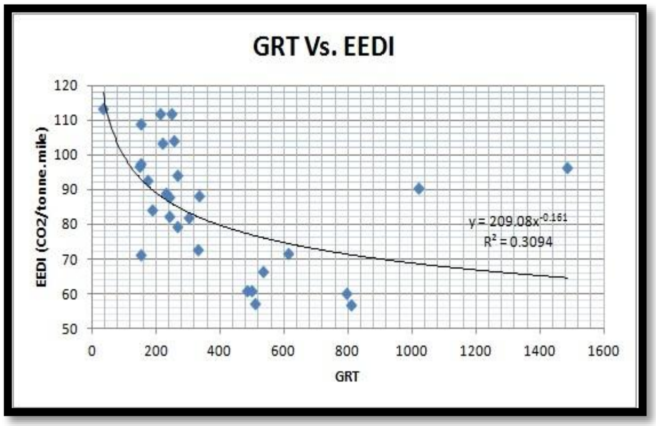

FIGURE. 2. Reference line for Bangladeshi Passenger vessel

RESULTS AND DISCUSSION

Consolidated results of all considered passenger vessels are shown in table 2. Ships with different dimension, capacity, speed and other hydrodynamic properties have different EEDI values. Analyzing table 2 and figure 2 efficiency criteria, that is, those characteristics that has made some vessels efficient and some vessels inefficient in terms of EEDI is understood for further investigation.

As described in section 3, a vessel when designed for a specific service speed condition and capacity, her maximum achievable EEDI is fixed. Since we have now a reference line, the new vessels EEDI cannot go beyond the boundary of the reference line and limited by a specific value of EEDI. So, when a vessel's EEDI goes beyond the boundary of the reference line, the design has to be modified and optimized to be more efficient so that she consume less fuel maintaining the same design speed and that is the target of IMO with EEDI. If we give a close look to the formulation the optimization with respect to EEDI will improve the propulsive efficiency, reduce hull resistance, increase the capacity of the vessel, reduce the power requirement by the vessel at certain speed and force the owner to have higher efficient and low fuel consumption engine and good quality of fuel. Another major intention of IMO is to implement innovative efficient technology (such as solar power or other renewable energy) which will reduce EEDI if we look at the equation.

At first look of the graph in figure 1 & 2 it could be misunderstood that small vessels are allowed to have higher EEDI allowing smaller vessels to emit higher CO_2 compared to a bigger vessel. This would falsely suggest that IMO is pushing the current design trend of ship to build smaller vessels whether we know that bigger vessels are more transport efficient than smaller one. So it does not make sense when we compare a small and large vessel in terms of EEDI from hydrodynamic point of view. Though the reference line allows having a higher EEDI for small vessels that does not mean that small vessel can attain low EEDI. In fact attained EEDI of smaller vessels is also high. In the next section where optimization of vessel with respect to EEDI is discussed, this issue would become clearer.

OPTIMIZATION OF INLAND VESSEL WITH RESPECT TO EEDI

In table 2, ships higher EEDI are colored in red and have some common characteristics compared to those other ships that have the same speed. Those characteristics are as follows:

- Higher EEDI ships have Higher Froude number (M.V. Swarnadip = 0.324, M.V. Jamal-3 = 0.29 and M.V. Modern Sun = 0.3) comparing with low EEDI ship (M.V. Eagle-3 = 0.22)
- Smaller vessels have high EEDI in general.
- Smaller vessel have low L/B ratio making those ship comparatively bulky.
- Higher EEDI vessels have low draft which do not allow large propeller.

From hydrodynamic point of view the above points are the most common issue to have larger engines and thus consume more fuel and emit more CO_2. Also we cannot forget the shallow water effect which .Now the question is

- Can these higher EEDI vessels (beyond the boundary of the reference line) be optimized to lower EEDI under the reference line?
- If possible, what are those criteria to optimize?

In order to have proper answer M.V. Swarndip is taken under consideration. The reference line value for this vessel is= 209.08 X GRT-0.169 = 209.08 X GRT-0.169 =209.08 X 150.8-0.169 = 89.64. Attained EEDI is = 109.115. In table 3, 1st row shows the original data of the said vessel. After optimization the attained EEDI must be lower than reference EEDI.1st attempt of optimization is carried out only by changing the principle particulars. The change in principle particulars and reduction in EEDI are as follows:

- Water line length increased by 1.9 meter.
- Beam is decreased by 0.7 meter increase L/B ratio from 4.64 to 5.5 and B/T ratio increased from 3.157 to 3.75.
- Reduction in EEDI is = 109.1155-102.03 = 7.0855

This means, simply by choosing appropriate principle particulars EEDI can be reduced by 6.5% (thus the fuel consumption and the energy efficiency of the ship). Table 3 also suggests that it is not possible to achieve the reference line by only choosing appropriate principle particulars for the said vessel. Speed must be reduced (thus the Froude number). 2nd attempt of the optimization is a carry over the 1st optimization but the speed is reduced to 10.4 knots which gives attained EEDI value 87.86 that is below the reference line value. This signifies that if the vessel does not go under any further improvement (increasing hull smoothness or having more favorable hull form or adoption of innovative technology) maximum achievable speed is 10.4 knots for the said vessel.

TABLE 3 Optimization ofBangladeshi small Inland Passenger Vessels, M.V. Swarnadip-4

Objective	**L WL (m)**	**B MLD (m)**	**L/B**	**C_B**	**T (m)**	**B/T**	**GRT**	**Speed (knot)**	**EEDI_att**	**EEDI_ref**
Parent data	31.09	6.70	4.64	0.54	1.47	3.16	150.8	11	109.12	89.64
1st attempt of optimization by only changing principle particulars for constant CB (without changing speed)	33.00	6.00	5.5	0.54	1.6	3.75	150.89	11	102.03	89.64
2nd attempt of optimization by only changing principle particulars for constant C_B (speed reduction considered)	33.00	6.00	5.5	0.54	1.6	3.75	150.89	10.4	87.86	89.64

Now let us consider another vessel which is one of the biggest passenger vessels plying within the riverine area of Bangladesh, M.V. Kirtankhola-2. All possible optimization at design stage is considered in order to lower attained EEDI and presented at table 4. Originally the vessel has EEDI was 96.36. It came down to 63.7 which mean 33.89% reduction is possible by changing the ship's original parameters within the reasonable range. How this happened? If we look table 4 closely, it can easily be understood that the new vessel was made slender by increasing water line length (Froude number reduced), decreasing breadth and block coefficient (making the vessel finer), increasing draft (allowing bigger propeller) and increasing GRT (increasing the denominator value of EEDI equation). It was possible to avail the original speed of 13 knots, which means new hull form will emit CO_2 and consume fuel 33.89% less than the original one.

TABLE 4. Optimization of Bangladeshi small Inland Passenger Vessels, M.V. Kirtankhola-2

Objective	L WL (m)	B MLD (m)	L/B	C_B	T (m)	B/T	GRT	Speed (knots)	EEDI_att	EEDI_ref
Parent data	82.82	14.64	5.66	0.7	2	7.32	1485.6	13	96.36	64.51
Optimization considering all parameters as variable	87.5	14	6.25	0.64	2.5	5.6	1605.4	13	63.7	63.7

CONCLUSION

Though EEDI is not an accurate emission indicator at present, it can be used as an emission control instrument at the design stage. In many cases, inland and coastal vessel designs are not optimized and energy efficient, especially in Bangladesh. On the other hand, due to draft restriction of the rivers of Bangladesh higher availing draft is very difficult. Shallow depth of the river causes shallow water effect on these ships increasing the required power even more. The installed power in M.V. Kirtankhola-2 is 3350 kW which is actually almost 100% higher than the required power at unrestricted water at the same speed. So design modification or optimization will also have to overcome this effect as much as possible. Development of the reference line for inland passenger vessel actually needs more verification. Measuring actual emission per tonne-mile for ship will give accurate result and establish the validity of the reference line produced.

REFERENCES

[1] IMO Resolution MEPC. 203 (62), Amendments to the annex of the protocol of 1997 to amend the international convention for the prevention of pollution from ships, 1973, as modified by the protocol of 1978 relating thereto (Inclusion of regulations on energy efficiency of ships in MARPOL annex VI), 2011.

[2] Jack Devanney, EEDI absurdities, Center for Tanker Ship Excellence, USA, 2011.

[3] IMO Knowledge Center, International Maritime Facts and Figures- Information Resources on Trade, Safety, Security, Environment, pp. 7, 2011.

[4] IMO, Second IMO GHG Study, 2009.

[5] United Nations, Kyoto Protocol to the United Nations Framework Convention on Climate Change (1998), 1-20.

[6] IMO, Consideration and Adoption of Amendments to Mandatory Instruments, MEPC 62/6/4, Agenda Item 6 (2011) 2-3.

[7]J. Holtrop, A Statistical Re-Analysis of Resistance and Propulsion Data, International Shipbuilding Progress, Vol. 31 (1984) 272-276.

International Conference on Mechanical Engineering 2015
(ICME 2015) 18 – 20 December, 2015, Dhaka, Bangladesh

Paper ID : 602

Electronic Chart Display and Information System (ECDIS): an Advanced Shipboard Operation and Safety System

Ram Krishna Saha[1], Md. Mashiur Rahaman[2,a)] and Laboni Afroz[2]

[1]*Bangladesh Forest Research Institute, Sholashahar,Chittagong-4211.*
[2]*Department of Naval Architecture and Marine Engineering, BUET, Dhaka-1000, Bangladesh.*

a) Corresponding author: mashiurrahaman@name.buet.ac.bd

Abstract. Electronic Chart Display and Information System (ECDIS) is used to maintain safety of navigation. It was identified that a major factor in the grounding of the CFL Performer on a sandbank off the UK east coast on 12 May 2008 is the poor training in use of the ECDIS. However, ECDIS will be of very little benefit in enhancing navigational safety if the watch- keeping officer is not fully trained and competent in its use. In addition, Human factor has been seen as the main source that contributes to accident in shipping. Therefore, New Technology and Training should go hands in hand that reduced marine accidents. For improving safety culture in shipping, it should be ensured that seafarer competency standards are kept up-to-date with ECDIS and other advanced bridge navigational equipment.

INTRODUCTION

The emergence and mounting popularity of sophisticated bridge equipment assure increased safety however, at the same time it places new demands on ship-owners and port authorities to provide appropriate training. Electronic Chart Display and Information Systems (ECDIS) is such kind of advanced tool, which intended to replace paper chart based navigation by providing increased benefits for safety and efficiency[1]. But this goose that is supposed to lay the golden egg of a safety culture is elusive for shipping if mariners are not well trained to use it properly. This paper first analyzes the grounding of CFL Performer then identifies the specific safety issues that are related to the accident, makes some recommendations for considering the upcoming revision of the Standards of Training, Certification and watch-keeping (STCW) convention for Seafarers from the maritime training and familiarity viewpoint before finally, the conclusion is drawn.

ANALYSIS OF THE GROUNDING OF CFL PERFORMER

Experience breeds wisdom. So, the purpose of the analysis is to help prevent similar accidents occurring in the future by determining the contributory causes and circumstances of the accident. According to the Marine Accident Investigation Branch (MAIB) on CFL Performer grounding at the North Sea on 12 May 2008, the vessels were taken on a planned route across Haisborough Sand, UK one of the vessels draught was considerably deeper than the charted depth of water. Also, the route was not adequately checked for navigational hazards either when planned or when being monitored and amended route was not cross-checked by the master[2]. In addition, the depth sounder was not switched on! [3]. On the other hand, MAIB found that neither chief officer nor second officer of the Dutch-flagged CFL Performer had been trained in the use of ECIDS even though it was the primary means of navigation onboard especially for paper chart-free ship. Moreover, none of the officers were aware of the significance of the safety contour, the safety depth, and the shallow deep contours, and did not know how to create a watch vector ahead of the vessel[5]. In addition, the master didnt inform the DPA or save the VDR data immediately. Figure 1 shows the Vessels original and revised planned routes

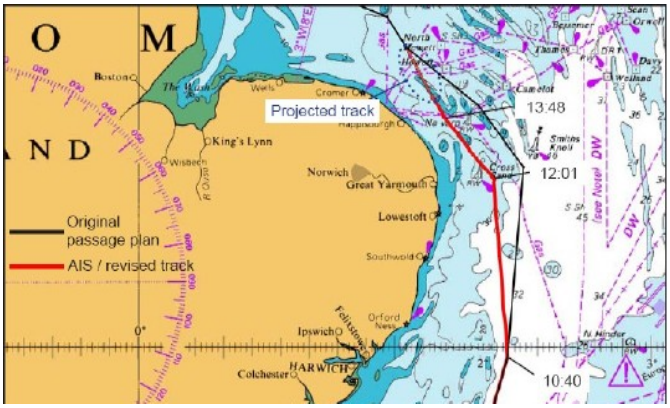

FIGURE 1: Vessels original and revised planned routes. Source: (Report on the investigation of the grounding of CFL Performer, 2008)

Safety Issues

The safety issues related to the accident based on the MAIB report on CFL grounding are: automatic route monitoring, reduction of human error, safety management and reduced workload.

Automatic Route Monitoring

ECDIS always helps a potentially invaluable asset to route planning by using user defined off track or channel limits. Here, the data displayer indicates to ships position, course and speed continuously[6]. When ship crossed the safety contour or selected danger then it showed red shaded area. However, regardless of the electronic aids available, there is a need for bridge watch-keepers to remain vigilant and continuously monitor a vessels position in relation to navigational hazards[7].

Reduction of Human Error

Human factor is seen as the main source that contributes to accident in shipping. During the automatic monitoring based on pre-established parameters including alarm, indications and other forms of warnings are set off by the watch officer. This system is used as a surveillance of the surrounding sea area, traffic situation and maneuvers.

Safety Management

Establishment of a safety management is paramount in the deliberations and actions of the international maritime community. In order to develop a safety management system, it must analyze previous accidents, hazardous incidents and other operational situations and make recommendations to protect the similar accident[2]. For improving the safety culture, the Officer in charge of a navigational watch on ships have to have sufficient knowledge of the characteristics of the various weather systems, reporting procedures and recording systems, which is part of ISM Code[8]. In addition, the masters responsibilities should be to provide the link between the shipboard training officer and the company training officer ashore that fulfill the role of continuity if the shipboard training officer is relieved during the voyage. At the same time, it should be ensured that all concerned are effectively carrying out the on- board training Programme[8]. Besides, performance checks and tests to navigation systems comply with manufacturers recommendations and good navigational practice is necessary[9].

Reduced Workload

The electronic chart contributes to improving the efficiency of shipboard operations and for compliance with required safety procedures. A study of U.S. Coast guard found that electronic chart systems reduced the navigation workload that allowed the mariner to concentrate more on collision avoidance and overall situational awareness[10]. On the base of above discussion, the proper use of ECDIS could lead to navigational efficiency and also contribute to enhanced safety. For that reason, IMO is phasing in the mandatory carriage of ECDIS over six years from July 2012, depending on ship type and age[11]. Therefore, the key recommendations for the upcoming revision of the Standard Technical Certification for Watch keeping (STCW) convention are:

- To ensure that seafarer competency standards are kept up-to-date with ECDIS and other advanced bridge navigational equipment training.
- To confirm that ENC will be available world wide by means of IHO Initiatives as ENC coverage are the primary means of using ECDIS

TRAINING AND FAMILIARITY OF ECDIS

ECDIS is designed to assist the mariner in route planning and route monitoring, and by displaying additional navigation-related information that always help to navigate ship [3]. That is why the Canadian ship owners mentioned that Safe navigation is good for business and when safe navigation is required ECDIS delivers. As stated by SGCG, bridge watch keepers need to be aware of the limitations of the equipment and the likely dangers, if there are any failures, such as loss of position input from GPS, or datum errors [10]. So training is the solution, as a well-trained crew always brings confidence. According to the Det Norske Veritas technical report (Report No: 2008-0048, rev. 01) grounding frequencies may be reduced by at least 302008). Therefore, this is the demand of time that ECDIS carriage should not longer become mandatory due to its benefit on the point of safety and environment. Prof. Dr Peter Ehlers, president, Federal Maritime and Hydrographic agency, Germany state that the electronic chart only benefits navigation safety if it is used correctly [6]. Consequently, it is necessary to prepare a manual for practical operations and to practice by a real-time complex simulator. It should cover through route planning and both visual and automatic route monitoring in typical navigational situations and sea areas. Therefore, STCW approved standardized IMO Model Training Course on the operational Use of ECDIS and which should be both generic and type-specific [6]. Generic training in the use of ECDIS is already available through the IMO model course. However, it is 14 years since the course was developed, and a review of its content may be beneficial to take into account the experience gained in the use of the system over that period [2]. On the other hand, the type-specific training might be conducted by manufactures by following requirements of the IMO model course in a condensed version using a ship operation simulator. So, through the comprehensive revision of the STCW Convention and the STCW Code, it should be ensured that seafarer competency standards are kept up-to-date with ECDIS and other advanced bridge navigational equipment [11].

ELECTRONIC NAVIGATION CHART COVERAGE

On the other hand, ENC coverage is the primary means of using ECDIS. At present, 85[7]. Therefore, it should be available in world wide before ECDIS mandatory. One good news is that a strategy has taken to enhance ENC data production in the region and acceleration of the carriage of several ships type with ECDIS through the HELCOM Declaration (2001) [6]. However, maximum benefit will depends in large part on how soon national Hydrographic Offices are able to provide sufficient ENC coverage and associated updating services required for use with ECDIS [6].

CONCLUSION

This paper is by no means comprehensive. The issues are much more complex and involved than what is presented here. The message however is clear. Information at sea is power, and the most powerful way to present navigation information is ECDIS. In contrast, ECDIS will be of very little benefit in enhancing navigational safety if the watch-keeping officer is not fully trained and competent in its use. For Example, MAIB has identified that a major factor in the grounding of the CFL Performer on a sandbank off the UK east coast on 12 May 2008 due to poor training in use of the ECDIS. Hence, an efficient navigational tool is needed to enhance the conduct of safe navigation, and it is possible when infrastructure such as the GPS and the use of official ENC data are significant complementary factors (Chua). Consequently, the proposed inclusion of specific ECDIS competences within the STCW Code is a very positive step, which merits strong and early support by IMO.

REFERENCES

[1] Weintrit A.The Electronic Chart Systems and their Classification,2001 RetrievedMarch16, 2009.

[2] Report on the investigation of the grounding of CFL Performer,Investigation No. 21/2008, Southampton, UK: Marine Accident Investigation Branch.

[3] Moon D. S. H., Advanced Shipboard Operation (ECDIS). Unpublished manuscript, Malm, Sweden,2009.
[4] Concern over ECDIS Training Standards, Nautilus, UK Telegraph,2009.
[5] Tetly L.,Calcutt D., Electronic Navigation Systems (3rd ed.), Oxford: Planta Tree,2001.
[6] Hecht H., Berking B., Buttgenbach G., Jonas M. and Alexander L., The Electronic Chart: Fuctions, Ptential and Limitations of a New Marine Navigation System,Lemmer, The Netherlands: GITC bv, 2002.
[7] IMO charts electronic future Fairplay Solutions(144), 2008.
[8] IMO,STCW Convention STCW Code. London,2001.
[9] Hecht H., Berking B., Buttgenbach G., Jonas M. and Alexander L. The Electronic Chart: Functions, Potential and Limitations of a New Marine Navigation System, WMU Journal of Maritime Affairs,Pp. 322,2006-2007.
[10] Gale C. H.,From Paper charts to ECDIS Seaways,2009.
[11] Bivre A. D., Feature: There is more to adequate manning of ships than meets the eye, BIMCO, April 2, 2008.

International Conference on Mechanical Engineering 2015
(ICME 2015) 18 – 20 December, 2015, Dhaka, Bangladesh

Paper ID : 607

Indigenous Development of Auscultatory Method based Semi Automatic Blood Pressure Monitor

Noor Mohammed[1,b)], Mohammad Zakir Hossain[2,c)] and Sumon Saha[3,a)]

[1] *Department of Biomedical Physics and Technology, University of Dhaka, Dhaka 1000, Bangladesh*
[2] *Department of Mechanical and Materials Engineering, University of Western Ontario, London, Ontario, N6A 5B9, Canada*
[3] *Department of Mechanical Engineering, Bangladesh University of Engineering and Technology, Dhaka 1000, Bangladesh*

a) Corresponding author: sumonsaha@me.buet.ac.bd
b) nirupom007@gmail.com
c) mhossai8@alumni.uwo.ca

Abstract. A blood pressure monitor is used to measure the blood pressure of a human body. In this paper, a semi-automatic blood pressure monitor is designed which can automatically inflate and deflate an arm cuff and measure the blood pressure with the help of a pressure sensor and a digital stethoscope. The detection of systolic and diastolic pressure is not fully automatic. It requires manual operation to capture pressure reading while the Korotkoff sounds are heard on the stethoscope. Here the measuring algorithm is the modified electronic version of mechanical auscultatory method.

INTRODUCTION

As the world population goes on increasing, the assurance of health safety of each individual has become challenging day by day. Through the advancement of modern science and technology, the human race is blessed with various biotechnological boons. However, this fact remains questionable in third world country like Bangladesh. Here the highly advanced biomedical technologies are far reaching for the primitive class. Besides, the existing medical monitoring devices are not so reliable in all cases of health issues due to higher cost. The abnormality in regular blood pressure (BP) indicates a variety of potential threats to health safety. In other words, it shows the symptoms of various fatal diseases like heart disease, diabetes, hypertension, kidney failure, obesity and so on. Drastic abnormality in blood pressure may lead to permanent health damage. Hence, like other regular medical parameters, measurement of blood pressure holds its own importance. A portable low cost reliable automatic BP monitoring device for general people can largely mitigate this serious health issue. The aim of the present work is to design and fabricate a blood pressure measuring device with the available technology, which can in turn be a reliable and economic BP monitoring device for all classes of people.

BLOOD PRESSURE

The term ‘blood pressure’ refers the arterial blood pressure exerted by the circulating blood upon the walls of blood vessels. In human body, blood pressure is pulsatile in nature. During each heartbeat, blood pressure varies between maximum (systolic) and minimum(diastolic) value [1].

Blood pressure is usually measured at one’s upper arm where brachial artery exists [2]. It is one of the major arteries in human body. The pumping action of heart enables cardio vascular circulation, which consists of pulmonary circulation and systemic circulation. During pulmonary circulation, blood flows from right ventricle to lungs. In lungs, the deoxygenated blood is oxygenated and flows toward left atrium and then left ventricle. After filling the left ventricular, the systemic circulation starts. The systemic circulation enables blood to flow through the various systems of the body to conduct various physiological works. After passing through aorta, arteries, arterioles and capillaries, blood returns to the right atrium of the heart via veins, venules and venacavas. Since blood flows from left ventricle to the rest of the body, the blood pressure at left ventricle is three times higher than the right ventricle. As a result, the blood pressure at the arteries is higher than the veins and hence, measurement is normally carried out at the brachial artery [3].

HEALTH ISSUES OF BLOOD PRESSURE

Determination of blood pressure is one of the most important measurements in clinical practice but still the most inappropriately performed measurement in the history of biomedical advancement. Among various cardio vascular diseases, hypertension is a major risk for the health safety of human life. Recent statistics of WHO (World Health Organization) reveals that about one third of the people of global population are under the potential threat of hypertension. So the importance of accurately measuring blood pressure cannot be neglected. From the data of various numerical observations, Pickering *et al.* [4] proposed the following classification of arterial blood pressure in human body as listed in Table 1.

TABLE 1. Classification of blood pressure in adult.

Classification	**BP (mmHg)**	
	Systolic	Diastolic
Normal	≤ 120	≤ 80
Pre-hypertension	120 – 139	80 – 89
Stage 1 hypertension	140 – 159	90 – 99
Stage 1 hypertension	≥ 160	≥ 100

BLOOD PRESSURE MEASUREMENT METHODS

For human body, various types of methods are available to measure arterial blood pressure. However we can classify these methods into two main categories as follows:

Invasive method

This method utilizes some medical instruments (e.g. needle, cannula) to penetrate the artery in order to measure the blood pressure using some pressure sensors. This method is normally used in critical stage under the supervision of experienced medical expert.

Non-invasive method

Non-invasive methods are simply the non-destructive methods, which are performed in external periphery of the human body. These methods do not need any insertion of needle or catheter in the artery during blood pressure measurement. The following methods are the most popular non-invasive techniques to measure arterial blood pressure.

Auscultatory method

The auscultatory method involves the use of inflatable arm cuff with a stethoscope to listen the Korotkoff sound [4] (a special tapping sound having five phases but not the sounds of heartbeat) during the blood pressure measurement. The cuff is placed around the upper arm (roughly the same vertical height as the heart position) and stethoscope chest piece is placed on the skin where brachial artery is positioned. The cuff is linked to a manual hand pump and either an aneroid manometer or a mercury manometer.

Initially the cuff is inflated to some high pressure to obstruct the blood flow in the brachial artery completely [1, 3, 4]. Then the cuff is deflated slowly with a constant pressure reduction rate. During deflation state, the blood starts to flow turbulently at some point. This sudden rush of turbulent blood flow creates vibration in the wall of the artery. As a result, a special tapping sound is heard on the stethoscope which is known as Korotkoff sound. The pressure in the cuff corresponded to this starting phase of Korotkoff sound is systolic pressure. The sound continues to some periods and finally becomes dimmed completely. At this ending phase of Korotkoff sound, we get the reading of diastolic pressure. Although the ending phase of Korotkoff sound is heard to detect via ordinary stethoscope, it is convenient to reduce 5 mm Hg from the value of last pressure reading [4]. After the ending phase of Korotkoff sound, the blood flow in the brachial artery becomes laminar.

Oscillometric method

The oscillometric method uses the oscillation of blood pressure at the deflating cuff from inflation state to detect the mean arterial pressure (MAP) in order to calculate the systolic and diastolic blood pressure from some empirical correlations. There are several ways to calculate MAP, which is the average of the arterial blood pressure. During each cardiac cycle, diastole usually lasts longer than systole. Therefore, the MAP is not simply the average value of systolic and diastolic pressure. At normal heart rates, systole usually requires one-third whereas diastole requires two-third of the cardiac cycle time, which can be expressed as follows:

$$P_m = \frac{P_s + 2P_d}{3}, \tag{1}$$

where, P_m is the mean arterial pressure, P_s is the systolic pressure and P_d is the diastolic pressure. However, this idealistic assumption is not true for the tachycardic (faster heart rate) patient. Because the percentage of time the heart spends in systole, increases as the heart rate increases. Therefore, most of the blood pressure monitors that involves non-invasive technique to measure blood pressure, calculate the MAP using actual blood pressure waveform for more accuracy [5].

At present, most of the automatic and manual BP measuring devices widely follow non-invasive techniques. Modern digital machines for BP measurement adopt oscillometric method which is not accurate in all cases. However, based on the auscultatory method of BP measurement, the manual machines are comparatively reliable. By considering the reliability factor and its accuracy, we have chosen the electronic auscultatory method.

HARDWARE DESCRIPTION

Basic power supply circuit

Figure 1 shows the circuit diagram used to supply 5V dc voltage into various parts of the central processing unit of the proposed BP measuring machine. The input source of this circuit is a 9V dc battery which is reduced to 5V by using a linear voltage regulator ‘L7805’ IC. This IC can givemaximum 1A current according to the requirement of the system load. Anelectrolytic capacitor with the capacity of 100F is used as a decoupling disc to ensure stable output voltage. This power supply circuit also provides 5V dc voltage to the digital stethoscope circuit. We have further used an external 6V dc supply consists of four AAA size 1.5V batteries in order to run the air pump.

Central processing unit

The central processing unit of the BP machine mainly consists of a microcontroller (MCU), a piezoresistive monolithic air sensor, a LCD (liquid crystal display) and a NPN silicon power transistor. The complete circuit diagram of the central processing unit is presented in Fig. 2. The heart of the processing unit is the microcontroller, which is an 8 bit ‘atmega8l’ type with operating voltage from 2.7 to 5.5V. It has 8kB ISP flash memory, six channels 10 bit ADC (for dual inline package) and 23 programmable input/output lines. The part number of the air pressure sensor is MPXV5050GP, which is ideally suitable for microcontroller-based system. The maximum range of operating pressure for the sensor is 50 kPa with 5V dc supply voltage. For displaying the measured blood pressure reading, a 16 characters and 2 lines ‘LM016L’ type LCD is connected with the microcontroller. It has built-in LSI HD44780 Hitachi controller and is operated by 5V dc supply. Moreover, the processing circuit consists of some basic passive elements such as watt resistors, capacitors (ceramics and electrolytes), 16 MHz crystal oscillator, three push buttons (reset button, pump start button, capture reading button), a diode to protect the MCU from the back emf of inductive load (dc motor of the micro air pump) and some connectors.

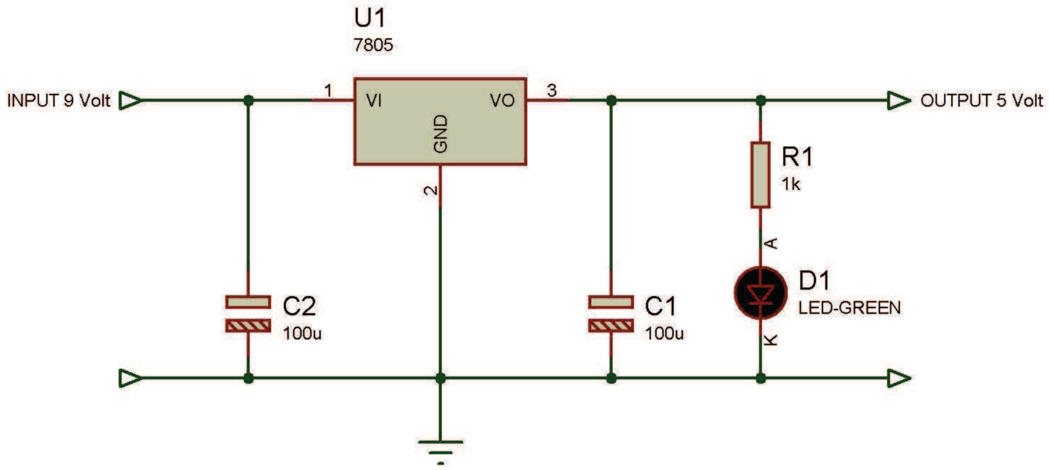

FIGURE 1. Circuit diagram of a basic 5V dc power supply.

Digital stethoscope circuit

The digital stethoscope hardware consists of a condenser microphone which senses the Korotkoff sound, a chest piece and a short medical grade tube of 6 cm length and 5 mm diameter [6]. The microphone is placed inside the tube at one end and the chest piece is connected on the other end of the tube. The stethoscope signal conditioning circuit(see Fig. 3) consists of an inverting preamplifier having a gain of 20, a second order Sallen-Key low pass filter with unity gain and a cut of frequency of 600 Hz [7, 8, 9], and a power audio amplifier (LM386) with a gain of 200 to drive the speaker of the earphone. The preamplifier and the filter are built using LM358N dual op-amp IC. To power the op-amps, 5V single supply with 2.5V biasing voltage is used [10, 11]. The other mechanical hardwares are a standard size adult arm cuff, some medical graded plastic tubes and a small mechanical gate valve coupled with the air pump by a small tee.

SOFTWARE DESCRIPTION

The code for the microcontroller is written using Arduino IDE. The compatible Arduino hardware for the atmega8l microcontroller is Arduino NG or older w/Atmega8 .The Arduino code is then loaded to the ‘atemaga8l’ microcontrollers ISP flash memory using serial communication. In order to write program in the microcontroller, a modified RS232 usb to serial converter with a TTL level converter (MAX232 IC) is used. The pressure sensor calibration software is developed using Processing IDE for 32-bit Windows XP operating system.

OPERATIONAL STEPS FOR BP MEASUREMENT

A schematic flow chart of the operational procedures of the proposed BP measurement machine included in the appendices (see Fig. 4). However, we briefly explain the operational steps as follows:

1. At first the power button will be pressed to switch on the whole circuit, which will be connected to the power supply system.
2. After powering on, the pump start button (which is connected to MCU) will be pressed to start the air pump by sending an electrical pulse to the air pump driver circuit.
3. When the air pump is in operation, the MCU will start to monitor the pressure from the pressure sensor and to check whether the pressure is higher than the fixed threshold value (i.e., 162 mm Hg) and will simultaneously show the real time pressure value on the LCD.
4. After increasing the pressure in the cuff up to the threshold value, the MCU will automatically stop the air pump.

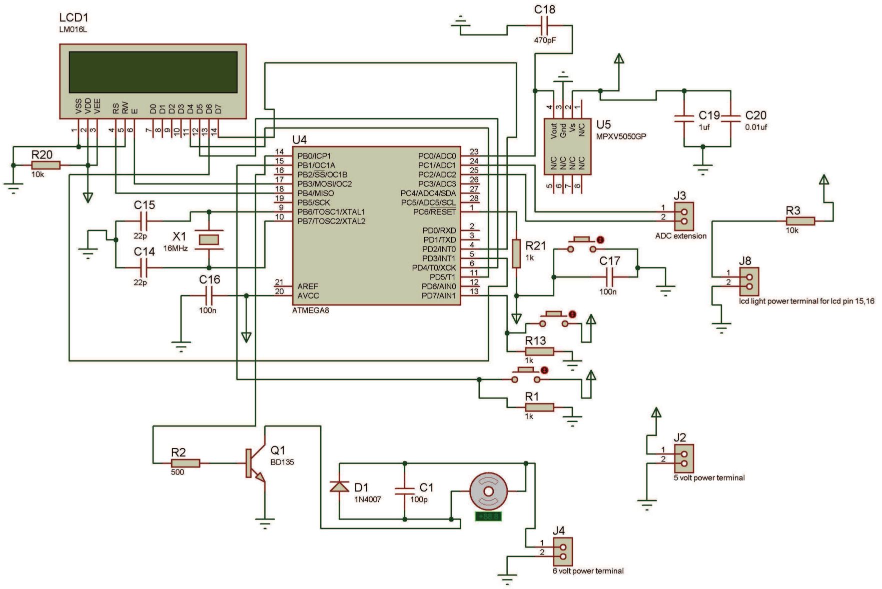

FIGURE 2. Circuit diagram of central processing unit along with air pump (excluding the digital stethoscope and power supply circuit).

5. Now the pressure in the cuff will be decreased continuously at a constant rate (5 mm Hg per sec). The gate valve will regulate the flow rate. It is to mention that the gate valve must be tuned initially at maximum cuff pressure to choose the desired flow rate. Since the flow rate of the pump is much higher than the pressure reduction rate through the valve, the semi-opened gate valve does not create any problem for the pump to reach the desired maximum pressure in the cuff.
6. At the same time, the observer will wear the earphone attached to the digital stethoscope and carefully hear the Korotkoff sound. (The earphone should be worn at the very beginning of the measurement.)
7. When the Korotkoff sound will be heard first, the observer will press the pressure reading capture button and when the sound will be heard no more the observer will press the same button again.
8. During the above operation, the MCU will record the instantaneous pressure value from the pressure sensor. In fact, it will record two different pressure values corresponding to the beginning and the ending of the Korotkoff sound, which indicate the systolic and the diastolic pressures respectively.
9. Finally, when the cuff is automatically deflated below the desired minimum pressure (i.e., less than 30 mm Hg), the MCU will display the systolic and the diastolic pressure in the LCD screen.
10. In order to measure the blood pressure for another set of reading, the pressure reading capture button should be pressed again and the procedures will start from step two.
11. Pressing master reset button will reset the central processing unit.

RESULT ANALYSIS FROM EXPERIMENTAL WAVE SIMULATION

We have taken some adult's blood pressure by our digital stethoscope. The output of the stethoscope (see Fig. 5) was recorded to a computer via mic in port [6]. Then the recorded sound was used as an input signal as shown in Fig. 6 to our final digital stethoscope circuit to study and simulate the amplified (gain 20) and the filtered output (see Fig. 7) and the corresponding output voltage after the filtering stage. The result was to the expected limit. Because when the Korotkoff sound starts, we heard an audible clean sound with a blinking led. Moreover, when the sound starts, the output voltage from filtered circuit fluctuates around to 2.3 to 3.9V with reference to 2.5V. That means, when the sound is not heard, the output voltage is constant to 2.5V.

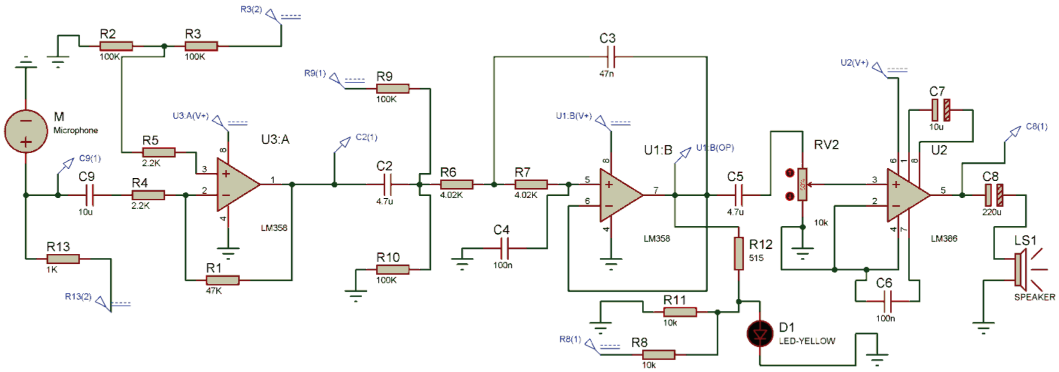

FIGURE 3. Circuit diagram of a digital stethoscope.

PRESSURE SENSOR CALIBRATION

The pressure sensor used in this project is calibrated to quantify the voltage output from the input pressure as shown in Fig. 8. The calibration results are presented below:

- Source offset voltage, $E_{off} = 0.25$V,
- Sensitivity, $S = 89.44$ mV/kPa,
- Best-fitted correlation, $E = 0.012P + 0.196$,
- Percentage of error in pressure reading from empirical relation is 0.22%.

BLOOD PRESSURE READING

The device has been used on seven subjects to study the performance and reliability of it. The results are then compared with the readings of traditional aneroid sphygmomanometer. Table 2 shows the summary of the results. From the above results, we can see that the variation of systolic pressure reading is higher than that of diastolic pressure reading. Thus, the device shows relatively higher error while detecting the systolic pressure.

TABLE 2. Blood pressure readings of the subjects.

Subject No.	Age (years)	P_{sys} (mmHg)	P_{dias} (mmHg)	P_{sys} (device) (mmHg)	P_{dias} (device) (mmHg)	P_{sys} error (%)	P_{dias} error (%)
1	25	125	90	120	92	4	2.2
2	30	130	80	124	78	4.6	2.5
3	24	120	85	112	88	6.7	3.5
4	35	143	92	132	95	7.7	3.3
5	32	135	82	125	80	7.4	2.4
6	25	127	78	122	80	3.9	2.6
7	23	120	80	115	82	4.2	2.5

RECOMMENDATIONS AND FUTURE SCOPES

Any kind of device related to the life science is very sensitive to background noise of the signal. Because most of the biosignals have very little amplitude and very poor signal to noise ratio. So most of the medical devices require amplifier with moderate to high gain according to the certain applications. As a result the background noises get amplified suppressing the original signal during the preamplification of the acquired signal. During the experiment, we failed to detect the starting phase and ending phase of the Korotkoff sound (K-sound has five different phases)

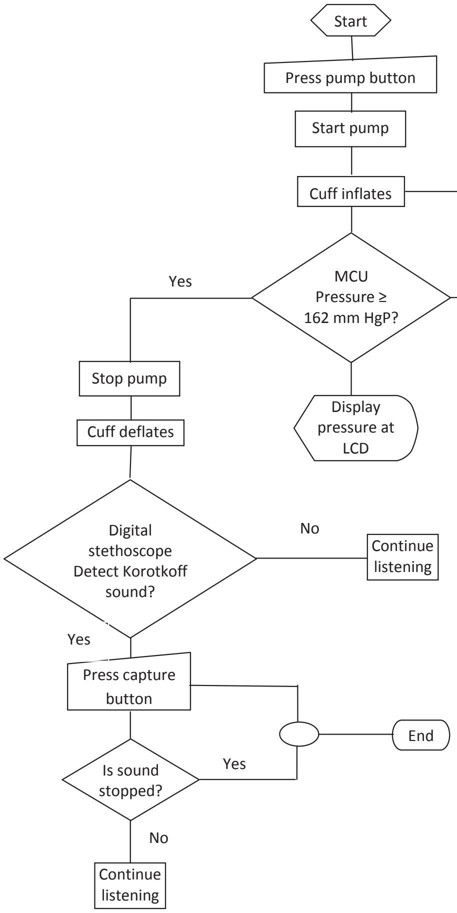

FIGURE 4. Flow chart of the operational procedures for BP measurement using electronic auscultatory method.

precisely which can be evident from the errors in the resulting pressure readings with respect to the readings of standard BP monitor. A more sensitive microphone like capacitive microphone can be used to minimize this problem. Besides the output of the microphone contains the interference from the 50 Hz main supply. So proper shielding of the device and signal paths are necessary for the improvement of signal to noise ratio.

Initially, we planned to develop a fully automated device using electronic auscultation. However, this method is later turned into semi-automatic because in real life we faced difficulty to process the output signal from the digital stethoscope in the microcontroller ADC. In order to investigate the reason we have used a hi-fi medical data acquisition device known as LabTutor. The result (see Fig. 9) from the LabTutor reveals that the korokoff sounds contain noise prior to the starting phase and after the ending phase. So inorder to suppress the noise we have to implement some higher order digital filter topology in the program firmware of the MCU. Again the the resolution of the adc also plays a vital role in the processing of the K-sound significantly. The consideration for filter topology is also equally applicable for the designing of analog signal conditioning circuit of the digital stethoscope. The cumulative effect of both analog and digital filters can play a vital role for the faithful production of the signals only.

CONCLUSION

In this research, a digital semi-automatic device is developed to monitor the human blood pressure. Though there are some hybrid BP monitors which involve digital pressure gauge to display only pressure readings but still require a manual hand pump to inflate the arm cuff during the measurement process. In comparison to these types of device, our machine involves automatic pumping action and digital stethoscope to have a clean audible Korotkoff sound. Final

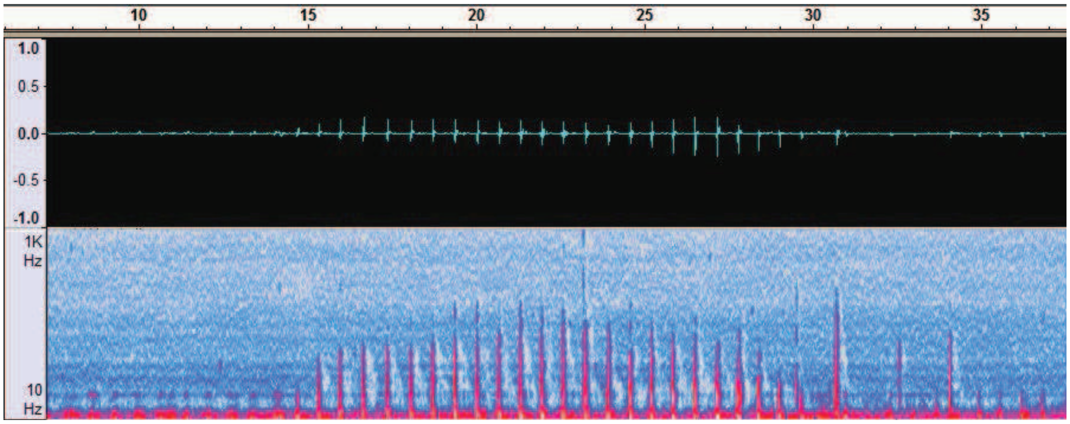

FIGURE 5. Korotkoff signal with frequency spectrum (amplitude and frequency versus time).

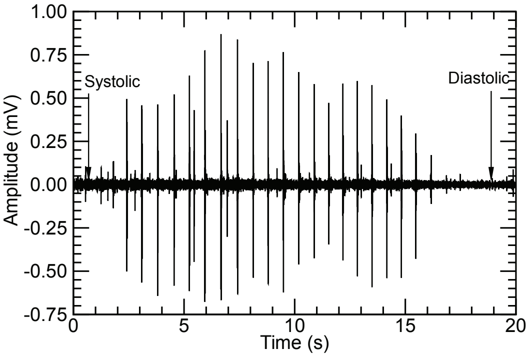

FIGURE 6. Input signal from the sound transducer.

goals of this project are to reduce the product cost, to manufacture a reliable device, to increase human comfort and to implement a new algorithm. Since using this semi-automatic device, any person can measure the blood pressure and thereby it can help to contribute significantly in healthy life style.

ACKNOWLEDGMENTS

The authors gratefully acknowledge the financial and technical supports of the department of Mechanical Engineering of Bangladesh University of Engineering and Technology, Bangladesh and the department of Biomedical Physics and Technology of University of Dhaka, Bangladesh.

REFERENCES

[1] C. G. Caro, *The Mechanics of the Circulation* (Cambridge University Press, 2012).
[2] W. Norman, *The Anatomy Lesson* (Georgetown University, Washington, 1999).
[3] L. Waite and J. M. Fine, *Applied Biofluid Mechanics* (McGraw-Hill, New York, 2007).
[4] T. G. Pickering, J. E. Hall, L. J. Appel, B. E. Falkner, J. Graves, M. N. Hill, D. W. Jones, T. Kurtz, S. G. Sheps, and E. J. Roccella, Hypertension **45**, 142–161 (2005).
[5] T. Ferns, G. Harris, T. McMahon, and K. Wright, Nursing Standard **25**, p. 40 (2010).
[6] A. Bhaskar, Advances in Physiology Education **36**, 360–362 (2012).
[7] V. Markandey, Digital stethoscope implementation on the TMS320C5515 DSP medical development kit (MDK), Application Report SPRAB38A (2010).

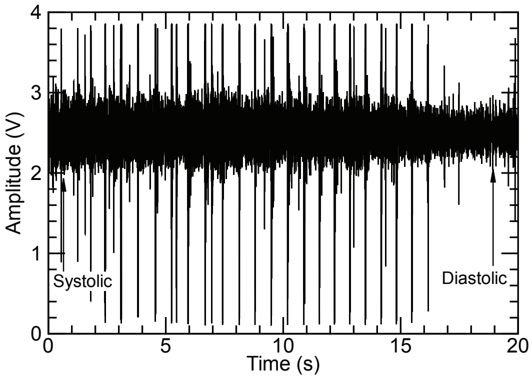

FIGURE 7. Filtered wave (cut-off frequency is 600Hz with unity gain and Sallen key LPF).

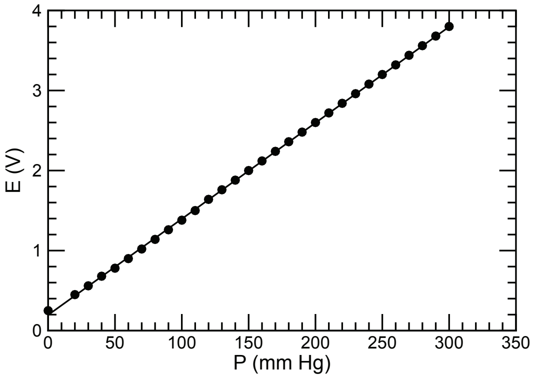

FIGURE 8. Calibration curve for the pressure sensor.

[8] J. DiCristina, Introduction to digital stethoscopes and electrical component selection criteria, TUTORIAL 4694 (2010).

[9] H. Uddin, S. M. Arif, M. Z. Hossain, and M. Z. Haq, "Design and fabrication of a computer interfaced stethoscope," in *9th Annual Paper Meet* (ME Division, IEB, Dhaka, Bangladesh, 2004).

[10] B. Carter, Filter design in thirty seconds, Application Report SLOA093 (2001).

[11] B. Carter, *Op Amps for Everyone* (Newnes, 2013).

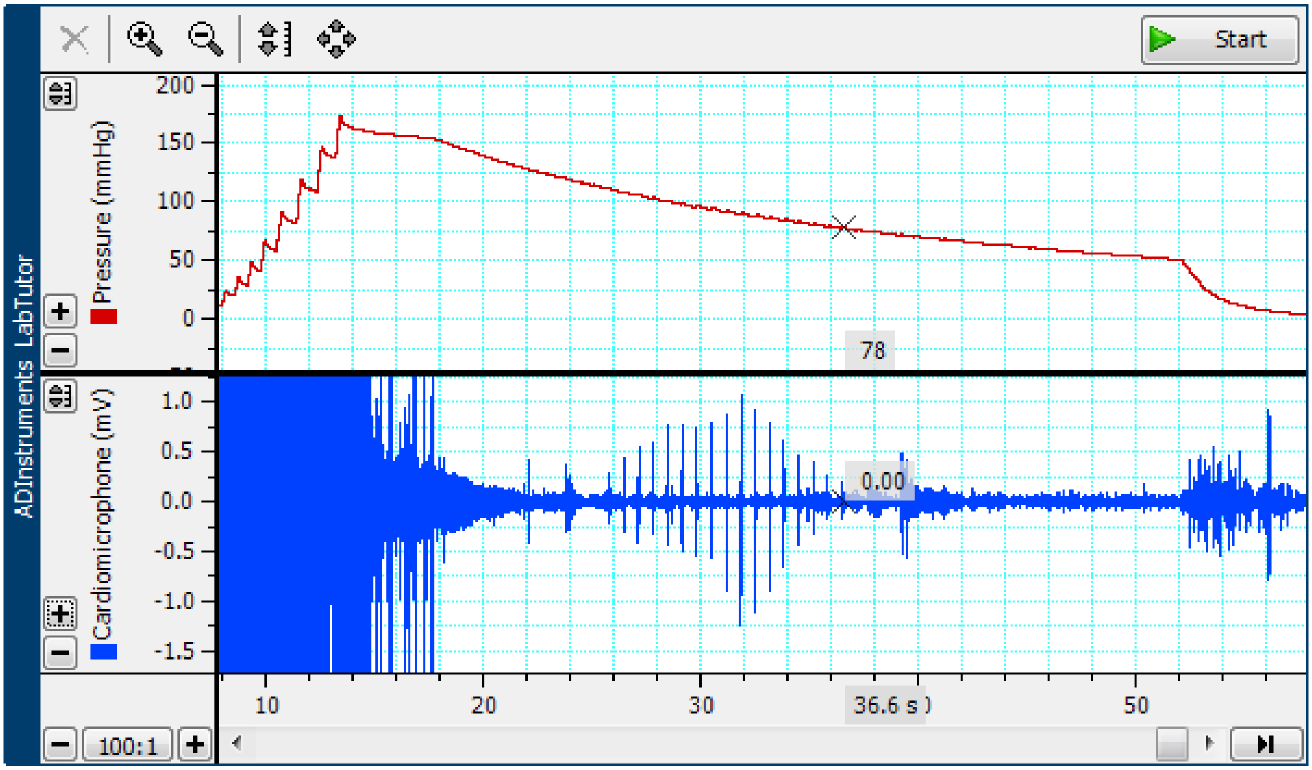

FIGURE 9. The pressure graph and the korotkoff sound (the regular pattern at the middle of the cardio microphone output) graph from the LabTutor (Here BP reading is 123/78 mm HgP).

International Conference on Mechanical Engineering 2015
(ICME 2015) 18 – 20 December, 2015, Dhaka, Bangladesh

Paper ID : 608

Tidal Power Potential of the Coastal Area of Bangladesh

Rubayat Islam[1,b)], Irfan Ahmed[1,c)], M. M. Razzaque[1,a)] and Md. Mahbubur Rahman[2]

[1]*Department of Mechanical Engineering, Bangladesh University of Engineering and Technology (BUET), Dhaka 1000, Bangladesh.*
[2]*Department of Mechanical Engineering, Military Institute of Science &Technology (MIST), Mirpur Cantonment, Dhaka-1216, Bangladesh.*

a)Corresponding author: mmrazzaque@me.buet.ac.bd
b)rubayat12@yahoo.com, c)irfanahmed.me@gmail.com

Abstract. In this paper an analysis of the tidal power potential at five different sites along the coastal area of Bangladesh is presented. The Swandip channel site located at the Meghna-Feni estuatry is found to have the maximum tidal power potential. The ongoing geological changes due to sedimentation seem gradually increasing the tidal power potential at this site.

INTRODUCTION

Bangladesh is a country of 1,47,570 sq. km area and 160 million people located in South Asia at 24° N latitude and 90° E longitude. It has a long coastline of 710 km with 2 to 8 m tidal range in the Bay of Bengal. The periodic variation of the height of sea water level corresponding to this tidal range can be used for power generation. Some recent studies [1, 2] suggest that the most of the coastal zone is covered with many embankments and sluice gates and has potential for harnessing tidal power by utilizing small scale tidal energy technology. Tidal power generation may solve the electricity crisis in the coastal zone and reduce load on the national power grid [3]. Tidal energy is one of the cleanest renewable energy sources. It has become one of the promising energy sources due to their continuous availability and predictable characteristics [4]. Recently, tidal energy resource assessment has been conducted in the coastal areas of Vancouver island [5], Malaysian islands [6], Nova Scotia [7] and Roosevelt island, New York [8]. However, the potential of tidal energy in the coastal areas of Bangladesh has not been fully studied yet. In this paper, the potential of tidal power at five locations along the coastline of the Bay of Bengal is presented. Detailed analysis is conducted only for the Sandwip island, which seems to be the most promising site for harnessing tidal energy.

TIDAL ENERGY

Tidal energy is generated by the interaction of the gravitational attraction among the Earth, Moon and Sun, and the rotation of the Earth-Moon and Earth-Sun systems. Under the action of these forces, ocean surface on the Earth deforms to a roughly egg-shape with two bulges. One ocean bulge is faced towards the Moon and the other is on the opposing side of the planet, facing away from the Moon. A similar interaction between the Earth and the Sun produces two other ocean bulges that line up towards and away from the Sun. Although the sun is 27 million times more massive than the Moon, the Moon is much closer to the Earth and for that reason has a greater gravitational pull on the Earth. In fact, the tide-generating force of the Moon on the Earth is more than twice of that of the Sun on the Earth. At a smaller scale, the magnitude of tides can be strongly influenced by the shape of the shoreline. Funnel-shaped bays in particular can dramatically alter tidal magnitude. Local wind and weather patterns also can affect tides. Strong offshore winds can move water away from coastlines, exaggerating low tide exposures [7, 8].

There are three basic tidal patterns. In general, most areas have two high tides and two low tides each day. When the two highs and the two lows are about the same height, the pattern is called a semi-daily or semidiurnal tide. If the high and low tides differ in height, the pattern is called a mixed semidiurnal tide. Some areas have only one high and one low tide each day. This is called a diurnal tide [9]. Due to the geographical location, the coastal area of Bangladesh experiences semi-daily or semidiurnal tide pattern.

SITE LOCATIONS AND DATA COLLECTION

Figure 1 shows a satellite view of the Bangladesh part of the coastline of the Bay of Bengal. There are many funnel shaped estuaries along the entire coastline which may be considered prospective sites for tidal power extraction. The Department of Hydrography of Bangladesh Inland Water Transport Authority (BIWTA) maintains 53 water level recording stations along the inland and coastal waterways of Bangladesh for monitoring water level round the year. The water level data acquired from these stations as well as from the commercial simulation models are processed and used for the production and publication of yearly tide tables and hydrographic charts. Among the funnel shaped estuaries along the coastline, five sites have been chosen in this work for studying the tidal power potential. The sites already have water level recording stations and the water level data for calculating the tidal power potential are collected from these tide tables [10] published by the BIWTA. The chosen sites are as follows.

Hiron Point: Hiron point is located at 21°48'54"N 89°27'43"E in the estuary of the river Kunga inside the mangrove forest Sundarban in the south-east region of the country in Khulna division.

Khepupara: Khepupara is located at 21°46'38"N 90°6'12"E in between the rivers Payra and Galachipa in the southern district Patuakhali under Barisal division.

Sandwip channel: Sandwip is an island in located at 22°29′ N 91°26.5′ E in the Bay of Bengal at the estuary of the rivers Meghna and Feni and separated from the Chittagong coast by Swandip channel.

Karnaphuli river - Sadarghat: This site is near the main river port in the Karnaphuli river in Chittagong and is located at 22°22′N 91°48′E.

Shahpuri Island: Shahpuri Island is located at 20° 46' N 92°19E in the estuary of the river Naf at the southeast end of Bangladesh.

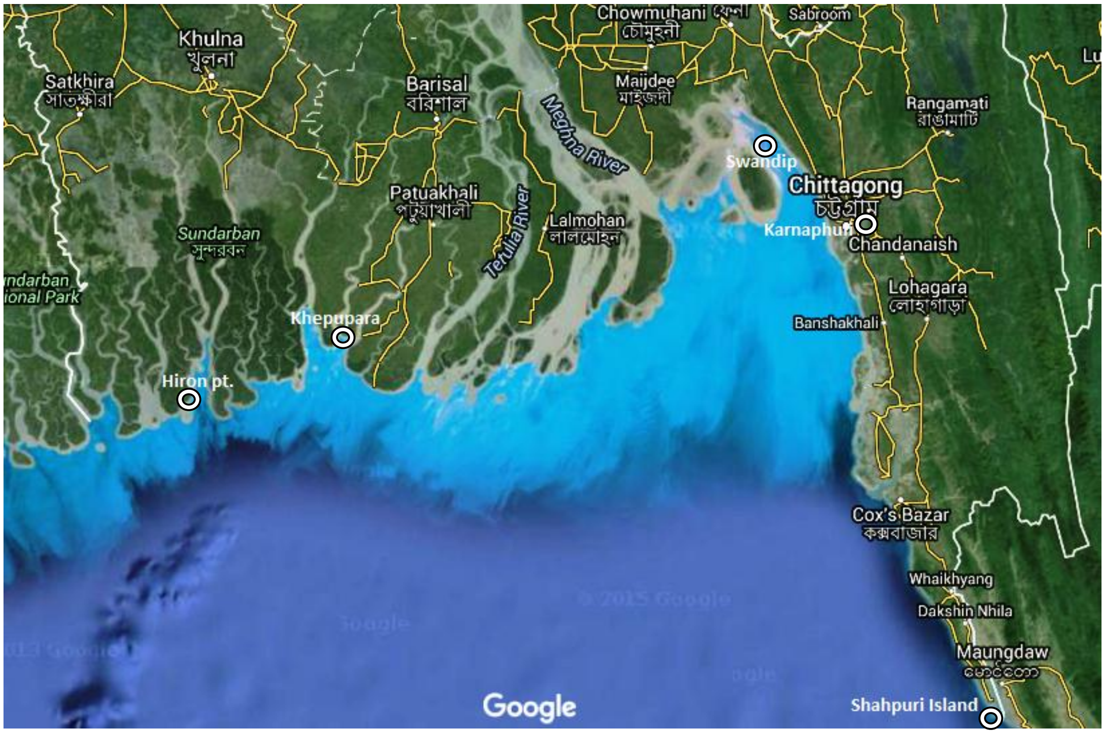

FIGURE 1. Bangladesh part of the coastline of the Bay of Bengal. The study sites are marked with ◎ sign.

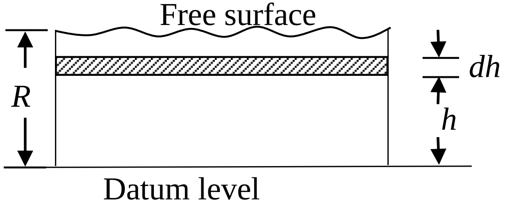

FIGURE 2. Calculation of the tidal energy potential.

CALCULATION

Consider a basin area A where the tidal range is R. The tidal range is the range of variation of water level during the high and low tides. If a volume element of height dh is chosen which spreads over the entire basin, then the mass of water contained in the volume is ρAdh. Thus the potential energy of the volume element becomes,

$$dE = \rho Adhgh = \gamma Ahdh \tag{1}$$

If h varies from 0 to R due to tidal effect, then the tidal potential energy becomes,

$$E = \int_0^R \gamma Ahdh = \gamma A \int_0^R hdh \tag{2}$$

So, the maximum value of the potential energy [9] would be,

$$E_{\max} = \frac{1}{2}\gamma AR^2 \tag{3}$$

In the coastal areas of Bangladesh, there are two high tides and two low tides every day. Therefore the maximum energy potential per day = $2E_{\max} = \gamma AR^2$ and the maximum power potential = $\gamma AR^2/t$, where, t = one lunar day.

Taking basin area A = 1 sq. Km, average daily tidal range R = 4.21 m and specific weight of sea water γ = 10055.25 N/m^3 and 1 lunar day = 24 hr 48 min. = 89280 sec, the energy potential per day is estimated to be 178.22 GJ/sq. km and the maximum power potential is estimated to be 2 MW/sq. km.

RESULTS AND DISCUSSION

The maximum power potentials are calculated using the tidal range data from tide tables [10]. The monthly averages of the maximum power potential of the five sites are presented in Table 1 for the year 2007.

TABLE 1. Monthly averaged maximum tidal power potential at the selected study sites during 2007

Month	Hiron-Point	Khepupara	Sandwip	Karnaphuli River_ Sadarghat	Shahpuri Island
January	0.271	0.385	1.867	0.903	0.487
February	0.328	0.403	1.978	1.040	0.530
March	0.379	0.458	2.327	1.120	0.567
April	0.385	0.504	2.190	1.150	0.533
May	0.356	0.540	1.967	0.980	0.483
June	0.295	0.482	1.853	0.860	0.442
July	0.314	0.505	1.847	0.883	0.474
August	0.368	0.559	2.077	1.083	0.556
September	0.422	0.594	2.207	1.167	0.584
October	0.365	0.577	2.043	1.067	0.549
November	0.302	0.509	1.773	0.920	0.490
December	0.267	0.407	1.683	0.797	0.475

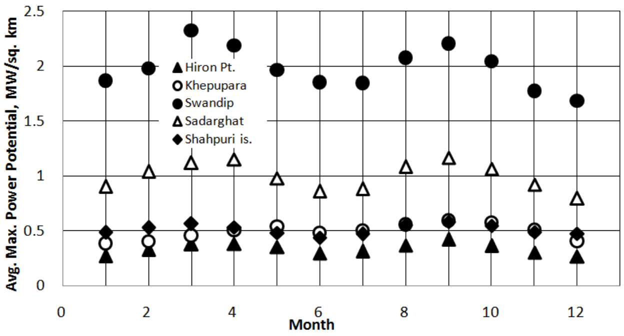

FIGURE 3. Averaged maximum tidal power potential during different months of year 2007 for all of the five sites.

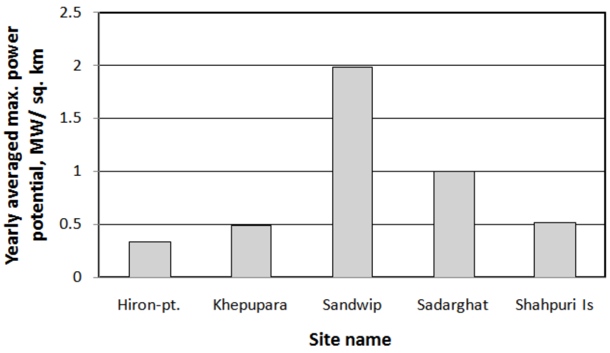

FIGURE 4. Yearly averaged maximum tidal power potential during 2007 at all of the five sites.

The plot of the monthly average maximum power potential vs. month in Fig. 3 shows that there are two peaks in the power potential occurring during the months of March and September. The distance between the Sun and the Earth changes every month and becomes the lowest twice in a year in the months of March and September. As a result the highest tidal power occurs in these months.

The maximum power potential averaged throughout the year in 2007 is plotted in Fig. 4 for all of the five sites. It is observed that among the five sites, the yearly averaged maximum power potential is the highest in the Sandwip site. Monthly averaged maximum power potentials for every other year between 2007 and 2015 have been calculated for Sandwip and listed in Table 2. It is seen that the time of the peak maximum power potentials slightly varies from year to year. The first peak occurs during March-April and the second peak occurs during August-September. The yearly averaged tidal power potentials at Sandwip site are plotted in Fig. 5 for different years. It is interesting that every year the tidal energy potential is gradually increasing at this site. This is possibly due to the geological changes like sedimentation occurring at the site every year.

TABLE 2. Monthly averaged maximum tidal power potential at Sandwip channel during 2007 - 2015

			Year		
Month	**2007**	**2009**	**2011**	**2013**	**2015**
January	1.867	1.837	1.783	2.058	1.989
February	1.978	2.050	2.197	2.212	2.300
March	2.327	2.400	2.251	2.492	2.361
April	2.190	2.218	2.282	2.509	2.457
May	1.967	1.987	2.065	2.356	2.208
June	1.854	1.877	1.884	2.201	2.078
July	1.847	1.875	2.048	2.154	2.120
August	2.077	2.081	2.428	2.234	2.479
September	2.207	2.230	2.363	2.312	2.648
October	2.044	2.082	2.264	2.230	2.495
November	1.774	1.822	1.983	2.090	2.137
December	1.684	1.678	1.890	2.006	1.940

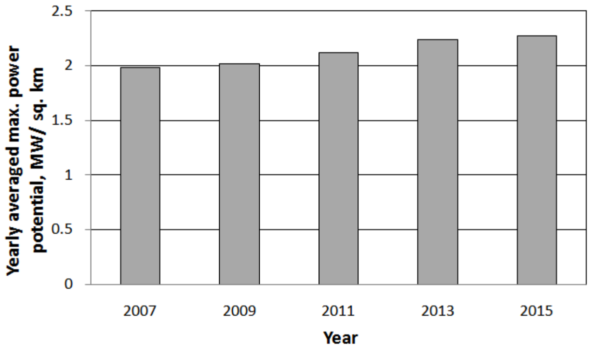

FIGURE 5. Yearly averaged maximum value of the tidal power potential at Sandwip channel site for the years 2007 - 2015.

CONCLUSIONS

Tidal power potential has been calculated at five different sites in the coastal area in Bangladesh. Among the sites, Sandwip channel has the highest potential for harnessing tidal power. The Sandwip channel area is dominated by tide throughout the year. Analysis of the yearly averaged maximum values of the tidal power potential shows a gradual increase every year possibly due to the geological changes at the site.

ACKNOWLEDGMENTS

Special thanks to BIWTA for providing the tide tables which were used in the calculation of tidal power potential.

REFERENCES

1. S. Ahmed, J. Civil Engineering, Inst. Engineers Bangadesh, **26**(1), 61-83, (1998).
2. M. Uddin, J. B. Alam, Z. H. Khan, G. M. J. Hasan and T. Rahman, Computational Water, Energy, and Environmental Engineering, **3**, 140-151, (2014), http://dx.doi.org/10.4236/cweee.2014.34015.
3. T. Ali, S. D. Gupta, I. Z. Arnab and S.M. Ferdous, Int. J. Renewable Energy Research, **2** (3), (2012).
4. S. M. R. Tousif and S. M. B. Taslim, Int. J. Scientific & Engineering Research, **2**(5), (2011).
5. G. Sutherland, M. Foreman and C. Garrett, Proc. IMechE, Part A: J. Power and Energy, Vol. 221, 147-157, (2007), http://dx.doi.org/10.1243/09576509JPE338.
6. Y. S. Lim and S. L. Koh, J. Renewable Energy, 35, 1024 - 1032, (2010), http://dx.doi.org/10.1016/j.renene.2009.10.016.
7. R. Karsten, "Tidal Energy Resource Assessment Map for Nova Scotia", report submitted to Offshore Energy Environmental Research (OEER) and Offshore Energy Technical Research (OETR), Nova Scotia, Canada (2012).
8. B. Gunawan, V. S. Neary and J. Colby, J. Renewable Energy, **71**, 509-517, (2014), http://dx.doi.org/10.1016/j.renene.2014.06.002.
9. A. M. Gorlov, Encyclopedia of Ocean Sciences, 2955–2960, (2001), http://dx.doi.org/10.1006/rwos.2001. 0032.
10. Bangladesh Tide Tables (2007 - 2015), Department of Hydrology, Bangladesh Inland Water Transport Authority (BIWTA).